Journal of Experimental and Theoretical Physics, Vol. 96, No. 1, 2003, pp. 1–7.
Translated from Zhurnal Éksperimental'noĭ i Teoreticheskoĭ Fiziki, Vol. 123, No. 1, 2003, pp. 5–12.

NUCLEI, PARTICLES, AND THEIR INTERACTION

Coherent Adiabatic Passage in Atomic Systems with a Closed Interaction Contour

S. V. Borisenok[a, *] and Yu. V. Rozhdestvenskiĭ[b, **]

[a]*Herzen State Pedagogical University, St. Petersburg, 191186 Russia*
[b]*Institute of Laser Physics, St. Petersburg, 199034 Russia*
**e-mail: sebori@mail.ru*
***e-mail: rozdyu@soi.spb.su*
Received April 24, 2002

Abstract—The effectiveness of coherent adiabatic passage in atomic systems with a closed interaction contour was studied. The dependence of coherent adiabatic passage on the algebraic sum of initial exciting field phases was demonstrated for the example of a double Λ-system of atomic levels. The conditions that should be met by interaction parameters for the occurrence of effective coherent adiabatic passage at various atomic contour phases were determined. © *2003 MAIK "Nauka/Interperiodica".*

1. INTRODUCTION

In the past decade, much attention has been given to coherent population transfer (coherent adiabatic passage) in atomic and molecular systems. The interest in this phenomenon stems from both the unique properties of adiabatic passage itself [1] and from the diversity of applications of this effect in atomic physics that these properties provide. For instance, coherent adiabatic passage is a promising method for laser cooling below the temperature determined by the recoil effect of atoms [2] and for creating high-effectiveness atomic wave packet splitters and developing atomic inteferometers based on these devices [3, 4]. In addition, such a passage in an atomic four-level system ("tripod" configuration) has made it possible to demonstrate the feasibility of atomic-wave lithography [5]. The use of coherent adiabatic passage in the specified applications is based on the high degree of population transfer between the limiting states of atomic systems, on the one hand, and the absence of population of intermediate states during the transfer (even in the case of the exact resonance between light fields and atomic transitions), on the other, if interaction parameters between an atom and an optical radiation field satisfy certain conditions.

In the simplest case of a three-level Λ-atom, the condition that should be met by interaction parameters (the so-called adiabaticity condition) is determined [6] by the region of overlap of laser pulses (Fig. 1). If laser pulses are bell-shaped, this region is determined by the ratio between the $\Omega_{1,2}(t)$ Rabi frequencies of $E_{1,2}(t)$ delayed laser pulses (with optical frequencies $\omega_{1,2}$ and pulse delay time δ),

$$1 \ll \Omega_0 \delta, \qquad (1)$$

where Ω_0 is the amplitude of laser fields. We assumed that the laser pulse frequencies coincided with the corresponding atomic transition frequencies and the sequence of pulses coincided with that shown in Fig. 1. If inequality (1) is satisfied, the effectiveness of coherent adiabatic passage reaches nearly 100%. As a result, the whole population can be transferred from level $|1\rangle$ to level $|2\rangle$ during laser pulse action without populating excited state $|3\rangle$ (Fig. 1).

Note that the absence of excited state population during the interaction process and effective population transfer are not characteristic features of coherent passage only. For instance, population transfer between the $|1\rangle$ and $|2\rangle$ states induced by a $\pi/2$ pulse at light field detunings much larger than the Rabi frequencies has similar properties. This allows high-rate selection of atoms to be performed in the field of two counterpropagating waves [7]. In contrast to population transfer by a $\pi/2$ pulse, coherent adiabatic passage, however, allows population to be effectively transferred also at zero frequency detunings, and the effectiveness of this transfer is almost insensitive to the shape of laser pulses [8] [only meeting (1) is required].

Naturally, such remarkable properties of coherent adiabatic passage stimulate studies of an increasingly large number of atomic systems in which such a passage can occur. Recently, coherent adiabatic passage with an interaction cycle closed by the optical field (a double Λ-system, see Fig. 1) was considered in the context of obtaining entangled quantum system states, which play an important role in quantum teleportation [9]. It is known [10, 11] that the special feature of all systems with closed interaction cycles is the dependence of the time evolution of population on some value Φ, called the atomic contour phase (in the simplest case, this

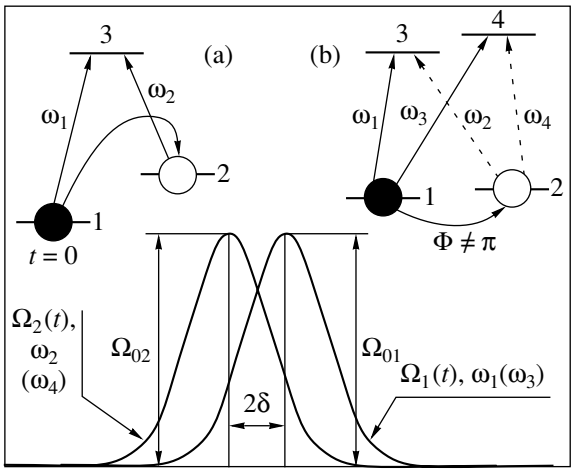

Fig. 1. Coherent adiabatic passage in (a) three-level and (b) double Λ systems. Shown in the bottom part of the figure is the sequence of light pulses necessary for effecting coherent adiabatic passage in these systems (so-called "counterintuitive pulse sequence"). For instance, in the three-level system, state $|1\rangle$ is initially populated and the sequence of light pulses is as follows: first, a laser pulse with frequency ω_2, which is in resonance with the $|2\rangle$–$|3\rangle$ transition, acts on the three-level system. The action of the second optical pulse with frequency ω_1, which is in resonance with the $|1\rangle$–$|3\rangle$ transition, is shifted by delay time 2δ. In the double Λ-system, state $|1\rangle$ is also initially populated, but the first pulse consists of two frequencies ω_2 and ω_4, which have the same envelope and are in resonance with the $|2\rangle$–$|3\rangle$ and $|2\rangle$–$|4\rangle$ transitions of the double Λ-system. The second optical pulse is shifted in time by 2δ and contains frequencies ω_1 and ω_3 close to the $|1\rangle$–$|3\rangle$ and $|1\rangle$–$|4\rangle$ transition frequencies, respectively.

phase is determined by the algebraic sum of the applied fields).

Note that, for the goals set in [9], it was sufficient to consider the case of a zero atomic contour phase $\Phi = 0$ and substantial frequency detunings of light waves. It was shown in [9] that the conditions of effective coherent adiabatic passage in three- and two-level Λ-systems nearly coincided. At the same time, the special features of precisely coherent adiabatic passage (in the sense specified above) in closed systems was excluded from consideration in [9]. These special features manifest themselves in population transfer at a nonzero phase value Φ under exact resonance conditions.

In this work, we show that both the effectiveness and the very existence of coherent adiabatic passage in a double Λ-system depend on phase Φ of the atomic contour. For instance, for phase values close to zero and at relatively low light field intensities, coherent adiabatic passage effectiveness is close to that for a three-level atomic system [6]. At the same time, at high light field intensities, the coherent adiabatic passage state is destroyed and the passage becomes incoherent even at near-zero contour phases. However, at phase $\Phi = \pi$, neither coherent nor incoherent passage occurs. In other words, atomic population transfer from one of the lower double Λ-system levels to another is then forbidden no matter whether or not condition (1) is satisfied. We also show that the effectiveness of coherent adiabatic passage in a double Λ-system at a nonzero Φ value is no longer determined by condition (1). We find a new adiabaticity condition which takes into account the dependence of passage effectiveness on the atomic contour phase.

We wish to emphasize that we consider passage under exact resonance conditions (that is, we assume all detunings to be zero) between light waves and atomic transitions in a double Λ-system. We nevertheless find that effective passage in the system under consideration occurs at atomic interaction contour phases close to zero. This circumstance is spectacular evidence of the special features of systems with closed interaction contours as opposed to open systems with an even number of states, for which coherent adiabatic passage states do not exist [12, 13].

2. ADIABATIC SEQUENCE CONDITION

Let us find such a condition to be met by interaction parameters (the so-called adiabatic sequence condition) under which transfer between limiting double Λ-system states occurs without populating intermediate states (that is, coherently). For this purpose, consider the time evolution of atomic populations. A description of the time evolution of populations in a double Λ-system in the absence of spontaneous relaxation is based on the system of equations for nonstationary probability amplitudes Ψ_m (m = 1–4),

$$ih\frac{\partial \mathbf{\Psi}}{\partial t} = H\mathbf{\Psi}. \qquad (2)$$

Here, Hamiltonian $H(t)$ in the resonance approximation is defined by the matrix

$$H(t) = \begin{pmatrix} 0 & 0 & \Omega_1(t) & \Omega_1(t)e^{-i\Phi} \\ 0 & 0 & \Omega_2(t) & \Omega_2(t) \\ \Omega_1(t) & \Omega_2(t) & 0 & 0 \\ \Omega_1(t)e^{-i\Phi} & \Omega_2(t) & 0 & 0 \end{pmatrix}, \qquad (3)$$

and $\mathbf{\Psi} = \{\Psi_1, \Psi_2, \Psi_3, \Psi_4\}^T$ is the column vector composed of probability amplitudes Ψ_m of finding the atom at time t in state m = 1–4. In Hamiltonian (3), we also introduced the time-dependent Rabi frequencies

$$\Omega_1(t) = \Omega_{01}\exp\left[-\frac{(t-\Delta t)^2}{T^2}\right],$$
$$\Omega_2(t) = \Omega_{02}\exp\left[-\frac{(t+\Delta t)^2}{T^2}\right], \qquad (4)$$

and the atomic contour phase $\Phi = \chi_1 + \chi_2 + \chi_3 - \chi_4$, where $\chi_m = \xi_m - \zeta_m$ and ξ_m and ζ_m are the phases of induced dipole moments and the initial phases of light waves, respectively. We assumed that the l–n transitions ($l = 1, 2$ and $n = 3, 4$) in the double Λ-system were electric dipole transitions, whereas the $|1\rangle$–$|2\rangle$ and $|3\rangle$–$|4\rangle$ transitions were forbidden in the dipole approximation (Fig. 1). The sequence of pulse actions was selected to correspond to coherent adiabatic passage (counterintuitive pulse order), and each light pulse contained two frequencies (see Fig. 1). A closed double Λ-system of another type [12, 13], for which our calculations are also valid, is shown in Fig. 2.

The solution to (2) can always be represented in the form

$$\Psi(t) = \sum a_n(t)\mathbf{u}_n(t)\exp\left[-\frac{i}{\hbar}\int\lambda_n(\tau)d\tau\right] \qquad (5)$$

with the initial condition $\Psi(0) = \sum a_n(t)\,\mathbf{u}_n(0)$ on the basis of instantaneous eigenfunctions $\mathbf{u}_n(t)$ of Hamiltonian (3),

$$H(t)\mathbf{u}_n(t) = \lambda_n(t)\mathbf{u}_n(t). \qquad (6)$$

Here, $a_n(t)$ are the expansion coefficients and $\lambda_n(t)$ are the eigenvalues.

Consider slow (or adiabatic) changes in Hamiltonian (3); precisely such changes occur in the interaction between the double Λ-system and two pairs of two-frequency laser pulses of Gaussian form [Eq. (4)]. According to the adiabatic theorem [14], if the system at $t = -\infty$ is in eigenstate $\mathbf{u}_n(t = -\infty)$ of Hamiltonian $H(t = -\infty)$, then, at time $t = \infty$, the system continuously transforms into eigenstate $\mathbf{u}_m(t = \infty)$ of Hamiltonian $H(t = \infty)$ provided the inequality

$$\left|\mathbf{u}_m \cdot \frac{d\mathbf{u}_n}{dt}\right| \ll \frac{|\lambda_m - \lambda_n|}{\hbar} \qquad (7)$$

is satisfied. The expansion coefficients in (5) can be taken to be $a_n(t) = a_n(0)$ if (7) is met. To consider the conditions of coherent adiabatic passage, the adiabatic theorem can be reformulated as follows: if, at $t = -\infty$, the system is in eigenstate $\mathbf{u}_n(t = \infty)$ of Hamiltonian $H(t = -\infty)$, then, at time $t = \infty$, the system remains in eigenstate $\mathbf{u}_n(t = \infty)$ of Hamiltonian $H(t = \infty)$ provided (7) is satisfied. In other words, condition (7) guarantees that the quantum system remains in the same quantum state $\mathbf{u}_n$. By $\mathbf{u}_m$ are meant the other eigenstates of the Hamiltonian, and (7) is actually the condition of smallness of the transition probability from one eigenstate to another compared with the difference of their energies.

To find the adiabatic sequence condition in the explicit form, let us find the eigenvectors of Hamiltonian (3). The characteristic equation for determining the eigenvalues of matrix (3) has the form

$$\lambda^4 - 2(\eta^2 + 1)\lambda^2 + 2\eta^2(1 - \cos\Phi) = 0, \qquad (8)$$

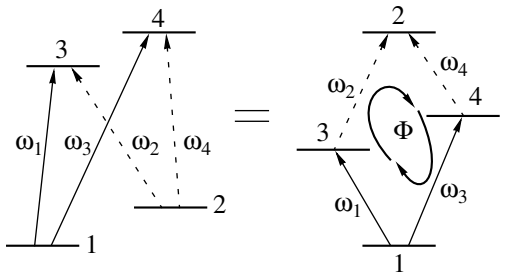

Fig. 2. Different configurations of four-level closed systems

where $\eta(t) = \Omega_2(t)/\Omega_1(t)$. Solving (8) yields eigenvalues $\lambda_n(t)$ in the form

$$\lambda_{1,2,3,4}(t) = \lambda^{\{\pm,\pm\}} = \pm[1 + \eta^2 \pm (\eta^4 + 2\eta^2\cos\Phi + 1)^{1/2}]^{1/2}, \qquad (9)$$

and the set of eigenvectors

$$\mathbf{u}_n(t) = C_1|1\rangle + C_2|2\rangle + C_3|3\rangle + C_4|4\rangle$$

is determined by the coefficients

$$C_1 = 1, \quad C_2 = \frac{r\sin\theta\cos\theta}{R}(1 + e^{i\Phi}),$$
$$C_3 = \frac{\sin\theta}{R}[r^2 - \cos^2\theta(1 - e^{i\Phi})], \qquad (10)$$
$$C_4 = \frac{\sin\theta}{R}[r^2 e^{i\Phi} + \cos^2\theta(1 - e^{i\Phi})],$$

where

$$r^{\{\pm,\pm\}} = \pm[1 \pm (\cos^4\theta + 2\sin\theta\cos^2\theta\cos\Phi + \sin^4\theta)^{1/1}]^{1/2},$$
$$R = r(r^2 - 2\cos^2\theta), \quad \tan\theta = \frac{\Omega_1}{\Omega_2}.$$

Eigenvalues (9) and eigenvectors (10) of Hamiltonian (3) allow the adiabatic sequence condition [Eq. (7)] in interaction with laser pulses of Gaussian form [Eq. (4)] to be written explicitly for an arbitrary atomic contour phase Φ value. To reveal the special features of the double Λ-system, namely, the contour phase dependence of the adiabatic sequence condition, consider the two most important situations with $\Phi = 0$ and $\Phi = \pi$.

2.1. Zero Atomic Contour Phase $\Phi = 0$

The coefficients of the eigenvectors [Eq. (10)] are then

$$C_1 = 1, \quad C_2 = \frac{2r\sin\theta\cos\theta}{R}, \quad C_3 = C_4 = \sin\theta\frac{r^2}{R}.$$

At $r^{\{\pm,-\}}$, we obtain $C_2 = -\tan\theta$ and $C_3 = C_4 = 0$, and the corresponding eigenvector is doubly degenerate. At

$r^{\{\pm,+\}} = \pm 2^{1/2}$, the coefficients are not so trivial, $C_2 = \cot\theta$ and $C_3 = C_4 = \pm 2^{-1/2}\sin\theta$. As eigenvectors are always determined up to an arbitrary factor, let us factor out $\cos\theta$ as a common factor from the first eigenvector at $\Phi = 0$ and $\sin\theta$ from the remaining eigenvectors. As a result, we obtain the following system of eigenvectors of Hamiltonian (3) for $\Phi = 0$:

$$|u_{1,2}^{\Phi=0}\rangle = \cos\theta|1\rangle - \sin\theta|2\rangle + 0(|3\rangle + |4\rangle), \quad (11a)$$

$$|u_{3,4}^{\Phi=0}\rangle = \frac{1}{2^{1/2}}\cos\theta|1\rangle - (\sin\theta|2\rangle + |3\rangle + |4\rangle). \quad (11b)$$

According to (11a), eigenvector $|u_{1,2}^{\Phi=0}\rangle$ is not related to intermediate levels $|3\rangle$ and $|4\rangle$ during the time interval of laser pulse action and coincides with the adiabatic passage state for a three-level atom [6].

Although we consider zero frequency detunings of light pulses from the $|3\rangle$ and $|4\rangle$ upper states, adiabatic passage state (11a) exists in a closed system with an even number of levels (that is, in the double Λ-system). This can be treated as one more distinguishing feature of atomic systems with a closed interaction contour, because, according to [12], adiabatic passage states of form (11a) do not exist in open systems with an even number of states at zero detunings and intermediate levels are always populated as a result of interactions.

Let us determine the adiabatic sequence condition in the explicit form under the requirement that nonadiabatic coupling between eigenvectors (11a) and (11b) is weak; that is, condition (7) is satisfied. Substituting eigenvectors (11a) and (11b) (with "+") into (7) then yields the adiabatic sequence condition in the form

$$\frac{d\theta}{dt} \ll \Omega_{\text{eff}} = (\Omega_1^2 + \Omega_2^2)^{1/2}. \quad (12a)$$

This condition can be transformed to

$$\eta(\delta, \tau) = 2^{1/2}\frac{\exp(\tau^2 + \delta^2)}{\cosh^{3/2}(4\delta\tau)} \ll \Omega_0 T, \quad (12b)$$

where $\tau = t/T$ and $\delta = \Delta t/T$.

Condition (12b) differs from condition (1) used in many works. Strictly, the adiabatic sequence condition is precisely (12b) rather than crude estimate (1). The matter is that we must average (12b) over the time interval of overlap of pulses [1] and set $\delta = 1$ [which, generally, substantially narrows the region of estimate (1) applicability]. Only then can the result be written in form (1).

Using (9) and (10), let us write the adiabatic sequence condition for small deviations μ of the atomic contour phase from $\Phi = 0$,

$$\eta(\delta, \tau)\left|1 + \frac{3\mu}{4\cosh(4\delta\tau)}\right| \leq \Omega_0 T. \quad (12c)$$

Averaging (12c) over the time interval of overlap of pulses allows us to obtain the "global" adiabatic sequence condition as distinguished from "local condition" (12c). According to (12c), the adiabatic sequence condition is satisfied and effective coherent adiabatic passage does occur if μ is small.

2.2. Atomic Contour Phase $\Phi = \pi$

Consider the other limiting case. Coefficients (10) of the eigenvectors are

$$C_1 = 1, \quad C_2 = 0, \quad C_3 = -C_4 = \frac{\sin\theta}{r}.$$

We then obtain $C_3 = -C_4 = \pm 2^{-1/2}$ at $r^{\{\pm,-\}} = \pm 2^{1/2}\sin\theta$. The coefficients are not so trivial at $r^{\{\pm,+\}} = \pm 2^{1/2}\cos\theta$, namely, $C_3 = C_4 = \pm 2^{-1/2}\tan\theta$. Let us factor out the $\cos\theta$ common factor from the first two eigenvectors to obtain the following system of eigenvectors of Hamiltonian (3) for $\Phi = \pi$:

$$|u_{1,2}^{\Phi=\pi}\rangle = \cos\theta|1\rangle + 0|2\rangle \pm 2^{-1/2}\sin\theta(|3\rangle - |4\rangle), \quad (13a)$$

$$|u_{3,4}^{\Phi=\pi}\rangle = 2^{-1/2}|1\rangle + 0|2\rangle \pm \frac{|3\rangle + |4\rangle}{2}. \quad (13b)$$

According to (13a), the $|u_{1,2}^{\Phi=\pi}\rangle$ eigenvector is always related to the $|3\rangle$ and $|4\rangle$ intermediate levels during laser pulse action. The adiabatic sequence condition [Eq. (7)] corresponding to (13a) can be written for small deviations ε from the $\Phi = \pi$ phase value in the form

$$\varepsilon\frac{d\theta}{dt} \ll 8^{1/2}(\cos^2\theta - \sin^2\theta)^2|\sin\theta - \cos\theta|\Omega_{\text{eff}}. \quad (14a)$$

Let us transform (14a) to form (12b),

$$\frac{\delta\varepsilon\exp(\tau^2 + \delta^2)\cosh(4\delta\tau)}{\sinh(2\delta\tau)\sinh^2(4\delta\tau)} \ll 8^{1/2}\Omega_0 T. \quad (14b)$$

This condition can never be satisfied because the left-hand side of (14b) tends to infinity at $\tau = 0$. Accordingly, for atomic contour phases close to $\Phi = \pi$, there is no condition under which coherent adiabatic passage can exist.

3. NUMERICAL CALCULATION RESULTS

In this section, we numerically solve (2) to obtain probability amplitudes Ψ_m (m = 1–4) and determine time-dependent populations of double Λ-system states excited by a pair of two-frequency pulses with a time delay (see Fig. 1).

The dependence of state $|2\rangle$ population on atomic contour phase Φ at $t \longrightarrow \infty$ (that is, after the action of light pulses) is shown in Fig. 3a [simple adiabatic sequence condition (1) is satisfied]. This dependence has a complex oscillatory character. For instance, for

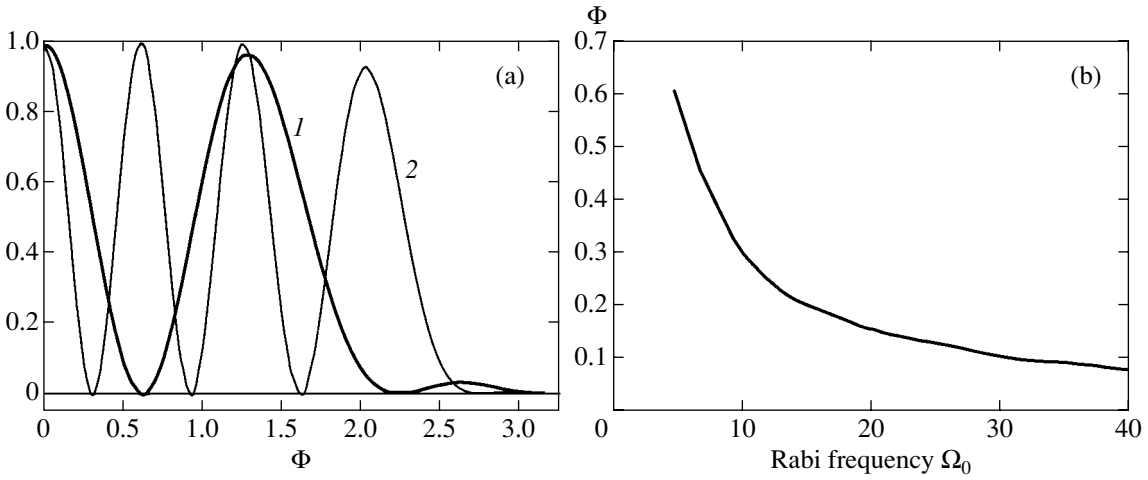

Fig. 3. (a) Dependences of the effectiveness of coherent adiabatic passage (final state $|2\rangle$ population after the action of laser pulses) on atomic contour phase Φ for light pulse amplitudes $\Omega_0 = 5$ (*1*) and 10 (*2*); (b) the position of the first minimum as a function of the amplitude of light pulses.

certain phase values, complete passage from state $|1\rangle$ to state $|2\rangle$ is observed, whereas no passage at all occurs at other Φ values. The number of oscillations of state $|2\rangle$ population determined by the atomic contour phase Φ increases with the intensity of light pulses.

The dependence of the position of the first state $|2\rangle$ population minimum on the amplitude of light fields is shown in Fig. 3b. One can see that the position of the transfer minimum closely approaches zero phase Φ as the intensity of pulses increases. This means that even at comparatively low light pulse intensities, a small change in the atomic contour phase causes a sharp change in the degree of transfer in the system. For instance, at a $\Phi \approx 0$ phase value, effective population transfer occurs in the system (Fig. 4a). Shown in Fig. 4a is coherent adiabatic passage when atomic contour phase Φ equals zero and adiabaticity condition (12b) is satisfied. The effectiveness of coherent adiabatic passage is then high, and the entire population is transferred from lower level $|1\rangle$ to another lower level $|2\rangle$ during the time interval of laser pulse action. The time evolution of the populations in the double Λ-system is then close to that observed in the simplest system of three levels, in complete agreement with the results obtained above.

Note also that the populations of the upper states $|3\rangle$ and $|4\rangle$ are close to zero during the time interval of laser pulse action; therefore, such a transfer can indeed be considered coherent adiabatic passage.

We stress once more that, in our problem, passage coherence (that is, the absence of population of intermediate states) is characteristic of zero light wave frequency detunings. This is also a special feature of closed systems, because, according to [12], population of intermediate levels always occurs in atomic systems with open interaction contours and an even number of levels; population transfer is then incoherent.

The time evolution of the population of states of the double Λ-system at a $\Phi = 0.3$ atomic contour phase value corresponding to the first state $|2\rangle$ population minimum after the action of laser pulses, that is, at $t = \infty$, is shown in Fig. 4b. It is seen that state $|2\rangle$ becomes slightly populated as laser pulses pass. After the passage of pulses, the whole population in the system is, however, equidistributed between the $|3\rangle$ and $|4\rangle$ upper states. The population transfer between states $|1\rangle$ and $|3\rangle$ and $|4\rangle$ then occurs "quasi-adiabatically," because the major population part always remains distributed between the $|1\rangle$, $|3\rangle$, and $|4\rangle$ states (the population of state $|2\rangle$ is comparatively small) and Rabi oscillations characteristic of fully nonadiabatic transfer processes are absent.

Note also that, because the time evolutions of states $|3\rangle$ and $|4\rangle$ are identical, we give for clarity the time dependences of the total population of these states.

The time evolution of populations for a $\Phi = 0.6$ atomic contour phase value corresponding to the state $|2\rangle$ population maximum after laser pulse decay ($t = \infty$) is shown in Fig. 4c. The transfer of population between states $|1\rangle$ and $|2\rangle$ is then completely incoherent, because intermediate states $|3\rangle$ and $|4\rangle$ are populated during laser pulse action.

The behavior of state populations at a $\Phi = 0.9$ phase value corresponding to the second state $|2\rangle$ population minimum is shown in Fig. 4d. Although level $|2\rangle$ is considerably populated during the time interval of pulse action, the final population of this state is close to zero after laser pulse decay. If the passage of pulses is interrupted at a certain time moment ($t \approx 3.8$), all states of the double Λ-system can be populated approximately equally (see Fig. 4d).

The time evolution of the populations at $\Phi = \pi$ is shown in Fig. 4e. The $|2\rangle$ level of the double Λ-system then remains unpopulated during the action of laser

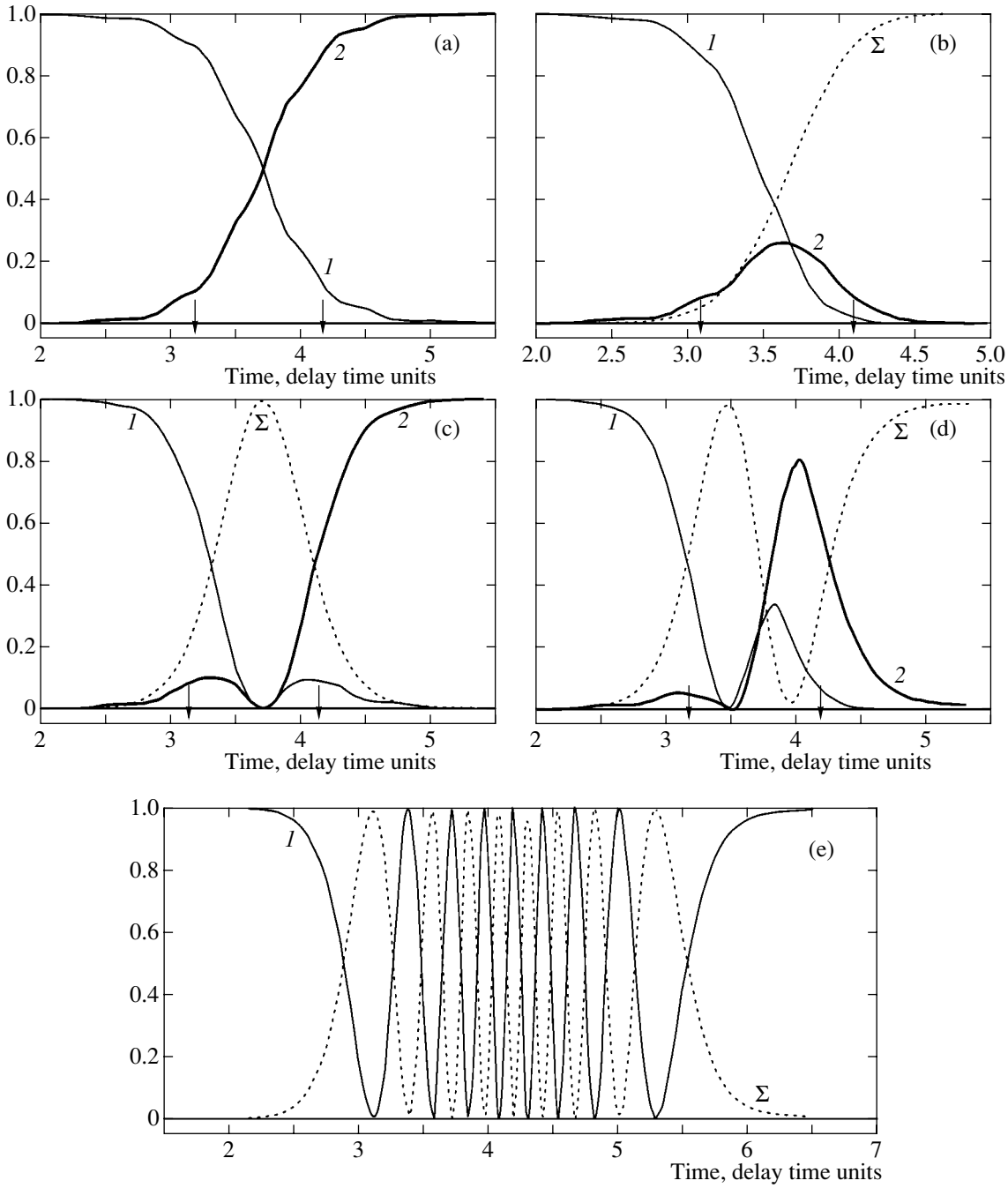

Fig. 4. Time evolution of populations in the double Λ-system of atomic levels for atomic contour phases $\Phi = 0$ (a), 0.3 (b), 0.6 (c), 0.9 (d), and π (e); (*1*) population of initial state $|1\rangle$ and (*2*) population of final state $|2\rangle$; $\sum$ is the sum of populations of intermediate states $|3\rangle$ and $|4\rangle$, arrows indicate Ω_2 and Ω_1 maxima at $t = 3.2$ and 4.2, respectively ($T = 1.5$). All values are in arbitrary units.

pulses, and there is no population transfer of any kind (coherent or incoherent). The whole population then oscillates between state $|1\rangle$ and intermediate states $|3\rangle$ and $|4\rangle$. Such a behavior of coherent adiabatic passage is caused by the complete disappearance of coherence between the $|1\rangle$ and $|2\rangle$ lower states of the double Λ-atom at a $\Phi = \pi$ phase value. The region of phases in which effective coherent adiabatic passage does not occur narrows as the Rabi frequency increases. For $\Phi = \pi$ phases, the effectiveness of any transfer is, however, always close to zero.

4. CONCLUSION

In conclusion, let us formulate the most important results of this work. We considered population transfer between the lower levels of a closed double Λ-system for arbitrary interaction contour phase values. We

found the adiabatic sequence conditions for such a system, that is, the conditions of the occurrence of effective coherent adiabatic passage from one of the lower system levels to another under exact resonance conditions between light waves and atomic transitions at small contour phase values. It was shown that, at $\Phi = (2n + 1)\pi$ phase values, the effectiveness of population transfer of any kind is always zero irrespective of the amplitude of light pulses and the delay time. This is a consequence of the destructive interference of different excitation channels. The dependence of the effectiveness of passage on the atomic contour phase in principle can be exploited to record optical information in a medium, because the equation for the phase contains the initial phases of exciting fields. As a result, a change in the phase of one of the optical fields changes the effectiveness of coherent adiabatic passage, which can be measured by probing field absorption at the corresponding atomic transition.

ACKNOWLEDGMENTS

The authors thank S.G. Przhibel'skii for interest in this work.

REFERENCES

1. K. Bergman, H. Theuer, and B. W. Shore, Rev. Mod. Phys. **70**, 1003 (1998).
2. T. Esslinger, F. Sander, M. Weidemuller, and T. W. Hansch, Phys. Rev. Lett. **76**, 2432 (1996).
3. M. Weitz, B. C. Young, and S. Chu, Phys. Rev. Lett. **73**, 2563 (1994); P. Marte, P. Zoller, and J. L. Hall, Phys. Rev. A **44**, R4118 (1991).
4. M. Ol'shanii, J. Vanicek, and M. Prentiss, Quantum Semiclassic. Opt. **8**, 655 (1996).
5. L. I. Plimak, Yu. V. Rozhdestvensky, M. K. Olsen, and M. J. Collet, Phys. Rev. A **63**, 023608 (2001).
6. M. Kasevich and S. Chu, Phys. Rev. Lett. **66**, 2297 (1991); E. A. Korsunskiĭ, D. V. Kosachev, B. G. Matisov, and Yu. V. Rozhdestvenskiĭ, Pis'ma Zh. Éksp. Teor. Fiz. **55**, 313 (1992) [JETP Lett. **55**, 311 (1992)].
7. U. Gaubatz, P. Rudecki, M. Becker, *et al.*, Chem. Phys. Lett. **149**, 463 (1988); J. R. Kuklinski, U. Gaubatz, F. T. Hioe, and K. Bergmann, Phys. Rev. A **40**, 6741 (1989).
8. T. A. Laine and S. Stenholm, Phys. Rev. A **53**, 2501 (1996).
9. R. G. Unanyan, B. W. Shore, and K. Bergmann, Phys. Rev. A **63**, 043405 (2001).
10. J. Oreg, B. W. Shore, K. Bergmann, and S. Rosenwaks, Phys. Rev. A **45**, 4888 (1992).
11. N. V. Vitanov and S. Stenholm, Phys. Rev. A **55**, 648 (1997).
12. D. V. Kosachiov, B. G. Matisov, and Yu. V. Rozhdestvensky, J. Phys. B **25**, 2473 (1992).
13. S. J. Buckle, S. M. Barnett, P. L. Knight, *et al.*, Opt. Acta **33**, 1129 (1986).
14. A. Messiah, *Quantum Mechanics* (Interscience, New York, 1961; Nauka, Moscow, 1979), Vol. 2, p. 247.

Translated by V. Sipachev

Journal of Experimental and Theoretical Physics, Vol. 96, No. 1, 2003, pp. 102–109.
Translated from Zhurnal Éksperimental'noĭ i Teoreticheskoĭ Fiziki, Vol. 123, No. 1, 2003, pp. 120–127.

SOLIDS
Electronic Properties

Spin-Flip Transitions of Two-Dimensional Electrons in Nonsymmetric Heterostructures

F. T. Vasko* and A. V. Korovin**

Institute of Semiconductor Physics, National Academy of Sciences of Ukraine, Kiev, 03028 Ukraine
**e-mail: ftvasko@yahoo.com*
***avkorovin@rambler.ru; korovin@lab2.semicond.kiev.ua*

Received June 6, 2002

Abstract—The absorption of far-infrared radiation due to electron transitions between spin-split states in nonsymmetric quantum wells excited by a plane-polarized electric field is considered. It is shown that a relative contribution of the exchange renormalization of spin-flip transitions decreases as the concentration of two-dimensional electrons increases. The shape of the absorption peak under resonance transitions is calculated for the case when the line broadening is determined using scattering by static defects. The effect of the Coulomb interaction on the shape of the peak is taken into account, and the suppression of spin-flip absorption due to temperature growth is described. © *2003 MAIK "Nauka/Interperiodica".*

1. INTRODUCTION

Resonance intersubband transitions in quantum wells are excited efficiently by an electric-field component perpendicular to a 2D layer, whereas the component polarized along the 2D plane is absorbed weakly in *n*-type quantum wells (see Section 8.2 in [1]). This fact is attributed to the selection rules of the dipole approximation for a simple model with an isotropic parabolic dispersion law. These rules of selection are violated either in quantum wells in semiconductors with ellipsoidal energy spectra [2] or when the variation of the effective mass along the growth axis of a structure is taken into account [3]. In addition, the absorption of radiation polarized in the 2D plane occurs in nonsymmetric heterostructures with spin degeneracy of the energy spectrum removed, where spin-flip transitions [4] under a planar electric field are allowed. This mechanism was discussed 20 years ago while investigating inversion layers in narrow-band materials [5]. Recent intense investigations of narrow-band InAs-based quantum wells with a noticeable spin splitting of the energy spectrum [6–8] have stimulated the study of the absorption of far-infrared radiation due to spin-flip transitions of 2D electrons in such structures. This process and the interaction between spin-flip transitions and 2D plasmons, which gives rise to spin–plasmon oscillations, have recently been considered in [9] within the self-consistent-field approximation.

In the present paper, we calculate the linear response of nonsymmetric quantum wells to submillimeter-wave radiation polarized in the 2D plane under spin-flip transitions of 2D electrons (the scheme of transitions is shown in Fig. 1) with regard to the exchange renormalization of such transitions. The specific features of the effect of electron–electron interaction on the shape of the absorption peak are associated with the fact that a depolarization shift is negligible (since the self-consistent field vanishes due to the translation invariance of the system in the 2D plane), while the exchange contribution shifts the line, thus reducing the energy of transitions and appreciably changing the shape of the absorption peak. The effect of collisions on the shape of the absorption peak is discussed for the model of scattering by static defects. The response depends on temperature even for strongly degenerate electron states, when the temperature is comparable with the spin-splitting energy.

In Section 2, we analyze a linearized quantum kinetic equation for the spin-dependent high-frequency component of the density matrix that takes into account exchange contributions. The shape of the absorption peak and its shift due to the exchange renormalization are considered in Section 3. Section 4 contains conclusive remarks and the discussion of the approximations used.

2. LINEAR RESPONSE

Consider a linear response of electrons in a nonsymmetric quantum well to an electric field of frequency ω polarized in the 2D plane and described by the Fourier component $\mathbf{E}\exp(-i\omega t)$. The electron states in the conduction band are determined by the following spin-dependent matrix Hamiltonian (see [1]):

$$\frac{\pi^2}{2m} + \hat{\boldsymbol{\sigma}} \cdot [\mathbf{v}_s \times \boldsymbol{\pi}], \qquad (1)$$

where m is the effective mass, $\boldsymbol{\pi} = \mathbf{p} + [i(e/\omega)\mathbf{E}e^{-i\omega t} + \text{c.c.}]$ is the longitudinal kinematic momentum, $\hat{\boldsymbol{\sigma}}$ are

the Pauli matrices, and $\mathbf{v}_s$ is a characteristic spin velocity that describes the efficiency of spin–orbit splitting of the spectrum and is directed along z axis. Neglecting the asymmetry of heteroboundaries, we can evaluate v_s as $|e|F_\perp/(4m\varepsilon_g)$, where ε_g is the effective width of the forbidden band of the quantum well in a homogeneous electric field $F_\perp$. Such an estimate, the discussion of the contribution of nonsymmetric heteroboundaries, as well as relevant references, are presented in [10]. The linearization of expression (1) with respect to a weak field yields a Fourier component, proportional to $e^{-i\omega t}$, of the perturbation operator

$$i\frac{e}{m\omega}(\mathbf{p}\cdot\mathbf{E}) + i\frac{e}{\omega}\hat{\boldsymbol{\sigma}}\cdot[\mathbf{v}_s\times\mathbf{E}]. \qquad (2)$$

Here arises the velocity operator $\mathbf{v} + [\hat{\boldsymbol{\sigma}}\times\mathbf{v}_s]$, which, together with the ordinary term $\mathbf{v} = \mathbf{p}/m$, contains a spin-dependent term. The induced current density is determined by the expression

$$\mathbf{J}_\omega = i\frac{e^2 n_{2D}}{m\omega}\mathbf{E} + \frac{e}{L^2}\mathrm{Sp}(\mathbf{v} + [\hat{\boldsymbol{\sigma}}\times\mathbf{v}_s])\widehat{\delta\rho}, \qquad (3)$$

where n_{2D} is the surface concentration of electrons, L^2 is the normalization area, and Sp includes averaging over the 2D momentum and summation over the spin variable.

The addition to the operator of one-electron density matrix $\widehat{\delta\rho}$ entering into formula (3) is determined by the Fourier component, proportional to $e^{-i\omega t}$, of a linearized kinetic equation that takes into account the Coulomb contributions of order e^2 in the Hartree–Fock approximation. The operator form of this equation is given by formulas (3)–(5) from [11]. Restricting the analysis to spin-flip transitions for the ground-state electrons only, we calculate $\mathbf{J}_\omega$ by the formula

$$\mathbf{J}_\omega = i\frac{e^2 n_{2D}}{m\omega}\mathbf{E} + \frac{e}{L^2}\sum_{\mathbf{p}}\mathrm{tr}_\sigma(\mathbf{v} + [\hat{\boldsymbol{\sigma}}\times\mathbf{v}_s])\widehat{\delta f}_\mathbf{p}, \qquad (4)$$

where tr_σ denotes the trace with respect to the spin variable, while the addition of $\widehat{\delta f}_\mathbf{p}$, proportional to $e^{-i\omega t}$, to the density matrix depends on the 2D momentum and the spin variable (i.e., it represents a 2×2 matrix). Using the results of [11], we obtain the following equation for $\widehat{\delta f}_\mathbf{p}$:

$$-i\omega\widehat{\delta f}_\mathbf{p} + \frac{i}{\hbar}[\hat{\hbar}_\mathbf{p}, \widehat{\delta f}_\mathbf{p}] + \frac{i}{\hbar}[\widehat{\delta h}_\mathbf{p}, \hat{f}_\mathbf{p}] = \hat{I}_{sc}(\widehat{\delta f}|\mathbf{p}), \qquad (5)$$

in which the (2×2) matrix $\hat{f}_\mathbf{p}$ describes the equilibrium distribution and $\hat{I}_{sc}(\widehat{\delta f}|\mathbf{p})$ is a linearized collision integral. In the case of scattering by static defects, the right-hand side of formula (5) is expressed as (see [12])

$$\hat{I}_{sc}(\widehat{\delta f}|\mathbf{p}) = \frac{1}{\hbar^2}\int_{-\infty}^{0} d\tau e^{(\lambda - i\omega)\tau}\int\frac{d\mathbf{p}}{(2\pi\hbar)^2}w_{|\mathbf{p}-\mathbf{p}_1|/\hbar} \qquad (6)$$
$$\times\{\hat{S}^\dagger_{\mathbf{p}\tau}(\widehat{\delta f}_{\mathbf{p}_1} - \widehat{\delta f}_\mathbf{p})\hat{S}_{\mathbf{p}_1\tau} - \hat{S}^\dagger_{\mathbf{p}_1\tau}(\widehat{\delta f}_\mathbf{p} - \widehat{\delta f}_{\mathbf{p}_1})\hat{S}_{\mathbf{p}\tau}\},$$

where $\hat{S}_{\mathbf{p}\tau} \equiv \exp[-i\hat{\hbar}_\mathbf{p}\tau/\hbar]$ is the electron evolution operator. Below, we also use the Gaussian correlator

$$w_{\Delta p} = w\exp[-(\Delta p l_c/\hbar)^2/2],$$

where l_c is the correlation length determining the characteristic scale of irregularities and w determines the intensity of scattering.

The stationary Hamiltonian $\hat{h}_\mathbf{p}$, which describes the motion in the 2D plane and takes into account the spin–orbit contribution and the exchange renormalization of the spectrum (for a translation invariant system, there is no self-consistent potential along the 2D plane), is given by

$$\hat{h}_\mathbf{p} = \varepsilon_p + (\hat{\boldsymbol{\sigma}}\cdot[\mathbf{v}_s\times\mathbf{p}]) \qquad (7)$$
$$-\sum_\mathbf{Q} v_Q\left|\int dz\varphi_z^2 e^{-iq_\perp z}\right|^2\hat{f}_{\mathbf{p}+\hbar\mathbf{q}}.$$

Here, $\varepsilon_p \equiv p^2/(2m)$, the reference point for the energy is the ground-state energy in the quantum well in the absence of spin splitting described by the wave function φ_z, and the summation is performed over all 3D wave vectors $\mathbf{Q} = \{\mathbf{q}, q_\perp\}$. Formula (7) also contains a Cou-

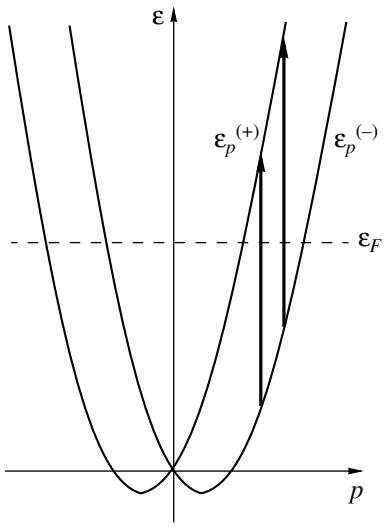

Fig. 1. The scheme of spin-flip transitions excited by an electric field of frequency ω parallel to the 2D layer. The arrows indicate transitions between branches with the dispersion laws $\varepsilon_p^{(\pm)} \equiv \varepsilon_p \pm v_s p$.

lomb matrix element $v_Q \equiv 4\pi e^2/(\epsilon Q^2 L^3)$ with homogeneous permittivity ϵ. Similarly, adding an exchange term to operator (2), we obtain the following (2×2) perturbation matrix that depends on the 2D momentum:

$$\widehat{\delta h}_{\mathbf{p}} = i\frac{e}{\omega}(\mathbf{v} + [\hat{\boldsymbol{\sigma}} \times \mathbf{v}_s]) \cdot \mathbf{E} - \sum_{\mathbf{Q}} v_Q \left| \int dz \varphi_z^2 e^{-iq_\perp z} \right|^2 \widehat{\delta f}_{\mathbf{p}+\hbar\mathbf{q}}. \quad (8)$$

Since the contribution of $ie(\mathbf{v} \cdot \mathbf{E})/\omega$ drops out of the commutators in the kinetic equation (5), the transitions under consideration are spin-flip transitions. Taking into consideration the equalities $\mathrm{tr}_\sigma[\hat{h}_{\mathbf{p}}, \widehat{\delta f}_{\mathbf{p}}] = 0$ and $\mathrm{tr}_\sigma[\widehat{\delta h}_{\mathbf{p}}, \hat{f}_{\mathbf{p}}] = 0$, we obtain $\mathrm{tr}_\sigma \widehat{\delta f}_{\mathbf{p}} = 0$ from Eq. (5), so that the scalar component of the addition to the density matrix vanishes. The equilibrium density matrix $\hat{f}_{\mathbf{p}}$ in Eq. (5) is rewritten as

$$\hat{f}_{\mathbf{p}} = f_F(\varepsilon_F - \varepsilon_p - (\hat{\boldsymbol{\sigma}} \cdot [\mathbf{v}_s \times \mathbf{p}])) = f_p^{(+)} + \frac{(\hat{\boldsymbol{\sigma}} \cdot [\mathbf{v}_s \times \mathbf{p}])}{v_s p} f_p^{(-)}, \quad (9)$$

where ε_F is the Fermi energy, $f_F(E)$ is the Fermi distribution function with temperature T, and

$$f_p^{(\pm)} \equiv [f_F(\varepsilon_F - \varepsilon_p - v_s p) \pm f_F(\varepsilon_F - \varepsilon_p + v_s p)]/2.$$

Note that $f_p^{(\pm)}$ drops out of the commutators in Eq. (5) and the contribution to the spin-flip absorption is made only by electrons close to the Fermi surface (if $T = 0$, then $f_p^{(-)}$ is replaced by -1 in the interval $\varepsilon_p - v_s p < \varepsilon_F < \varepsilon_p + v_s p$ and vanishes for other p).

Separating the factor $f_p^{(-)}$ introduced by Eq. (9) from $\widehat{\delta f}_{\mathbf{p}}$, we seek a solution to (5) in the form $\widehat{\delta f}_{\mathbf{p}} = (\hat{\boldsymbol{\sigma}} \cdot \mathbf{R}_{\mathbf{p}}) f_p^{(-)}$, so that formula (5) gives the following equation for the vector $\mathbf{R}_{\mathbf{p}}$:

$$-i\omega(\hat{\boldsymbol{\sigma}} \cdot \mathbf{R}_{\mathbf{p}}) + \frac{i}{\hbar}[\tilde{h}_{\mathbf{p}}, (\hat{\boldsymbol{\sigma}} \cdot \mathbf{R}_{\mathbf{p}})] + \frac{i}{\hbar}\left[\widetilde{\sigma h}_{\mathbf{p}}, \frac{(\hat{\boldsymbol{\sigma}} \cdot [\mathbf{v}_s \times \mathbf{p}])}{v_s p}\right] = \hat{\boldsymbol{\sigma}} \cdot \hat{\mathbf{I}}_{sc}(\mathbf{R}|\mathbf{p}). \quad (10)$$

The spin-dependent contributions to the renormalization Hamiltonian of 2D electrons (7) and the perturbation operator (8), marked by tildes in what follows, are rewritten as

$$\tilde{h}_{\mathbf{p}} = \hat{\boldsymbol{\sigma}} \cdot \left\{ [\mathbf{v}_s \times \mathbf{p}] - \int \frac{d\mathbf{p}_1}{2\pi m} M_{|\mathbf{p}-\mathbf{p}_1|/\hbar} f_{p_1}^{(-)} \frac{[\mathbf{v}_s \times \mathbf{p}]}{v_s p_1} \right\} \quad (11)$$

and

$$\delta\tilde{h}_{\mathbf{p}} = \hat{\boldsymbol{\sigma}} \cdot \left\{ i\frac{e}{\omega}[\mathbf{v}_s \times \mathbf{E}] - \int \frac{d\mathbf{p}_1}{2\pi m} M_{|\mathbf{p}-\mathbf{p}_1|/\hbar} f_{p_1}^{(-)} \mathbf{R}_{\mathbf{p}_1} \right\}. \quad (12)$$

Here, we introduce the integral kernel

$$M_q = \int dz \varphi_z^2 \int dz' \varphi_{z'}^2 \frac{e^{-1|z-z'|}}{qa_B} \approx \frac{1}{qa_B} \quad (13)$$

depending on the transfer of two-dimensional wave vector q; to derive this expression, we performed integration with respect to $q_\perp$ in general formulas (7) and (8) and introduced the Bohr radius $a_B = \epsilon\hbar^2/me^2$. The right equality in (13) applies to the two-dimensional limit case $qd \ll 1$ (d is the quantum-well width, which determines the maximum of $|z - z'|$). The relaxation term in the kinetic equation (10) is obtained from the general expression (6). Restricting ourselves to small spin-splitting of the spectrum near the Fermi energy, which corresponds to the condition $v_s \ll v_F \equiv \sqrt{2\varepsilon_F/m}$, we substitute

$$\hat{S}_{\mathbf{p}\tau} \approx \exp[-i\varepsilon_{\mathbf{p}}\tau/\hbar]$$

into formula (6) to obtain the following collision integral in (10):

$$\hat{I}_{sc}(\widehat{\delta f}|\mathbf{p}) \approx f_p^{(-)} \hat{\boldsymbol{\sigma}} \cdot \frac{2\pi}{\hbar} \int \frac{d\mathbf{p}_1}{(2\pi\hbar)^2} w_{|\mathbf{p}-\mathbf{p}_1|/\hbar} \times \delta(\varepsilon_p - \varepsilon_{p_1})(\mathbf{R}_{\mathbf{p}_1} - \mathbf{R}_{\mathbf{p}}) \equiv f_p^{(-)} \hat{\boldsymbol{\sigma}} \cdot \hat{\mathbf{I}}_{sc}(\mathbf{R}|\mathbf{p}), \quad (14)$$

where the contributions of spin-flip processes during collisions are small with respect to the parameter v_s/v_F.

Substituting matrices (11) and (12) into (10), we obtain the following vector equation for $\mathbf{R}_{\mathbf{p}}$:

$$\omega\mathbf{R}_{\mathbf{p}} - \frac{2i}{\hbar}\left\{ [[\mathbf{v}_s \times \mathbf{p}] \times \mathbf{R}_{\mathbf{p}}] - \int \frac{d\mathbf{p}_1}{2\pi m} f_{p_1}^{(-)} M_{|\mathbf{p}-\mathbf{p}_1|/\hbar} \times \left(\frac{[[\mathbf{v}_s \times \mathbf{p}_1] \times \mathbf{R}_{\mathbf{p}}]}{v_s p_1} - \frac{[[\mathbf{v}_s \times \mathbf{p}] \times \mathbf{R}_{\mathbf{p}_1}]}{v_s p} \right) \right\} + i\hat{\mathbf{I}}_{sc}(\mathbf{R}|\mathbf{p}) = \frac{2e}{\hbar\omega} \frac{[[\mathbf{v}_s \times \mathbf{p}] \times \mathbf{E}]}{v_s p} \mathbf{v}_s, \quad (15)$$

where the inhomogeneous term is perpendicular to the 2D plane. Separating the planar, $\mathbf{r}_{\mathbf{p}}$, and transversal, $r_{\mathbf{p}}^\perp$, contributions to $\mathbf{R}_{\mathbf{p}}$, we obtain the following system of equations from (15):

$$\omega\mathbf{r}_{\mathbf{p}} - \frac{2iv_s}{\hbar}\mathbf{p}r_{\mathbf{p}}^\perp + \frac{2i}{\hbar}\int \frac{d\mathbf{p}}{2\pi m} \frac{\hbar}{a_B|\mathbf{p}-\mathbf{p}_1|} f_{p_1}^{(-)} \left(\frac{\mathbf{p}_1}{p_1} r_{\mathbf{p}}^\perp - \frac{\mathbf{p}}{p} r_{\mathbf{p}_1}^\perp \right) = i\frac{2\pi}{\hbar}\int \frac{d\mathbf{p}}{(2\pi\hbar)^2} w_{|\mathbf{p}-\mathbf{p}_1|/\hbar} \delta(\varepsilon_p - \varepsilon_{p_1})(\mathbf{r}_{\mathbf{p}_1} - \mathbf{r}_{\mathbf{p}}),$$

$$\omega r_{\mathbf{p}}^{\perp} + \frac{2iv_s}{\hbar}(\mathbf{p}\cdot\mathbf{r}_{\mathbf{p}}) - \frac{2i}{\hbar}\int\frac{d\mathbf{p}}{2\pi m}\frac{\hbar}{a_B|\mathbf{p}-\mathbf{p}_1|} \tag{16}$$

$$\times f_{p_1}^{(-)}\left(\frac{(\mathbf{p}_1\cdot\mathbf{r}_{\mathbf{p}})}{p_1} - \frac{(\mathbf{p}\cdot\mathbf{r}_{1\mathbf{p}})}{p}\right) = i\frac{2\pi}{\hbar}\int\frac{d\mathbf{p}}{(2\pi\hbar)^2}$$

$$\times w_{|\mathbf{p}-\mathbf{p}_1|/\hbar}\delta(\varepsilon_p - \varepsilon_{p_1})(r_{\mathbf{p}_1}^{\perp} - r_{\mathbf{p}}^{\perp}) + \frac{2e(\mathbf{p}\cdot[\mathbf{E}\times\mathbf{v}_s])}{p\hbar\omega}.$$

Here, the kernel of Coulomb contribution (13) is written for the two-dimensional limit case.

The induced current (4) is expressed in terms of $\mathbf{r}_{\mathbf{p}}$ by the formula

$$\mathbf{J}_{\omega} = i\frac{e^2 n_{2D}}{m\omega}\mathbf{E} + 2e\int\frac{d\mathbf{p}}{(2\pi\hbar)^2}f_p^{(-)}[\mathbf{v}_s\times\mathbf{r}_{\mathbf{p}}]; \tag{17}$$

therefore, to describe the absorption due to spin-flip transitions, one has to solve the system of integral equations (16) and calculate the real contribution to the induced current (17).

3. THE SHAPE OF THE ABSORPTION PEAK

Using the energy–angle variables (ε, ϕ) such that the vectors $\mathbf{p} = p_\varepsilon\mathbf{n}_\phi$ with $p_\varepsilon = \sqrt{2m\varepsilon}$ and $\mathbf{n}_\phi = (\cos\phi, \sin\phi)$ determine the orientation of the 2D momentum, one can easily verify that the vector function $\mathbf{r}_{\mathbf{p}}$ defined by system (16) is oriented along the 2D momentum, i.e., $\mathbf{r}_{\mathbf{p}} = \mathbf{n}_\phi r_{\varepsilon,\phi}^{\parallel}$. As a result, we obtain the following system of equations for $r_{\varepsilon,\phi}^{\parallel,\perp}$

$$\omega r_{\varepsilon,\phi}^{\parallel} - i\omega_\varepsilon r_{\varepsilon,\phi}^{\perp} + \frac{2i}{a_B}\int_0^\infty d\varepsilon_1 f_{\varepsilon_1}^{(-)}$$

$$\times\int_0^{2\pi}\frac{d\Delta\phi}{2\pi}\frac{r_{\varepsilon,\phi}^{\perp}\cos\Delta\phi - r_{\varepsilon_1,\phi+\Delta\phi}^{\perp}}{\sqrt{p_\varepsilon^2 + p_{\varepsilon_1}^2 - 2p_\varepsilon p_{\varepsilon_1}\cos\Delta\phi}}$$

$$= i\nu\int_0^{2\pi}\frac{d\Delta\phi}{2\pi}w_{\varepsilon,\Delta\phi}(r_{\varepsilon,\phi+\Delta\phi}^{\parallel}\cos\Delta\phi - r_{\varepsilon,\phi}^{\parallel}), \tag{18}$$

$$\omega r_{\varepsilon,\phi}^{\perp} + i\omega_\varepsilon r_{\varepsilon,\phi}^{\parallel} - \frac{2i}{a_B}\int_0^\infty d\varepsilon_1 f_{\varepsilon_1}^{(-)}$$

$$\times\int_0^{2\pi}\frac{d\Delta\phi}{2\pi}\frac{(r_{\varepsilon,\phi}^{\parallel} - r_{\varepsilon_1,\phi+\Delta\phi}^{\parallel})\cos\Delta\phi}{\sqrt{p_\varepsilon^2 + p_{\varepsilon_1}^2 - 2p_\varepsilon p_{\varepsilon_1}\cos\Delta\phi}}$$

$$= i\nu\int_0^{2\pi}\frac{d\Delta\phi}{2\pi}w_{\varepsilon,\Delta\phi}(r_{\varepsilon,\phi+\Delta\phi}^{\parallel} - r_{\varepsilon_1,\phi}^{\parallel}) + \frac{2eEv_s}{\hbar\omega}\sin\phi.$$

Here, $\omega_\varepsilon = 2v_s p_\varepsilon/\hbar$ is the frequency of a spin-flip transition for an electron with energy ε, $\nu = \pi\rho_{2D}\omega/\hbar$ is the relaxation frequency in the case of short-range scattering, and the function $\omega_{\varepsilon,\Delta\phi} = \exp[-(p_\varepsilon l_c/\hbar)^2(1 - \cos\Delta\phi)/4]$ takes into account the finiteness of the correlation length. Since the kernels of the integral summands (18) depend only on $\cos\Delta\phi$, the angular dependence of solutions to (18) is determined by $\sin\phi$:

$$r_{\varepsilon,\phi}^{\parallel,\perp} = \frac{2eEv_s}{\hbar\omega}\chi_\varepsilon^{\parallel,\perp}\sin\phi. \tag{19}$$

For the functions $\chi_\varepsilon^{\parallel,\perp}$ thus introduced, we obtain the system of integral equations

$$(\omega + i\nu_\varepsilon^{(2)})\chi_\varepsilon^{\parallel} - i\omega_\varepsilon\chi_\varepsilon^{\perp}$$

$$+\frac{2i}{a_B p_\varepsilon}\int_0^\infty d\varepsilon_1 f_{\varepsilon_1}^{(-)}A_1\left(\frac{\varepsilon_1}{\varepsilon}\right)(\chi_\varepsilon^{\perp} - \chi_{\varepsilon_1}^{\perp}) = 0,$$

$$(\omega + i\nu_\varepsilon^{(1)})\chi_\varepsilon^{\perp} + i\omega_\varepsilon\chi_\varepsilon^{\parallel} - \frac{2i}{a_B p_\varepsilon}\int_0^\infty d\varepsilon_1 f_{\varepsilon_1}^{(-)} \tag{20}$$

$$\times\left[A_1\left(\frac{\varepsilon_1}{\varepsilon}\right)\chi_\varepsilon^{\parallel} - A_2\left(\frac{\varepsilon_1}{\varepsilon}\right)\chi_{\varepsilon_1}^{\parallel}\right] = 1,$$

where the relaxation frequencies are given by $(n = 1, 2)$

$$\nu_\varepsilon^{(n)} = \nu\int_0^{2\pi}\frac{d\Delta\phi}{2\pi}w_{\varepsilon,\Delta\phi}(1 - \cos^n\Delta\phi). \tag{21}$$

These frequencies decrease as $p_F l_c/\hbar$ increases and weakly depend on ε near the Fermi energy $p_F^2/(2m) = \varepsilon_F$ (see Fig. 2). The Coulomb integral terms in Eqs. (20) are expressed through the kernel

$$A_n(z) = \int_0^{2\pi}\frac{d\Delta\phi}{2\pi}\frac{\cos^n\Delta\phi}{\sqrt{1 + z - 2\sqrt{z}\cos\Delta\phi}}, \tag{22}$$

which diverge logarithmically for $z = 1$ (see Fig. 3).

The complex conductivity σ_ω is expressed in terms of $\chi_\varepsilon^{\parallel}$ after a simple integration with respect to angle in formula (17). Then, for the relative absorption ξ_ω of a 2D layer, which is determined by the ratio of the energy flux absorbed in the quantum well to that transmitted through the 2D layer, $\xi_\omega = 4\pi\mathrm{Re}\,\sigma_\omega/(c\sqrt{\epsilon})$, we obtain

$$\xi_\omega = \frac{e^2}{c\sqrt{\epsilon}}\frac{4\pi\rho_{2D}v_s^2}{\hbar\omega}\int_0^\infty d\varepsilon f_\varepsilon^{(-)}\mathrm{Re}\chi_\varepsilon^{\parallel}. \tag{23}$$

For $T \ll \varepsilon_F$, the function $f_\varepsilon^{(-)}$ is different from zero only in a narrow region near the Fermi energy.

When a uniform broadening of the peak dominates, we can neglect the energy dependence of $\chi_\varepsilon^{\parallel,\perp}$ near the

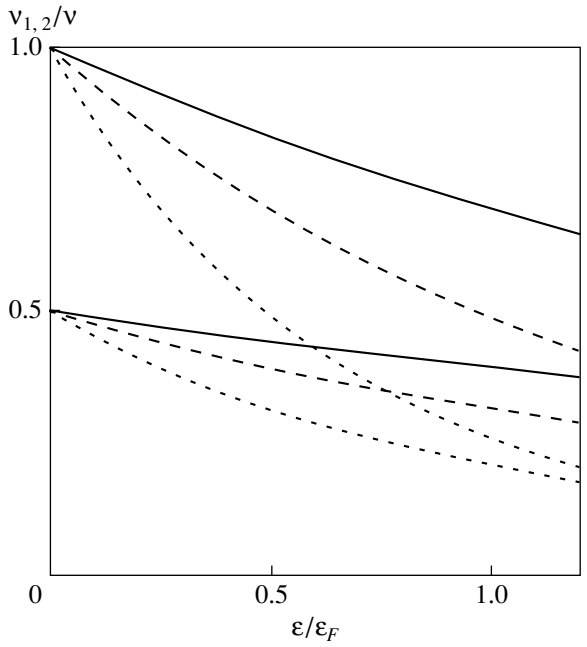

Fig. 2. Dimensionless relaxation frequencies versus energy (see Eq. (20)) for the following values of the parameter $p_F l_c/\hbar$: 0.5 (solid curve), 1 (dashed curve), and 2 (dotted curve).

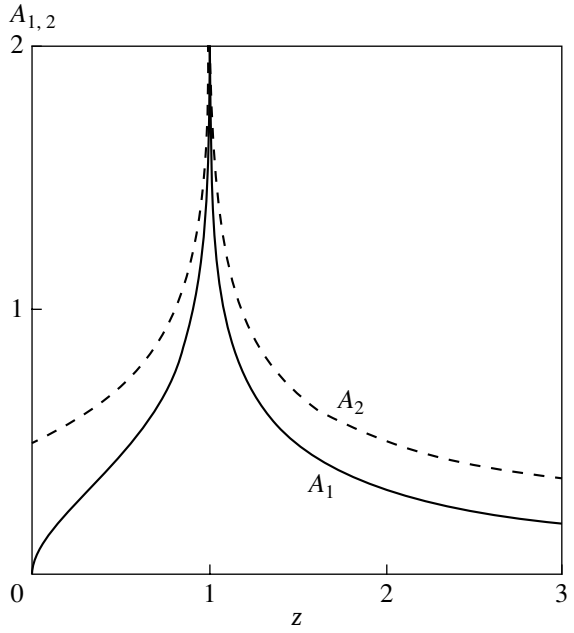

Fig. 3. Dimensionless functions $A_{1,2}(z)$.

Fermi energy. Thus, Eqs. (20) reduce to a linear algebraic system for $\chi_F^{\parallel,\perp} \equiv \chi_{\varepsilon_F}^{\parallel,\perp}$:

$$\begin{pmatrix} \omega + i\nu_F^{(1)} & -i\omega_F \\ i(\omega_F + \Delta\omega) & \omega + i\nu_F^{(2)} \end{pmatrix} \begin{pmatrix} \chi_F^{\parallel} \\ \chi_F^{\perp} \end{pmatrix} = \begin{pmatrix} 0 \\ 1 \end{pmatrix}, \qquad (24)$$

where $\omega_F = 2v_s p_F/\hbar$, the relaxation frequencies $\nu_F^{(2)}$ and $\nu_F^{(1)}$ are determined by Eq. (21) with $\varepsilon = \varepsilon_F$, and the exchange renormalization of the transition frequency is defined by the expression

$$\Delta\omega = \frac{2}{a_B p_F}\int_0^\infty d\varepsilon_1 f_{\varepsilon_1}^{(-)}\left[A_2\left(\frac{\varepsilon_1}{\varepsilon_F}\right) - A_1\left(\frac{\varepsilon_1}{\varepsilon_F}\right)\right]. \qquad (25)$$

The relative absorption (23) of the 2D layer is expressed in terms of $\chi_F^{\parallel}$ according to the equation (for $\nu_{\text{eff}} \ll \tilde{\omega}$)

$$\xi_\omega \approx \frac{e^2}{c\sqrt{\epsilon}\hbar^2}\frac{m v_s^2 \nu_{\text{eff}}}{[(\omega - \tilde{\omega})^2 + \nu_{\text{eff}}^2]}, \qquad (26)$$

so that we obtain a Lorentz absorption peak whose width is determined by the frequency $\nu_{\text{eff}} = (\nu_F^{(1)} + \nu_F^{(2)})/2$. The maximum absorption corresponds to the frequency $\tilde{\omega} = \sqrt{\omega_F(\omega_F + \Delta\omega)}$ and is shifted toward lower frequencies because of the exchange renormalization of the spin-flip transition.

If the variation of the transition frequency in the energy interval $|\varepsilon - \varepsilon_F| < \hbar\omega_F/2$ and the integral terms in (20) are comparable with ν_{eff} (or exceed the collision broadening), one should consider the system of integral equations (20). In this case, both the energy dependence of the renormalized frequency $\bar{\omega}_\varepsilon$ of the spin-flip transition, which is introduced by

$$\bar{\omega}_\varepsilon = \omega_\varepsilon - \frac{2}{a_B p_\varepsilon}\int_0^\infty d\varepsilon_1 f_{\varepsilon_1}^{(-)} A_1\left(\frac{\varepsilon_1}{\varepsilon}\right), \qquad (27)$$

and the integral terms in Eqs. (20) attributed to the nonlocal character of the exchange prove to be significant. Thus, instead of algebraic system (24), one should consider the equality

$$\begin{pmatrix} \omega + i\nu_\varepsilon^{(1)} & -i\bar{\omega}_\varepsilon \\ i\bar{\omega}_\varepsilon & \omega + i\nu_\varepsilon^{(2)} \end{pmatrix} \begin{pmatrix} \chi_\varepsilon^{\parallel} \\ \chi_\varepsilon^{\perp} \end{pmatrix}$$

$$= \begin{pmatrix} 0 \\ 1 \end{pmatrix} + \frac{2i}{a_B p_\varepsilon}\int_0^\infty d\varepsilon_1 f_{\varepsilon_1}^{(-)} \begin{pmatrix} A_1\left(\frac{\varepsilon_1}{\varepsilon}\right)\chi_{\varepsilon_1}^{\perp} \\ -A_2\left(\frac{\varepsilon_1}{\varepsilon}\right)\chi_{\varepsilon_1}^{\parallel} \end{pmatrix}. \qquad (28)$$

Here, the functions $\chi_\varepsilon^{\perp,\parallel}$ for zero temperature are defined on the interval $|\varepsilon - \varepsilon_F| < 2v_s p_F$ because $f_\varepsilon^{(-)}$

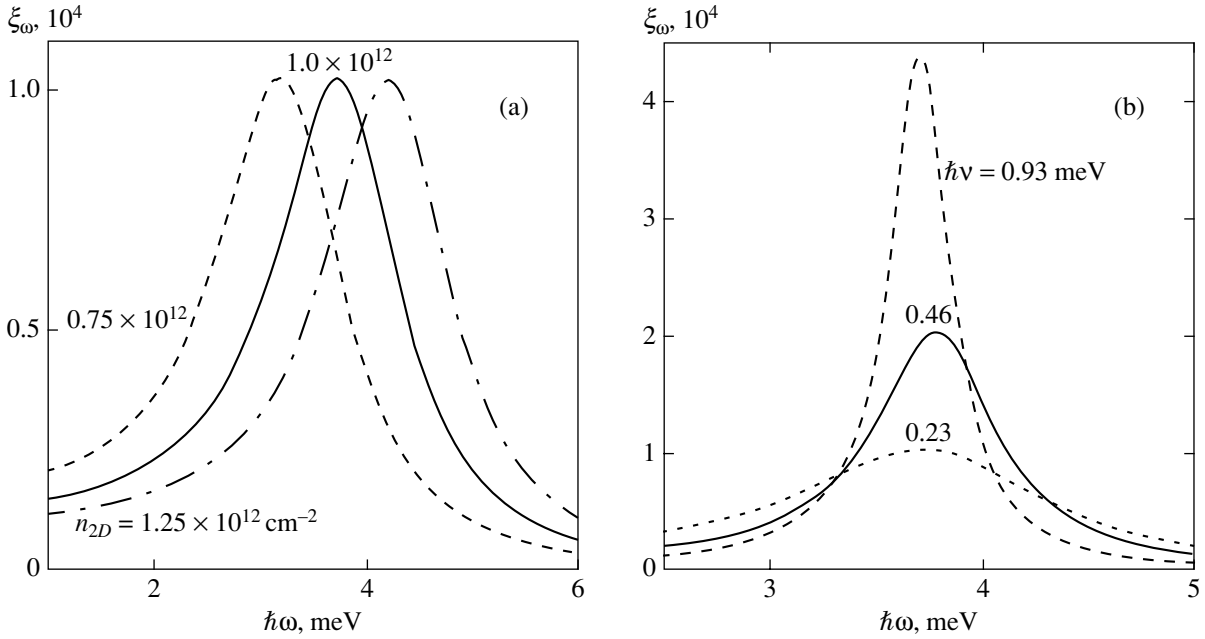

Fig. 4. The spectral characteristics of the absorption coefficient for $T = 0$ (a) for various concentrations n_{2D} at $\hbar\nu = 0.93$ meV and (b) for various broadening energies $\hbar\nu$ at $n_{2D} = 10^{12}$ cm^{-2}.

vanishes outside this interval. Numerical solutions to such a system were obtained by a direct method, while the absorption spectra are obtained by integrating with respect to energy in formula (23).

Figure 4 shows the spectra of the absorption coefficient at $T = 0$ (a) for variations in the electron concentration n_{2D} and (b) for various line broadenings $\hbar\nu$ for a fixed 2D concentration of $n_{2D} = 10^{12}$ cm^{-2}. The calculations are performed for the case of short-range scattering with a carrier mobility of $\mu = 5.5 \times 10^5$ cm^2/(V s) and a spin velocity of 1.2×10^6 cm/s (borrowed from the experimental data of [13]), which correspond to a

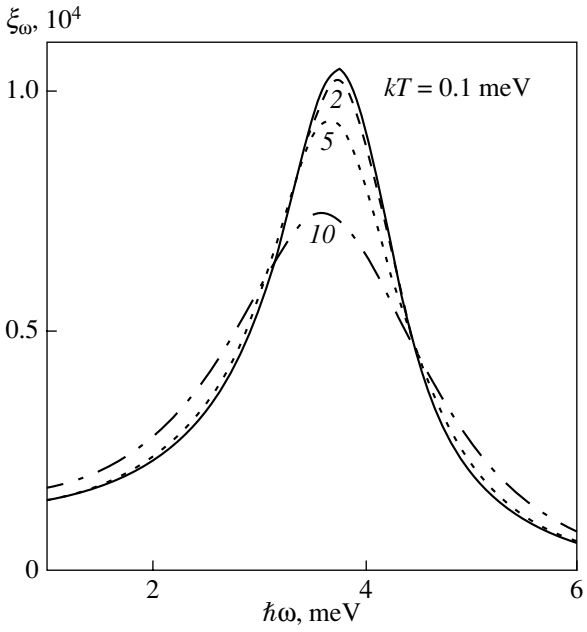

Fig. 5. Suppression of the absorption peak with increasing temperature for $n_{2D} = 10^{12}$ cm^{-2}and $\hbar\nu = 0.93$ meV.

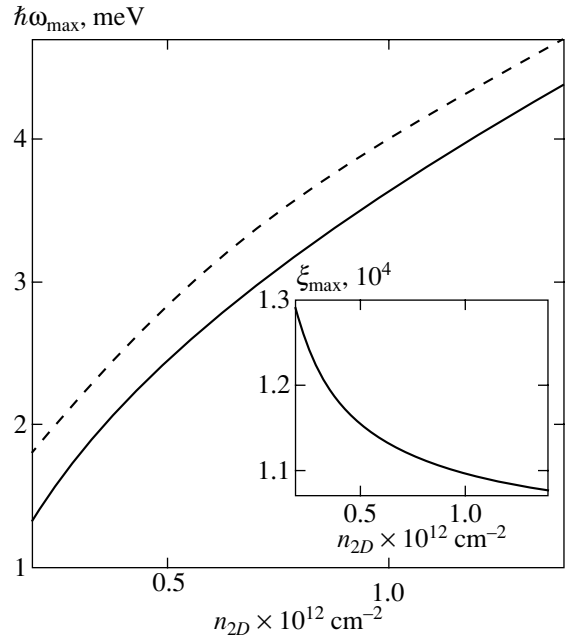

Fig. 6. The energy of the absorption peak and its maximal value (the inset) as functions of the 2D concentration.

broadening energy of 0.93 meV and a transition energy of $\hbar\omega_F = 4$ meV. The peak is shifted toward lower energies as the concentration decreases and is suppressed as the broadening energy increases; moreover, the shape of this peak proves to be nonsymmetric. Figure 5 shows the suppression of absorption as temperature increases (the results correspond to $n_{2D} = 10^{12}$ cm^{-2} and $\hbar\nu = 0.93$ meV); in this case, the shape of the peak is also changed and the peak itself is shifted toward lower energies, which is associated with a decrease in the Coulomb contribution with increasing temperature.

These results are summarized in Fig. 6, which demonstrates the shift of the absorption line and the maximum absorption (in the inset) as functions of concentration at zero temperature. The line shift proves to be almost proportional to $\sqrt{n_{2D}}$ (for comparison, the dashed curve represents the spin-splitting energy) because the exchange contribution is almost independent of $\sqrt{n_{2D}}$ due to weak dependence of the integral term in formula (28) on p_F. However, these integral contributions substantially change the shape of the absorption peak; in contrast to the one-particle result, when the absorption peak is steplike for small $\hbar\nu$ [9], the peak nearly always has a Lorentz shape. The broadening energy slowly decreases as the concentration increases (from 0.8 to 0.7 meV for the variation of concentration from 0.25×10^{12} to 1.75×10^{12} cm^{-2}); we do not present this weak dependence here.

4. CONCLUSION

In this paper, we have considered the shape of the absorption peak due to intersubband transitions excited by an electric-field component parallel to the 2D layer. Both the uniform broadening of the peak due to the scattering by static defects and the exchange renormalization of spin-flip transitions have been taken into account. It has been shown that such renormalization not only reduces the transition energy but also appreciably changes the shape of the peak. It has been established that the absorption peak is rapidly suppressed as temperature increases (when T becomes comparable with the transition energy, but still $T \ll \varepsilon_F$). Numerical results are presented for typical parameters of nonsymmetric InAs-based heterostructures.

Let us dwell on the main approximations used in these calculations. Hamiltonian (1) of two-dimensional electrons is represented in the effective-mass approximation, while spin-dependent phenomena are described by the characteristic velocity $\mathbf{v}_s$, which can be interpreted as a phenomenological parameter. These approximations, just as the consideration of solely the Coulomb contributions of order e^2 in the linearized kinetic equation (5) (see [11]), are generally accepted. The model of scattering by static defects that are characterized by correlation length l_c and determine the uniform line broadening can easily be generalized to the case of elastic scattering by acoustic phonons (which may be significant in GaAs-based heterostructures with sufficiently high mobility). An additional contribution to the uniform broadening also arises due to the direct Coulomb scattering of electrons; however, this contribution is of the order of e^4 and does not exceed 0.1 meV for the concentrations considered in this paper (see the references to the calculations and the experimental data in [14]). In addition, the use of uniform permittivity in formulas (7), (8), and (23) presumes that the variation of permittivity across a heterostructure is small and that the surface phenomena are neglected. Finally, the use of a two-dimensional approximation for Coulomb kernel (13) and the assumption that the transition energy, peak width, and temperature are small compared to the Fermi energy is justified in heavily doped quantum wells. Thus, the approximations made do not impose considerable restrictions on our description of the shape of the peak of spin-flip absorption as a function of v_s, concentration, and temperature.

The results presented in this paper describe the far-infrared-absorption peak due to spin-flip transitions of 2D electrons, which can be investigated both by spectral measurements and by measuring the dependence of this peak on transverse voltage (which modulates the spin velocity v_s) or on temperature. In addition, a similar description of the collision broadening and the exchange renormalization of spin-flip transitions is needed for considering the excitation of spin–plasmon 2D oscillations (see [9]) and spin-flip scattering processes.

REFERENCES

1. F. T. Vasko and A. V. Kuznetsov, *Electron States and Optical Transitions in Semiconductor Heterostructures* (Springer-Verlag, New York, 1998).
2. Y. Zhang, N. Baruch, and I. Wang, Appl. Phys. Lett. **63**, 1068 (1993); I. S. Park, R. P. G. Karunasiri, and K. L. Wang, Appl. Phys. Lett. **60**, 103 (1992).
3. R. Q. Yang, Phys. Rev. B **52**, 11958 (1995); F. T. Vas'ko and Yu. N. Soldatenko, Fiz. Tekh. Poluprovodn. (Leningrad) **20**, 920 (1986) [Sov. Phys. Semicond. **20**, 579 (1986)].
4. É. I. Rashba, Usp. Fiz. Nauk **84**, 557 (1964) [Sov. Phys. Usp. **7**, 823 (1965)].
5. F. T. Vas'ko and N. A. Prima, Fiz. Tverd. Tela (Leningrad) **21**, 1734 (1979) [Sov. Phys. Solid State **21**, 994 (1979)]; F. T. Vas'ko, Pis'ma Zh. Éksp. Teor. Fiz. **30**, 574 (1979) [JETP Lett. **30**, 541 (1979)].
6. J. P. Heida, B. J. van Wees, J. J. Kuipers, *et al.*, Phys. Rev. B **57**, 11911 (1998).
7. J. Nitta, T. Akazaki, H. Takayanagi, and T. Enoki, Phys. Rev. Lett. **78**, 1335 (1997).

8. J. Luo, H. Munekata, F. F. Fang, and P. J. Stiles, Phys. Rev. B **41**, 7685 (1990).

9. L. I. Magaril, A. V. Chaplik, and M. V. Éntin, Zh. Éksp. Teor. Fiz. **119**, 175 (2001) [JETP **92**, 153 (2001)].

10. F. T. Vas'ko, Fiz. Tekh. Poluprovodn. (Leningrad) **19**, 1958 (1985) [Sov. Phys. Semicond. **19**, 1207 (1985)]; E. A. de Andrada e Silva, G. C. La Rocca, and F. Bassani, Phys. Rev. B **55**, 16293 (1996); F. T. Vasko and O. Keller, Phys. Rev. B **58**, 15666 (1998).

11. F. T. Vas'ko, Zh. Éksp. Teor. Fiz. **120**, 1468 (2001) [JETP **93**, 1270 (2001)].

12. I. B. Levinson, Zh. Éksp. Teor. Fiz. **57**, 660 (1969) [Sov. Phys. JETP **30**, 362 (1970)]; F. T. Vas'ko, Fiz. Tekh. Poluprovodn. (Leningrad) **10**, 70 (1976) [Sov. Phys. Semicond. **10**, 41 (1976)].

13. S. Yamada, Y. Sato, S. Gozu, and T. Kikutani, Physica E (Amsterdam) **7**, 992 (2000).

14. K. Kempa, P. Bakshi, J. Engelbrecht, and Y. Zhou, Phys. Rev. B **61**, 11083 (2000); M. Hartig, J. D. Ganishre, P. E. Selbmann, *et al.*, Phys. Rev. B **60**, 1500 (1999).

Translated by I. Nikitin

Journal of Experimental and Theoretical Physics, Vol. 96, No. 1, 2003, pp. 110–117.
Translated from Zhurnal Éksperimental'noĭ i Teoreticheskoĭ Fiziki, Vol. 123, No. 1, 2003, pp. 128–136.

SOLIDS
Electronic Properties

Magnetic Properties of Anion-Deficient $La_{1-x}Ba_xMnO_{3-x/2}$ ($0 \le x \le 0.30$) Manganites

S. V. Trukhanov[a, *], I. O. Troyanchuk[a], N. V. Pushkarev[a], and H. Szymczak[b]

[a]*Institute of Solid-State and Semiconductor Physics, National Academy of Sciences of Belarus, Minsk, 220072 Republic of Belarus*

[b]*Institute of Physics, Polish Academy of Sciences, Warsaw, PL-02-668 Poland*

**e-mail: truhanov@ifttp.bas-net.by*

Received June 24, 2002

Abstract—An experimental investigation is performed of the crystal structure and magnetic and electrical properties of anion-deficient compositions of $La^{3+}_{1-x}Ba^{2+}_xMn^{3+}O^{2-}_{3-x/2}$ ($0 \le x \le 0.30$) which do not contain manganese ions of different vacancies. It is found that all reduced samples are single-phase perovskites with *O*-orthorhombic ($x = 0$, 0.05), rhombohedral ($x = 0.10$, 0.15, 0.20, 0.25), and cubic ($x = 0.30$) symmetry of the unit cell. It is observed that systems of the compounds being treated experience a transition from a weakly ferromagnetic ($x = 0$) to a nonuniform ferromagnetic ($0 \le x \le 0.10$) state. An increase in the degree of nonstoichiometry with respect to oxygen leads to the emergence of the antiferromagnetic orbitally disordered phase. For compounds with $x > 0.20$, clearly defined properties are observed that are characteristic of cluster spin glass with the freezing temperature of magnetic moments $T_F \sim 45$ K. The maximal amount of the ferromagnetic component is registered for $x = 0.15$. All of the reduced samples are semiconductors. As the substitution level increases, the electrical resistivity (at room temperature) first decreases in magnitude ($0 \le x \le 0.15$) and then increases ($x > 0.15$). The magnetoresistance of all reduced samples increases gradually upon transition to a magnetically ordered state and reaches its maximal value at the liquid nitrogen temperature. A hypothetical magnetic phase diagram is constructed for the system of anion-deficient compositions of $La^{3+}_{1-x}Ba^{2+}_xMn^{3+}O^{2-}_{3-x/2}$ ($0 \le x \le 0.30$) being treated. The investigation results contribute to understanding the nature of 180-degree indirect superexchange interactions between ions of trivalent manganese. It is assumed that the Mn^{3+}–O–Mn^{3+} superexchange interactions are negative in the orbitally disordered phase in the case of pentahedral coordination of Mn^{3+} ions. © *2003 MAIK "Nauka/Interperiodica".*

1. INTRODUCTION

Substituted $Ln_{1-x}D_xMnO_3$ manganites with a perovskite structure (Ln = La, Pr, Nd, etc., and D = Ca, Sr, Ba, etc.) have been attracting the attention of researchers for well over 50 years [1]. Compounds of this type exhibit unique correlations between the chemical composition, crystal structure, and magnetic and electrical properties [2]. The early investigations of these materials were caused by the need for development and use of dielectric ferromagnets of high spontaneous magnetization for high-frequency applications, and later investigations were performed to study and use the so-called "colossal" magnetoresistance (CMR) revealed in substituted manganites in the early 1990s [3]. Although the nature of the physical processes occurring in manganites is still unclear, even today these compounds find wide application. They are used in magnetic recording for recording and readout, as solid electrolytes of fuel cells, as catalysts, and as magnetic field sensors [4–6].

The conditions of preparation and magnetic and electrical properties of ceramic samples in a series of solid solutions of $La_{1-x}D_xMnO_3$ (D = Ca, Sr, Ba) were first reported by Jonker and Van Santen [1]. They observed a correlation between the electrical conductivity and magnetization during substitution of bivalent alkaline-earth ions for lanthanum manganite. It was found that, in the calcium concentration range of $0.20 \le x \le 0.50$, this compound becomes ferromagnetic and exhibits metallic conduction at temperatures below the Curie point. The magnetoresistance and other transport properties for manganites were first described by Volger [7], who demonstrated that the magnetoresistance of $La_{0.8}Sr_{0.2}MnO_3$ is negative with a peak somewhat below T_C. Searle and Wang [8] were the first to investigate the magnetic transport properties of single crystals of a $La_{1-x}Pb_xMnO_3$ ($0.20 \le x \le 0.44$) system. They revealed metallic conduction below T_C and a significant negative magnetoresistance of about 20% in a field of 1 T.

The initial compound $LaMnO_3$ is an antiferromagnetic semiconductor with a magnetic structure of the *A* type [9]. A weak ferromagnetic component arises as a result of Dzyaloshinsky–Moriya interactions. The Neél temperature for this compound is approximately

140 K. The presence of Jahn–Teller Mn^{3+} ions with the electronic configuration $t_{2g}^3 e_g^1$ ($S = 2$), which enter into stoichiometric $La^{3+}Mn^{3+}O_3^{2-}$, causes the so-called *O*'-orthorhombic symmetry of the unit cell of this compound. The substitution of Ca^{2+} ions for La^{3+} ions leads to the emergence of Mn^{4+} ions with the electronic configuration t_{2g}^3 ($S = 3/2$). With the concentration of substituent ions of $x \sim 0.10$, a transition is observed from the *O*'-orthorhombic symmetry of the unit cell to the *O*-orthorhombic symmetry, which is explained by the removal of cooperative static Jahn–Teller distortions [10]. At $x = 0.20$, a significant increase is observed in spontaneous magnetization and in the magnetic ordering temperature, as well as a transition to metallic conduction below T_C.

Barium-substituted manganites are studied much less than compounds substituted by calcium and strontium ions. This is partly due to the difficulty of preparing quality samples in a concentration range of substituent ions [11]. In the case of calcium, a complete series of solid solutions is produced by synthesis in air, while in the case of strontium, the range of solubility is limited to $x = 0.70$. In order to obtain a complete series ($0 \le x \le 1$) of solid solutions with strontium, a reducing medium is required in which the synthesis must be performed [12]. The solubility limit for barium ions was found to be $x = 0.45$ [13]. This is due to the tendency of manganese ions to pass to a tetravalent state by forming hexagonal $Ba^{2+}Mn^{4+}O_3^{2-}$ in air. The uniform series of manganites substituted by barium ions was recently extended to $x = 0.50$ [14] using two-stage redox synthesis. Moreover, a similar method was used to prepare single-phase $La_{1/3}Ba_{2/3}MnO_3$ perovskite, which has an orthorhombic symmetry of the unit cell and exhibits the metal–insulator transition at 230 K [15].

Of other manganites, the Ba-substituted ones attract attention because they have a Curie point above room temperature; for example, for $La_{0.65}Ba_{0.35}MnO_3$, we have $T_C = 362$ K with a peak of magnetoresistance observed in the vicinity of this point. The high value of T_C is attributed to the large mean ionic radius in the *A* sublattice of the ABO_3 perovskite structure [16]. The phase transition temperatures close to room temperature render the materials being treated promising from the standpoint of their practical uses.

The basic theory explaining the properties of substituted manganites is the theory by Zener of the so-called double exchange [17, 18]. This theory is based on the real transition of an electron from a half-filled e_g-orbital of an Mn^{3+} ion to a free e_g-orbital of a Mn^{4+} ion. The double exchange mechanism favors ferromagnetism and a metallic type of conduction. A deviation from the stoichiometric composition with respect to oxygen causes a variation of the mean valency of manganese. The removal of a single ion of oxygen from the crystal lattice leads to the $2Mn^{3+} \longrightarrow 2Mn^{4+}$ transition. At $\gamma = x/2$, $Ln_{1-x}^{3+}A_x^{2+}Mn_{1-x+2\gamma}^{3+}Mn_{x-2\gamma}^{4+}O_{3-\gamma}^{2-}$ contains only Mn^{3+} ions. In view of the foregoing, it is of interest to investigate anion-deficient samples of $La_{1-x}^{3+}Ba_x^{2+}Mn^{3+}O_{3-x/2}^{2-}$, whose magnetic and electrical properties are defined by monovalent ions of Mn^{3+}.

2. EXPERIMENT

Ceramic compositions of $La_{1-x}^{3+}Ba_x^{2+}Mn_{1-x}^{3+}Mn_x^{4+}O_3^{2-}$ ($x = 0$, 0.05, 0.10, 0.15, 0.20, 0.25, 0.30) were prepared using the conventional ceramic technology. La_2O_3 and Mn_2O_3 oxides and, especially, pure carbonate $BaCO_3$ were weighed in the desired cationic ratio (Ln : Ba : Mn = $[1 - x]$: $[x]$: 1) and thoroughly mixed. The resultant mixtures were ground in an agate mortar with an addition of a small amount of ethyl alcohol. Prior to weighing, lanthanum oxide was annealed in air at 1000°C for 2 h to remove moisture and carbon dioxide. Preliminary roasting was performed in air at 1100°C for 2 h with subsequent grinding. The final synthesis was performed in air at 1550°C for 2 h. The chemical equation describing the preparation of compounds of initial compositions has the following form:

$$\left\{\frac{1-x}{2}\right\}La_2O_3 + xBaCO_3 + 0.50Mn_2O_3 \longrightarrow La_{1-x}Ba_xMnO_z + xCO_2\uparrow. \quad (1)$$

During synthesis, the samples were placed on a platinum substrate. In order to produce compositions with the oxygen content close to stoichiometric, the samples were quenched from 1000°C to room temperature. The X-ray analysis of the reaction products was performed using a DRON-3 diffractometer, under conditions of K_α radiation of Cr at room temperature at angles in the range of $30° \le 2\theta \le 100°$. A graphite monochromator was used for filtering out the K_β radiation of Cr. The oxygen content was determined by thermogravimetric analysis. According to our investigation results, the samples synthesized in air in the range of $0 \le x \le 0.15$ had an oxygen content somewhat above stoichiometric. The excess oxygen decreased gradually with the concentration of Ba ions from $\delta \sim 0.11$ ($x = 0$) to $\delta \sim 0$ ($x = 0.20$). Samples with $x = 0.25$ and 0.30 were stoichiometric with respect to oxygen.

Anion-deficient compositions of $La_{1-x}^{3+}Ba_x^{2+}Mn^{3+}O_{3-x/2}^{2-}$ ($x = 0$, 0.05, 0.10, 0.15, 0.20, 0.25, 0.30) were prepared by the method of topotactic reactions. The samples were placed into evacuated ($P \sim 10^{-4}$ Pa) quartz ampules along with a certain amount of metallic tantalum, which was used as an oxygen absorber. Quartz ampules were held at 850°C for 20 h with subsequent

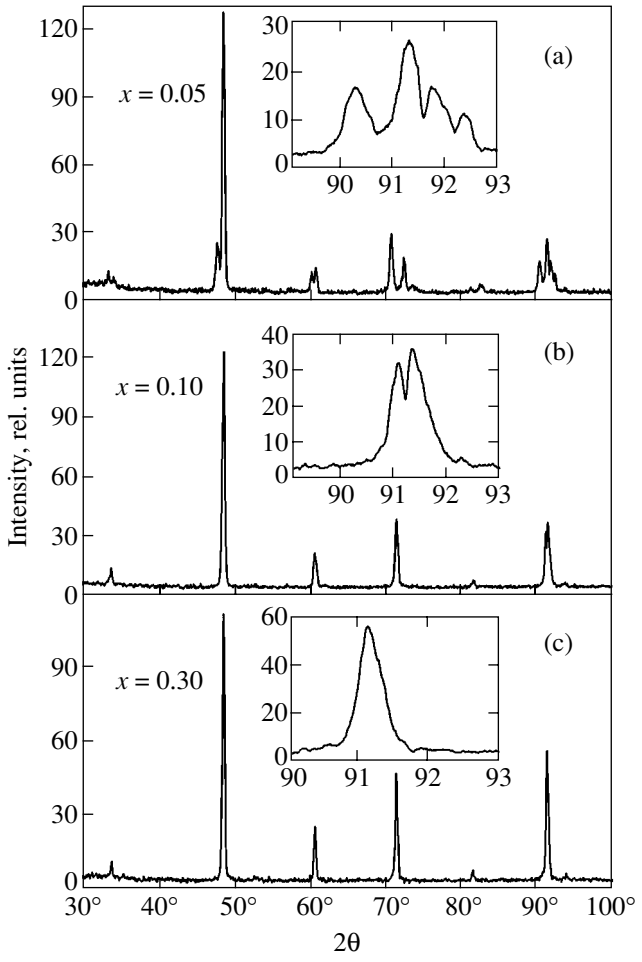

Fig. 1. Powder X-ray diffraction patterns at room temperature for $La_{1-x}Ba_xMnO_{3-x/2}$ compounds of anion-deficient compositions with $x = 0.05$ (a), 0.10 (b), 0.30 (c). The insets demonstrate reflections of (a) 132 + 024 + 312 + 204, (b) $21\bar{1}$ + 211 + $\bar{2}11$, and (c) 211.

cooling to room temperature at a rate of 100 deg/h. The chemical equation of reduction is as follows:

$$La_{1-x}Ba_xMnO_{3+\delta} + \left\{\frac{2\delta + x}{5}\right\}Ta \longrightarrow La_{1-x}Ba_xMnO_{3-x/2} + \left\{\frac{2\delta + x}{10}\right\}Ta_2O_5. \quad (2)$$

The oxygen content for reduced samples was determined by weighing prior to and after reduction, by the variation of the mass. The chemical formula of reduced compounds may be written as $La_{1-x}Ba_xMnO_{3-x/2\pm0.01}$.

The magnetization was investigated using a commercially available OI-3001 vibrating-coil magnetometer in the temperature range from 4 to 300 K. The temperature dependence of magnetization was measured after cooling in a fairly weak magnetic field of 100 Oe (FC) and after cooling without a field (ZFC). The magnetic ordering temperature (T_{mo}) was defined as the temperature of the FC-magnetization derivative minimum (dM_{FC}/dT). The value of spontaneous magnetic moment (M_s) was determined by the field dependence by extrapolation to zero field. The electrical resistance was measured in samples sized $10 \times 2 \times 2$ mm by the standard four-point probe method in the temperature range from 77 to 300 K. The magnetoresistance was calculated in accordance with the formula

$$MR[\%] = \{[\rho(H) - \rho(0)]/\rho(0)\} \times 100\%, \quad (3)$$

where MR[%] is the negative isotropic magnetoresistance expressed in percent, $\rho(H)$ is the electrical resistivity in a magnetic field of 9 kOe, and $\rho(0)$ is the electrical resistivity in zero magnetic field. The direction of electric current coincided with the longer side of the samples. The magnetic field was applied in parallel with electric current in the sample.

3. EXPERIMENTAL RESULTS AND THEIR DISCUSSION

According to the results of X-ray analysis, all of the reduced samples of $La_{1-x}Ba_xMnO_{3-x/2}$ (x = 0, 0.05, 0.10, 0.15, 0.20, 0.25, 0.30) represent a single-phase product with a perovskite structure (Fig. 1). The parameters were calculated on the assumption of the following symmetries of the unit cell: *O*'-orthorhombic (*O*') for x = 0, 0.05); rhombohedral (*R*) for $0.10 \le x \le 0.25$; and cubic (*C*) for $x = 0.30$. The parameters are given in the table. According to Goodenough [19], the *O*'-orthorhombic symmetry is caused by the cooperative static Jahn–Teller effect. This effect is due to the presence of Jahn–Teller ions (for example, high-spin Mn^{3+} or Cu^{2+}) in equivalent crystallographic positions. As soon as the concentration of the Jahn–Teller ions becomes less than 90%, a transition is observed to the local dynamic Jahn–Teller effect and, along with that, to *O*-orthorhombic distortions of the unit cell. The true symmetry of the unit cell in the case of *O*'- and *O*-orthorhombic distortions is monoclinic [20]. However, we observed a transition to rhombohedral distortions at $x = 0.10$. It is known that the crystal lattice of perovskite may be distorted as a result of two factors, namely, (i) the inconsistency of the size of cations to the size of the pores they occupy and (ii) the Jahn–Teller effect. In the former case, the transition to a minimum of free energy is caused by cooperative rotation of oxygen octahedrons. In the latter case, distortions arise as a result of removal of electronic e_g levels of Jahn–Teller ions in the octahedral field of oxygen anions [4]. Therefore, it is possible that the size factor dominates over the Jahn–Teller factor for Ba-substituted manganites, and the concentration of oxygen vacancies $\gamma = 0.05$ is insufficient for removing Jahn–Teller distortions; as a result, the *O*' $\longrightarrow$ *R* transition is observed. It is interesting to note that, as the concentration of substituent ions

increases, a gradual decrease is observed in the specific (per cell) volume of the unit cell. It is known that La^{3+} and Ba^{2+} ions with a coordination number that is a multiple of 12 have effective ionic radii of 1.36 and 1.61 Å, respectively [21]. Consequently, the substitution of Ba^{2+} ions for La^{3+} ions must bring about an increase in the unit cell volume. However, a reduction of this volume is observed, which may be attributed to the decrease in the coordination number of Mn^{3+} ions and to the emergence of oxygen vacancies. The effective ionic radii of Mn^{3+} for the octahedral and pentahedral types of symmetry are 0.645 and 0.580 Å, respectively [21].

The $La_{0.95}Ba_{0.05}MnO_{2.98}$ sample exhibits an increase in the FC magnetization (Fig. 2) at a temperature below 150 K. This temperature is close to the Neél temperature and amounts to approximately 140 K for $LaMnO_3$. The ZFC and FC curves differ very strongly immediately below T_{mo}. The ZFC magnetization exhibits a small peak in the neighborhood of T_{mo} and, after that, is almost independent of temperature upon cooling. Such a behavior is possible in the case of a high magnetic anisotropy of the sample. The $La_{0.90}Ba_{0.10}MnO_{2.95}$ sample has T_{mo} = 153 K. The ZFC and FC curves come to differ from each other far below this temperature. The ZFC magnetization reaches its maximal value at the critical temperature T_C = 138 K and then decreases gradually. The transition to the paramagnetic state is quite abrupt, which is characteristic of magnetically homogeneous magnetic substances. The lowest temperature, T_{mo} = 124 K, is exhibited by the $La_{0.85}Ba_{0.15}MnO_{2.93}$ sample.

The $La_{0.80}Ba_{0.20}MnO_{2.90}$ compound (Fig. 3) is characterized by an abrupt decrease in the ZFC curve below T_{cr} = 60 K. The magnetic ordering temperature for this composition is 137 K. Such a behavior of the ZFC magnetization is characteristic of the process of gradual freezing of magnetic moments of randomly distributed clusters. However, the transition to the demagnetized state is rather abrupt. The most clearly defined properties of cluster spin glass are observed for the $La_{0.70}Ba_{0.30}MnO_{2.85}$ compound. The ZFC curve exhibits a sharp peak in the vicinity of 45 K. We take this temperature to be the freezing temperature T_{fr} of magnetic moments of clusters. For $La_{1-x}Ba_xMnO_{3-x/2}$ compositions with x = 0.25, 0.30, the transition to the paramagnetic state is very wide; therefore, we did not apply the standard procedure for determining T_{mo}.

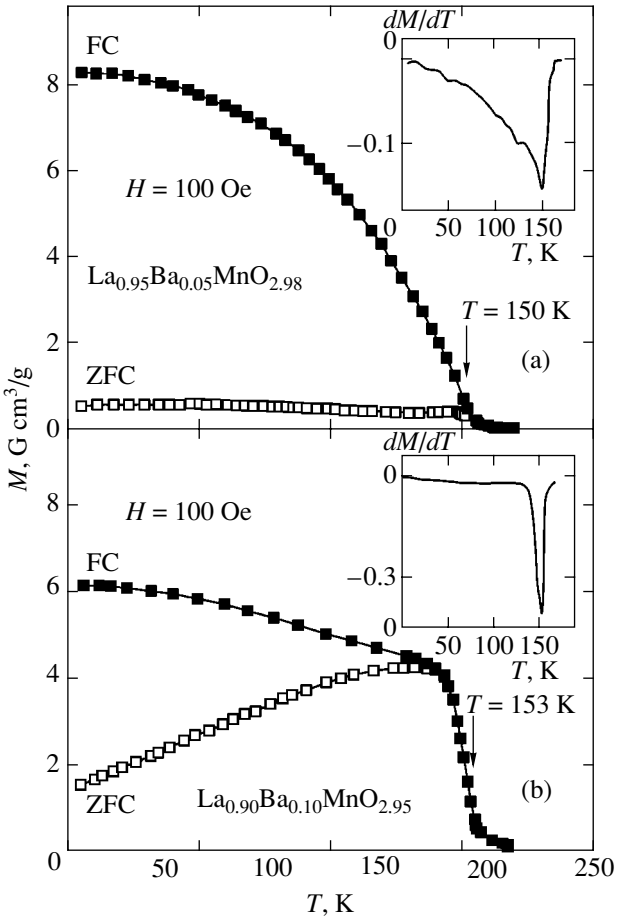

Fig. 2. Temperature dependence of ZFC (light symbols) and FC (dark symbols) magnetization in a magnetic field of 100 Oe for anion-deficient compositions of (a) $La_{0.95}Ba_{0.05}MnO_{2.98}$ and (b) $La_{0.90}Ba_{0.10}MnO_{2.95}$. The insets demonstrate the temperature dependence of the derivative of FC magnetization.

The type of symmetry and the unit cell parameters for samples of a $La_{1-x}Ba_xMnO_{3-x/2}$ ($0 \le x \le 0.30$) system of anion-deficient compositions

Compounds	Symmetry	*a*, Å	*b*, Å	*c*, Å	α	*V*, Å^3
$LaMnO_3$	*O*'-orthorhombic	5.537	5.749	7.692	–	244.72
$La_{0.95}Ba_{0.05}MnO_{2.98}$	*O*'-orthorhombic	5.524	5.675	7.802	–	244.58
$La_{0.90}Ba_{0.10}MnO_{2.95}$	rhombohedral	3.939	–	–	90.41°	61.13
$La_{0.85}Ba_{0.15}MnO_{2.93}$	rhombohedral	3.938	–	–	90.29°	61.09
$La_{0.80}Ba_{0.20}MnO_{2.90}$	rhombohedral	3.938	–	–	90.16°	61.07
$La_{0.75}Ba_{0.25}MnO_{2.88}$	rhombohedral	3.937	–	–	90.02°	61.03
$La_{0.70}Ba_{0.30}MnO_{2.85}$	cubic	3.937	–	–	–	61.02

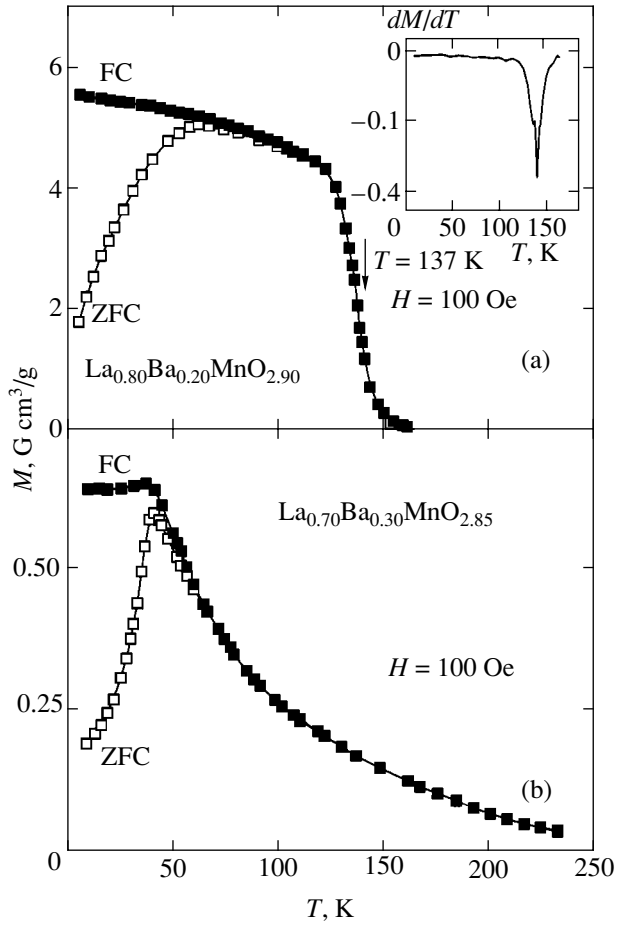

Fig. 3. Temperature dependence of ZFC (light symbols) and FC (dark symbols) magnetization in a magnetic field of 100 Oe for anion-deficient compositions of (a) $La_{0.80}Ba_{0.20}MnO_{2.90}$ and (b) $La_{0.70}Ba_{0.30}MnO_{2.85}$. The inset demonstrates the temperature dependence of the derivative of FC magnetization.

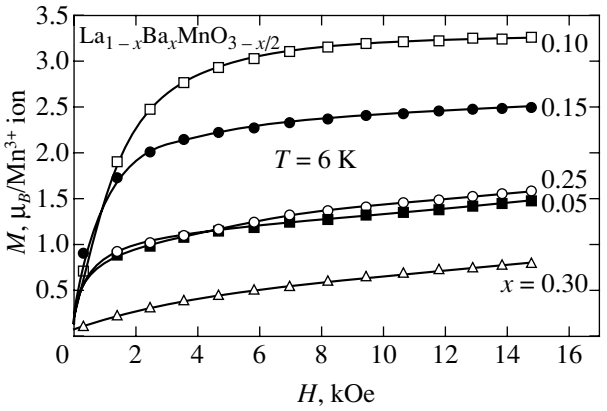

Fig. 4. Field dependences of magnetization at a temperature of 6 K, obtained in the decreasing field mode for anion-deficient compositions of $La_{1-x}Ba_xMnO_{3-x/2}$ with $x = 0.05$ (dark squares), 0.10 (light squares), 0.15 (dark circles), 0.25 (light circles), and 0.30 (light triangles).

Figure 4 gives the field dependence of magnetization at a temperature of 6 K, obtained in the decreasing field mode, for some reduced compositions of $La_{1-x}Ba_xMnO_{3-x/2}$. The magnetization is not saturated in fields of up to 16 kOe; therefore, it is quite difficult to determine the magnitude of spontaneous magnetic moment. The $La_{0.95}Ba_{0.05}MnO_{2.98}$ compound exhibits the M_s value equal to $0.81\mu_B/Mn^{3+}$ ion. It will be recalled that the M_s value of $4\mu_B$ corresponds to a fully ferromagnetic state (magnetic moment of Mn^{3+} ion). One can see in Fig. 4 that, as the level of substitution rises, M_s first increases to $3\mu_B/Mn^{3+}$ ion ($x = 0.10$) and then decreases to $0.20\mu_B/Mn^{3+}$ ion ($x = 0.30$).

The temperature dependences of electrical resistivity and magnetoresistance for reduced compositions of $La_{1-x}Ba_xMnO_{3-x/2}$ with $x = 0.05$, 0.10, 0.20, and 0.30 are given in Fig. 5. All samples exhibit resistivity of the activated type. No anomalies were observed on the curve of the dependence of electrical resistivity in the region of transition to the magnetically ordered state. As the level of substitution rises, the electrical resistivity at room temperature first decreases in magnitude to $x = 0.15$ and then gradually increases up to $x = 0.30$. The least value of electrical resistivity at room temperature is exhibited by the sample with $x = 0.15$, which is characterized by a significant ferromagnetic component. The magnetoresistance for all samples correlates with the absence of any anomalies of electrical resistivity in the vicinity of the temperature of transition to the magnetically ordered state and gradually decreases to reach its maximal value at liquid nitrogen temperature. Such a behavior of magnetoresistance is characteristic of granulated film systems and polycrystalline samples and is probably due to intergranular electric transport. A maximal value of magnetoresistance of about 34% is observed for the sample with $x = 0.30$.

The following reasoning helps us to understand the nature of the magnetic processes occurring in reduced samples of $La_{1-x}Ba_xMnO_{3-x/2}$. The double exchange may be realized in a system with mixed valency of manganese (Mn^{3+}/Mn^{4+}). The samples of the system being treated formally contain only Mn^{3+} ions. Therefore, we believe that for interpreting the magnetic properties, one must use the inferences of Goodenough's theory [22] for 180-degree indirect superexchange interactions. The Mn^{3+}–O–Mn^{3+} superexchange interactions are anisotropic in the orbitally ordered phase (positive in the (001) plane and negative along the [001] direction) but isotropic in the orbitally disordered phase (positive along all directions). As a result of realization of the Jahn–Teller effect, antiferrodistortion orbital ordering (ordering of d_{z^2} orbitals) is observed for $LaMnO_3$; therefore, the Mn^{3+}–O–Mn^{3+} superexchange interactions are antiferromagnetic. The small ferromagnetic component is defined by the antisymmetric

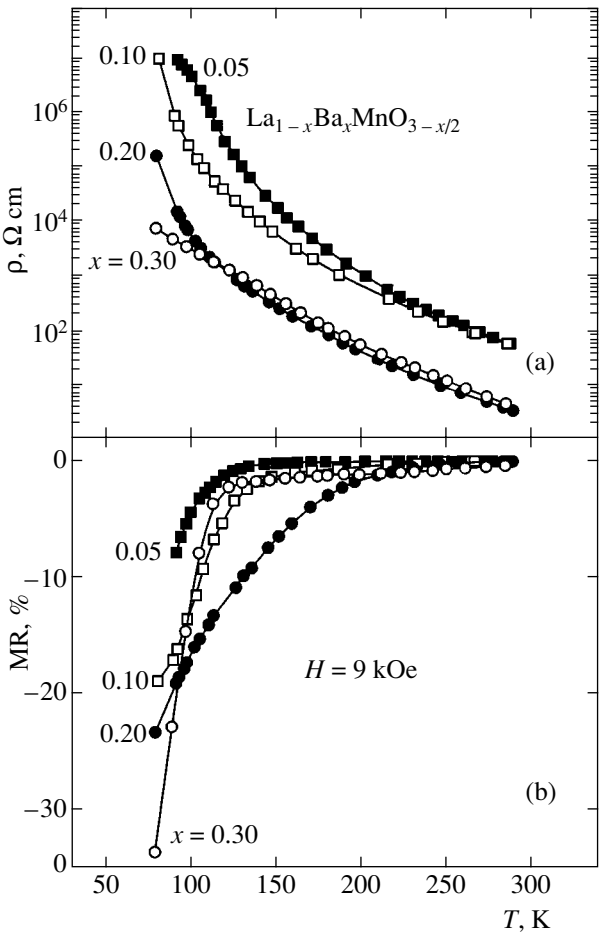

Fig. 5. (a) Electrical resistivity and (b) magnetoresistance in a field of 9 kOe as functions of temperature for anion-deficient compositions of $La_{1-x}Ba_xMnO_{3-x/2}$ with $x = 0.05$ (dark squares), 0.10 (light squares), 0.20 (dark circles), and 0.30 (light circles).

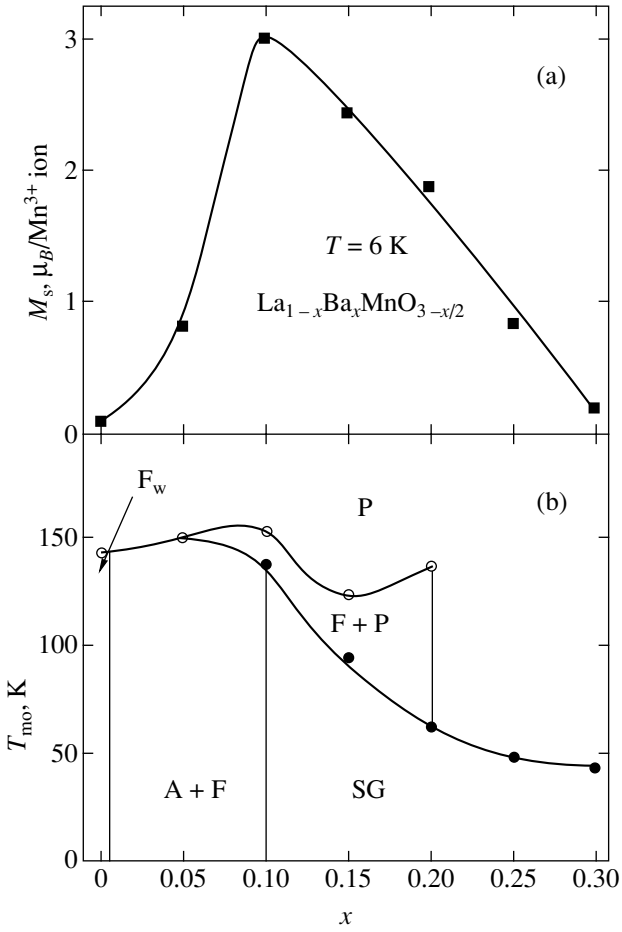

Fig. 6. (a) Spontaneous magnetization and (b) tentative magnetic phase diagram for a system of anion-deficient compositions of $La_{1-x}Ba_xMnO_{3-x/2}$ ($0 \le x \le 0.30$); F_w indicates a weakly ferromagnetic state, A + F indicates a nonuniform magnetic state representing a mixture of antiferromagnetic and ferromagnetic phases, SG indicates a state similar to cluster spin glass, F + P indicates a nonuniform magnetic state in the case of which short-range ferromagnetic correlations are observed, and P indicates the paramagnetic state. The light circles indicate the magnetic ordering temperature, and the dark circles indicate the critical freezing temperature of magnetic moments of clusters.

exchange of Dzyaloshinsky and Moriya [23]. In view of these facts, we can conclude that $LaMnO_3$ is a weak ferromagnet (Fig. 6). Information about the phase states of stoichiometric Ba-substituted manganites can be found in [1, 24–27]. As the concentration of substituent ions increases above the critical value $x \sim 0.1$, the cooperative static Jahn–Teller effect is gradually removed along with orbital ordering. Therefore, the reduced compounds in the $0 \le x \le 0.10$ range must exhibit an increase in the ferromagnetic component, as is observed experimentally. The removal of the cooperative static Jahn–Teller effect is further promoted by the emergence of oxygen vacancies [28]. The transition to ferromagnetism apparently proceeds via the non-single-phase magnetic state. The results of numerous investigations demonstrate that this possibility may be realized [29]. However, the process of decrease in the coordination of manganese ions is superimposed on the process of removal of orbital ordering. It is known that $Ca^{2+}Mn^{3+}O^{2-}_{2.50}$ with a perovskite-like structure, in which the Mn^{3+} ion is in pentahedrons, is an antiferromagnet [30, 31]. Therefore, it is reasonable to assume that the Mn^{3+}–O–Mn^{3+} superexchange interaction for pentahedral symmetry of manganese ions is antiferromagnetic, and the uniform ferromagnetic state for $0 \le x \le 0.10$ cannot be realized for yet another reason, namely, because of the emergence of oxygen vacancies (Fig. 6). We believe that the compounds in this region of compositions represent, from the magnetic standpoint, a mixture of antiferromagnetic (orbitally ordered and disordered) and ferromagnetic (orbitally disordered) phases. For $x > 0.10$, the volume of the antiferromagnetic orbitally disordered phase starts increasing significantly, which causes a reduction of spontaneous magnetic moment. The competition in interaction

between antiferromagnetically and ferromagnetically ordered clusters apparently leads to a state of the type of cluster spin glass with a gradually decreasing freezing temperature of magnetic moments of clusters. The possibility of this is demonstrated by a clearly defined peak on the curve of the temperature dependence of ZFC magnetization. The gradual decrease in T_{fr} is indicative of the decrease in the size of ferromagnetically ordered clusters. A state of the type of cluster spin glass is often observed in inhomogeneous magnetic systems such as granulated Co–Cu and Co–Ag films [32, 33]. In the systems, ferromagnetic granules are implanted in a nonferromagnetic matrix. A significant temperature interval below T_{cr}, where the ZFC curve almost coincide with FC curve for compositions with $0.10 \le x \le 0.20$, may be indicative of the existence of short-range ferromagnetic correlations during transition to a demagnetized state; i.e., the ferromagnetic ordering temperature is higher than the antiferromagnetic ordering temperature. For compositions with $0.20 < x \le 0.30$, the properties of cluster spin glasses are defined the most clearly.

A simple model may be suggested for interpreting the electric and magnetic transport properties. As the concentration of substituent ions increases, the volume of ferromagnetic clusters increases and brings about a simpler displacement of charge carriers, as expressed by the increase in resistivity for $x \le 0.15$. Outside the ferromagnetic clusters, the distribution of spins over directions is characterized by a lower degree of order than that within these clusters. As the volume of antiferromagnetic (orbitally disordered) phase for $x > 0.15$, the scattering of charge carriers by randomly distributed spins increases along with resistivity. In addition, one must take into account the intergranular effect. The diffusion coefficient for oxygen anions on the surface of granules is an order of magnitude higher than that for anions within the granules [34]; therefore, microdomains depleted in oxygen anions are formed on the surface of granules during reduction. It is known that, in the case of reduction, the size of granules is reduced and their number increases [35]. So, the reduction brings about predomination of the intergranular contribution to electric transport and to an increase in resistivity. The inference about the intergranular contribution to electric transport is further supported by the behavior of magnetoresistance. The application of external magnetic field causes an increase in the degree of order for spins outside ferromagnetic clusters. This brings about the emergence of magnetoresistance. Thus, the increase in the degree of order must be the higher, the lower the temperature and the lower the degree of order of spins before the application of magnetic field. For this reason, the maximal magnetoresistance is observed for a sample with the most clearly defined properties of cluster spin glass (with $x = 0.30$) at liquid nitrogen temperature.

4. CONCLUSION

We have performed an experimental investigation of the crystal structure and magnetic and electrical properties of anion-deficient compositions of $La_{1-x}Ba_xMnO_{3-x/2}$ ($0 \le x \le 0.30$) which do not contain different-valency ions of manganese. It has been found that all reduced samples are single-phase perovskites with *O'*-orthorhombic ($x = 0$, 0.05), rhombohedral ($x =$ 0.10, 0.15, 0.20, 0.25), and cubic ($x = 0.30$) symmetry of the unit cell. As the concentration of substituent ions increases, a gradual decrease in the specific volume of the unit cell is observed. It has been found that the compounds of the system being treated experience a transition from a weakly ferromagnetic ($x = 0$) to a nonuniform ferromagnetic ($0 < x \le 0.10$) state. An increase in the degree of nonstoichiometry with respect to oxygen leads to the emergence of the antiferromagnetic orbitally disordered phase. The competition between antiferromagnetic and ferromagnetic interactions brings about the state of cluster spin glass. For compounds with $x > 0.20$, clearly defined properties are observed that are characteristic of cluster spin glass with the freezing temperature of magnetic moments $T_{fr} \sim 45$ K. The maximal value of the ferromagnetic component is registered for the sample with $x = 0.10$. All of the reduced compounds are semiconductors. As the substitution level increases, the electrical resistivity of the samples first decreases in magnitude at room temperature ($0 \le x \le 0.15$) and then increases ($x > 0.15$). The magnetoresistance of all reduced samples increases gradually upon transition to a magnetically ordered state and reaches its maximal value at liquid nitrogen temperature. A hypothetical magnetic phase diagram is constructed for the system of anion-deficient compositions of $La_{1-x}Ba_xMnO_{3-x/2}$ ($0 \le x \le 0.30$) being treated. The experimental data may be interpreted using Goodenough's theory for 180-degree indirect superexchange interactions. It is assumed that the Mn^{3+}–O–Mn^{3+} superexchange interactions are negative in the orbitally disordered phase in the case of pentahedral coordination of Mn^{3+} ions.

ACKNOWLEDGMENTS

This study was supported in part by the Foundation for Basic Research of the Republic of Belarus (project no. F02M-069) and by the Committee of Science of the Polish Republic (KBN grant no. 5 PO3B 016 20).

REFERENCES

1. G. H. Jonker and J. H. van Santen, Physica (Utrecht) **16**, 337 (1950).
2. M. B. Salamon and M. Jaime, Rev. Mod. Phys. **73**, 583 (2001).
3. J. M. D. Coey, M. Viret, and S. von Molnar, Adv. Phys. **48**, 167 (1999).
4. E. L. Nagaev, Phys. Rep. **346**, 387 (2001).

5. D. Hawe, Sens. Actuators A **81**, 268 (2000).
6. Y. Xu, U. Memmert, and U. Hartmann, Sens. Actuators A **91**, 26 (2001).
7. J. Volger, Physica (Amsterdam) **20**, 46 (1954).
8. C. Searle and S. T. Wang, Can. J. Phys. **47**, 2703 (1969).
9. G. Matsumoto, J. Phys. Soc. Jpn. **29**, 606 (1970).
10. I. O. Troyanchuk, Zh. Éksp. Teor. Fiz. **102**, 132 (1992) [Sov. Phys. JETP **75**, 132 (1992)].
11. I. O. Troyanchuk, D. D. Khalyavin, S. V. Trukhanov, *et al.*, J. Phys.: Condens. Matter **11**, 8707 (1999).
12. K. Kikuchi, H. Chiba, M. Kikuchi, and Y. Syono, J. Solid State Chem. **146**, 1 (1999).
13. I. O. Troyanchuk, S. V. Trukhanov, D. D. Khalyavin, and H. Szymczak, J. Magn. Magn. Mater. **208**, 217 (2000).
14. B. Raveau, C. Martin, A. Maignan, and M. Hervieu, J. Phys.: Condens. Matter **14**, 1297 (2002).
15. S. L. Yuan, Y. Jiang, X. Y. Zeng, *et al.*, Phys. Rev. B **62**, 11347 (2000).
16. F. Millange, A. Maignan, V. Caignaert, *et al.*, Z. Phys. B **101**, 169 (1996).
17. C. Zener, Phys. Rev. **82**, 403 (1951).
18. P.-G. De Gennes, Phys. Rev. **118**, 141 (1960).
19. J. B. Goodenough, Phys. Rev. **100**, 564 (1955).
20. V. M. Loktev and Yu. G. Pogorelov, Fiz. Nizk. Temp. **26**, 231 (2000) [Low Temp. Phys. **26**, 171 (2000)].
21. R. D. Shannon, Acta Cryst. A **32**, 751 (1976).
22. J. B. Goodenough, A. Wold, R. J. Arnott, and N. Menyuk, Phys. Rev. **124**, 373 (1961).
23. I. Dzialoshinsky, J. Phys. Chem. Solids **4**, 241 (1958).
24. F. K. Lotgering, Philips Res. Rep. **25**, 8 (1970).
25. C. Roy and R. C. Budhani, J. Appl. Phys. **85**, 3124 (1999).
26. R. C. Budhani, C. Roy, L. Lewis, *et al.*, J. Appl. Phys. **87**, 2490 (2000).
27. H. L. Ju, Y. S. Nam, J. E. Lee, and H. S. Shin, J. Magn. Magn. Mater. **219**, 1 (2000).
28. I. O. Troyanchuk, S. V. Trukhanov, D. D. Khalyavin, *et al.*, Fiz. Tverd. Tela (St. Petersburg) **42**, 297 (2000) [Phys. Solid State **42**, 305 (2000)].
29. G. Allodi, R. De Renzi, G. Guidi, *et al.*, Phys. Rev. B **56**, 6036 (1997).
30. K. R. Poeppelmeier, M. E. Leonowicz, and J. M. Longo, J. Solid State Chem. **44**, 89 (1982).
31. K. R. Poeppelmeier, M. E. Leonowicz, J. C. Scanlon, *et al.*, J. Solid State Chem. **45**, 71 (1982).
32. S. Nafis, J. A. Woollam, Z. S. Shan, and D. J. Sellmyer, J. Appl. Phys. **70**, 6050 (1991).
33. F. Conde, C. Gomez-Polo, and A. Hernando, J. Magn. Magn. Mater. **138**, 123 (1994).
34. K. A. Thomas, P. S. I. P. N. de Silva, L. F. Cohen, *et al.*, J. Appl. Phys. **84**, 3939 (1998).
35. J. M. Gonzalez-Calbet, E. Herrero, N. Rangavittal, *et al.*, J. Solid State Chem. **148**, 158 (1999).

Translated by H. Bronstein

Journal of Experimental and Theoretical Physics, Vol. 96, No. 1, 2003, pp. 118–128.
From Zhurnal Éksperimental'noĭ i Teoreticheskoĭ Fiziki, Vol. 123, No. 1, 2003, pp. 137–148.

SOLIDS
Electronic Properties

Reconstruction of the 2D Hole Gas Spectrum for Selectively Doped *p*-Ge/$Ge_{1-x}Si_x$ Heterostructures¶

Yu. G. Arapov[a], G. I. Harus[a], V. N. Neverov[a], N. G. Shelushinina[a], M. V. Yakunin[a, *], and O. A. Kuznetsov[b]

[a] *Institute of Metal Physics, Russian Academy of Sciences, GSP-170, Yekaterinburg, 620219 Russia*
[b] *Scientific-Research Institute at Nizhni Novgorod State University, Nizhni Novgorod, Russia*
**e-mail: yakunin@imp.uran.ru*
Received July 22, 2002

Abstract—The magnetic field ($0 \le B \le 32$ T) and temperature ($0.1 \le T \le 15$ K) dependences of longitudinal and Hall resistivities have been investigated for *p*-$Ge_{0.93}Si_{0.07}$/Ge multilayers with different Ge layer widths $12 \le d_w \le 20$ nm and hole densities $p_s = (1–5) \times 10^{15}$ m^{-2}. An extremely high sensitivity of the experimental data (the structure of magnetoresistance traces, relative values of the inter-Landau-level gaps deduced from the activation magnetotransport, etc.) to the quantum well profile is revealed in the cases where the Fermi level reaches the second confinement subband. An unusually high density of localized states between the Landau levels is deduced from the data. Two models for the long-range random impurity potential (the model with randomly distributed charged centers located outside the conducting layer and the model of the system with a spacer) are used to evaluate the impurity potential fluctuation characteristics: the random potential amplitude, the nonlinear screening length in the vicinity of integer filling factors $\nu = 1$ and $\nu = 2$, and the background density of states (DOS). The described models are suitable for explanation of the observed DOS values, while the short-range impurity potential models fail. For half-integer filling factors, a linear temperature dependence of the effective quantum Hall effect plateau–plateau (PP) transition widths $\nu_0(T)$ is observed, contrary to the expected scaling behavior of the systems with short-range disorder. The finite $T \longrightarrow 0$ width of the PP transitions may be due to an effective low-temperature screening of a smooth random potential due to the Coulomb repulsion of electrons. © *2003 MAIK "Nauka/Interperiodica".*

1. INTRODUCTION

The *p*-type modulation-doped heterostructures on the basis of Si, Ge, and their alloys are of interest in device physics, in view of Si-based chip technology for fabrication of high-performance transistors, intrachip optical interconnects, and possible applications in fiber-optic telecommunications. Many quantum physical aspects could be foreseen in investigations of this heterosystem because of specific features of the valence band structure, which might be varied dramatically by the extent of the hole confinement and uniaxial stress arising from the lattice mismatch. Because the band offset in the Ge–Si heterosystem is almost entirely located in the valence band, the confinement of electrons is hardly achievable and 2D conductance is mainly due to holes.

Until now, the research has mostly been performed on Si side compounds, like the Si/$Si_{1-x}Ge_x$/Si quantum well (QW), to be best compatible with the Si substrate [1]. In this case, the hole conductivity is via the Si–Ge alloy. In this paper, we present the results obtained on a high-quality two-dimensional hole gas (2DHG) realized in the heterosystems on the Ge side, in the *p*-$Ge_{1-x}Si_x$/Ge heterostructures with a small amount of Si. In this case, the 2DHG is confined not in an alloy with randomly distributed Ge and Si atoms within the crystal lattice, but in a uniform Ge crystal layer, which works towards a decrease in the number of imperfections [2].

Much knowledge on the valence band properties can be obtained under conditions of its magnetic field quantization, especially in the case where it is spatially quantized in addition. Some information on the intricate Landau level (LL) structure of the valence band can be obtained from the quantum cyclotron resonance [2, 3]. This experiment yields distances between the adjacent levels positioned in each series on the opposite sides of the Fermi level. Similar probing of the LL diagram within its cut by the Fermi level can be realized by means of activation magnetotransport analysis under the quantum Hall regime. Distances between the adjacent LLs are then extracted irrespective of their classification in certain series because there are no restrictions due to optical selection rules. Moreover, a detailed scrutiny of the states distributed between the adjacent LLs can be achieved from scanning them by the Fermi level in experiments of this kind.

¶This article was submitted by the authors in English.

The analysis of temperature dependence of the Hall and longitudinal magnetoresistivity both in the plateau and in the plateau-plateau transition regions allows extracting such electron spectrum parameters as the energy separation between adjacent LLs, the relative fractions of localized and extended states, the density of localized states, and the width of extended state bands. Experimental reconstruction of the energy spectrum is especially important for *p*-type systems with a complex valence band spectrum, in which the LL picture is not determined by only the cyclotron energy with a given effective mass as for the *n*-type system with a simple parabolic conduction band.

2. EXPERIMENTAL TECHNIQUE

A series of multilayered *p*-$Ge_{1-x}Si_x$/Ge ($x \approx 0.07$) heterostructures differing in the Ge layer width in the range d_w = 12–20 nm and the hole density per single Ge layer $p_s = (1–5) \times 10^{15}$ m^{-2} were grown by hydride vapor deposition on the Ge(111) substrate. The undoped Ge buffer was grown first, followed by the undoped $Ge_{1-y}Se_y$ buffer and then by several undoped $Ge_{1-x}Si_x$/Ge periods and a certain number of periods with $Ge_{1-x}Si_x$ barriers doped symmetrically with boron in their central parts (having undoped spacers about 1/4 the barrier width on both sides of the barriers): see the inset in Fig. 2 below. The relation between the Si content in the buffer (*y*) and in the multilayers (*x*) predetermines the distribution of mismatch stress between the Ge and $Ge_{1-x}Si_x$ layers. The barriers are sufficiently wide to avoid inter-Ge-layer tunneling. The low-temperature hole mobilities are in the range 1–1.7 m^2/(V s). Double cross Hall bridges were fabricated by the photolithography and subsequent wet etching technique and contacts attached by thermocompression. Hall and longitudinal magnetoresistivities were measured on the dc current in normal magnetic fields up to 12 T in the steady regime and up to 32 T in ~10 ms pulses within the temperature range $0.1 \le T \le 15$ K.

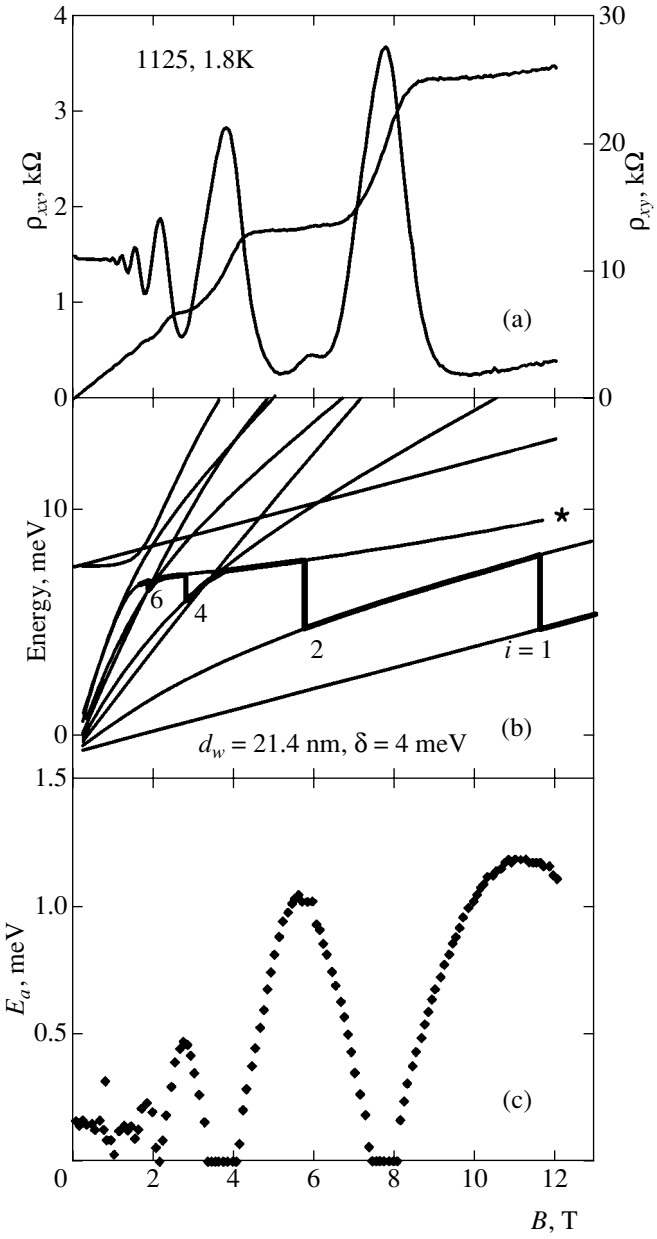

Fig. 1. Comparison of the calculated LL picture and the Fermi level motion (b) with the experimental recordings (a) and deduced activation energies (c) for sample 1125a$_7$. Mobility gaps are estimated from (c) as twice the maximum $E_a(B)$ values.

3. GENERAL PICTURE OF LANDAU LEVELS DEDUCED FROM THE QUANTUM HALL EFFECT

3.1. Manifestations of the Second Subband in $\rho_{xx}(B)$ and $\rho_{xy}(B)$ Experimental Traces

The simplest situation occurs for the narrowest Ge layers with the lowest hole densities. In this case, the QW profile approaches a rectangular shape and only the lowest confinement subband is filled with holes. Although the system of Landau levels in the valence band is rather complicated [4] due to heavy and light hole hybridization complemented by the effects of confinement and uniaxial stress (Fig. 1b), the experimental recordings of the longitudinal and Hall magnetoresistivities, $\rho_{xx}(B)$ and $\rho_{xy}(B)$, have a regular structure similar to that observed in a simple nondegenerate conduction band (Fig. 1a). The $\rho_{xy}(B)$ traces contain plateaus of the integer quantum Hall effect (QHE) at fundamental values $\rho_{xy} = h/ie^2$, with *i* an integer, concomitant with minima in $\rho_{xx}(B)$, both kinds of peculiarities being regularly spaced in the reciprocal magnetic field and monotonicallly damped with a decrease in the field. The peculiarities correspond to i = 1, 2, 4, 6, …; i.e., the even-numbered QH peculiarities dominate in weak fields. This is analogous to a simple conductivity band for small Zeeman splitting.

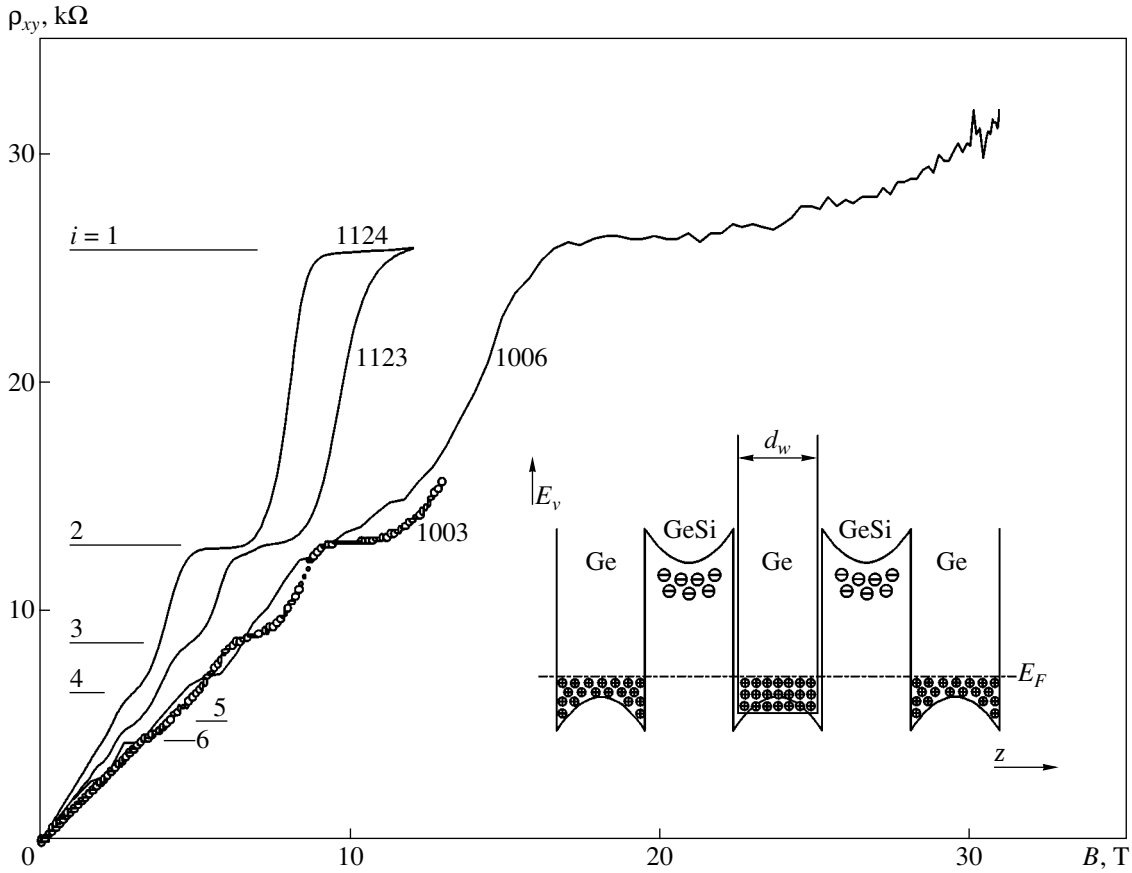

Fig. 2. Quantum Hall effect in different samples. Inset: a schematic valence band energy diagram of the samples studied.

Magnetoresistivities of an entirely different structure were detected for samples with wider Ge layers and higher hole densities [5]. In Figs. 2 and 3, the Hall and longitudinal magnetoresistivities are depicted for the samples presented in the table. For the longitudinal magnetoresistivity, the amplitudes of the traces are normalized to the highest peak and in their positions are normalized by scaling them versus the inverse filling factor $\nu = p_s h/eB$. The common feature of these five samples is that, in spite of different QW widths and hole densities, their traces contain plateaus in $\rho_{xy}(B)$ and concomitant $\rho_{xx}(B)$ minima for $i = 1$ and 2. But the structures of these curves differ significantly below the plateau with $i = 2$.

For samples 1006, 1124, and 1125, the plateau with $i = 4$ comes next on the low-field side after the plateau with $i = 2$ and the other even-numbered plateaus dominate. For the other two samples, 1123 and 1003, the plateau with $i = 3$ comes next after the one with $i = 2$, the plateau with $i = 4$ is missed, and the odd numbered plateaux dominate. These features are even more pronounced in the $\rho_{xx}(B)$ curves (Fig. 3). To explain this, we have calculated the Ge valence band energy spectra quantized by both the magnetic field and the confinement. The model of an infinitely deep rectangular well was used [4]. Examples of these calculations are presented in Figs. 1b and 4. The behavior of the Fermi level is presented for extremely sharp LLs and constant total hole densities.

The calculations show that, in sample 1006, the Fermi level moves within the ground confinement sub-

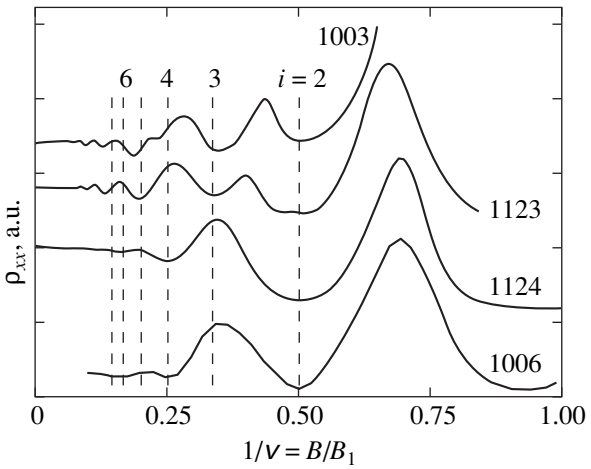

Fig. 3. Longitudinal magnetoresistivity of the samples shown in Fig. 2 scaled versus the inverse filling factor.

band. Its levels are grouped in pairs, similarly to the LL picture for the conduction band with a small spin splitting. This is why the even-numbered peculiarities dominate here.

Upon lowering the magnetic field, the Fermi level approaches the lowest LL of the second subband (the level marked with "*" in Figs. 1b and 4). In samples 1124 and 1125, it enters this LL, but this event does not lead to significant changes in the experimental recordings (Figs. 1a, 1b).

The degree of the second subband involvement increases with $p_s d_w^2$, and the samples in the table are sorted in rows according to this parameter. As follows from the calculations (Fig. 4), the value $p_s d_w^2 \approx 1.9$ for sample 1123 is sufficient for the Fermi level to rather deeply penetrate the second subband; as a result, a single step for $i = 2$ in the Fermi level motion between the ground subband LLs is divided into two steps with $i = 2$ and $i = 3$. This is how the $i = 3$ peculiarity arises in the experimental data.

Another consequence of the embedding of the additional level is that step no. 4 for sample 1123 no longer corresponds to the transition at the distance of about the cyclotron energy between the orbitally split spin couples of the ground subband; instead, it corresponds either to the transition onto this additional level or, if the embedded level is lower than the Fermi level, to the transition within the spin split couples. In the latter case, the numbers of observed peculiarities, i.e., the corresponding integer filling factors, are merely shifted one unit higher because of an additional level emerging below the Fermi level (changing their numbers from even to odd). In both cases, the energy distance for the $i = 4$ peculiarity can become much smaller than the cyclotron energy, leading to its disappearance. The crucial role of the second confinement subband position relative to the Fermi level is therefore evident. On the other hand, this position is very sensitive to the width and the shape of the QW, which should be reflected in a high sensitivity of the structure of experimental curves to diverse changes in the system. Indeed, in sample 1003 with parameters not strongly different from those of sample 1123, a small peculiarity with $i = 4$ has been detected. In the inset in Fig. 4, we show the evolution of magnetoresistivity of sample 1123 with a tilt of the magnetic field from the normal to the sample plane. The tilt introduces some changes to the LL picture that revive the peculiarity with $i = 4$, initially absent.

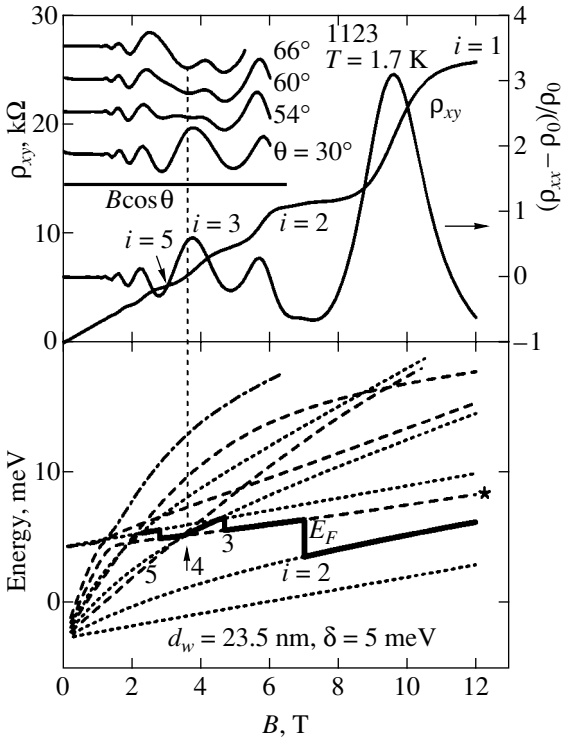

Fig. 4. Radical changes in the structure of QHE due to involvement of the second subband.

3.2. Activation Magnetotransport in the Quantum Hall Mobility Gaps

It is now commonly accepted that the existence of quantized plateaus in the $\rho_{xy}(B)$ dependences with vanishing values of ρ_{xx} is caused by the existence of disorder-induced mobility gaps in the DOS of a 2D system. When the Fermi level is settled down in the gap, the thermally activated behavior of ρ_{xx} (or σ_{xx}) is observed due to the excitation of electrons to the narrow band of extended states (with a width γ) near the middle of a disorder-broadened LL.

As a rule, it is assumed that the delocalized states have discrete energies $E = E_N$ separated by the (mobility) gap $\Delta \gg k_B T$, which leads to the expression [6–9]

$$\sigma_{xx} \propto \exp\left(-\frac{E_a}{k_B T}\right), \qquad (1)$$

where $E_a = |E_F - E_N|$. In the valence band of 2D Ge, a nonlinear dependence of LLs on the magnetic field results in the strong inequality $\Delta \gg k_B T$ is not valid even at fields as high as $B \approx 10$ T, and a more general expres-

Sample parameters

Sample	μ, m²/Vs	p_s, 10^{15} m^{-2}	d_w^*, nm	$p_s d_w^2$
1006-1	1.4	4.9	12.5	0.77
$1124b_3$	1.0	2.8	20 (21.4)	1.28
$1125a_7$	1.7	2.8	20 (22)	1.36
$1123a_6$	1.4	3.4	20 (23.5)	1.88
1003-2	1.5	4.8	22	2.32

* In brackets, we present the corrected values obtained from our analysis.

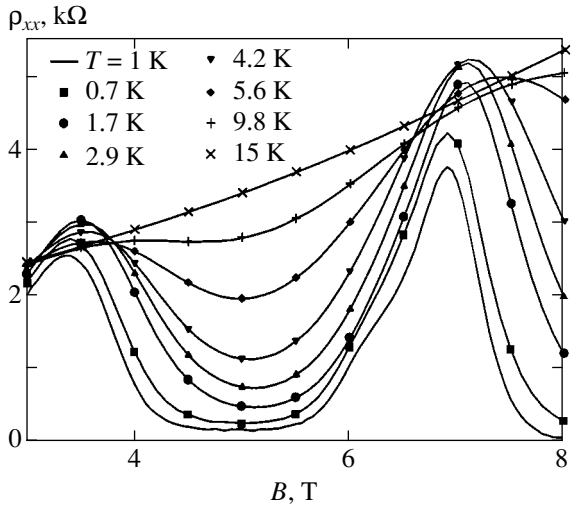

Fig. 5. Variations of the magnetoresistivity with the temperature.

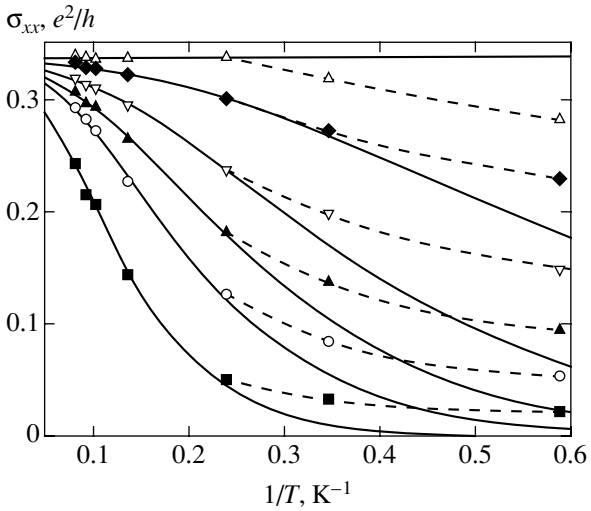

Fig. 6. Activation behavior of the conductivity: B = (△) 8, (◆) 8.2, (▽) 8.5, (▲) 8.8, (○) 9.2, (■) 11.2 T.

sion must be used for the temperature-dependent conductivity $\sigma_{xx}(T)$:

$$\sigma_{xx}(T) = \int \sigma(E) \frac{\partial f(E)}{\partial E} dE. \quad (2)$$

Here, $f(E)$ is the Fermi–Dirac distribution function, and $\sigma(E)$ is a partial conductivity at the energy E. For an extremely narrow band of delocalized states ($\gamma \ll k_B T$), Eq. (2) yields

$$\sigma_{xx}(T) = \sigma_0 \frac{\gamma}{k_B T} \frac{\partial f(E)}{\partial E}\bigg|_{E = E_a}, \quad (3)$$

where σ_0 is on the order of the minimal metallic conductivity.

In the structures investigated, the magnetoresistivity was measured (Fig. 5) and the thermally activated conductivity was found in the range T = (3–15) K for fixed values of B in the quantum Hall plateau regions (see Fig. 6). The solid curves correspond to expression (3) with E_a and γ as fitting parameters ($\sigma_0 = 0.5e^2/h$). Deviations of the experimental points from the calculated curves for $T < 3$ K (connected by lines as guides to the eye in Fig. 6) are explained by variable range hopping among localized states at E_F, which usually dominates for sufficiently low T.

The activation energy E_a is presented in Figs. 1c and 7 as a function of B or the filling factor ν in the vicinity of ν = 1, 2, and 4 for two of the investigated samples. The activation energy achieves its maximum value $E_a^{\max}$ at integer values of ν. The mobility gap width estimated as $\Delta = 2E_a^{\max}$ is close to the energy separation $\Delta \approx |E_N - E_{N'}|$ between the adjacent LLs within uncertainty on the order of γ. In a simple parabolic band, the activation energy for the integer filling factor corresponds to half the cyclotron energy, $E_a^{\max} \approx \hbar\omega_c/2$ [8, 9]. Because of a pronounced sublinearity in the B dependence of the valence band energy levels (Figs. 1b and 4) and the interference with the second subband levels, estimations of the cyclotron energy from the low-field Shubnikov–de Haas oscillations may strongly contradict the inter-LL distances obtained from the activation analysis in high fields. Thus, $\hbar\omega_c$ should be about 10 meV at B = 10 T for samples 1124 and 1125 with the value $m = 0.1m_0$ obtained from oscillations, while we have found Δ = (2.4–2.6) meV and Δ = (1.8–2.2) meV for ν = 1 and 2, respectively, from the activation conductivity.

Considering that the mobility gap corresponds to most of the inter-LL distance, leaving just an infinitesimal part for the stripe of delocalized states in the middle of LLs, the values of mobility gaps thus obtained can be compared with the calculated inter-LL distances. In comparison with a qualitative analysis of the structure of experimental magnetoresistivity traces described in the preceding paragraph, the activation analysis yields a quantitative tool to probe inter-LL distances.

An example of such an analysis for sample $1125a_7$ is presented in Fig. 1, where the steps in the Fermi level motion with the magnetic field due to jumps between the calculated LLs are juxtaposed with both the experimental recordings and the deduced activation energies. While a pronounced step in $E_F(B)$ indicates only the existence of QH peculiarities in $\rho_{xx}(B)$ and $\rho_{xy}(B)$, a quantitative analysis can be done on the basis of the deduced activation energies. Thus, we can note that if the entire process were developed in the first subband, then the i = 2 mobility gap would be about 30% wider than that for i = 1 (Fig. 1b). The ratio of the gap for i = 2 to that for i = 1 is reduced by fitting the obtained activation energies when the second confinement subband is

considered. We achieved the best coincidence for sample 1125 by taking the Ge layer width d_w = 21.4 nm, slightly higher than the nominal value of 20.0 nm.

Involvement of the second subband offers a possibility of explaining the difference between the activation energies in samples 1125 and 1124 with nominally similar parameters. For the latter sample, the ratio of the mobility gap for $i = 2$ to the one for $i = 1$ is about a quarter lower than for the former (Fig. 7, lower part). As seen from the quantized structure of the 2D Ge valence band in the upper part of Fig. 7, the decrease in the mobility gap ratio in sample 1124 may be explained by some lowering of the second subband (dashed lines for LLs and Fermi energy in Fig. 7) due to an increase in the Ge layer width. The necessary correction to the Ge layer width is small, from 21.4 to 22.0 nm, due to a strong (approximately quadratic) sensitivity of the second subband energy to the layer width.

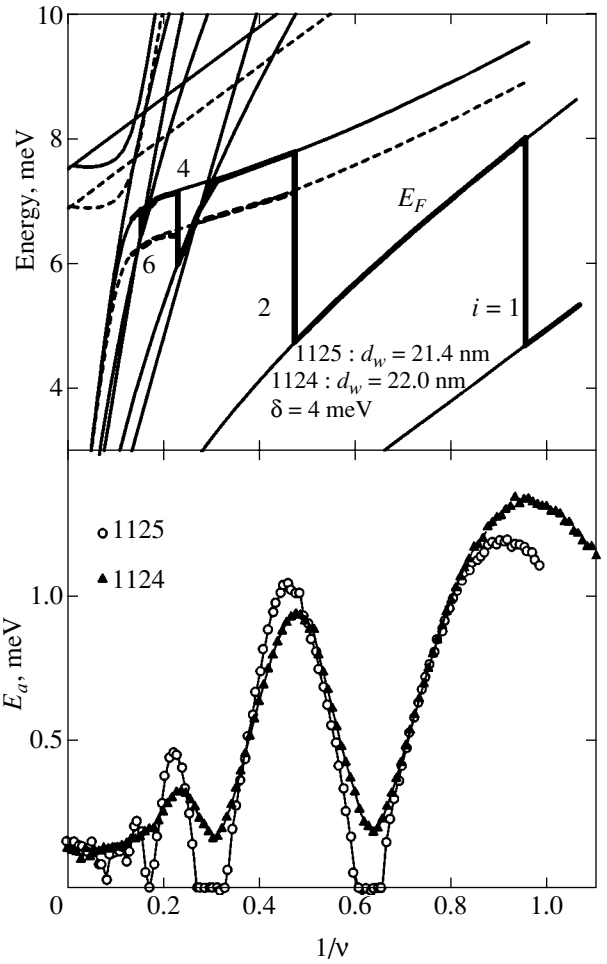

Fig. 7. Activation energies for sample 1125 compared with the data for sample 1124 (bottom) and explanation of the difference by the involvement of the second confinement subband (top: solid lines for 1125 and dashed lines for 1124).

4. SCANNING THE DENSITY OF STATES BETWEEN AND WITHIN THE LANDAU LEVELS

The nature of the QHE is known to be closely related to the electron localization phenomenon in 2D disorder systems in quantizing magnetic fields. For the QHE to exist, narrow bands of extended states must be present close to the center of each of the Landau subbands provided that all other states are localized [10, 11]. When the magnetic field values are in the plateau regions, the system is in the localized regime and the temperature dependence of the dissipative conductivity σ_{xx} (and the resistivity $\rho_{xx} \approx \sigma_{xx}/\sigma_{xy}^2$) has an exponential character, $\sigma_{xx}(T) \longrightarrow 0$ as $T \longrightarrow 0$ [7, 8]. If the magnetic field is in the plateau–plateau (PP) transition region, the Fermi level passes through the narrow strip of extended states at the Landau level center and the system behaves as a metal with nonzero conductivity as $T \longrightarrow 0$ and a peaklike form of the $\sigma_{xx}(B)$ dependence.

This section is organized as follows. The results for the QHE plateau regions are presented in Section 4.1, where the background density of localized states is evaluated from the analysis of activated magnetoresistivity. Two random impurity potential models are used for evaluation of the impurity potential fluctuation parameters, the random potential amplitude and the nonlinear screening length in the vicinity of integer filling factors (FFs), In Section 4.2, the data for the QHE PP transition regions are reported and the temperature dependence of the width of the extended state band is extracted and analyzed in terms of the theory of critical phenomena. The effect of the Coulomb interaction on smooth disorder potential screening is discussed.

4.1. The Density of States in the Mobility Gap

The DOS in mobility gaps can be evaluated from the data on the activation energy E_a as a function of the LL filling factor $\nu = n/n_B$ (where n is the electron density and $n_B = eB/hc$). The filling factor can be tuned by the change in either the carrier density [6] or the magnetic field [7–9]. We use the method of activated magnetoresistivity for the reconstruction of the 2D hole gas DOS under quantizing magnetic fields in the p-Ge/$Ge_{1-x}Si_x$ system. The DOS was calculated taking thermal activation of both electrons and holes on adjacent LLs into account [6, 12].

From the $E_a(B)$ dependences, the density of localized states in the mobility gap can be constructed as [8, 9]

$$g(E_F) = \left[\frac{dE_a(n)}{dn}\right]^{-1} = \frac{\nu e}{2\pi\hbar c}\left(\frac{dE_a(B)}{dB}\right)^{-1}. \qquad (4)$$

In Fig. 8, we show the typical results for the mobility gap DOS as a function of energy. Even in the middle of the gap, the density of localized states was found to have an unexpectedly high value, comparable to that for two filled confinement subbands without the magnetic

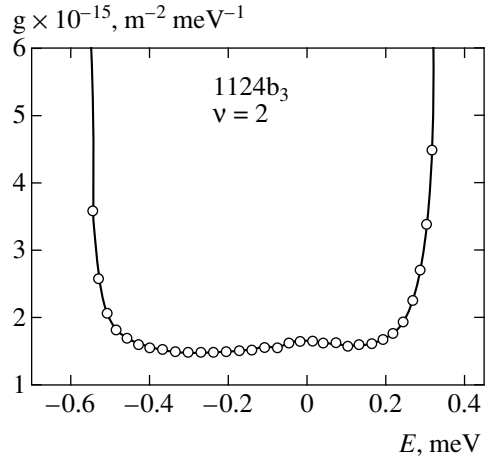

Fig. 8. The background density of states for sample 1124 as deduced from the activation energy; $E = 0$ corresponds to the middle of the energy interval between two LLs.

field, $g_0 = m/(\pi\hbar^2) \approx 1 \times 10^{15}$ m^{-2} meV^{-1}. Moreover, $g(E)$ is practically independent of E in the overwhelming part of the energy interval between adjacent LLs: $g(E) = g_c = (1–1.5) \times 10^{15}$ m^{-2} meV^{-1} for $\nu = 1$ and 2. This result is consistent with those obtained for AlGaAs/GaAs [8, 9] and InGaAs/InP [7] heterostructures and Si MOSFET structures [6] with *n*-type conductivity.

Because all the short-range impurity potential models lead to an exponential drop in the DOS between Landau levels, a clear picture of the DOS in the QHE regime can be presented only in terms of the long-range potential fluctuations in combination with the oscillating dependence of the DOS on the filling factor. This idea was advanced in the early work by Shklovskii and Efros [13] and was later developed in a series of works by Efros *et al.* (see [14, 15] and references therein). In a selectively doped heterostructure, the smooth random potential is formed by fluctuations in the concentration of remote impurities.

For a random potential $V(r)$, which is smooth at the scale of the magnetic length l_B, the localization in the QHE regime can be discussed in terms of semiclassical quantization and percolation [16]. In the semiclassical limit, the electron energy in the quantizing magnetic field can be written as

$$E_N(r_0) = \hbar\omega_c\left(N + \frac{1}{2}\right) + V(r_0), \qquad (5)$$

where r_0 is the oscillator center coordinate. A smooth potential therefore removes the degeneracy in r_0 and makes the LL energy dependent on spatial coordinates.

An order of magnitude evaluation of the spatial scale and amplitude of the random potential in p-Ge/Ge$_{1-x}$Si$_x$ heterostructures in the QHE regime can be obtained from the analysis of the mobility gap DOS. Two models for the random impurity potential were used.

(i) The model with randomly distributed charged centers located within a thick layer close to the 2D electron (hole) gas [13], for which the relation between the fluctuation amplitude F and scale L is

$$F(L) = \beta\frac{e^2\sqrt{NL}}{\kappa}, \qquad (6)$$

where β is a numerical coefficient ($\beta \approx 0.1$ [14]), N is the density of charged impurities (per volume), and κ is the static dielectric constant.

(ii) The model of the system with a spacer: a condenser with the 2D electron (hole) gas as one plate and randomly distributed charged centers as the other plate, separated by a distance d_s [14, 15]. In this case,

$$F(L) = \frac{e^2\sqrt{2\pi C}}{\kappa}\sqrt{\ln\frac{L}{2d_s}}, \qquad (7)$$

where C is the average impurity density (per area).

It can be seen from Eqs. (6) and (7) that, without screening, the amplitude F diverges at large L. When the filling factor is close to an integer (i), a very small concentration of electrons $\delta n \ll n_B$ can be redistributed in space, and so-called nonlinear screening [13–15] occurs ("threshold" screening [17]). For $\nu = i$ exactly, the screening is realized only due to electrons and holes induced by an overlap of the adjacent fluctuating Landau levels, and the random potential amplitude is therefore on the order of the corresponding LL gap.

For the investigated heterostructures, $N \approx 10^{23}$ m^{-3} ($C = Nd_a \approx 10^{15}$ m^{-2}) and the mean distance between impurities $N^{-1/3} \approx 20$ nm is comparable to both the width of 2D Ge layer $d_w \approx 20$ nm and the width of the doped part of the sample $d_a \approx 10$ nm. Thus, these models are not valid precisely, but are suitable to obtain a range of random potential parameter values.

In the nonlinear screening regime, the respective DOS in the middle of the mobility gap [13–15] of width $W \approx 2$ meV for the two models are given by

(i)

$$g\left(\frac{W}{2}\right) = \frac{4\beta e^2 N}{\kappa W^2} \approx 7.5 \times 10^{10}\ \text{cm}^{-2}\ \text{meV}^{-1}, \qquad (8)$$

(ii)

$$g\left(\frac{W}{2}\right) = \frac{2\sqrt{C}}{7Wd_s} \approx 9.5 \times 10^{10}\ \text{cm}^{-2}\ \text{meV}^{-1}. \qquad (9)$$

Without any fitting parameter, we therefore obtain a rather reasonable evaluation of the background DOS, and the two models yield values close to each other. For a random potential amplitude comparable to the mobility gap, $F \approx W$, we obtain the nonlinear screening length (the scale of optimum fluctuation) $L_c \approx 100$ nm for model (i) (see Eq. (6)) and $L_c \approx 40$ nm for model (ii)

(see Eq. (7)). We see that, in both cases, the spatial scale of fluctuations is substantially larger than the magnetic length ($l_B \approx 8$ nm at $B = 10$ T), and therefore, the random potential can indeed be regarded as a smooth one.

Therefore, order-of-magnitude evaluations of the random impurity potential parameters for the p-Ge/Ge$_{1-x}$Si$_x$ heterostructures indicate that, in the vicinity of integer filling factors $\nu = 1$ and $\nu = 2$ (i.e., in the regions of QHE plateaux), a sharp broadening of LL occurs. It is believed that, for a filling factor close to a half-integer (the regions of the plateau–plateau transition), the potential fluctuations must be small because of the effective (linear) electron screening [13–15].

4.2. The Width of the Extended State Band

The QHE regime can be regarded as a sequence of quantum phase insulator-metal–insulator transitions when the DOS of the 2D system in quantizing magnetic fields is scanned by the Fermi energy. In accordance with this concept, the transition regions between the adjacent QHE plateaux, as well as the widths of the appropriate $\rho_{xx}(B)$ peaks, must become narrower as the temperature approaches zero. In the theoretical framework of scaling (see, e.g., [18] and references therein), the width of the transition regions tends to zero as

$$\delta B_{i \to (i+1)} \propto T^{\kappa}, \qquad (10)$$

where $\kappa = 1/z\nu$, $\nu = 7/3$ is the critical index of localization length, and $z = 1$ is the dynamical critical index.

The pioneer experimental study on low-mobility InGaAs/InP heterostructures by Wei *et al.* [19] strongly supports the power-law behavior in Eq. (10). The evolution of the width of the ρ_{xx} peaks and of the inverse maximal slope of the ρ_{xy} steps, $(d\rho_{xy}/dB)^{-1}_{\max}$, as a function of the temperature, corresponds to (10) with a nearly universal value of the exponent $\kappa = 0.4 \pm 0.04$ for several LLs. The scaling behavior with $\kappa = (0.42–0.46)$ was later reported for the QHE plateau–plateau transition in GaAs/AlGaAs heterostructures [20] and in p-SiGe quantum wells [21] and for the QHE-to-insulator transition in GaAs/AlGaAs [20] and InGaAs/InP heterostructures [22].

In other series of experimental works, the universality of the exponent κ was questioned (see references in review article [16]). For instance, the measured values of κ increased from 0.28 to 0.81 with decreasing mobility in AlGaAs/GaAs heterostructures [23], or the values of κ between 0.2 and 0.65 were obtained for six subbands of Si MOSFETs [24].

In a recent work by Shahar *et al.* [25], a novel transport regime distinct from the critical scaling behavior was reported to exist asymptotically close to the transition at very low temperatures. Studying the QHE-to-insulator transition in a variety of GaAs/AlGaAs and InGaAs/InP samples at temperatures down to 70 mK,

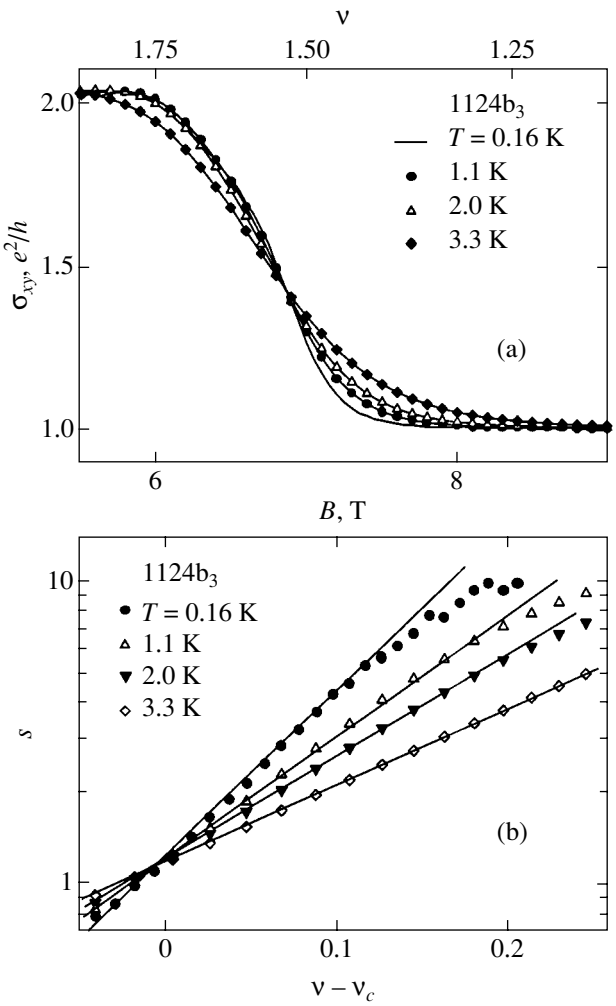

Fig. 9. Hall conductivity for sample 1124b$_3$ (a), plotted as a function of filling factor ν and scattering parameter s (b). The latter is derived from the σ_{xy} data shown in (a).

they found an exponential dependence of ρ_{xx} on the filling factor on both sides of the critical FF value ν_c ($\Delta\nu = |\nu - \nu_c|$),

$$\rho_{xx} = \exp(-\Delta\nu/\nu_0(T)), \qquad (11)$$

and emphasized that the effective transition width $\nu_0(T)$ appears to vary as $\alpha T + \beta$ rather than exhibit the T^{κ} scaling behavior. This implies that, even at $T = 0$, the transition has a finite width unless a different conduction mechanism takes over at even lower temperatures. The authors noted that some of their In-GaAs/InP samples were from the same growth as the sample in [19] and that they also revised their own previous data for GaAs/AlGaAs samples [20].

To estimate the width of the band of delocalized states in our Ge/Ge$_{1-x}$Si$_x$ samples, we have analyzed the magnetoresistance data in the transition region between the first and the second QHE plateaux in two

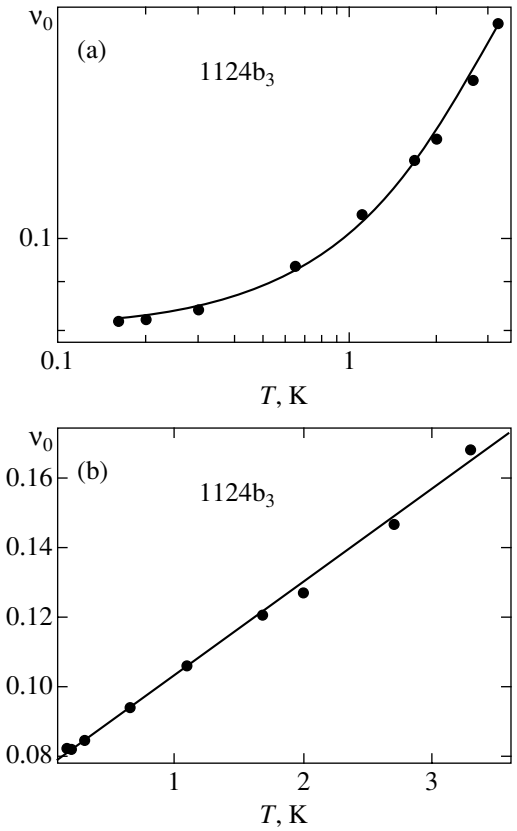

Fig. 10. (a) A log–log graph of $\nu_0(T)$ in Eq. (12) plotted against T. (b) The same as (a) plotted using a linear graph. Solid lines are the best fit.

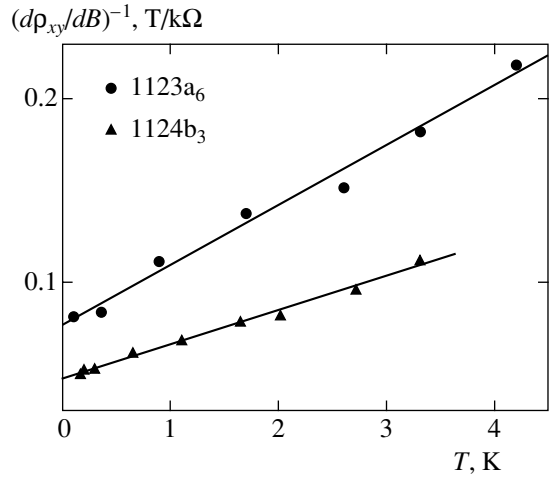

Fig. 11. The inverse maximum slope of $(d\rho_{xy}/dB)^{-1}_{\max}$ as a function of temperature for two samples 1123a$_6$ and 1124b$_3$.

ways. First, we used the description of $\sigma_{xy}(B)$ dependences in terms of the so-called scattering parameter [26]

$$s = \exp(-\Delta\nu/\nu_0(T)). \quad (12)$$

For the 1 ⟶ 2 plateau–plateau transition, the scattering parameter can be extracted as [21, 27]

$$\sigma_{xy} = 2 - s^2/(1 + s^2). \quad (13)$$

The other way that we used was to find the maximum slope of $(d\rho_{xy}/dB)_{\max}$ in a transition region and to draw its inverse in reliable units against the temperature as in [19].

In Figs. 9a and 9b, we show the $\sigma_{xy}(B)$ and $s(\nu)$ dependences for one of the investigated samples, 1124b$_3$. Figures 10a and 10b depict the $\nu_0(T)$ dependences extracted in accordance with Eq. (12) in a log-log graph and on a linear scale. It can be seen from Fig. 10a that the data cannot be satisfactorily described by a power law $\nu_0 \longrightarrow T^\kappa$ (it is not a straight line on the log–log plot). On the other hand, the data are much more compatible with the linear dependence

$$\nu_0(T) = \alpha T + \beta \quad (14)$$

with $\alpha = 0.076$, $\beta = 0.027$, and $\beta/\alpha = 2.8$ K (Fig. 10b).

Qualitatively, the frontal treatment of the data by the inverse maximum slope of $\rho_{xy}(B)$ yields the same but slightly less accurate result in Eq. (14) with $\beta/\alpha = 2.6$ K for sample 1124b$_3$ and $\beta/\alpha = 2.3$ K for sample 1123a$_6$ (Fig. 11).

As pointed out in [25], the ratio β/α defines a temperature T^* that is found to be characteristic of the material system. Thus, T^* turned out to be close to 0.5 K for InGaAs/InP samples and 50 mK for GaAs/AlGaAs samples [25]. It can be seen that the characteristic temperature is about 2.5 K (2.3–2.8 K) for Ge/GeSi samples studied here.

In the theoretical work by Pruisken *et al.* [28] and in the experimental work by van Schaijk *et al.* [22], it is emphasized that short-range random potential scattering is essentially important in studying scaling phenomena because the long-range potential fluctuations dramatically complicate their observability. In their opinion, the linear behavior ($\nu_0 = \alpha T + \beta$) is semiclassical in nature and should be observed at finite T and in samples with predominantly slowly varying potential fluctuations.

The simplest and most natural reason for the linear $\nu_0(T)$ dependence, namely, the thermal broadening of a quantum critical phase transition, is suggested and confirmed by calculations in the work by Coleridge and Zawadzki [27]. It is shown there that the thermal broadening not only yields a linear increase in $\nu_0(T)$ but also leads to a temperature-dependent increase in the σ_{xx} peak height as the temperature is lowered. This was observed in their experiment.

There is nothing about the temperature dependence of the ρ_{xx} (or σ_{xx}) peak value in the work by Shahar *et al.* [25]. But we observe a linear $\nu_0(T)$ dependence in Ge/GeSi samples within the temperature interval where the peak values of σ_{xx} undoubtedly decrease with low-

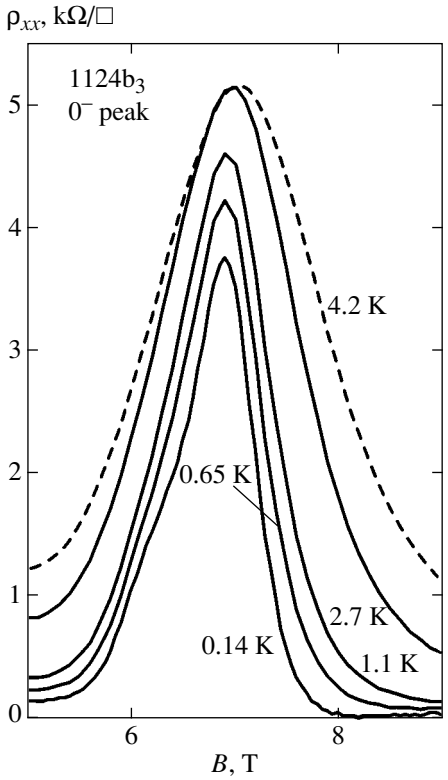

Fig. 12. The 0^- ρ_{xx}^{peak} value for sample 1124b$_3$ at different temperatures.

ering T (Fig. 12). Then, we are not in the conditions of thermal broadening, in contrast to the experiment in [27].

We believe that the answer to the main question about the finite width of QHE transitions as $T \longrightarrow 0$ can be found in the works treating the effect of Coulomb interactions on the screening of smooth disorder potentials [29–31]. The theory involves screening within the Thomas–Fermi approximation appropriate for a smooth disorder.

The effect of the electron—electron interaction manifests itself in that the regions of the third kind occur in the sample in addition to the local areas of filled and empty LLs present in the noninteracting system. The new "metallic" regions are those where the local electron density is between zero and that of the filled LL. The percolation description must then be revised because the metallic region percolates through the sample over a finite range of magnetic field near the critical value. We therefore expect the transition between Hall plateaus to have a finite width in filling factors even in the low-temperature limit.

It is notable that the value of $\nu_0(T \longrightarrow 0)$ gives an empirical estimate of the fraction of extended states in the total number of states per magnetic quantum level $n_B = eB/hc$.

We have $\nu_0(T \longrightarrow 0) = 0.08$ for the 0^- LL in sample 1124b$_3$ (see Fig. 10b). It can be seen that a tiny fraction of states are extended, i.e., most of them are localized, as they should be in the QHE regime.

5. CONCLUDING REMARKS

Scanning the quantized valence band of the Ge layers by the Fermi level in the quantum Hall regime yields opportunities to reconstruct the Landau level pattern of the band, including the levels at the bottom of the second confinement subband, to feel the shift of the second subband introduced by tiny changes in the QW profile. Furthermore, this experimental approach allows going beyond the model of delta-shaped LLs and investigating the distribution of localized and extended states throughout the entire LL picture in detail.

In selectively doped p-Ge/Ge$_{1-x}$Si$_x$ heterostructures investigated here, the main scattering mechanism for quasi-2D holes in Ge quantum wells at low temperatures is the scattering on remote ionized boron impurities located at Ge$_{1-x}$Si$_x$ barriers. The fluctuations in the density of randomly distributed remote impurities act as a source of the smooth disorder potential causing localization effects in the quantum Hall regime. Screening of this disorder assumes a very different character depending on the value of the filling factor. When the Fermi level is near the center of the Landau subband (half-integer filling factors), electrons are free to adjust their density and screening of random potential is good, but when it lies in the mobility gap between LLs (nearly integer filling factors), they cannot, and screening is poor.

We could explain the unusually high values of the background DOS obtained from the analysis of thermally activated magnetoresistance in the QHE plateau regions in the vicinity of $\nu = 1$ and $\nu = 2$ only in the framework of disorder potential, smooth at the scale of the magnetic length. In the models with nonlinear screening of a long-range random impurity potential, we obtain a reasonable estimate both for the density of localized states and for the spatial scale of potential fluctuation, which actually turns out to be rather large compared with the magnetic length.

On the other hand, for half-integer filling factors, the linear temperature dependence of the effective QHE plateau–plateau transition width $\nu_0(T) = \beta + \alpha T$ is observed in our Ge/Ge$_{1-x}$Si$_x$ samples in contrast to the scaling behavior inherent to systems with a short-range disorder. This result is in accordance with the data of recent experimental work [25] for other semiconductor systems. It is tempting to consider the finite width of the QHE transition, even as $T \longrightarrow 0$, as a consequence of an effective screening of smooth random potential due to the Coulomb repulsion of electrons [29–31].

ACKNOWLEDGMENTS

The work is supported by the Russian Foundation for Basic Research (project no. 02-02-16401, 01-02-17685, 02-02-06864, and 02-02-06168), INTAS YSF 01/1-156, and the 6th expert competition of the Russian Academy of Sciences (1999, no. 68).

REFERENCES

1. F. Schaffer, Semicond. Sci. Technol. **12**, 1515 (1997).
2. C. M. Engelhard, D. Toebben, M. Aschauer, *et al.*, Solid-State Electron. **37**, 949 (1994).
3. R. Winkler, M. Merkler, T. Darnhofer, and U. Rössler, Phys. Rev. B **53**, 10858 (1996).
4. Yu. G. Arapov, N. A. Gorodilov, V. N. Neverov, *et al.*, Pis'ma Zh. Éksp. Teor. Fiz. **59**, 247 (1994) [JETP Lett. **59**, 268 (1994)].
5. Yu. G. Arapov, V. N. Neverov, G. I. Harus, *et al.*, Fiz. Tekh. Poluprovodn. (St. Petersburg) **32**, 721 (1998) [Semiconductors **32**, 649 (1998)].
6. M. G. Gavrilov and T. V. Kukushkin, Pis'ma Zh. Éksp. Teor. Fiz. **43**, 79 (1986) [JETP Lett. **43**, 103 (1986)].
7. H. P. Wei, A. M. Chang, D. C. Tsui, and M. Rozeghi, Phys. Rev. B **32**, 7016 (1985).
8. D. Weiss, E. Stahl, G. Weiman, *et al.*, Surf. Sci. **170**, 285 (1986).
9. P. Svoboda, G. Nachtwei, C. Breitlow, *et al.*, cond-mat/9612053.
10. R. B. Laughlin, Phys. Rev. B **23**, 5632 (1981).
11. B. I. Halperin, Phys. Rev. B **25**, 2185 (1982).
12. Yu. G. Arapov, G. I. Harus, V. N. Neverov, *et al.*, Nanotechnology **11**, 351 (2000); cond-mat/0103343.
13. B. I. Shklovskiĭ and A. L. Éfros, Pis'ma Zh. Éksp. Teor. Fiz. **44**, 520 (1986) [JETP Lett. **44**, 669 (1986)].
14. A. L. Efros, Solid State Commun. **70**, 253 (1989).
15. A. L. Efros, F. G. Pikus, and V. G. Burnett, Phys. Rev. B **47**, 2233 (1993).
16. B. Huckestein, Rev. Mod. Phys. **67**, 357 (1995).
17. I. V. Kukushkin, S. V. Meshkov, and V. B. Timofeev, Usp. Fiz. Nauk **155**, 219 (1988) [Sov. Phys. Usp. **31**, 511 (1988)].
18. D. Liu and S. Das Sarma, Phys. Rev. B **49**, 2677 (1994).
19. H. P. Wei, D. C. Tsui, M. A. Paalanen, and A. M. M. Pruisken, Phys. Rev. Lett. **61**, 1294 (1988).
20. D. Shahar, D. C. Tsui, M. Shayegan, *et al.*, cond-mat/9611011.
21. P. T. Coleridge, cond-mat/9902103.
22. R. T. F. van Schaijk, A. de Visser, S. Olsthoorn, *et al.*, Phys. Rev. Lett. **84**, 1567 (2000); cond-mat/9812035.
23. S. Koch, R. J. Haug, K. von Klitzing, and K. Ploog, Phys. Rev. B **43**, 6828 (1991).
24. M. D'Iorio, V. M. Pudalov, and S. M. Semenchinsky, in *High Magnetic Fields in Semiconductor Physics*, Ed. by G. Landwehr (Springer-Verlag, Berlin, 1992), p. 56.
25. D. Shahar, M. Hilke, C. C. Li, *et al.*, Solid State Commun. **107**, 19 (1998); cond-mat/9706045.
26. D. H. Lee, Z. Wang, and S. Kivelson, Phys. Rev. Lett. **70**, 4130 (1993).
27. P. T. Coleridge and P. Zawadzki, Solid State Commun. **112**, 241 (1999).
28. A. M. M. Pruisken, B. Ščorić, and M. A. Baranov, Phys. Rev. B **60**, 16838 (1999); cond-mat/9807241.
29. S. Luryi, in *High Magnetic Fields in Semiconductor Physics*, Ed. by G. Landwehr (Springer-Verlag, Berlin, 1987).
30. A. L. Efros, Phys. Rev. B **45**, 11354 (1992).
31. N. R. Cooper and J. T. Chalker, Phys. Rev. B **48**, 4530 (1993).

Journal of Experimental and Theoretical Physics, Vol. 96, No. 1, 2003, pp. 129–139.
Translated from Zhurnal Éksperimental'noĭ i Teoreticheskoĭ Fiziki, Vol. 123, No. 1, 2003, pp. 149–160.

SOLIDS
Electronic Properties

Quantum Spin Liquid in the FCC Lattice

E. V. Kuz'min

Kirensky Institute of Physics, Siberian Division, Russian Academy of Sciences, Akademgorodok, Krasnoyarsk, 660036 Russia
e-mail: dir@iph.krasn.ru
Received January 26, 2002

Abstract—The properties of the spin system in the FCC lattice described by the Heisenberg model ($s = 1/2$) with antiferromagnetic interactions between the nearest neighbors were studied. It was shown within the framework of spin-wave theory that long-range antiferromagnetic order was absent because of frustration of exchange coupling and transverse quantum spin fluctuations. The system was in the quantum spin liquid state. A method for describing it within linear second-order theory with self-consistently calculated parameters was suggested. It was proved that the ground spin liquid state was singlet. The thermodynamic properties of the spin liquid in the whole temperature range and the character of spatial spin correlations, which had alternating signs and a finite correlation length, were determined. The theory was constructed based on the method of two-time Green temperature functions. © *2003 MAIK "Nauka/Interperiodica".*

1. INTRODUCTION: A CRITERION OF ANTIFERROMAGNETISM IN THE FCC LATTICE

A system of localized spins is described by the Heisenberg model with the Hamiltonian

$$H = -\frac{1}{2}\sum_{\mathbf{f},\mathbf{R}} J(\mathbf{R})\mathbf{s}_\mathbf{f}\cdot\mathbf{s}_{\mathbf{f}+\mathbf{R}}, \qquad J(\mathbf{R}) = J(-\mathbf{R}), \quad J(0) = 0, \tag{1}$$

defined on an ideal lattice with periodic boundary conditions. Here, $\mathbf{f}$ are the coordinates of lattice sites, $J(\mathbf{R})$ are the exchange integrals at intersite distance $\mathbf{R}$, and $\mathbf{R}$, $\mathbf{s}_\mathbf{f} = (s_\mathbf{f}^+, s_\mathbf{r}^-, s_\mathbf{f}^z)$ is the spin operator on site $\mathbf{f}$. For three-dimensional systems, Hamiltonian (1) is largely used to describe long-range magnetic order. The exact first-order equation of motion ($\hbar = 1$) is linearized (the Tyablikov splitting) as

$$i\dot{s}_\mathbf{f} \approx \sum_R J(\mathbf{R})(\langle s_{\mathbf{f}+\mathbf{R}}^z\rangle s_\mathbf{f}^+ - \langle s_\mathbf{f}^z\rangle s_{\mathbf{f}+\mathbf{R}}^+) \tag{2}$$

on the assumption that $\langle s_\mathbf{f}^z\rangle \neq 0$. Equation (2) is the base equation of spin-wave theory at various regular exchange $J(\mathbf{R})$ distributions and mean $\langle s_\mathbf{f}^z\rangle$ values. To describe collinear antiferromagnetic states, subsystems A ($N/2$ sites $\boldsymbol{\alpha}$ with spins "upward," N is the number of sites) and B ($N/2$ sites $\boldsymbol{\beta}$ with spins "downward") are introduced. We then have $\langle s_\boldsymbol{\alpha}^z\rangle = \bar{s}$, $s_\boldsymbol{\beta}^z = -\bar{s}$, where $\bar{s} = \bar{s}(T)$ and T is the temperature in energy units.

Of special interest is the FCC lattice with exchange antiferromagnetic interactions between the nearest neighbors: $J(\boldsymbol{\Delta}) = -J$, $J > 0$, where $\boldsymbol{\Delta}$ are the vectors connecting $z_1 = z = 12$ nearest neighbors. There are four types of ordering in the FCC lattice [1]. For any of them, frustrated (energetically unfavorable) exchange J-couplings always arise. For instance, for antiferromagnetic order of the first type characterized by alternating ferromagnetic xy planes with spins upward and downward, that is, antiferromagnetically coupled planes, all four J-couplings in these planes are frustrated. The remaining eight (interplanar) antiferromagnetic couplings are, however, normal, and the effective molecular field is $\pm 4J\bar{s}$ ("plus" sign for spins upward and "minus" for spins downward). Stabilizing such an antiferromagnetic structure requires taking into account at least ferromagnetic exchange between next-nearest neighbors, $J(\mathbf{a}) = K$, $K > 0$, where $\mathbf{a}$ are the vectors connecting $z_2 = 6$ next-nearest neighbors ($|\mathbf{a}| = a$ is the FCC lattice parameter, and $|\boldsymbol{\Delta}| = a/\sqrt{2}$).

Lines [2, 3] showed that antiferromagnetic order could only exist at $K \neq 0$ in a quantum spin system with Hamiltonian (1) in the FCC lattice. This conclusion is valid for the first ($K > 0$) and third ($K < 0$) types of ordering. In any event, the $\bar{s} = \bar{s}(\lambda)$ order parameter and the $T_N(\lambda)$ Neél temperature are functions of the $\lambda = |K|/J$ ratio and vanish at $\lambda = 0$ ($K = 0$). Apart from frustrations, this phenomenon is related to the substantial role played by transverse quantum spin fluctuations, which, at $\lambda = 0$, destroy long-range antiferromagnetic order. Note that the antiferromagnetic state "survives" in the system of classical spins [4, 5].

The conclusion on the absence of antiferromagnetic order at $K = 0$ also follows from work [6]. The authors considered a primitive cubic cell with antiferromagnetic interactions J_1 and J_2 for the nearest and next-nearest neighbors, respectively ($s = 1/2$), and intro-

duced the $p = J_2/(J_1 + J_2)$ parameter. At $J_1 = 0$, we nearly have the FCC spin lattice, and antiferromagnetic order is absent in this limit ($p = 1$).

To summarize, it follows from [2, 3, 6] that long-range antiferromagnetic order is absent in the FCC lattice for quantum spins with antiferromagnetic exchange J only between the nearest neighbors. What is the state of such a system? Below, we suggest the concept of a spin liquid.

2. QUANTUM SPIN LIQUID

We continue our consideration of a system with Hamiltonian (1) and total spin operator **S** taking into account antiferromagnetic exchange interactions J only between the nearest neighbors,

$$h = \frac{H}{zJ} = \frac{1}{2z}\sum_{\mathbf{f},\Delta}\mathbf{s}_\mathbf{f}\cdot\mathbf{s}_{\mathbf{f}+\Delta}, \quad \mathbf{S} = \sum_\mathbf{f}\mathbf{s}_\mathbf{f}, \quad s = \frac{1}{2}. \tag{3}$$

In the absence of stabilizing factors, there is no antiferromagnetic FCC lattice state. Let us therefore analyze the spin system with dimensionless Hamiltonian (3) as a quantum spin liquid.

We define the spin liquid as a system without symmetry loss and without long-range magnetic order in which

(1) spin correlation functions are isotropic,

$$\begin{aligned}\frac{1}{N}\sum_\mathbf{f}\langle s_\mathbf{f}^x s_{\mathbf{f}+\mathbf{r}}^x\rangle &= \frac{1}{N}\sum_\mathbf{f}\langle s_\mathbf{f}^y s_{\mathbf{f}+\mathbf{r}}^y\rangle \\ &= \frac{1}{N}\sum_\mathbf{f}\langle s_\mathbf{f}^z s_{\mathbf{f}+\mathbf{r}}^z\rangle \equiv \frac{1}{4}K_r,\end{aligned} \tag{4}$$

and only depend on the modulus of distance $r = |\mathbf{r}|$; in addition, $K_0 = 1$ (the sum rule);

(2) the mean values for an arbitrary spin component on lattice sites and for an arbitrary total spin operator component are zero,

$$\langle s_\mathbf{f}^\alpha\rangle = 0, \quad \langle S^\alpha\rangle = 0, \tag{5}$$

where $\alpha = x, y, z$ or $+, -, z$;

(3) the mean values of the products of spin operators on an odd number of different sites are zero,

$$\langle s_\mathbf{f}^\alpha s_\mathbf{m}^\beta s_\mathbf{n}^\gamma\rangle = 0, \quad \mathbf{f}\neq\mathbf{m}\neq\mathbf{n}. \tag{6}$$

Here and throughout, the symbol $\langle\ldots\rangle$ denotes thermodynamic averaging at temperature $\tau = T/zJ$ and over the ground state wave function at $\tau = 0$.

The whole collection of the properties of the spin liquid, namely, its ground state, the excitation spectrum, and the thermodynamic properties, should be described based on Hamiltonian (3) and postulates (4)–(6). Note that postulate (6) was introduced for the first time by this author in [7]; the corollaries to it will be considered below. It will be shown that the ground state is singlet and has a total spin of $S = 0$, which is equivalent to the equality

$$\langle\mathbf{S}^2\rangle_{\tau=0} = 0. \tag{7}$$

The properties of the spin liquid state are largely determined by the spatial and temperature dependences of the $K_r(\tau)$ spin correlation functions. The spin liquid state energy per bond in J units is

$$\varepsilon = \frac{\langle H\rangle}{(1/2)zNJ} = -\frac{3}{4}K_1, \tag{8}$$

where $K_{|\Delta|} = -K_1$ ($K_1 > 0$) is the correlator between the nearest neighbors.

To describe the state of the spin liquid, we use the Fourier transforms of the spin operators

$$s^\alpha(\mathbf{q}) = \frac{1}{\sqrt{N}}\sum_\mathbf{f} e^{i\mathbf{q}\cdot\mathbf{f}}s_\mathbf{f}^\alpha$$

(similarly for all the other operators), where vectors **q** belong to the first Brillouin zone of the FCC lattice, and we introduce the Fourier transform of the correlation function

$$\begin{aligned}K(\mathbf{q}) &= \sum_r e^{-i\mathbf{q}\cdot\mathbf{r}}K_r \\ &= 4\langle s^z(\mathbf{q})s^z(-\mathbf{q})\rangle = 2\langle s^+(\mathbf{q})s^-(-\mathbf{q})\rangle,\end{aligned} \tag{9}$$

$$K_r = \frac{1}{N}\sum_\mathbf{q} e^{i\mathbf{q}\cdot\mathbf{r}}K(\mathbf{q})$$

with the obvious property $K(\mathbf{q}) = K(-\mathbf{q})$. Calculations of $K(\mathbf{q})$ are performed by the method of two-time Green temperature functions [8]. Because the correlators are isotropic, it suffices to calculate the retarded commutator Green function

$$\langle\langle s^z(\mathbf{q})|s^z(-\mathbf{q})\rangle\rangle_\omega \equiv G(\mathbf{q},\omega), \tag{10}$$

where ω is the dimensionless spectral variable used to determine $K(\mathbf{q})$ by the spectral theorem,

$$\begin{aligned}\frac{1}{4}K(\mathbf{q}) &= \langle s^z(\mathbf{q})s^z(-\mathbf{q})\rangle = \int_{-\infty}^{\infty} J(\mathbf{q},\omega;\tau)d\omega, \\ J(\mathbf{q},\omega;\tau) &= \frac{e^{\omega/\tau}}{e^{\omega/\tau}-1}\left(-\frac{1}{\pi}\right) \\ &\times \operatorname{Im}\langle\langle s^z(\mathbf{q})|s^z(-\mathbf{q})\rangle\rangle_{\omega+i0},\end{aligned} \tag{11}$$

where $J(\mathbf{q},\omega;\tau)$ is the spectral intensity.

3. EQUATIONS OF MOTION AND THE GREEN FUNCTION OF LINEAR SECOND-ORDER THEORY

The theory of spin liquids is based on equations of an order not lower than second because $\langle s_{\mathbf{f}}^{\alpha} \rangle = 0$, and, in contrast to spin-wave theory, first-order equations can not be linearized. The exact equations of motion have the form ($\hbar = 1$)

$$\begin{aligned} i\dot{s}_{\mathbf{f}}^{+} &= \frac{1}{z}\sum_{\Delta}(s_{\mathbf{f}}^{z}s_{\mathbf{f}+\Delta}^{+} - s_{\mathbf{f}+\Delta}^{z}s_{\mathbf{f}}^{+}), \\ i\dot{s}_{\mathbf{f}}^{z} &= \frac{1}{2z}\sum_{\Delta}(s_{\mathbf{f}}^{+}s_{\mathbf{f}+\Delta}^{-} - s_{\mathbf{f}+\Delta}^{+}s_{\mathbf{f}}^{-}) \equiv M_{\mathbf{f}}, \end{aligned} \tag{12}$$

$$i\dot{M}_{\mathbf{f}} = -\frac{\partial^2 s_{\mathbf{f}}^{z}}{\partial t^2} = \frac{1}{2z^2}\sum_{\Delta}(s_{\mathbf{f}}^{z} - s_{\mathbf{f}+\Delta}^{z}) + R_{\mathbf{f}}, \tag{13}$$

where

$$\begin{aligned} R_{\mathbf{f}} &= \frac{1}{z^2}\sum_{\Delta\neq\Delta'}[s_{\mathbf{f}}^{z}s_{\mathbf{f}+\Delta}^{+}s_{\mathbf{f}+\Delta'}^{-} \\ &+ (s_{\mathbf{f}+\Delta-\Delta'}^{z} - s_{\mathbf{f}+\Delta'}^{z})s_{\mathbf{f}}^{+}s_{\mathbf{f}+\Delta}^{-} - s_{\mathbf{f}+\Delta}^{z}s_{\mathbf{f}}^{+}s_{\mathbf{f}+\Delta-\Delta'}^{-}]. \end{aligned} \tag{14}$$

The second-order equation takes into account the kinematic properties of the spin operators on one node.

Let us truncate the chain of linked equations at the second step by linearizing the $R_{\mathbf{f}}$ operator, which contains the products of the spin operators on three different nodes. We suggest the following linearization scheme:

$$\begin{aligned} s_{\mathbf{f}}^{z}s_{\mathbf{n}}^{+}s_{\mathbf{m}}^{-} &\approx s_{\mathbf{f}}^{z}\alpha_{|\mathbf{n}-\mathbf{m}|}\langle s_{\mathbf{n}}^{+}s_{\mathbf{m}}^{-}\rangle \\ &= \frac{1}{2}\alpha_{|\mathbf{n}-\mathbf{m}|}K_{|\mathbf{n}-\mathbf{m}|}s_{\mathbf{f}}^{z}, \quad \mathbf{f}\neq\mathbf{n}\neq\mathbf{m}, \end{aligned} \tag{15}$$

where $\alpha_{|\mathbf{n}-\mathbf{m}|}$ are the parameters that introduce corrections into the splitting (linearization). This scheme is a simple generalization of the linearization procedure applied in [6, 7, 9–11]. Using (15), we obtain

$$\begin{aligned} (R_{\mathbf{f}})_{\text{lin}} &= \frac{1}{2z^2}\sum_{\substack{\Delta,\Delta' \\ (\Delta\neq\Delta')}}[\alpha_{|\Delta-\Delta'|}K_{|\Delta-\Delta'|}(s_{\mathbf{f}}^{z} - s_{\mathbf{f}+\Delta}^{z}) \\ &+ \alpha_1 K_1(s_{\mathbf{f}+\Delta'}^{z} - s_{\mathbf{f}+\Delta'-\Delta}^{z})], \quad K_{|\Delta|} = -K_1. \end{aligned} \tag{16}$$

The sum over Δ' in the first term is

$$\begin{aligned} \tilde{K} &\equiv \frac{1}{z}\sum_{\substack{\Delta' \\ (\Delta'\neq\Delta)}}\alpha_{|\Delta-\Delta'|}K_{|\Delta-\Delta'|} \\ &= \frac{1}{12}(-4\alpha_1 K_1 + 2\alpha_2 K_2 + 4\alpha_3 K_3 + \alpha_4 K_4), \end{aligned} \tag{17}$$

where indices 1, 2, 3, and 4 denote the coordination zones with the corresponding $|\Delta - \Delta'|$ distances. The linearized $R_{\mathbf{f}}$ operator can now be written as

$$\begin{aligned} (R_{\mathbf{f}})_{\text{lin}} &= \frac{1}{2}\left[\left(\tilde{K} + \frac{\alpha_1 K_1}{z}\right)\frac{1}{z}\sum_{\Delta}(s_{\mathbf{f}}^{z} - s_{\mathbf{f}+\Delta}^{z})\right. \\ &\left. + \frac{\alpha_1 K_1}{z^2}\sum_{\Delta,\Delta'}(s_{\mathbf{f}+\Delta}^{z} - s_{\mathbf{f}+\Delta+\Delta'}^{z})\right], \end{aligned} \tag{18}$$

where the $\Delta' \neq \Delta$ restriction is removed in the second term.

The above transformations allow us to replace the exact equation (13) by the linearized one,

$$\begin{aligned} (i\dot{M}_{\mathbf{f}})_{\text{lin}} &= \left(-\frac{\partial^2 s_{\mathbf{f}}^{z}}{\partial t^2}\right)_{\text{lin}} \\ &= \frac{1}{2z^2}\sum_{\Delta}(s_{\mathbf{f}}^{z} - s_{\mathbf{f}+\Delta}^{z}) + (R_{\mathbf{f}})_{\text{lin}}, \end{aligned} \tag{19}$$

which, after the Fourier transform, takes the form

$$\begin{aligned} (i\dot{M}(\mathbf{q}))_{\text{lin}} &= \left(-\frac{\partial^2 s^{z}(\mathbf{q})}{\partial t^2}\right)_{\text{lin}} = \frac{1}{2}(1-\Gamma_{\mathbf{q}}) \\ &\times\left[\left(\tilde{K} + \frac{1+\alpha_1 K_1}{z}\right) + \alpha_1 K_1\Gamma_{\mathbf{q}}\right]s^{z}(\mathbf{q}) \equiv \Omega_{\mathbf{q}}^2 s^{z}(\mathbf{q}). \end{aligned} \tag{20}$$

Here,

$$\begin{aligned} \Gamma_{\mathbf{q}} &= \frac{1}{z}\sum_{\Delta}e^{i\mathbf{q}\cdot\Delta} = \frac{1}{3}(c_x c_y + c_x c_z + c_y c_z), \\ c_j &\equiv \cos\frac{q_j}{2}. \end{aligned} \tag{21}$$

Using the notation

$$\frac{\alpha_1 K_1}{2} \equiv \lambda^2, \quad \frac{\tilde{K} + (1+\alpha_1 K_1)/z}{\alpha_1 K_1} \equiv D, \tag{22}$$

we can write

$$\Omega_{\mathbf{q}}^2 = \lambda^2(1-\Gamma_{\mathbf{q}})(D+\Gamma_{\mathbf{q}}) \equiv \lambda^2 E_{\mathbf{q}}^2. \tag{23}$$

Applying the Fourier transform to equations of motion (12) and (13) yields the following equations for the Green functions:

$$\begin{aligned} \omega G(\mathbf{q},\omega) &= \langle\langle M(\mathbf{q})|s^{z}(-\mathbf{q})\rangle\rangle_{\omega}, \\ \omega\langle\langle M(\mathbf{q})|s^{z}(-\mathbf{q})\rangle\rangle_{\omega} &= A_{\mathbf{q}} + \langle\langle i\dot{M}(\mathbf{q})|s^{z}(-\mathbf{q})\rangle\rangle_{\omega}, \end{aligned}$$

where

$$A_{\mathbf{q}} = \langle [M(\mathbf{q}), s^z(-\mathbf{q})] \rangle = \frac{K_1}{2}(1-\Gamma_{\mathbf{q}}). \quad (24)$$

Using the $i\dot{M}(\mathbf{q}) \approx (i\dot{M}(\mathbf{q}))_{\text{lin}}$ approximation [see (20)], we obtain the Green function of linear second-order theory in the form

$$G(\mathbf{q}, \omega) = \frac{A_{\mathbf{q}}}{\omega^2 - \Omega_{\mathbf{q}}^2}. \quad (25)$$

Its spectral intensity (11) is

$$J(\mathbf{q}, \omega; \tau) = \frac{e^{\omega/\tau}}{e^{\omega/\tau}-1}\frac{A_{\mathbf{q}}}{2\Omega_{\mathbf{q}}} \times [\delta(\omega - \Omega_{\mathbf{q}}) - \delta(\omega + \Omega_{\mathbf{q}})], \quad \Omega_{\mathbf{q}} \geq 0. \quad (26)$$

By the spectral theorem, the one-time average is

$$\langle s^z(\mathbf{q}) s^z(-\mathbf{q}) \rangle \equiv \frac{1}{4}K(\mathbf{q}) = \int_{-\infty}^{\infty} J(\mathbf{q}, \omega; \tau) d\omega = \frac{A_{\mathbf{q}}}{2\Omega_{\mathbf{q}}} \coth\frac{\Omega_{\mathbf{q}}}{2\tau}$$

or

$$K(\mathbf{q}) = \frac{K_1}{\lambda}\frac{1-\Gamma_{\mathbf{q}}}{E_{\mathbf{q}}(D)} \coth\frac{\lambda E_{\mathbf{q}}(D)}{2\tau}. \quad (27)$$

Equation (27) shows that the suggested version of spin liquid theory contains three unknown parameters, which are functions of temperature, namely, the modulus of the correlator between the nearest neighbors $K_1(\tau)$, the "stiffness" parameter of the excitation spectrum $\lambda(\tau)$, and the pseudogap in the spectrum $D(\tau)$. All these parameters should be calculated self-consistently from three equations (see below). Note in advance that, because $-1/3 \leq \Gamma_{\mathbf{q}} \leq 1$ in the Brillouin zone of the FCC lattice, we can conveniently separate the limiting spectrum point (–1/3) and write the D parameter as

$$D = 1/3 + \delta, \quad \delta = \delta(\tau) \geq 0, \quad (28)$$

which is necessary for satisfying the $\Omega_{\mathbf{q}} \geq 0$ or $E_{\mathbf{q}}(\delta) \geq 0$ condition.

4. THE SELF-CONSISTENCY EQUATION

Using the definition of spatial correlators K_r [Eq. (9)], we obtain the system of equations

$$K_0 = 1 = \frac{1}{N}\sum_{\mathbf{q}} K(\mathbf{q}) = \frac{K_1}{\lambda} I_0(\delta, \tau),$$

$$K_1 = \frac{1}{N}\sum_{\mathbf{q}} (-\Gamma_{\mathbf{q}}) K(\mathbf{q}) = \frac{K_1}{\lambda} I_1(\delta, \tau), \quad (29)$$

$$K_{\text{tot}} = \frac{1}{N}\sum_{\mathbf{q}} (\Gamma_{\mathbf{q}})^2 K(\mathbf{q}) = \frac{K_1}{\lambda} I_2(\delta, \tau),$$

where

$$I_n(\delta, \tau) = \frac{1}{N}\sum_{\mathbf{q}} (-\Gamma_{\mathbf{q}})^n \frac{1-\Gamma_{\mathbf{q}}}{E_{\mathbf{q}}(\delta)} \coth\frac{\lambda E_{\mathbf{q}}(\delta)}{2\tau},$$

$$E_{\mathbf{q}}(\delta) = \sqrt{(1-\Gamma_{\mathbf{q}})\left(\frac{1}{3} + \Gamma_{\mathbf{q}} + \delta\right)}, \quad (30)$$

$$K_{\text{tot}} = \frac{1}{z^2}\sum_{\Delta, \Delta'} K_{|\Delta + \Delta'|} = \frac{1 - 4K_1 + 2K_2 + 4K_3 + K_4}{z}, \quad z = 12.$$

Equations (29) have the formal solution (the arguments of the functions are omitted)

$$\lambda = I_1, \quad K_1 = I_1/I_0, \quad K_{\text{tot}} = I_2/I_0, \quad \alpha_1 = 2I_0 I_1. \quad (31)$$

Note that the $D = 1/3 + \delta$ parameter [see Eq. (28)] is written as a complex combination of unknown correlators and splitting parameters. Calculating them separately is meaningless. For this reason, we further calculate the δ value as one of the most important characteristics of the system, which describes correlations in an "extended" cluster. We cannot, however, determine δ from (31) and will therefore use the method of moments [7] to calculate it self-consistently.

Let us define and exactly calculate the first three moments,

$$M_0 \equiv \langle s_{\mathbf{f}}^z(t) s_{\mathbf{f}}^z(0) \rangle_{t=0} = \langle s_{\mathbf{f}}^z s_{\mathbf{f}}^z \rangle = \frac{1}{4},$$

$$M_1 \equiv \left\langle i\frac{\partial s_{\mathbf{f}}^z(t)}{\partial t} s_{\mathbf{f}}^z(0) \right\rangle_{t=0} = \left\langle \frac{1}{2z}\sum_{\Delta} (s_{\mathbf{f}}^+ s_{\mathbf{f}+\Delta}^- - s_{\mathbf{f}+\Delta}^+ s_{\mathbf{f}}^-) s_{\mathbf{f}}^z \right\rangle = \frac{K_1}{4},$$

$$M_2 \equiv \left\langle \left(-\frac{\partial^2 s_{\mathbf{f}}^z(t)}{\partial t^2}\right) s_{\mathbf{f}}^z(0) \right\rangle_{t=0} = \left\langle \left(\frac{1}{2z^2}\sum_{\Delta} (s_{\mathbf{f}}^z - s_{\mathbf{f}+\Delta}^z) + R_{\mathbf{f}}\right) s_{\mathbf{f}}^z \right\rangle = \frac{1}{8}\left(\frac{K_1}{z} + K_{\text{tot}}\right). \quad (32)$$

These calculations are performed using the rules of the multiplication of operators on one node and the definitions of $K_1 = -K_{|\Delta|}$ and K_{tot} [see Eq. (30)]; importantly,

by virtue of condition (6), only the first term of the $R_{\mathbf{f}}$ operator [Eq. (14)] contributes to the $\langle R_{\mathbf{f}} s^z_{\mathbf{f}} \rangle$ mean.

Based on the spectral theorem, the one-node mean can be represented as

$$\langle s^z_{\mathbf{f}}(t) s^z_{\mathbf{f}}(0) \rangle = \int_{-\infty}^{\infty} e^{-i\omega t} J_0(\omega) d\omega,$$
$$J_0(\omega) = \frac{1}{N} \sum_{\mathbf{q}} J(\mathbf{q}, \omega; \tau), \tag{33}$$

where the $J(\mathbf{q}, \omega; \tau)$ spectral intensity generally corresponds to the exact Green function $G(\mathbf{q}, \omega)$. It follows from (33) that

$$M_0 = \int_{-\infty}^{\infty} J_0(\omega) d\omega, \quad M_1 = \int_{-\infty}^{\infty} \omega J_0(\omega) d\omega,$$
$$M_2 = \int_{-\infty}^{\infty} \omega^2 J_0(\omega) d\omega. \tag{34}$$

Above, we calculated approximate Green function (25). The corresponding $J(\mathbf{q}, \omega; \tau)$ spectral intensity is given by (26). It follows that

$$J_0(\omega) = \frac{K_1}{4\lambda} \frac{1}{N} \sum_{\mathbf{q}} \frac{e^{\omega/\tau}}{e^{\omega/\tau} - 1} \frac{1 - \Gamma_{\mathbf{q}}}{E_{\mathbf{q}}}$$
$$\times [\delta(\omega - \Omega_{\mathbf{q}}) - \delta(\omega + \Omega_{\mathbf{q}})], \quad \Omega_{\mathbf{q}} = \lambda E_{\mathbf{q}}. \tag{35}$$

Let us impose the requirement that exact equations (34) should be satisfied in the linear second-order theory under consideration. The M_0 zero moment is given by the equation that precisely reproduces the sum rule $K_0 = 1$. It is easy to see that substituting (35) into (34) to obtain M_1 leads to an identity. Substituting (35) into (34) to determine M_2, however, yields

$$M_2 = \frac{\lambda K_1}{4} P(\delta),$$
$$P(\delta) \equiv \frac{1}{N} \sum_{\mathbf{q}} (1 - \Gamma_{\mathbf{q}}) E_{\mathbf{q}} \coth \frac{\Omega_{\mathbf{q}}}{2\tau}. \tag{36}$$

Using the exact expression for M_2 [Eq. (32)] and solutions (31), we obtain the equation for self-consistently calculating gap parameter δ,

$$P(\delta) = \frac{I_2(\delta) + I_1(\delta)/12}{2I_1^2(\delta)}, \quad \delta = \delta(\tau). \tag{37}$$

It follows that consistent linear second-order theory is based on the observance of the sum rule $K_0 = 1$, the definitions of the K_1 and K_{tot} correlators [Eqs. (29)], and the requirement of the exact second moment value, which leads to (37). Equation (37) plays an important role. Indeed, it makes the theory of spin liquids internally closed, and there appears a possibility of self-consistently calculating all system parameters.

The sums over the Brillouin zone in the equations for I_n and P will be written in terms of integrals with the density of states $D(\varepsilon)$. The $D(\varepsilon)$ density of states that corresponds to the isoenergy surfaces $\Gamma_{\mathbf{q}} = \varepsilon$ in the FCC lattice should satisfy the exact relations

$$D_0 = \int_{-1/3}^{1} D(\varepsilon) d\varepsilon = 1,$$
$$D_1 = \int_{-1/3}^{1} \varepsilon D(\varepsilon) d\varepsilon = 0, \tag{38}$$
$$D_2 = \int_{-1/3}^{1} \varepsilon^2 D(\varepsilon) d\varepsilon = \frac{1}{z}.$$

The $D(x)$ density of states was approximated as

$$D(x) = \begin{cases} A(x), & -1/3 \le x \le 0 \\ B(x), & 0 \le x \le 1, \end{cases} \tag{39}$$

where

$$A(x) = -0.366664 \ln \left[0.0671182 \left(x + \frac{1}{3} \right) \right] - 0.456693x,$$
$$B(x) = 0.226573 \sqrt{1 - x} + \frac{0.202745}{x + 0.151142} - 0.174703.$$

In selecting this approximation, we were first and foremost guided by the logarithmic divergence of $D(\varepsilon)$ at $\varepsilon = -1/3$ and the fulfillment of integral equations (38), because self-consistency equations (31) and (37) are also integral.

Combining (31) and (37) yields the system of three equations for self-consistently calculating the spin liquid parameters,

$$\lambda = I_1, \tag{40a}$$
$$K_1 = I_1/I_0, \tag{40b}$$
$$P = \frac{I_2 + I_1/12}{2I_1^2}. \tag{40c}$$

Here,

$$I_n(\delta, t) = \int_{-1/3}^{1} d\varepsilon D(\varepsilon) (-\varepsilon)^n \frac{1 - \varepsilon}{E(\varepsilon, \delta)} \coth \frac{E(\varepsilon, \delta)}{2t},$$
$$P(\delta, t) = \int_{-1/3}^{1} d\varepsilon D(\varepsilon) (1 - \varepsilon) E(\varepsilon, \delta) \coth \frac{E(\varepsilon, \delta)}{2t}, \tag{41}$$

$$E(\varepsilon, \delta) = \sqrt{(1-\varepsilon)\left(\frac{1}{3}+\varepsilon+\delta\right)}, \quad t = \frac{\tau}{\lambda}.$$

5. THE GROUND STATE

Consider the properties of the spin liquid at $\tau \equiv 0$ (the hyperbolic cotangent equals one). The I_n and P integrals only depend on $\delta(0)$, and $K_1 = I_1/I_0$ monotonically decreases as $\delta(0)$ increases and has a maximum at $\delta(0) = 0$. Equation (40c) at $\tau \equiv 0$ is an equation with respect to $\delta(0)$ and has the solution $\delta(0) = 1.04 \times 10^{-3} \neq 0$. We therefore have the following characteristics of the ground state of the system:

$$\begin{gathered}\delta(0) = 1.04\times10^{-3}, \quad \lambda(0) = 0.538,\\ K_1(0) = 0.178, \quad \varepsilon_0 = -0.133.\end{gathered} \tag{42}$$

In addition, $I_0 = 3.026$, $I_2 = 0.212$, $\alpha_1 = 3.256$, and $P = 0.442$.

Solution (42) being available, it is pertinent to make some comments on the method for linearizing (15). It is known that, in first-order theory, the linearization (Tyablikov splitting) is performed without any correcting factor (the correcting factor is taken to be one). With α_i set equal to one in the second-order theory under consideration, equations (29) have no solutions of any kind. If all $\alpha_i = \alpha$ are equal, we can, without invoking the method of moments, obtain the gap parameter in the form

$$\delta = \frac{I_2(\delta)}{I_1(\delta)} - \frac{1}{4} - \frac{1}{12}\frac{2I_0(\delta)I_1(\delta)-1}{2I_1^2(\delta)}.$$

This equation has the solution $\delta^*(0) = 0.0435$ at $\tau = 0$, and we obtain

$$\begin{gathered}\lambda^*(0) = 0.319, \quad K_1^*(0) = 0.143,\\ \varepsilon_0^* = -0.107, \quad \alpha = 1.418.\end{gathered}$$

Clearly, this variant gives a substantial loss in the ground state energy compared with (42). Note also that the singlet state energy obtained by applying the method of moments [7] to the spin liquid in a square lattice is $\varepsilon_0 = -0.352$, which is lower than the energy of the antiferromagnetic state at $\tau = 0$.

Let us show that the ground state is singlet (total spin $S = 0$). We will introduce the function (the mean of the square of the total spin of the system referred to one spin)

$$\begin{aligned}S^2(\tau) &\equiv \frac{1}{N}\langle \mathbf{S}^2\rangle = \frac{1}{N}\sum_{\mathbf{fm}}\langle \mathbf{s}_\mathbf{r}\cdot\mathbf{s}_\mathbf{m}\rangle\\ &= \sum_\mathbf{r}\frac{1}{N}\sum_\mathbf{f}\langle \mathbf{s}_\mathbf{f}\cdot\mathbf{s}_{\mathbf{f}+\mathbf{r}}\rangle = \frac{3}{4}\sum_\mathbf{r}K_\mathbf{r} = \frac{3}{4}K(0),\end{aligned} \tag{43}$$

which can be expressed via the Fourier transform of correlation function (27) at $\mathbf{q} = 0$. At $\tau \equiv 0$, it follows from (27) that $K(0) = 0$ and $S^2(0) = 0$, which proves the singlet character of the ground state in conformity with (7). On the other hand, (43) can be treated as the limit

$$\begin{aligned}K(0) &= \lim_{\mathbf{q}\to 0}K(\mathbf{q}) = \frac{K_1}{\lambda}\lim_{\mathbf{q}\to 0}\frac{1-\Gamma_\mathbf{q}}{E_\mathbf{q}(\delta)}\coth\frac{\lambda E_\mathbf{q}(\delta)}{2\tau}\\ &= \frac{4\tau}{\alpha_1\left(\frac{1}{3}+\Gamma_0+\delta\right)}.\end{aligned} \tag{44}$$

From this equation, we again obtain $K(0)$ as $\tau \longrightarrow 0$ (a singlet). At $\tau \neq 0$, triplet excitations, however, arise in the system, which results in $S^2(\tau) \neq 0$. Equation (44) will be used to analyze the temperature properties of the spin liquid.

6. CALCULATIONS OF THE THERMODYNAMIC PROPERTIES OF THE SPIN LIQUID

System (40) was solved numerically. A t value was set, and δ was found by (40c). At these t and $\delta(t)$, the I_0, $I_1 = \lambda$, $K_1 = I_1/I_0$, and $\alpha_1 = 2I_0I_1$ integrals and temperature $\tau = \lambda t$ were calculated. As a result, all the parameters found numerically were functions of temperature $\tau = T/zJ$ ($z = 12$).

The calculated temperature dependence of the $\delta(\tau)$ gap parameter is shown in Fig. 1. In the low-temperature region, $\delta(\tau)$ grows almost as a power function of τ, $\delta(\tau) \propto \tau^2$ according to our data. However, already at $\tau \geq 0.5$, the $\delta(\tau)$ parameter virtually coincides with its asymptotic value 4τ.

The temperature dependence of the $\lambda(\tau)$ stiffness parameter of the excitation spectrum with the asymptotic behavior $\lambda(\tau) \propto 1/\sqrt{\tau}$ is shown in Fig. 2.

It is known that the thermodynamic properties of a system are determined by its excitation spectrum. The temperature evolution of the spectrum

$$\Omega_\mathbf{q}(\tau) = \sqrt{1-\Gamma_\mathbf{q}}\lambda(\tau)\sqrt{1/3+\Gamma_\mathbf{q}+\delta(\tau)}$$

is shown in Fig. 3; it was obtained by self-consistently calculating the $\lambda(\tau)$ and $\delta(\tau)$ parameters. The spectrum is gapless and acoustic; that is, $\Omega_\mathbf{q} \propto q$ as $q \longrightarrow 0$ (as with phonons or antiferromagnetic magnons). The mean excitation energy (recall that all the energy parameters of the system are reduced to the dimensionless form through dividing by zJ) is

$$\begin{aligned}\bar{\Omega}(\tau) &= \lambda(\tau)\sum_{-1/3}^{1}D(\varepsilon)E(\varepsilon, \delta(\tau))d\varepsilon\\ &\approx \lambda(\tau)\sqrt{\delta(\tau)}.\end{aligned} \tag{45}$$

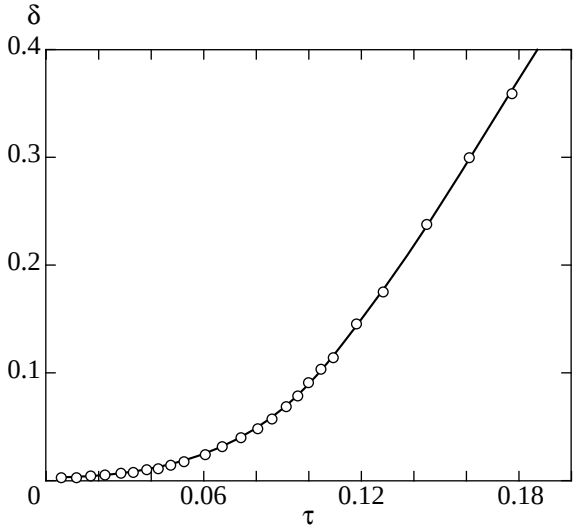

Fig. 1. Dependence of gap parameter δ on dimensionless temperature $\tau = T/zJ$ at low temperatures.

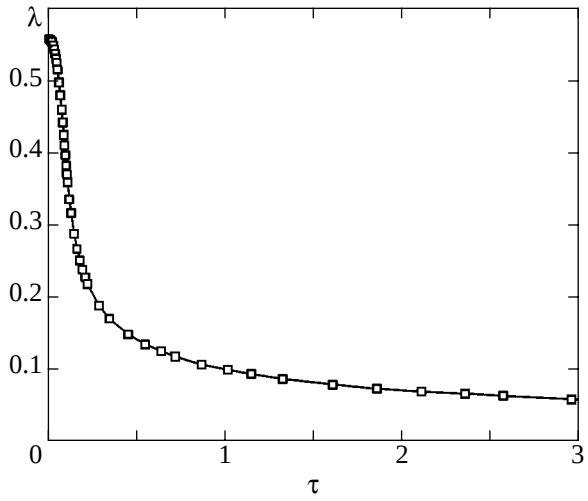

Fig. 2. Temperature dependence of spectrum stiffness parameter λ(τ).

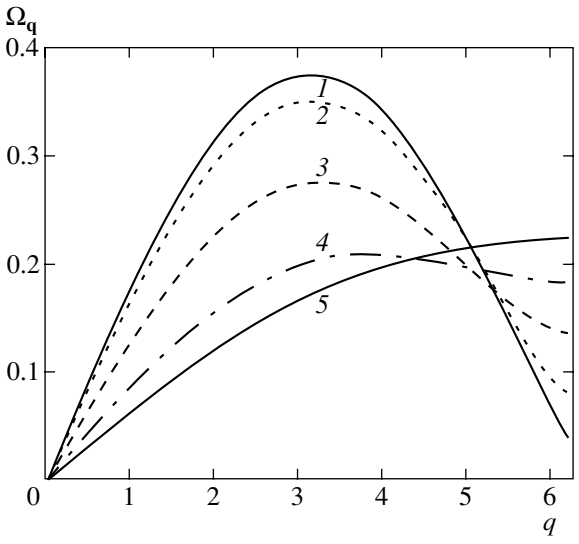

Fig. 3. Temperature evolution of excitation spectrum $\Omega_{\mathbf{q}}(\tau)$ in the [001] direction at self-consistently calculated δ(τ) and λ(τ) parameters: (*1*) τ = 0, λ = 0.56, and δ = 0.0032; (*2*) τ = 0.05, λ = 0.518, and δ = 0.0172; (*3*) τ = 0.1, λ = 0.385, and δ = 0.091; (*4*) τ = 0.2, λ = 0.23, and δ = 0.47; and (*5*) τ = 1.0, λ = 0.1, and δ = 3.68.

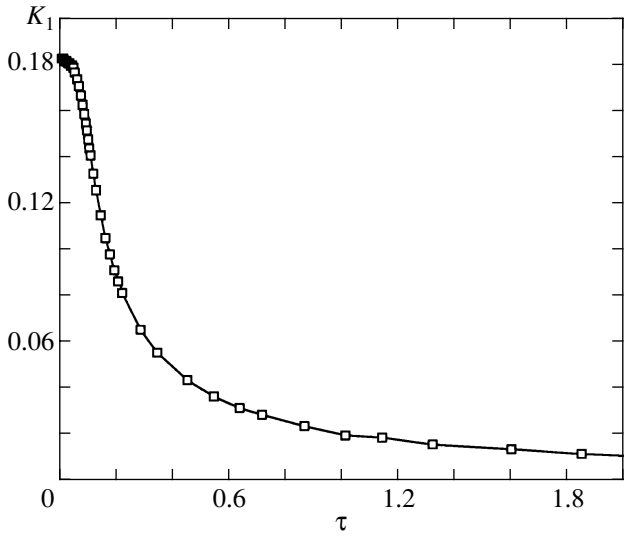

Fig. 4. Temperature dependence of the correlator modulus between nearest neighbors $K_1(\tau)$; system energy $\varepsilon(\tau) = -(3/4)K_1(\tau)$.

This is an increasing function of temperature, which reaches "saturation" at τ > 2; that is, $\bar{\Omega} \longrightarrow 0.2$.

The temperature behavior of the $K_1(\tau)$ modulus of the correlator between the nearest neighbors is shown in Fig. 4. At τ ≥ 0.5, its temperature dependence is close to asymptotic, $K_1(\tau) \propto 1/\tau$. According to the calculations, the dimensionless heat capacity

$$c(\tau) = \frac{\partial \varepsilon(\tau)}{\partial \tau} = -\frac{3}{4}\frac{\partial K_1(\tau)}{\partial \tau} \qquad (46)$$

has a form similar to that of the heat capacity of a two-level system (Schottky anomaly), namely, it has a maximum at $\tau \approx 0.1 \approx \bar{\Omega}/2$ and the $c(\tau) \propto 1/\tau^2$ asymptotic behavior. In the low-temperature region, it, however, exhibits the behavior of a power function, $c(\tau) \propto \tau^3$.

Magnetic susceptibility. The dynamic susceptibility of a spin system in dimensionless units is determined by the equation [8]

$$\chi^{\alpha\beta}(\mathbf{q}, \omega) = -\langle\langle s^{\alpha}(\mathbf{q}) | s^{\beta}(-\mathbf{q})\rangle\rangle_{\omega}.$$

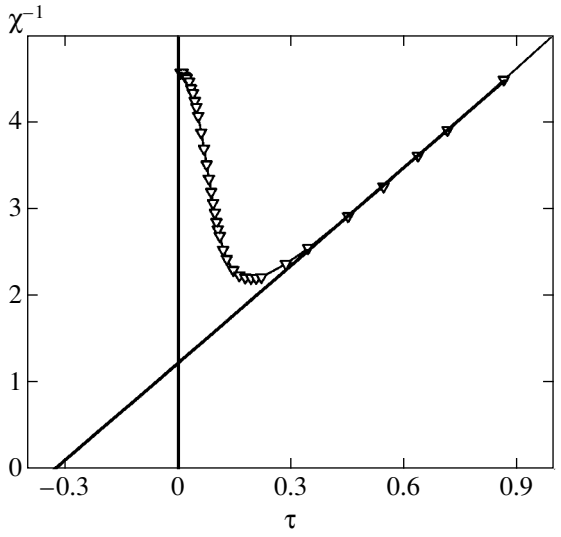

Fig. 5. Temperature dependence of reciprocal susceptibility χ^{-1}; at $\tau > 0.5$, the $\chi^{-1}(\tau)$ function virtually reaches its asymptotic value with the Curie paramagnetic point $\Theta = 1/3$.

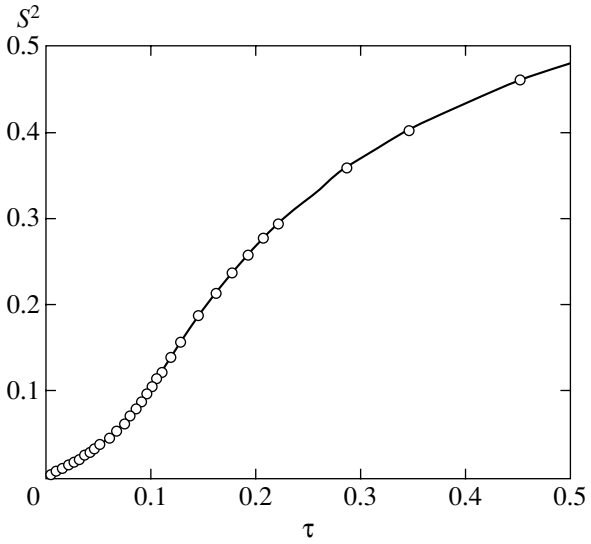

Fig. 6. Low-temperature behavior of the $S^2(\tau) \equiv N^{-1}\langle \mathbf{S}^2 \rangle$ function, where $\mathbf{S}$ is the total spin operator of the system; asymptotically, $S^2(\tau) \longrightarrow 3/4$.

In the spin liquid state under consideration, we have

$$\chi^{+-}(\mathbf{q}, \omega) = 2\chi^{zz}(\mathbf{q}, \omega) = -2G(\mathbf{q}, \omega)$$

because of the isotropic character of the correlation functions. According to (24) and (25), the expression for the static susceptibility ($\omega = 0$) has the form

$$\chi^{zz}(\mathbf{q}, 0) = \frac{K_1}{2}\frac{1-\Gamma_\mathbf{q}}{\Omega_\mathbf{q}^2} = \frac{K_1}{2\lambda^2}\frac{1}{1/3 + \Gamma_\mathbf{q} + \delta} = \frac{1}{\alpha_1}\frac{1}{1/3 + \Gamma_\mathbf{q} + \delta}. \quad (47)$$

It follows from (47) that

$$\chi^{zz}(0, 0) \equiv \chi(\tau) = \frac{1}{\alpha_1(\tau)[4/3 + \delta(\tau)]}, \quad \chi^{zz}(0, 0)|_{\tau = 0} \equiv \chi(0) = 0.23, \quad (48)$$

$$\chi^{zz}(\mathbf{Q}_{1,2}, 0) = \frac{1}{\alpha_1(\tau)\delta(\tau)}, \quad \chi^{zz}(\mathbf{Q}_{1,2}, 0)|_{r = 0} = 295.31, \quad (49)$$

where $\mathbf{Q}_1 \equiv X = (0, 0, 2\pi)$ and $\mathbf{Q} \equiv W = (\pi, 0, 2\pi)$ are the special points of the FCC lattice Brillouin zone at which $\Gamma_{\mathbf{Q}_1} = \Gamma_{\mathbf{Q}_2} = -1/3$. Because $\delta(0) \neq 0$ in the spin liquid, (49) does not diverge as $\tau \longrightarrow 0$, which is evidence of spin liquid stability with respect to short-wave perturbations corresponding to the $\mathbf{Q}_{1,2}$ wave vectors and of correlation length finiteness.

Compare susceptibility (48) with the longitudinal thermodynamic susceptibility. By definition [8], it is given by

$$\tilde{\chi}^{zz}(\tau) = \frac{1}{\tau}[\langle (s^z(0))^2 \rangle - \langle s^z(0) \rangle^2] \equiv \frac{1}{\tau}\chi_0(\tau), \quad (50)$$

where $s^z(0)$ is the operator Fourier transform at $\mathbf{q} = 0$. As $\langle s^z(0) \rangle = 0$ in the spin liquid state, it follows from the isotropic character of the spin correlators that

$$\chi_0(\tau) = \frac{1}{N}\langle (S^z)^2 \rangle = \frac{1}{3}S^2(\tau) = \frac{1}{4}K(\mathbf{q} = 0) = \frac{\tau}{\alpha_1(3/4 + \delta)}, \quad (51)$$

where the $S^2(\tau)$ function is given by (43). A comparison of expressions (50) and (51) with (48) shows that the longitudinal thermodynamic susceptibility coincides with the dynamic susceptibility at $\omega = 0$ and $\mathbf{q} = 0$; that is, $\tilde{\chi}^{zz}(\tau) = \chi(\tau)$. In addition,

$$3\tau\chi(\tau) = S^2(\tau). \quad (52)$$

The $\chi^{-1}(\tau)$ reciprocal susceptibility calculated numerically is shown in Fig. 5. This function has a minimum at $\tau \approx 0.2$ and becomes close to the $\chi^{-1}(\tau) \approx \tau + \Theta$ function already at $\tau \geq 0.5$; here, $\Theta = 1/3$ is an analog of the paramagnetic Curie point for antiferromagnets. The $S^2(\tau)$ function calculated by (52) is shown in Fig. 6. The $\alpha_1(\tau)$ parameter rapidly reaches its asymptotic value (one) at $\tau \geq 0.5$.

7. INTERPRETATION OF THE RESULTS

In the region of maximally low temperatures, the $\coth(x/2) = 1 + 2n(x)$ representation, where $n(x)$ is the Bose distribution function, can conveniently be used. The spectrum in this region is acoustic (proportional to q), and the parameters in this region therefore behave as power functions,

$$\lambda(\tau) = \lambda(0) - B\tau^4, \quad K_1(\tau) = K_1(0) - A\tau^4. \quad (53)$$

As the energy of the system is $\varepsilon = -(3/4)K_1$, the heat capacity of the spin liquid in this region,

$$c(\tau) = \partial\varepsilon/\partial\tau = 4A\tau^3, \quad (54)$$

is similar to the heat capacity of Debye phonons (or antiferromagnetic magnons).

At temperatures $\tau \geq \tau_0$, where $\tau_0 = \lambda(0)(2/\sqrt{3})\sqrt{\delta(0)}$ is the excitation energy at the boundary ($\varepsilon = -1/3$ or $\mathbf{q} = \mathbf{Q}_{1,2}$), the thermodynamic properties of the system become more complex, because this region also contributes to the temperature dependence of the parameters. Initially, the quadratic dependence of δ predominates, but, at $\tau > 1$, the dependence becomes linear.

Asymptotic behavior ($\tau \longrightarrow \infty$). The coefficients of the asymptotic behaviors of all the functions when correlations disappear can be determined analytically using the following obvious physical conditions:

(1) $S^2(\tau) \longrightarrow 3/4$; 3/4 is the value of the square of the spin on a lattice site.

(2) $\alpha_1(\tau) \longrightarrow 1$; that is, the uncoupling parameter for noncorrelated spins becomes equal to one.

The first condition leads to the Curie law for susceptibility (52),

$$\chi(\tau) = \frac{S^2(\tau)}{3\tau} \longrightarrow \frac{1}{4\tau}.$$

On the other hand, the other (equivalent) definition of susceptibility [Eq. (48)] gives

$$\chi(\tau) \longrightarrow \frac{1}{4/3 + \delta(\tau)}$$

when both conditions are satisfied. For the Curie law to be obeyed, it is necessary that

$$\delta(\tau) \longrightarrow 4\tau. \quad (55)$$

Asymptotically, the integrals take the form

$$I_n(\tau) \longrightarrow \frac{1}{2\lambda(\tau)} \int_{-1/3}^{1} D(\varepsilon)(-\varepsilon)^n \left(1 - \frac{\varepsilon}{4\tau}\right) d\varepsilon.$$

This result and properties (38) of the density of states give

$$I_0(\tau) \longrightarrow \frac{1}{2\lambda(\tau)}, \quad I_1(\tau) \longrightarrow \frac{1}{z}\frac{1}{2\lambda(\tau)}\frac{1}{4\tau}, \quad I_2(\tau) \longrightarrow \frac{1}{z}\frac{1}{2\lambda(\tau)}, \quad z = 12. \quad (56)$$

As $I_1 = \lambda$ [according to self-consistency equation (40a)], it follows from (56) that $\lambda^2 = 1/8z\tau$; that is,

$$\lambda \longrightarrow \frac{1}{\sqrt{2z}}\frac{1}{2\sqrt{\tau}}, \quad \bar{\Omega} = \lambda\sqrt{\delta} = \frac{1}{\sqrt{2z}}. \quad (57)$$

To summarize, the behavior of the thermodynamic characteristics of the system (spin liquid) as $\tau \longrightarrow \infty$ is as follows:

$$\chi(\tau) \longrightarrow \frac{1}{4\tau}, \quad \delta(\tau) \longrightarrow 4\tau,$$
$$\lambda(\tau) \longrightarrow \frac{\bar{\Omega}}{2}\frac{1}{\sqrt{\tau}} = \frac{0.102}{\sqrt{\tau}}, \quad (58)$$
$$K_1(\tau) \longrightarrow \frac{\bar{\Omega}^2}{2}\frac{1}{\tau} = \frac{0.021}{\tau}.$$

8. SPATIAL CORRELATIONS IN THE SPIN LIQUID

By definition,

$$K_r = 4\frac{1}{N}\sum_{\mathbf{f}} \langle s^z_{\mathbf{f}} s^z_{\mathbf{f}+\mathbf{r}} \rangle = \frac{4}{3}\frac{1}{N}\sum_{\mathbf{f}} \langle \mathbf{s}_{\mathbf{f}} \mathbf{s}_{\mathbf{f}+\mathbf{r}} \rangle.$$

The general equation for the spatial correlation functions [see (14) and (34)] has the form

$$K_r = \frac{1}{N}\sum_{\mathbf{q}} e^{i\mathbf{q}\cdot\mathbf{r}} K(\mathbf{q}),$$
$$K(\mathbf{q}) = \frac{K_1}{\lambda}\frac{1 - \Gamma_{\mathbf{q}}}{E_{\mathbf{q}}(\delta)} \coth\frac{\lambda E_{\mathbf{q}}(\delta)}{2\tau},$$

where the $g \equiv K_1/\lambda$ and δ parameters are functions of temperature.

Consider the character of spatial correlations in the ground (singlet) spin liquid state. At $\tau \equiv 0$, we have

$$K(\mathbf{q}) = g(0)R(\mathbf{q}), \quad R(\mathbf{q}) \equiv \sqrt{\frac{1 - \Gamma_{\mathbf{q}}}{1/3 + \Gamma_{\mathbf{q}} + \delta(0)}}. \quad (59)$$

The determination of K_r at arbitrary r is a technically complex computational problem because the summation (integration) is over the first Brillouin zone, which has a fairly complex form in the FCC lattice [12].

First, note that Eq. (43),

$$\sum_{\mathbf{r}} K_r = 0,$$

is evidence that spatial correlation functions are alternating in the ground singlet spin liquid state and cancel each other when the summation is performed.

It follows from (59) that the largest contribution to the formation of spatial correlations is made by those Brillouin zone regions in which $\Gamma_{\mathbf{q}} \longrightarrow -1/3$; that is, by the neighborhoods of points $\mathbf{Q}_1 = (0, 0, 2\pi)$ and $\mathbf{Q}_2 = (\pi, 0, 2\pi)$ and other points with similar symmetry properties.

The neighborhood of point $\mathbf{Q}_1$. Set $\mathbf{q} = \mathbf{Q}_1 + \mathbf{p}$, where $|\mathbf{p}| = p \ll 1$. In this region,

$$\Gamma_{\mathbf{Q}_1+\mathbf{p}} \approx -\frac{1}{3} + \frac{1}{12}p_z^2,$$
$$R(\mathbf{Q}_1 + \mathbf{p}) \approx \frac{4}{\sqrt{p_z^2 + \kappa^2}}, \quad \kappa^2 \equiv z\delta(0) \tag{60}$$

and the Fourier transform of the correlation function is anisotropic and has a singular direction (z). Then,

$$K_r \approx 4ge^{i\mathbf{Q}_1\cdot\mathbf{r}} C_{an}(r),$$
$$C_{an}(r) = \frac{1}{(2\pi)^3}\int\limits_{(p_0)} d\mathbf{p}\frac{e^{i\mathbf{p}\cdot\mathbf{r}}}{\sqrt{p_z^2 + \kappa^2}}. \tag{61}$$

The integration is performed in the spherical coordinates over a sphere of small radius p_0 (the $\mathbf{r}$ vector is directed along z axis),

$$C_{an}(r) = \frac{1}{2\pi^2}\int\limits_0^{p_0} p^2 dp \int\limits_0^1 \frac{dx\cos(prx)}{\sqrt{p^2x^2 + \kappa^2}}$$
$$= \frac{1}{2\pi^2}\int\limits_0^{p_0} p^2 dp \frac{1}{p}\int\limits_0^{pr}\frac{dz\cos z}{\sqrt{z^2 + A^2}},$$

where $A^2 = r^2\kappa^2$. At large r values, the integral is [13]

$$\int\limits_0^\infty \frac{dz\cos z}{\sqrt{z^2 + A^2}} \approx \frac{\pi}{2A}e^{-A}, \quad A \gg 1.$$

As a result, we obtain the following asymptotic behavior:

$$C_{an}(r) \propto \frac{\exp(-r/\xi)}{\sqrt{r/\xi}}, \quad \xi = \frac{1}{\kappa} = \frac{1}{\sqrt{z\delta(0)}}, \tag{62}$$

where ξ is the correlation length. As $\delta(0) \approx 10^{-3}$ and $z = 12$, we have $\xi \approx 8.95$; that is, approximately nine lattice parameters or 12–13 distances between the nearest neighbors. It follows from these estimates that short-range order is fairly well established in the spin liquid.

The $\coth x \approx 1/x$ approximation can be used at high temperatures to obtain

$$K(\mathbf{q}) \approx \frac{4\tau}{\alpha_1(\tau)}\frac{1}{1/3 + \Gamma_{\mathbf{q}} + \delta(\tau)} \tag{63}$$

[recall that, asymptotically, $\alpha_1(\tau) \longrightarrow 1$ and $\delta(\tau) \longrightarrow 4\tau$]. We then have

$$K_r = \frac{4\tau}{\alpha_1(\tau)}\frac{1}{v_B}\int\limits_{(v_B)} d\mathbf{q}\frac{e^{i\mathbf{q}\cdot\mathbf{r}}}{1/3 + \Gamma_{\mathbf{q}} + \delta(\tau)},$$
$$v_B = 4(2\pi)^3,$$

where v_B is the volume of the Brillouin zone. As previously, the neighborhoods of the points at which $\Gamma = -1/3$ are assumed to make the major contribution to the integral. In the neighborhood of point $\mathbf{Q}_1$, we have

$$K_r \approx \frac{z\tau}{\alpha_1(\tau)}C^*_{an}(r),$$
$$C^*_{an}(r) = \frac{1}{(2\pi)^3}\int\limits_{(p_0)} d\mathbf{p}\frac{e^{i\mathbf{p}\cdot\mathbf{r}}}{p_z^2 + \kappa^2}. \tag{64}$$

As opposed to $C_{an}(r)$, the $C^*_{an}(r)$ function contains a linear term rather than a root in the denominator. The integration by the method specified above gives

$$C^*_{an}(r) \approx \frac{p_0^2}{(2\pi)^2} r\int\limits_0^\infty \frac{dz\cos z}{z^2 + \kappa^2 r^2}$$
$$= \frac{p_0^2}{(2\pi)^2} r\frac{\pi}{2\kappa r}e^{-\kappa r} \propto e^{-\kappa r}. \tag{65}$$

The $\xi = 1/\kappa$ correlation length becomes small under high-temperature conditions ($\xi \propto 1/\sqrt{\tau}$). As a result, virtually the only remaining correlations are those between the nearest neighbors.

It follows that spatial correlations in the main directions oscillate with a $\mathbf{Q}_1 \cdot \mathbf{r} = 2\pi r$ period and decay following the behavior of the $C_{an}(r)$ function.

9. CONCLUSION

Let us summarize the results obtained in this work.

In systems with frustrated exchange interactions between the nearest neighbors (as in the FCC lattice), quantum fluctuations of transverse spin components become substantial and can destroy the Ising antiferromagnetic state in the absence of additional stabilizing factors (exchange between the next-nearest neighbors or anisotropy).

In the absence of a long-range order in the FCC lattice, the system is in the spin liquid state. This state is characterized by an isotropic spin correlation function (Hamiltonian symmetry is not destroyed), and the

ground state of the spin liquid is singlet (the total spin of the system is $S = 0$), in conformity with the quantum-mechanical classification of states according to the total spin value.

We described the spin liquid within second-order theory by the method of Green functions. A method for self-consistently calculating spin liquid parameters, namely, the parameter of excitation spectrum stiffness λ, the modulus of the spin correlator between the nearest neighbors K_1, and the gap parameter δ, as functions of the temperature was suggested. The spin liquid energy (in units of exchange parameter per bond) is $\varepsilon = -(3/4)K_1$, and the ground state energy is $\varepsilon_0 = -0.133$. The $\delta \neq 0$ parameter plays an important role. It preserves the translational invariance of the principal lattice in the spin system, determines correlation length $\xi = 1/\sqrt{z\delta}$, and leads to the Curie law for the magnetic susceptibility of the spin liquid at high temperatures.

The spin liquid has a short-range order similar to the antiferromagnetic order with alternating spin correlation functions. The behavior of reciprocal susceptibility is also close to that characteristic of antiferromagnets (even to the existence of the paramagnetic Curie point).

The antiferromagnetic state can compete with the spin liquid state if there are stabilizing factors. The conclusion can be drawn that systems with a long-range magnetic order transform into the spin liquid state at temperatures above critical.

ACKNOWLEDGMENTS

The author thanks V.V. Val'kov, V.I. Zinenko, and S.G. Ovchinnikov for useful discussions and criticism. This work was financially supported by the Russian Foundation for Basic Research (project no. 00-02-16110).

REFERENCES

1. S. V. Vonsovskiĭ, *Magnetism: Magnetic Properties of Dia-, Para-, Ferro-, Antiferro-, and Ferrimagnets* (Nauka, Moscow, 1971), p. 704.
2. M. E. Lines, Proc. R. Soc. London, Ser. A **271**, 105 (1963).
3. M. E. Lines, Phys. Rev. **135**, A1336 (1964).
4. H. T. Diep and H. Kawamura, Phys. Rev. B **40**, 7019 (1989).
5. M. T. Heinila and A. S. Oja, Phys. Rev. B **48**, 16514 (1993).
6. A. F. Barabanov, V. M. Beresovsky, and E. Zasinas, Phys. Rev. B **52**, 10177 (1995).
7. E. V. Kuz'min, Fiz. Tverd. Tela (St. Petersburg) **44**, 1075 (2002) [Phys. Solid State **44**, 1122 (2002)].
8. S. V. Tyablikov, *Methods in the Quantum Theory of Magnetism*, 2nd ed. (Nauka, Moscow, 1975; Plenum, New York, 1967), p. 216.
9. H. Shimahara and S. Takada, J. Phys. Soc. Jpn. **60**, 2394 (1991).
10. A. F. Barabanov and V. M. Berezovskiĭ, Zh. Éksp. Teor. Fiz. **106**, 1156 (1994) [JETP **79**, 627 (1994)].
11. A. F. Barabanov and V. M. Beresovsky, Phys. Lett. A **186**, 175 (1994).
12. H. Jones, *The Theory of Brillouin Zones and Electronic States in Crystals* (North-Holland, Amsterdam, 1960; Mir, Moscow, 1968).
13. H. B. Dwight, *Tables of Integrals and Other Mathematical Data*, 4th ed. (Macmillan, London, 1961; Nauka, Moscow, 1978).

Translated by V. Sipachev

Journal of Experimental and Theoretical Physics, Vol. 96, No. 1, 2003, pp. 140–149.
From Zhurnal Éksperimental'noĭ i Teoreticheskoĭ Fiziki, Vol. 123, No. 1, 2003, pp. 161–171.

SOLIDS
Electronic Properties

Electronic Structure of Carbon Nanoparticles¶

V. A. Osipov[a, *], E. A. Kochetov[a, *], and M. Pudlak[b, **]

[a]*Bogolyubov Laboratory of Theoretical Physics, Joint Institute for Nuclear Research, Dubna, Moscow oblast, 141980 Russia*

[b]*Institute of Experimental Physics, Slovak Academy of Sciences, Kosice, 043 53 Slovak Republic*

**e-mail: osipov@thsun1.jinr.ru, kochetov@thsun1.jinr.ru*

***e-mail: pudlak@saske.sk*

Received April 19, 2002

Abstract—The electronic structure of graphitic nanoparticles is investigated within a gauge field-theory model. The local and total densities of states (DOS) near the pentagonal defects (disclinations) are calculated for three geometries: sphere, cone, and hyperboloid. It is found that the low-energy electron states have a rather specific dependence on both the energy and the distance from a disclination line. In particular, the low-energy total DOS has a cusp that drops to zero at the Fermi energy for disclinations with the Frank index $\nu < 1/2$, while a region of a nonzero DOS across the Fermi level is formed for $\nu = 1/2$. The true zero-mode fermion state is found for the graphitic hyperboloid. The appearance of an enhanced charge density near the Fermi level for nanocones with a 60° opening angle (180° disclination) is predicted. © *2003 MAIK "Nauka/Interperiodica".*

1. INTRODUCTION

Carbon nanoparticles, which are expected to have important implications for the development of electronic devices, flat panel displays, nanoswitches, etc., have recently received great attention from both experimentalists and theorists (see, e.g., reviews [1, 2]). The high flexibility of carbon allows producing variously shaped carbon nanoparticles: nanotubes, fullerenes, cones, toroids, graphitic onions, and nanohorns. Particular attention has been given to the peculiar electronic states due to topological defects that have been observed in different kinds of carbon nanoparticles by scanning tunneling microscopy (STM). For example, STM images with fivefold symmetry (due to pentagons in the hexagonal graphitic network) have been obtained in the C_{60} fullerene molecule [3]. The peculiar electronic properties at the ends of carbon nanotubes (which include several pentagons) have been probed experimentally in [4, 5]. Recently, the electronic structure of a single pentagon was revealed on an atomic scale by STM in [6], where the enhanced charge density at the pentagon, which was located at the apex of the conical protuberance of the graphitic particle, was experimentally clarified.

By its nature, the pentagon occurring in a graphite sheet is a topological defect. Actually, as mentioned in [7], fivefold coordinated particles are orientational disclination defects in the otherwise sixfold coordinated triangular lattice. Moreover, disclinations are generic defects in closed carbon structures, fullerenes, and nanotubes, because, in accordance with Euler's theorem, these microcrystals can only be formed with the total disclination 4π. According to the geometry of the hexagonal network, this implies the presence of twelve pentagons (60° disclinations) on the closed hexatic surface.

We note that graphitic cones are of special interest because they can contain a single pentagon at the apex, in contrast to twelve pentagons in fullerene molecules and nanotubes. This fact makes nanocones attractive for experimental study of peculiar electronic states due to topological defects that were theoretically predicted in [8, 9]. In particular, analysis within the effective-mass theory shows that a specific $\sqrt{3} \times \sqrt{3}$ superstructure induced by pentagon defects can appear with the wave functions decaying as $r^{-1/5}$ [8]. Recently, this prediction was experimentally verified in [6]. A recent study [10] within both tight-binding and *ab initio* calculations shows the presence of sharp resonant states in the region close to the Fermi energy. The strength and position of these states with respect to the Fermi level were found to depend sensitively on the number and relative positions of the pentagons constituting the conical tip. In particular, a prominent peak occurring just above the Fermi level was found for the nanocone with three symmetric pentagons (which corresponds to a 60° opening angle or, equivalently, to a 180° disclination). On the other hand, the continuum model suggested in [9] predicts apical enhancement of the density of states (DOS) at the Fermi energy (E_F) in the vicinity of the apex for cones with 120° disclinations.

It is interesting to note that the problem of specific electronic states at the Fermi level due to disclinations is similar to that of the fermion zero modes in topologically nontrivial manifolds. In field theory, zero modes

¶This article was submitted by the authors in English.

were found to play an important role in understanding anomalies [11] and charge fractionalization that results in unconventional charge–spin relations (e.g., paramagnetism of charged fermions) [12]. As mentioned in [12], this finding has been experimentally verified in trans-polyacetylene chains for one spatial dimension. The Dirac equation for massless fermions in three-dimensional space–time in the presence of a magnetic field was found to yield $N - 1$ zero modes in the N-vortex background field [13]. As we have shown in [14], the problem of the local electronic structure of fullerene is closely related to Jackiw's analysis [13]. We note that the field-theory models for Dirac fermions in a plane and on a sphere [15, 16] were invoked to describe the variously shaped carbon materials. More recently, the importance of the fermion zero modes was discussed in the context of high-temperature chiral superconductors [17–19] and fullerene molecules [16].

Investigation of the electronic structure requires formulating a theoretical model describing electrons on arbitrary curved surfaces with disclinations taken into account. An important ingredient of this model can be provided by the self-consistent effective-mass theory describing the electron dynamics in the vicinity of an impurity in graphite intercalation compounds [20]. The most important fact found in [20] is that the electronic spectrum of a single graphite plane linearized around the corners of the hexagonal Brillouin zone coincides with that of the Dirac equation in (2 + 1) dimensions. This finding stimulated formulation of some field-theory models for Dirac fermions on hexatic surfaces to describe the electronic structure of variously shaped carbon materials: fullerenes [14, 15], nanotubes [21], and cones [9, 22].

In this paper, we study the problem of electron states in carbon nanostructures for three geometries: sphere, cone, and hyperboloid. We note that, in our approach, the gauge theory of disclinations on fluctuating elastic surfaces [23] is basically used. More specifically, we formulate the Dirac equation on a curved surface with a flux due to a pentagonal apical disclination represented by an Abelian gauge field. Both the local and the total density of states are calculated in each case. Special attention is given to the correct inclusion of the spin connection for fermions. Actually, our analysis shows that the spin connection leads to a redefinition of wave functions but leaves Dirac equations unchanged. In other words, the spin connection does not influence the electron spectrum, but affects the DOS.

The paper is organized as follows. The general formalism for studying electron states in the curved two-dimensional background is presented in Section 2. We formulate a field-theory model for Dirac fermions on hexatic surfaces of an arbitrary geometry with both electrons and disclinations taken into account. The flux due to the pentagonal defect is represented by an Abelian gauge field within a self-consistent gauge model. In Section 3, we apply the model to the problem of electron states in the fullerene molecule. We calculate the local and the total DOS and study zero-energy electronic states. In Section 4, we consider two arbitrary geometries for the description of nanocones, conical and hyperbolical. The results obtained are compared with other approaches. Section 5 is devoted to concluding remarks.

2. GENERAL FORMALISM

Our consideration is based on the effective-mass theory that was applied in [20] to study the screening of a single intercalant within a graphite host, with a two-dimensional approximation used for the description of the graphite host. The effective-mass expansion is equivalent to the $\mathbf{k} \cdot \mathbf{p}$ expansion of the graphite energy bands around the $\mathbf{K}$ point in the Brillouin zone when the intercalant potential is equal to zero. In fact, there are two degenerate Bloch eigenstates, $\Psi_{1,2}(\mathbf{K}, \mathbf{r})$ at $\mathbf{K}$, and the electron wave function on a graphite lattice can therefore be approximated by

$$\Psi(\mathbf{k}, \mathbf{r}) = f_1(\boldsymbol{\kappa})e^{i\boldsymbol{\kappa}\cdot\mathbf{r}}\Psi_1(\mathbf{K}, \mathbf{r}) + f_2(\boldsymbol{\kappa})e^{i\boldsymbol{\kappa}\cdot\mathbf{r}}\Psi_2(\mathbf{K}, \mathbf{r}),$$

where $\mathbf{k} = \mathbf{K} + \boldsymbol{\kappa}$. Keeping the terms of the order of $\boldsymbol{\kappa}$ in the Schrödinger equation results in a secular equation for the amplitudes $f_{1,2}(\boldsymbol{\kappa})$, which after diagonalization finally yields the two-dimensional Dirac equation [20]

$$i\gamma^\mu\partial_\mu\psi(\mathbf{r}) = E\psi(\mathbf{r}). \quad (1)$$

Here, γ^μ are the Dirac matrices that in 2D reduce to the conventional Pauli matrices, the energy E is measured relative to the Fermi energy, and the two-component wave function $\psi \propto (f_1, f_2)^T$ represents two graphite sublattices. As mentioned in [20], the $\mathbf{k} \cdot \mathbf{p}$ approximation essentially amounts to replacing the graphite bands by conical dispersions at the Fermi energy.

For our purpose, we need a generalization of Eq. (1) incorporating both a disclination field and a nontrivial background geometry. A possible description of disclinations on arbitrary two-dimensional elastic surfaces is offered by the gauge approach [23]. In accordance with the basic assumptions of this approach, disclinations can be incorporated in the elasticity theory Lagrangian by introducing a compensating $U(1)$ gauge field W_μ. It is important that the gauge model admits vortexlike solutions for wedge disclinations [23], thus representing a disclination as a vortex of elastic medium. The physical meaning of the gauge field is that the elastic flux due to rotational defect, which is directly related to the Frank vector (see Section 3), is completely determined by the circulation of the W_μ field around the disclination line. In the gauge theory context, the disclination field can be straightforwardly incorporated in (1) by the standard substitution

$$\partial_\mu \longrightarrow \partial_\mu - iW_\mu.$$

Within the linear approximation to gauge theory of disclinations (which amounts to the conventional elasticity theory with linear defects), the basic field equation that describes the $U(1)$ gauge field in a curved background is given by

$$D_\mu F^{\mu k} = 0, \quad F^{\mu k} = \partial^\mu W^k - \partial^k W^\mu, \tag{2}$$

where the covariant derivative $D_\mu := \partial_\mu + \Gamma_\mu$ involves the Levi-Civita (torsion-free, metric compatible) connection

$$\Gamma^k_{\mu\lambda} := (\Gamma_\mu)^k_\lambda = \frac{1}{2} g^{kl}\left(\frac{\partial g_{l\lambda}}{\partial x^\mu} + \frac{\partial g_{\mu l}}{\partial x^\lambda} - \frac{\partial g_{\mu\lambda}}{\partial x^l}\right), \tag{3}$$

with $g_{\mu k}$ being the metric tensor on a Riemannian surface Σ with local coordinates $x^\mu = (x^1, x^2)$. For a single disclination on an arbitrary elastic surface, a singular solution to (2) is found to be [23]

$$W^k = -\nu \varepsilon^{k\lambda} D_\lambda G(x, y), \tag{4}$$

where

$$D_\mu D^\mu G(x^1, x^2) = \frac{2\pi\delta^2(x^1, x^2)}{\sqrt{g}}, \tag{5}$$

with $\varepsilon_{\mu k} = \sqrt{g}\,\epsilon_{\mu k}$ being the totally antisymmetric tensor on Σ, $\epsilon_{12} = -\epsilon_{21} = 1$. We note that Eqs. (2)–(5) self-consistently describe a defect located on an arbitrary surface [23].

To describe fermions in a curved background, we need a set of orthonormal frames $\{e_\alpha\}$ for the metric $g_{\mu\nu}$; local $SO(2)$ rotations act on the frames as

$$e_\alpha \longrightarrow e'_\alpha = \Lambda^\beta_\alpha e_\beta, \quad \Lambda^\beta_\alpha \in SO(2).$$

It then follows that

$$g_{\mu\nu} = e^\alpha_\mu e^\beta_\nu \delta_{\alpha\beta},$$

where e^μ_α is the zweibein, with the orthonormal frame indices being $\alpha, \beta = \{1, 2\}$ and the coordinate indices $\mu, \nu = \{1, 2\}$. As usual, to ensure that physical observables are independent of a particular choice of the zweibein fields, a local $so(2)$-valued gauge field ω_μ must be introduced. The gauge field of the local Lorentz group is known as the spin connection. For the theory to be self-consistent, the zweibein fields must be chosen to be covariantly constant [24],

$$\mathcal{D}_\mu e^\alpha_\nu := \partial_\mu e^\alpha_\nu - \Gamma^\lambda_{\mu\nu} e^\alpha_\lambda + (\omega_\mu)^\alpha_\beta e^\beta_\nu = 0,$$

which determines the spin connection coefficients explicitly,

$$(\omega_\mu)^{\alpha\beta} = e^\alpha_\nu D_\mu e^{\beta\nu}. \tag{6}$$

Finally, Dirac equation (1) on a surface Σ in the presence of the U(1) external gauge field W_μ is written as

$$i\gamma^\alpha e^\mu_\alpha (\nabla_\mu - iW_\mu)\psi = E\psi, \tag{7}$$

where $\nabla_\mu = \partial_\mu + \Omega_\mu$ with

$$\Omega_\mu = \frac{1}{8}(\omega_\mu)^{\alpha\beta}[\gamma_\alpha, \gamma_\beta] \tag{8}$$

being the spin connection term in the spinor representation.

3. SPHERICAL FULLERENE MOLECULES

Variously shaped fullerene molecules appear in the process of graphite vaporization. The more spherical of them is the C_{60} molecule, also nicknamed the "bucky ball." Others are either slightly (as C_{70}, whose shape is more like an elliptical deformation) or remarkably deformed. We are interested here in the C_{60} molecule and in its spherical generalizations like the C_{240} and C_{540} molecules.

3.1. The Model

To describe a sphere, we use the polar projective coordinates

$$x^1 = r \quad x^2 = \varphi; \quad 0 \le r < \infty, \quad 0 \le \varphi < 2\pi,$$

where R is the radius of the sphere. In these coordinates, the metric tensor becomes

$$g_{rr} = \frac{4R^4}{(R^2 + r^2)^2}, \quad g_{\varphi\varphi} = \frac{4R^4 r^2}{(R^2 + r^2)^2}, \tag{9}$$
$$g_{r\varphi} = g_{\varphi r} = 0,$$

and therefore,

$$\sqrt{g} := \sqrt{\det\|g_{\mu\nu}\|} = \frac{4R^4 r}{(R^2 + r^2)^2}.$$

Nonvanishing coefficients of connection (3) are given by

$$\Gamma^r_{rr} = -\frac{2r}{R^2 + r^2}, \quad \Gamma^r_{\varphi\varphi} = -r\frac{R^2 - r^2}{R^2 + r^2},$$

$$\Gamma^\varphi_{r\varphi} = \frac{1}{r}\frac{R^2 - r^2}{R^2 + r^2},$$

and the general representation for the zweibeins is

$$e^1_r = e^2_\varphi = \frac{2R^2\cos\varphi}{R^2 + r^2}, \quad e^1_\varphi = -e^2_r = -\frac{2R^2\sin\varphi}{R^2 + r^2},$$

which in view of Eq. (6) gives

$$\omega_r^{12} = \omega_r^{21} = 0, \quad \omega_\varphi^{12} = -\omega_\varphi^{21} = \frac{2r^2}{R^2 + r^2} =: 2\omega. \quad (10)$$

The following solution to Eqs. (4) and (5) can be easily found:

$$G = \ln r, \quad W_r = 0, \quad W_\varphi = \nu, \quad r \neq 0.$$

Locally, it describes a topological vortex on the Euclidean plane, which confirms the observation that disclinations can be viewed as vortices in elastic media.

The elastic flow through a surface on the sphere is given by the circular integral

$$\frac{1}{2\pi}\oint \mathbf{W} d\mathbf{r} = \nu.$$

Generally, there are no restrictions on the value of the winding number ν apart from $\nu > -1$ for topological reasons. But if we take the symmetry group of the underlying crystal lattice into account, the possible values of ν become "quantized" in accordance with the group structure (e.g., $\nu = 1/6, 1/3, 1/2, \ldots$ for the hexagonal lattice). We note that the elastic flux is characterized by the Frank vector $\boldsymbol{\omega}$, $|\boldsymbol{\omega}| = 2\pi\nu$, with ν being the Frank index. Thus, the elastic flux is "classical" in its origin; i.e., there is no quantization (in contrast to the magnetic vortex). In some physically interesting applications, however, vortices with a fractional winding number have already been considered (see, e.g., the discussion in [17]). We also note that a detailed theory of magnetic vortices on the sphere has been presented in [25].

In 2D, the Dirac matrices can be chosen as the Pauli matrices, $\gamma^1 = -\sigma^2$ and $\gamma^2 = \sigma^1$; Eq. (8) then reduces to

$$\Omega_\varphi = i\omega\sigma^3. \quad (11)$$

As a result, the Dirac operator

$$\hat{\mathcal{D}} := i\gamma^\alpha e_\alpha^\mu (\nabla_\mu + iW_\mu)$$

on the two-sphere becomes

$$\hat{\mathcal{D}} = \hat{\mathcal{D}}^\dagger = \frac{r^2 + R^2}{2R^2}\begin{Bmatrix} 0 & e^{-i\varphi}\left(-\partial_r + \dfrac{i\partial_\varphi + \nu}{r} + \dfrac{\omega}{r}\right) \\ e^{i\varphi}\left(\partial_r + \dfrac{i\partial_\varphi + \nu}{r} - \dfrac{\omega}{r}\right) & 0 \end{Bmatrix}. \quad (12)$$

In proving that the operator $\hat{\mathcal{D}}$ is Hermitian, we use that in the presence of a metric,

$$\partial_r^\dagger = -\partial_r - \frac{1}{2}\partial_r \ln g.$$

For massless fermions, σ^3 serves as a conjugation matrix, and the energy eigenmodes are symmetric with respect to $E = 0$:

$$\sigma^3 \psi_E = \psi_{-E}.$$

The generator of the local Lorentz transformations $\Lambda_\alpha^\beta \in SO(2)$ takes the form $-i\partial_\varphi$, and the generator of the Dirac spinor transformations $\rho(\Lambda)$ is

$$\Sigma_{12} = \frac{i}{4}[\gamma_1, \gamma_2] = \frac{1}{2}\sigma^3.$$

The total angular momentum of the 2D Dirac system is therefore given by

$$L_z = -i\partial_\varphi + \frac{1}{2}\sigma^3,$$

which commutes with operator (12). Consequently, the eigenfunctions are classified with respect to the eigenvalues of $J_z = j + 1/2$, $j = 0, \pm 1, \pm 2, \ldots$ and are to be taken in the form

$$\psi = \begin{pmatrix} u(r)e^{i\varphi j} \\ v(r)e^{i\varphi(j+1)} \end{pmatrix}. \quad (13)$$

As follows from Eq. (12), the spin connection term can be taken into account by redefining the wave function as

$$\psi = \tilde{\psi}\sqrt{R^2 + r^2}, \quad (14)$$

which reduces eigenvalue problem (7) to

$$\begin{aligned} \partial_r \tilde{u} - \frac{(j - \nu)}{r}\tilde{u} &= \tilde{E}\tilde{v}, \\ -\partial_r \tilde{v} - \frac{(j + 1 - \nu)}{r}\tilde{v} &= \tilde{E}\tilde{u}, \end{aligned} \quad (15)$$

where

$$\tilde{E} = \frac{2R^2 E}{R^2 + r^2}.$$

3.2. Extended Electron States

The general solution to (15) is not available, unfortunately. But because we are mainly interested in electronic states near the disclination line, we can restrict our consideration to the case of small r. In this case, a solution to (15) (with (14) taken into account) is found to be

$$\begin{pmatrix} u \\ v \end{pmatrix} = A\begin{pmatrix} J_\eta(2Er) \\ \pm J_{\bar\eta}(2Er) \end{pmatrix}, \tag{16}$$

where

$$\eta = \pm(j-\nu), \quad \bar\eta = \pm(j-\nu+1),$$

and A is a normalization factor. Therefore, there are two independent solutions with $\eta(\bar\eta) > 0$ and $\eta(\bar\eta) < 0$. We note that the respective signs "±" in (16) correspond to states with $E > 0$ and $E < 0$. As already noted, σ^3 serves as the conjugation matrix for massless fermions and the energy eigenmodes are symmetric with respect to $E = 0$. We can therefore consider either case, for instance, $E > 0$.

The important restrictions come from the normalization condition

$$\int(|u|^2 + |v|^2)\sqrt{g}dx^1dx^2 = 1. \tag{17}$$

From (16), it follows that $A^2 \propto E$. On the other hand, the integrand in (17) must be nonsingular at small Er. This imposes a restriction on possible values of j. Namely, for $\eta, \bar\eta > 0$, we obtain $j - \nu > -1/2$, and for $\eta, \bar\eta < 0$, we have $j - \nu < -1/2$. It follows that possible values of j do not overlap at any ν.

In the vicinity of a pentagon, the electron wave function is given by

$$\begin{pmatrix} u \\ v \end{pmatrix} \propto \begin{pmatrix} E^{1/2+\eta}r^\eta, \\ E^{1/2+\bar\eta}r^{\bar\eta} \end{pmatrix}. \tag{18}$$

In particular, in the leading order, we obtain

$$\Psi \propto \begin{cases} \sqrt{E}, & \nu = 0, \\ E^{1/3}r^{-1/6}, & \nu = 1/6, \\ E^{1/6}r^{-1/3}, & \nu = 1/3. \end{cases}$$

Because the local density of states diverges as $r \longrightarrow 0$, it is more appropriate to consider the total density of states on a patch $0 < r \le \delta$ for small δ, rather than the local quantities. For this, we must integrate the electron density over a small disk $|r| < \delta$. (We recall that r and φ are stereographically projected coordinates on the sphere.) The result is

$$D(E,\delta) \propto \begin{cases} (E\delta)\delta, & \nu = 0, \\ (E\delta)^{2/3}\delta, & \nu = 1/6, 5/6, \\ (E\delta)^{1/3}\delta, & \nu = 1/3, 2/3, \\ \delta, & \nu = 1/2. \end{cases} \tag{19}$$

For the defect-free case ($\nu = 0$), we obtain the well-known behavior of the total DOS in the δ disk given by $D(E,\delta) \propto E\delta^2$ (in accordance with the previous analysis [20]). For $\nu = 1/6, 1/3, 2/3, 5/6$, the low-energy total DOS has a cusp that drops to zero at the Fermi energy. Most intriguing is the case where $\nu = 1/2$ and a region of a nonzero DOS across the Fermi level is formed. This implies local metallization of graphite in the presence of a 180° disclination. In the fullerene molecule, however, there are twelve 60° disclinations, and therefore, the case $\nu = 1/6$ is actually realized.

3.3. Zero-Energy Modes

An interesting issue to be addressed is the existence of zero-energy modes. For the two-sphere, this problem can be solved exactly (see [13, 14]). Namely, for $E = 0$, Eq. (15) reduces to

$$\begin{aligned} \partial_r\tilde u_0 - \frac{(j-\nu)}{r}\tilde u_0 &= 0, \\ -\partial_r\tilde v_0 - \frac{(j+1-\nu)}{r}\tilde v_0 &= 0. \end{aligned} \tag{20}$$

We can construct self-conjugate solutions $\begin{pmatrix} \tilde u_0 \\ 0 \end{pmatrix}$ and $\begin{pmatrix} 0 \\ \tilde v_0 \end{pmatrix}$, where

$$\tilde u_0 = Ar^{j-\nu}, \quad \tilde v_0 = Ar^{-(j-\nu+1)}. \tag{21}$$

The normalization condition

$$\int|\psi_0|^2\sqrt{g}drd\varphi = 1 \tag{22}$$

yields

$$2\pi A^2\int_0^\infty \frac{4R^4r^{2l}}{R^2+r^2}rdr = 1, \tag{23}$$

where $l = j - \nu$ for u_0 and $l = -(j - \nu + 1)$ for v_0. Finally,

$$A^2 = \frac{\sin\pi\bar\eta}{4\pi^2R^{2(1+\bar\eta)}},$$

for u_0 and

$$A^2 = -\frac{\sin\pi\eta}{4\pi^2 R^{2(1-\eta)}}$$

for v_0. We note that the restriction $-1 < j - \nu < 0$ serves to avoid divergence in (22). In the defect-free case ($\nu = 0$), this yields no zero modes on the sphere. We note that this agrees with the general observation that the Dirac operator can have no zero modes on a manifold with an everywhere positive Ricci scalar curvature $\mathcal{R}$. Indeed, we easily find that $\hat{\mathcal{D}}^2 = \Delta + \mathcal{R}/4$, where the Laplace–Beltrami operator Δ has nonnegative eigenvalues [26]. For the two-sphere, $\mathcal{R} = 1/R^2$, and therefore, $\hat{\mathcal{D}}^2 > 0$.

In the case where $\nu = 1/6$, in which we are interested here, the only possible value of j is $j = 0$, and therefore, $u_0 \propto r^{-1/6}$ and $v_0 \propto r^{-5/6}$ near the disclination line. Thus, our analysis shows that two normalizable zero modes can exist on the sphere in the presence of a disclination vortex. We note that this conclusion agrees with [15] (where a different continuum model was formulated) and differs from [13, 14], where either u_0 or v_0 was found to be normalizable. The reason is that, in [13, 14], the external gauge field was assumed to be well-behaved at the origin. In this paper, we admit singular solutions as well.

The total density of states on the patch $0 < r \le \delta$ becomes

$$D(\delta) \propto \begin{cases} \delta^{1/3}, & \nu = 1/6, 5/6, \\ \delta^{2/3}, & \nu = 1/3, 2/3, \\ \delta, & \nu = 1/2. \end{cases} \quad (24)$$

It follows that this behavior differs from (19) and therefore allows recognizing the zero-eigenvalue states in experiment.

4. NANOCONES

A conelike structure (an exposed surface) is formed when a pentagon is introduced into a graphite sheet. There are two possible scenarios for modeling nanocones. First, the cut-and-paste procedure can be accomplished in which the pentagon is constructed in the hexagonal network by cutting out a 60° sector from the graphene sheet (a single layer of graphite). In this case, we have a real cut with the consequent departure from the flat surface. Pentagonal defects in cones can therefore be considered as apical disclinations, and the opening angle is directly connected to the Frank index of the disclination. Because of the symmetry of the graphite sheet, only five types of cones can be created from a continuous sheet of graphite. The total disclinations of all these cones are multiples of 60°, corresponding to the presence of a given number (n) of pentagons at the apices. It is important to mention that carbon nanocones with the cone angles of 19°, 39°, 60°, 85°, and 113° have been observed in a carbon sample [27]. We note that these angles might correspond to 300°, 240°, 180°, 120°, and 60° disclinations in graphite, respectively. Disks ($n = 0$) and one-open-end nanotubes ($n = 6$) have also been observed in the same sample [27]. This case was theoretically studied in [9, 10, 22]. At the same time, cones with the apex angles of 30°, 50°, and 70° have also been found [28, 29]. These angles are forbidden within the above scenario. In [28, 29], the appearance of such cones was explained in terms of the open cone model.

Second, a single disclination on a finite graphite sheet is known to be buckled to screen its energy, thus leading to a curved hexagonal network [7]. In this context, the pentagon in graphene can result in a curved conelike structure. The most appropriate conelike figure is the hyperboloid. We note that this agrees with a suggestion made in [1] that nonsymmetric fullerenes of a special form can serve as nucleating centers for the nanocone. We consider both these scenarios below.

4.1. Cone Geometry

4.1.1. The model. In the polar coordinates $(r, \varphi) \in R^2$, a cone can be regarded as the embedding

$$(r, \varphi) \longrightarrow (ar\cos\varphi, ar\sin\varphi, cr),$$
$$0 < r < 1, \quad 0 \le \varphi < 2\pi,$$

with a and c being the cone parameters. From this, the components of the induced metric can easily be obtained as

$$g_{rr} = a^2 + c^2, \quad g_{\varphi\varphi} = a^2 r^2, \quad g_{r\varphi} = g_{\varphi r} = 0. \quad (25)$$

The opening angle of the cone, θ, is determined by

$$\sin(\theta/2) = a/\sqrt{a^2 + c^2}.$$

Because the cone itself appears when one or more sectors are removed from graphene, all possible angles are divisible by $\pi/3$. Therefore, the Frank index of the apical disclination can be specified by

$$\nu = 1 - \sin(\theta/2).$$

At $\nu = 0$, we obtain a flat graphene sheet ($\theta = \pi$). For convenience, we introduce the parameter

$$\xi = 1 + c^2/a^2$$

such that

$$\sin(\theta/2) = 1/\sqrt{\xi}$$

and

$$1/\sqrt{\xi} = 1 - \nu.$$

Nonvanishing coefficients of connection (3) are now given by

$$\Gamma^r_{\varphi\varphi} = -\frac{r}{\xi}, \quad \Gamma^\varphi_{r\varphi} = \Gamma^\varphi_{\varphi r} = \frac{1}{r}.$$

The general representation for the zweibeins is found to be

$$e_r^1 = \sqrt{a^2 + c^2}\cos\varphi, \quad e_\varphi^1 = -ar\sin\varphi,$$
$$e_r^2 = \sqrt{a^2 + c^2}\sin\varphi, \quad e_\varphi^2 = ar\cos\varphi,$$

which in view of Eq. (6) gives

$$\omega_r^{12} = \omega_r^{21} = 0,$$
$$\omega_\varphi^{12} = -\omega_\varphi^{21} = 1 - 1/\sqrt{\xi} =: 2\omega. \tag{26}$$

The external gauge potential is then $W_r = 0$, $W_\varphi = \nu$, and the Dirac operator on the cone takes the form

$$\hat{\mathcal{D}} = \hat{\mathcal{D}}^\dagger = \begin{bmatrix} 0 & e^{-i\varphi}\left(-\dfrac{\partial_r}{\sqrt{a^2 + c^2}} + \dfrac{1}{ar}(i\partial_\varphi + \nu + \omega)\right) \\ e^{i\varphi}\left(\dfrac{\partial_r}{\sqrt{a^2 + c^2}} + \dfrac{1}{ar}(i\partial_\varphi + \nu - \omega)\right) & 0 \end{bmatrix}.$$

Making the substitution

$$\psi = \tilde{\psi} r^\alpha, \quad \alpha = \sqrt{\xi}\omega,$$

we reduce the eigenvalue problem in Eq. (7) to

$$\partial_r \tilde{u} - \frac{\sqrt{\xi}}{r}(j - \nu)\tilde{u} = \tilde{E}\tilde{v},$$
$$-\partial_r \tilde{v} - \frac{\sqrt{\xi}}{r}(j + 1 - \nu)\tilde{v} = \tilde{E}\tilde{u}, \tag{27}$$

where $\tilde{E} = \sqrt{\xi}\, aE$.

4.1.2. Electron states. In contrast to the previous case of the two-sphere, the cone is essentially a flat manifold (the scalar curvature $\mathcal{R} = 0$ everywhere on the cone, except at the origin), and as a result, (27) allows an exact solution. Namely, the general solution to (27) is found to be [22]

$$\begin{pmatrix} \tilde{u} \\ \tilde{v} \end{pmatrix} = Ar^{-\alpha}\begin{pmatrix} J_\eta(\tilde{E}r) \\ \pm J_{\bar{\eta}}(\tilde{E}r) \end{pmatrix}, \tag{28}$$

where

$$\eta = \pm(\sqrt{\xi}(j - \nu + 1/2) - 1/2),$$
$$\bar{\eta} = \pm(\sqrt{\xi}(j - \nu + 1/2) + 1/2).$$

As earlier, we consider the case where $E > 0$. Normalization condition (17) now becomes

$$2\pi\sqrt{\xi}a^2A^2\int_0^1 (J_\eta^2(\tilde{E}r) + J_{\bar{\eta}}^2(\tilde{E}r))rdr = 1. \tag{29}$$

The normalization factor can be extracted from the asymptotic formula for Bessel functions at large arguments. Indeed, $\bar{\eta} - \eta = 1$ in our case, and therefore,

$$J_\eta^2 + J_{\bar{\eta}}^2 \longrightarrow 2/\pi\tilde{E}r \quad \text{for} \quad \tilde{E}r \gg 1.$$

Substituting this in (29) yields

$$A^2 = \frac{E}{4a}.$$

Clearly, (29) must be nonsingular at small r. This imposes a restriction on possible values of j. For $\eta, \bar{\eta} > 0$, we obtain $j > -1$ (i.e., $j = 0, 1, 2, \ldots$), and for $\eta, \bar{\eta} < 0$, we have $j < -2\nu$ ($j = -1, -2, \ldots$ at $\nu < 1/2$).

We are interested in the electron states near the apex of the cone. As follows directly from (28), the wave functions behave as

$$\begin{pmatrix} u \\ v \end{pmatrix} \propto \begin{pmatrix} E^{1/2+\eta}r^\eta, \\ E^{1/2+\bar{\eta}}r^{\bar{\eta}} \end{pmatrix} \tag{30}$$

for small r. In the leading order, we obtain

$$\Psi \propto E^{(1-2\nu)/2(1-\nu)}r^{-\nu/(1-\nu)}.$$

In particular, we obtain

$$\Psi \propto \begin{cases} \sqrt{E}, & \nu = 0, \\ E^{2/5}r^{-1/5}, & \nu = 1/6, \\ E^{1/4}r^{-1/2}, & \nu = 1/3. \end{cases}$$

Finally, the total density of states on the patch $0 <$

$r \le \delta$ is given by

$$D(E, \delta) \propto \begin{cases} E^{(1+2\nu)/(1-\nu)}\delta^{(\nu+2)/(1-\nu)}, & \eta, \bar{\eta} > 0, \\ E^{(1-2\nu)/(1-\nu)}\delta^{(2-3\nu)/(1-\nu)}, & \eta, \bar{\eta} < 0. \end{cases} \quad (31)$$

It should be stressed that, according to (31), a specific behavior of $D(E, \delta)$ occurs only for $\nu = 1/2$, where $D \propto E^0\delta$. This prediction of our model agrees with a finding in [10], where the prominent peak just above the Fermi level was found for the nanocone with three symmetric pentagons (180° disclination). In the leading order, it follows from (31) that

$$D(E, \delta) \propto \begin{cases} E\delta^2, & \nu = 0, \\ E^{4/5}\delta^{9/5}, & \nu = 1/6, \\ E^{1/2}\delta^{3/2}, & \nu = 1/3, \\ \delta, & \nu = 1/2. \end{cases} \quad (32)$$

As can be seen, the extended states with a nonzero density of states at E_F appear only at $\nu = 1/2$. This conclusion disagrees with the results obtained in [9], where a nonzero DOS at E_F was found to occur at $\nu = 1/3$. We now comment on this disagreement briefly. There is an important point where our consideration differs from [9]. Our model is based on the gauge-theory approach where defects on an elastic curved surface are described by an Abelian gauge field. As a result, the flux due to pentagonal apical disclination (elastic vortex) is explicitly incorporated into the Dirac equation. On the other hand, the model in [9] treats the appropriate boundary conditions for electron states resulting from the cut-and-paste procedure. In that approach, the gauge field carries information about the boundary conditions. In fact, both models are similar but not identical, which is exemplified by the different predictions.

To examine the electron states at the Fermi energy, we return to (27) and set $E = 0$. The solution reads

$$u_0 = Ar^{-1/2+\tilde{j}\sqrt{\xi}}, \quad v_0 = Br^{-1/2-\tilde{j}\sqrt{\xi}}, \quad (33)$$

where $\tilde{j} = j - \nu + 1/2$. A simple analysis shows that, for $j = 0$, both u_0 and v_0 are normalizable on the cone of a finite size. Both solutions are singular. For $\nu = 1/6$, we obtain

$$|u_0|^2 \propto r^{-1/5}/a^2, \quad |v_0|^2 \propto r^{-9/5}/a^2.$$

For any other j, either u_0 or v_0 is found to be normalizable and the solutions become nonsingular. As before, the total DOS can be considered for singular states. It is easy to find that $D \propto \delta^{1/5}$ for u_0 and $D \propto \delta^{9/5}$ for v_0. This result differs from [8], where, although in a different framework, the states on a finite cone with a single-pentagon defect have been found at the Fermi energy (these states decay away from the apex as $|\psi|^2 \propto r^{-2/5}$). At the same time, our study confirms the principal conclusion in [8, 30] that the states contributing to the nonzero DOS at the Fermi energy exhibit a power-law behavior for a single-pentagon defect. We also note that there are no zero-energy electronic states on a single disclination in monolayer graphite of an infinite length ($a \longrightarrow \infty$). We emphasize that this conclusion agrees with the results of numerical calculations in [30], where the local density of states at the Fermi level was found to be zero for five-membered rings (pentagons). We also note that, for $\nu = 1/2$, $D \propto \delta$ for both u_0 and v_0.

4.2. Hyperboloid Geometry

4.2.1. The model. The upper half of a hyperboloid can be regarded as the embedding

$$(\chi, \varphi) \longrightarrow (a\sinh\chi\cos\varphi, a\sinh\chi\sin\varphi, c\cosh\chi),$$
$$0 \le \chi < \infty, \quad 0 \le \varphi < 2\pi.$$

From this, the components of the induced metric can be obtained as

$$g_{\chi\chi} = a^2\cosh^2\chi + c^2\sinh^2\chi, \quad g_{\varphi\varphi} = a^2\sinh^2\chi, \quad g_{\varphi\chi} = g_{\chi\varphi} = 0, \quad (34)$$

which yields

$$\Gamma^{\chi}_{\chi\chi} = \frac{(a^2 + c^2)\sinh 2\chi}{2g_{\chi\chi}},$$
$$\Gamma^{\chi}_{\varphi\varphi} = -\frac{a^2\sinh 2\chi}{2g_{\chi\chi}}, \quad \Gamma^{\varphi}_{\varphi\chi} = \Gamma^{\varphi}_{\chi\varphi} = \coth\chi \quad (35)$$

for the nonvanishing coefficients of the connection. In a rotating $SO(2)$ frame, the zweibeins become

$$e^1_\chi = \sqrt{g_{\chi\chi}}\cos\varphi, \quad e^2_\chi = \sqrt{g_{\chi\chi}}\sin\varphi,$$
$$e^1_\varphi = -a\sinh\chi\sin\varphi, \quad e^2_\varphi = a\sinh\chi\cos\varphi, \quad (36)$$

which, in view of Eq. (6), gives the spin connection coefficients

$$\omega^{12}_\chi = \omega^{21}_\chi = 0,$$
$$\omega^{12}_\varphi = -\omega^{21}_\varphi = \frac{1}{2}\left[1 - \frac{a\cosh\chi}{\sqrt{g_{\chi\chi}}}\right] =: \omega, \quad (37)$$

and therefore,

$$\Omega_\varphi = i\omega\sigma^3. \quad (38)$$

The external gauge potential is then $W_\chi = 0$, $W_\varphi = \nu$, and the Dirac operator on the hyperboloid takes the form

$$\hat{\mathcal{D}} = \begin{bmatrix} 0 & e^{-i\varphi}\left(-\frac{\partial_\chi}{\sqrt{g_{\chi\chi}}} + \frac{1}{a\sinh\chi}(i\partial_\varphi + \nu + \omega)\right) \\ e^{i\varphi}\left(\frac{\partial_\chi}{\sqrt{g_{\chi\chi}}} + \frac{1}{a\sinh\chi}(i\partial_\varphi + \nu - \omega)\right) & 0 \end{bmatrix}.$$

It can be verified that $\hat{\mathcal{D}} = \hat{\mathcal{D}}^\dagger$.

The substitution

$$\tilde{\psi} = \psi\sqrt{\sinh\chi}$$

reduces the eigenvalue problem in Eq. (7) to

$$\begin{aligned} \partial_\chi\tilde{u} - \sqrt{\coth^2\chi + b^2}\,\tilde{j}\tilde{u} &= \tilde{E}\tilde{v}, \\ -\partial_\chi\tilde{v} - \sqrt{\coth^2\chi + b^2}\,\tilde{j}\tilde{v} &= \tilde{E}\tilde{u}, \end{aligned} \tag{39}$$

where

$$\tilde{E} = \sqrt{g_{\chi\chi}}E, \quad b = c/a, \quad \tilde{j} = j - \nu + 1/2.$$

4.2.2. Electron states. To study electronic states on the hyperboloid, we must analyze Eqs. (39). Because of the nonvanishing scalar curvature, the general solution to the Dirac equation on the hyperboloid (as well as on the sphere) is not available and we are forced to simplify the problem. Fortunately, we are interested in the behavior of the electron states near the apex and can therefore consider only the case of small χ. We then obtain

$$\begin{aligned} \partial_\chi\tilde{u} - \frac{\tilde{j}}{\chi}\tilde{u} &= Ea\tilde{v}, \\ -\partial_\chi\tilde{v} - \frac{\tilde{j}}{\chi}\tilde{v} &= Ea\tilde{u}, \end{aligned} \tag{40}$$

with the obvious solutions

$$\begin{aligned} \tilde{u} &= A\sqrt{Ea\chi}J_{|j-\nu|}(Ea\chi), \\ \tilde{v} &= A\sqrt{Ea\chi}J_{|j-\nu+1|}(Ea\chi). \end{aligned}$$

As can be seen, this is exactly the case of a sphere, which should not be surprising, because these two manifolds are locally diffeomorphic. Evidently, the total DOS on a finite hyperboloid is the same as on the sphere (see (19)).

We now consider the zero-energy modes, setting $E = 0$ in (39). The general solution is found to be

$$\begin{aligned} \tilde{u}(\chi) &= A\left[(k\cosh\chi + \Delta)^{2k}\frac{\Delta - \cosh\chi}{\Delta + \cosh\chi}\right]^{\tilde{j}/2}, \\ \tilde{v}(\chi) &= A\left[(k\cosh\chi + \Delta)^{2k}\frac{\Delta - \cosh\chi}{\Delta + \cosh\chi}\right]^{-\tilde{j}/2}, \end{aligned} \tag{41}$$

where

$$k = \sqrt{1 + b^2}, \quad \Delta = \sqrt{1 + k^2\sinh^2\chi}.$$

An important restriction comes from the normalization condition (see (17)) which on a finite hyperboloid yields $\tilde{j} > -1/2$ for $u(\chi)$ and $\tilde{j} < 1/2$ for $v(\chi)$. We see that, for $-1/2 < \tilde{j} < 1/2$, both $u(\chi)$ and $v(\chi)$ are normalizable simultaneously. For the zero-energy mode, the total DOS on a finite hyperboloid is found to be the same as on the sphere (see (24)).

Although the local electronic structures are similar on the hyperboloid and the sphere, there is a principal global distinction. We consider an unbounded hyperboloid (full locus). In this case, additional restrictions at the upper limit of the integral in (17) must be taken into account. We obtain $-1/2 < \tilde{j} < -1/2k$ for $u(\chi)$ and $1/2k < \tilde{j} < 1/2$ for $v(\chi)$. Therefore, either $u(\chi)$ or $v(\chi)$ becomes normalizable on the hyperboloid of infinite volume. We see that, as $c/a \longrightarrow 0$, a normalizable solution does not exist. In fact, the hyperboloid then becomes a plane. Consequently, our results are in accordance with the planar case. The total density of states on an infinite hyperboloid for a variety of defects is as follows:

$$D(\delta) \propto \begin{cases} \delta^{1/3}, & \nu = 1/6, \quad c/a > \sqrt{5}/2, \\ \delta^{2/3}, & \nu = 1/3, \quad c/a > 2\sqrt{2}, \\ \delta^{2/3}, & \nu = 2/3, \quad c/a > 2\sqrt{2}, \\ \delta^{1/3}, & \nu = 5/6, \quad c/a > \sqrt{5}/2. \end{cases} \tag{42}$$

We note that normalizable zero-energy states do not exist for the defect with $\nu = 1/2$ nor for the defect-free case $\nu = 0$. The most important conclusion from our consideration is that there is a possibility for the true zero-mode fermion state on the hyperboloid. As we have shown, the normalized zero-mode states on both the sphere and the cone exist only for a finite system size and disappear in the infinite-size limit. For an infinite hyperboloid, a normalized zero-energy electron state can exist in the presence of a disclination flux.

5. CONCLUSIONS

We have formulated a gauge field-theory model describing electron states on graphitic nanoparticles. The topological nature of the pentagonal defect is found to markedly modify the low-energy electronic

structure. In particular, the total density of extended states has a rather specific dependence on both the energy and the distance from the disclination line. We have found that the low-energy total DOS has a characteristic cusp at the Fermi energy for any disclinations with $\nu < 1/2$. In particular, this finding suppresses the extended electron states with a nonzero DOS at E_F in the fullerene molecule with $\nu = 1/6$. For zero-mode states, the total DOS on the patch $0 < r < \delta$ behaves as $\delta^{1/3}$. A similar behavior is found for a graphitic hyperboloid. There is, however, a principal distinction due to the possibility for the true zero-mode fermion state to occur on the hyperboloid. Namely, the normalized zero-energy electron state can exist even on an infinite-size hyperboloid.

We have shown that the local and the total DOS at the apices of nanocones are strongly dependent on the pentagon concentration. In particular, our model predicts anomalous behavior of $D(E, \delta)$ only for $\nu = 1/2$ (three pentagons at the apex), where $D \propto E^0\delta$; that is, the enhanced charge density at E_F is located at the apex of the cone at a 60° opening angle. This implies local metallization, thus suggesting some important applications of nanocone-based structures in microelectronic devices. First of all, such a remarkable increase of the DOS must provoke the corresponding enhancement of the field emission current, thereby decreasing the threshold voltage for emitted electrons. We note that this conclusion agrees well with the results in [10], where the prominent peak appearing just above the Fermi level was established in a nanocone with three pentagons at the apex. It was proposed that such peculiar nanocones are good candidates for nanoprobes in scanning probe microscopy and excellent candidates for field-emission devices. As was also mentioned in [10], the nanocones with free pentagons at the tip have the highest probability of nucleation and are frequently observed [27]. It is expected that localized states at the Fermi level may give rise to materials with novel electronic and magnetic properties. We hope that our predictions will motivate further measurements of electronic properties of graphitic nanoparticles.

ACKNOWLEDGMENTS

This work was supported by the Science and Technology Department of Moscow oblast and the Russian Foundation for Basic Research (project no. 01-02-97021) and by the Slovak Scientific Grant Agency (grant no. 7043(MP)).

REFERENCES

1. Yu. E. Lozovik and A. M. Popov, Usp. Fiz. Nauk **167**, 751 (1997) [Phys. Usp. **40**, 717 (1997)].
2. A. V. Eletskiĭ, Usp. Fiz. Nauk **167**, 945 (1997) [Phys. Usp. **40**, 899 (1997)].
3. J. G. Hou *et al.*, Phys. Rev. Lett. **83**, 3001 (1999).
4. D. L. Carroll *et al.*, Phys. Rev. Lett. **78**, 2811 (1997).
5. P. Kim *et al.*, Phys. Rev. Lett. **82**, 1225 (1999).
6. B. An *et al.*, Appl. Phys. Lett. **78**, 3696 (2001).
7. D. R. Nelson and L. Peliti, J. Phys. (Paris) **48**, 1085 (1987).
8. K. Kobayashi, Phys. Rev. B **61**, 8496 (2000).
9. P. E. Lammert and V. H. Crespi, Phys. Rev. Lett. **85**, 5190 (2000).
10. J.-C. Charlier and G.-M. Rignanese, Phys. Rev. Lett. **86**, 5970 (2001).
11. R. Jackiw and C. Rebbi, Phys. Rev. D **16**, 1052 (1977).
12. R. Jackiw and J. R. Schrieffer, Nucl. Phys. B **190**, 253 (1981).
13. R. Jackiw, Phys. Rev. D **29**, 2375 (1984).
14. V. A. Osipov and E. A. Kochetov, Pis'ma Zh. Éksp. Teor. Fiz. **72**, 295 (2000) [JETP Lett. **72**, 199 (2000)].
15. J. González, F. Guinea, and M. A. H. Vozmediano, Phys. Rev. Lett. **69**, 172 (1992).
16. J. González, F. Guinea, and M. A. H. Vozmediano, Nucl. Phys. B **406**, 771 (1993).
17. G. E. Volovik, Pis'ma Zh. Éksp. Teor. Fiz. **63**, 763 (1996) [JETP Lett. **63**, 802 (1996)].
18. G. E. Volovik, Pis'ma Zh. Éksp. Teor. Fiz. **70**, 609 (1999) [JETP Lett. **70**, 645 (1999)].
19. G. E. Volovik, Pis'ma Zh. Éksp. Teor. Fiz. **70**, 739 (1999) [JETP Lett. **70**, 792 (1999)].
20. D. P. DiVincenzo and E. J. Mele, Phys. Rev. B **29**, 1685 (1984).
21. C. L. Kane and E. J. Mele, Phys. Rev. Lett. **78**, 1932 (1997).
22. V. A. Osipov and E. A. Kochetov, Pis'ma Zh. Éksp. Teor. Fiz. **73**, 631 (2001) [JETP Lett. **73**, 562 (2001)].
23. E. A. Kochetov and V. A. Osipov, J. Phys. A: Math. Gen. **32**, 1961 (1999).
24. M. B. Green, J. H. Schwartz, and E. Witten, *Superstring Theory* (Cambridge Univ. Press, Cambridge, 1988; Mir, Moscow, 1990), Vol. 2.
25. B. A. Ovrut and S. Tomas, Phys. Rev. D **43**, 1314 (1991).
26. M. Stone, Nucl. Phys. B **314**, 557 (1989).
27. A. Krishnan *et al.*, Nature **388**, 451 (1997).
28. N. A. Kiselev *et al.*, Carbon **36**, 1149 (1998).
29. H. Terrones *et al.*, Chem. Phys. Lett. **343**, 241 (2001).
30. R. Tamura and M. Tsukada, Phys. Rev. B **49**, 7697 (1994); **52**, 6015 (1995).

Journal of Experimental and Theoretical Physics, Vol. 96, No. 1, 2003, pp. 150–164.
Translated from Zhurnal Éksperimental'noĭ i Teoreticheskoĭ Fiziki, Vol. 123, No. 1, 2003, pp. 172–188.

SOLIDS
Electronic Properties

Topological Transitions in Size-Quantized Heterostructures

A. A. Gorbatsevich* and O. V. Zhabitsky**
Moscow Institute of Electronic Engineering, Moscow, 103498 Russia
**e-mail: aag@qdn.miee.ru*
***e-mail: Oleg.Zhabitsky@motorola.com*
Received August 1, 2002

Abstract—An exact solution is obtained to the problem of the spectrum of holes, described by the Luttinger Hamiltonian, in a quantum well of finite depth under arbitrary uniaxial stresses in the well and the barrier. Conditions for the topological transitions accompanied by the variation in the connectivity of the isoenergetic surface are found. It is shown that, for certain values of model parameters, the effective mass of holes in the ground-state subband of size quantization becomes negative. *© 2003 MAIK "Nauka/Interperiodica".*

1. INTRODUCTION

An important role in the application of modern methods of band-structure engineering to the development of new types of heterostructures is played by qualitative ideas about the specific features of the formation of the charge-carrier energy spectrum with regard to size quantization. For nondegenerate states in the conduction band, these ideas are rather trivial and are reduced to the results of an exactly solvable problem on the bound states of an electron in a quantum well of finite depth [1]. A more complicated situation occurs in the valence band due to the mixing of light- and heavy-hole states under nonzero values of the transverse quasimomentum of charge carriers (in the plane of the quantum well). The simplest model describing this phenomenon is the Luttinger Hamiltonian, which takes into account the band that is split off due to spin–orbit interaction. An exact solution to the problem with the Luttinger Hamiltonian for a quantum well with infinitely high barriers was obtained by Nedorezov [2] and improved in [3, 4]. In recent years, there has been considerable interest in strained heterostructures, which is primarily attributed to numerous engineering applications of these structures [5]. The use of the deformation potential as an additional control parameter opens new possibilities for developing heterostructures with prescribed properties. The growth of various types of strained heterostructures (that are compressed or stretched in the plane of the quantum well) allows one to alter the forbidden band and the effective density of states and thus to control the radiation wavelength and the threshold current in semiconductor lasers [6, 7] and enhance the sensitivity of detectors in electrooptical modulators [8]. The application of strained layers enables one to increase the mobility and concentration of charge carriers in the channel of a field-effect transistor with modulated doping [9] and to enhance the efficiency of the emitter and increase the band transport factor of a heterojunction bipolar transistor [9]. The Nedorezov solution in the case of a strained quantum well was generalized in [10]. The basic principles of the hole spectrum of real semiconductor systems with different Luttinger parameters in the well and the barrier, with a finite height of the potential barrier, and with regard to stresses were established in [11] by numerical calculation, where the authors used analytic expressions for the eigenfunctions of the Luttinger Hamiltonian. A variety of results of numerical calculations of the energy spectra of holes in size-quantized semiconductor heterostructures have been expounded in modern monographs and textbooks [7, 12–14].

In the present work, we obtain an exact solution for the energy spectrum of holes, described by the Luttinger Hamiltonian, in a quantum well of finite depth under the assumption that the Luttinger parameters in the well and the barrier are identical, while elastic stresses in the well and the barrier may be different. The relations obtained show that, in certain parameter domains of the system, the effective mass of holes in the ground-state subband E_{h1} of size quantization becomes negative, while the isoenergetic surface becomes multiconnected; these phenomena can manifest themselves differently in experiments. Actually, we deal with a new mechanism of topological transition in the energy spectrum [15].

The paper is set up as follows. In Section 2, by example of a model problem of a quantum well with infinitely high barriers, we establish the main factors that determine the details of the energy spectrum of holes in size-quantized heterostructures, in particular, a relation between the transverse effective mass (with respect to the quantization axis) and the sequence order (in energy) of the subbands of size quantization. In modern literature [7, 13, 14], one usually applies various approximations to the qualitative interpretation of the results of numerical calculations, which reduce to neglecting the warping of the bulk dispersion law. We show that neglecting the warping may lead to a loss of

important features of the transverse dispersion law of holes. In Section 3, we obtain an exact solution to the model problem of the spectrum of holes in a quantum well of finite depth, find conditions for the topological transitions accompanied by variation of the connectivity of the isoenergetic surface, and construct topological diagrams that determine the boundaries of the existence domains of multiconnected isoenergetic surfaces as a function of stresses in the well and the barrier. We show that the presence of stretching deformations in the quantum well is favorable to the topologically nontrivial structure of the energy spectrum. In Section 4, as an example of the realization of topological transitions in specific physical systems, we present the results of numerical calculations, carried out by the envelope-function method, of the energy spectrum in strained InP/InGaAs and GaAs/SiGe heterostructures. Possible experimental manifestations of topological transitions are discussed in Section 4 and in the Conclusion.

2. MIXING OF LIGHT AND HEAVY HOLES, WARPING, AND SIZE QUANTIZATION IN A QUANTUM WELL WITH INFINITELY HIGH BARRIERS

Consider an isolated symmetric quantum well of width L. Suppose that the plane of the well is perpendicular to axis z. To describe the effects of size quantization, we apply the effective-mass (envelope-function) approximation. The Luttinger Hamiltonian for envelope functions, which describes the subbands of heavy holes, is given by ($\hbar = 1$)

$$H(z) = -\begin{pmatrix} P+Q & L & M & 0 \\ L^* & P-Q & 0 & M \\ M^* & 0 & P-Q & -L \\ 0 & M^* & -L^* & P+Q \end{pmatrix} + U(z), \quad (1)$$

where

$$P = \frac{\gamma_1}{2m_0}(k_x^2 + k_y^2 + k_z^2),$$

$$Q = \frac{\gamma_2}{2m_0}(k_x^2 + k_y^2 - 2k_z^2),$$

$$L = -\frac{i\sqrt{3}\gamma_3}{m_0}(k_x - ik_y)k_z,$$

$$M = \frac{\sqrt{3}\gamma_2}{2m_0}(k_x^2 - k_y^2) - i\frac{\sqrt{3}\gamma_3}{m_0}k_xk_y,$$

$U(z)$ is the potential of the heterostructure ($U(z) = U_0$ for the barrier and $U(z) = 0$ in the well); m_0 is the mass of a free electron; and γ_1, γ_2, and γ_3 are the Luttinger parameters, which, generally speaking, are different for the well and the barrier. Hamiltonian (1) is expressed on the basis of the eigenfunctions $Y_{3/2}^{\pm 3/2, \pm 1/2}$ of angular momentum. Everywhere below, we refer to the band corresponding to the projection of momentum 3/2 (1/2) onto axis z for $k_x = k_y = 0$ as the band of heavy h (light l) holes.

The energy spectrum of Hamiltonian (1) in the bulk of semiconductor ($U(z) = \text{const}$) is well known:

$$E_{h,l} = -P \pm \sqrt{Q^2 + |L|^2 + |M|^2}. \quad (2)$$

In addition to the Kramers degeneracy, each energy level (2) is degenerate in the states of light and heavy holes. A distinctive feature of energy spectrum (2) is the warping, which disappears when $\gamma_2 = \gamma_3$.

The size-quantized energy spectrum of nondegenerate (disregarding the Kramers degeneracy) bands (the conduction band of widely used semiconductors) can be obtained directly from the expression for the bulk dispersion law. To this end, one should substitute the quantized values of the longitudinal quasimomentum, which correspond to the motion along the size-quantization axis and are determined by the matching conditions of the wave functions and their derivatives at the heterointerfaces, into the expression for the bulk dispersion law [7, 12, 14]. In this case, each quantized value of the longitudinal quasimomentum k_n corresponds to its own subband $E_n(k_\perp)$ of size quantization that describes the dependence of energy on the transverse quasimomentum $k_\perp$ (corresponding to the motion in the plane of the well). When quantizing degenerate states (2) of the valence band of widely used semiconductors, the mixing of heavy- and light-hole branches at finite values of the transverse quasimomentum considerably complicates the calculation of the size-quantized spectrum.

When the transverse quasimomentum is equal to zero, Hamiltonian (1) is diagonal, the states of light and heavy holes are decoupled, and their longitudinal quasimomenta are quantized independently. In this case, the problem of quantizing the longitudinal quasimomentum is reduced to determining the spectrum of nondegenerate states in a quantum well of finite depth [1]. If we neglect the difference between the effective masses (Luttinger parameters) in the well and the barrier, then the size-quantized longitudinal quasimomenta of light and heavy holes coincide ($k_{nh0} = k_{nl0} = k_{n0}$; the effective mass is not included in the condition of size quantization [1]), and the edges of the subbands are determined by the bulk effective masses:

$$E_{nh,l0} = -\frac{k_{n0}^2}{2m_{h,l}} = -\frac{(\gamma_1 \mp 2\gamma_2)k_{n0}^2}{2m_0}. \quad (3)$$

This relation implies that the first subband of size quantization for heavy holes is higher in energy than the first subband of light holes.

Table 1. Calculation of transverse effective masses $m_{h1,2}$ (11) for the first two subbands of heavy holes for various semiconductors. Parameters ν, m_h, m_{hr}, and $m_{h\perp 0}$ are defined in (5), (3), (4), and (8), respectively. The last column contains references to the sources of the values of $\gamma_{1,2,3}$

Material	ν	m_0/m_h	m_0/m_{hr}	$m_0/m_{h\perp 0}$	m_0/m_{h1}	m_0/m_{h2}	Reference
Si	1.45	3.44	4.61	–11.3408	3.47929	4.68684	[14]
GaP	1.64	3.07	4.54	–48.0206	–0.010403	7.03924	[16]
GaP	2.75	2.24	5.18	–3.25551	4.06544	11.9147	[14]
AlAs	2.55	2.12	4.58	–2.79707	3.65245	8.73729	[16]
AlAs	2.30	2.09	4.13	–3.21162	3.25151	6.75966	[14]
AlP	2.47	1.93	4.06	–2.33254	3.26109	7.20948	[16]
AlSb	2.7	2.8	6.37	–3.41378	5.08869	13.5452	[16]
AlN	2.92	0.98	2.39	–2.2217	1.76406	7.29171	[16]
GaN	3.56	1.17	3.42	–1.42	2.71259	22.8286	[16]
GaAs	3.88	2.86	9.04	–3.46228	7.1656	224.439	[16]
GaAs	4.17	2.65	8.95	–3.06429	7.1139	–155.477	[14]
Ge	4.51	4.85	17.6	–5.25372	14.0416	–102.141	[14]
InP	4.40	1.88	6.68	–1.58875	5.39928	–45.4664	[16]
InP	4.92	2.12	8.36	–2.62692	6.61613	–27.9207	[14]
InN	5.2	1.2	4.98	–1.34595	3.96514	–12.5272	[16]
GaSb	5.31	3.74	15.83	–4.76623	12.5128	–38.0669	[14]
GaSb	5.7	4	18.1	–4.87872	14.3526	–33.9338	[16]
InAs	12.33	3	28.5	–1.37294	23.1966	–8.71673	[16]
InAs	12.43	2.93	28.04	–2.89337	22.5455	–10.4123	[14]
InSb	17.32	3.8	50.3	–2.39355	40.7622	–10.4437	[16]
InSb	17.46	3.8	50.72	–4.12938	40.7881	–12.4159	[14]

An interesting feature of the energy spectrum $E_n(k_\perp)$ of size-quantized systems, which was revealed as early as in the first calculations for quantum wells [3], is the fact that the effective mass in the transverse dispersion law of the first subband of size quantization (the subband of heavy holes) is less than the effective mass of the next subband. This phenomenon is called a mass reversal in the literature [7, 13, 14]. Various arguments have been used to qualitatively validate this phenomenon, which ultimately reduce to the rejection of off-diagonal terms in the Luttinger Hamiltonian (1) [7, 13, 14]. In this case, we obtain the following expression for the transverse dispersion law:

$$E_{nh,l}(k_\perp) = E_{nh,l0} - \frac{k_\perp^2}{m_{h,lr}} = E_{nh,l0} - \frac{(\gamma_1 \pm \gamma_2)k_\perp^2}{2m_0}; \quad (4)$$

i.e., formula (4) indeed implies that the coefficient multiplying the square of the transverse quasimomentum in the expression for the energy of heavy holes is greater than the corresponding term in the expression for light holes. However, the reversed masses in (4) that result from such a manipulation depend neither on the geometrical parameters of a size-quantized heterostructure nor on the number of the subband; they do not reproduce the real situation even qualitatively. Table 1 displays the results of the exact solution [2, 3] (which is discussed below) for the effective mass of transverse motion for the first two subbands of size quantization for heavy holes ($m_{h1,2}$, the sixth and seventh columns in Table 1) and for the first subband of light holes (m_{l1}, the sixth column in Table 2) for thin films of various materials (quantum wells with infinitely high barriers). For comparison, the fourth column presents the numerical values of reversed masses $m_{h,lr}$ (4). For the materials in the upper part of the table (Si-like materials), the effective mass of light holes is indeed greater than the "transverse" mass of heavy holes. However, the numerical values of transverse masses $m_{h,l1}$ have nothing to do with the values of reversed masses. For most materials from the upper part of Table 1, the transverse effective masses of light holes are negative. For the materials from the lower part of Table 1 (Ge-like materials), the transverse masses of light holes prove to be less than those of heavy holes. It can easily be shown that, for the materials presented in the lower part of Table 1, the second subband of size quantization for

Table 2. Calculation of transverse effective masses m_{l1} (11) for the first subband of light holes for various semiconductors. Parameters ν, m_l, m_{lr}, and m_{l0} are defined in (5), (3), (4), and (8), respectively

Material	ν	$m_0/m_{l\perp 0}$	m_0/m_{lr}	$m_0/m_{l\perp 0}$	m_0/m_{l1}	Reference
Si	1.45	5	3.83	19.7808	1.71036	[14]
GaP	1.64	5.03	3.56	56.1206	–7.02045	[16]
GaP	2.75	6.16	3.22	11.6555	–5.45039	[14]
AlAs	2.55	5.4	2.94	10.3171	–2.84356	[16]
AlAs	2.30	4.81	2.77	10.1116	–1.38447	[14]
AlP	2.47	4.77	2.64	9.03254	–1.89515	[16]
AlSb	2.7	7.56	3.99	13.7738	–5.40956	[16]
AlN	2.92	2.86	1.45	6.0617	–4.54101	[16]
GaN	3.56	4.17	1.92	6.76	–18.7366	[16]
GaAs	3.88	11.1	4.92	17.4223	–213.816	[16]
GaAs	4.17	11.05	4.75	16.7643	165.876	[14]
Ge	4.51	21.85	9.1	31.9537	122.365	[14]
InP	4.40	8.28	3.48	11.7488	53.3047	[16]
InP	4.92	10.44	4.2	15.1869	37.2528	[14]
InN	5.2	6.24	2.46	8.78595	18.066	[16]
GaSb	5.31	19.86	7.77	28.3662	55.421	[14]
GaSb	5.7	22.8	8.7	31.6787	53.005	[16]
InAs	12.33	37	11.5	41.3729	29.1383	[16]
InAs	12.43	36.41	11.3	42.2334	29.0831	[14]
InSb	17.32	65.8	19.3	71.9935	138.109	[16]
InSb	17.46	66.36	19.44	74.2894	135.703	[14]

heavy holes lies higher in energy than the first subband for light holes. In other words, as follows from (3), the relation

$$\nu = \frac{m_h}{m_l} > 4 \tag{5}$$

or

$$\gamma_1 < \frac{10}{3}\gamma_2$$

holds for these materials. The transverse effective mass of the second subband of heavy holes in these materials is always greater than the effective mass of the first subband. Thus, an exact statement is that the reversal of transverse masses occurs for the first and second subbands of size quantization with respect to energy (the effective mass of the first subband is lower than that of the second) rather than for the subbands of light and heavy holes. Note that, according to calculations, the transverse effective masses of all subbands substantially depend both on the film thickness (the width of the quantum well) and on the subband number, and are not even qualitatively reproduced by formula (4).

It should be noted that the rejection of off-diagonal terms in Hamiltonian (1), which leads to relations (4), is not justified even formally because the coefficient γ_3, to which the off-diagonal terms in (1) are proportional, is greater than the coefficient γ_2, which determines the difference between the effective masses of light and heavy holes, for all widely used semiconductors [14, 16]. Moreover, rejecting the off-diagonal terms, we lose information on such a significant feature of the bulk spectrum as warping. At the same time, the contribution of the off-diagonal terms of the Luttinger Hamiltonian to the size-quantized spectrum can easily be taken into account in perturbation theory if one assumes that the ratio

$$\frac{k_\perp}{k_n} \ll 1 \tag{6}$$

is a small parameter. Expanding (2) in terms of parameter (6), we obtain

$$E_{h,l} \approx -E_{h,l0} - \frac{k_\perp^2}{2m_{h,l\perp 0}}, \tag{7}$$

where we have the following expression for the "bare" transverse effective mass $m_{h,l\perp 0}$:

$$\frac{m_0}{m_{h,l\perp 0}} = \gamma_1 \pm \gamma_2 \mp \frac{3\gamma_3^2}{\gamma_2}. \tag{8}$$

When $\gamma_2 = \gamma_3$ (in the absence of warping), the bare transverse masses coincide with the bulk masses $m_{h,l}$ (3). The reversed masses (4) are obtained from (8) if we set the Luttinger parameter γ_3 equal to zero. It is clear that, up to the second-order terms in $k_\perp$ in energy, this is equivalent to the elimination of the off-diagonal terms from the Luttinger Hamiltonian.

As was pointed out by the authors of [17], the bare transverse effective mass of heavy holes is negative in many semiconductors with a sufficiently large ratio of parameters γ_3 and γ_2 (see Table 1). This is a direct consequence of the warping in the bulk dispersion law for heavy holes. At the same time, the bare effective mass (8) is different from the transverse effective mass observed in the experiment since formula (8) does not take into account the dependence of the quantized quasimomentum k_n on the transverse quasimomentum $k_\perp$, which results from the mixing of light- and heavy-hole branches at finite $k_\perp$. Let us represent this dependence as follows:

$$k_{nh,l} = k_{nh,l0} + \frac{\alpha_{h,l}k_\perp^2}{k_{nh,l0}}. \tag{9}$$

Here, the second term on the right-hand side is called a phase shift because it determines the variation in the phase of a wave function under the variation of the transverse momentum. With regard to the phase shift, the expression for the effective mass of transverse motion of holes is rewritten as

$$\begin{aligned}\frac{m_0}{m_{h,l\perp}} &= \frac{m_0}{m_{h,l\perp 0}} + \delta\left(\frac{m_0}{m_{h,l\perp 0}}\right)\\ &= \gamma_1 \pm \gamma_2 \mp \frac{3\gamma_3^2}{\gamma_2} + 2\alpha_{h,l}(\gamma_1 \mp 2\gamma_2)k_{nh,l0},\end{aligned} \tag{10}$$

where $(m_0/m_{h,l\perp 0})$ is the variation of the effective mass of transverse motion associated with the phase shift.

To determine the phase shift, one has to solve the eigenvalue problem for Hamiltonian (1) with regard to the matching condition on the boundaries of the quantum well. In a quantum well with infinitely high barriers, the matching condition is reduced to the vanishing of the wave function on the boundary. For a given value of energy, Luttinger Hamiltonian (1) has eight linearly independent solutions (including the states that differ in the direction of the longitudinal quasimomentum $\pm k_{nh,l}$) that form a basis. Therefore, the boundary conditions in the well with infinitely high barriers lead to a system of eight homogeneous linear equations for the expansion coefficients of the wave eigenfunction over this basis. This problem was solved for the first time by Nedorezov [2] (in [2], an error was made in sign while substituting specific values of the Luttinger parameters; this error was corrected in [3]). A solution for the transverse effective mass (in which a phase shift is taken into account) is given by [2, 3]

$$\begin{aligned}\frac{m_0}{m_{h,l\perp}} &= \frac{m_0}{m_{h,l\perp 0}}\\ &+ \begin{cases} +\dfrac{3\gamma_3^2}{\gamma_2^2}\dfrac{m_0}{\sqrt{m_h m_l}}\dfrac{1}{\pi n}\cot\dfrac{n\pi\nu^{\mp 1/2}}{2}, & n = 2m+1,\\ -\dfrac{3\gamma_3^2}{\gamma_2^2}\dfrac{m_0}{\sqrt{m_h m_l}}\dfrac{1}{\pi n}\tan\dfrac{n\pi\nu^{\mp 1/2}}{2}, & n = 2m,\end{cases}\end{aligned} \tag{11}$$

where $m_{h,l}$ are the bulk effective masses of heavy and light holes (3), $m_{h,l\perp 0}$ are the bare transverse effective masses (8), and the parameter ν is defined in (5). The second term on the right-hand side of (11) determines a contribution associated with the phase shift to the effective mass. The calculated effective masses of different semiconductors are presented in Tables 1 and 2.

Formula (11) shows that, for the ground-state subband of size quantization ($n = 1$), the phase shift makes a positive contribution to the inverse transverse effective mass of heavy holes (because $\nu > 1$) and a negative contribution to the effective mass of light holes for Si-like materials ($\nu < 4$), in which the second subband in energy is the ground-state subband of light holes.

For Ge-like materials ($\nu > 4$), the second subband in energy is the subband of heavy holes with $n = 2$, and formula (11) shows that the contribution of the phase shift to the inverse transverse effective mass for this subband is negative. Thus, it is the dependence of the momentum of size quantization on the transverse quasimomentum (the phase shift in our terminology) that accounts for the basic principles determining the value of the transverse effective mass in various materials.

Qualitatively, the physical reason for the positive sign of the phase shift α_h of the quasimomentum of size quantization (an increase in k_z with increasing $k_\perp$) for the ground-state subband of size quantization can be interpreted as follows. When $k_\perp \neq 0$, a wave corresponding to the branch of light holes with the same energy as that for heavy holes but with lesser k_z is coupled to the wave corresponding to the branch of heavy holes. The standing-wave condition (the condition of constructive interference) requires that a certain average momentum of coupled states should be on the order of the momentum k_{z0} defined by the interference condition in the absence of mixing of the light- and heavy-hole branches (for $k_\perp \neq 0$). When $k_\perp = 0$, the quasimomentum $k_{h0} = k_{z0}$, while $k_{l0} < k_{z0}$. The coupling of a wave with lesser quasimomentum (k_{z0}) to the wave with $k_{h0} = k_{z0}$ decreases their mean effective momentum. Therefore, for the effective mean momentum to remain on the order of k_{z0} as the momentum $k_\perp$ (which determines the degree of mixing) increases, the quasimomentum k_h should also increase with $k_\perp$. This trend will weaken if

we make k_h and k_l closer to each other, for example, by moving the branch of heavy holes downward and the branch of light holes upward along the energy axis due to a stretching stress applied to the system.

A similar result is obtained by reducing the barrier height. In this case, the momentum k_{h0} of size quantization decreases [1] and the difference between k_{h0} and k_{l0}, as well as the phase shift, also decreases. This mechanism of suppressing the phase shift can be strengthened by applying a compressing stress that increases the barrier height for light holes and decreases it for heavy holes. The following section is devoted to solving the problem of size quantization of the energy spectrum of the Luttinger Hamiltonian for a quantum well of finite depth in a strained heterostructure.

3. SIZE QUANTIZATION OF THE HOLE SPECTRUM IN A STRAINED QUANTUM WELL OF FINITE DEPTH

Consider a strained heterostructure consisting of a quantum well and symmetric barriers of finite height. Let ζ and η be the shifts of energy levels due to mechanical stresses in the well and the barrier regions, respectively. Suppose that the stresses do not break the spatial symmetry of the system and that they are identical in the left and right barriers. To take into account these stresses, we have to make the following change in the variable Q in the well and the barriers:

$$Q^w \longrightarrow Q^w + \zeta, \quad Q^b \longrightarrow Q^b + \eta. \tag{12}$$

For notational convenience, introduce the normalized stresses

$$\zeta_{h,l} = \frac{m_0\zeta}{\gamma_2 k_{h,l}^2}, \quad \eta_{h,l} = \frac{m_0\eta}{\gamma_2 q_{h,l}^2}. \tag{13}$$

In a quantum well of finite depth, in addition to the boundary conditions imposed on the wave functions, one should take into account the conditions imposed on the derivatives of these functions. The dimensions of the Hamiltonian and the corresponding matrix of boundary conditions can be reduced by applying the basis transformation of Broido and Sham [18], which guarantees that the matrix elements of the momentum p_z vanish. Later, this transformation was generalized to a 6×6 Hamiltonian [19, 20]. On the new basis, the Hamiltonian is reduced to a block-diagonal form whose elements are two identical 2×2 Hamiltonians:

$$\tilde{H}(z) = -\begin{pmatrix} P+Q & \tilde{M} \\ \tilde{M}^* & P-Q \end{pmatrix} + U(z). \tag{14}$$

Here,

$$\tilde{M} = |M| + i\frac{\sqrt{3}\gamma_3}{m_0}|k_\perp|k_z,$$

where M is defined in (1). Everywhere below, we will use boundary conditions of conventional form that guarantee the continuity of flow across the heterointerfaces at $z = 0$ and $z = L$:

$$\begin{aligned} \psi_l(0_-) &= \psi_w(0_+), \quad \psi_w(L_-) = \psi_r(L_+), \\ \hat{j}_l\psi_l(0_-) &= \hat{j}_w\psi_w(0_+), \quad \hat{j}_w\psi_w(L_-) = \hat{j}_r\psi_r(L_+), \end{aligned} \tag{15}$$

where the flow operator $\hat{j}$ is given by [12]

$$\hat{j} = -e\frac{\delta}{\delta\hat{k}_z}\tilde{H}(\hat{k}_z, \mathbf{k}_\perp). \tag{16}$$

Here, $\tilde{H}(\hat{k}_z, \mathbf{k}_\perp)$ is Hamiltonian (14) and the subscripts l, r, and w refer to the left and right barriers and the quantum well, respectively. Possible deviations from standard boundary conditions (15) and related physical phenomena were considered in [21].

Expanding the matrix of boundary conditions over the basis of eigenfunctions of Hamiltonian (14), we obtain the following expression that determines the energy spectrum of holes in the quantum well of finite depth:

$$\begin{aligned} S(u,t) + S(s,v) &= D(s,t,u,v,k_l,k_h) \\ &+ D(t,s,v,u,k_h,k_l), \end{aligned} \tag{17}$$

where

$$S(u,t) = |u||\tilde{u}||t||\tilde{t}|\sin(k_lL + \phi_{\tilde{u}} - \phi_u)\sin(k_hL + \phi_{\tilde{t}} - \phi_t),$$

$$D(s,t,u,v,k_1,k_2) = |s||\tilde{t}|[|\tilde{u}||v|\sin(k_1L + \phi_{\tilde{u}} - \phi_s)$$

$$\times \sin(k_2L + \phi_{\tilde{t}} - \phi_v) + |u||\tilde{v}|\sin(\phi_s - \phi_u)\sin(\phi_{\tilde{t}} - \phi_{\tilde{v}})],$$

$$u, \tilde{u} = (k_l \pm iq_h)(R_l^b M_l^{w*} - R_l^w M_l^{l,r}),$$

$$v, \tilde{v} = (k_h \pm iq_h)(R_l^b M_h^{w*} - R_h^w M_l^{l,r}),$$

$$s, \tilde{s} = (k_l \pm iq_l)(R_h^b M_l^{w*} - R_l^w M_h^{l,r}),$$

$$t, \tilde{t} = (k_h \pm iq_l)(R_h^b M_h^{w*} - R_h^w M_h^{l,r}),$$

$$M_{h,l}^l = |M| - \frac{\sqrt{3}\gamma_3}{m_0}|k_\perp|q_{h,l},$$

$$M_{h,l}^r = |M| + \frac{\sqrt{3}\gamma_3}{m_0}|k_\perp|q_{h,l},$$

$$M_{h,l}^w = |M| + i\frac{\sqrt{3}\gamma_3}{m_0}|k_\perp|k_{h,l}, \quad R_i^j = Q_i^j - P_i^j - E,$$

ϕ_i is the phase of the appropriate coefficient, and E is energy. In the limit of small $k_\perp$, the pairs of coefficients c and $\tilde{c}$ ($c = \{u, v, s, t\}$) satisfy the following relation:

$$c = -\tilde{c}^*.$$

In the limit as U_0, $q \longrightarrow \infty$, formula (17) reduces to the spectrum formula from [2, 10].

Expression (8) for the bare (without taking into account the phase shift) effective masses of the subbands of heavy and light holes with regard to stresses is rewritten as

$$\frac{m_0}{m_{h,l\perp 0}} = \gamma_1 \pm \gamma_2 \mp \frac{3\gamma_3^2}{\gamma_2(1-\zeta_{h,l})}. \quad (18)$$

As we discussed above, the third term in this expression is related to the warping of the bulk spectrum. Owing to the coefficient $(1 - \zeta_{h,l})$ in the denominator of the third term, positive stresses $\zeta_{h,l}$ increase the contribution of warping, whereas negative stresses, conversely, reduce this contribution. Moreover, for sufficiently large stresses, the coefficient $1 - \zeta_{h,l}$ may change the sign of the contribution of warping to the effective mass.

Taking into account the stresses and the phase shift, we obtain the following expression for the effective masses of the subbands of heavy and light holes:

$$\frac{m_0}{m_{h,l}} = \gamma_1 \pm \gamma_2 \mp \frac{3\gamma_3^2}{\gamma_2(1-\zeta_{h,l})} + 2(\gamma_1 \mp 2\gamma_2)\alpha_{h,l}. \quad (19)$$

For a barrier of finite height when $k_\perp \ll k_{z0}$, formula (17) yields the following expression for the coefficient $\alpha_{h,l}$ in (19) that determines the phase shift and the sign of the effective mass:

$$\alpha_{h,l} = \frac{3\gamma_3^2}{2\gamma_2^2}\frac{q_{h,l}}{2+q_{h,l}L}\frac{1}{(1-\zeta_h)(1-\zeta_l)(1+\eta_h)(1+\eta_l)}\left\{\frac{(1-\zeta_{l,h})(q_{h,l}-q_{l,h})}{k_{h,l}q_h q_l}\left(1+\frac{\eta_{h,l}q_{h,l}^2-\zeta_{h,l}k_{h,l}^2}{k_{h,l}^2+q_{h,l}^2}\right)\right.$$

$$\pm\frac{1-\zeta_{l,h}}{q_{h,l}}\frac{k_{h,l}}{k_{h,l}^2+q_{h,l}^2}\frac{2\gamma_2}{\gamma_1\mp 2\gamma_2}(1+\eta_{l,h})(\eta_{h,l}+\zeta_{h,l})+\frac{1}{k_l k_h}\left[1+\frac{\zeta_h(q_h-q_l)k_h^2+q_h\eta_h(k_h^2+q_h q_l)}{q_l(k_h^2+q_h^2)}\right] \quad (20)$$

$$\left.\times\left[1+\frac{\zeta_l(q_l-q_h)k_l^2+q_l\eta_l(k_l^2+q_h q_l)}{q_h(k_l^2+q_l^2)}\right]\left[\frac{1+\cos\phi_{l,h}}{\sin\phi_{l,h}}+\frac{(\eta_{l,h}+\zeta_{l,h})(q_{h,l}-q_{l,h})k_{l,h}q_{l,h}}{q_{h,l}(k_{l,h}^2+q_{l,h}^2)\pm\zeta_{l,h}(q_l-q_h)k_{l,h}^2+\eta_{l,h}q_{l,h}(k_{l,h}^2+q_l q_h)}\right]\right\},$$

where

$$\phi_{l,h} = k_{l,h}L - 2\operatorname{arccot}\frac{k_{l,h}}{q_{l,h}}.$$

The first term on the right-hand side of (20) comes from the dependence of the barrier height on the transverse quasimomentum, which arises in the presence of stresses even when the Luttinger parameters of the well and the barrier are identical. The second term on the right-hand side is attributed to the dependence of the phases ϕ_c in the arguments of sines on the left-hand side of (20) on the transverse quasimomentum and vanishes when the barrier height tends to infinity. The last term on the right-hand side of (20) represents the Nedorezov contribution [2] modified for finite values of the barrier height and stresses. In a well with infinitely high barriers, the phase shift α_h for heavy holes is always positive and compensates for the contribution of the term associated with the warping to the effective mass. In this case, conversely, the phase shift and, accordingly, the contribution of light holes to the inverse effective mass is negative. As a result, the effective mass of transverse motion for light holes in the quantum well may become greater than that for heavy holes. However, within the limits that admit analytic investigation, coefficient α_h is positive and its contribution to the effective mass of transverse motion is greater than the contribution of the negative third term on the right-hand side [10]. For arbitrary values of the parameters, formula (20) requires numerical analysis.

Figures 1 and 2 represent the topological diagrams of the subbands of light and heavy holes in the plane (ζ, η) for a model structure for various widths of the quantum well. The values $\zeta, \eta > 0$ correspond to compression along the axis and stretching in the plane of the heterostructure. According to (1), (13), and (14), a stress of any sign moves the subbands of light and heavy holes in opposite directions in energy: under stretching in the plane of the quantum well, the subbands of heavy holes move downward and the subbands of light holes move upward in energy, whereas, under compression, the situation is opposite. Under sufficiently large positive stresses in absolute value (axial compression or stretching in the plane), the first subband of light holes becomes the ground-state subband and lies higher in energy than the first subband of heavy holes. The barrier height for heavy (light) holes is determined by the parameter

$$U_{h,l} = U \mp \zeta \pm \eta. \quad (21)$$

Consider the characteristic domains of topological diagrams in greater detail.

The boundary of the existence domain for the first subband of heavy holes is specified by the conditions $U_h = 0$ and $k_{h1} = q_{h1} = 0$. When $U_h < 0$, the quantities k_h and q_h are purely imaginary and the wave function

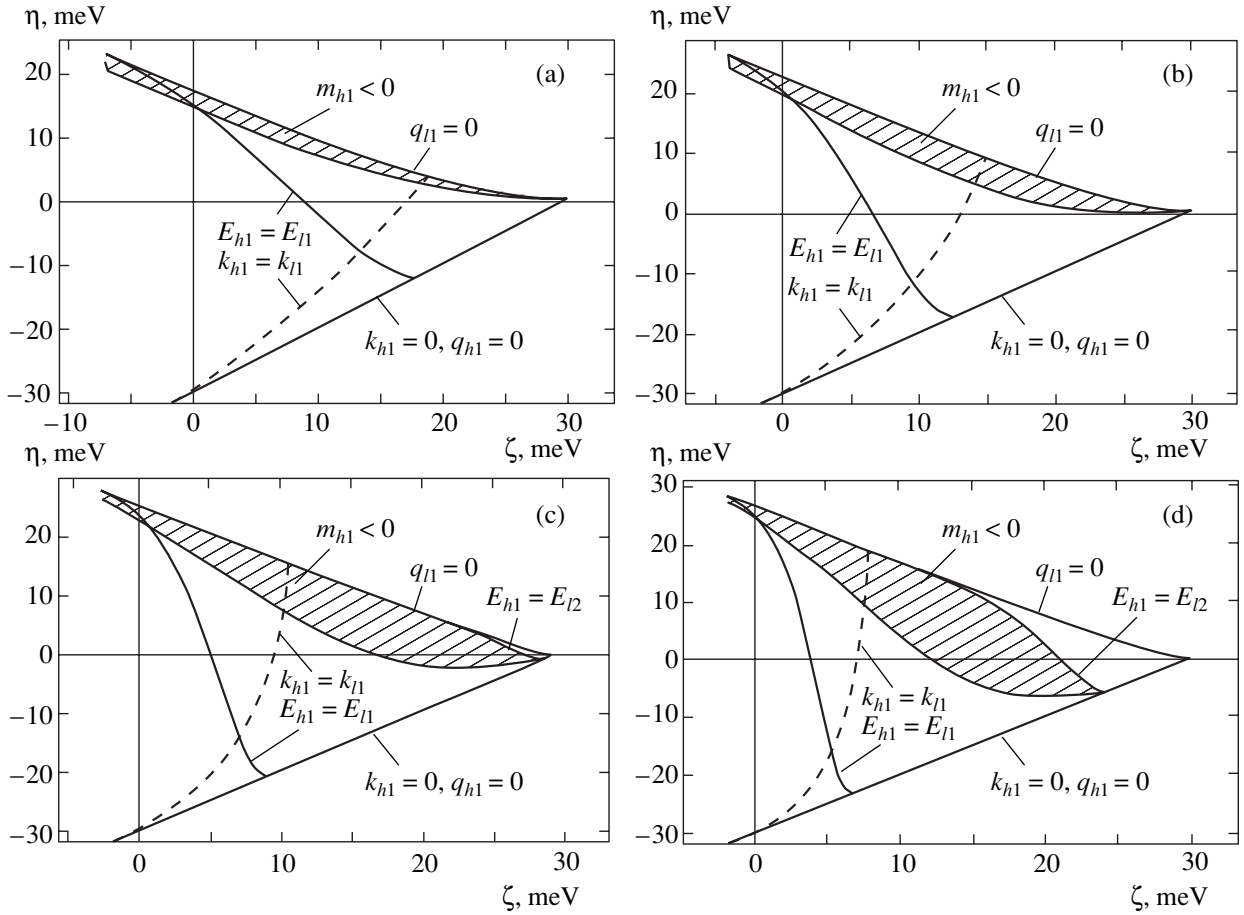

Fig. 1. Topological diagram for the first subband of heavy holes in the plane ζ, η for a model structure as a function of the width of the quantum well: L = (a) 50, (b) 75, (c) 100, and (d) 125 Å. The barrier height is 30 meV, and the Luttinger parameters are $\gamma_1 = 7.0$, $\gamma_2 = 2.5$, and $\gamma_3 = 3.5$.

contains components that do not decay as $z \longrightarrow \pm\infty$. Near this line, the parameter U_h (21), which determines the barrier height for heavy holes, is small. Since $\zeta_h^{-1} \longrightarrow 0$ (13), the major contribution to coefficient α_h is made in this domain by the second term in curly brackets in (20). After simple manipulations, we obtain the following expression for the phase shift α_h:

$$\alpha_h \approx -\frac{1}{\zeta_h}\frac{3\gamma_3^2}{2\gamma_2(\gamma_1 - 2\gamma_2)} \longrightarrow 0,$$

while the effective mass of the first subband of heavy holes with regard to $\zeta_h^{-1} \longrightarrow 0$ is equal to the bare mass (18):

$$\frac{m_0}{m_{h\perp}} = \gamma_1 + \gamma_2. \tag{22}$$

Near the boundary of the existence domain of the first subband of light holes (the line $k_{l1} = 0$, $q_{l1} = 0$), the barrier height U_l (21) for light holes serves as a small parameter. In this case, we have the following expression for the phase shift α_l:

$$\alpha_l \approx -\frac{1}{\zeta_l}\frac{3\gamma_3^2}{2\gamma_2(\gamma_1 + 2\gamma_2)} \longrightarrow 0,$$

while the effective mass of the first subband of light holes is equal to

$$\frac{m_0}{m_{l\perp}} = \gamma_1 - \gamma_2. \tag{23}$$

Thus, near the boundaries $k_{h1} = q_{h1} = 0$ and $k_{l1} = q_{l1} = 0$ of the existence domains of the subbands, the transverse effective masses are positive and independent of stresses in the well and the barrier.

Near the second boundary of the existence domain of the subbands of heavy and light holes, we have

$$q_{l1} \longrightarrow +0, \quad q_{h1} \longrightarrow +0$$

for Figs. 1 and 2, respectively. This case is of interest because the effective mass of the first subband of heavy holes in Fig. 1 is negative for $q_{l1} \longrightarrow 0$. After simple

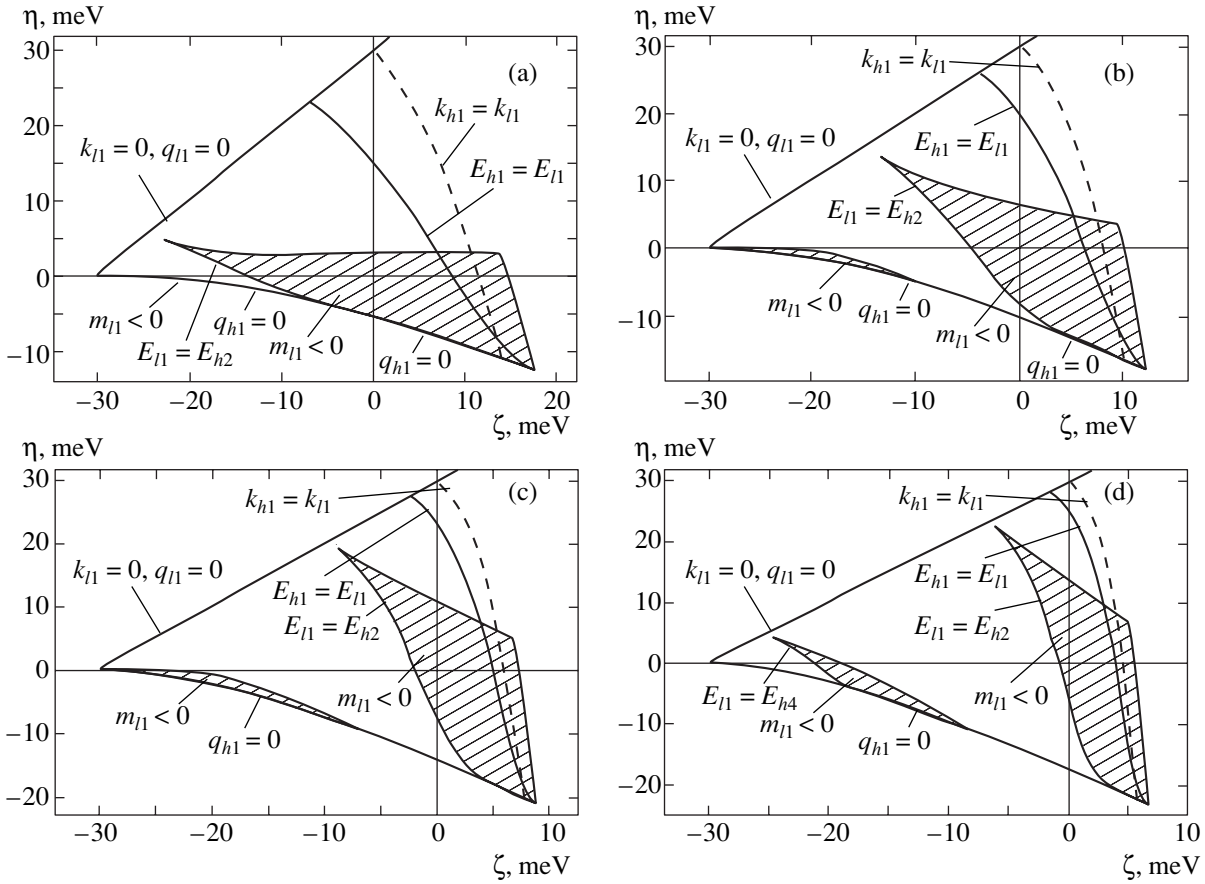

Fig. 2. Same as in Fig. 1 for the first subband of light holes.

manipulations, we obtain the following expression for the phase shift in this approximation:

$$\alpha_{h,l} = \frac{3\gamma_3^2}{2\gamma_2^2}\frac{q_{h,l}}{2 + q_{h,l}L}$$

$$\times \frac{\eta_{h,l} + \zeta_{h,l}}{(1-\zeta_h)(1-\zeta_l)(1+\eta_{h,l})}\frac{k_{h,l}^2}{k_{h,l}^2 + q_{h,l}^2}$$

$$\times \left\{\frac{q_{h,l}}{k_{l,h}}\left(\frac{q_{h,l}}{k_{l,h}} - \tan\frac{k_{l,h}L}{2}\right) \pm \frac{2\gamma_2(1-\zeta_{l,h})}{\gamma_1 \mp 2\gamma_2}\right\}.$$

In the general case, one cannot obtain a simple expression for the effective masses of the first subbands of heavy and light holes. Numerical calculations show that, for all compound semiconductors [14], there exists an interval of values (ζ, η) near the boundary $q_{l1} = 0$ in which the effective mass of the first subband of heavy holes is negative. It should also be noted that there exist combinations of parameters (γ_1, γ_2, γ_3) such that there is no such interval for negative effective masses m_{h1}; namely, when $\gamma_3 \longrightarrow \gamma_2$, i.e., in the spherical approximation, the effective mass of the first subband of heavy holes is positive near the boundary $q_{l1} = 0$. An increase in the ratio γ_3/γ_2 first gives rise to a domain of negative effective masses m_h and then results in an expansion of this domain.

Consider the domain of topological diagrams near the dashed line $k_{l1} = k_{h1}$. The relation between the quasimomenta k_l and k_h for $k_\perp = 0$ is described by the equation

$$k_l^2(\gamma_1 + 2\gamma_2) = k_h^2(\gamma_1 - 2\gamma_2) + 4m_0\zeta.$$

In this case, exact values of the quasimomenta and the normalized stresses are given by

$$k_{h,l} = \sqrt{\frac{m_0\zeta}{\gamma_2}}, \quad \zeta_{h,l} = 1.$$

The examination of the last coefficient in square brackets in expression (20) for the phase shift shows that it is proportional to a small quantity $(1 - \zeta_{l,h})$ near line $k_l = k_h$. Thus, all three terms in curly brackets in (20) are proportional to the small parameter $1 - \zeta_{l,h}$, while the phase shift itself has a singularity,

$$\alpha_{h,l} \propto \frac{1}{1-\zeta_{h,l}}, \tag{24}$$

in (19), this singularity is compensated for by the third term associated with the warping of the bulk spectrum. It also follows from (24) that the phase shift changes its sign on the line $k_l = k_h$. To the left of this line, the phase shift is positive for heavy holes and negative for light ones, whereas, to the right of this line, it is negative for heavy holes and positive for light ones. Figures 1 and 2 show that the effective masses of the first subbands of heavy and light holes in this domain may either be positive or negative.

The point of intersection of the curves $q_{l1} = 0$ and $k_{l1} = k_{h1}$ in Fig. 1 is of interest. At this point, the phase shift vanishes, while the effective mass of the first subband of heavy holes is given by

$$\frac{m_0}{m_h} = \gamma_1 + \gamma_2 - \frac{3\gamma_3^2}{\gamma_2};$$

i.e., it exactly coincides with the bare effective mass (8) of the subband of heavy holes in the absence of stresses and depends only on the Luttinger parameters. As we have already noted, this mass is negative for all widely used compound semiconductors.

The characteristic feature of Figs. 1 and 2 is the presence of intersection lines of the edges ($k_\perp = 0$) of various subbands of heavy and light holes under the variation of stress for large L: the intersection of the subband E_{h1} with E_{l2}, and the intersection of the subband E_{l1} with E_{h2}, E_{h3}, and E_{h4}. As the width L of the quantum well increases, the conditions for the intersection of subbands under the variation of stresses in the structure are weakened because the energy separation between two neighboring subbands decreases and the number of subbands increases. When $\zeta > 0$ (axial compression or in-plane stretching), the bottom of the potential well for light holes lies higher by 2ζ in energy than the bottom of the potential well for heavy holes, while the depth of the potential well increases for light holes and decreases for heavy holes. Therefore, as the stresses ζ increase, the subbands of light holes move upward in energy, while the subbands of heavy holes move downward; the number of subbands of heavy holes decreases, while that of light holes increases. Under negative stresses, $\zeta < 0$, the situation is diametrically opposite: the height of the potential barrier decreases for light holes and increases for heavy holes; the subbands of heavy holes move upward in energy, while the subbands of light holes move downward.

The intersection of energy subbands substantially affects the phase shifts (20) and, consequently, the effective masses (19). Indeed, consider the first term of the last cofactor in (20):

$$\frac{1 + \cos\phi_{l,h}}{k_{l,h}\sin\phi_{l,h}} = \frac{\cot(\phi_{l,h}/2)}{k_{l,h}}.$$

This term has a singularity at $\phi_{l,h} = 2\pi n$, where n is an integer. Hence, at the intersection line of energies $E_{h,l1}$ and even energies $E_{l,hn}$, the phase shift $\alpha_{h,l}$ has a singularity of the form

$$\alpha_{h,l} \propto \cot(\pi n).$$

For the first subband of light holes, to the right of the lines E_{h2} and E_{h4} (see the family of curves in Fig. 2), the phase shift has a singularity $\alpha_l \longrightarrow -\infty$ and, to the left, a singularity $\alpha_l \longrightarrow \infty$. Hence, the effective mass m_l has a singularity $m_l \longrightarrow -0$ to the right and a singularity $m_l \longrightarrow +0$ to the left of these lines. Similarly, for the first subband of heavy holes, to the right of the lines E_{l2} (see the family of curves in Fig. 1), the phase shift has a singularity $\alpha_h \longrightarrow +\infty$ and, to the left, a singularity $\alpha_h \longrightarrow -\infty$. Hence, the effective mass m_h has a singularity $m_h \longrightarrow +0$ to the right and a singularity $m_h \longrightarrow -0$ to the left of these lines.

Consider the effect of the width L of the quantum well on the characteristics of the first subband of heavy holes. As L increases, the quasimomentum k_h decreases, while the quasimomenta q_h and q_l increase. Therefore, the boundary $q_{l1} = 0$ moves to greater values of stress η (see Fig. 1). Another consequence of the decrease in the quasimomentum k_h with increasing the width of the well is the shift of the line $k_{l1} = k_{h1}$ considered above to the left. As we noted above, the parameter $\zeta_h > 1$ is greater than 1 to the right of this line. A numerical analysis shows that, for large ζ, the phase shift α_h changes insignificantly under the variation of L, while the third term in the bare effective mass (19) is positive and, conversely, sharply decreases as L increases. Thus, it is the decrease in the bare effective mass (19) for large ζ that is responsible for the expansion of the region of negative effective masses m_h.

In the case of the first subband of light holes, the basic factor that determines the effect of the width L of the quantum well on the parameters of the topological diagram and the transverse effective mass is the dependence of the phase shift, whose contribution to the effective mass (19) for light holes is several times greater than for heavy holes, on the width L of the well.

The condition

$$k_{h0} = k_{l0}$$

is satisfied at the intersection line of the first subbands of heavy and light holes. In this case, it follows from (20) that, when approaching this line, the phase shifts $\alpha_{h,l}$ tend to infinity and the inverse masses tend to zero. Therefore, in the expansion of dispersion relation (17) in powers of $k_\perp$, one should take into account the terms of higher order than $k_\perp^2$; this requires a numerical analysis. Appropriate calculations for real strained heterostructures are presented in the next section.

The line of intersection of the first subband of light and the second subband of heavy holes is characterized by the fact that a conical point arises in the dispersion

law; in this case, the first term in the expansion of a quasimomentum is linear in $k_\perp$:

$$k_h = k_{h0} + \alpha_h k_\perp, \quad k_l = k_{l0} + \alpha_l k_\perp.$$

Calculations yield the following expression for the expansion coefficients $\alpha_{h,l}$ at the intersection of the nth subband of heavy holes and the mth subband of light holes:

$$\alpha_h^2 = \frac{3\gamma_3^2 q_h q_l}{2\gamma_2^2 k_h k_l}\frac{1-(-1)^{n+m}}{(2+q_h L)(2+q_l L)}$$

$$\times \frac{1}{(1-\zeta_h)(1-\zeta_l)(1+\eta_h)(1+\eta_l)}$$

$$\times\left[1+\frac{\zeta_h(q_h-q_l)k_h^2+q_h\eta_h(k_h^2+q_h q_l)}{q_l(k_h^2+q_h^2)}\right]$$

$$\times\left[1+\frac{\zeta_l(q_l-q_h)k_l^2+q_l\eta_l(k_l^2+q_h q_l)}{q_h(k_l^2+q_l^2)}\right],$$

$$\alpha_l = \alpha_h\frac{k_h}{k_l}\frac{\gamma_1-2\gamma_2}{\gamma_1+2\gamma_2}.$$

The emergence of a conical point at the crossing of subbands of different parity has been pointed out in [10] while analyzing the dispersion law for a strained quantum well with infinitely high barriers, and in [22], where $(\mathbf{k}\hat{\mathbf{p}})$ perturbation theory has been developed for the hole spectrum of a quantum well of finite depth.

Summarizing, we can formulate the main characteristic features of the topological diagrams in the following form. The line $q_{l,h} = 0$ specifies the boundaries of the existence domain of localized states. To the left of the line $E_{h10} = E_{l10}$ ($E_{h,ln0} = E_{h,ln}(k_\perp = 0)$), the subband E_{h1} lies higher in energy than E_{l1}, whereas, to the right of this line, this subband lies lower. On the line $k_h = k_l$, the phase shift has a singularity ($\zeta_h = \zeta_l = 1$); in the expression for the effective mass (10), this singularity is compensated for by an appropriate singular term in the bare effective mass (8). On this line, the phase shift changes its sign. To the left of this line, the phase shift is positive for heavy holes and negative for light ones. The shaded domains in the diagrams correspond to negative effective masses of transverse motion (10). In these domains, each subband has four extrema situated in the $\langle 110\rangle$ directions and the isoenergetic surfaces near the extrema of the subbands are quadruply connected. The negative sign of the bare effective mass (8) associated with the warping in the bulk dispersion law is primarily responsible for the sign reversal of the mass of heavy holes, whereas the sign reversal of the effective mass of light holes is attributed to the negative sign of the phase shift. In Figs. 1 and 2, the values of parameters for which the ground-state subband of size quantization has a negative effective mass correspond to cross-hatched regions near lines $E_{h10} = E_{l10}$ (this is the subband E_{h1} to the left and E_{l1}, to the right). In a narrow interval of parameter values in the vicinity and to the left of the line $E_{h10} = E_{l10}$ in the shaded domain of the diagram in Fig. 2, subband E_{h1} has five extrema (one extremum at the center of the Brillouin zone and four in the $\langle 110\rangle$ directions). In this domain, subbands E_{h1} and E_{l1} exhibit anticrossing behavior. On line $E_{h2} = E_{l1}$ on the diagram of Fig. 2, which corresponds to the crossing of the first subband of light holes and the second subband of heavy holes, a conical point arises at the center of the Brillouin zone in the energy spectrum.

We can draw the following main conclusion from the analysis of the topological diagrams of model systems in Figs. 1 and 2. There exist parameter domains in strained heterostructures in which the ground-state subband of size quantization has a negative effective mass. To analyze the possibility of existence of negative effective masses and multiconnected isoenergetic surfaces in real strained heterostructures, one should take into account the difference between the Luttinger parameters in the well and the barrier. This problem requires numerical calculations that are described in the next section.

4. TOPOLOGICAL TRANSITIONS IN STRAINED HETEROSTRUCTURES OF GROUP IV SEMICONDUCTORS AND A_3B_5 COMPOUNDS

Strained layers are widely used in modern optoelectronic and transistor heterostructures. In field-effect transistor heterostructures, stresses are the inevitable price that one has to pay for increasing the band offset in a heterojunction in order to increase the concentration of charge carriers in the quantum well and for using materials that have lower effective masses and higher mobilities than the substrate material. In bipolar transistor heterostructures, where one uses variable-composition materials in order to develop a spatial gradient of the band-gap energy, stresses also arise as a concomitant phenomenon and do not play an independent role. Conversely, in laser heterostructures and radiation detectors, stresses represent an important parameter that determines the configuration of the subbands of size quantization of light and heavy holes and the effective density of states, which determines the amplification and absorption factors of a structure associated with interband transitions [7].

In recent years, considerable progress has been made toward the development of intersubband quantum cascade lasers [23, 24]. One of the problems faced when designing such devices is a competition between photon recombination and intersubband phonon relaxation. Upon emitting phonons, charge carriers are accumulated in the minimum of the lower subband. This fact impedes the development of inverse population and requires special measures to remove the charge carriers

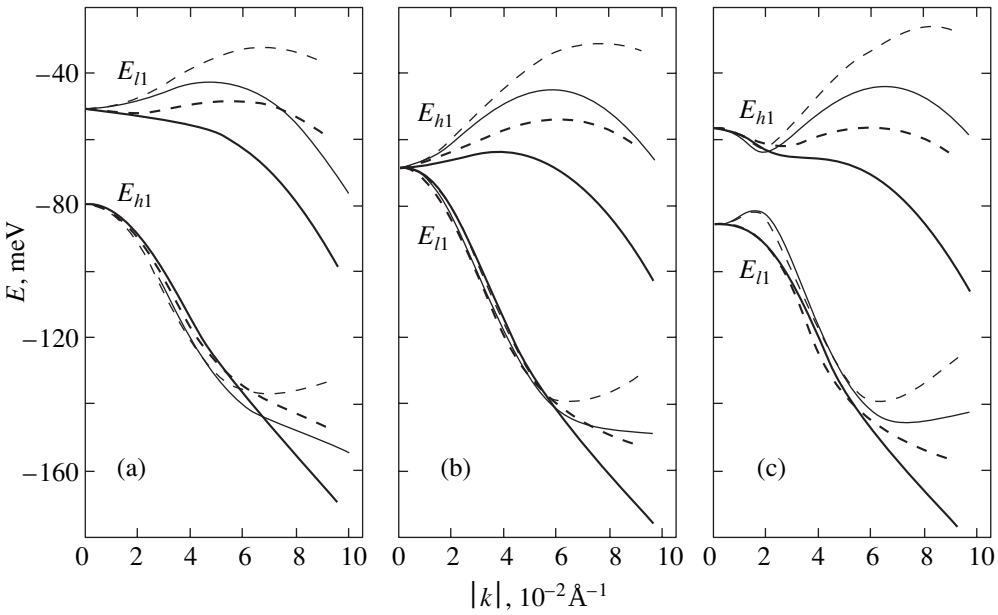

Fig. 3. Dispersion laws of the first subbands of heavy (E_{h1}) and light (E_{l1}) holes in the symmetric InP–$In_xGa_{1-x}As$–InP structure for various compositions of the material of the well: x = (a) 0.2, (b) 0.3, and (c) 0.4. At $k = 0$, (a) $E_{l1} > E_{h1}$, (b) $E_{l1} = E_{h1}$, and (c) $E_{l1} < E_{h1}$. The thick lines represent the results of calculations with nonsymmetrized boundary conditions [20], and the thin lines represent similar results for symmetrized boundary conditions [12, 26]. The solid and dashed curves represent the dispersion laws in the directions ⟨100⟩ and ⟨110⟩, respectively. The width of the well is L = 35 Å.

from the lower subband, which substantially complicate the design of the device. In the preceding section, we showed that, under certain relations between the parameters of a system, the minima of the ground-state subband of size quantization of holes are displaced from the center Γ of the Brillouin zone to the region with finite values of the wave vector. This creates favorable conditions for the development of intersubband hole-population inversion because, after radiative recombination at point Γ, the holes, scattered by phonons, move away from the recombination domain to the side minima of the subband.

Among known strained heterostructures, systems in which a quantum well is in a compressed state have found the widest application. These are, in particular, GaAs–$In_xGa_{1-x}As$ and Si–Ge_xSi_{1-x} heterostructures. However, the layers grown under stretching stresses exhibit more perfect morphology than the layers grown under compressing stresses [25]. Stretching stresses in a quantum well can be attained in systems based on phosphorous-containing compounds. Consider an InP–$In_xGa_{1-x}As$–InP heterostructure. When $x > 0.53$, the quantum well is in the compressed state, whereas, when $x < 0.53$, it is in the stretched state. Numerical calculations were performed within the standard envelope-function method for Hamiltonian (1). Both symmetrized [12, 26] and nonsymmetrized [20] boundary conditions, which differently take into account the discontinuity of the Luttinger parameters on the heteroboundary [27], were used in the calculations. The following Luttinger parameters were taken for the well and the barrier: $\gamma_1 = 6.98$, $\gamma_2 = 2.06$, and $\gamma_3 = 2.93$ for GaAs; $\gamma_1 = 20.0$, $\gamma_2 = 8.5$, and $\gamma_3 = 9.2$ for InAs; and $\gamma_1 = 5.08$, $\gamma_2 = 1.60$, and $\gamma_3 = 2.1$ for InP [16]. The band offsets and the Luttinger parameters of the ternary compound were calculated by the Wegard rule using a linear interpolation of appropriate parameters for InP–InAs and InP–GaAs heterojunctions [16]. Figure 3 displays the evolution of the dispersion law for the first subbands of heavy (E_{h1}) and light (E_{l1}) holes near the line of topological transition $E_{h1} = E_{l1}$ as the stress ζ in the well increases. On this line, the effective mass changes its sign at the point Γ, and, hence the connectivity of the isoenergetic surface is changed. Note that the dispersion of the side maximum of the subband of light holes in the plane k_xk_y is weakly pronounced and, actually, there is a loop of extrema in the system with a singularity in the density of states. Figures 4 and 5 show two-dimensional dispersion laws for the first two subbands of size quantization for x = 0.2 (Fig. 3a) and x = 0.4 (Fig. 3c).

Another example of a heterostructure with stretching stresses in the quantum well is given by a GaAs–Si_xGe_{1-x}–GaAs system. Both the Luttinger parameters and the band offsets are calculated by the Wegard rule. The following Luttinger parameters are taken for the well and the barrier: $\gamma_1 = 6.98$, $\gamma_2 = 2.06$, and $\gamma_3 = 2.93$ for GaAs [16]; $\gamma_1 = 4.22$, $\gamma_2 = 0.39$, and $\gamma_3 = 1.44$ for Si; and $\gamma_1 = 13.35$, $\gamma_2 = 4.25$, and $\gamma_3 = 5.69$ for Ge [14]. The dispersion laws for the first subbands of heavy (E_{h1}) and

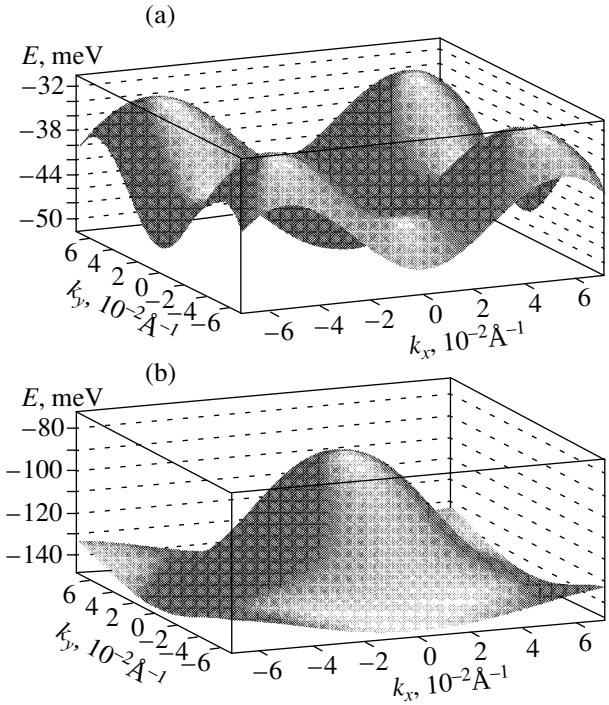

Fig. 4. Two-dimensional dispersion laws for the first subbands of heavy, E_{h1} (a), and light, E_{l1} (b), holes in the symmetric InP–$In_{0.2}Ga_{0.8}As$–InP structure (symmetrized boundary conditions). The width of the well is L = 35 Å.

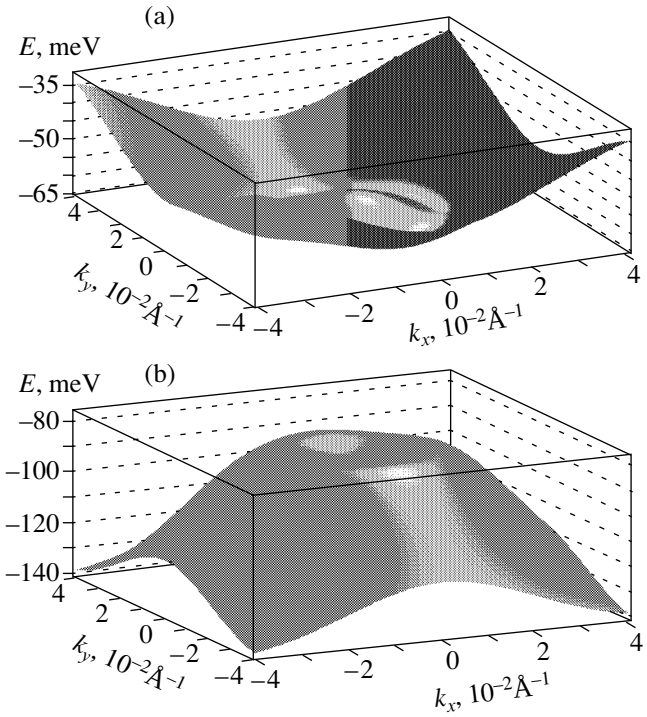

Fig. 5. Same as in Fig. 4 in the symmetric InP–$In_{0.4}Ga_{0.6}As$–InP structure.

light (E_{l1}) holes near the line $E_{h1} = E_{l1}$ are depicted in Fig. 6.

The Luttinger Hamiltonian does not take into account the contribution of a band that is split off due to the spin–orbit interaction. One should expect that, at least when the intersubband energy separation is less than the energy of the spin–orbit interaction, the results of our calculations will not significantly differ from the results of more accurate calculations involving a 6×6 Hamiltonian.

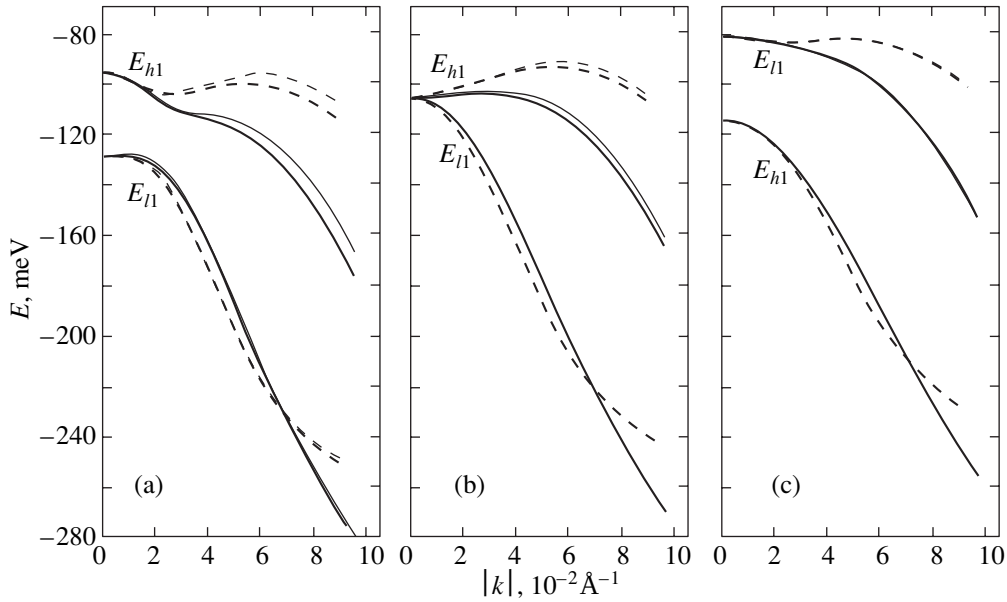

Fig. 6. Same as in Fig. 3 in the symmetric GaAs–Si_xGe_{1-x}–GaAs structure for various compositions of the material of the well: (a) x = 0.3, (b) 0.45, and (c) 0.6. At k = 0, (a) $E_{l1} < E_{h1}$, (b) $E_{l1} = E_{h1}$, and (c) $E_{l1} > E_{h1}$.

The scheme, described above, for the development of inverse population in the hole subbands is based on the fact that the radiative recombination and the accumulation of charge carriers due to the phonon relaxation occur in different domains of the **k** space. This condition is fulfilled when the effective mass is negative in the second (in energy) subband, rather than in the lower subband of size quantization. As follows from the results of Sections 2 and 3, the situation when the effective mass is negative in the second subband of size quantization is typical for most (including unstressed) heterostructures. However, it should be noted that, to efficiently implement the mechanism described, the energy separation between the subbands of size quantization must be greater than the energy of an optical phonon to guarantee fast intersubband relaxation. In the heterostructures, considered in this section, that are characterized by a negative effective mass of the ground-state subband of size quantization, this condition is not fulfilled and intersubband relaxation occurs via acoustic phonons. At the same time, when the effective mass is negative for the second (in energy) subband of size quantization, the energy separation of the subbands can easily be controlled by varying the width of the quantum well. The investigation of the conditions for the development of the intersubband inverse population of holes requires a careful numerical analysis of the kinetics of nonequilibrium charge carriers and deserves special consideration. In view of deep interest in silicon-based sources of coherent electromagnetic radiation, the investigation of $Si–Ge_xSi_{1-x}$ systems is of special importance.

CONCLUSION

In this paper, we have established the basic principles of the formation of the energy spectra of holes in size-quantized heterostructures. We have shown that the details of the transverse (with respect to the quantization axis) dispersion law are determined by the competition of two factors, the warping in the bulk dispersion law and the dependence of the quantized (longitudinal with respect to the quantization axis) momentum on the transverse quasimomentum. In unstressed heterostructures, the second (in energy) subband of size quantization in deep quantum wells has, as a rule, a negative effective mass. In this work, we have obtained an exact solution for the energy spectrum of holes, described by the Luttinger Hamiltonian, in a quantum well of finite depth with regard to stresses in the well and the barrier. On the basis of the exact solution, we have demonstrated that, for a certain relation between the parameters of a system subject to stretching stresses, the ground-state subband of size quantization in the quantum well can also have a negative effective mass. A variation in the parameters of the system in unstressed heterostructures gives rise to topological transitions accompanied by variation in the connectivity of the isoenergetic surface.

Together with the population inversion of the hole subbands mentioned above, the sign reversal of the mass of transverse motion may also have other experimentally observable consequences. The variation in the connectivity of the isoenergetic surface can be detected in cyclotron-resonance experiments. It should be expected that, at sufficiently low temperatures, electron–electron interactions will lift the fourfold degeneracy of energy minima by developing a certain long-range ordering, similar to the lifting of intervalley degeneracy in inversion layers [28]. In this situation, the instability will additionally increase due to the presence of the van Hove singularity in the density of states, which is associated with a variation in the topology of isoenergetic surfaces. Recently, the possibility of using artificial heterostructures for the development of conditions that guarantee the implementation of one or another mechanism of superconductivity has been discussed [29, 30]. In view of this fact, the situation with a variation in the topology of the spectrum described in this paper is of interest for verifying the conditions under which the superconductivity mechanisms associated with a singularity in the density of states are implemented.

ACKNOWLEDGMENTS

One of the authors (A.A.G.) is grateful to R. Winkler for useful discussions.

This work was supported by the Russian Foundation for Basic Research (project no. 02-02-16994) and the Ministry of Education of the Russian Federation.

REFERENCES

1. L. D. Landau and E. M. Lifshitz, *Course of Theoretical Physics*, Vol. 3: *Quantum Mechanics: Non-Relativistic Theory*, 3rd ed. (Nauka, Moscow, 1974; Pergamon, New York, 1977).
2. S. S. Nedorezov, Fiz. Tverd. Tela (Leningrad) **12**, 2269 (1970) [Sov. Phys. Solid State **12**, 1814 (1970)].
3. A. Matulis and K. Piragas, Fiz. Tekh. Poluprovodn. (Leningrad) **11**, 2202 (1975) [Sov. Phys. Semicond. **9**, 1432 (1975)].
4. M. I. D'yakonov and A. V. Khaetskiĭ, Zh. Éksp. Teor. Fiz. **82**, 1584 (1982) [Sov. Phys. JETP **55**, 917 (1982)].
5. G. S. Osbourn, Phys. Rev. B **27**, 5126 (1983).
6. A. R. Adams, Electron. Lett. **22**, 249 (1986).
7. W. W. Chow and S. W. Koch, *Semiconductor Laser Fundamentals*: *Physics of the Gain Materials* (Springer, New York, 1999).
8. S.-C. Hong, G. P. Kothial, N. Debbar, *et al.*, Phys. Rev. B **37**, 878 (1988).
9. M. Shur, *Physics of Semiconductor Devices* (Prentice Hall, Englewood Cliffs, N.J., 1990; Mir, Moscow, 1992), Vol. 1.
10. O. V. Kibis and L. D. Shvartsman, Poverkhnost **7**, 119 (1985).

11. L. C. Andreani, A. Pasquarelo, and F. Bassani, Phys. Rev. B **36**, 5887 (1987).
12. G. Bastard, J. A. Brum, and R. Ferreira, Solid State Phys. **44**, 229 (1991).
13. C. Weisbuch and B. Vinter, *Quantum Semiconductor Structures*: *Fundamentals and Applications* (Academic, San Diego, 1991).
14. M. Cardona and H. Yu, *Fundamentals of Semiconductors*: *Physics and Materials Properties* (Springer, Berlin, 1999).
15. I. M. Lifshits, Zh. Éksp. Teor. Fiz. **38**, 1569 (1960) [Sov. Phys. JETP **11**, 1130 (1960)].
16. I. Vurgaftman, J. R. Meyer, and L. R. Ram-Mohan, Phys. Rev. B **89**, 5815 (2001).
17. A. A. Gorbatsevich and O. V. Zhabitsky, in *Proceedings of 7th International Symposium on Nanostructures*: *Physics and Technology* (St. Petersburg, 1999), p. 368.
18. D. A. Broido and L. J. Sham, Phys. Rev. B **31**, 888 (1985); Phys. Rev. B **34**, 3917 (1986).
19. C. Y.-P. Chao and S. L. Chuang, Phys. Rev. B **46**, 4110 (1992).
20. B. A. Foreman, Phys. Rev. B **48**, 4964 (1993).
21. I. V. Tokatly, A. G. Tsibizov, and A. A. Gorbatsevich, Phys. Rev. B **65**, 165328 (2002).
22. O. V. Kibis, Fiz. Tekh. Poluprovodn. (Leningrad) **23**, 820 (1989) [Sov. Phys. Semicond. **23**, 514 (1989)].
23. J. Faist, F. Capasso, D. L. Sivco, *et al.*, Science B **264**, 553 (1994).
24. A. F. Kazarinov and R. A. Suris, Fiz. Tekh. Poluprovodn. (Leningrad) **5**, 797 (1971) [Sov. Phys. Semicond. **5**, 707 (1971)].
25. J. E. Guyer, S. A. Barnett, and P. W. Voorhees, J. Cryst. Growth **217**, 1 (2000).
26. W. Potz, W. Porod, and D. K. Ferry, Phys. Rev. B **32**, 3868 (1985).
27. S. De Franceschi, J.-M. Jancu, and F. Beltram, Phys. Rev. B **59**, 9691 (1999).
28. T. Ando, A. B. Fowler, and F. Stern, in *Electronic Properties of Two-Dimensional Systems* (Am. Phys. Soc., New York, 1982; Mir, Moscow, 1985).
29. P. M. Platzman and T. Lenosky, Phys. Rev. B **52**, 10327 (1995).
30. V. V. Kapaev and Yu. V. Kopaev, Pis'ma Zh. Éksp. Teor. Fiz. **68**, 211 (1998) [JETP Lett. **68**, 223 (1998)].

Translated by I. Nikitin

Journal of Experimental and Theoretical Physics, Vol. 96, No. 1, 2003, pp. 19–24.
Translated from Zhurnal Éksperimental'noĭ i Teoreticheskoĭ Fiziki, Vol. 123, No. 1, 2003, pp. 25–31.

NUCLEI, PARTICLES, AND THEIR INTERACTION

On Compression of Electromagnetic Pulses in Dielectric Plates

S. N. Vlasov* and E. V. Koposova

Institute of Applied Physics, Russian Academy of Sciences, ul. Ul'yanova 46, Nizhni Novgorod, 603600 Russia
**e-mail: vlasov@appl.sci-nnov.ru*

Received July 8, 2002

Abstract—The results of theoretical investigation of propagation of electromagnetic wave pulses in nonlinear dielectric plates, taking into account the dispersion introduced by the plate to the maximum possible extent, are presented. The investigation is aimed at obtaining the shortest possible pulses of electromagnetic waves. Pulse compression is based on the collapse of electromagnetic waves in transparent dielectrics with electronic nonlinearity. The integral equation for describing the pulse compression is derived, and conditions under which a pulse is compressed relative to time and one of the transverse coordinates are determined. Numerical simulation shows that quite short (on the order of a few femtoseconds) pulses can be obtained in this way. © *2003 MAIK "Nauka/Interperiodica".*

1. Pulse compression is one of the basic methods of increasing radiation power. For this purpose, use can be made of the collapse [1–3] of electromagnetic waves in transparent nonlinear cubic dielectrics with permittivity

$$\varepsilon = \varepsilon_l(1 + \Delta\varepsilon_n),$$

where ε_l and $\Delta\varepsilon_n$ are the linear and the nonlinear parts of permittivity, the latter being proportional (in the steady state) to the intensity,

$$\Delta\varepsilon_n \propto |E|^2,$$

E being the electric field amplitude. In order to obtain short pulses, collapse must be caused by a nonlinearity with a short relaxation time t_r. This is observed for electronic nonlinearity, which is self-focusing as a rule with coefficient $\Delta\varepsilon_n > 0$. This nonlinearity ensures the compression of the field structure along coordinates perpendicular to the direction of pulse propagation. Pulse compression along the longitudinal coordinate is possible only for a dispersion for which the condition

$$\frac{\partial^2 k}{\partial\omega^2} < 0$$

holds, where k is the modulus of the wave vector at the carrier frequency ω. However, dispersion in dielectrics is such that temporal compression occurs only at fairly long waves, e.g., in quartz at a wavelength of $\lambda \geq 1.35$ μm in vacuum. However, pulse compression in three dimensions (two spatial coordinates and one temporal coordinate) occurs so that the energy of the self-compressing part decreases with the pulse duration even at such wavelengths. Such a property is not observed for a collapse in two dimensions (one spatial and one temporal coordinate), but this may take place during the propagation of electromagnetic waves in planar single-mode waveguides, when the field structure is fixed relative to the coordinate perpendicular to the waveguide plane. Waves propagating in plane dielectric plates exhibit approximately the same properties. In this case, "material" dispersion of the dielectric is significant in the long-wave part of the optical range. It turns out that the dispersion of propagating waves becomes "collapsing" for the optimal choice of the plate thickness up to wavelengths shorter that $\lambda \sim 0.7$ μm. In this communication, we present the results of a theoretical study of propagation of electromagnetic wave pulses in nonlinear dielectric plates, in which the dispersion introduced by a plate is taken into account to the maximum possible extent. First, we formulate the integrodifferential equation for describing pulse compression and determine the conditions under which a pulse is compressed in time and along one of the transverse coordinates. Then we describe and discuss the results of numerical simulation, indicating that short pulses (on the order of a few femtoseconds) can be obtained in this way.

2. Following the approach used in [4], we obtain the equation describing the propagation of wave packets in a dielectric plate of thickness T; we assume that the y axis is perpendicular to the plane of the plate, a wave propagates along the z axis, and the midplane of the plane coincides with the xz plane (Fig. 1). In such a plate, in the linear approximation, localized TE and TM waves can propagate. We confine our analysis to the TE waves. The structure of the electric field of such a wave in the case when it is independent of coordinate x is shown in Fig. 1 (we have only one component E_x). The

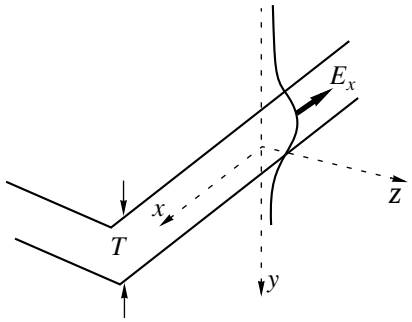

Fig. 1. Dielectric plate.

propagation constant h for such waves can be determined from the equation [5]

$$\sqrt{h^2 - k^2} = \sqrt{\varepsilon_l\left(\frac{k}{k_f}\right)k^2 - h^2} \times \tan\left(\sqrt{\varepsilon_l\left(\frac{k}{k_f}\right)k^2 - h^2}\frac{T}{2}\right), \quad (1)$$

where $k = \omega/c$, c being the velocity of light in vacuum. Equation (1) takes into account the dispersion of permittivity of the dielectric as well as the dependence of ε_l on frequency (wavelength in vacuum), which is defined by the semiempirical formulas [6]

$$\begin{aligned}\varepsilon_l &= A_1 + A_2\lambda^2 + A_3\lambda^{-2} + A_4\lambda^{-4} + A_5\lambda^{-6} + A_6\lambda^{-8} \\ &= A_1 + A_2\left(\frac{k_f}{k}\right)^2 + A_3\left(\frac{k_f}{k}\right)^{-2} + A_4\left(\frac{k_f}{k}\right)^{-4} \\ &\quad + A_5\left(\frac{k_f}{k}\right)^{-6} + A_6\left(\frac{k_f}{k}\right)^{-8},\end{aligned} \quad (2)$$

where $A_1, \ldots, A_6$ are the coefficients in the formula for dispersion and λ is the wavelength in vacuum in micrometers. This dependence contains the normalization frequency

$$f_f = \frac{\omega_f}{2\pi} \approx 3 \times 10^{14}\ \text{Hz},$$

at which the wavelength in vacuum is 1 μm, its wave vector being $k_f = \omega_f/c$.

We assume that the dependence of the field structure on the y coordinate can be described by a single localized mode, which is true if the plate thickness is smaller than the wavelength in vacuum or is equal to it for conventional values of permittivity $\varepsilon_l \approx 2.1$–$2.5$.

Let us consider the evolution of a wave packet with the propagation vector components k_x and h_z. If we know the dispersion characteristic of one of the types of waves,

$$h_z = F\left(\frac{\omega}{c}, k_x\right) = \sqrt{h^2 - k_x^2}, \quad (3)$$

we find, repeating the arguments used in [4], that the evolution of the electric field E_x of such a packet can be described (in the absence of nonlinearity) by the integral relation

$$\frac{\partial F_x}{\partial z} = -\frac{i}{(2\pi)^2}\iint\sqrt{h^2(\omega) - k_x^2} \times \exp[\Delta]E_x(t', x')dt'dx'd\omega dk_x, \quad (4)$$

where

$$\Delta(\omega, t, k_x, x, t', x') = i(\omega t - k_x x) - i(\omega t' - k_x x')$$

and $h(\omega)$ is the solution to Eq. (1). Introducing the notation

$$LE_x = \frac{1}{(2\pi)^2}\iint\sqrt{h^2(\omega) - k_x^2} \times \exp[\Delta(\omega, t, k_x, x, t', x')]E_x(t', x')dt'dx'd\omega dk_x$$

and passing to the field amplitude with the help of the formula

$$A_0 = E_x\exp[ih_c z - i\omega_c t],$$

where h_c is the constant of wave propagation at the central frequency ω_c, we can write Eq. (4) in the form

$$\frac{\partial A_0}{\partial z} = -iLA_0 + ih_c A_0. \quad (5)$$

We describe the nonlinear component of permittivity by the equation [1, 7] taking into account the nonlinearity relaxation time,

$$\frac{d\Delta\varepsilon_n}{dt} + \frac{\Delta\varepsilon_n}{t_r} = \frac{\varepsilon'|E|^2}{t_r}, \quad (6)$$

where ε' is the nonlinearity coefficient. Applying the approach used in [7], we obtain the following expression from $\Delta\varepsilon_n$ from Eq. (6):

$$\Delta\varepsilon_n = \exp\left(\frac{t}{t_r}\right)\int_0^t \varepsilon'|E^2|\exp\left(-\frac{t_0}{t_r}\right)dt_0. \quad (7)$$

Integrating this equation by parts and retaining the first two terms in the small parameter (relaxation time), we obtain the nonlinear permittivity component in the form

$$\Delta\varepsilon_n = \varepsilon'|E^2| - t_r\frac{d(\varepsilon'|E^2|)}{dt}. \quad (8)$$

In order to describe the propagation of packets in a nonlinear cubic dielectric, we use this expression, supplementing equality (5) with a term approximately equal to

$$\left(C|A_0|^2 - t_r\frac{d}{dt}C|A_0|^2\right)A_0.$$

According to [9], the value of coefficient C is given by

$$C \approx \frac{3h_c\varepsilon'}{8},$$

if the amplitude A_0 corresponds to the average density of the dielectric. This leads to the following equation describing the propagation of a pulse:

$$\frac{\partial A_0}{\partial z} = -iLA_0 + ih_cA_0 - i\left(C|A_0|^2 - t_r\frac{d}{dt}C|A_0|^2\right)A_0. \quad (9)$$

Let us pass to the frame of reference $z\bar{t}$, comoving with the pulse, in accordance with the formulas

$$z = z, \quad t = \bar{t} + \frac{z}{v_{gr}},$$

where

$$v_{gr} = \frac{c}{\partial h/\partial k_{\omega=\omega_c}}.$$

Using the expression

$$\frac{\partial A_0}{\partial \bar{t}} = \frac{1}{(2\pi)^2}\int i\bar{\omega}A_0\exp[\Delta(\bar{\omega}, \bar{t}, k_x, \bar{t}', x')]d\bar{t}'d\bar{\omega}dx'dk_x,$$

where $\bar{\omega} = \omega - \omega_c$, we reduce Eq. (9) to the form

$$\frac{\partial A_0}{\partial z} = -\frac{i}{(2\pi)^2}\int\left(h_z - \frac{\bar{\omega}}{c}\frac{\partial h_z}{\partial k_{k=kc}}\right) \times A_0\exp[\Delta(\bar{\omega}, \bar{t}, k_x, x, \bar{t}', x')]d\bar{t}'d\bar{\omega}dx'dk_x \quad (10)$$

$$+ ih_cA_0 - i\left(C|A_0|^2 - t_r\frac{d}{dt}C|A_0|^2\right)A_0.$$

Note that the presentation of the nonlinear permittivity component in form (8) formally coincides with the description of weak nonlinear dispersion, which was proposed in [8]:

$$(\Delta\varepsilon_n)E = \varepsilon'|E^2|E + i\omega_c\left(t_{r,1}|E^2|\frac{dE}{dt} + t_{r,2}E^2\frac{dE^*}{dt}\right),$$

where the asterisk denotes complex conjugation and $t_{r,1}$ and $t_{r,2}$ are certain constants characterizing a given substance, which can be regarded as purely imaginary and identical. Equation (10) can be used for describing pulses with duration of the envelope comparable with the nonlinearity relaxation time.

3. We will estimate the pulse parameters using the paraxial approximation, in which the time spectrum of the pulse $\Delta k/k_c \ll 1$, where $k_c = \omega_c/c$, and its width in the x direction, which is equal to $2a_x$, is considerably larger than the wavelength:

$$2a_x \gg \lambda_c = \frac{2\pi}{k_c}.$$

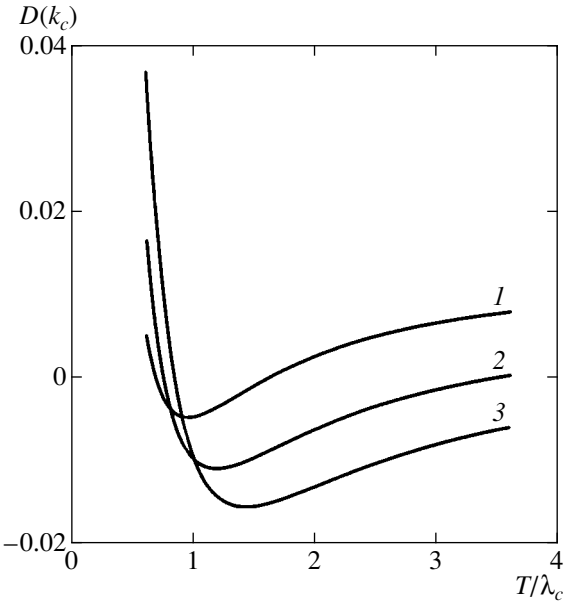

Fig. 2. Dependence of parameter D on the relative thickness of the plate for different values of $\lambda_c/\lambda_f = 0.8$ (*1*), 1.0 (*2*), and 1.2 (*3*).

The integral operator in Eq. (10) in this case can be represented in the form

$$-i\frac{1}{(2\pi)^2}\int\left[h_c + \frac{\bar{\omega}}{c}\frac{\partial h_z}{\partial k_{k=k_c}} + \frac{(\bar{\omega})^2}{2c^2}\frac{\partial^2 h_z}{\partial k^2_{k=k_c}} + \frac{(\Delta k_x)^2}{2}\frac{\partial^2 h_z}{\partial k_x^2} - \frac{\bar{\omega}}{c}\frac{\partial h_z}{\partial k_{k=k_c}}\right] \times \exp[\Delta(\bar{\omega}, \bar{t}, k_x, x, \bar{t}', x')]A_0d\bar{t}'d\bar{\omega}dx'dk_x = \frac{i}{2c^2}\frac{\partial^2 h}{\partial k^2}\frac{\partial^2 A_0}{\partial \bar{t}^2} - \frac{i}{2h_c}\frac{\partial^2 A_0}{\partial x^2}.$$

We pass to the dimensionless variables

$$\zeta = h_cz, \quad \tau = \bar{t}\omega_c, \quad \xi = h_cx, \quad A = \sqrt{\frac{2C}{h_c}}A_0 \quad (11)$$

and omit in Eq. (10) the terms describing the nonlinearity relaxation. In this approximation, Eq. (10) becomes parabolic:

$$\frac{\partial^2 A}{\partial \xi^2} - D\frac{\partial^2 A}{\partial \tau^2} - 2i\frac{\partial A}{\partial \zeta} + |A|^2A = 0. \quad (12)$$

The characteristic properties of solutions to Eq. (12) are well known [1]. Their behavior depends considerably on the sign of the coefficient

$$D = \frac{k_c^2}{h_c}\frac{\partial^2 h}{\partial k^2_{k=k_c}}.$$

For the pulse compression problem, the negative value of D, for which the solution to Eq. (12) has the form of a collapse, is of special importance. The dependence of coefficient D on the thickness of a quartz glass plate [6] for several values of the ratio of the carrier frequency ω_c to frequency ω_f are shown in Fig. 2. It can be seen from the figure that there exists a range of plate thicknesses for which D is negative and, hence, the pulse is compressed. As the frequency increases, this region becomes narrower and vanishes for a wavelength shorter than 0.7 μm in vacuum. The minimal value of coefficient D corresponds to a plate thickness approximately equal to the wavelength in vacuum at the carrier frequency.

Equation (12) has a homogeneous solution of the form

$$A = A_\perp(x, \tau)\exp(-iH\zeta), \tag{13}$$

which is an analog of the "Townes" beam propagating in space [1]. It describes a pulse propagating in the direction of the ζ axis without changing its shape. The cross section of such a pulse by the $\xi\tau$ "plane" is an ellipse. The ratio of the beam "width" $2a_\tau$ in the τ direction (pulse duration multiplied by the velocity of light) to the beam width $2a_x$ in the x direction is

$$\frac{a_\tau}{a_x} = \frac{k_c\sqrt{\frac{k_c^2}{h_c}\frac{\partial^2 h}{\partial k^2}}}{ch_c} \approx \frac{\sqrt{-D}}{c\sqrt{\varepsilon_l}}.$$

In accordance with the results of calculations, the "duration" of such a pulse (in wavelengths) for the minimal value of D is an order of magnitude smaller than its transverse dimension.

The energy of such a pulse is defined as

$$W_{\rm cr} = \sqrt{\frac{3}{2}}P_{\rm cr}\frac{k_c}{h_c c}\left[\frac{T}{2} + \frac{\lambda_c \sin\chi_y k_c T}{2\chi_y}\right]\sqrt{-D}, \tag{14}$$

where $P_{\rm cr}$ is the critical power of self-focusing and $\chi_y \approx \sqrt{\varepsilon - 1}$ is the y component of the dimensionless wave number inside the plate. In expression (14), we disregard the pulse energy outside the plate. In the regimes of interest for pulse compression, this energy is small. We can write the following order-of-magnitude estimate for the pulse energy:

$$W_{\rm cr} \approx P_{\rm cr}\frac{T}{c}\sqrt{-D} \approx 10^{-9}\ \text{J}.$$

In accordance with the theory of instability of plane waves in self-focusing media, a uniform distribution splits approximately into pulses with the structure of a homogeneous beam, each of which is compressed in the approximation of Eq. (12) to zero length.

4. It is interesting to analyze the change in the pulse structure in the framework of a more exact equation (10) taking into account dispersion in a wide range of angles and frequencies [4]. We integrated Eq. (10) numerically for beams with a small energy excess over the critical value. Introducing the dimensionless coefficients

$$k_x = \frac{k_x}{k_c}, \quad \omega_w = \frac{\bar{\omega}}{\omega_c}, \quad \frac{k_c}{k_f} = K, \quad k_c T = T_w,$$

we obtain Eq. (10) in dimensionless form:

$$\frac{\partial A}{\partial \zeta} = -\frac{i}{(2\pi)^2\chi_c}$$
$$\times \int\left[\sqrt{\chi^2(1+\omega_w)^2 - \kappa_x^2} - \omega_w\frac{\partial\chi}{\partial k_{\omega=\omega_c}}\right] \tag{15}$$
$$\times \exp[i\Delta(\omega_w, \tau, \kappa_x, \xi, \tau', \xi')]A d\tau' d\omega_w d\xi' d\kappa_x$$
$$+ iA - i\frac{1}{2}\left[|A|^2 - \alpha\frac{\partial|A^2}{\partial\tau}\right]A,$$

where $\chi(\omega_w, T_w, K)$ is the root of the equation

$$\sqrt{\chi^2 - 1} - \sqrt{\varepsilon[K(1+\omega_w)] - \chi^2}$$
$$\times \tan\left(\sqrt{\varepsilon[K(1+\omega_w)] - \chi^2}\frac{T_w(1+\omega_w)}{2}\right) = 0, \tag{16}$$

$\alpha = \omega_c t_r$.

It is more convenient, however, to carry out the numerical solution in the variables

$$\xi_b = \sqrt{|D|}\xi, \quad \tau = \tau, \quad \zeta_b = \zeta\sqrt{|D|}, \quad A_b = \frac{A}{|D|^{1/4}},$$

in which a beam of form (13) would have a circular cross section. In these new variables, Eq. (15) assumes the form

$$\frac{\partial A_b}{\partial \zeta_b} = -\frac{i}{(2\pi)^2\chi_c}$$
$$\times \int\frac{1}{\sqrt{|D|}}\left[\sqrt{\chi^2(1+\omega_w)^2 - |D|\kappa_x^2} - \omega_w\frac{\partial\chi}{\partial k_{\omega=\omega_c}}\right]$$
$$\times \exp[i\omega_w(\tau - \tau') - ik_x(\xi_b - \xi_b')] \tag{17}$$
$$\times A_b d\tau' d\omega_w d\xi_b' d\kappa_x + iA_b$$
$$- i\frac{1}{2}\left[|A_b|^2 - \alpha\frac{\partial|A_b|^2}{\partial\tau}\right]A_b;$$

accordingly, approximate equation (12) assumes the form

$$\sqrt{|D|}\frac{\partial^2 A_b}{\partial \xi_b^2} + \frac{\partial^2 A_b}{\partial \tau^2} - 2i\frac{\partial A_b}{\partial \zeta_b} + |A_b|^2 A_b = 0. \qquad (18)$$

We solved the system of equations (16), (17) using one of the simplest versions of the splitting method [10] in the $L \times L$ square in variables $\xi_b\tau$ using an $N \times N$ mesh. In the version of the method used by us, this corresponds to computations in variables $\kappa_x\omega_w$ in a square of the size

$$\Delta\kappa_x \times \delta\omega_w = \left(\frac{2\pi}{L}N\right)^2.$$

It follows from this formula that an increase in the number of intervals in the $\xi_b\tau$ space corresponds to an increase in the bands of both temporal and spatial frequencies.

The results of calculations for $L = 628$ and $N = 160$ are given below. The frequency band used lies at the boundary of the region in which formula (2) is valid for describing the permittivity dispersion.

5. Let us consider the results of computations for a wavelength of $\lambda_c = 1$ μm and a quartz plate thickness of $T = 1$ μm. The initial function had the Gaussian form:

$$A_b(\xi_b, \tau, 0) = \bar{A}_0 \exp\left[-\frac{\xi_b^2 + \tau^2}{2a^2}\right]$$

with parameter $2a \approx 181$ ($2a_x(0) \approx 20$ μm), which corresponds to the pulse duration $t_i \approx 9$ fs (at half the amplitude) for the parameter D chosen in accordance with Fig. 2.

The behavior of the field at the peak of the pulse as a function of the longitudinal coordinate ζ is shown in Fig. 3. Curve *1* characterizes the increase in the peak value in the case when Eq. (18) is solved in the paraxial approximation for the initial value $\bar{A}_0 = 0.003$, which corresponds to $W/W_{cr} \approx 2.25$. In accordance with the prevailing concepts of collapse in the (1 + 2) space, the field turns to infinity at a certain point. The peak value corresponds to "computer" infinity and, hence, characterizes the accuracy of computations. Curve *2* illustrates the behavior of the peak for a pulse described by Eq. (17) for $W/W_{cr} \approx 2.25$ and zero relaxation time. The pulse is compressed to a slightly larger duration than that attained in the paraxial approximation. Rigorous inclusion of linear dispersion in this problem changes the pulse structure at the compression stage, but the compression ratio turns out to be so large that the minimal duration is smaller than the initial wavelength at the carrier frequency. It can be seen that instability develops in the descending branch of the pulse. The introduction of a finite relaxation time limits the increase in the amplitude the most strongly. This is illustrated by curve *3* in Fig. 3.

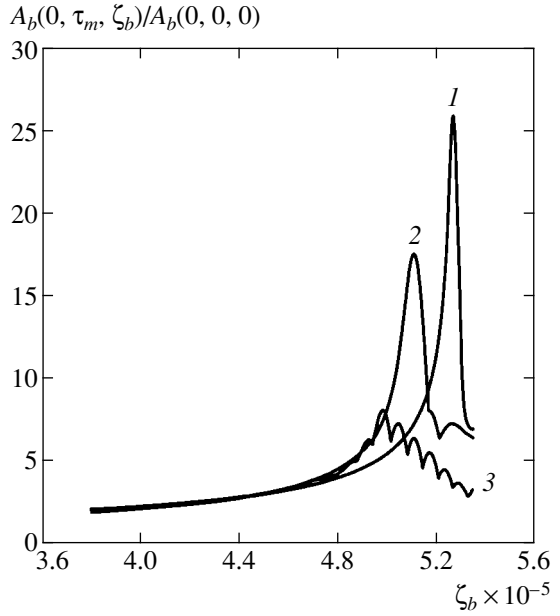

Fig. 3. Dependence of the amplitude at the peak of a beam with $W/W_{cr} \approx 2.25$ on coordinate ζ_b: paraxial approximation (*1*), total dispersion, $t_r = 0$ (*2*), and total dispersion, $t_r = 3 \times 10^{-15}$ s (*3*).

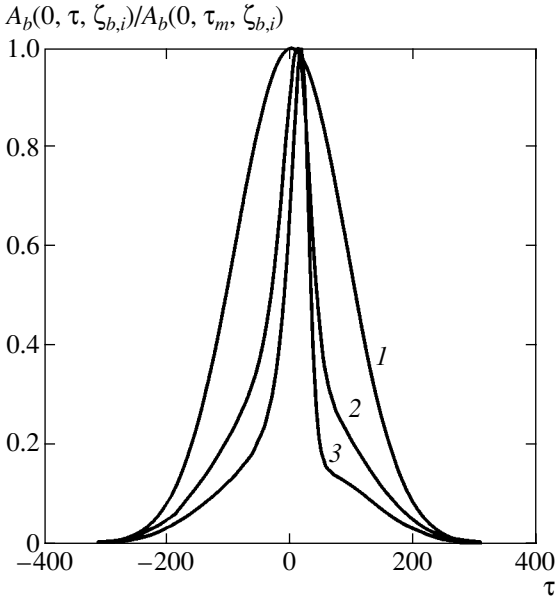

Fig. 4. Time variation of the pulse structure with $W/W_{cr} \approx 2.25$ and with relaxation time $t_r = 3 \times 10^{-15}$ s for $\zeta_{b,1} = 0$ (*1*), $\zeta_{b,2} = 390020$ (*2*), and $\zeta_{b,3} = 455500$ (*3*).

Figure 4 shows the change in the pulse structure with time for three different states $\zeta_{b,i}$ ($i = 1$ corresponds to the starting point, $i = 2$ corresponds to coordinate ζ_b at which the amplitude is doubled, and $i = 3$

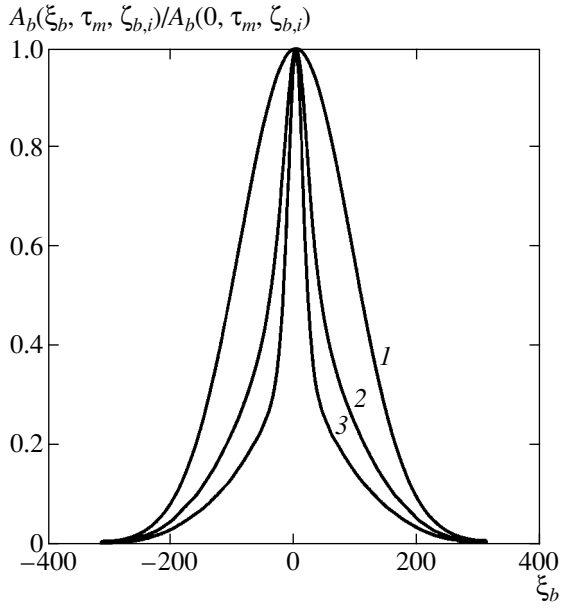

Fig. 5. Dependence of the pulse structure with $W/W_{cr} \approx 2.25$ and with relaxation time $t_r = 3 \times 10^{-15}$ s on the transverse coordinate for $\zeta_{b,1} = 0$ (*1*), $\zeta_{b,2} = 390020$ (*2*), and $\zeta_{b,3} = 455500$ (*3*).

corresponds to coordinate ζ_b at which the amplitude is tripled).

In the latter case, the pulse duration becomes equal to the wavelength. The maximum value is attained for a certain value of dimensionless time τ_m depending on longitudinal coordinate ζ_b. It is displaced in the forward direction relative to the origin of the reference frame; i.e., it propagates at a velocity slightly exceeding the group velocity. The pulse becomes asymmetric in time: its leading front becomes steeper. The spatial structure of the pulse in this case remains smoother than in Fig. 5, where the amplitude structure of the beam is shown as a function of the transverse coordinate for three values of longitudinal coordinate ζ_b.

As the pulse propagates further ($\zeta > \zeta_{b,3}$), it acquires high-frequency modulation with a period smaller than the period of the carrier wave due to the development of instability. For this reason, the electromagnetic pulse can be compressed to times smaller than the period of oscillations at the carrier frequency. A correct description of this process requires a more rigorous inclusion of nonlinearity, its dispersion, and its saturation; in particular, harmonic generation must be taken into account.

ACKNOWLEDGMENTS

The authors are grateful to V.I. Talanov for fruitful discussions.

This study was supported by the Russian Foundation for Basic Research (project no. 00-15-96772) in accordance with the program Nonlinear Dynamics and Solitons of the Presidium of the Russian Academy of Sciences.

REFERENCES

1. S. N. Vlasov and V. I. Talanov, *Wave Self-Focusing* (Inst. Prikl. Fiz. Ross. Akad. Nauk, Nizhni Novgorod, 1997).
2. V. E. Zakharov, Zh. Éksp. Teor. Fiz. **62**, 1745 (1972) [Sov. Phys. JETP **35**, 908 (1972)].
3. A. Silberberg, Opt. Lett. **15**, 1282 (1990).
4. V. V. Bakhanov and V. I. Talanov, in *Near-Surface Layer of the Ocean. Physical Processes and Remote Sounding* (Inst. Prikl. Fiz. RAN, Nizhni Novgorod, 1999), Vol. 1, p. 81.
5. L. A. Vaĭnshteĭn, *Electromagnetic Waves*, 2nd ed. (Radio i Svyaz', Moscow, 1988).
6. *Physical Quantities. Handbook*, Ed. by I. S. Grigor'ev and E. Z. Meilikhov (Énergoatomizdat, Moscow, 1991).
7. A. V. Grudinin, E. M. Dianov, D. V. Korobkin, *et al.*, Tr. Inst. Obshch. Fiz. Akad. Nauk SSSR **23**, 3 (1990).
8. V. I. Bespalov, A. G. Litvak, and V. I. Talanov, in *Proceedings of 2nd All-Union Symposium on Nonlinear Optics* (Nauka, Novosibirsk, 1968), p. 428.
9. Y. Codama and A. Hasegava, IEEE J. Quantum Electron. **23**, 510 (1987).
10. G. I. Marchuk, *Methods of Splitting* (Nauka, Moscow, 1988).

Translated by N. Wadhwa

Journal of Experimental and Theoretical Physics, Vol. 96, No. 1, 2003, pp. 25–33.
Translated from Zhurnal Éksperimental'noĭ i Teoreticheskoĭ Fiziki, Vol. 123, No. 1, 2003, pp. 32–41.

NUCLEI, PARTICLES, AND THEIR INTERACTION

Squeezed States of Light as Self-Similar Structures

V. A. Mironov

Institute of Applied Physics, Russian Academy of Sciences,
ul. Ul'yanova 46, Nizhni Novgorod, 603950 Russia
e-mail: fraiman@appl.sci-nnov.ru

Received August 15, 2002

Abstract—A new approach to investigating a broad class of dynamic states for a quantum oscillator is suggested. It is based on an invariant transformation of the equation to a new time determined by the quantum dispersion of the corresponding state. The squeezed states of a quantum system generated by the ground-state wave function are constructed. In coordinate representation, these states are described by a self-similar wave function localized near a classical trajectory. The statistics of the squeezed state of light is analyzed in the single-mode approximation. The parametric excitation of squeezed states for a quantum harmonic oscillator is considered. © *2003 MAIK "Nauka/Interperiodica".*

1. INTRODUCTION

The study of light with a reduced level of quantum fluctuations (nonclassical light) is still a pressing problem of quantum optics. Apart from other applications [1, 2], unremitting interest in the corresponding states of light stems from the prospects of using them in modern information systems, in which the squeezed states are basic [3].

The state of a system in which the dispersion of the distribution of one of the canonical variables is smaller than that in the ground (vacuum) state is called a squeezed state. Although the basic concepts are simple, the statistical properties of the squeezed state of light are difficult to analyze (see, e.g., [1]). The single-mode approach essentially deals with the class of dynamic solutions for a quantum harmonic oscillator that minimize the uncertainty relation. Squeezed single-mode states are created from an unsqueezed (generally vacuum) state using the transformation of canonical variables or by the Stoller unitary operator. Being created from a vacuum state, the squeezed state is clearly a fundamentally quantum state.

The formal procedure for constructing a squeezed state of light makes this object an exotic structure. On the other hand, nonclassical light is generally excited in dynamic quantum parametric processes. This forces us to look at the problem of the squeezed states of light from a slightly different perspective and to consider the dynamic procedure for constructing such states.

Here, we suggest a new approach to investigating the squeezed states of light based on invariant canonical transformations of the equations for a quantum harmonic oscillator to a new time. By considering the system evolution in the new time determined by the squeezed-state dispersion, we can construct (and excite) the corresponding states using a dynamic invariant transformation. These states are described by the dynamic self-similar distributions that are the ground-state wave functions in the proper (nonuniform) time. In Section 2, we suggest two invariant dynamic transformations (squeezing and passage to an oscillating frame of reference) of the equations for a quantum oscillator and construct the self-similar solutions generated by the ground-state wave function. In Section 3, by sequentially using these transformations, we find the self-similar structures that describe the squeezed coherent states of the system and study the spectrum of these states. In Section 4, we consider the parametric excitation of squeezed states.

2. FORMULATION OF THE PROBLEM: INVARIANT TRANSFORMATIONS

The Hamiltonian of a quantum harmonic oscillator,

$$\hat{H} = (\hat{p}^2 + \omega^2(t)\hat{q}^2)/2,$$

with a time-dependent frequency $\omega(t)$ specifies the following equations of motion for the Heisenberg operators:

$$\frac{d\hat{q}}{dt} = \hat{p}, \quad \frac{d\hat{p}}{dt} = -\omega^2(t)\hat{q}. \tag{1}$$

2.1. Squeezing Transformation

Let the evolution of the coordinate, $\hat{Q}$, and momentum, $\hat{P}$, operators in the new time τ be described by equations of the same type,

$$\frac{d\hat{Q}}{d\tau} = \hat{P}, \quad \frac{d\hat{P}}{d\tau} = -\Omega^2\hat{Q}, \tag{2}$$

with the same commutation relation

$$([\hat{P}, \hat{Q}] = -i).$$

It is easy to see that the unitary transformation of the canonical variables

$$\hat{q} = b(t)\hat{Q}(\tau), \qquad \hat{p} = \hat{P}(\tau)/b(t) + b_t(t)\hat{Q}(\tau) \tag{3}$$

reduces Eqs. (1) to Eqs.(2) if the scale $b(t)$ varies as

$$b_{tt} + \omega^2(t)b = \frac{\Omega^2}{b^3}. \tag{4}$$

Here, we use the following notation for the derivatives:

$$b_t = \frac{db}{dt}, \quad b_{tt} = \frac{d^2b}{dt^2}.$$

The new evolutionary variable τ is related to the old variable t by

$$d\tau = \frac{dt}{b^2(t)}. \tag{5}$$

First, note the following. The above transformation (3)–(5) differs markedly from the invariant transformations commonly used in quantum theory in that it contains the transformation of the evolutionary variable (5). Through this transformation, Eqs. (1) for an oscillator with a variable frequency can be reduced, for example, to the corresponding equation (2) with a constant frequency, Ω = const. The scale parameter $b(t)$ relates the dispersions of the processes in the new and old times. Thus, for the processes with a zero mean ($\langle\hat{q}\rangle = \langle\hat{Q}\rangle = 0$), we derive the following relations for the dispersions of the canonical variables:

$$\langle\hat{q}^2\rangle = b^2(t)\langle\hat{Q}^2\rangle, \tag{6}$$

$$\langle\hat{p}^2\rangle = \frac{\langle\hat{P}^2\rangle}{b^2} + b_t^2\langle\hat{Q}^2\rangle. \tag{7}$$

In other words, if the dispersion of the system coordinate in some state (6) is equal to $\langle\hat{q}^2\rangle$ ($\langle\hat{q}^2\rangle = b^2(t)\langle\hat{Q}^2\rangle$), then the dispersion in the new (proper) time (5), which is virtually determined by this state, is $\langle\hat{Q}^2\rangle$. Of particular interest are the dynamic states of the system that are the ground (vacuum) state in the proper time (5). These are the squeezed states of the system.

The nonlinear equation (4) for the scale parameter is latently linear. It is convenient to represent its solution as

$$b = (u^2 + \Omega^2 v^2/w^2)^{1/2}, \tag{8}$$

where u and v are the two linearly independent solutions of the equation for an oscillator

$$x_{tt} + \omega^2(t)x = 0 \tag{9}$$

with the initial conditions

$$u(0) = A, \quad u_t(0) = B, \quad v(0) = 0, \quad v_t(0) \neq 0;$$

w is the Wronskian:

$$w = uv_t - u_tv = \text{const}.$$

For a harmonic oscillator, $\omega = \Omega = \omega_0 = \text{const}$, the scale parameter varies as

$$b(t) = \sqrt[4]{K}\left(\cos^2\omega_0 t + \frac{1}{K}\sin^2\omega_0 t\right)^{1/2}, \tag{10}$$

where the squeezing factor $K = (b_{max}/b_{min})^2$ characterizes the modulation of the dispersion at double frequency. This periodic variation of the dispersion between its maximum,

$$b^2_{max}(t = 0) = \sqrt{K},$$

and its minimum,

$$b^2_{min}(t = \pi/2\omega_0) = 1/\sqrt{K},$$

serves as evidence for a squeezed state of light.

To get a more detailed picture, we continue to analyze a quantum harmonic oscillator with a unit frequency ($\omega = \Omega = \omega_0 = 1$). Consider the pseudoannihilation operator

$$\hat{A} = \frac{\hat{Q} + i\hat{P}}{\sqrt{2}}. \tag{11}$$

Using (3), we represent it in terms of the standard production and annihilation operators

$$\hat{a}^+ = (\hat{q} - i\hat{p})/\sqrt{2}, \quad \hat{a} = (\hat{q} + i\hat{p})/\sqrt{2}.$$

As a result, we obtain

$$\hat{A} = \frac{1}{2}\left(b + \frac{1}{b} - ib_t\right)\hat{a} + \frac{1}{2}\left(-b + \frac{1}{b} - ib_t\right)\hat{a}^+. \tag{12}$$

Let us assume that the system described by the operators $\hat{Q}$ and $\hat{P}$ in the new time τ is in the ground state $|0\rangle$. Acting on it by pseudoannihilation operator (12), we derive the following relation for the corresponding dynamic state $|\psi\rangle$ in real time:

$$\left(b + \frac{1}{b} - ib_t\right)\hat{a}|\psi\rangle + \left(-b + \frac{1}{b} - ib_t\right)\hat{a}^+|\psi\rangle = 0. \tag{13}$$

Hence, for example, using the coordinate representation for the operators $\hat{a}$ and $\hat{a}^+$, we obtain the wave function of the squeezed vacuum state

$$\psi = \sqrt[4]{\frac{1}{\pi b^2}}\exp\left(-\frac{q^2}{2b^2} - \frac{ib_t}{2b}q^2\right), \tag{14}$$

where $b(t)$ is defined by expression (10) with $\omega_0 = 1$. It has a self-similar structure and can be obtained from the Schrödinger equation with a parabolic potential by an appropriate transformation to the self-similar variables [$\eta = q/b(t)$].

Using the steady-state expansion of $|\psi\rangle$, we can obtain the following recurrence relations for the probability amplitudes c_n of the oscillator being at neighboring levels:

$$\left(b + \frac{1}{b} - ib_t\right)(n+1)^{1/2}c_{n+1} + \left(-b + \frac{1}{b} - ib_t\right)(n-1)^{1/2}c_{n-1} = 0. \quad (15)$$

Hence, we derive the probabilities of the oscillator being in the 2nth state

$$w_{2n} = |c_2|^{2n} = \frac{2(2n)!}{2^{2n}(n!)^2}\left(\frac{\sqrt{K}-1}{\sqrt{K}+1}\right)^{2n}\frac{\sqrt[4]{K}}{\sqrt{K}+1}. \quad (16)$$

Naturally, this expression can be derived by expanding (14) in terms of the steady-state eigenfunctions for the quantum oscillator.

The mean number of the modes,

$$\bar{n} = \sum_{n=0}^{\infty} nw_n, \quad (17)$$

that form the squeezed vacuum state (16) is

$$\bar{n} = \frac{(1-\sqrt{K})^2}{4\sqrt{K}}. \quad (18)$$

Thus, the enrichment of the spectrum with increasing squeezing factor follows the law $\bar{n} \sim \sqrt{K}$. Note that relation (13) corresponds to the standard definition of the squeezed state of light [1]. However, because of its structure, it also contains a simple description of system dynamics (14).

2.2. Transformation to an Oscillating Frame of Reference

Consider another invariant transformation. Let there be a solution $\bar{x}(t)$ of the classical equation for a harmonic oscillator with $\omega_0 = 1$. Transform the canonical variables

$$\hat{q}(t) = \hat{Q}(t) + \bar{x}(t)\hat{I}, \quad \hat{p}(t) = \hat{P}(t) + \bar{x}_t(t)\hat{I} \quad (19)$$

in Eq. (1) with $\omega(t) = 1$. In (19), $\hat{I}$ is a unit operator. Since the basic equation is linear, the evolution of the new canonical variables $\hat{Q}$ and $\hat{P}$ is clearly described by the same Eqs. (1) with $\omega(t) = 1$ if $\bar{x}(t)$ and $\bar{x}_t(t)$ are the coordinate and velocity of classical motion, respectively.

In essence, transformation (19) is the transformation of the quantum equations of motion (1) to the noninertial (oscillating) frame of reference associated with a classical trajectory. For the state pseudoannihilation operator in the oscillating frame of reference $\hat{A} = (\hat{Q} + i\hat{P})/\sqrt{2}$, we obtain

$$\hat{A} = \hat{a} - (\bar{x}(t) + i\bar{x}_t(t))\hat{I}/\sqrt{2}. \quad (20)$$

If the quantum system in the oscillating frame of reference is in the ground state $|0\rangle$, then the real state $|\psi\rangle$ is described by the operator equation

$$\hat{a}|\psi\rangle = (\bar{x}(t) + i\bar{x}_t(t))\hat{I}|\psi\rangle/\sqrt{2}; \quad (21)$$

i.e., the wave function is the eigenfunction of the pseudoannihilation operator and, by definition, describes the coherent states of the system [1]. In energy representation, this equation can be easily solved. As a result, we obtain the Poisson distribution for the probability of the oscillator being in the nth state, which is well known in quantum optics [1, 2, 4]:

$$w_n = \frac{N^n}{n!}\exp(-N), \quad (22)$$

where N is the number of photons in classical motion.

To conclude this section, we note the following. The unitary transformation of the canonical variables (3) in the Schrödinger equation (i.e., in coordinate representation),

$$i\frac{\partial\psi}{\partial t} + \frac{\partial^2\psi}{\partial q^2} - \frac{\omega^2(t)}{4}q^2\psi = 0, \quad (23)$$

corresponds to a self-similar substitution of the form

$$\psi = \frac{1}{\sqrt{b(t)}}S(q/b)\exp\left(-i\frac{b_t}{4b}q^2\right). \quad (24)$$

It is easy to verify that the self-similar function $S(q/b)$ is described in the new time τ (5) by the Schrödinger equation

$$i\frac{\partial S}{\partial\tau} + \frac{\partial^2 S}{\partial\eta^2} - \frac{\Omega^2}{4}\eta^2 S = 0, \quad (25)$$

where $\eta = q/b(t)$. The dispersion $b(t)$ of the wave function (24) is defined by Eq. (4). Using the steady-state solution of Eq. (25) that corresponds to the ground state of the quantum oscillator, we determine the dynamic wave function (14) using (24).

Note that the passage to the self-similar function (24), (25) for $\Omega = \text{const}$ is accompanied by an increase in the symmetry of the system under consideration. Equation (25) is invariant relative to a shift in nonuniform time ($\tau \longrightarrow \tau + \tau_0$) and, for $\Omega = 0$, relative to trans-

lation in the space of self-similar variable η ($\eta \longrightarrow \eta + \eta_0$).

The transformation of the wave function to an oscillating frame of reference is given in [4].

3. SQUEEZED COHERENT STATES

Sequentially applying the above transformations [squeezing (3) and passage to an oscillating frame of reference (19)] extends the class of dynamic solutions of the equation for a quantum oscillator.

3.1. Perfectly Squeezed States

Let us first consider the following possibility. We first pass to an oscillating frame of reference (19) and then make a squeezing transformation [$q(t)$, $p(t) \longrightarrow Q(\tau)$, $P(\tau)$] according to (3)–(5). As a result, we obtain a generalized transformation of Eqs. (1) to (2):

$$\begin{aligned}\hat{q} &= b(t)\hat{Q}(\tau) + \bar{x}(t)\hat{I},\\ \hat{p} &= \frac{\hat{P}(t)}{b(t)} + b_t(t)\hat{Q}(\tau) + \bar{x}_t(t)\hat{I}.\end{aligned} \tag{26}$$

For simplicity, as above, we assume that $\omega(t) = \Omega = 1$. For the pseudoannihilation operator $\hat{A} = (\hat{Q}(\tau) + i\hat{P}(t))/\sqrt{2}$ in the proper time (5) determined by the state dispersion, we derive

$$\begin{aligned}\hat{A} = \frac{1}{2}\left(b + \frac{1}{b} - ib_t\right)\hat{a} + \frac{1}{2}\left(-b + \frac{1}{b} - ib_t\right)\hat{a}^+\\ -\left[\left(\frac{1}{b} - ib_t\right)x + ibx_t\right]\frac{\hat{I}}{\sqrt{2}}.\end{aligned} \tag{27}$$

Assuming then that the transformed (in the oscillating frame of reference and in the new time τ) state in the vacuum state $|0\rangle$, we arrive at the operator equation for the corresponding dynamic state of the system $|\psi(t)\rangle$:

$$\begin{aligned}\left(b + \frac{1}{b} - ib_t\right)\hat{a}|\psi\rangle + \left(-b + \frac{1}{b} - ib_t\right)\hat{a}^+|\psi\rangle\\ = \left(\left(\frac{1}{b} - ib_t\right)\bar{x} + ib\bar{x}_t\right)\sqrt{2}\hat{I}|\psi\rangle.\end{aligned} \tag{28}$$

It is a generalization of (13) and (21) to a squeezed coherent state. Here, it is important to note that the squeezing transformation acts differently on the coordinate and velocity of classical motion [see the right-hand side of Eq. (28)].

In coordinate representation, the following expression can be easily obtained for the wave function of a coherent squeezed state:

$$\begin{aligned}\Psi &= \left(\frac{1}{\pi b^2}\right)^{1/4}\\ &\times \exp\left[-\left(\frac{1}{b^2} - i\frac{b_t}{b}\right)\frac{(q - \bar{x}(t))^2}{2} + i\bar{x}_t q\right].\end{aligned} \tag{29}$$

It describes a self-similar wave field localized near the oscillating classical trajectory $\bar{x}(t)$ of the center of mass,

$$\bar{x} = \bar{q} = \int q|\Psi|^2 dq,$$

with frequency $\omega_0 = 1$. The dispersion b^2 of (29) varies with a double frequency [see (10)]. Obviously, the spectral features of the coherent squeezed state are determined by the phase difference between the oscillations of the center of mass $x(t)$ and the dispersion parameter $b_t = 0$, $b(t) = \sqrt[4]{K}$ at $t = 0$.

The probability of the oscillator being in the nth state can be obtained in energy representation by appropriately generalizing relation (15) to a squeezed coherent state. It is easier to act by expanding (29) in terms of the steady-state wave functions for the oscillator (Hermitean function ψ_n). Calculating the coefficients of this expansion,

$$c_n = \int \Psi\Psi_n^* dq,$$

yields

$$\begin{aligned}|c_n|^2 = \frac{2\sqrt[4]{K}}{\sqrt{K}+1}\left(\frac{1-\sqrt{K}}{1+\sqrt{K}}\right)^n \left|H_n\left(\frac{ix_0 - x_t(0)\sqrt{K}}{\sqrt{K-1}}\right)\right|^2\\ \times (2^n n!)^{-1}\exp\left(\frac{x_0^2 + x_t^2(0)\sqrt{K}}{\sqrt{K}+1}\right),\end{aligned} \tag{30}$$

where $x_0 = \bar{x}(t = 0)$ and $x_t(0) = \bar{x}_t(t = 0)$ are, respectively, the coordinate and velocity of classical motion (the center of mass) when the squeezing transformation is "turned on"; H_n is the nth Hermitean polynomial. Note that such expressions can be found, in particular, in [1, 4]. However, in contrast to the corresponding relation in [1, 4], our expressions (30) are determined by the classical system parameters and by the squeezing factor. Thus, we can analyze in more detail the features of the spectrum for a squeezed coherent state (30).

The following averaged characteristics of the distribution $w_n = |c_n|^2$ for the probability of the oscillator being in the nth state are indicative:

$$\bar{n} = \sum_0^\infty n w_n, \quad \overline{n^2} = \sum_0^\infty n^2 w_n. \tag{31}$$

Details of calculating the spectral moments (31) for distribution (30) are given in the Appendix. Here, we present the following results. The mean of distribution (30) is

$$\bar{n} = \frac{x_0^2 + x_t^2(0)}{2} + \frac{(1-\sqrt{K})^2}{4\sqrt{K}}. \quad (32)$$

It is the sum of the corresponding mean numbers of photons in classical motion (the mean for the Poisson distribution), N, and in a squeezed vacuum state (18).

Based on the expression for the second moment and (32), we can derive the relation

$$\Delta = \overline{n^2} - (\bar{n}^2 + \bar{n})$$
$$= \frac{(1-\sqrt{K})^2(1+K)}{8K} + \frac{\sqrt{K}-1}{2}\left[x_0^2 - \frac{x_t^2(0)}{\sqrt{K}}\right]. \quad (33)$$

This relation is used in quantum optics [1] to describe the deviations of the photon statistics from Poissonian statistics.

Note that the squeezing transformation acts differently on the coordinate x_0 and velocity $x_t(0)$ of the classical motion "dressed" by the quantum dispersion. This circumstance leads to a number of features in the photon statistics. It is easy to derive a relation between K, x_0, and $x_t(0)$ that makes the right-hand side of expression (33) vanish. In this sense, the statistics is Poissonian ($\Delta = 0$). Depending on the sign of Δ, the photon statistics of the squeezed coherent state can be super-Poissonian ($\Delta > 0$) and sub-Poissonian ($\Delta < 0$). The limiting case is realized, for example, if the squeezing ($K > 0$) is turned on at a zero center-of-mass velocity of classical motion [$x_t(0) = 0$]. The corresponding states of the wave system are defined as quadrature-squeezed [1].

If the squeezing is done when the coordinate is zero ($x_0 = 0$) and the velocity $x_t(0)$ is at a maximum, then Δ can be less than zero ($\Delta < 0$) for the number of photons $N = x_t^2(0)/2$ in classical motion:

$$N > \frac{(\sqrt{K}-1)(K+1)}{8\sqrt{K}}. \quad (34)$$

The dispersion $D = \overline{n^2} - \bar{n}^2$ of such a state for $N \gg K \gg 1$ is

$$D \approx N/\sqrt{K};$$

i.e., it is appreciably smaller than the mean number of photons (32). For this reason, it is called squeezed by the number of photons [1].

Consider the features of spectrum (30) for these two types of squeezed states of the system for $K > 1$. In the first case, [$x_t(0) = 0$], using the asymptotic expression [6]

$$|H_n(ix)| \approx \frac{2^{n/2}}{\sqrt{2}}\left(\frac{n}{e}\right)^{n/2}\exp\left(-\frac{x^2}{2}\right) + \sqrt{2n}x \quad (35)$$

for $1 \ll |x|^2 \ll n$ yields the expression

$$|c_n|^2 = \frac{1}{2\sqrt[4]{K}\sqrt{2\pi n}}\exp\left(-\frac{2(\sqrt{n}-\sqrt{N})^2}{\sqrt{K}}\right). \quad (36)$$

To simplify it, we used the Stirling formula for $n!$ and the condition of a strongly squeezed coherent multiphoton state $N \gg K \gg 1$.

Thus, the spectrum of a quadrature-squeezed state (36) is a shifted Gaussian function that depends on $\sqrt{n}$. Near the maximum ($n^* = N$) and for $n \gg N$, function (36) behaves more smoothly than does the standard Gaussian function of n. This causes an appreciable increase in the dispersion of (36) compared with $\sqrt{K}$ to $N\sqrt{K}$, which corresponds to (6).

In the second case, where the squeezing acts on a system whose classical motion has a maximum velocity ($x_0 = 0$), the corresponding distribution (30) is defined by Hermitean polynomials of a real argument. For $K \gg 1$, (30) simplifies to

$$|c_n|^2 = \frac{2}{\sqrt[4]{K}2^n n!}\exp\left(-\frac{2n}{\sqrt{K}}\right)$$
$$\times H_n^2\left(\sqrt{\frac{2NK}{K-1}}\right)\exp\left(-\frac{2N\sqrt{K}}{\sqrt{K}+1}\right). \quad (37)$$

The Hermitean polynomial $H_n(x)$ reaches its maximum at $x^2 \approx 2n$, i.e., in our case, for n^* equal to the number of photons in classical motion ($n^* = N$). In this region, the asymptotic behavior of $H_n(x)$ for $n \gg 1$ and $x \gg 1$ is determined by the Airy function [6]. As a result, we obtain from (37)

$$|c_n|^2 = \frac{2}{\sqrt[4]{K}}\frac{3^{2/3}\sqrt{2}}{\pi^{3/2}n^{1/6}}\mathrm{Ai}^2(t)\exp\left(\frac{2(N-n)}{\sqrt{K}}\right), \quad (38)$$

where

$$t = 2\sqrt[3]{3}n^{1/6}(\sqrt{n}-\sqrt{N}).$$

Thus, distribution function (37) for the state squeezed by the number of photons exhibits the following behavior. For $n < N$, the increase of (38) is essentially determined by the Airy function Ai(t). The decrease of (38) for $n > N$ is described by the exponential factor in (38). As a result, the two-scale distribution (38) localized near $n = N$ has a combined dispersion, which we determined by using the method of moments (33) and (32).

3.2. A Generalized Coherent Squeezed State

There is also another possibility. We first perform the squeezing transformation (3)–(5) and then pass to an oscillating frame of reference (19) associated with a classical trajectory. As a result, we obtain the following transformation of the canonical variables:

$$\begin{aligned}\hat{q} &= b(t)(\hat{Q}(\tau) + \eta(\tau)\hat{I}),\\ \hat{p} &= \frac{(\hat{P}(t) + \eta_\tau(\tau)\hat{I})}{b(t)} + b_t(t)(\hat{Q}(\tau) + \eta(\tau)\hat{I}),\end{aligned} \tag{39}$$

where $\eta(\tau)$ and $\eta_\tau(\tau)$ are the coordinate and velocity of classical oscillatory motion in the new time. As above, $\omega = \omega_0 = \Omega = 1$. Repeating the same operations as in the previous case yields the expression for the pseudoannihilation operator:

$$\begin{aligned}\hat{A} &= \frac{1}{\sqrt{2}}\left(\frac{1}{b} - ib_t\right)\hat{q}\\ &+ \frac{1}{\sqrt{2}}(ib)\hat{p} - [\eta(\tau) + i\eta_\tau(\tau)]\frac{\hat{I}}{\sqrt{2}}.\end{aligned} \tag{40}$$

Thus, the ground state of the system in the new time τ is described by the operator equation

$$\left(\left(\frac{1}{b} - ib_t\right)\hat{q} + (ib)\hat{p}\right)\Psi = [\eta(\tau) + i\eta_\tau(\tau)]\Psi, \tag{41}$$

whence we derive the following expression for the wave function in coordinate representation:

$$\begin{aligned}\psi &= \left(\frac{1}{\pi b^2}\right)^{1/4}\\ &\times \exp\left(-\frac{1}{2}\frac{(q - \eta(\tau)b(t))^2}{b^2(t)} + i\frac{b_t}{2b^2}q^2 + i\frac{\eta_\tau}{b}q\right).\end{aligned} \tag{42}$$

It has, at least outwardly, a more complex self-similar structure than do (14) and (29). Expression (42) describes the wave packet localized near a classical trajectory:

$$\bar{q} = b(t)\eta(\tau) \equiv \bar{x}(t). \tag{43}$$

Clearly, this is the same oscillating trajectory as that for distribution (29), $\bar{q} = \bar{x}(t)$. This can easily be verified, because $\eta_{\tau\tau} = -\eta$, $d\tau = dt/b^2$, and b is the solution of Eq. (4) for $\omega = \Omega = 1$. Thus, basically, distribution (42) differs from (29) in that the parameters of the classical trajectory dressed by it are determined by the dispersion of state (42).

Consider the spectrum (in Hermitean functions) of wave function (42). It can also be directly obtained from (41) by expressing $\hat{p}$ and $\hat{q}$ in terms of the production and annihilation operators in the Fock representation. However, it is easier to use the correspondence between (42) and (29). As above, the oscillation phase $\eta(\tau)$ is reckoned from the time when $b_t(t = 0) = 0$ and $b(t = 0) = \sqrt[4]{K}$. As a result, we obtain for the probability of the oscillator being in the nth state

$$\begin{aligned}|c_n|^2 &= \frac{2\sqrt[4]{K}}{\sqrt{K}+1}\left(\frac{1-\sqrt{K}}{1+\sqrt{K}}\right)^n\left|H_n\left(\frac{(i\eta_0 - \eta_t(0))\sqrt[4]{K}}{\sqrt{K-1}}\right)\right|^2\\ &\times (2^n n!)^{-1}\exp\left\{-\frac{\eta_0^2\sqrt{K} + \eta_t^2(0)}{\sqrt{K}+1}\right\},\end{aligned} \tag{44}$$

where $\eta_0 = \eta(t = 0)$ and $\eta_\tau(\tau = 0) = \eta_\tau(0)$. It can be derived from (30) by the substitution

$$x_0 \longrightarrow \sqrt[4]{K}\eta_0, \quad x_t(0) \longrightarrow \eta_\tau(0)/\sqrt[4]{K}, \tag{45}$$

which is determined by modification (43) of the classical equation of motion. In other words, the difference between (44) and (30) is that for the classical trajectory (43), the initial conditions specify

$$x(t) = b(t)\cos\int_0^t \frac{dt}{b^2(t)}, \tag{46}$$

which is determined by the quantum dispersion $b(t)$. In this sense, our transformations [squeezing and passage to an oscillating frame of references $x(t)$] can be said to commute.

To conclude this section, we note the following. The system state (42) and (45) under consideration is a generalized coherent squeezed state [1]. The corresponding expression (14) is given, for example, in [1] [see formula (21.5.25)]. It is so cumbersome that the authors refused to analyze this expression. The conclusions reached when discussing the first two moments of the photon distribution [formulas (21.5.26) and (21.5.28)] were not very definitive either. In our approach, substitution (45) in (32) and (33) does not result in an appreciable complication:

$$\bar{n} = \frac{\eta_0^2\sqrt{K} + \eta_\tau^2(0)/\sqrt{K}}{2} + \frac{(1-\sqrt{K})^2}{4\sqrt{K}}, \tag{47}$$

$$\Delta = \frac{(1-\sqrt{K})^2(1+K)}{8K} + \frac{\sqrt{K}-1}{2}(\sqrt{K}\eta_0^2 - \eta_\tau^2(0)/K). \tag{48}$$

Clearly, analysis of these expressions and the spectral features of squeezed coherent states [quadrature-squeezed (36) and squeezed by the number of photons (38)] differs little from that described in the first part of this section.

4. THE EXCITATION OF SQUEEZED STATES

The transformations of squeezing (3) and passage to an oscillating frame of reference (19) basically reduce the solution of a broad class of nonstationary quantum problems to Eq. (9) with a variable frequency. Of particular interest in exciting squeezed states of light is the study of resonance processes. Since the dispersion of

the wave function in a squeezed state varies at the double frequency of a reference harmonic oscillator, it would be natural to use a parametric resonance to excite such states. Consider the degenerate parametric down conversion whose dynamics is described by the Hamiltonian

$$\hat{H} = (\hat{p}^2 + (1 + \varepsilon\sin 2t)\hat{q}^2)/2,$$

where $\varepsilon \ll 1$.

As a result, we obtain Eq. (1) for a quantum oscillator with the frequency varying as

$$\omega^2(t) = 1 + \varepsilon\sin 2t. \quad (49)$$

The choice of such a periodic function ($\sin 2t$) corresponds to the phase relations used above. Let us first consider the excitation of a vacuum state (14) and then generalize the derived expressions to squeezed coherent states.

4.1. The Excitation of a Squeezed Vacuum State

In our approach, the problem of exciting a squeezed state reduces to analyzing the equation for the dispersion of a quantum system

$$b_{tt} + (1 + \varepsilon\sin 2t)b = 1/b^3. \quad (50)$$

As above (8), the solution of this equation should be represented ($b^2 = u^2 + v^2$) via the linearly independent solutions $u(t)$ and $v(t)$ of the oscillator equation

$$y_{tt} + (1 + \varepsilon\sin 2t)y = 0 \quad (51)$$

with the same initial conditions [$u(0) = 1$, $u_t(0) = 0$, $v(0) = 0$, $v_t(0) \neq 0$).

Hence, we derive the following expression for the quantum-state dispersion $b(t)$ for the parametric resonance conditions under consideration:

$$b(t) = (\cos^2 t + \exp(-4\gamma t)\sin^2 t)^{1/2}\exp\gamma t, \quad (52)$$

where the increment of parametric instability is $\gamma = \varepsilon/4$. Thus, dispersion (52) changes twice in the oscillator period from its maximum value $b_{\max} = \exp(\gamma t)$ to its minimum value $b_{\min} = \exp(-\gamma t)$. The squeezing factor

$$K = b^2_{\max}/b^2_{\min} = \exp(\varepsilon t) \quad (53)$$

increases exponentially with time. Thus, the expression for the quantum dispersion

$$b(t) = \sqrt[4]{K(t)}\left(\cos^2 t + \frac{1}{K(t)}\sin^2 t\right) \quad (54)$$

retains its original form (10) with the squeezing factor $K(t)$ increasing slowly (on the scale of the dispersion oscillation period) with time. In this approximation, the state wave function (14) and spectrum (16) are slowly evolving functions as the squeezing factor (53) increases.

4.2.The Excitation of a Squeezed Coherent State

The wave function for a squeezed coherent state is defined by two parameters: the dispersion and trajectory of the center-of-mass motion. The quantum-state dispersion is described by expression (54) with the squeezing factor (53). The wave function (29) is localized near the classical trajectory

$$\bar{x}_{tt} + (1 + \varepsilon\sin 2t)\bar{x} = 0. \quad (55)$$

The two linearly independent solutions of this equation in the same approximation as above ($\varepsilon \ll 1$) are

$$\bar{x}_1(t) = A\exp(\varepsilon t/4)\cos t, \quad (56)$$

$$\bar{x}_2(t) = B\exp(-\varepsilon t/4)\sin t. \quad (57)$$

Thus, two regimes are possible. In the first case, the increase in the modulation depth of dispersion (54) is accompanied by an increase in the amplitude of the coherent component described by expression (56). The growth of parametric instability of the center-of-mass motion of the wave field (56) results in the excitation of a quadrature-squeezed coherent state.

In the other case, the initial phase relation between the oscillations of the center of the wave field (57) and dispersion (54) are such that a state squeezed by the number of photons is formed. This process is peculiar in that the oscillatory center-of-mass motion (57) is suppresed as the amplitude of the quantum dispersion (54) increases exponentially. As a result, the energy of the coherent component decreases and, consequently, a state more similar to a squeezed vacuum state is excited.

4.3. Processes in Reverse Order of Transformations

Next, consider the application of the transformations in reverse order, i.e., (39), but for a quantum oscillator with a variable frequency (49). In this case, the wave function that describes a nonstationary squeezed coherent state is localized, like (42), near the classical trajectory

$$\bar{x}(t) = b(t)\eta(\tau). \quad (58)$$

It follows from the method of constructing this squeezed coherent state that the dispersion is described by Eq. (50) and that $\eta(\tau)$ is the equation for a harmonic oscillator

$$\eta_{\tau\tau} + \eta = 0$$

in the new time

$$d\tau = dt/b^2(t).$$

It is easy to see that $\bar{x}(t)$ defined by relation (58) is the solution to Eq. (55). In other words, (58) is a different representation of the solution to steady-state equation (55) via the solution to the equation for a harmonic oscillator in the new time. Thus, as in the case of dynamic transformation (39), the problem reduces to specifying the initial conditions when solving Eq. (55), expressed in representation (58) in terms of the initial quantum state dispersion at time $t = 0$. The properties of the excitation of a quadrature-squeezed state and a state squeezed by the number of photons here are the same as those in Section 4.2.

5. CONCLUSION

The procedure for obtaining the dynamic solutions of the equation for a quantum oscillator outlined above has a number of advantages over the commonly used procedure [7–9]. Using invariant transformations of the canonical variables and time ultimately reduces the solution of the problem to a classical oscillator with a variable frequency. As a result, the solution of the quantum problem can be expressed in terms of the parameters of a classical system. In particular, the solutions generated by the ground(vacuum)-state wave function correspond to squeezed states of the system. They are self-similar in structure. In the new (nonuniform) time determined by the state dispersion, the self-similar solution matches the ground-state wave function. In our approach, the distributions localized near classical oscillatory motion (coherent state) correspond to squeezed coherent states. The situation here is in many respects similar to the Feynmann representation of quantum mechanics in classical trajectories [10] supplemented with a transformation of the evolutionary variable. The clear structure of the wave function allows us to easily analyze the conditions (phase relations between the invariant transformations) under which quadrature-squeezed states and states squeezed by the number of photons are realized and to consider the parametric excitation of squeezed states for the system.

In conclusion, we note the following. The suggested dynamic transformations of the canonical variables are a convenient tool for studying the applications of nonclassical light. Thus, for example, when considering the interaction of squeezed coherent light with atoms, passing to the new time determined by the quantum dispersion reduces the problem in the new canonical variables to the better studied problem of the interaction between coherent radiation and matter.

Similar dynamic transformations of the canonical variables also take place in the more complex case of a quantum oscillator with dissipation [9] described by the Hamiltonian

$$\hat{H} = \exp(-2F(t))\hat{p}^2/2 + \omega^2(t)\exp(2F(t))\hat{q}^2/2.$$

The corresponding generalization of transformations (3) and (4) is

$$\hat{q} = b\exp(-F)\hat{Q}(\tau),$$

$$\hat{p} = \frac{\exp(F)}{b}\hat{P}(\tau) + (b_t - F_t b)\exp(F)\hat{Q}(\tau),$$

$$b_{tt} + (\omega^2(t) - F_{tt} - F_t^2)b = \frac{1}{b^3}.$$

As above, operators $\hat{Q}(\tau)$ and $\hat{P}(\tau)$ in the new time $d\tau = dt/b^2(t)$ describe a quantum harmonic oscillator (2) with $\Omega = 1$. Clearly, this circumstance appreciably simplifies analysis of such a dissipative system.

ACKNOWLEDGMENTS

I am grateful to G.A. Vugalter, A.G. Litvak, V.E. Semenov, and G.M. Fraiman for helpful discussions. This study was supported by the Russian Foundation for Basic Research (project no. 01-02-17388).

APPENDIX

To determine the moments of the photon number distribution,

$$w_n = \frac{2\sqrt[4]{K}}{\sqrt{K}+1}\left(\frac{1-\sqrt{K}}{1+\sqrt{K}}\right)^n \left| H_n\left(\frac{ix_0 - x_t(0)\sqrt[4]{K}}{\sqrt{K-1}}\right)\right|^2 \times (2^n n!)^{-1}\exp\left(-\frac{(x_0^2 + x_t^2(0)\sqrt{K})}{\sqrt{K}+1}\right), \quad (59)$$

we use the relation [11]

$$\frac{1}{\sqrt{1-z^2}}\exp\left(\frac{2xyz - z^2(x^2+y^2)}{1-z^2}\right) = \sum_0^\infty \frac{(z/2)^n}{n!}H_n(x)H_n(y). \quad (60)$$

If we use the notation

$$z = (1-\sqrt{K})/(1+\sqrt{K}),$$

$$x = (ix_0 - x_t(0)\sqrt[4]{K})/(\sqrt{K}-1), \quad (61)$$

$$y = x^* = -(ix_0 + x_t(0)\sqrt[4]{K})/(\sqrt{K}-1)$$

in (60), then we obtain an expression for the normalization of distribution (59). In this notation, distribution (59) can be written as

$$w_n = \frac{z^n|H_n(x)|^2}{g(z, x, y = x^*)}, \quad (62)$$

where

$$gt(z, x, y = x^*) = \frac{1}{\sqrt{1-z^2}}\exp\left(\frac{2xyz - z^2(x^2+y^2)}{1-z^2}\right). \quad (63)$$

The normalization of distribution (59) is given by the relation

$$\sum_{n=0}^{\infty}\frac{z^n}{2^n n!}|H_n(x)|^2 = g(z, x, y = x^*). \quad (64)$$

To determine the first moment of distribution (62),

$$\bar{n} = \sum_{0}^{\infty} n w_n, \quad (65)$$

we differentiate (60) with respect to z. Multiplying the derived expression by z/g yields the following expression for the first moment:

$$\bar{n} = \frac{z}{g(z, x, y = x^*)}\left(\frac{\partial g(z, x, y)}{\partial z}\right)_{x = x,\, y = x^*}. \quad (66)$$

Here, after the differentiation, we should set $y = x^*$. By transforming (66) using (61), we determine $\bar{n} = \bar{n}(K, x_0, x_t(0))$ in form (32).

Making the same operations [differentiating (66) with respect to z and multiplying by z/g] yields the expression for the second moment of (62)

$$\overline{n^2} = \sum_{n=0}^{\infty} n^2 w_n = \left(\frac{z}{g}\right)\frac{\partial}{\partial z}\left(\left(\frac{z}{g}\right)\frac{\partial g}{\partial z}\right). \quad (67)$$

Here, as above, we should set $y = x^*$ in the final expressions.

Higher order moments can be determined in exactly the same way.

REFERENCES

1. L. Mandel and E. Wolf, *Optical Coherence and Quantum Optics* (Cambridge Univ. Press, Camdridge, 1995; Nauka, Moscow, 2000).
2. M. O. Scully and M. S. Zubairy, *Quantum Optics* (Cambridge Univ. Press, Cambridge, 1997).
3. *The Physics of Quantum Information*, Ed. by D. Boumeesfer, A. K. Ekert, and A. Zelingev (Springer, Berlin, 2000).
4. L. D. Landau and E. M. Lifshitz, *Course of Theoretical Physics*, Vol. 3: *Quantum Mechanics: Non-Relativistic Theory*, 4th ed. (Nauka, Moscow, 1989; Pergamon, New York, 1977).
5. J. Perina, *Quantum Statistics of Linear and Nonlinear Optical Phenomena* (Reidel, Dordrecht, 1984; Mir, Moscow, 1987).
6. G. Szego, *Orthogonal Polynomials* (Am. Math. Soc., New York, 1959; GIFML, Moscow, 1962).
7. A. M. Perelomov, *Generalized Coherent States and Their Applications* (Nauka, Moscow, 1987; Springer, New York, 1986).
8. I. A. Malkin and V. I. Man'ko, *Dynamic Symmetry and Coherent States of Quantum Systems* (Nauka, Moscow, 1979).
9. V. V. Dodonov and V. I. Man'ko, in *Invariants and the Evolution of Nonstationary Quantum Systems*, Ed. by M. A. Markov (Nauka, Moscow, 1987; Nova Sci., New York, 1989).
10. R. Feynman and A. R. Hibbs, *Quantum Mechanics and Path Integrals* (McGraw-Hill, New York, 1965; Mir, Moscow, 1968).
11. A. P. Prudnikov, Yu. A. Bychkov, and O. I. Marichev, *Integrals and Series*, Vol. 2: *Special Functions* (Nauka, Moscow, 1983; Gordon and Breach, New York, 1986).

Translated by V. Astakhov

Journal of Experimental and Theoretical Physics, Vol. 96, No. 1, 2003, pp. 34–39.
Translated from Zhurnal Éksperimental'noĭ i Teoreticheskoĭ Fiziki, Vol. 123, No. 1, 2003, pp. 42–48.

NUCLEI, PARTICLES, AND THEIR INTERACTION

Cross Sections of Inelastic Processes in Collisions between Relativistic Structured Heavy Ions and Atoms

V. I. Matveev* and E. S. Gusarevich

Lomonosov Pomorskii State University, Arkhangel'sk, 163006 Russia
Arkhangel'sk State Technical University, Arkhangel'sk, 163002 Russia
**e-mail: matveev.victor@pomorsu.ru*

Received September 17, 2002

Abstract—A nonperturbative method is developed for the calculation of cross sections of inelastic processes in collisions between structured high-charge heavy ions moving at relativistic velocities and atoms. By structure ions are meant partly stripped ions consisting of an ion nucleus and a number of bound electrons which partly compensate the core charge and form the electron "coat" of the ion. The single ionization cross section of hydrogen atom and single and double ionization cross sections of helium atom are calculated. It is demonstrated that the inclusion of the extent of ion charge may bring about a marked variation of the respective cross sections compared to ionization by point ions of the same charge and energy. © *2003 MAIK "Nauka/Interperiodica".*

1. INTRODUCTION

Numerous experiments performed in heavy-ion accelerators involve the use of partly stripped ions of high charges and energies (see, for example, [1–7] and the references cited there). As a rule, the calculation procedures describe such screened ions as point charges. Relatively few papers are devoted to theoretical investigation of the processes of excitation or ionization of target atoms by partly stripped ions, which are described as extended charges with an electronic structure. At the same time, it appears that one must treat an incident ion as an extended structured particle with the size on the order of electron shells of the ion rather than as a point particle. The strong field of a multiply charged ion prevents one from applying perturbation theory. Therefore, as a rule, the ionization cross sections were calculated (see, for example, [8, 9]) using the widely employed method of classical trajectories. Quantum-mechanical nonperturbative treatment using the sudden perturbation approximation was performed by Yudin [10, 11]. He managed to derive only the dependences of the ionization probability in a limited range of impact parameters. In order to calculate the total ionization cross section, one had to introduce a semiempirical procedure of "renormalizing" the Born approximation. In [12, 13], where the eikonal approximation was used, only the energy loss in collisions of relativistic structured heavy ions with atoms was calculated. Intensive theoretical and experimental studies are presently underway (see, for example, [17–19]) into the processes of the loss of electrons which belong to bombarding ions.

We used the eikonal approximation and the joining method suggested in [14–16] to develop a nonperturbative method for the calculating cross sections of the processes of excitation or ionization of target atoms by partly stripped relativistic high-charge ions described as extended charges. By way of example, the single ionization cross section of hydrogen atom and single and double ionization cross section of helium atom were calculated. It has been demonstrated that the inclusion of the extent of ion charge may bring about a marked variation of the respective cross sections compared to cross sections calculated for ionization by point ions of the same charge and energy.

2. CALCULATION TECHNIQUE

According to [14, 15], the cross section of transition of a nonrelativistic (prior to and after collision) N-electron atom, which is at rest at origin, from the $|0\rangle$ to $|n\rangle$ state upon collision with a relativistic ion moving at velocity v in the small-angle eikonal approximation has the form (here and below, atomic units are used)

$$\sigma_n = \int d^2b \left| \langle n | 1 - \exp\left\{ -\frac{i}{v} \int_{-\infty}^{\infty} U(X, \mathbf{b}; \{\mathbf{r}_a\}) dX \right\} | 0 \rangle \right|^2. \quad (1)$$

The scattering Coulomb potential $U = U(X, \mathbf{b}; \{\mathbf{r}_a\})$ is a function of both the ion coordinates $\mathbf{R} = (X, \mathbf{b})$ and the positions of atomic electrons, whose coordinates are denoted by $\{\mathbf{r}_a\}$; $a = 1, \ldots, N$. We will follow [11, 20–22] and write the Coulomb interaction of a partly screened ion which contains N_i electrons in its shells and is located at point $\mathbf{R}$, with atomic electrons located at points $\mathbf{r}_a$, in the form

$$U(\mathbf{R}; \{\mathbf{r}_a\}) = -\sum_a \left\{ \frac{Z(1-\nu)}{|\mathbf{r}_a - \mathbf{R}|} + \frac{Z\nu}{|\mathbf{r}_a - \mathbf{R}|} \exp\left(-\frac{1}{\lambda} |\mathbf{r}_a - \mathbf{R}| \right) \right\}, \quad (2)$$

1063-7761/03/9601-0034$24.00

where λ is the screening parameter (effective ion size), equal to

$$\lambda = g\frac{\nu^{2/3}}{1-\nu/7}\frac{1}{Z^{1/3}},$$

$$g = 0.3\frac{3\pi^2}{50}\Gamma\left(\frac{1}{3}\right) \approx 0.48.$$

Here, we introduce the relative number of ion electrons, $\nu = N_i/Z$. The characteristic feature of collisions between high-charge ions and atoms consists in that the cross sections of inelastic processes are, as a rule, fairly large and significantly exceed the atomic dimensions. In view of this, we will assume that $r_a/R \ll 1$; then, the integral in Eq. (1) may be rewritten as

$$-\frac{i}{v}\int_{-\infty}^{\infty} U dX = i\mathbf{q}\cdot\sum_a \mathbf{r}_a, \tag{3}$$

where

$$\mathbf{q} = \frac{2Z^*}{vb}\left[1 + \frac{\nu}{1-\nu}\frac{b}{\lambda}K_1\left(\frac{b}{\lambda}\right)\right]\frac{\mathbf{b}}{b}. \tag{4}$$

As a result, Eq. (1) will take the form

$$\sigma_n = \int d^2b\left|\langle n|\exp\left\{i\mathbf{q}\cdot\sum_a \mathbf{r}_a\right\}|0\rangle\right|^2. \tag{5}$$

Obviously, vector $\mathbf{q}$ has the meaning of momentum transferred to atomic electrons upon collision with an ion with the impact parameter $\mathbf{b}$; $Z^* = Z(1-\nu)$ is the visible charge of a partly stripped ion; and $K_1(x)$ is the Macdonald function. The limiting values of $\mathbf{q}$ have a transparent physical meaning: $\mathbf{q} \longrightarrow 2Z(1-\nu)\mathbf{b}/vb^2$ at $b \longrightarrow \infty$, which corresponds to the scattering by a screened ion of charge $Z(1-\nu)$; $\mathbf{q} \longrightarrow 2Z\mathbf{b}/vb^2$ at $b \longrightarrow 0$, which corresponds to the scattering by a bare ion of charge Z.

We will first treat a collision between a relativistic structured multiply charged ion and a hydrogen atom. In calculating the cross sections of inelastic processes, we will follow [14, 15] and use the joining method, which enables one to derive formulas for cross sections in an analytical form. For this purpose, we will divide the entire range $0 < b < \infty$ of possible values of impact parameter b into two regions corresponding to the small and large impact parameters,

$$(A)\ 0 < b < b_0, \quad (B)\ b_0 < b < \infty, \tag{6}$$

where

$$b_0 \sim v\gamma, \quad \gamma = \frac{1}{\sqrt{1-\beta^2}}, \quad \beta = \frac{v}{c},$$

c being the velocity of light. In region A of small impact parameters, the strong field of a high-charge ion cannot be included using perturbation theory; therefore, we will calculate the cross section by formula (5). In region B of large impact parameters, one can assume the field developed by an ion to be weak, describe the ion as a point charge Z^*, and use perturbation theory for the calculation of σ_n. We calculate σ_n in each of the regions according to Eqs. (6) and add them together to obtain the resultant cross section. In doing so, the knowledge of the exact value of the boundary between the regions is unimportant, because the dependence of σ_n on the parameter b_0 in any region turns out to be logarithmic. This results in correct joining of the contributions by adjacent regions, and, in the final result, σ_n is independent of joining parameter b_0. As a result, the ionization cross section of a hydrogen atom may be represented in the form (cf. [18])

$$\sigma_i = 8\pi\frac{Z^{*2}}{v^2}\lambda_i\left(\ln\frac{2\alpha_i v^2\gamma}{\eta Z^*\omega_i} - \frac{\beta^2}{2}\right), \tag{7}$$

where $\eta = \exp B = 1.781$, $B = 0.5772$ is the Euler constant, $\omega_i = 0.711$ is the so-called [15] "mean" ionization energy, $\lambda_i = 0.283$, and the coefficients α_i are calculated by the formula

$$\alpha_i = \lim_{b_0\to\infty}\frac{Z^*}{vb_0}\exp\left\{\frac{1}{\lambda_i}\frac{v^2}{8\pi Z^{*2}}\int_0^{b_0} 2\pi b db \times \int d\mathbf{k}|\langle\mathbf{k}|\exp(i\mathbf{q}\cdot\mathbf{r})|0\rangle|^2\right\}. \tag{8}$$

Formula (7) is not dissimilar in aspect to the respective formula given in [15] for the cross section of ionization by point charge Z^*. However, in contrast to the case of point charge, in which $\alpha_i = 3.264$ is [15] a number independent of the ion charge and velocity, in the case of extended charge, by virtue of determining the transferred momentum by formula (4), α_i turns out to be a function of the ion velocity v and the relative number ν of electrons in the ion "coat." Figure 1 gives the cross sections of ionization of a hydrogen atom by partly stripped U^{6+} ions (with the number of electrons $N_i = 86$ in the ion shells corresponding to the visible ion charge $Z^* = 6$) calculated by formula (7). Although partly stripped ions are frequently used in collision experiments, no experimental data are available in the literature on the cross sections of ionization of atoms by relativistic structured heavy ions in the ranges of ion energies and charges of interest to us, in which the corrections due to the extent of ion charge are significant. However, because we describe the corrections due to the ion charge extent by point particles relative to the ionization cross sections, we found it necessary to give (in Figs. 1–3) by way of illustration the experimental data on the cross sections of ionization of atoms by partly stripped ions in the ranges of ion energies and charges for which, according to our calculation proce-

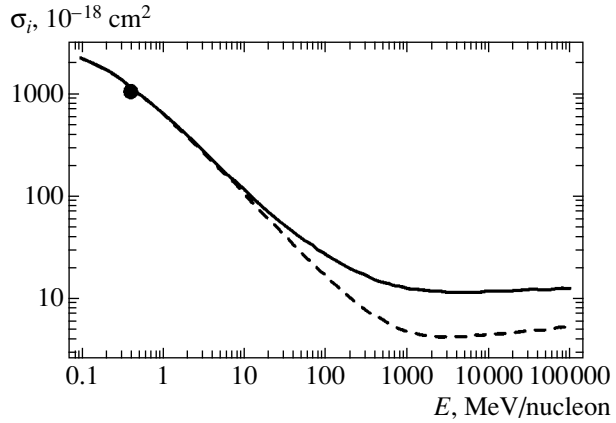

Fig. 1. The cross section of ionization of a hydrogen atom by partly stripped U^{6+} ions as a function of the ion energy. The solid curve indicates the predicted cross section for an extended ion, the dashed curve indicates the cross section of ionization by a point ion for the same values of energy (per nucleon) and charge, and the solid dot indicates the experimental results of [5] (for C^{6+} + H collisions).

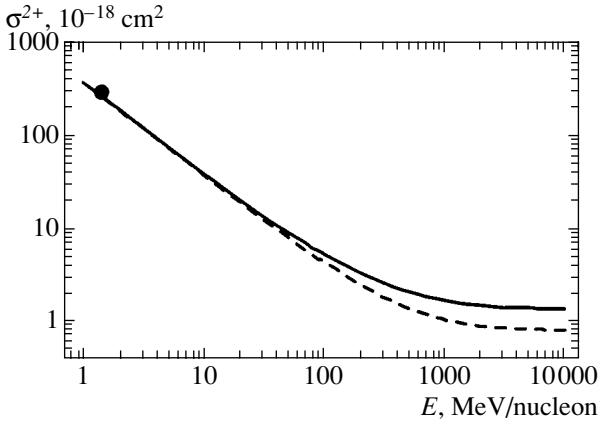

Fig. 2. The cross section of double ionization of a helium atom by partly stripped Fe^{15+} ions as a function of the ion energy. The solid curve indicates the predicted cross section for an extended ion, the dashed curve indicates the cross section of double ionization by a point ion for the same values of energy and charge, and the solid dot indicates the experimental results of [6] (for Fe^{15+} + He collisions).

dure, the cross sections of ionization by extended and point ions are close to one another.

We will now consider the double ionization of a helium atom. According to [14, 15], there is no need to use the joining method for calculation of the respective cross section. Therefore, the double ionization cross section may be obtained directly from formula (5), in which the integration is extended to the entire plane of the impact parameter and has the form

$$\sigma^{2+} = \int\int\int |\langle \mathbf{k}_1, \mathbf{k}_2 | \exp\{i\mathbf{q}\cdot(\mathbf{r}_1+\mathbf{r}_2)\}|0,0\rangle|^2 d\mathbf{k}_1 d\mathbf{k}_2 d^2b. \quad (9)$$

Here, $|0, 0\rangle$ is the wave function of the ground state of helium atom and $|\mathbf{k}_1, \mathbf{k}_2\rangle$ is the wave function of a helium atom with two electrons in continuum with the respective momenta $\mathbf{k}_1$ and $\mathbf{k}_2$; when integrating with respect to these momenta in Eq. (9), one must take care that the final states were not taken into account twice. In calculations, the wave functions were represented in the form of symmetrized products of hydrogen-like one-electron wave functions with the same values of the effective charge of the helium atom nucleus Z_a = 1.97 (according to [15], this value of effective charge brings about good agreement with the experimental data for double ionization of helium by bare relativistic ion impact). The calculation results are given in Fig. 2.

The single ionization cross section of a helium atom, which corresponds to one of the electrons getting into any state of continuum and the other electron getting into any state of discrete spectrum (or into any state of the complete set of discrete and continuous spectra, in which case one must deduct a contribution which corresponds to finding two electrons in the states of a two-electron continuum, i.e., in the states of double ionization), is (cf. [15])

$$\sigma^{1+} = 16\pi\frac{Z^{*2}}{Z_a^2 v^2}\lambda_i\left(\ln\frac{2\alpha_i v^2\gamma}{\eta Z_a Z^* \omega_i} - \frac{\beta^2}{2}\right) - 2\sigma^{2+}. \quad (10)$$

Here [15], Z_a = 1.37 is the effective charge of a helium atom nucleus for one-electron ionization (according to [15], this value of effective charge brings about good

Relative corrections for the cross sections σ_i, σ^{1+}, and σ^{2+} and the relative contribution ξ to the ionization cross section by the processes of excitation of the electron coat of ion

χ	Ion energy, 10^3 MeV/nucleon								
	0.01	0.05	0.1	0.5	1	5	10	50	100
χ_H	0.0774	0.3850	0.6304	1.3689	1.6067	1.6913	1.6214	1.4389	1.3682
χ_{He}^{1+}	0	0.0007	0.0025	0.014	0.019	0.022	0.021	0.018	0.017
χ_{He}^{2+}	0.0004	0.017	0.0473	0.1855	0.2406	0.2933	0.2974	0.2990	0.2991
$\xi \times 10^4$	1.6	1.3	1.1	0.96	0.92	0.88	0.83	0.78	0.72

agreement with the experimental data). We used formula (10) to calculate the dependence of a single ionization cross section of a helium atom in collisions with Fe^{15+} iron ions on the ion energy, with the results qualitatively reproducing the previously described behavior of the ionization cross section of a hydrogen atom. However, the corrections proved to be minor because of the considerable magnitude of the single ionization cross section (see table). Therefore, we calculated the single ionization cross section of a helium atom in collisions with U^{15+} uranium ions with the same visible ion charge $Z^* = +15$ but with a much larger charge of the nucleus and a larger number of bound electrons as compared to Fe^{15+}. The obtained dependence of the ionization cross section on the ion energy is given in Fig. 3.

Because the effects of the ion charge extent proved to be very appreciable, it appears necessary to discuss the correctness of representing the field of the structured ion by the potential according to Eq. (2).

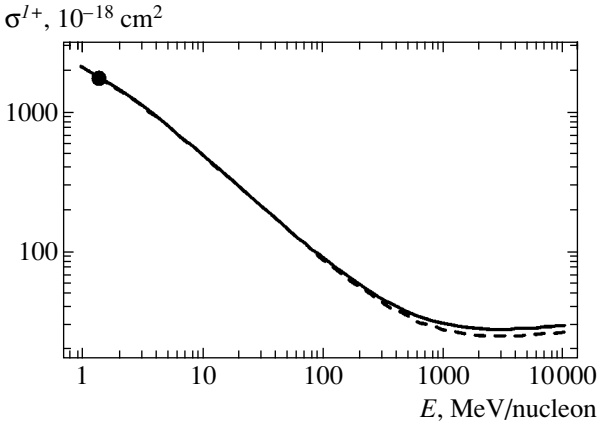

Fig. 3. The cross section of single ionization of a helium atom by partly stripped U^{15+} ions as a function of the ion energy. The solid curve indicates the predicted cross section for an extended ion, the dashed curve indicates the cross section of ionization by a point ion for the same values of energy and charge, and the solid dot indicates the experimental results of [6] (for Fe^{15+} + He collisions).

3. CHOICE OF INTERACTION POTENTIAL

Strictly speaking, the potential given by Eq. (2) may be obtained as follows. We will introduce the potential of projectile–target interaction $V(\mathbf{r}, \boldsymbol{\rho}, \mathbf{R}(t))$, where $\mathbf{r}$ denotes the set of coordinates of the target electrons, $\boldsymbol{\rho}$ denotes the set of coordinates of the projectile electrons, and $\mathbf{R}(t)$ is the distance between the projectile and target nuclei in the rest frame of the target. Then, the potential according to Eq. (2) is calculated by averaging over the projectile electron coordinates $\boldsymbol{\rho}$,

$$U(\mathbf{R}; \{\mathbf{r}_a\}) = \langle \varphi | V(\mathbf{r}, \boldsymbol{\rho}, \mathbf{R}(t)) | \varphi \rangle, \qquad (11)$$

where $\varphi = \varphi(\boldsymbol{\rho})$ is the wave function of the ground state of the projectile electrons. If the Lenz–Jensen model [23–25] (which refines [23] the Thomas–Fermi model) is used to describe the distribution of the electron number density of the projectile, one can see in Fig. 4 constructed by the data of [22] that the potential according to Eq. (2) is a good approximation for the averaged potential according to Eq. (11).

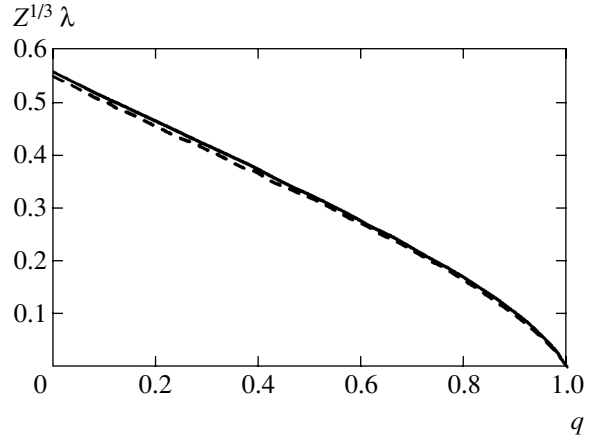

Fig. 4. The effective ion size λ as a function of the degree of ionization $q = Z^*/Z$, where Z^* is the visible ion charge and Z is the ion nucleus charge. The solid curve indicates the screening parameter in the potential given by Eq. (2) (Brandt–Kitagawa model [22]), and the dashed curve indicates the ion size in the Lenz–Jensen model [23–25].

In order to reveal the importance of the shell structure and the contribution by electron transitions between the shells of an incident ion, one can formulate a more general problem of the investigation of inelastic processes simultaneously occurring in the target proper and in the projectile. Consider a collision in which the target makes a transition from the initial state $|0\rangle$ to the final state $|n\rangle$, while the projectile electrons change from the initial state $|0\rangle$ into the final state $|m\rangle$. The cross section of such a process will be written as

$$\sigma_{0\to n}^{0\to m} = \int P_{0\to n}^{0\to m}(b) d^2 b = 2\pi \int_0^\infty P_{0\to n}^{0\to m}(b) b db, \qquad (12)$$

where the expression $P_{0\to n}^{0\to m}(b)$ denotes the probability of detecting the target and projectile in the final states $|n\rangle$ and $|m\rangle$, respectively, after collision with impact parameter b. The electron transitions occurring in the target and projectile may be treated as independent processes. Therefore, the probability of transition may be represented in the form (which is apparently a natural generalization to the given case of the integrand in formula (5))

$$P_{0\to n}^{0\to m} = \left| \langle \varphi_m(\boldsymbol{\rho}) | \exp\left(i\mathbf{q}_2 \cdot \sum_j \boldsymbol{\rho}_j \right) | \varphi_0(\boldsymbol{\rho}) \rangle \right|^2 \times \left| \langle \Phi_n(\mathbf{r}) | \exp\left(i\mathbf{q}_1 \cdot \sum_a \mathbf{r}_a \right) | \Phi_0(\mathbf{r}) \rangle \right|^2, \qquad (13)$$

where $\varphi(\boldsymbol{\rho})$ and $\Phi(\mathbf{r})$ are the electron wave functions of the projectile and target, respectively; and $\mathbf{q}_1$ and $\mathbf{q}_2$ are the momenta transferred upon collision, with $\mathbf{q}_1$ having the meaning of momentum transferred by the projectile to the target electrons, and $\mathbf{q}_2$, that of momentum transferred by the target to the projectile electrons. Therefore, one can use formula (12) to calculate the cross sections of various inelastic processes which lead, upon collision, to a simultaneous excitation of the electron shells of the target and projectile. In order to determine the contribution of electron transitions between the shells of the bombarding ion, we calculated σ_2, the cross section of inelastic collision of hydrogen-like Fe^{25+} iron ions (projectile) and He^{1+} helium ions (target) at which the ionization of the He^{1+} target occurs with excitation of the Fe^{25+} target to any state of discrete and continuous spectra, as well as σ_1, the cross section of the process in which the target is ionized and the projectile remains in the ground state. In order to estimate the contribution by the processes of excitation of the electron coat of the ion, we will introduce the relative contribution $\xi = (\sigma_2 - \sigma_1)/\sigma_1$. If ξ is much less than unity, the contribution by the excitations of the electron shells of the target may be ignored and the bombarding ion may be treated as an extended charge. Our calculation of the values of ξ as a function of the kinetic energy of the bombarding ion, the results of which are given in the table (fourth line), reveals that, if we treat collisions of heavy ions of visible charge $Z^* \gg 1$ with light atoms or with ions of a nuclear charge much less than Z^*, the excitations of the electron coat of the projectile may be ignored.

4. DISCUSSION OF THE RESULTS

Figures 1 and 2 are constructed on a logarithmic scale, which enables one to cover a wide range of ion energy but poorly reflects the details. Therefore, for qualitative illustration of the effect of inclusion of the extent of ion charge, we will introduce relative corrections

$$\chi_H = \frac{\sigma_i - \sigma_{i(\text{point})}}{\sigma_{i(\text{point})}},$$

where $\sigma_{i(\text{point})}$ is the cross section of ionization of a hydrogen atom by a point ion of the same charge Z^* as the visible charge of an incident extended ion and at the same relative velocity. Similarly introduced are the relative corrections for single and double ionization of a helium atom,

$$\chi_{He}^{1+} = \frac{\sigma^{1+} - \sigma_{(\text{point})}^{1+}}{\sigma_{(\text{point})}^{1+}}, \quad \chi_{He}^{2+} = \frac{\sigma^{2+} - \sigma_{(\text{point})}^{2+}}{\sigma_{(\text{point})}^{2+}}.$$

Given in the table are the values of χ_H for U^{6+} + H collisions, as well as of χ_{He}^{1+} and χ_{He}^{2+} for Fe^{15+} + He collisions. One can see in the table that corrections to the ionization cross section as a result of inclusion of the ion charge extent may turn out to be significant. One can see in Figs. 1–3 that, as the energy of the incident ion increases, the effects of ion charge extent may bring about a significant growth of the single and double ionization cross sections compared to respective cross sections calculated for a point ion. Such a behavior is apparent from physical reasoning: indeed, in collisions with large impact parameters, atomic electrons interact with an incident ion as with a point charge equal to the visible charge of a screened ion (in our notation, Z^*). As to collisions with small impact parameters, atomic electrons perceive an ion as a bare charge Z. All regions of impact parameters contribute to the cross sections, and, because Z is larger than Z^*, atomic electrons effectively interact with an ion whose charge exceeds Z^*, this leading to an increase in cross sections that may turn out to be significant in the case of $Z \gg Z^*$. In order to estimate the effect of the ion charge extent, we will introduce the effective radius r such that $\sigma_{i(\text{point})} = \pi r^2$. Then (based on geometric reasoning, according to which an ion is treated as a sphere of radius λ), a cross section in view of the ion charge extent is to be estimated at $\sigma_i \sim \pi(r + \lambda)^2$. For $\lambda^2 \ll r^2$ (in the cases treated by us, this inequality may be taken to be valid for estimation purposes), one can easily estimate the correction χ_H in terms of the predicted value $\sigma_{i(\text{point})}$ of the cross section of ionization by the point ion and the effective ion radius λ,

$$\chi_H \sim \frac{2\lambda}{r} = \frac{2\pi^{1/2}\lambda}{[\sigma_{i(\text{point})}]^{1/2}}.$$

Because λ in formula (2) is independent of the kinetic energy of the ion, the relative correction χ_H increases, while $\sigma_{i(\text{point})}$ decreases with increasing energy. One can readily see that the figures and the data given in the table demonstrate this particular behavior of cross sections, which is apparently common to the remaining cross sections of inelastic processes that accompany collisions of relativistic structured heavy ions with atoms.

ACKNOWLEDGMENTS

This study received financial support from the Russian Foundation for Basic Research (project no. 01-02-17047) and from the Ministry of Education of the Russian Federation (grant no. E00-3.1-390).

REFERENCES

1. H. F. Krause, C. R. Vane, S. Datz, *et al.*, Phys. Rev. A **63**, 032711 (2001).
2. T. Ludziejewski, Th. Stohlker, D. C. Ionescu, *et al.*, Phys. Rev. A **61**, 052706 (2000).
3. E. Wells, I. Ben-Itzhak, K. D. Carnes, *et al.*, Phys. Rev. A **60**, 3734 (1999).

4. M. Tschersich, R. Drozdowski, M. Busch, *et al.*, J. Phys. B **32**, 5556 (1999).
5. M. B. Shah and H. B. Gilbody, J. Phys. B **16**, L449 (1983).
6. J. H. McGuire, A. Mueller, B. Schuch, *et al.*, Phys. Rev. A **35**, 2479 (1987).
7. H. Berg, J. Ullrich, E. Bernstein, *et al.*, J. Phys. B **25**, 3655 (1992).
8. M. Purkait, A. Dhara, S. Sounda, and C. R. Mandal, J. Phys. B **34**, 755 (2001).
9. C. Illescas, B. Pons, and A. Riera, Phys. Rev. A **63**, 062722 (2001).
10. G. L. Yudin, Dokl. Akad. Nauk SSSR **282**, 874 (1985) [Sov. Phys. Dokl. **30**, 488 (1985)].
11. G. L. Yudin, Zh. Tekh. Fiz. **55**, 9 (1985) [Sov. Phys. Tech. Phys. **30**, 4 (1985)].
12. V. I. Matveev, Zh. Tekh. Fiz. **72** (5), 10 (2002) [Tech. Phys. **47**, 523 (2002)].
13. V. I. Matveev, Zh. Éksp. Teor. Fiz. **121**, 260 (2002) [JETP **94**, 217 (2002)].
14. T. Ludziejewski, Th. Stohlker, D. C. Ionescu, *et al.*, Phys. Rev. A **61**, 052706 (2000).
15. A. B. Voitkiv, C. Muller, and N. Grun, Phys. Rev. A **62**, 062701 (2000).
16. C. Muller, A. B. Voitkiv, and N. Grun, Phys. Rev. A **66**, 012716 (2002).
17. V. I. Matveev and S. G. Tolmanov, Zh. Éksp. Teor. Fiz. **107**, 1780 (1995) [JETP **80**, 989 (1995)].
18. V. I. Matveev and Kh. Yu. Rakhimov, Zh. Éksp. Teor. Fiz. **114**, 1646 (1998) [JETP **87**, 891 (1998)].
19. V. I. Matveev and D. U. Matrasulov, J. Phys. B **33**, 2721 (2000).
20. G. Maynard, D. Gardes, M. Chabot, *et al.*, Nucl. Instrum. Methods Phys. Res. B **146**, 88 (1998).
21. G. Maynard, M. Chabot, and D. Gardes, Nucl. Instrum. Methods Phys. Res. B **164/165**, 139 (2000).
22. W. Brandt and M. Kitagawa, Phys. Rev. B **25**, 5631 (1982).
23. P. Gombas, *Die Statistische Theorie des Atoms und ihre Anwendungen* (Springer, Vienna, 1949).
24. W. Lenz, Z. Phys. **77**, 713 (1932).
25. H. Jensen, Z. Phys. **77**, 722 (1932).

Translated by H. Bronstein

Journal of Experimental and Theoretical Physics, Vol. 96, No. 1, 2003, pp. 40–52.
Translated from Zhurnal Éksperimental'noĭ i Teoreticheskoĭ Fiziki, Vol. 123, No. 1, 2003, pp. 49–63.

PLASMA, GASES

Propagation of a High-Pressure Microwave Discharge in Prebreakdown Fields: Formation of Plasma Structures

P. V. Vedenin[a] and N. A. Popov[b, *]

[a]*Moscow Physical Society, Moscow, 119991 Russia*
[b]*Skobel'tsyn Research Institute of Nuclear Physics, Moscow State University, Moscow, 119992 Russia*
**e-mail: yura@mics.msu.su*

Received July 17, 2002

Abstract—A 3D model is developed, which describes the propagation of an initiated high-pressure microwave discharge in a linearly polarized wave beam. The equations for the electric field amplitude are solved self-consistently with the set of equations of plasmochemical kinetics. Plasma structures of the experimentally observed "snake" and "chain" types are obtained using this model. The calculation results enable one to determine the conditions of formation of one or another spatial structure, as well as the parameters of the plasmoids being formed. The results of calculation of the discharge propagation toward the radiation source are compared with the available experimental data. © *2003 MAIK "Nauka/Interperiodica".*

1. INTRODUCTION

Microwave discharges in electromagnetic wave beams represent a relatively new phenomenon in the physics of gas discharge; the investigation of this phenomenon was given new momentum by the advent of powerful microwave oscillators. Experimental investigations of microwave discharges in prebreakdown fields revealed that a complex spatially nonuniform discharge structure is formed in high-pressure gases ($\nu \gg \omega$, where ν is the transport frequency of electron collisions and ω is the circular frequency of the field) [1–5]. In this way, the types of structures qualitatively vary depending on the discharge conditions [4].

The ignition of a microwave discharge in prebreakdown fields requires an initiator used to develop local regions of above-breakdown field or an external preionization source forming the plasma background. Usually, no external ionization source is present in an initiated discharge, which distinguishes this discharge from a non-self-sustained discharge. The initiating elements are provided by metal needles, multipoint brushes, metal–dielectric plates, and so on. As is observed by the majority of researchers, in a steady-state mode of propagation, the discharge structure and its other characteristics do not depend on the type of initiator [1–4].

In [3–5] and in other papers, the possibility is observed of a jumplike propagation of an initiated microwave discharge toward the radiation source in the form of dipole plasma channels oriented along the electric field vector (dipole mode of propagation). Figure 1 is a photograph (borrowed from [4]) of a discharge in the $\mathbf{kE}_0$ plane ($\mathbf{k}$ is the wave vector, and $\mathbf{E}_0$ is the electric field of an incident wave). One can see that the channel length, somewhat exceeding $\lambda/2$ (λ is the microwave radiation wavelength), is always much greater than the channel radius. The dipole mode was observed in the following range of values of reduced field:

$$0.65(E/N)_{\mathrm{br}} \le (E/N)_0 \le (E/N)_{\mathrm{br}};$$

here, N is the concentration of molecules and $(E/N)_{\mathrm{br}}$ is the breakdown value of the field. The factor 0.65 experimentally obtained for nitrogen and air varied little upon transition to argon, helium, hydrogen, and CO_2.

Figure 2 gives the rate of discharge propagation as a function of the quantity $(E/N)_0$, obtained in [4] for air at $\lambda = 4.3$ cm. According to [3, 4], similar dependences are observed for argon, helium, nitrogen, CO_2, and other gases. The kink on the curve of dependence of velocity at $(E/N)_0 \approx 0.65(E/N)_{\mathrm{br}}$ (for air, $0.65(E/N)_{\mathrm{br}} \approx$ 80 Td) may be attributed to the change of the mechanism of discharge propagation. Also indicative of this are the photographs which point to a significant variation of the discharge structure at $(E/N)_0 < 0.65(E/N)_{\mathrm{br}}$ [4]. Note that, in accordance with Fig. 2, the velocity of the discharge front motion at a fixed value of $(E/N)_0$ in the dipole mode depends little on the gas pressure. Similar results were previously obtained in krypton at $\lambda =$ 6.7 mm and $P = 200$–650 Torr [6] and in argon at $\lambda =$ 4.3 cm and $P = 100$–735 Torr [7].

Two types of plasmoid arrangement were experimentally observed during the discharge motion toward the radiation source, namely, a "chain" and a "snake." The first type is characterized by successive lining up of a chain of plasma dipoles spaced at a distance of approximately $\lambda/4$ from one another. The chain was formed in almost the entire range (specified above) of values of the parameter $(E/N)_0$ in all investigated gases [3–5]. The snake arrangement of plasmoids may

Fig. 1. An integral photograph of a "snake" structure [4]. Air, P = 100 Torr, $(E/N)_0$ = 100 Td, λ = 4.3 cm. The microwave radiation propagates from left to right.

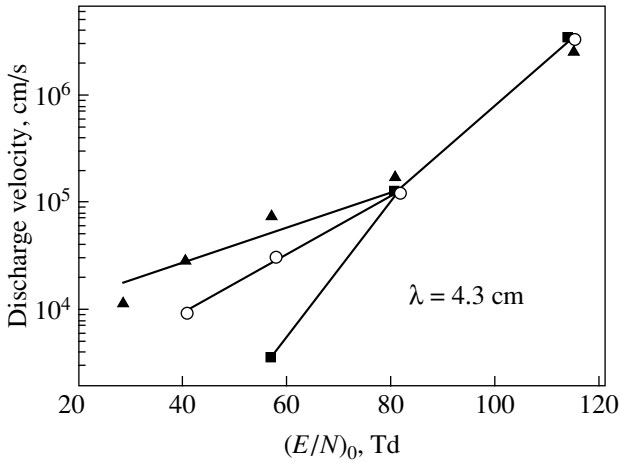

Fig. 2. The average rate of microwave discharge propagation as a function of the reduced field $(E/N)_0$ in air [4]; P = 50 (■), 70 (○), and 100 (▲) Torr.

be most readily registered in the $\mathbf{kB}_0$ plane, in which the discharge performs longitudinal and transverse diagonal jumps in the vicinity of the longitudinal direction and moves generally toward the radiation source [3]. The sequence of production of plasmoids in an ideal snake (propagating toward the radiation source in the negative direction of the x axis) may be schematically represented as

$$\begin{aligned}((X_j, Y_j, Z_j) &\longrightarrow (X_j - d_x, Y_j \pm d_y, Z_j)\\ &\longrightarrow (X_j - 2d_x, Y_j, Z_j)\\ &\longrightarrow (X_j - 3d_x, Y_j \pm d_y, Z_j)\\ &\longrightarrow (X_j - 4d_x, Y_j, Z_j) \longrightarrow \ldots,\end{aligned}$$

where X_j, Y_j, and Z_j are coordinates of the center of the jth plasmoid. This type of motion was observed only in molecular gases in a narrow transition region in the range of fields of $(E/N)_0 \approx (0.65\text{–}0.75)(E/N)_{\text{br}}$ [3].

This suggested mechanism of jumplike propagation of an initiated high-pressure microwave discharge is based on the interference between the incident electromagnetic wave and that reflected from plasmoids. As a result, regions of above-breakdown field arise, in which the avalanche multiplication of electrons and the formation of the next plasmoid begin. This recurring process may be interpreted as the discharge motion toward the radiation source. The propagation mechanism described above may be *a priori* regarded as field ionization mechanism (though, at late stages of channel formation, the gas heating will naturally have its effect).

A number of researchers (see the review [8] and other papers) treated yet another mechanism of structure formation in a high-pressure microwave discharge ($\nu \gg \omega$), which brings about the stratification of an initially homogeneous discharge into individual plasma filaments oriented along the electric field vector [8]. This mechanism is based on the overheating ionization instability. The time of discharge stratification is defined by the characteristic time of heating and gasdynamic rarefaction of the plasma channel. Therefore, in a wide range of discharge parameters, the field ionization and overheating ionization mechanisms may be separated as regards the time of development, because the structure formation by the former of these mechanisms occurs during pregasdynamic times.

Papers [9–11] deal with theoretical investigations of the dipole mode of microwave discharge propagation. Mnatsakanyan and Naĭdis [9] treated a discharge in krypton for the experimental conditions of [6] within the model of plane plasma sheets. The calculated dependences of the average rate of discharge propagation on gas pressure and $(E/N)_0$ agree with the values measured in [6] (the difference does not exceed a factor of two–three). However, the maximal number density of electrons and the width of plasma sheets in the calculations were $N_e = 10^{16}$ cm^{-3} and Δ = 0.1 mm, respectively, while the maximal number density of electrons in the experiments did not exceed $N_e^{\max} = 10^{14}$ cm^{-3}, with a plasmoid radius of r = 0.25 mm. It must be emphasized that the dipoles in the experiment were represented by relatively thin plasma filaments. The electromagnetic wave reflection from such filaments differs significantly from its reflection from plasma sheets (employed in the model); it is apparently this fact that results in the above-mentioned difference between prediction and experimental results.

In order to simulate the dipole mode of microwave discharge propagation, one needs a description of the electromagnetic wave interaction with a system of thin plasma channels oriented along the electric field vector. One of the questions to be answered by the simulation results is whether it is possible to reach a degree of gas

ionization (and, accordingly, a reflection coefficient) in plasmoids such as to provide for the possibility of discharge propagation in the entire range of values of the reduced field of $0.65(E/N)_{br} \le (E/N)_0 \le (E/N)_{br}$. Thus, these values of the degree of ionization must be reached during the time of plasmoid formation τ_e,

$$\tau_e = \frac{d_x}{V}, \tag{1}$$

where V is the average velocity of discharge front and d_x is the distance between plasmoids in the direction of vector **k**.

It is the purpose of this study to perform a self-consistent simulation of the electrodynamics and plasmochemical kinetics of the dipole mode of microwave discharge in air and to describe the main types of spatial structures being formed and the conditions of their emergence, as well as to determine the velocity of discharge propagation and the parameters of the plasmoids being formed.

2. DERIVATION OF THE INITIAL SET OF ELECTRODYNAMIC EQUATIONS

Plasma channels (plasmoids) are located in the field of a monochromatic linearly polarized electromagnetic wave,

$$E_v(x, t) = 0.5E_z(x)\exp(-i\omega t) + \text{c.c.},$$

$$E_z(x) = E_0\exp(ikx).$$

It is assumed that (i) the plasmoids are identical in shape and represent ellipsoids of revolution extended along the z axis in parallel with the electric field vector, which have their centers in the xy plane (**kB**$_0$ plane) and semiaxes $l_{zm} > l_{\rho m}$; (ii) the plasma within the mth plasmoid is distributed uniformly with n_{em} = const; and (iii) the plasmoid radius $l_{\rho m}$ is markedly less than the distance between plasmoids and satisfies the condition

$$\alpha_m \ll 1, \tag{2}$$

where $\alpha_m = kl_{\rho m}$. We will emphasize that Eq. (2) is realized in all experimental investigations of microwave discharges known to us.

First of all, we will derive equations describing the electromagnetic wave scattering from a solitary plasmoid.

We will align the plasma channel axis with the z axis and place the channel center at the origin of the coordinates. In the presence of axial symmetry in the distribution of plasma concentration, it is natural to perform the investigation in cylindrical coordinates,

$$x = \rho\cos\varphi, \quad y = \rho\sin\varphi.$$

Under the effect of a plane linearly polarized electromagnetic wave, which has, in cylindrical coordinates, the electromagnetic field components

$$e_z = J_0(k\rho) + 2\sum_{m=1}^{\infty} i^m J_m(k\rho)\cos m\varphi,$$
$$b_\rho = e_z\sin\varphi, \quad b_\varphi = e_z\cos\varphi, \tag{3}$$

where $(b_{\rho,\varphi}; e_z) = (B_{\rho,\varphi}; E_z)/E_0$ and $J_m(x)$ is the Bessel function of the mth kind, all field components with a complete spectrum of azimuthal harmonics are excited in the plasmoid. It is clear, however, that the degree of the effect of higher harmonics (and, via these harmonics, of the e_φ and b_z components) on the reflectivity of the plasma channel decreases with the radius of the latter. For example, in the limit of infinitely long filament $l_z \longrightarrow \infty$, we have

$$e_{z1}(\rho > l_\rho)/e_{z0}(\rho > l_\rho) \sim \alpha^2/4$$

(see [13]); here, e_{z1} and e_{z0} are the complex amplitudes of the first and zero harmonics, respectively. In this paper, we will restrict ourselves to treating the case of Eq. (2) and find the solution of the set of Maxwell equations only for zero harmonics of the b_φ, e_z, and e_ρ components.

The formal solution of the equation

$$\left(\frac{1}{\rho}\frac{\partial}{\partial\rho}\rho\frac{\partial}{\partial\rho} - \frac{1}{\rho^2} + \frac{\partial^2}{\partial z^2} + k^2\varepsilon\right)b_\varphi^{(\text{in})} = 0, \tag{4}$$

as well as the expressions for $e_z^{(\text{in})}$ and $e_\rho^{(\text{in})}$ within the plasmoid, can be written using the e_z function ($\rho = 0, z$) which is not yet known,

$$b_\varphi^{(\text{in})}(\rho, z) = -i\sqrt{\varepsilon}\sum_{l=0}^{\infty} h_l J_{l+1}(\chi)e_z^{(2l)}(0, z),$$
$$\mathbf{e} = \frac{i}{k\varepsilon}\text{curl}\mathbf{b}, \tag{5}$$

where

$$h_l = \frac{(-1)^l}{l!}\left(\frac{\rho_*}{2L^2\gamma}\right)^l,$$

$$\chi = \gamma\rho_*, \quad \gamma = \alpha\sqrt{\varepsilon}, \quad L = \frac{l_z}{l_\rho}, \quad \rho_* = \frac{\rho}{l_\rho},$$

$$\beta = kl_z, \quad \varepsilon = 1 + i\sigma_*, \quad \sigma_* = \frac{4\pi\sigma}{\omega};$$

$\sigma = e^2n_e/m\nu$ is the plasma conductivity,

$$e_z^{(m)} = \frac{d^m e_z}{dz_*^m}, \quad z_* = \frac{z}{l_z}.$$

One can use expressions (5) (which are valid both for an ellipsoid and for any body of revolution) and deter-

mine the $e_z(0, z)$ dependence to find the field at each point of the plasma channel.

We write the formal solution to Maxwell equations for $e_z(\mathbf{r})$ in an integral form and use Eqs. (5) to derive the equation sought for $e_z(0, z)$,

$$e_z(0,z) = \frac{1}{\varepsilon}\left(1 + \frac{i\sigma_* L}{2}\iint d\xi d\eta \xi^2 \times \frac{D(\xi,\eta,\gamma)e_z(0,\eta)(1-i\alpha R_*)\exp(i\alpha R_*)}{R_*^3}\right), \quad (6)$$

where

$$R_* = \sqrt{\xi^2 + L^2(z_* - \eta)^2},$$

$$D(\xi,\eta,\gamma)e_z(0,\eta) = [\xi\delta(\vartheta)J_0(\gamma\xi) + \gamma J_1(\gamma\xi)]e_z(0,\eta) + \frac{1}{L^2}\sum_{l=0}^{\infty} h_l\left\{\frac{\delta(\vartheta)J_{l+1}(\gamma\xi)}{\gamma}\left[\eta - \frac{\xi^2}{2(l+1)}\frac{d}{d\eta}\right] - \frac{\xi J_{l+2}(\gamma\xi)}{2(l+1)}\frac{d}{d\eta}\right\}e_{z0}^{(2l+1)}(0,\eta),$$

$\delta(\vartheta)$ is the delta function, and $\vartheta = \sqrt{\xi^2 + \eta^2} - 1$.

The expression for the complex amplitude of electric field outside of the plasma channel, made up by the external field and the field $e_z^-(\rho, z)$ of a scattered axially symmetric wave, has the form

$$e_z^{(ex)}(\mathbf{r}) = \exp(ikx) + \frac{i\sigma_* L}{4\pi}\frac{1}{\rho_*}\frac{\partial}{\partial\rho_*}\rho_*\iiint d\xi d\eta d\psi \times \frac{\xi\cos\psi D(\xi,\eta)e_z(0,\eta)\exp(i\alpha R_*)}{R_*}, \quad (7)$$

where

$$R_* = \sqrt{\rho_*^2 + \xi^2 - 2\rho_*\xi\cos\psi + L^2(z_* - \eta)^2},$$

and $e_z(0, z)$ is the solution to Eq. (6).

In describing the interaction between an electromagnetic wave and a group of plasmoids in equations for the longitudinal profile of the field $e_{zm}(X_m, Y_m, z)$ within the mth plasma channel with the center at point $(X_m, Y_m, 0)$, one must take into account the electric field contribution from all of the remaining channels,

$$\varepsilon_m e_{zm}(z) - \frac{i\sigma_{*m}L_m}{2}\iint d\xi d\eta \xi^2 D(\xi,\eta,\gamma_m)e_{zm}(\eta) \times \frac{(1-i\alpha_m R_{*mm})\exp(i\alpha_m R_{*mm})}{R_{*mm}^3} = \exp(ikX_m) + \frac{i}{4\pi}\sum_{n\neq m}^{N}\frac{\sigma_{*n}}{\rho_{*mn}}\frac{\partial}{\partial\rho_{*mn}}\rho_{*mn} \quad (8)$$

$$\times\iiint d\xi d\eta d\psi \xi\cos\psi D(\xi,\eta,\gamma_n)e_{zn}(\eta) \times \frac{\exp(i\alpha_m R_{*mn})}{R_{*mn}},$$

where

$$R_{*mn} = \sqrt{\rho_{*mn}^2 + \xi^2 - 2\rho_{*mn}\xi\cos\psi + L^2(z_* - \eta)^2},$$

$$\rho_{mn} = \sqrt{(X_m - X_n)^2 + (Y_m - Y_n)^2},$$

$\rho_{*mn} = \rho_{mn}/l_{\rho n}$, $z_* = z/l_{zn}$, $m = 1, \ldots, N$, and N is the number of plasmoids. We assume in Eq. (8) that $\varepsilon_m = 1$ to immediately derive expressions for the external field $e_z^{(ex)}(\mathbf{r})$ produced by a system of dipoles at point (X_m, Y_m, z).

We will dwell on a number of corollaries to the foregoing equations and compare them with the previously obtained results.

2.1. Relations (5) give the radial distribution of the amplitude of electromagnetic field components. In the case of $\Lambda = \sigma_*\alpha^2/4 \gg 1$ (for air and nitrogen, $\Lambda \approx n_e l_\rho^2 10^6/N_0\lambda$, where λ and l_ρ are in cm), the channel radius significantly exceeds the skin depth and the field in the internal region exponentially decreases toward the center,

$$J_0(|\rho_*\gamma| \gg 1) \propto \exp(\rho_*\sqrt{2\Lambda})/\sqrt{\rho_*}.$$

At $\Lambda < 1$ (this condition is realized in the majority of experiments), the electric field amplitude varies weakly over distances less than the channel radius.

2.2. At the potential stage in the β, $\Lambda \ll 1$ limit, the result of integration of Eq. (6) is the following expression for the complex amplitude:

$$e_z(0,z) = e_{\text{cpot}} = \left[1 + \frac{i\sigma_*}{L^2-1}\left(\frac{L\ln(L - \sqrt{L^2-1})}{\sqrt{L^2-1}} - 1\right)\right]^{-1}. \quad (9)$$

Because $e_z(0, z) = \text{const}$, we use Eqs. (5) to derive the well-known result of [12],

$$e_\rho^{(\text{in})}(\rho,z) = 0, \quad b_\varphi^{(\text{in})}(\rho,z) = 0.$$

2.3. In the $l_z \longrightarrow \infty$ limit, the distribution of the amplitude of a longitudinal electric field along the plasmoid axis is uniform. Therefore, assuming that

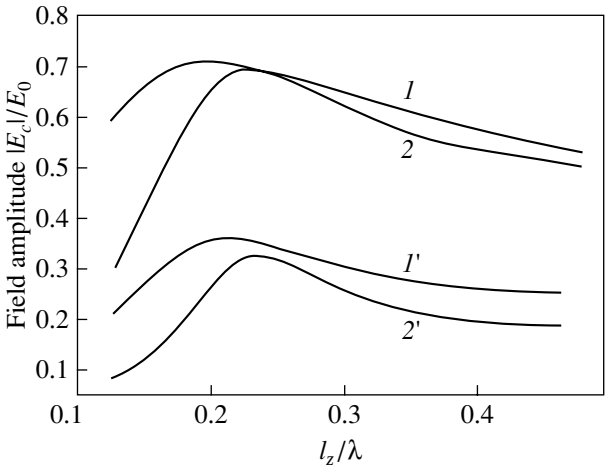

Fig. 3. The amplitude of electric field $|E_c|/E_0$ at the channel center as a function of the channel half-length l_z/λ for different values of the parameters α and Λ: (*1*) $\alpha = 0.4$, $\Lambda = 0.4$; (*2*) $\alpha = 0.1$, $\Lambda = 0.4$; (*1'*) $\alpha = 0.4$, $\Lambda = 1.4$; (*2'*) $\alpha = 0.1$, $\Lambda = 1.4$.

$e_z(0, \eta) = e_{cw} = \text{const}$ in the integrands of formulas (6) and (7), we find

$$e_{cw} = -\frac{2i}{\alpha\pi}\frac{1}{J_0(\gamma)H_1^{(1)}(\alpha) - \sqrt{\varepsilon}J_1(\gamma)H_0^{(1)}(\alpha)}, \quad (10)$$

$$e_z^{(\mathrm{ex})}(\rho > l_\rho) = \exp(ikx) + \frac{i\pi e_{cw}}{2}H_0^{(1)}(k\rho) \times [\gamma J_0(\alpha)J_1(\gamma) - \alpha J_0(\gamma)J_1(\alpha)], \quad (11)$$

where $H_m^{(1)}(x)$ is the Hankel function of the *m*th kind corresponding to a diverging wave,

$$H_m^{(1)}(x \gg 1) \propto \exp(ix)/\sqrt{x}.$$

Expressions (10) and (11) were derived in [13] as a particular case of solving the problem on the scattering of a plane linearly polarized electromagnetic wave from a plasma filament of infinite length with a nonuniform (over the radius and azimuth) distribution of the plasma concentration.

2.4. The calculated dependence of the normalized field amplitude $|e_c|$ at the center of a plasma channel on the channel length is given in Fig. 3 for different values of the parameters α and Λ. One can see that the resonance pattern of these curves is the more pronounced, the thinner the plasma channel is. As the parameter Λ increases, the channel length, at which the first main resonance of the amplitude of longitudinal electric field and, accordingly, of the current density is attained, increases to approach the value of $2l_z = \lambda/2$. The resonance of the current density at $2l_z = \lambda/2$ for a thin ($|1/\ln\alpha| \ll 1$) metal dipole vibrator was obtained by Leontovich and Levin [14]. This result may now be generalized to fit a plasma channel of finite conductivity.

2.5. We will treat the reflecting properties of a plasmoid and, first of all, identify the regions of spatial localization of the maximal field amplitude. In these regions (all other conditions being favorable), new channels may then arise to form the discharge structures described in the Introduction. Consider formula (7). When the distance from the plasmoid center to the observation point ($r = \sqrt{\rho^2 + z^2}$) exceeds the maximal characteristic size of the plasmoid (l_z), the expression for the field amplitude may be rewritten in the form

$$\left|e_z^{(\mathrm{ex})}(\rho, z)\right| \approx \sqrt{1 + \left|e_z^-(\rho, z)\right|^2 + 2\left|e_z^-(\rho, z)\right|\cos\Psi}. \quad (12)$$

Here,

$$e_z^-(\rho, z) \approx i\frac{4}{3}\Lambda e_c \exp(ikr)\frac{l_z}{r} \times \left(\frac{\rho^2}{r^2} + \frac{1}{kr}\left(\frac{3\rho^2}{r^2} - 2\right)\left(i - \frac{1}{kr}\right)\right)F(\gamma),$$

$$F(\gamma) \approx \left(1 - \frac{\gamma^2}{10}\right),$$

if $\Lambda < 1.5$, and

$$\Psi(x, y, z) = k(r - x) + \psi(x, y, z),$$

where $\psi(x, y, z)$ is the phase dependent both on the plasma channel parameters and on the distance from the observation point ($0 < \psi < \pi$).

The surfaces with $M_n^{(3)}(x, y, z) = 0$, on which the condition $\cos\Psi = 1(|e_z^{(\mathrm{ex})}(x, y, z)| \approx 1 + |e_z^-(x, y, z)|)$ is realized, are described by the following equation:

$$y^2 + z^2 \approx \Psi_n(x, y, z)(\Psi_n(x, y, z) + 2x), \quad (13)$$

where

$$\Psi_n(x, y, z) = \frac{\lambda}{2}\left(2n - \frac{\psi(x, y, z)}{\pi}\right), \quad n > 0.$$

If $2n \gg \psi/\pi$, the surfaces with $M_n^{(3)}(x, y, z) = 0$ are close to the surfaces of paraboloids of revolution with the x axis of symmetry and with vertexes at points $X_n \approx -n\lambda/2$. In the case of $n = 1$, the $M_1^{(3)}(x, y, z) = 0$ surface may also be approximated by the respective paraboloid of revolution; however, this may only be done in the $kr \gg 1$ region in which the ψ phase is already weakly dependent on the coordinates of the observation point. In the neighborhood of point (X_1, 0, 0) (at which the absolute maximum of the electric field amplitude $|E_z|_{\max} \equiv E_0 K_{\mathrm{ref}}$

is realized and K_{ref} is reflection coefficient of the channel) determined from the equation

$$X_1 \approx -\Psi_1(X_1, 0, 0)/2,$$

the shape of the $M_1^{(3)}(x, y, z) = 0$ surface is determined by the coordinate dependence of the phase. It is obvious that, in the region defined by $M_1^{(3)}(x, y, z) = 0$, amplitude $|e_z^{(ex)}|$ exhibits no extrema (in particular, on the $x > 0$ semiaxis).

Analysis of expression (13) reveals that the curve $M_1^{(2)}(x, y) = 0$ in the xy plane is markedly convex toward the radiation source ($y \approx 2\sqrt{X_1(X_1 - x)}$), while in the xz plane, the curve $M_1^{(2)}(x, z) = 0$ is almost parallel to the z axis ($x(z) \approx x(0)$) as long as $|z| < \lambda/2$. The foregoing illustrates the experimentally observed tendency of plasma channels to somewhat curve toward the radiation source in the $\mathbf{kB}_0$ plane (xy plane) while remaining parallel to the electric field.

2.6. Figure 4 gives graphs of the function $K_{ref}(\Lambda)$ for $\alpha = 0.4$ and different values of the half-length β of a plasma channel. Similar dependences were obtained for other values of dimensionless radius α in the range from 0.2 to 0.4. An important result of these calculations is weak dependence of the reflection coefficient K_{ref} on α and β at $\alpha = 0.2$–0.4 and $\beta = 1.6$–2.2, which enables one to significantly simplify the model by regarding the channel radius and length as the parameters of the problem.[1] Note further the rapid decrease in the derivative $dK_{ref}(\Lambda)/d\Lambda$ at $\Lambda > 1$. This indicates that, by just increasing parameter Λ in the region of $\Lambda > 1$, one cannot appreciably increase the reflection coefficient of the structure being treated (see below for more detail).

Based on the foregoing and on Fig. 4, we will estimate the lower limit of the range of values of parameter $(E/N)_0$, in which a discharge may propagate in the form of a chain of dipoles,

$$(E/N)_0 \approx 0.7(E/N)_{br}. \quad (14)$$

Note that the estimate given by Eq. (14) agrees quite well with the experimentally obtained relation (see the Introduction).

2.7. Given in Fig. 5 for a chain structure is the dependence of the distance $d_x^{(ch)}$ between plasmoids on their length $2l_z$ for different values of the dimensionless radius α. One can see that the value of $d_x^{(ch)}$ appreciably exceeds the dimension $\lambda/4$ at $0.3\lambda \le 2l_z \le 0.4\lambda$. If $2l_z > 0.7\lambda$, the curves group together in the vicinity of the value of $d_x^{(ch)} \approx \lambda/4$. As the parameter α increases, the distance $d_x^{(ch)}$ in the range of plasmoid length $2l_z > \lambda/2$ of interest to us increases. Comparison of these results with the experimentally obtained values of $d_x^{(ch)}$ enables one to restrict the treatment to the following values of the effective radius and length of plasmoids:

$$l_\rho < 0.05\lambda \ (\alpha \le 0.3), \quad 2l_z \ge 0.65\lambda \ (\beta \ge 2). \quad (15)$$

These estimates agree with the respective data obtained from photographs of microwave discharges. In what

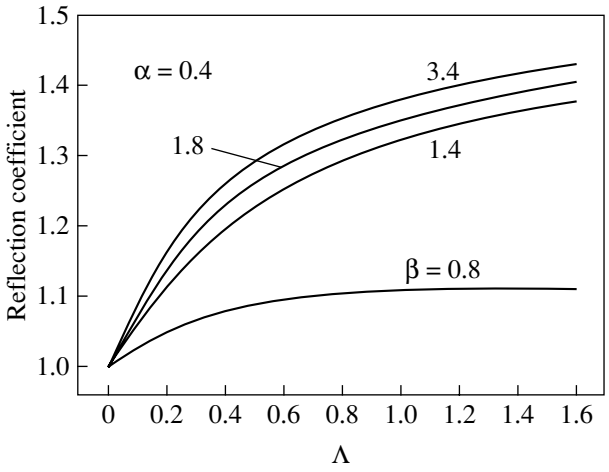

Fig. 4. The reflection coefficient of electromagnetic wave as a function of parameter Λ for $\alpha = 0.4$ and for different values of $\beta = 2\pi l_z/\lambda$.

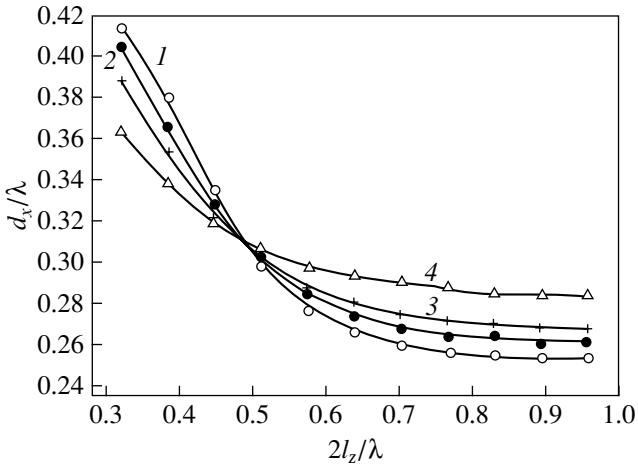

Fig. 5. The average distance d_x/λ between plasmoids as a function of their length $2l_z/\lambda$ for different values of α and Λ: (*1*) $\alpha = 0.2$, $\Lambda = 0.6$; (*2*) $\alpha = 0.2$, $\Lambda = 1$; (*3*) $\alpha = 0.4$, $\Lambda = 0.6$; (*4*) $\alpha = 0.1$, $\Lambda = 0.6$.

[1] In application to the parameter β, this result may be illustrated by Eq. (12) and Fig. 3: because $K_{ref} \approx 1 + |e_z^-(X_1, 0, 0)|$ and $|e_z^-| \propto |e_c(\beta)|\beta$, the product $|e_c(\beta)|\beta$ remains virtually unchanged in the most steeply sloping region of $\beta \approx 1.6$–2.2 of the function $|e_c(\beta)|$. As was revealed by analysis of Eq. (6) in the $\Lambda \ll 1$, $L \gg 1$ limit, the field amplitude at the plasmoid center depends logarithmically weakly on the plasmoid radius; therefore, $|e_z^-| \propto |e_c(\ln 2/\alpha)|$.

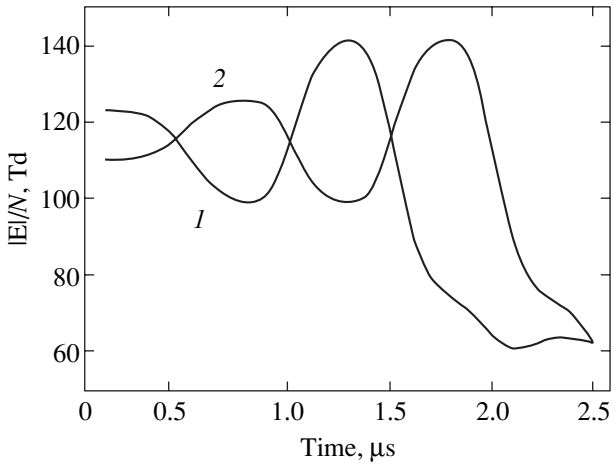

Fig. 6. The dynamics of the reduced field $|E|/N$ in the fourth (curve *1*) and fifth (curve *2*) plasmoids. $(E/N)_0$ = 115 Td, P = 100 Torr.

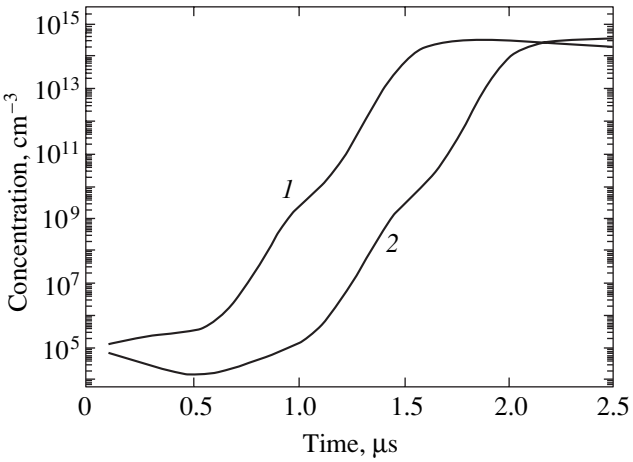

Fig. 7. The dynamics of the electron number density in the fourth (curve *1*) and fifth (curve *2*) plasmoids. $(E/N)_0$ = 115 Td, P = 100 Torr.

follows, we will give the results of numerical calculations for the evolution of the main characteristics of chain and snake structures at $\beta = 2$ and $\alpha = 0.25$.

3. DESCRIPTION OF THE MODEL

The formation of a system of plasma channels was investigated in a quasi-optical wave beam ($\partial(\ldots)/\partial x \ll k$),

$$E_{vz}(\mathbf{r}, t) = 0.5E_z(x, y, z)\exp(-i\omega t) + \text{c.c.},$$

$$E_z(x, y, z) = E_0 G(x)\exp\left[-\frac{(y^2 + z^2)G(x)}{a_f^2}\right], \quad (16)$$

$$G(x) = \frac{1}{1 + 2ix/ka_f^2},$$

the radius a_f of whose focus was a parameter of the problem. The plasmoids were simulated by identical ellipsoids of revolution extended along the electric field and uniformly filled with plasma, with centers in the xy plane ($\mathbf{kB}_0$ plane). The plasmoid length was taken to be constant; i.e., it was assumed that the extension of the arising plasma channel occurs during periods of time much shorter than τ_e in Eq. (1). Channels with a fixed number density of electrons were used as initiators.

Judging by the available photographs of discharges (see Figs. 11 and 12 below), the formed plasmoids markedly differ from ellipsoids of revolution and more closely resemble ellipsoids with semiaxes $l_x < l_y \ll l_z$. In view of this, the question arises of the possibility of replacing such a plasmoid by an "effective" ellipsoid of revolution. It has been demonstrated in [13] that, in determining the field amplitude at the center of an infinitely long plasma channel with a nonuniform profile of electron number density,

$$f(\rho) = N_e(\rho)/N_{ec}, \quad N_{ec} = N_e(\rho = 0),$$

this channel can be replaced by a plasmoid with a uniform distribution of

$$N_e(\rho) = N_{ec}$$

and an effective radius of

$$\rho_{\text{eff}} = \sqrt{2\int_0^\infty f(\rho)\rho d\rho}.$$

The possibility of such a replacement is attributed to the fact that the field amplitude both at the channel center and outside the channel depends on the radius only in

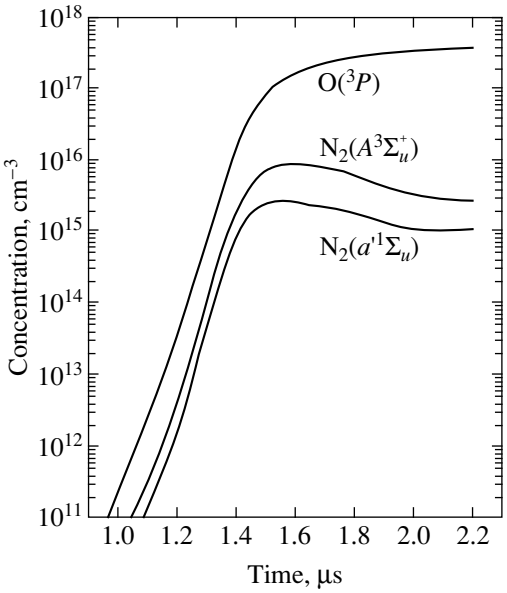

Fig. 8. The time dependence of the concentration of O(^3P) atoms and excited $N_2(A^3\Sigma_u^+)$ and $N_2(a'^1\Sigma_u^-)$ molecules in the fourth plasmoid. $(E/N)_0$ = 115 Td, P = 100 Torr, λ = 4.3 cm.

terms of parameter Λ; it is this latter parameter that must be replaced by

$$\Lambda_{\text{eff}} \propto N_{ec}\pi\rho_{\text{eff}}^2 = 2\pi\int_0^\infty N_e(\rho)\rho d\rho.$$

All of the foregoing holds also for a plasma dipole for which

$$\rho_{\text{eff}} \equiv l_\rho = \sqrt{\frac{1}{\pi}\int\int_{(S)} dx\,dy\, f(x, y, 0)}, \qquad (17)$$

where the integration is performed over the entire area taken up by the plasma. In the case of a homogeneous plasma ellipsoid, we have

$$l_\rho \equiv \rho_{\text{eff}} = \sqrt{l_x l_y}, \quad \Lambda_{\text{eff}} = \sigma_* l_x l_y/4.$$

An analytical investigation of expressions (6) and (7) in the limits of $\Lambda \ll 1$ and $l_z \gg l_x, l_y$ brought about a similar result.

The following computational algorithm was employed. Because of the electromagnetic wave scattering by a system of plasmoids, local maxima of the electric field amplitude were observed. At these maxima were placed the centers of new plasmoids which were included in the scattering group. Then, the above-described process was repeated. The number density of charged particles within the next plasmoid was calculated at its center in conformity with the field; i.e., any variation of the electron number density resulted in the redistribution of the field amplitude in the entire space and, consequently, affected the rate of ionization and excitation of gas in all channels.

It was assumed that, under the conditions being treated, the excitation and ionization of molecules in a discharge are accomplished for the most part by electron impact from the ground electron state. The dependences of the rates of respective processes on the value of E/N and on the degree of vibrational excitation of molecules were borrowed from [15, 16]. Note that the data of [15] were obtained for discharges in a constant electric field. However, a number of researchers (see the review [16]) have demonstrated that the use of these data at $\nu \gg \omega$ in application to microwave discharges is justified given the proper choice of the effective rate of electron–molecule collisions.

In the case of high energy contributions to gas, which are realized under the conditions being treated, one must expect a significant vibrational excitation of nitrogen molecules. The presence of vibrationally excited molecules brings about an increase in the number of high-energy electrons and appreciable rise of the rates of processes with thresholds exceeding the mean energy of electrons. Dyatko *et al.* [17, 18] suggested the formula

$$\log\left(\frac{k_{\text{vib}}}{k_0}\right) = C\exp\left(-\frac{h\omega}{T_v}\right)\Big/\left(\frac{E}{N}\right)^2 \qquad (18)$$

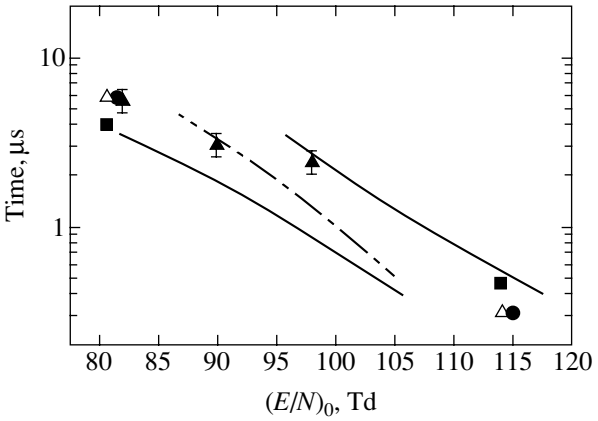

Fig. 9. The time τ_e of formation of plasmoids in air as a function of the reduced field $(E/N)_0$: P = (△) 50, (●) 70, and (■) 100 Torr, λ = 4.3 cm, data of [4]; P = 200 Torr (▲), λ = 8.5 cm, data of [5]. The curves indicate the calculation results for P = 100 Torr: (*1*) snake, (*2*) chain (λ = 4.3 cm); the dash-and-dot curve indicates a chain structure (λ = 8.5 cm).

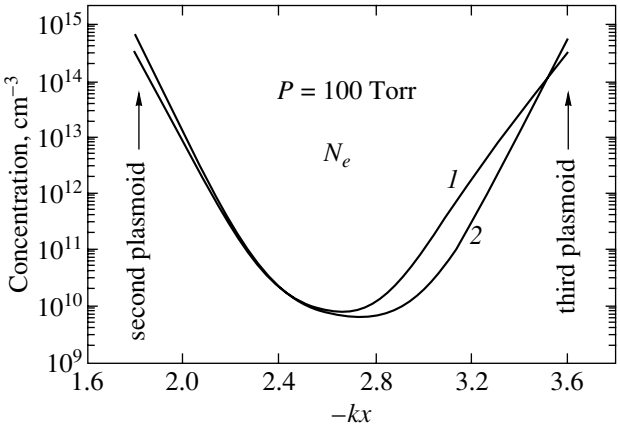

Fig. 10. The spatial distribution of the electron number density between the second and third plasmoids at $(E/N)_0$ = 115 Td (curve *1*) and 100 Td (curve *2*); P = 100 Torr, λ = 4.3 cm.

for describing this effect, where k_{vib} *i*s the constant of the respective process, $h\omega$ is the energy of vibrational quantum, and T_v is the vibrational temperature of molecules. According to [17], $C \approx$ const for all electron processes with high thresholds.

The equation

$$\frac{dN_e}{dt} = N_e(\nu_{\text{ion}} - \nu_{\text{att}}) + Q_{\text{ass}} - Q_{\text{rec}} + Q_{\text{det}} + Q_{\text{photo}} \qquad (19)$$

was solved for the electron number density. Here, ν_{ion} and ν_{att} are the rates of ionization and attachment of electrons, Q_{ass} and Q_{rec} denote the contributions by the reactions of associative ionization [19] and electron–ion recombination, Q_{det} denotes all processes of electron detachment from negative ions (at $O(^3P)$ atoms,

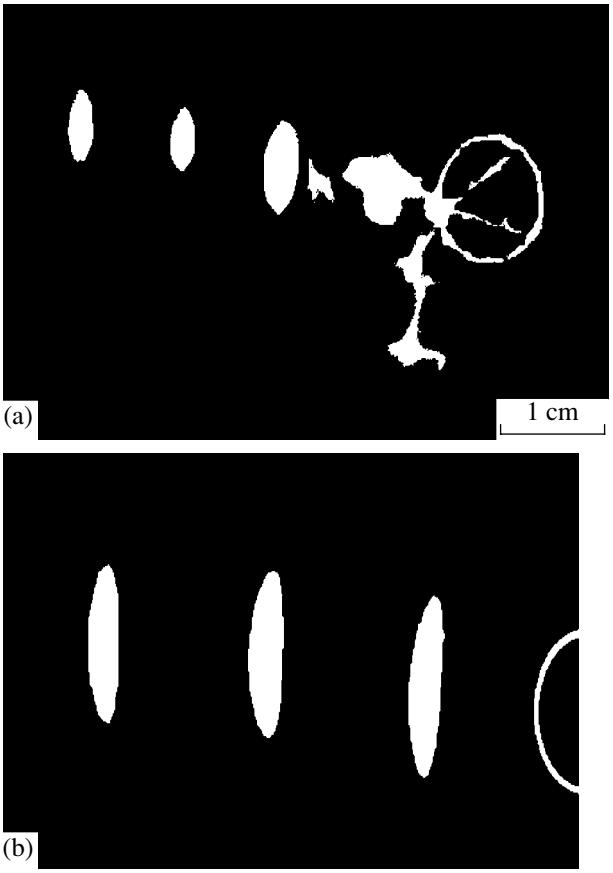

Fig. 11. A chain discharge structure in the $\mathbf{kB}_0$ plane. Air, P = 100 Torr, λ = 4.3 cm; microwave radiation propagates from left to right: (a) integral photograph of the structure [4], (b) numerical calculation results.

$O_2(a^1\Delta_g)$ molecules, and others), and Q_{photo} denotes the formation of charged particles at the expense of the photoionization processes. Similar balance equations were written for all charged particles. Nine species of positive and negative ions were taken into account, namely, O_2^+, O_4^+, N_2^+, N_4^+, NO^+, O^-, O_2^-, O_3^-, O_4^-. A system of ion–molecular reactions was used as the base [19].

In describing the ionization of unexcited air by UV radiation of already formed plasmoids, the model of Aleksandrov and Kochetov [20] was used. It was assumed that the ionization occurred during the absorption by oxygen of the radiation of molecular bands of N_2 in the wavelength range λ = 98.0–102.5 nm. Then, for the axisymmetric case, at a distance ρ from the plasmoid being treated, we have

$$Q_{\text{photo}}(\rho) \approx \frac{\pi + 2}{8\sqrt{2}\ln(\chi_1/\chi_2)} \times \frac{N_e V_{\text{dr}} \xi \theta}{1 + P/P_0} \frac{\exp(-P_{O_2}\chi_1\rho)}{(\rho/l_\rho)^2}. \quad (20)$$

Here, N_e and V_{dr} denote the number density and drift velocity of electrons in an emitting plasmoid, respectively; θ is the average (in the given wavelength range) number of ionizing photons produced by an electron per unit path length; ξ is the mean probability of photoionization; χ_1 = 0.035 cm^{-1} Torr^{-1} and χ_2 = 2.0 cm^{-1} Torr^{-1} are the coefficients of absorption by oxygen of radiation with the wavelengths of 102.5 and 98.0 nm, respectively [20]; and P is the gas pressure (the parameter P_0 = 30 Torr allows for the collisional quenching of emitting states of nitrogen).

The dynamics of the gas temperature was described by the equation

$$C_v N \frac{dT}{dt} = \frac{\varepsilon_v - \varepsilon_v(T)}{\tau_{VT}} + W_r, \quad (21)$$

where C_v is the specific heat of gas at constant volume, ε_v is the average amount of vibrational quanta per N_2 molecule, τ_{VT} is the characteristic time of VT relaxation of vibrational excitation of $N_2(v)$, and W_r is the rate of gas heating in chemical reactions.

Taken into account in describing the source of heating due to chemical processes were the reactions of preassociation of highly excited electron states of oxygen (which are populated either by electron impact or during the quenching of excited states of N_2), the reactions of quenching of excited $O(^1D)$ atoms by nitrogen molecules, and others. The employed model of heating the gas was described in detail in [21], where the results of respective test calculations are also given.

Under the conditions being treated, the characteristic time of gasdynamic expansion of a plasma channel is several microseconds. At $(E/N)_0$ = 80–90 Td, this time may be comparable to the time of formation of the next plasmoid. As is demonstrated by the results of our model calculations, the gasdynamic processes have no appreciable effect on the reflectivity of plasmoids, though significantly affecting their ultimate parameters. We investigated the possibility of describing the dynamics of jumplike propagation of a discharge disregarding the overheating ionization instability mechanism; therefore, the effect of gasdynamic processes was ignored.

4. CALCULATION RESULTS

Characteristic curves reflecting the evolution of the amplitude of reduced electric field E/N and of the electron number density in the fourth and fifth plasmoids at $(E/N)_0$ = 115 Td, P = 100 Torr, and λ = 4.3 cm for a structure of the chain type are given in Figs. 6 and 7. The spatial distribution of the field amplitude at t = 0, which is the result of interaction between an electromagnetic wave and the plasma channel initiating the discharge, is described in detail in Section 2.5. The initial number density of electrons in an arising plasma channel is 10^4–10^6 cm^{-3} and is defined by the balance

of the processes of photoionization (UV radiation from the preceding plasmoid) and dissociative attachment to oxygen molecules. The increase of N_e in prebreakdown fields is largely associated with the increase in the concentration of $O(^3P)$ atoms on which the effective detachment of electrons occurs. At $\Lambda > 0.01$ ($N_e \geq (4–6) \times 10^{12}$), a redistribution of the field amplitude occurs: the field in a plasmoid decreases because of self-screening and the reflection coefficient increases. The final value of the electron number density for the values of the channel dimensionless radius $kl_\rho = 0.25$ is $(2–4) \times 10^{14}$ cm^{-3}. In this way, the reflection coefficient reaches the value of 1.24 and the field in the plasmoid decreases to approximately 60 Td. A fairly dense plasma is maintained under these conditions owing to the reactions of associative ionization [22],

$$\begin{aligned} &N_2(A^3\Sigma_u^+) + N_2(a'^1\Sigma_u^-) \\ &\longrightarrow e + N_4^+ \ (5 \times 10^{-11} \text{ cm}^3/\text{s}), \\ &N_2(a'^1\Sigma_u^-) + N_2(a'^1\Sigma_u^-) \\ &\longrightarrow e + N_4^+ \ (2 \times 10^{-10} \text{ cm}^3/\text{s}). \end{aligned} \quad (22)$$

The main channel of the loss of charged particles at this stage becomes the electron–ion recombination, because the concentration of oxygen atoms already exceeds 10^{17} cm^{-3} (see Fig. 8) and the destruction of negative ions proceeds at a much faster rate than their formation.

For the same conditions, Fig. 8 gives the results of calculating the dynamics of concentration of $O(^3P)$ atoms and metastable electron-excited molecules of $N_2(A^3\Sigma_u^+)$ and $N_2(a'^1\Sigma_u^-)$ involved in reactions of associative ionization (22). With $t \geq 1.4$ μs, the rate of formation of charged particles in reactions (22) exceeds 3×10^{20} cm^{-3}/s.

According to Figs. 6 and 7, the time dependences of the field amplitude and of the electron number density in two successive plasmoids (in view of the time shift by the constant quantity τ_e) are almost constant. Figure 9 gives the values of τ_e obtained by formula (1) using the experimental data on the rate of propagation of the discharge front at $\lambda = 4.3$ cm [4] and $\lambda = 8.5$ cm [5]. Note the very strong dependence of τ_e on $(E/N)_0$ (for a chain and a snake at $\lambda = 4.3$ cm, we have $\tau_e \propto E_0^9$), as well as the fairly weak dependence of τ_e on the gas pressure and on the wavelength of microwave radiation.

The same figure gives the results of calculating the time of plasmoid formation for structures of chain and snake types in a microwave discharge in air at P = 100 Torr and wavelengths of $\lambda = 4.3$ cm (solid curves) and $\lambda = 8.5$ cm (dot-and-dash line). In calculations in determining τ_e, the time reading started from the moment when the field in the channel being treated exceeded the breakdown value and terminated when the coefficient of electromagnetic wave reflection from this channel turned out to be sufficient for reaching the breakdown value of the field in the next plasmoid. The calculation results for $P = 100$ Torr enable one to adequately describe the respective experimental data. However, the predicted dependence of τ_e on the gas pressure ($P\tau_e \approx$ const) is stronger than that observed in experiment. The reason for this difference is not yet clear.

We attribute some disagreement between the numerical simulation results and experimental data at $(E/N)_0 = 115$ Td (Fig. 9) to the violation of the condition of "instantaneousness" of the channel extension, which was mentioned previously in describing the model. Note further that, in the case of a marked increase in time τ_e of plasmoid formation (in the range of values of $(E/N)_0 \approx 90$ Td for the chain mode and $(E/N)_0 \approx 80$ Td for the snake mode), the approximation of invariability of the plasma channel radius becomes invalid and the need arises to take into account the evolution of the effective channel radius.

In order to determine the degree of effect of the radii of plasma channels on the time of their formation, calculations were performed for different fixed values of the parameter $\alpha = kl_\rho = 0.2–0.3$. The scatter of $\delta\tau_e$ turned out to be relatively small,

$$\frac{\tau_e(\alpha = 0.3)}{\tau_e(\alpha = 0.2)} \approx 1.2–1.3,$$

which is a result of the weak dependence $K_{\text{ref}}(\alpha)$ (Fig. 4). In addition, the effect of the processes of photoionization on τ_e was investigated. For this purpose, model calculations were performed in which the rate of photoionization given by Eq. (20) increased (or decreased) by a factor of 5. Even so significant a variation of Q_{photo} failed to bring about a marked variation of τ_e.

Given in Fig. 9 for a snake structure are the results of calculation of τ_e in a discharge with $\lambda = 8.5$ cm (dot-and-dash curve). One can see that the time of plasmoid formation increases with the wavelength of microwave radiation: the less the value of reduced field $(E/N)_0$, the greater the increase in this time. The reason for this is that, in the case of a constant dimensionless channel radius α, the reflectivity of the channel depends only on the value of the parameter Λ proportional to the product $N_e\lambda$. Therefore, for one and the same value of $(E/N)_0$, the maximal electron number density in plasmoids proves to be lower in discharges with a longer wavelength. As a result, both the production of atomic oxygen (ensuring the destruction of negative ions) and the formation of excited molecules participating in processes of associative ionization are delayed.

Figure 10 gives the distribution of the electron number density in the region between the second and third plasma channels at the moment of time $t = 5$ μs for $(E/N)_0 = 100$ and 115 Td. The extreme points in the figure indicate the electron number density in the channels. Such distributions become steady following the

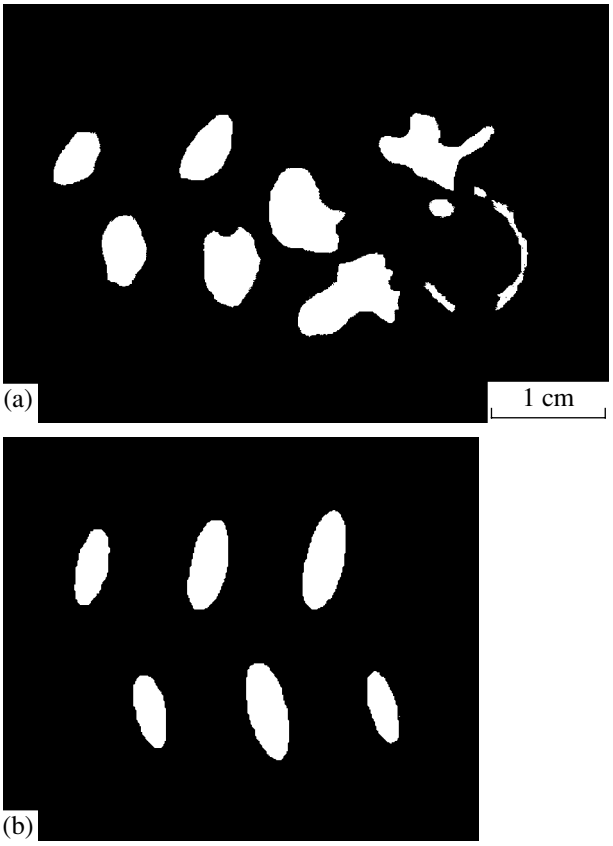

Fig. 12. A snake discharge structure in the $\mathbf{kB}_0$ plane. Air, P = 100 Torr, λ = 4.3 cm; microwave radiation propagates from left to right: (a) integral photograph of the structure [3], (b) numerical calculation results.

formation of the next fourth plasmoid and hardly vary after that. The increase in the gas temperature at so low a concentration of background plasma in a field with a decreasing amplitude does not exceed three degrees, which prevents the overheating ionization instability from developing in the interplasmoid space. The latter fact indicates that the mechanism of structure formation investigated by Vikharev *et al.* [8] and other researchers is not realized under the given conditions (for the dipole mode of microwave discharge).

It follows from Fig. 9 that plasma structures of two types may exist in the field range of $(E/N)_0$ = 85–115 Td. The time of plasmoid formation in a chain (curve *2*) is longer than that in a snake (curve *1*) because of the higher reflectivity of the latter. The fact that only a chain is experimentally observed in the region of their competition $(E/N)_0/(E/N)_{br}$ = 0.75–1 [4] is presumably associated with the method of initiation of the given discharge (see below).

We will dwell in more detail on the properties of discharge structures being formed and conditions of their initiation.

Figure 11a depicts an integral photograph (borrowed from [4]) of a chain discharge structure in the $\mathbf{kB}_0$ plane, and Fig. 11b gives the results of numerical calculation of spatial distribution of relative radiation intensity of a 2^+ nitrogen system ($N_2(C^3\Pi_u) \longrightarrow N_2(B^3\Pi_g) + h\nu$ transition) [23]. The light-colored regions lie within the isoline of relative intensity $0.2I_{max}$. One can see that the plasmoids are markedly curved towards the source of microwave radiation. The semiaxial ratio in the photograph approximately corresponds to the predicted value of $l_y/l_x \approx 3$–$3.5 (l_\rho \equiv \rho_{eff} \approx 2l_x)$. Note further that, both in theory and in experiment, the line connecting the channel centers is arranged at an angle to the wave beam axis. The latter fact is associated with the transverse shift of the initiating system from the axis of a highly focused wave beam. At $a_f > 3\lambda$, this effect almost fully disappears.

A chain structure exhibits approximately the same reflectivity as a solitary plasmoid (the difference between the values of the absolute maximum of the amplitude $K_{ref}(\Lambda)$ is several percent (Fig. 4)). So insignificant a difference is attributed to the rapid decrease in the scattered wave amplitude ($\propto 1/r$) with increasing distance from the axis of the reflecting channel. Therefore, a solitary plasmoid may be regarded as the base element of a chain structure.

The shift of initiating dipoles in the transverse (relative to vector $\mathbf{k}$) direction brings about a significant improvement in the reflectivity of a plasma system. We performed calculations of the formation of plasma structures in a wide wave beam ($a_f \longrightarrow \infty$) with two identical initiators located on the y axis at a distance of $|\Delta Y|$ from each other. In this case, the location of the region of maximum amplitude is, naturally, equidistant from both reflecting objects. An increase in $|\Delta Y|$ was accompanied by an increase in the amplitude E_{max} to the maximal value (reached at $|\Delta Y_{max}| \approx \lambda/2$) followed by a decrease in this amplitude. The plasmoids spaced at a distance $|\Delta Y| > \lambda$ from one another had almost no effect on one another and reflected as solitary independent objects. At $|\Delta Y| = |\Delta Y_{max}|$, the value of $K_{ref}(\Lambda)$ ($\Lambda = \Lambda_1 = \Lambda_2$) was appreciably higher than the respective value for a solitary channel. For example, given Λ = 1, $K_{ref} \approx 1.35$ for a solitary channel and $K_{ref} \approx 1.7$ for two spaced plasmoids.

Therefore, the reflectivities of a system of plasmoids are appreciably improved if these plasmoids can be spaced from one another in the transverse (relative to vector $\mathbf{k}$) direction. Time τ_e of formation of plasma channels decreases accordingly, and the velocity of discharge propagation increases.

Figure 12a depicts an integral photograph of a snake structure in the $\mathbf{kB}_0$ plane, and Fig. 12b gives the results of respective numerical calculation. Note approximate agreement of the predicted orientation of channel cross sections with their photographic image. When this structure is realized, the $K_{ref}^{(sn)}(\Lambda)$ curve lies higher than the respective curves for a solitary plasmoid and for a

chain structure. Therefore, the threshold of the dipole mode of propagation of a microwave discharge is lower in the case of a snake structure. Calculations revealed that

$$\frac{(E/N)_{0\ \min}^{(\mathrm{sn})}}{(E/N)_{\mathrm{br}}} \approx 0.6\,.$$

The formation of a plasma structure of a certain type depends primarily on the method of discharge initiation. Indeed, by arranging the initiators in one or another manner, we "impose" on the discharge, from the very outset, the algorithm of its structure formation. For example, if we use base elements of the chain or snake type as the initiating group, we can only reproduce these plasma structures. If base elements of different types are contained in the initiation region, the pattern of the spatial structure realized in the discharge will be defined by other factors (for example, by $(E/N)_0$, the parameter a_f, and others).

Note that these results do not contradict the experimental data (referred to in the Introduction) that indicate that the discharge structure is independent of the type of initiator, because the majority of these data were obtained for $(E/N)_0 \le 0.6(E/N)_{\mathrm{br}}$ and do not pertain to the dipole structure zone. But most important is the fact that the initiators employed in experiments contain no "asymmetric" elements that must form the basic set for structures of the snake type. Therefore, all of the initiators used in [1–4] may be regarded to be of the same type from the standpoint of structure formation.

Within their initiation regions, discharge structures are fairly stable and regularly reproducible in calculations. For a discharge structure of the snake type, the mean distance between plasmoids is

$$d_x^{(\mathrm{sn})}/\lambda \approx 0.17$$

in the direction of discharge propagation,

$$d_y^{(\mathrm{sn})}/\lambda \approx 0.4$$

in the transverse direction, and

$$d_x^{(\mathrm{ch})}/\lambda \approx 0.25\text{–}0.3$$

for a chain (see Fig. 4). These values depend little on the discharge parameters and agree with the experimental data of [3, 4]. If the initiator coordinates are other than d_x and d_y, then, starting with some plasmoid (whose number depends on the degree of initial misalignment), the structure "arrives" at its characteristic scales all the same. This inference also agrees with the observation results of [1–4], which indicate that the discharge characteristics depend little on the type of initiator.

So, in the range of

$$(E/N)_0/(E/N)_{\mathrm{br}} = 0.6\text{–}0.7,$$

a discharge is capable of moving toward the radiation source only in the form of a snake, and, in the range of

$$(E/N)_0/(E/N)_{\mathrm{br}} = 0.7\text{–}1,$$

either one of the plasma structures may be realized. It follows from Fig. 9 that the velocity of discharge propagation must be determined by the discharge structure. That is, as a result of using two different initiating elements, one can (all other things being equal) attain different rates of discharge propagation.

By varying the relative positions of two identical initiators, we managed to identify three initiation regions in the *xy* plane, which started a chain, a snake, and a new structure consisting of three parallel chains. We will omit the details and note only that, for the latter structure to form, the initiating plasmoids must be spaced in the transverse direction at a distance exceeding λ. An initiating system with a small transverse dimension ($< 0.4\lambda/\pi$) is capable of forming only a chain structure.

5. CONCLUSION

We have developed a 3D model for describing the propagation of an initiated high-pressure microwave discharge in a linearly polarized wave beam. The suggested model is used to self-consistently solve equations for the electric field amplitude and plasmochemical kinetics, as well as equations for the gas temperature and for the mean number of stored vibrational quanta of nitrogen molecules.

The results of calculating the characteristic time τ_e of formation of plasma channels agree with the available experimental data. The value of τ_e with a fixed value of reduced field $(E/N)_0$ depends little on the wavelength of microwave radiation, which is also confirmed by experimental data. However, the predicted pressure dependence of the time of plasmoid formation is stronger than the experimentally obtained dependence.

The developed model was used to obtain the experimentally observed types of plasma structures formed, namely, the snake and chain types. These discharge structures are fairly stable and regularly reproducible in calculations. The mean distances between plasmoids both in a snake and in a chain depend little on the discharge parameters and agree with the experimentally measured values.

The reflectivity of a system of plasma channels improves considerably if the plasmoids are spaced from one another in the transverse (relative to the vector **k**) direction. This is accompanied by an increase in the rate of discharge propagation and by the extension of the range of reduced electric fields $(E/N)_0$ in which the given discharge structure may exist.

The investigation results enable one to determine the conditions of formation of one or another spatial structure, as well as the parameters of plasmoids being formed. By varying the positions of initiators, the focal distance a_f, and other characteristics of the discharge, one can purposefully control the parameters of the discharge structure and individual plasmoids in order to attain the desired result.

Interest has recently increased in investigations of the effect of gas discharges on shock-wave processes [24–26] with a view to reducing the intensity (Mach number) of the latter processes. The use, for this purpose, of microwave discharges of the type described herein appears to be very promising, because, in the case of this highly inhomogeneous discharge, the energy is absorbed only in plasma channels that are highly heated as a result. According to Artem'ev *et al.* [26], the presence of a system of hot channels must contribute to effective destruction of shock waves in the zone of discharge action, as was observed by Grachev *et al.* [27].

ACKNOWLEDGMENTS

We are grateful to V.G. Brovkin and Yu.F. Kolesnichenko for the photographs of discharge structures and valuable discussion of our results.

REFERENCES

1. G. M. Batanov, S. I. Gritsinin, I. A. Kossyĭ, *et al.*, Tr. Fiz. Inst. im. P. N. Lebedeva, Akad. Nauk SSSR **160**, 174 (1985).
2. S. V. Golubev, S. I. Gritsinin, V. G. Zorin, *et al.*, in *High-Frequency Discharge in Wave Fields*, Ed. by A. G. Litvak (Inst. Prikl. Fiz. Akad. Nauk SSSR, Gor'ki, 1988), p. 136.
3. V. G. Brovkin, Yu. F. Kolesnichenko, and D. V. Khmara, in *Ball Lightning in Laboratory*, Ed. by R. F. Avramenko *et al.* (Khimiya, Moscow, 1994), p. 119.
4. V. G. Brovkin and Yu. F. Kolesnichenko, J. Mosc. Phys. Soc. **5**, 23 (1995).
5. L. P. Grachev, I. I. Esakov, G. I. Mishin, and K. V. Khodataev, Zh. Tekh. Fiz. **65** (5), 21 (1995) [Tech. Phys. **40**, 416 (1995)].
6. N. A. Bogatov, Yu. Ya. Brodsky, S. V. Golubev, and V. G. Zorin, in *Proceedings of XVIII International Conference PIG* (Swansea, 1987), p. 864.
7. V. G. Brovkin and Yu. F. Kolesnichenko, in *Proceedings of International Conference on Strong Microwaves in Plasmas* (1994), Vol. 1, p. 271.
8. A. L. Vikharev, V. B. Gil'denburg, A. V. Kim, *et al.*, in *High-Frequency Discharge in Wave Fields*, Ed. by A. G. Litvak (Inst. Prikl. Fiz. Akad. Nauk SSSR, Gor'ki, 1988), p. 41.
9. A. Kh. Mnatsakanyan and G. V. Naĭdis, Fiz. Plazmy (Moscow) **16**, 481 (1990).
10. N. Yu. Babaeva, A. Kh. Mnatsakanyan, and G. V. Naĭdis, Fiz. Plazmy (Moscow) **18**, 1055 (1992).
11. I. V. Bezmenov, V. V. Rusanov, and V. B. Silakov, Tr. Inst. Obshch. Fiz., Ross. Akad. Nauk **47**, 74 (1994).
12. L. D. Landau and E. M. Lifshitz, *Electrodynamics of Continuous Media*, 2nd ed. (Nauka, Moscow, 1982; Pergamon Press, Oxford, 1984).
13. P. V. Vedenin, Fiz. Plazmy (Moscow) **25**, 384 (1999).
14. M. Leontovich and M. Levin, Zh. Tekh. Fiz. **14**, 481 (1944).
15. N. L. Aleksandrov, F. I. Vysikaĭlo, R. Sh. Islamov, *et al.*, Teplofiz. Vys. Temp. **19**, 22 (1981).
16. N. A. Dyatko, I. V. Kochetov, and A. N. Napartovich, in *High-Frequency Discharge in Wave Fields*, Ed. by A. G. Litvak (Inst. Prikl. Fiz. Akad. Nauk SSSR, Gor'ki, 1988), p. 9.
17. A. Kh. Mnatsakanyan and G. V. Naĭdis, in *Plasma Chemistry*, Ed. by B. M. Smirnov (Énergoatomizdat, Moscow, 1987), No. 14, p. 227.
18. N. L. Aleksandrov and I. V. Kochetov, Teplofiz. Vys. Temp. **25**, 1062 (1987).
19. I. A. Kossyi, A. Y. Kostinsky, A. A. Matveev, and V. P. Silakov, Plasma Sources Sci. Technol. **1**, 201 (1992).
20. M. B. Zheleznyak, A. Kh. Mnatsakanyan, and G. V. Naĭdis, Teplofiz. Vys. Temp. **20**, 423 (1982).
21. N. A. Popov, Fiz. Plazmy (Moscow) **27**, 940 (2001).
22. H. Brunet and J. Rocca-Serra, J. Appl. Phys. **57**, 1574 (1985).
23. A. M. Pravilov, *Photoprocesses in Molecular Gases* (Énergoatomizdat, Moscow, 1992).
24. *Proceedings of II Weakly Ionized Gases Workshop* (Norfolk, Virginia, 1998).
25. Yu. F. Kolesnichenko, V. G. Brovkin, V. A. Lashkov, *et al.*, AIAA Pap. **2001-0345** (2001); AIAA Pap. **2001-3060** (2001).
26. V. I. Artem'ev, V. I. Bergel'son, I. V. Nemchinov, *et al.*, Mat. Model. **8**, 1 (1989).
27. L. P. Grachev, I. I. Esakov, G. I. Mishin, and K. V. Khodataev, Zh. Tekh. Fiz. **55**, 972 (1985) [Sov. Phys. Tech. Phys. **30**, 586 (1985)].

Translated by H. Bronstein

Journal of Experimental and Theoretical Physics, Vol. 96, No. 1, 2003, pp. 53–58.
Translated from Zhurnal Éksperimental'noĭ i Teoreticheskoĭ Fiziki, Vol. 123, No. 1, 2003, pp. 64–70.

SOLIDS
Structure

Raman Scattering and Interaction and Interference of Optical Vibrations in a γ-Li_3PO_4 Superionic Crystal

B. N. Mavrin[a, *], V. V. Asonov[a], V. V. Fomichev[b], A. K. Ivanov-Shits[c], and V. V. Kireev[c]

[a]*Institute of Spectroscopy, Russian Academy of Sciences, Troitsk, Moscow oblast, 142190 Russia*
[b]*Lomonosov State Academy of Fine Chemical Technology, pr. Vernadskogo 86, Moscow, 117571 Russia*
[c] *Institute of Crystallography, Russian Academy of Sciences, Moscow, 117333 Russia*
**e-mail: mavrin@isan.troitsk.ru*

Received July 11, 2002

Abstract—Polarized Raman spectra of a γ-Li_3PO_4 single crystal are investigated at temperatures approximately up to 700 K. It is shown that vibrations of PO_4 tetrahedrons and cations of the lithium sublattice can be separated in the spectra. It is found that an increase in temperature leads to interference of one-phonon optical modes of symmetry B_{2g} and A_g, which is accompanied by antiresonance in a frequency range near 190 cm^{-1}. Numerical analysis of the spectrum in the region of interaction of optical modes reveals a strong temperature dependence of the interaction constant, which is determined by anharmonic coupling of optical and acoustic modes. © *2003 MAIK "Nauka/Interperiodica".*

1. INTRODUCTION

The high-temperature lithium phosphate γ-Li_3PO_4 is a promising solid electrolyte with a high ionic conductivity [1]. Its vibrational spectra have been studied insufficiently and only for multiphase ceramic [2] and polycrystalline [3] samples in a limited frequency region. It would also be interesting to study the effect of anharmonic motion of (Li^+) conduction ions, which is intensified upon heating, on the vibrational spectra.

In this work, we analyze the Raman spectra of an oriented γ-Li_3PO_4 single crystal, which is metastable at room temperature [4], in various scattering geometries. The observed spectral lines are assigned, in accordance with the vibration symmetry types and with group-theoretical analysis, to (external and internal) vibrations of isolated PO_4 tetrahedrons, which are structural elements of the crystals, and cations of the lithium sublattice. Temperature variations of the spectra enabled us to detect the interference of one-phonon states, which is manifested in the emergence of antiresonance and in deformation of profiles of interacting lines, which is typical of the resonance of a discrete level with a continuous spectrum. Numerical analysis of the spectra reveals a strong temperature dependence of the constant of interaction between one-phonon states.

2. GROUP-THEORETICAL ANALYSIS OF VIBRATIONS

The structure of γ-Li_3PO_4 is formed by isolated PO_4 tetrahedrons linked via lithium tetrahedrons [4]. The measurements of electron density distribution revealed the covalent type of the P–O bonds in a PO_4 tetrahedron and only a certain covalent component of the Li–O bonds [5]. The space group of the crystal belongs to the centrosymmetric rhombic group D_{2h}^{16} (four structural units in a primitive cell) [4]. Considering that eight Li atoms occupy position C_1; 4 Li, 4 P, and 8 O atoms occupy position $C_s(xz)$, and 8 O atoms are in position C_1, we can find the total vibrational representation [6]:

$$\Gamma = 14A_g + 10B_{1g} + 14B_{2g} + 10B_{3g} + 10A_u + 14B_{1u} + 10B_{2u} + 14B_{3u}. \quad (1)$$

All the *g* modes are Raman active, while vibrations of the classes B_{1u}, B_{2u}, and B_{3u} are active in the IR absorption, except three acoustic modes ($1B_{1u} + 1B_{2u} + 1B_{3u}$).

In view of the fact that PO_4 tetrahedrons are isolated and the P–O bonds are of the covalent type, it is expedient in the complete representation (1) to single out the vibrations of PO_4 tetrahedrons and the vibrations of cations of the lithium sublattice. The vibrations of PO_4 tetrahedrons can be divided into internal and external. Internal vibrations of the $[PO_4]^{3-}$ ion (symmetry T_d) include the following four modes [7]: $\nu_1(A_1)$ at 970 cm^{-1}, ν_2(E) at 358 cm^{-1}, $\nu_3(F_2)$ at 1080 cm^{-1}, and $\nu_4(F_2)$ at 500 cm^{-1}. In view of dynamic interaction of the four PO_4 tetrahedrons in the unit cell and due to the removal of degeneracy under the action of the static crystal field, these modes in the γ-Li_3PO_4 crystal must split into the following Raman active components [6]: $\nu_1 \longrightarrow A_g + B_{2g}$, $\nu_2 \longrightarrow A_g + B_{1g} + B_{2g} + B_{3g}$, ν_3, $\nu_4 \longrightarrow 2A_g + B_{1g} + 2B_{2g} + B_{3g}$. External vibrations (translations and libra-

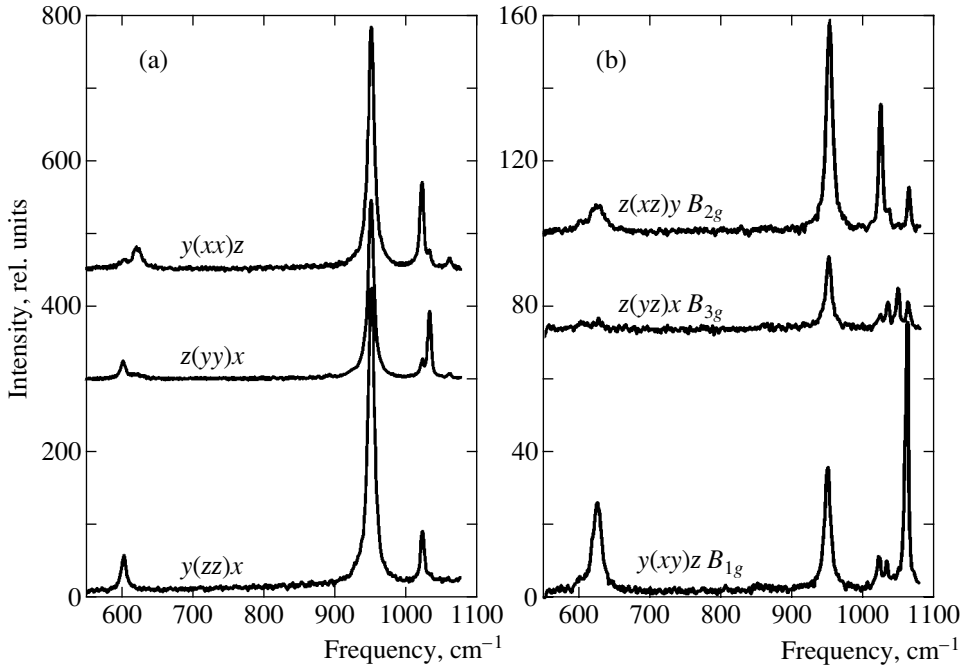

Fig. 1. Raman spectra of a γ-Li_3PO_4 crystal in a frequency range above 600 cm^{-1}: (a) vibrations of symmetry A_g; (b) vibrations of symmetries B_{1g}, B_{2g}, and B_{3g}.

tions of a PO_4 tetrahedron), which are Raman active, can be classified as follows [6]:

$$\begin{aligned}\Gamma^{\text{transl}} &= 2A_g + B_{1g} + B_{2g} + B_{3g},\\ \Gamma^{\text{libr}} &= A_g + 2B_{1g} + B_{2g} + 2B_{3g}.\end{aligned} \quad (2)$$

Subtracting the vibrations of the PO_4 tetrahedron from complete representation (1), we obtain Raman active types of vibrations, which must involve lithium atoms:

$$\Gamma^{\text{Li}} = 5A_g + 4B_{1g} + 5B_{2g} + 4B_{3g}.$$

3. EXPERIMENTAL TECHNIQUE

The crystals of γ-Li_3PO_4 were grown by crystallization from polycrystalline lithium orthophosphate from solution in melt Li_3PO_4 : Li_2MoO_4 : LiF (mass ratio 50 : 34 : 16). A platinum rod was used as a crystallization seed. After complete dissolution of lithium orthophosphate in the melt (at 1030°C), the solution was cooled to 990°C, after which crystallization was carried out by cooling slowly (0.15 deg/h) to 950°C. Crystals grown to a size of $2 \times 5 \times 7$ mm were extracted from the melt and cooled to room temperature.

Raman spectra of the crystal were obtained in the standard 90° geometry with excitation by a line of 514.5 nm wavelength emitted by an argon laser and with detection using a multichannel spectrometer operating in the range 50–1050 cm^{-1} and having a resolution of 3.5 cm^{-1}. Exciting and scattered radiation propagated in our experiments along the crystallographic axes. For temperature measurements, a crystal was placed in an oven whose temperature was maintained to within ±2 K in a temperature range up to 700 K.

4. DISCUSSION OF RAMAN SPECTRA

Force constants of the Li–O bond correlate with its length [8]. Considering that the average length of the Li–O bond in a γ-Li_3PO_4 crystal is approximately equal to 2 Å [4], we can expect that vibrations of lithium cations in the tetrahedral surrounding correspond to frequencies from the range below 500 cm^{-1} [8]. Consequently, in the frequency range above 500 cm^{-1}, Raman spectra can display only vibrations of the PO_4 tetrahedron. Moreover, taking into account the covalent nature of the P–O bond, we can expect that the Raman lines corresponding to vibrations of a PO_4 tetrahedron are more intense than the vibrations of Li–O. We used these assumptions in interpreting the Raman spectrum of the γ-Li_3PO_4 crystal.

Let us first consider the spectra in the frequency range above 500 cm^{-1} (Fig. 1). Figure 1a shows the A_g vibrational spectra for three tensor components α_{xx}, α_{yy}, and α_{zz}, which turned out to be different due to the anisotropy of the crystal. The most intense line of frequency 950 cm^{-1} must be assigned to vibration ν_1 (according to both its intensity and the closeness to the position of the line in the spectrum of a free $[PO_4]^{3-}$ ion). The pair of lines above 950 cm^{-1} (1022 and 1032 cm^{-1}) can be assigned to the two expected vibra-

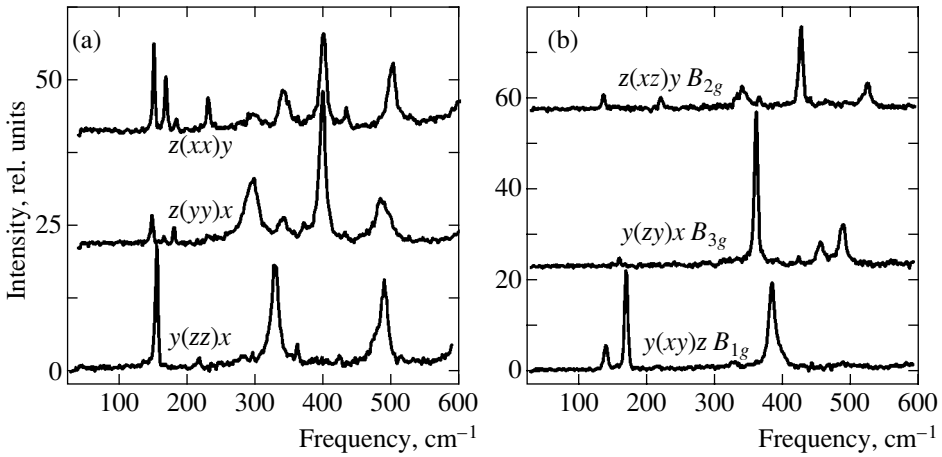

Fig. 2. Raman spectra of a γ-Li_3PO_4 crystal in a frequency range below 600 cm^{-1}: (a) vibrations of symmetry A_g; (b) vibrations of symmetries B_{1g}, B_{2g}, and B_{3g}.

tions: ν_3 ($2A_g$), while the pair of lines below 950 cm^{-1} (602 and 622 cm^{-1}) can be assigned to ν_4. The doublet 602–622 cm^{-1} cannot be assigned so unambiguously to ν_4 since frequency ν_4 for a free ion is close to 500 cm^{-1}. When doing so, we proceeded from the relative intensities of the lines (the lines lying below 600 cm^{-1} are weaker than the doublet) and the low probability of the emergence of other lines in this spectral region. While interpreting the spectra of vibrations B_{1g}, B_{2g}, and B_{3g} (Fig. 1b), we took into account the fact that these vibrations must be close in frequency to the corresponding A_g vibrations in ν_1, ν_3, and ν_4. The results are compiled in the table.

The identification of spectral lines below 600 cm^{-1} (Fig. 2) was complicated due to overlapping of lines (and, accordingly, mixing of the forms of vibrations) corresponding to internal vibration ν_2 of a PO_4 tetrahedron with external vibrations of the PO_4 tetrahedron and vibrations of lithium cations.

While assigning lines to the ν_2 vibration, we took into account the fact that the intensities of these lines must be higher as compared to other lines in the spectrum below 500 cm^{-1}, and the lines must be close to 400 cm^{-1}, i.e., the position of ν_2 in the spectrum of a free $[PO_4]^{3-}$ ion. In addition, we can expect that the widths of the ν_2 lines are smaller than the widths of the lines corresponding to vibrations of Li (in view of superionic motion of Li ions even at room temperature). In the spectrum of A_g vibrations (Fig. 2a), we assigned the intense line at frequency 388 cm^{-1} to the ν_2 vibration. It remains unclear, however, why this line predominates in the spectrum of tensor components α_{xx} and α_{yy}, but is practically absent in the spectrum of the α_{zz} component. We can assume that this is due to the structure of the crystal in which PO_4 tetrahedrons form chains along the z axis, and neighboring chains are formed by tetrahedrons oriented in opposite directions [4]. The most intense lines at frequencies 381, 424, and 363 cm^{-1} corresponding to symmetries B_{1g}, B_{2g}, and B_{3g} (Fig. 2b) are assigned to the ν_2 vibration from the same considerations as for symmetry A_g (see table).

The frequencies of the external vibrations of a PO_4 tetrahedron are usually observed in the range below 250 cm^{-1} (e.g., in KH_2PO_4 [9]). According to group-theoretical analysis (2), three modes of each type are expected in the Raman spectra of external vibrations in γ-Li_3PO_4. External vibrations are manifested most

Frequencies of spectral lines (in cm^{-1}) of a γ-Li_3PO_4 crystal and their classification

Frequency	Classification		Frequency	Classification	
Internal vibrations of PO_4 tetrahedron					
363	B_{3g}	ν_2	948	B_{2g}	ν_1
381	B_{1g}		950	A_g	
388	A_g		1022, 1032	A_g	ν_3
424	B_{2g}		1045	B_{1g}	
602, 622	A_g	ν_4	1021, 1060	B_{2g}	
602	B_{1g}		1031	B_{3g}	
602, 626	B_{2g}				
602	B_{3g}				
External vibrations of PO_4 tetrahedron					
140, 157, 219	A_g		136, 160, 217	B_{2g}	
138, 169, 218	B_{1g}			B_{3g}	
Vibrations of lithium ions					
284, 327, 360, 474, 489	A_g		336, 360, 459, 485, 517	B_{2g}	
325, 358, 399, 488	B_{1g}		322, 455, 487, 562	B_{3g}	

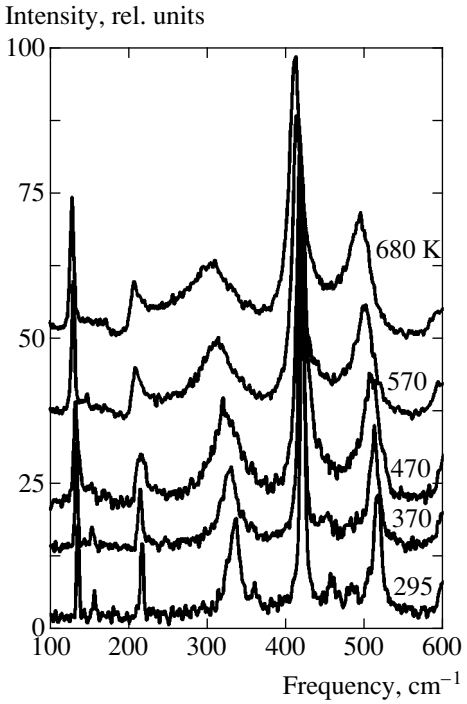

Fig. 3. Raman spectra of a γ-Li_3PO_4 crystal in the scattering geometry $x(zx)y$ (vibrations of symmetry B_{2g}) at different temperatures.

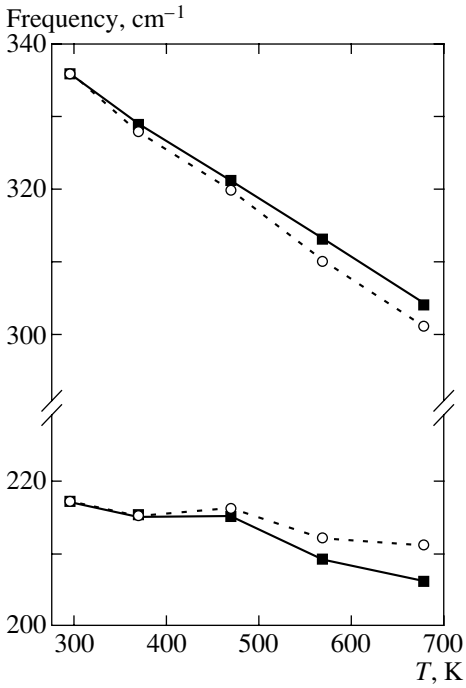

Fig. 4. Temperature dependence of the frequencies of interacting modes: solid lines correspond to measured positions of frequency and dashed lines correspond to the positions of frequencies calculated disregarding the interaction.

clearly in the spectrum of A_g vibrations ($z(xx)y$ geometry, Fig. 2a). This spectrum contains three low-frequency lines at frequencies 140, 157, and 219 cm^{-1} (a weak line at a frequency of 169 cm^{-1} can be seen due to the penetration of an intense line from the $y(xy)z$ geometry). A distinguishing feature of these lines is that their width is small as compared to the lines with higher frequencies and can be assigned, in all probability, to external vibrations of the PO_4 tetrahedron. External vibrations of other symmetry types (B_{1g}, B_{2g}, and B_{3g}) of the PO_4 tetrahedron must lie in the same frequency range (see Fig. 2b and table).

The remaining lines in the frequency range below 600 cm^{-1} (Fig. 2), except those assigned to vibrations of the PO_4 tetrahedron, must be associated with vibrations involving Li atoms (see table).

5. TEMPERATURE MEASUREMENTS AND INTERFERENCE OF ONE-PHONON STATES

The ionic conductivity in γ-Li_3PO_4 increases exponentially with temperature and obeys the Arrhenius law [1]. While heating the γ-Li_3PO_4 crystal approximately to 700 K, we did not observe any changes in the spectra that could indicate a phase transition in this temperature range; at the same time, all Raman lines were broadened significantly (especially the lines corresponding to vibrations of lithium atoms) due to anharmonicity and experienced a low-frequency shift upon an increase in temperature.

Here, we pay attention to the interaction of optical phonons upon heating, which is manifested most strongly in the $x(zx)y$ geometry, in which the B_{2g} vibrations are active (Fig. 3). At room temperature, two intense lines of symmetry B_{2g} are observed in the frequency range 170–380 cm^{-1} at frequencies 217 and 337 cm^{-1}. As the temperature increases, line 337 cm^{-1} experiences a considerable temperature shift of frequency (~0.09 cm^{-1}/K), while the temperature shift of line 217 cm^{-1} is much smaller (Figs. 3 and 4). The width of the 337 cm^{-1} line increases from 17 cm^{-1} at room temperature to 75 cm^{-1} at 680 K, the wings of the line 337 cm^{-1} overlapping with the 217 cm^{-1} line, and these lines experience interference at 570 and 680 K (see Fig. 3). Interference is manifested in a change in the shape of the 217 cm^{-1} line, which becomes asymmetric and acquires a deep minimum (antiresonance) near 190 cm^{-1}.

Such a shape of the band appears, for example, in the case of a Fermi resonance of a discrete level with a continuous spectrum [10] and indicates unambiguously that the Raman tensor components of the discrete level and continuous spectrum have opposite signs. However, the interference in our case cannot be regarded as a Fermi resonance since it occurs between one-phonon states. Mixing of one-phonon states becomes possible [11] if we take into account indirect coupling between optical

phonons via an anharmonic interaction of each optical phonon with two acoustic phonons into which the optical phonons can decay. The interference of one-phonon states was observed earlier during the interaction between soft and hard modes in the Raman spectra of $AlPO_4$ [12] as well as in the hyper-Raman spectra [13] and IR absorption spectra [14] of $SrTiO_3$. If the positions of interacting optical phonons ν_s and ν_h are not yet close, as in our case (Fig. 4), the intensity of the Raman spectrum in the region of interaction of the phonons can be described by the imaginary part of susceptibility [10, 13]:

$$\chi(\nu) = \chi_s(\nu) + \chi_h(\nu) + \chi_{sh}(\nu)$$
$$= \frac{M_s^2}{G_s^{-1} - \gamma^2 G_h} + \frac{M_h^2}{G_h^{-1} - \gamma^2 G_s} + \frac{2\gamma M_s M_h G_h}{G_s^{-1} - \gamma^2 G_h}, \quad (3)$$

where the subscripts s and h correspond to the "soft" mode at 337 cm^{-1} and the "hard" mode at 217 cm^{-1}, M_i are the Raman tensor components ($i = s$ or h), $G_i = (\nu - \nu_i - id_i)^{-1}$ are Green's functions of modes ν_s and ν_h with a damping factor of $2d_i$, γ is the interaction constant for the modes, $\chi_i(\nu)$ are the spectral distribution functions for each mode disregarding the interaction, and $\chi_{sh}(\nu)$ is the interference term. The functions $\mathrm{Im}\chi_i(\nu)$ are positive at all frequencies, while the sign of $\mathrm{Im}\chi_{sh}(\nu)$ depends on the signs of M_i and, in addition, is reversed between the frequencies ν_s and ν_h.

It was noted above that the shape of the spectra in Fig. 3 indicates that the tensor components M_s and M_h have opposite signs. The experimental spectra can also be used for determining the damping factors for each mode at any temperature. In order to fit the spectra calculated by formula (3) to the experimental spectra, we must determine interaction constant γ and the temperature dependence of M_i. Disregarding the interaction, we could unambiguously determine the frequencies of both modes ν_s and ν_h for given values of γ and M_i from the coincidence of the peaks for the relative lines in the calculated and experimental spectra. In the course of fitting, we discovered the following circumstances.

In order to obtain an antiresonance in the spectra near 190 cm^{-1} at 570 and 680 K, interaction constant γ must be large (not smaller than 25 cm^{-1}). If we assume that γ has a constant value at all temperatures, the value of M_h must be reduced by a factor of 2.5 (accordingly, the intensity of the 217 cm^{-1} band must be reduced by a factor of $(M_h)^2$) upon heating from room temperature to 680 K for a satisfactory fitting of the relative intensities of modes ν_s and ν_h. The spectra show that the integrated intensity of the band at frequency 337 cm^{-1} (and, hence, component M_s) remains virtually unchanged at all temperatures after the inclusion of the occupancy factor. On the other hand, if we assume that M_h is constant at all temperatures, fitting requires a variation of the interaction constant (its smooth increase with temperature).

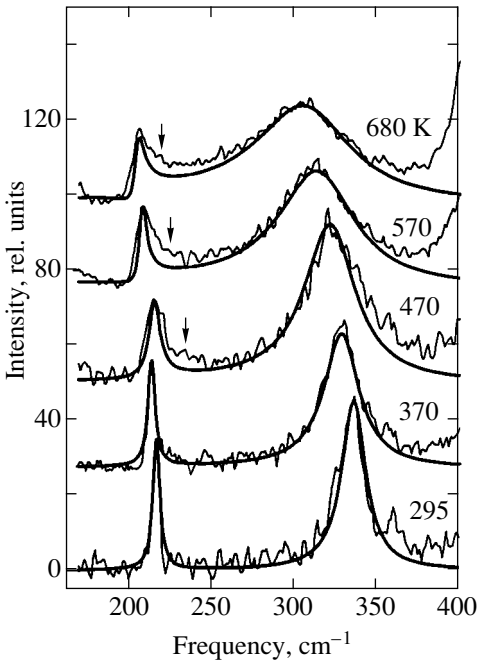

Fig. 5. Comparison of calculated and experimental spectra in the region of interaction between the modes 217 and 337 cm^{-1}.

A γ-Li_3PO_4 crystal is transparent in the visible range, and the Raman spectra excited by a line of 514.5 nm were obtained under nonresonant conditions. For this reason, there are no grounds for such a strong decrease in the intensity of the 217 cm^{-1} line upon heating as compared to other spectral lines. However, the interaction constant may increase with temperature [11] since the frequency of the 337 cm^{-1} mode decreases significantly upon heating (see Figs. 3 and 4), and the position of this mode relative to the two-phonon acoustic continuum responsible for the interaction between modes ν_s and ν_h may change.

The result of fitting the theoretical spectra to the experimental spectra for constant values of M_s and M_h at all temperatures is shown in Fig. 5. In our calculations, we assumed that lines ν_s and ν_h had Lorentz profiles in the absence of the interaction. The line widths were determined from the experimental spectra. The parameters M_s and M_h were determined by fitting the calculated spectrum to the experimental spectrum obtained at room temperature under the assumption that $\gamma = 0$. At other temperatures, parameter γ mainly determined the relative intensities of the interacting modes, while the optimal choice of ν_s and ν_h ensured the coincidence of the peaks of the relevant bands in the calculated and experimental spectra. With increasing temperature, we had to increase the value of γ for fitting the relative intensities of spectral bands (7, 13, 21, and 25 cm^{-1} at 370, 470, 570, and 680 K, respectively). The choice of the value of $\gamma = 0$ at room temperature was arbitrary. If we assume that $\gamma = \gamma_0 \neq 0$ at room tempera-

ture, the values of γ at other temperatures must be increased by γ_0.

A satisfactory agreement between the calculated and experimental spectra can be reached for temperatures 295 and 370 K. At temperatures above 370 K, the contribution from the intense 424 cm^{-1} line increases, and a discrepancy between the calculated and experimental spectra appears in the frequency range 200–250 cm^{-1} (shown by the arrow in Fig. 5). We can assume that, as in the case of Raman spectra for $AlPO_4$ [12], an additional band emerging in the frequency range 200–250 cm^{-1} upon an increase in temperature, i.e., for ν_s approaching ν_h, is associated with two-phonon acoustic states, which have been enhanced as a result of resonance with the approaching vibration ν_s. This additional contribution, which was disregarded in fitting, could also affect the interference in this frequency range. It can be seen from Fig. 4 that the inclusion of the interaction does not significantly change the position of modes ν_s and ν_h below 500 K, and the difference in these positions becomes noticeable only above 500 K due to a decrease in the separation between the modes and an increase in the constant of interaction of these modes.

We did not observe interference phenomena in the spectra of vibrations B_{1g} and B_{3g} upon heating approximately to 700 K. The spectrum of A_g vibrations (in the $y(xx)z$ geometry) displayed an antiresonance in the vicinity of 190 cm^{-1} due to the interference of phonons with frequencies 219 and 284 cm^{-1}. The 284 cm^{-1} line was displaced upon heating towards lower frequencies, broadened considerably, and overlapped with the 219 cm^{-1} line. However, the band profiles were less reliable for numerical analysis in view of low intensities of the interacting modes.

Thus, we have described for the first time the Raman spectra of a γ-Li_3PO_4 crystal in various polarizations, which enables us to classify the observed spectral lines according to the types of vibrations and to separate the vibrations of PO_4 tetrahedrons and of the lithium sublattice. Temperature analysis of the spectra revealed the interference of one-phonon states of the lithium sublattice, associated with anharmonic interaction between optical and acoustic phonons. The exponential increase in the cation conductivity with temperature [1] enhances anharmonic movements of lithium ions and, hence, the interaction between the optical phonons associated with vibrations of lithium ions and acoustic modes. Analysis of the spectra revealed a strong temperature dependence of the constant of optical phonon interaction, which can be assigned, in all probability, to an increase in conductivity with temperature as well as a change in the position of interacting modes relative to the two-phonon acoustic continuum, which is responsible for the interaction of optical modes.

REFERENCES

1. A. K. Ivanov-Shits, V. V. Kireev, O. K. Mel'nikov, and L. N. Dem'yanets, Kristallografiya **46**, 938 (2001) [Crystallogr. Rep. **46**, 864 (2001)].
2. E. B. De Araujo, J. A. C. De Paiva, J. A. Freitas, and A. S. B. Sombra, J. Phys. Chem. Solids **59**, 689 (1998).
3. T. Riedener, Y. Shen, R. J. Smith, and K. L. Bray, Chem. Phys. Lett. **321**, 445 (2000).
4. O. S. Bondareva, M. A. Simonov, and N. V. Belov, Dokl. Akad. Nauk SSSR **240**, 75 (1978) [Sov. Phys. Dokl. **23**, 287 (1978)].
5. O. V. Yakubovich and V. S. Urusov, Kristallografiya **42**, 301 (1997) [Crystallogr. Rep. **42**, 261 (1997)].
6. G. N. Zhizhin, B. N. Mavrin, and V. F. Shabanov, *Optical Vibrational Spectra of Crystals* (Nauka, Moscow, 1984), p. 39.
7. K. Nakamoto, *Infrared Spectra of Inorganic and Coordination Compounds* (Wiley, New York, 1963; Mir, Moscow, 1966), p. 151.
8. A. N. Lazarev, A. P. Mirgorodskiĭ, and I. S. Ignat'ev, *Vibrational Spectra of Complex Oxides* (Nauka, Leningrad, 1975), p. 118.
9. C. Y. She, T. W. Broberg, and D. F. Edwards, Phys. Rev. B **4**, 1580 (1971).
10. M. V. Belousov, D. E. Pogarev, and S. V. Pogarev, in *Oxide Lattice Vibrations* (Nauka, Leningrad, 1980), p. 249.
11. A. Zavadovski and J. Ruvalds, Phys. Rev. Lett. **24**, 1111 (1970).
12. J. F. Scott, Phys. Rev. Lett. **24**, 1107 (1970).
13. V. N. Denisov, B. N. Mavrin, V. B. Podobedov, and J. F. Scott, J. Raman Spectrosc. **14**, 276 (1983).
14. J. L. Servoin, Y. Luspin, and F. Gervais, Phys. Rev. B **22**, 5501 (1980).

Translated by N. Wadhwa

Journal of Experimental and Theoretical Physics, Vol. 96, No. 1, 2003, pp. 59–65.
Translated from Zhurnal Éksperimental'noĭ i Teoreticheskoĭ Fiziki, Vol. 123, No. 1, 2003, pp. 71–78.

SOLIDS
Structure

Hyperfine Interactions in $Sc_{1-x}Y_xFe_2$ Cubic Laves Alloys

V. S. Pokatilov

Moscow State Institute of Radioengineering, Electronics, and Automation (Technical University), pr. Vernadskogo 78, Moscow, 119454 Russia

e-mail: pokatilov@mirea.ru

Received July 15, 2002

Abstract—Effects of hybridization of 3*d* bands of iron with 3*d* bands of scandium and 4*d* bands of yttrium in $Sc_{1-x}Y_xFe_2$ cubic Laves alloys ($0 \le x \le 1$) are studied by the nuclear magnetic resonance method. The concentration dependences of the lattice parameters *a*, saturation magnetization σ, and hyperfine fields at the ^{57}Fe, ^{45}Sc, and ^{89}Y nuclei—as well as the ^{27}Al impurity nuclei, whose atoms substitute iron atoms in the lattices of these alloys—are measured. The "local" and "induced" contributions to hyperfine fields at the ^{57}Fe nuclei are separated and the magnetic moments at iron atoms are estimated. It is found that the hybridization effect leads to the formation of magnetic moments at Sc and Y atoms (whose direction is opposite to the direction of the magnetic moment at iron atoms) and is responsible for the ferrimagnetic structure in $Sc_{1-x}Y_xFe_2$ alloys. © *2003 MAIK "Nauka/Interperiodica".*

1. INTRODUCTION

Alloys of iron with rare earth elements of the RFe_2 type, which are know as Laves compounds, have been objects of investigations for many years since these alloys form the basis of many widely used magnetic materials and are of interest for researchers engaged in the study of interactions between atoms of iron and rare earth elements. One of such interactions is the hybridization of 3*d* bands of iron atoms and 3*d* bands of scandium atoms in these alloys (R = Sc), 3*d* bands of iron atoms and 4*d* bands of atoms R = Y, Zr, Nb, Mo, and 3*d* bands of iron atoms and 5*d* bands of atoms in Laves alloys RFe_2 (R = Ce–Lu) [1–7]. It was shown in [1–7] that hybridization leads to the formation of magnetic moments at Sc, Y, Zr, and Nb atoms, which are directed oppositely to the magnetic moment of iron atoms, and to the ferrimagnetic structure in such alloys. In the Laves compound of iron with R atoms (Ce, Gd, Tb, and Lu) containing 4*f* 5*d* electrons, the hybridization of 3*d* bands of iron and 5*d* bands of R atoms leads to the formation of an additional negative magnetic moment at rare earth atoms (in addition to the magnetic moment due to 4*f* electrons [6, 7]). However, the experimental facts confirming the emergence of negative magnetic moments at R atoms are scarce. The magnetic moments at rare earth atoms in RFe_2 compounds (R = Y, Zr, Ce, Lu) were detected and measured by the method of polarized neutrons in [8–11], while the NMR method was used for the same purpose in the case of R = Sc, Y, Zr, Ce, Lu, Gd [12–15]. It was shown that, in accordance with theoretical calculations, these alloys have a ferrimagnetic structure, and the magnetic moments μ(R) at R atoms, which were measured by these two methods, are in good agreement (if we take into account the peculiar features of these methods). The effect of hybridization of 3*d* bands of iron and *d* bands of rare earth atoms in ternary Laves alloys with various rare earth atoms $(R_{1-x}R'_x)Fe_2$ has not been investigated comprehensively. Only one publication [15] is devoted to the study of the hybridization effects in Laves alloys $(Sc,Zr)Fe_2$ using the NMR method. It was proved that negative magnetic moments are formed at lattice sites occupied by scandium and zirconium atoms and their concentration dependence was measured.

This work aims at an analysis of the hybridization of 3*d* bands of iron with 3*d* bands of scandium and 4*d* bands of yttrium in $Sc_{1-x}Y_xFe_2$ ternary Laves alloys with a cubic structure in the concentration range $0 \le x \le 1$. The hybridization effect may lead to a change in the magnetic moments at iron atoms the emergence of magnetic moments at rare earth atoms, and a change in the hyperfine fields at the nuclei, which are determined to a considerable extent by the magnetic moments at magnetic atoms. In order to detect this effect, we measured the hyperfine fields (by the NMR method) at ^{57}Fe, ^{45}Sc, and ^{89}Y nuclei as well as at ^{27}Al impurity nuclei (with a concentration less than 1 at.%), whose atoms substitute iron atoms in these compounds.

At present, the following information concerning the $(Sc,Y)Fe_2$ system is known from the literature. Analysis of the electronic structure has proved that the hybridization effect leads to the emergence of magnetic moments at Sc atoms in $ScFe_2$ (with a hexagonal structure of the $MgZn_2$ type) [1, 4] and at Y atoms in YFe_2 [2–4], whose direction is opposite to the direction

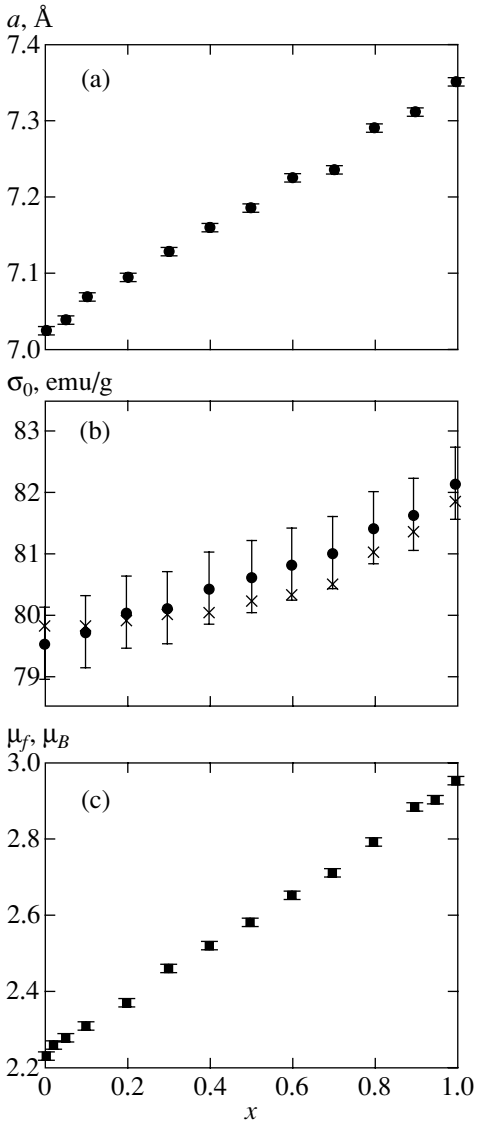

Fig. 1. Concentration dependences of (a) lattice parameters a at 293 K, (b) magnetization σ (77 K) (crosses correspond to $Sc_{1-x}Y_xFe_{1.97}Al_{0.03}$ and circles to $(Sc,Y)Fe_2$), and (c) magnetic moment μ_f per structural unit of the compound.

of the magnetic moment μ(Fe) at iron atoms. For $ScFe_2$, it was found that $\mu(Fe_1) = 1.54\mu_B$, $\mu(Fe_2) = 1.60\mu_B$ (there exist two nonequivalent crystallographic states of iron in the $ScFe_2$ compound with a hexagonal structure of the $MgZn_2$ type), and $\mu(Sc) = -0.52\mu_B$, while for YFe_2, $\mu(Fe) = 1.71\mu_B$ and $\mu(Y) = -0.49\mu_B$. The magnetic moments of iron and yttrium were also measured by the method of polarized neutrons in the YFe_2 alloy: $\mu(Fe) = (1.77 \pm 0.08)\mu_B$ and $\mu(Y) = (-0.67 \pm 0.04)\mu_B$ [8]. The magnetic moments at iron, scandium, and yttrium atoms in $ScFe_2$ (with a cubic structure of the $MgCu_2$ type) and YFe_2 alloys were estimated in [12–14] using the NMR method. For the $ScFe_2$ compound, it was found that $\mu(Fe) = 1.56\mu_B$ and $\mu(Sc) = -(0.97 \pm 0.05)\mu_B$, while for YFe_2, $\mu(Fe) = 1.71\mu_B$ and $\mu(Y) = -(0.52 \pm 0.05)\mu_B$.

2. SAMPLES AND MEASURING TECHNIQUE

Ingots of $Sc_{1-x}Y_xFe_2$ and $Sc_{1-x}Y_xFe_{1.97}Al_{0.03}$ alloys weighing 5–7 g were made of high-purity metals in highly pure argon atmosphere in an argon-arc furnace. The ingots in the argon atmosphere were crushed and pressed into pellets, after which they were remelted. This procedure was repeated three times to obtain homogeneous samples. The samples were not subjected to thermal treatment to avoid the formation of second phases in $ScFe_2$ due to polymorphism, typical of such alloys [16]. Yttrium was added to $ScFe_2$ in amounts ≥2 at.% to stabilize the cubic structure of $ScFe_2$ and to prevent polymorphic transformations in this compound. The cubic structure of $ScFe_2$ alloys was also ensured by an excess of scandium (3.5 at. %) relative to the stoichiometric Sc concentration, which was created during the manufacture of this alloy as described in [16]. The specimens were in the form of powders with a particle size less than 70 μm, which were prepared in an argon atmosphere. The crystal structure of the alloys and the lattice parameter were measured using X-ray radiography at room temperature. The chemical and plasma-spectroscopic analyses showed that the specimens had preset compositions to within 0.2 at. %. The saturation magnetization σ was measured at 77 K in magnetic fields up to 15 kOe on a vibrating-coil magnetometer with a compensating coil. The error in the measurements of σ was determined from the spread in the values of magnetization measured on four specimens for each composition and was less than 2%. The NMR spectra were measured at 4.2 K by the pulsed NMR method from points in the frequency range 10–130 MHz using an amplification gauge in amplifier blocks and measuring the amplitude of high-frequency pulses exciting an echo signal at each point of the NMR spectrum. The experimental conditions of the nuclear spin echo excitation and measurement of the frequency dependence $A(f)$ of echo amplitudes were such that $A \propto f^2$.

3. EXPERIMENTAL RESULTS

Figure 1 shows the concentration dependences of the lattice parameters a at room temperature, the saturation magnetization σ at 77 K, and the magnetic moments (per structural unit) μf, calculated from σ, for $(Sc,Y)Fe_2$ alloys. It can be seen from the figures that the replacement of a scandium atom (with outer $3d^14s^2$ electrons) by yttrium atoms (with outer $4d^15s^2$ electrons) with the same number of outer d and s electrons in the system leads to considerable changes in the lattice parameters a and the magnetic moments μ_f of the compounds under investigation.

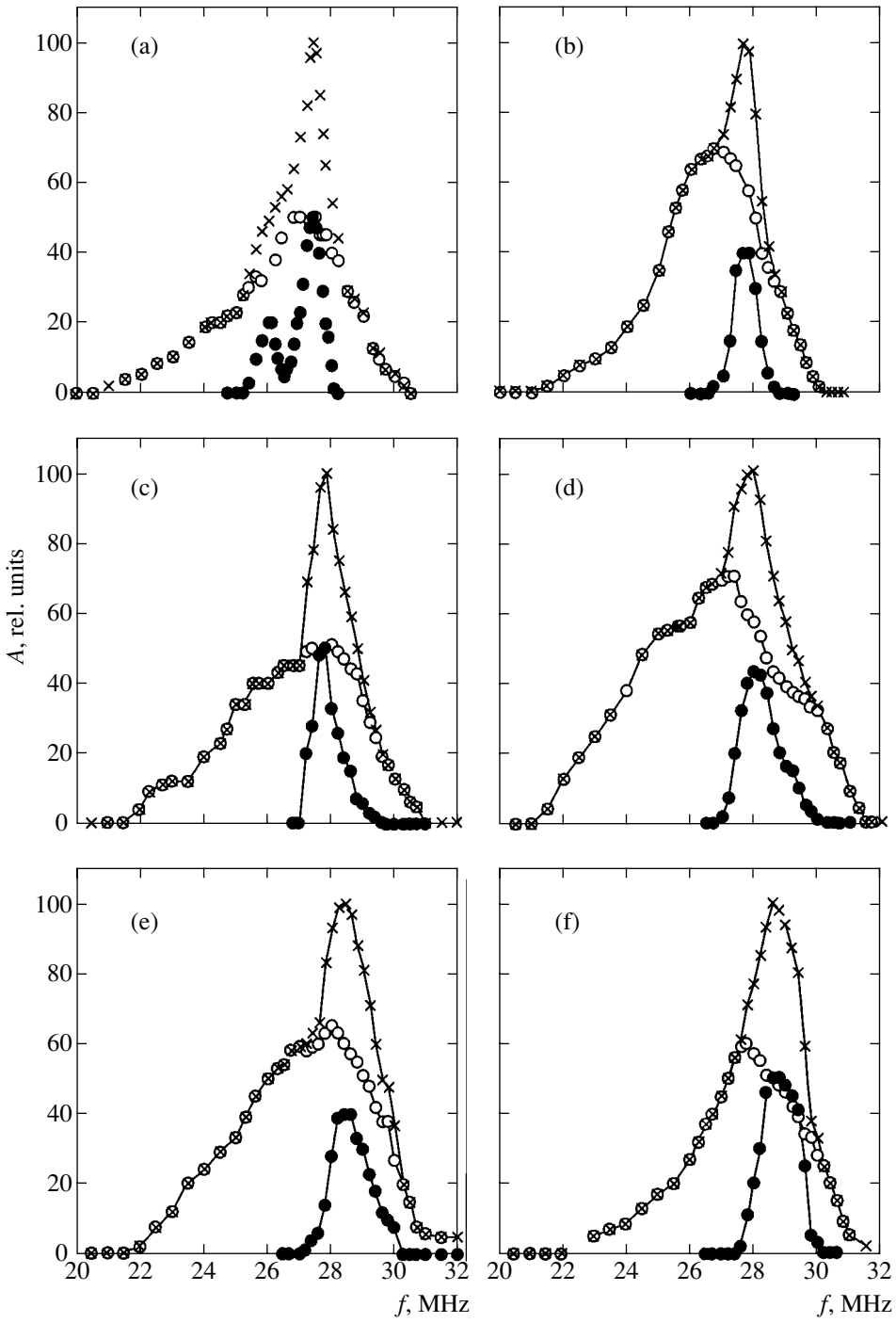

Fig. 2. NMR spectra at the ^{57}Fe nuclei (●) in alloys $Sc_{1-x}Y_xFe_2$, at the ^{57}Fe + ^{27}Al nuclei (×), and at the ^{27}Al nuclei (○) in $(Sc_{1-x}Y_x)Fe_{1.97}Al_{0.03}$ alloys at 4.2 K: x = 0 (a), 0.1 (b), 0.3 (c), 0.5 (d), 0.7 (e), and 0.9 (f).

Figure 2 shows the NMR spectra at ^{57}Fe nuclei in these alloys at 4.2 K. The spectra of $ScFe_2$ and YFe_2 alloys are completely identical to analogous spectra obtained in [17, 18] for the given alloys. The NMR spectra of ^{57}Fe nuclei in these compounds display two peaks with an intensity ratio of 1 : 3, which are typical of Laves iron-based alloys with a cubic structure and are due to the existence of two magnetically nonequivalent states of iron atoms in a lattice of the $MgCu_2$ type, when the easy magnetization axis coincides with the ⟨111⟩ direction. For a low yttrium concentration in $ScFe_2$ or, conversely, for a low concentration of scandium in YFe_2, the NMR spectra of ^{57}Fe nuclei are narrow; however, the spectra are broadened slightly in the concentration range $0.2 < x < 0.8$. It should be noted that an iron atom in the first coordination sphere is sur-

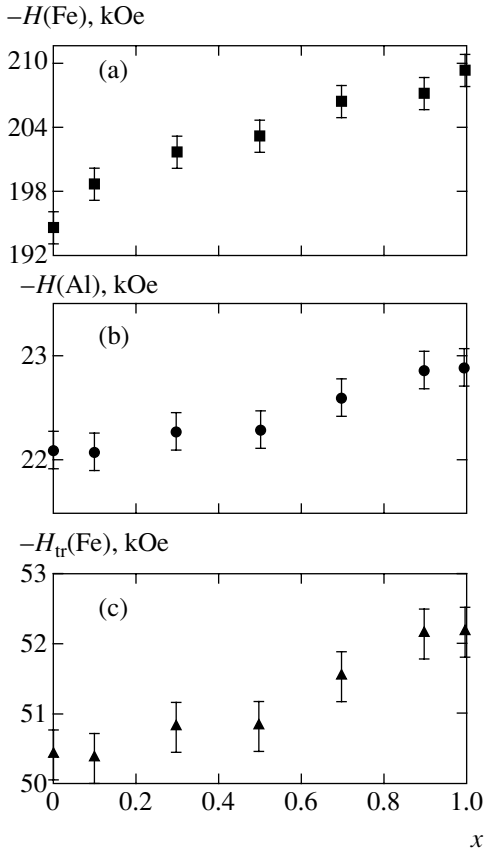

Fig. 3. Concentration dependences of (a) hyperfine fields at ^{57}Fe nuclei, (b) at ^{27}Al nuclei, and (c) induced contribution H_{tr}(Fe) calculated by formula (3) for $(Sc_{1-x}Y_x)Fe_2$ alloys.

rounded by six iron atoms, 6Fe, while the second coordination sphere has six positions occupied by scandium and/or yttrium atoms, i.e., 6(Sc,Y). Figure 3a shows mean hyperfine fields H(Fe) at ^{57}Fe nuclei in the (Sc,Y)Fe_2 system. These fields were determined from the average resonance frequencies f_{av}, which in turn were estimated from the center of gravity of the spectra:

$$f_{av} = \int fP(f)df \Big/ \int P(f)df,$$

where $P(f)$ is the distribution of resonance frequencies f shown in Fig. 2.

Figure 2 also shows the NMR spectra measured in the frequency range 20–32 MHz for (Sc,Y)$Fe_{1.97}Al_{0.03}$ alloys. In this frequency range, NMR signals from both the ^{57}Fe nuclei and the ^{27}Al impurity nuclei are observed; consequently, these spectra are formed by the signal from the ^{57}Fe nuclei as well as from the ^{27}Al nuclei. The NMR spectra in (Sc,Y)Fe_2 and (Sc,Y)$Fe_{1.97}Al_{0.03}$ alloys were recorded under identical conditions of echo signal excitation; and echo amplitudes were measured in microvolts with the help of a calibrated rf pulse at each point of the spectrum. A comparison of the NMR spectra of ^{57}Fe and combined spectra from the ^{27}Al and ^{57}Fe nuclei shows that the NMR spectra of the ^{27}Al nuclei are much broader than the NMR spectra of the ^{57}Fe nuclei. The echo amplitudes are normalized per gram of substance. Considering that the echo excitation conditions were the same in the measurements of the NMR spectra at the ^{57}Fe nuclei in (Sc, Y)Fe_2 alloys and the combined NMR spectra at the ^{57}Fe and ^{27}Al nuclei in (Sc,Y)$Fe_{1.97}Al_{0.03}$ alloys and assuming that absolute amplitudes of the echo were measured in each case, the NMR spectrum of the ^{57}Fe nuclei in (Sc,Y)Fe_2 alloys was subtracted from the combined NMR spectra at the ^{57}Fe and ^{27}Al nuclei in (Sc,Y)$Fe_{1.97}Al_{0.03}$ alloys to obtain the NMR spectra of the ^{27}Al impurity nuclei in the alloys under investigation. We assume here that aluminum impurity atoms in an amount smaller than 1 at.% do not perturb the electronic and magnetic properties of the alloys as well as the hyperfine fields at the ^{57}Fe nuclei in (Sc,Y)Fe_2. Figure 2 also shows the NMR spectra of the ^{27}Al impurity nuclei, while Fig. 3b shows the concentration dependence of the mean hyperfine fields, H(Al), at the ^{27}Al nuclei in the Laves compounds investigated here. The H(Al) fields were determined from average resonance frequencies estimated from the centers of gravity of the spectra. It can be seen that the values of mean hyperfine fields at the ^{27}Al impurity nuclei whose atoms substitute iron atoms in the cubic lattice increase with yttrium concentration in the alloy. Aluminum impurity atoms substituting iron atoms in a cubic lattice of the $MgCu_2$ type have the same surroundings as the iron atoms themselves, i.e., 6Fe in the first coordination sphere and 6(Sc,Y) in the second sphere. The H(Al) curve describes the concentration dependence of hyperfine fields induced by the magnetic moments of atoms in the nearest coordination spheres at a site occupied by an iron or aluminum atom.

Figures 4a and 4b show the NMR spectra of the ^{89}Y and ^{45}Sc nuclei, respectively, in (Sc,Y)Fe_2 compounds at 4.2 K. It can be seen that the spectra of these nuclei are narrow for a low yttrium concentration in $ScFe_2$ for small admixtures of scandium in YFe_2. The NMR spectra at the ^{45}Sc and ^{89}Y nuclei become broad for compositions with $0.2 < x < 0.8$. Figure 5 shows the concentration dependences H(Sc) and H(Y) of the mean hyperfine fields at the ^{45}Sc and ^{89}Y nuclei in the $(Sc_{1-x}Y_x)Fe_2$ alloys. These fields were also determined from the average values of resonance frequencies. We assume that the hyperfine fields at the given nuclei are negative in accordance with the sign of the hyperfine field at the ^{45}Sc nuclei in $ScFe_2$ [17] and at the ^{89}Y nuclei in YFe_2 [18]. Our results show that when yttrium atoms substitute scandium atoms in (Sc,Y)Fe_2 alloys, the absolute values of the hyperfine fields at the ^{45}Sc and ^{89}Y nuclei decrease, while the values of these fields increase at the ^{57}Fe nuclei and at the ^{27}Al impurity nuclei whose atoms substitute iron atoms. It should be

noted that scandium or yttrium atoms in the cubic lattice of the RFe_2 alloy contain 12Fe in the first coordination sphere and 4R (R = Sc, Y) in the second sphere.

4. DISCUSSION

Hyperfine fields at the nuclei of magnetic atoms (e.g., at the ^{57}Fe nuclei of iron atoms) contain three main contributions (see, for example, [19]),

$$H(\mathrm{Fe}) = H_{\mathrm{cp}}(\mathrm{Fe}) + H_s(\mathrm{Fe}) + H_{\mathrm{tr}}(\mathrm{Fe}), \quad (1)$$

where H_{cp}(Fe) is the contribution to the hyperfine field from the polarization of *s* electrons from inner shells of an iron atom by the magnetic moment μ(Fe) of the iron atom, H_s(Fe) is the contribution to the hyperfine field from the polarization of the outer *s* electrons by the magnetic moment μ(Fe) of the iron atom, and H_{tr}(Fe) is the contribution to the hyperfine field from the polarization of conduction electrons by the magnetic moments of atoms in the nearest coordination spheres. Here, $H_{\mathrm{tr}}(\mathrm{Fe}) = \sum a_i \mu_i N_i$, where *i* is the number of the coordination sphere, μ_i is the average magnetic moment of magnetic atoms in the *i*th sphere, and N_i is the number of magnetic atoms in the *i*th sphere (for details see, for example, [14]). The first and second contributions to the hyperfine field come from the iron atom at whose nucleus the NMR is observed and are proportional to the magnetic moment μ(Fe) of the iron atom itself; i.e.,

$$H_{\mathrm{cp}}(\mathrm{Fe}) = P_1(\mathrm{Fe})\mu(\mathrm{Fe}), \quad H_s(\mathrm{Fe}) = P_2(\mathrm{Fe})\mu(\mathrm{Fe}),$$

$$H_{\mathrm{cp}}(\mathrm{Fe}) + H_s(\mathrm{Fe}) = P(\mathrm{Fe})\mu(\mathrm{Fe}) = H_{\mathrm{loc}}(\mathrm{Fe}).$$

The hyperfine field at the nucleus of a magnetic atom is usually represented as the sum of two contributions:

$$H(\mathrm{Fe}) = H_{\mathrm{loc}}(\mathrm{Fe}) + H_{\mathrm{tr}}(\mathrm{Fe}), \quad (2)$$

where H_{loc}(Fe) is the so-called local contribution to the hyperfine field and *P*(Fe) is the field at the ^{57}Fe nucleus per Bohr magneton; *P*(Fe) are constants whose values for some *d* elements are estimated in [19]. Formula (1) usually contains two more small contributions, one of which (H_{dip}) is associated with dipole effects and the other (H_{Lor}) is associated with the Lorentz field. The value of H_{dip} in cubic alloys is small. In our analysis, we took into account the contribution from the field H_{Lor}. This field was calculated by using the data on magnetization σ (Fig. 1) and density of the alloys, which were estimated from the lattice parameter *a* (see Fig. 1). The field H_{Lor} varies from 2.1 to 2.3 kOe upon an increase in the yttrium concentration in the alloys from $x = 0$ to $x = 1$. In order to determine the effect of hybridization of the *d* bands of iron with *d* bands of scandium or yttrium in the Laves alloys under investigation, we must estimate the magnetic moments μ(Fe), μ(Sc), and μ(Y) at iron, scandium, and yttrium atoms from the data on hyperfine fields and compare them with the values of μ(Fe) which could be observed at iron atoms in

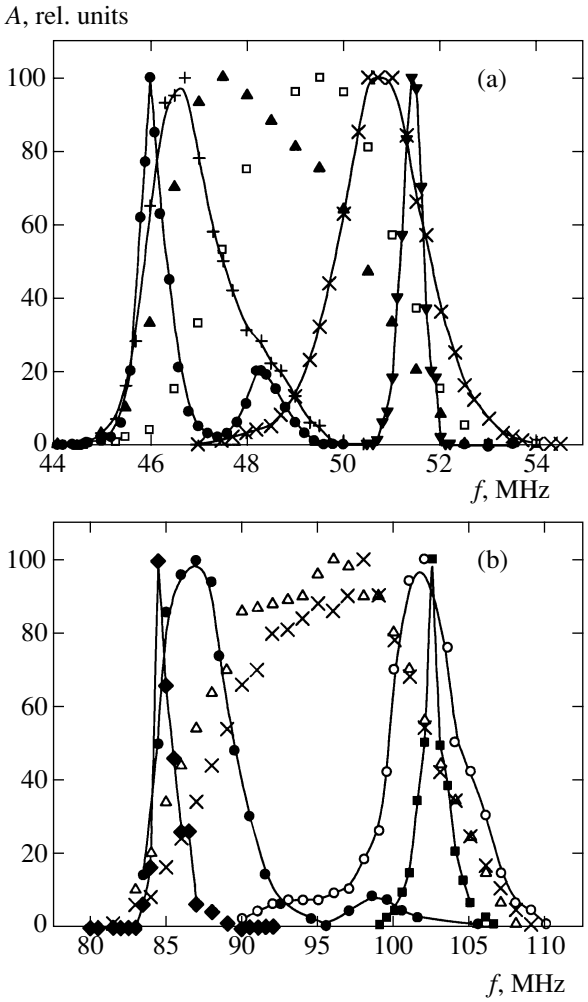

Fig. 4. NMR spectra (a) at ^{89}Y nuclei: $x = 0.1$ (▼), 0.3 (×), 0.5 (□), 0.7 (▲), 0.9 (+), and 0.98 (●); (b) at ^{45}Sc nuclei: 0.1 (■), 0.2 (○), 0.7 (△), 0.5 (×), 0.9 (●), and 0.95 (◆) in $(Sc_{1-x}Y_x)Fe_2$ alloys.

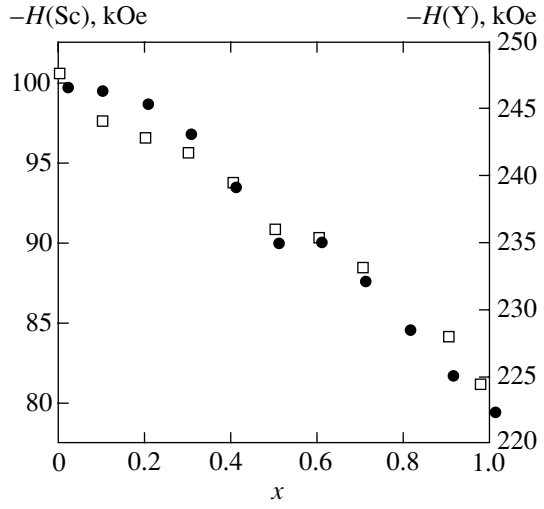

Fig. 5. Concentration dependences of hyperfine fields at ^{89}Y (●) and ^{45}Sc (□) nuclei in $(Sc_{1-x}Y_x)Fe_2$ alloys.

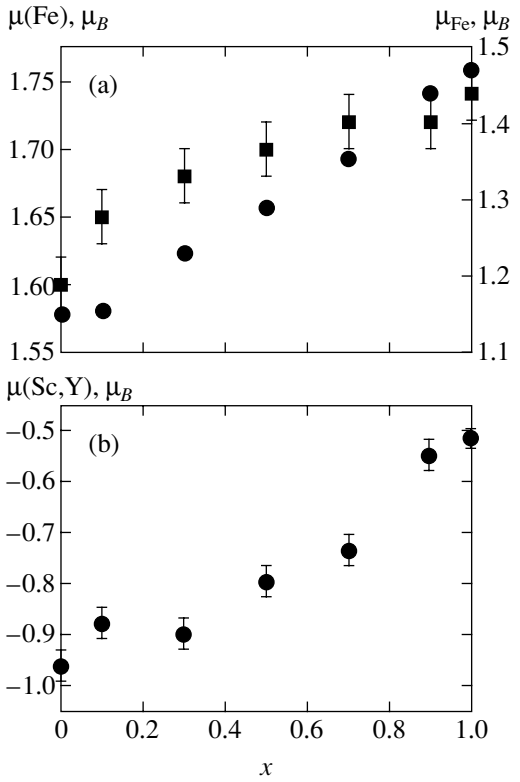

Fig. 6. Concentration dependences of (a) average magnetic moments μ_{Fe} at iron atoms, calculated by the formula $\mu_f = 2\mu_{Fe}$ under the assumption that Sc and Y atoms have zero magnetic moments (●) and magnetic moments μ(Fe) at iron atoms, estimated from the local contribution H_{loc}(Fe) (■); (b) average magnetic moments μ(Sc, Y) at lattice sites occupied by scandium and yttrium atoms in $(Sc_{1-x}Y_x)Fe_2$ alloys.

the absence of hybridization (i.e., when μ(Sc) and μ(Y) are equal to zero). Formula (2) implies that we would be able to evaluate the local magnetic moment at iron atoms from the experimental values of the hyperfine field at the ^{57}Fe nucleus if we could estimate the local contribution H_{loc}(Fe) at the ^{57}Fe nuclei to the experimental hyperfine interaction H(Fe) in formula (2). This is almost impossible at present, and researchers try to estimate the second main contribution, H_{tr}(Fe), to the hyperfine field at the nucleus of a magnetic atom. Two methods exist for estimating H_{tr}(Fe) [14, 20]. The method described in [20] requires knowledge of hyperfine fields at the impurity nuclei of the 3*d* atoms substituting iron atoms in each of the alloys investigated. The second method is described in detail in [14]. It is shown that, in order to estimate the value of H_{tr}(Fe) in iron-based alloys, it is sufficient to use hyperfine fields at impurity nuclei of nonmagnetic atoms of aluminum or copper if aluminum or copper atoms substitute iron atoms in iron-based alloys, including Laves compounds. We measured the hyperfine fields at the ^{27}Al impurity nuclei. According to [14], contribution H_{tr}(Fe) can be estimated from the data on hyperfine fields H(Al) at the ^{27}Al impurity nuclei from the relation

$$H_{tr}(\mathrm{Fe}) = H(\mathrm{Al})A_s(\mathrm{Fe})/A_s(\mathrm{Al}), \qquad (3)$$

where A_s(Fe) and A_s(Al) are the hyperfine interaction constants for iron and aluminum atoms [21]: A_s(Fe) = 1780 kOe per *s* electron and A_s(Al) = 789 kOe per *s* electron. Using the experimental values of hyperfine fields H(Al) at the ^{27}Al nuclei and formula (3), we estimated the induced contributions H_{tr}(Fe) and then the local contributions H_{loc}(Fe) from formula (2). Considering that P(Fe) = –90 kOe [19], we determined the local magnetic moments μ(Fe) at iron atoms in $Sc_{1-x}Y_xFe_2$ alloys; the values of these moments are presented in Fig. 6a. It can be seen from the figure that the substitution of yttrium for scandium in $Sc_{1-x}Y_xFe_2$ compounds increases the magnetic moments μ(Fe) at iron atoms from $1.60\mu_B$ to $1.74\mu_B$. If we assume that the only magnetic atoms in $(Sc,Y)Fe_2$ alloys are iron atoms (i.e., there is no hybridization, and the magnetic moments at scandium and yttrium atoms are equal to zero), then $\mu_f = 2\mu_{Fe}$ and the magnetic moments μ_{Fe} at iron atoms in the system of alloys under investigation vary from $1.11\mu_B$ ($x = 0$) to $1.48\mu_B$ ($x = 1$) (see Fig. 6a). It can be seen that the real values of μ(Fe) differ significantly from μ_{Fe} which would be observed at iron atoms in the absence of the hybridization effect.

Our experimental results show that the magnetic moment μ_f per structural unit, as well as the absolute values of hyperfine fields at the ^{57}Fe nuclei and at the ^{27}Al impurity nuclei whose atoms substitute iron atoms in a lattice of the $MgCu_2$ type, increases when scandium is replaced by yttrium. Consequently, the increase in the hyperfine field at the ^{57}Fe and ^{27}Al nuclei could be explained by an increase in the magnetic moments at iron atoms also in the absence of the hybridization effect. If we assume that scandium and yttrium atoms have zero magnetic moments, the hyperfine fields at the ^{45}Sc and ^{89}Y nuclei should also increase since these atoms are surrounded only by magnetic iron atoms from the nearest coordination spheres, and the hyperfine field at the ^{45}Sc and ^{89}Y nuclei would be determined only by the contribution H_{tr} proportional to the magnetic moments of iron atoms in the nearest coordination spheres. Our experiments show, however, that the absolute values of the hyperfine field at the ^{45}Sc and ^{89}Y nuclei decrease significantly upon the substitution of yttrium for scandium with increasing magnetic moments at iron atoms. These results indicate that scandium and yttrium atoms must possess magnetic moments and, hence, the hyperfine fields at the ^{45}Sc and ^{89}Y nuclei must contain, in addition to the induced fields H_{tr}, significant local fields H_{loc}(Sc) and H_{loc}(Y) due to the intrinsic magnetic moments μ(Sc) and μ(Y).

Systematic data on hyperfine fields at various impurity nuclei of *s* and *p* atoms substituting R atoms in the

RFe_2 Laves alloys have not been obtained either. This does not allow us to estimate the main contributions to the hyperfine field at the nuclei of R atoms in this (or other) system of alloys of a rare earth element with iron. However, we can estimate μ(Sc) and μ(Y) from the experimental data on the magnetic moments μ_f and from the local magnetic moments μ(Fe) at iron atoms estimated above (see Fig. 6a) assuming that $\mu_f = 2\mu(Fe) + \mu(R)$ in RFe_2 Laves alloys. The values of the magnetic moments μ(Sc, Y) at the lattice sites occupied by scandium and/or yttrium atoms calculated in this way are shown in Fig. 6b. It can be seen that the magnetic moments μ(Sc, Y) are negative, i.e., opposite to the magnetic moments of iron atoms. As the yttrium concentration in the alloy increases, the absolute value of μ(Sc, Y) in the alloy decreases from about 1 to $0.5\mu_B$.

Thus, our results proved that compounds $Sc_{1-x}Y_xFe_2$ ($0 \le x \le 1$) exhibit hybridization of the *d* bands of iron with *d* bands of scandium or *d* bands of yttrium. This effect leads to the formation of considerable magnetic moments at scandium and yttrium atoms (these moments being directed oppositely to the magnetic moments of iron atoms) and the formation of a ferrimagnetic structure in these alloys.

REFERENCES

1. Sh. Ishida and S. Asano, J. Phys. Soc. Jpn. **54**, 4688 (1985).
2. P. Mohn and K. Schwarz, Physica B & C (Amsterdam) **130**, 26 (1985).
3. H. Yamada and M. Shimizu, J. Phys. F: Met. Phys. **16**, 1039 (1986).
4. S. Asano and Sh. Ishida, J. Magn. Magn. Mater. **70**, 187 (1987).
5. K. Terao and M. Shimizu, Phys. Status Solidi B **139**, 485 (1987).
6. M. S. S. Brooks, O. Eriksson, and B. Johansson, J. Phys.: Condens. Matter **1**, 5861 (1989).
7. M. S. S. Brooks, L. Nordstom, and B. Johansson, J. Appl. Phys. **69**, 5683 (1991).
8. C. Ritter, J. Phys.: Condens. Matter **1**, 2765 (1989).
9. S. J. Kennedy, P. J. Brown, and B. R. Coles, J. Phys.: Condens. Matter **5**, 5169 (1993).
10. D. Givord, A. R. Gregory, and J. Schweizer, J. Magn. Magn. Mater. **15–18**, 293 (1980).
11. P. Warren, J. B. Forsyth, G. J. McInture, and N. Bernhoeft, J. Phys.: Condens. Matter **4**, 5795 (1992).
12. V. S. Pokatilov, Metallofizika (Kiev) **11**, 51 (1989).
13. V. S. Pokatilov, Zh. Éksp. Teor. Fiz. **93**, 944 (1987) [Sov. Phys. JETP **66**, 531 (1987)].
14. V. S. Pokatilov, J. Magn. Magn. Mater. **189**, 189 (1998).
15. V. S. Pokatilov, V. V. Golikova, and E. F. Sidokhin, Zh. Éksp. Teor. Fiz. **95**, 2079 (1989) [Sov. Phys. JETP **68**, 1202 (1989)].
16. *Handbook: State Diagrams of Binary and Multicomponent Systems Based on Iron* (Metallurgiya, Moscow, 1986), p. 81.
17. V. S. Pokatilov, V. V. Sadchikov, E. F. Sidokhin, and O. V. Utenkova, Fiz. Met. Metalloved. **62**, 69 (1986).
18. A. Oppelt and K. H. J. Buschow, Phys. Rev. B **13**, 4998 (1976).
19. M. B. Stearns, Phys. Rev. B **4**, 4081 (1971).
20. J. Boysen, A. Heidari, and A. Brewer, J. Magn. Magn. Mater. **59**, 15 (1986).
21. I. A. Campbell, J. Phys. C **2**, 1338 (1969).

Translated by N. Wadhwa

Journal of Experimental and Theoretical Physics, Vol. 96, No. 1, 2003, pp. 66–77.
Translated from Zhurnal Éksperimental'noĭ i Teoreticheskoĭ Fiziki, Vol. 123, No. 1, 2003, pp. 79–91.

SOLIDS
Structure

The Effective Properties of Macroscopically Nonuniform Ferromagnetic Composites: Theory and Numerical Experiment

A. A. Snarskii[a, *], M. V. Shamonin[b], and M. I. Zhenirovsky[a]

[a]*National Technical University, Kiev, 03056 Ukraine*
[b]*H. ROSEN Engineering GmbH, D-49811 Lingen* (*Ems*), *Germany*
**e-mail: asnar@yandex.ru*

Received August 5, 2002

Abstract—Various theoretical models (self-consistent field, local linearization, and percolation theory methods and an analytic solution of the linear problem for an ordered medium) for calculating the magnetostatic properties of two-phase composites containing one ferromagnetic phase were considered. The concentration and field dependences of the effective magnetic permeability were found. A method for determining the coercive force and remanent magnetization as functions of the ferromagnetic phase concentration was suggested. Numerical experiments were performed for composites with a periodic distribution of circular inclusions. The results were compared with the analytically calculated effective magnetic permeability. © *2003 MAIK "Nauka/Interperiodica".*

1. INTRODUCTION

The magnetic properties of composites containing ferromagnetic inclusions have been studied in many experimental and theoretical works (e.g., see [1–6]). They are of interest because the potentialities of pure (single-phase, uniform, and homogeneous) materials have to a substantial extent been exhausted. An important role in creating new materials is played by macroscopically nonuniform media, whose properties can be controlled in fairly wide ranges [7].

Composites with the required combination of properties not characteristic of pure phases can in certain instances be synthesized depending on the structure, the concentration, and the local properties of the phases. Such materials are extensively used in various electrotechnical applications. For instance, soft magnetic powder composites combining the ferromagnetic properties of metal particles and elasticity of polymeric (nonmagnetic) matrices are used as screening elements in wideband communication systems.

The primary goal of a theoretical description of any composite material is the determination of the dependences of its effective properties on the concentrations of the phases, the geometric characteristics of phase distribution, and phase local physical properties.

In this work, we consider the effective properties of two-phase composites one phase of which is ferromagnetic, $\mathbf{B} = \mu_1(\mathbf{H})\mathbf{H}$, and the second one is some linear medium, $\mathbf{B} = \mu_2\mathbf{H}$ (this is usually a polymeric matrix with $\mu_2 = \mu_0 = 4\pi \times 10^{-7}$ H m^{-1}). In such composites [1], complex nonlinear dependences of the response of the whole sample to applied magnetic fields and sharp concentration dependences of the effective coefficients related to their percolation behavior are observed. The specified peculiarities make calculations of the effective properties of a composite a very complex problem of theoretical physics, which can be solved either for a simple geometric arrangement of phases (layers or ordered balls) or in certain approximations, whose applicability limits are difficult to estimate.

Apart from the difficulties mentioned above, magnetic composites are characterized by at least two distinguishing features fundamental in character.

The first is specific nonlinearity of local magnetic permeability (Fig. 1). Depending on the local magnetic field strength, the magnetic permeability of the ferromagnetic phase can be of the order of, or much larger than, the magnetic permeability of the nonmagnetic phase. The permeability ratio (the nonuniformity parameter) varies from about one to a thousand. Magnetic field values in a nonuniform medium can be substantially different in different regions, and nonuniformity parameters are therefore also fairly different. This means that, generally, such a two-phase medium can be considered neither weakly nor strongly nonuniform.

In certain instances, we cannot ignore hysteresis in the magnetic phase. It is shown below that a theoretical description of such composites should include phenomena similar to thermoelectric (that is, systems with two thermodynamic forces, electric field and temperature gradient, and two fluxes, current density and heat flow density, should be considered).

Of the diverse structures of two-phase media which are uniform in the mean, two structures will be consid-

ered. This is, first, a randomly nonuniform medium, in which the arrangement of none of the phases can be considered determining. A discrete model of such a structure that ignores the shape of inclusions is a mesh with nodes (or bonds) having the properties of the first and second phases. Structures of the second type are media with periodically distributed inclusions of one of the phases in the matrix of the other. The phases cannot then be considered geometrically equivalent; figuratively, black spheres in a white medium and white spheres in a black medium do not transform into each other under changes in concentration.

The effective properties of randomly nonuniform media for which hysteresis can be ignored are considered in Section 2.1. A method for calculating the effective coefficients and coercive force of a randomly nonuniform ferromagnetic composite is suggested in Section 2.2. The effective properties of a two-dimensional composite with periodically distributed circular inclusions are studied in Section 3. For determining them, we must solve Maxwell equations combined with material balance equations for one unit cell and perform averaging. The numerical simulation results are given in Section 4. We use the finite element method, which has recently become the main instrument in mathematical simulations of engineering and fundamental electromagnetism problems (e.g., see [8, 9]). The advantages of the finite element method over alternative numerical methods for solving partial derivative equations (finite difference and boundary element methods) is the simplicity of modeling complex boundaries, simple generalization to approximations of higher orders, effective discretization, and the use of sparse matrices.

2. RANDOMLY NONUNIFORM DISORDERED MEDIA

2.1. A Ferromagnetic Phase with a Zero Hysteresis Loop

The most important characteristic of nonuniform media is the effective kinetic coefficients. In the problem under consideration, these are effective magnetic permeability μ_{eff} and effective reluctance λ_{eff}, which, by definition, relate volume-average magnetic field strength $\langle \mathbf{H} \rangle$ to volume-average magnetic induction $\langle \mathbf{B} \rangle$,

$$\langle \mathbf{B} \rangle = \mu_{eff} \langle \mathbf{H} \rangle, \quad \langle \mathbf{H} \rangle = \lambda_{eff} \langle \mathbf{B} \rangle, \tag{1}$$

where $\langle \ldots \rangle = V^{-1} \int \ldots dV$ denotes averaging over volume V. It is assumed that the averaging dimension (on the order of $V^{1/3}$) is in all directions many times larger than the correlation radius; that is, self-averaging occurs in such a system, and the effective kinetic coefficient values do not depend on the particular realization of a random distribution of phases.

The approximation that can most successfully be used to calculate the effective kinetic coefficients in

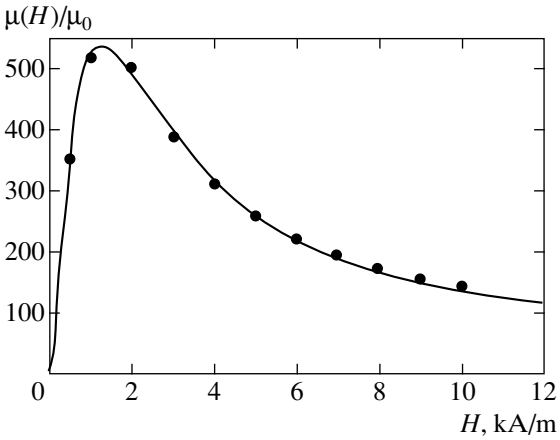

Fig. 1. Magnetic field dependence of relative permeability in a nonlinear ferromagnetic phase; closed circles are permeabilities for a particular material, and the solid line corresponds to the analytic function (see Appendix) approximating the experimental values.

nearly the whole concentration range, taking into account the influence of inclusions of one phase on the other, is the Bruggeman–Landauer self-consistent field approximation (effective medium theory) [10, 11]. A large number of effective medium theory variants can be found in [12]. In the linear case, this theory gives a good approximation for all concentrations and all ratios between local kinetic coefficients except the immediate vicinity of the percolation threshold at large nonuniformity values. In the nonlinear case, this approximation is inapplicable and should be generalized. One of such generalizations is suggested in [13, 14] and applied to power-type nonlinearity (so-called strong nonlinearity [15, 16]).

Let us calculate λ_{eff}. According to the key approximation of the method suggested in [13, 14], local field $\mathbf{B}$ within inclusions is considered independent of the coordinates (this is only valid for elliptically shaped inclusions and only when interaction between inclusions can be ignored), and the λ value in the nonlinear phase, $\lambda_1 = \lambda_1(\mathbf{B})$, is replaced by constant $\tilde{\lambda}_1$,

$$\tilde{\lambda}_1 = \langle \lambda_1(\mathbf{B}) \rangle_1, \tag{2}$$

where averaging is performed over the nonlinear phase volume, $\langle \ldots \rangle = (1/V_1) \int_{V_1} \ldots dV$.

The second approximation is a replacement which, in terms of the present work, has the form

$$\tilde{\lambda}_1 = \langle \lambda_1(\mathbf{B}) \rangle_1 \longrightarrow \lambda_1(\sqrt{\langle \mathbf{B}^2 \rangle_1}). \tag{3}$$

The two-phase medium with coefficients $\lambda_1(\mathbf{B}(\mathbf{r}))$ and $\lambda_2 = 1/\mu_0$ (the second phase is nonmagnetic) is replaced by a two-phase medium with $\lambda_1(\sqrt{\langle \mathbf{B}^2 \rangle_1})$ and λ_2, that is, a medium in which the local λ_1 value is independent of local field $\mathbf{B} = \mathbf{B}(\mathbf{r})$. At a given external field $\langle \mathbf{B} \rangle$, the

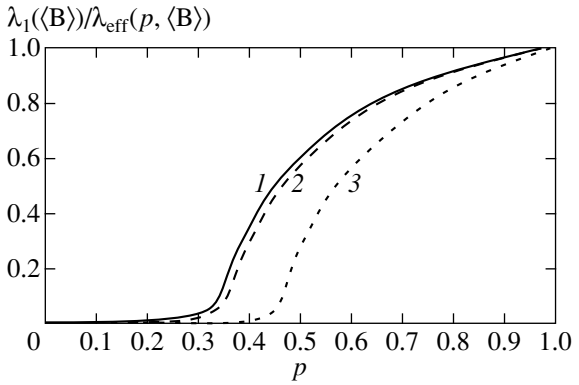

Fig. 2. Dependence of effective reluctance λ_{eff} on the ferromagnetic phase concentration at different values of magnetic induction $\langle \mathbf{B} \rangle$ applied to the sample: (*1*) 0.15, (*2*) 0.2, and (*3*) 0.5 T.

whole first phase has the same coefficient $\lambda_1 = \tilde{\lambda}_1$ determined by the $\langle \mathbf{B}^2 \rangle_1$ value.

It follows that, on the one hand, we can use the standard effective medium theory approximation to determine λ_{eff} of a two-phase medium with coefficients $\tilde{\lambda}_1$ and λ_2,

$$\lambda_{\text{eff}}^{(3D)} = \frac{1}{2}\Big\{(3p-2)\tilde{\lambda}_1 + (1-3p)\lambda_2 + \sqrt{[(3p-2)\tilde{\lambda}_1 + (1-3p)\lambda_2]^2 + 8\lambda_2\tilde{\lambda}_1}\Big\}, \quad (4)$$

where p is the concentration of the ferromagnetic phase. On the other hand, the $\langle \mathbf{B}^2 \rangle_1$ value can be found using the equality $\langle \mathbf{B} \cdot \mathbf{H} \rangle = \langle \mathbf{B} \rangle \cdot \langle \mathbf{H} \rangle$ (e.g., see [17]). According to this equality,

$$\lambda_{\text{eff}} \langle \mathbf{B} \rangle^2 = p\lambda_1 \langle \mathbf{B}^2 \rangle_1 + (1-p)\lambda_2 \langle \mathbf{B}^2 \rangle_2,$$

where $\langle \ldots \rangle_{1,2}$ denotes averaging over the first or second phase. Eventually,

$$\langle \mathbf{B}^2 \rangle_1 = \frac{\langle \mathbf{B} \rangle^2}{p} \frac{\partial \lambda_{\text{eff}}}{\partial \tilde{\lambda}_1}. \quad (5)$$

In the two-dimensional case, (4) is replaced by

$$\lambda_{\text{eff}}^{(2D)} = \frac{1}{2}\Big\{(2p-1)(\tilde{\lambda}_1 - \lambda_2) + \sqrt{[(2p-1)(\tilde{\lambda}_1 - \lambda_2)]^2 + 4\lambda_2\tilde{\lambda}_1}\Big\}. \quad (6)$$

Substituting (4) or (6) into (5) yields a nonlinear equation for determining $\langle \mathbf{B}^2 \rangle_1$. Using the obtained $\langle \mathbf{B}^2 \rangle_1$ value in (4) or (6), we obtain λ_{eff} as a function of external magnetic field $\langle \mathbf{B} \rangle$, concentration, and nonlinearity function parameters.

Similarly, for μ_{eff}, we have [18, 19]

$$\mu_{\text{eff}}^{(3D)} = \frac{1}{4}\{(3p-1)\tilde{\mu}_1 + (2-3p)\mu_2 + \sqrt{[(3p-1)\tilde{\mu}_1 + (2-3p)\mu_2]^2 + 8\mu_2\tilde{\mu}_1}\}, \quad (7)$$

$$\mu_{\text{eff}}^{(2D)} = \frac{1}{2}\Big[(1-2p)(\mu_2 - \tilde{\mu}_1) + \frac{1}{2}\sqrt{(1-2p)^2(\mu_2 - \tilde{\mu}_1)^2 + 4\mu_2\tilde{\mu}_1}\Big], \quad (8)$$

where $\mu_2 = \mu_0$, and (5) is replaced by a similar equation for $\langle \mathbf{H}^2 \rangle_1$, namely,

$$\langle \mathbf{H}^2 \rangle_1 = \frac{\langle \mathbf{H}^2 \rangle}{p} \frac{\partial \mu_{\text{eff}}}{\partial \tilde{\mu}_1}. \quad (9)$$

The dependence of $(\lambda_{eff}/\lambda_1)^{-1}$ on the concentration of the ferromagnetic phase obtained as described above is shown in Fig. 2. According to this figure, a sharp change (increase) in λ at small $\langle \mathbf{B} \rangle$ values occurs close to the three-dimensional percolation threshold, which equals 1/3 according to the effective medium theory approximation. The concentration at which this increase is observed shifts to the right as $\langle \mathbf{B} \rangle$ increases, which is likely to be an artifact of the method. We were unable to find smooth solutions to the system of nonlinear equations at $\langle \mathbf{B} \rangle$ values higher than 0.5 T. Calculations of μ_{eff} in the three- and two-dimensional cases are performed similarly, see [18, 19] for details. As with λ_{eff}, the concentration dependence curve exhibits a sharp increase in μ_{eff}. In contrast to the problem with λ_{eff}, we were, however, able to find solutions to the system of nonlinear equations for all applied field $\langle \mathbf{H} \rangle$ values.

2.2. A Ferromagnetic Phase with a Nonzero Hysteresis Loop: The Local Linearization Method

If the ferromagnetic phase has a nonzero hysteresis loop, then, generally, neither local and nor effective magnetic permeability can be determined unambiguously. The local magnetic permeability ceases to be single-valued because its value depends on the prehistory of sample magnetization. The problem can therefore be completely solved to determine the effective magnetic permeability and its dependences on $\langle \mathbf{B} \rangle$ and $\langle \mathbf{H} \rangle$ only if the magnetization "history" is known. However, even then (for instance, the sample was first brought to technical saturation, after which demagnetization proceeded along the so-called back of the hysteresis loop, see arrow in Fig. 3), there arises a nonstandard situation with determining effective characteristics. Namely, *B*

remains nonzero at $H = 0$, which is precisely the remanent magnetization effect. We will describe a method for calculating the effective coefficients of a composite when one of the phases has a hysteresis loop. We will also determine the dependence of coercive force H_c (remanent magnetization B_r) of the composite on the ferromagnetic phase concentration and coercive force h_c (remanent magnetization b_r) in this phase.

For definiteness, let us call this method the local linearization method. The method was earlier applied to calculate the effective conduction of strongly nonlinear composites [20].

The first approximation in the local linearization method is the local linearization of the equation

$$\mathbf{H}(\mathbf{r}) = \lambda(\mathbf{B})\mathbf{B}(\mathbf{r}) \tag{10}$$

for a certain induction $\tilde{\mathbf{B}}$ value (Fig. 3). Local nonlinearity (10) at $\mathbf{B} = \tilde{\mathbf{B}}$ is replaced by the linearized dependence

$$\mathbf{H} = \lambda_d(\tilde{\mathbf{B}})\mathbf{B} + \Lambda(\tilde{\mathbf{B}}), \tag{11}$$

where

$$\Lambda(\tilde{\mathbf{B}}) = \mathbf{H}(\tilde{\mathbf{B}}) - \lambda_d(\tilde{\mathbf{B}})\tilde{\mathbf{B}} = [\lambda(\tilde{\mathbf{B}}) - \lambda_d(\tilde{\mathbf{B}})]\tilde{\mathbf{B}} \tag{12}$$

and

$$\lambda_d(\tilde{\mathbf{B}}) = \left.\frac{dH(B)}{dB}\right|_{B=\tilde{B}}. \tag{13}$$

Next, we assume that field $\langle H\rangle$ is brought to values corresponding to technical saturation of the ferromagnetic phase and then decreases. It follows that the medium is situated on the upper backward branch of the hysteresis loop, if the hysteresis loop is considered in the H (abscissa) and B (ordinate) axes.

In determining the effective coefficients for a system obeying laws of type (11), which relate the local field to the induction,

$$\langle\mathbf{H}\rangle = \lambda_e(\langle\mathbf{B}\rangle)\langle\mathbf{B}\rangle + \Lambda_e, \tag{14}$$

we must find the Λ_e value (in a sample with the prehistory under consideration, this value equals the effective coercive force H_c of the whole sample) and calculate λ_e as for systems with a linear law, for instance, the effective medium theory law.

Formally, (14) means that a nonzero field exists in the composite at a zero induction [$\langle\mathbf{B}\rangle = 0$ in (14)]; that is, there exists a factor different from $\langle\mathbf{B}\rangle$ that sustains the field. To determine Λ_e, let us draw an analogy between (11) and a thermoelectric medium,

$$\mathbf{e} = p\mathbf{j} - \frac{\alpha}{\kappa}\mathbf{q}, \tag{15}$$

where α is the thermal electromotive force coefficient, ρ is the specific resistance, κ is the specific heat conductivity, and $\mathbf{q} = -\kappa\nabla T$ is the heat flow. Law (15) is valid at a low thermoelectric Q value ($T\alpha^2/\rho\kappa \ll 1$, where T is the temperature). A comparison of (15) and (14) shows that these laws are similar if $(\alpha/\kappa)\mathbf{q} = \text{const}$ in each phase. As the α/κ ratio is independent of the coordinates in both phases, the $\mathbf{q}$ value should also be so. It is easy to see that this condition can only be satisfied if $\kappa_1 = \kappa_2$. Then,

$$\mathbf{q} = \text{const} \tag{16}$$

for the whole sample. This is the second approximation of the local linearization method.

We assume that condition (16) is satisfied. Equations (11)–(14), which describe a nonlinear medium after local linearization, then coincide with those for the thermoelectric system up to the denotation changes

$$\begin{gathered} -\frac{\alpha}{\kappa}q \longleftrightarrow \Lambda_1, \quad -\frac{\alpha_e}{\kappa}q \longleftrightarrow \Lambda_e, \\ \rho_1 \longleftrightarrow \lambda_d(\tilde{\mathbf{B}}), \quad \rho_2 \longleftrightarrow \lambda_2 = \frac{1}{\mu_0}, \quad \rho_e \longleftrightarrow \lambda_e, \end{gathered} \tag{17}$$

where ρ_e is the effective resistance of a thermoelectric linear system with local relations (15),

$$\langle\mathbf{e}\rangle = \rho_e\langle\mathbf{j}\rangle - \frac{\alpha_e}{\kappa}\mathbf{q}. \tag{18}$$

According to the standard effective medium theory model [21] (also see [22]), the ρ_e and α_e effective coefficients in the three-dimensional case are related as

$$\alpha_e(3D) = p\alpha_1\frac{\rho_e + 2\rho_2}{\rho_e + 2[p(\rho_2 - \rho_1) + \rho_1]}, \tag{19}$$

where ρ_e is the effective specific resistance in a medium with $\rho_1 = \lambda_d$ and $\rho_2 = \lambda_2$. In the effective medium theory approximation, ρ_e is determined from the equation

$$p\frac{\rho_e - \rho_1}{\rho_e + 2\rho_1} + (1-p)\frac{\rho_e - \rho_2}{\rho_e + 2\rho_2} = 0. \tag{20}$$

Determining ρ_e by (20) and substituting it into (19), we obtain α_e. Substituting α_e into (18) and taking into account denotation changes (17) and the equalities $H_c = \Lambda_e$ and $h_c = \Lambda_1$ yields

$$H_c^{(3D)} = h_c p\frac{\lambda_e + 2\lambda_2}{\lambda_e + 2[p(\lambda_2 - \lambda_d) + \lambda_d]}, \tag{21}$$

where, according to (20),

$$\begin{aligned} \lambda_e^{(3D)} &= \frac{1}{2}\{(1-3p)\lambda_2 + (3p-2)\lambda_d \\ &+ \sqrt{[(1-3p)\lambda_2 + (3p-2)\lambda_d]^2 + 8\lambda_d\lambda_2}\} \end{aligned} \tag{22}$$

and h_c is the local coercive force in the ferromagnetic phase.

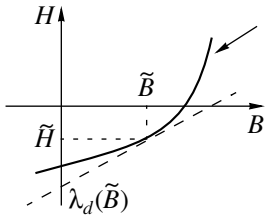

Fig. 3. Illustration for the local linearization method. For each $\tilde{B}$ value, a nonlinear $H = H(B)$ dependence (solid line) is replaced by a linear dependence (dashed line) that intersects the H axis at the point $\lambda_d(\tilde{B})$. The arrow points to the back of the hysteresis loop.

Let us substitute (21) and (22) into (14) and set $\tilde{\mathbf{B}} = \langle \mathbf{B} \rangle$. Taking into account (1), we obtain

$$\lambda_{\text{eff}}^{(3D)} = \frac{p(2\lambda_2 + \lambda_e)(\lambda - \lambda_d)}{2p(\lambda_2 - \lambda_d) + 2\lambda_d + \lambda_e} + \lambda_e. \quad (23)$$

In the two-dimensional problem, (20) and (22) are replaced by

$$p\frac{\rho_e - \rho_1}{\rho_e + \rho_1} + (1-p)\frac{\rho_e - \rho_2}{\rho_e + \rho_2} = 0, \quad (24)$$

$$\lambda_e^{(2D)} = \frac{1}{2}\{(2p-1)(\lambda_d - \lambda_2) + \sqrt{[(2p-1)(\lambda_d - \lambda_2)]^2 + 4\lambda_d\lambda_2}\} \quad (25)$$

and (21) and (23), by

$$H_c^{(2D)} = h_c p\frac{\lambda_e + \lambda_2}{p(\lambda_2 - \lambda_d) + \lambda_d + \lambda_e}, \quad (26)$$

$$\lambda_{\text{eff}}^{(2D)} = \frac{p(\lambda_2 + \lambda_e)(\lambda - \lambda_d)}{p(\lambda_2 - \lambda_d) + \lambda_d + \lambda_e} + \lambda_e. \quad (27)$$

The effective magnetic permeability μ_{eff} and remanent magnetization B_r are calculated quite similarly. We will only give the results of these calculations:

$$\mu_{\text{eff}}^{(3D)} = \frac{p\mu_e(2\mu_e + \mu_0)(\mu - \mu_d)}{2p\mu_e(\mu_d - \mu_0) + 2\mu_0\mu_e + \mu_d\mu_0} + \mu_e, \quad (28)$$

$$\mu_{\text{eff}}^{(2D)} = \frac{p\mu_e(\mu_e + \mu_0)(\mu - \mu_d)}{p\mu_e(\mu_d - \mu_0) + \mu_0(\mu_e + \mu_d)} + \mu_e, \quad (29)$$

$$B_r^{(2D)} = \frac{pb_r\mu_e(\mu_e + \mu_0)}{p\mu_e(\mu_d - \mu_0) + \mu_0(\mu_e + \mu_d)}, \quad (30)$$

$$B_r^{(3D)} = \frac{pb_r\mu_e(2\mu_e + \mu_0)}{2p\mu_e(\mu_d - \mu_0) + 2\mu_0\mu_e + \mu_d\mu_0}, \quad (31)$$

where

$$\mu_e^{(3D)} = \frac{1}{4}[3p(\mu_d - \mu_0) + 2\mu_0 - \mu_d + \sqrt{[3p(\mu_d - \mu_0) + 2\mu_0 - \mu_d]^2 + 8\mu_d\mu_0}], \quad (32)$$

$$\mu_e^{(2D)} = \frac{1}{2}[(2p-1)(\mu_d - \mu_0) + \sqrt{[(2p-1)(\mu_d - \mu_0)]^2 + 4\mu_d\mu_0}], \quad (33)$$

$$\mu_d = \frac{dB(H)}{dH}, \quad (34)$$

b_r is the remanent magnetization in the ferromagnetic phase, and it is taken that $\tilde{\mathbf{H}} = \langle \mathbf{H} \rangle$, as in (23) and (27).

The dependence of coercive force H_c on the concentration of the ferromagnetic phase with local coercive force h_c and the dependence of remanent magnetization B_r on the concentration of the ferromagnetic phase with local remanent magnetization b_r are shown in Figs. 4a and 4b, respectively.

2.3. Ferromagnetic Phase with a Zero Hysteresis Loop Close to the Percolation Threshold

Let us return to the problem of calculating μ_{eff} in the absence of a hysteresis. It should be clearly understood that the generalization of effective medium theory and the local linearization method used above to calculate μ_{eff} contains several serious assumptions [for instance, (3)], which are difficult to justify and whose effect on the final result is not obvious. The use of the percolation theory method is based on the percolation structure model and does not require such assumptions to be made.

As is shown below, the use of percolation theory when local permeability nonlinearity is of the type under consideration (Fig. 1) is only possible under very strict limitations on the problem parameters. Although the region of parameters for which the results of percolation theory are valid is comparatively small, percolation theory allows us to obtain dependences of μ_{eff} free of assumptions of type (3) and thereby to show to what extent these assumptions influence calculation results.

Calculations of μ_{eff} by percolation theory methods will be performed using the percolation structure models [23–28] above the percolation threshold, below this threshold, and at the percolation threshold proper (that is, in the smearing region). Processes that occur in percolation structures are described in many works on percolation theory in terms of current passage. For this reason, we will first obtain all equations in these terms and then use an analogy between the problem of stationary electric current density distributions j in a medium

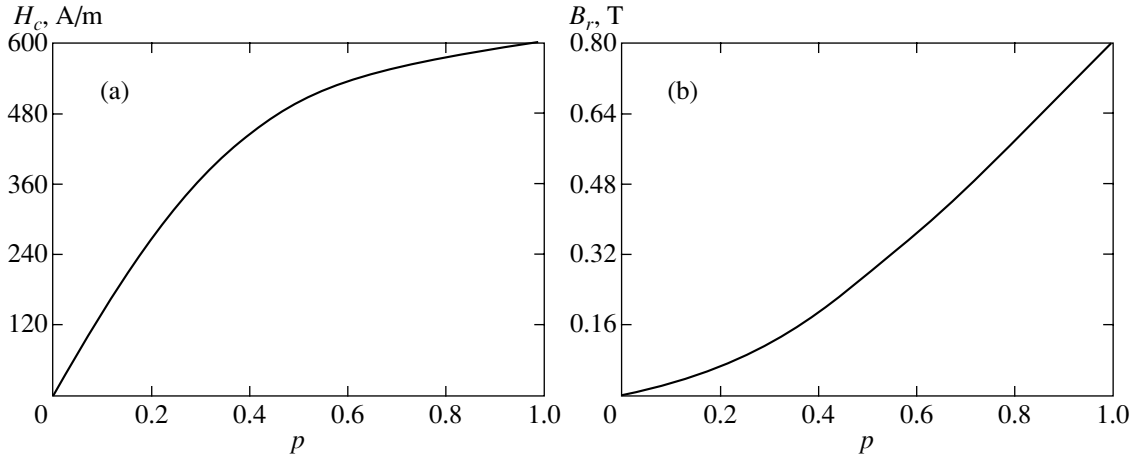

Fig. 4. Dependences of coercive force H_c (a) and remanent magnetization B_r (b) on the concentration of the ferromagnetic phase with (a) local coercive force h_c = 600 A/m and (b) remanent magnetization b_r = 0.8 T.

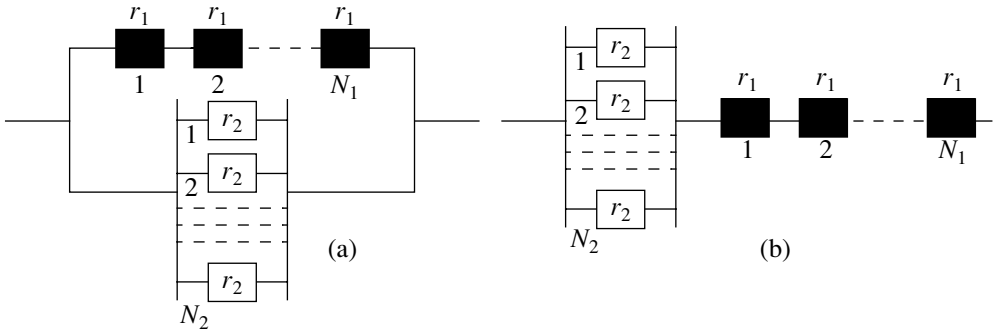

Fig. 5. Hierarchical percolation structure model. The main elements of the structure are (a) above the percolation threshold, a bridge of high-conductivity phase resistances (black resistances) connected in series and (b) below the percolation threshold, an interlayer of low-conductivity phase resistances connected in parallel.

with conductivities σ_1 and σ_2 ($\sigma_1 \gg \sigma_2$) and the problem of stationary magnetic field **B** induction distributions in a medium with magnetic permeabilities μ_1 and μ_2 ($\mu_1 \gg \mu_2$),

$$\begin{gathered}\mathrm{div}\mathbf{B} = 0 \longleftrightarrow \mathrm{div}\mathbf{j} = 0,\ \mathrm{rot}\,\mathbf{H} = 0 \longleftrightarrow \mathrm{rot}\,\mathbf{E} = 0,\\ \mathbf{B} = \mu\mathbf{H} \longleftrightarrow \mathbf{j} = \sigma\mathbf{E},\\ \mathbf{H} = -\mathrm{grad}\psi \longleftrightarrow \mathbf{E} = -\mathrm{grad}\varphi,\\ \mu_1(H) \longleftrightarrow \sigma_1(E),\quad \mu_2 \longleftrightarrow \sigma_2,\end{gathered} \tag{35}$$

where E is the electric field intensity and φ and ψ are the electric and magnetic field potentials, respectively.

First, consider effective magnetic permeability calculations for a randomly nonuniform system above the percolation threshold p_c ($p > p_c$) and outside the smearing region Δ. According to [24–28], the simplest percolation structure model in a volume with characteristic dimensions of the order of the correlation radius ξ, which takes into account the finite $\mu_2/\mu_1 \ll 1$ ratio (the magnetic field "percolates" through the phases with both large and small magnetic permeability values), consists of two elements (Fig. 5). In the "current" terminology, the total current J that percolates through the correlation volume passes (1) a bridge consisting of N_1 resistances of the high-conductivity phase connected in series and (2) an interlayer consisting of N_2 resistances of the low-conductivity phase connected in parallel. The voltage drops across the bridge, $\Delta\varphi_1$, and the interlayer, $\Delta\varphi_2$(=$\Delta\varphi_1$), are written via volume-average field $\langle E\rangle$ as follows:

$$\langle E\rangle\xi = \Delta\varphi = \Delta\varphi_2 = \Delta\varphi_1, \tag{36}$$

where $\Delta\varphi$ is the voltage drop across the correlation volume. We assume that the voltage largely drops on the main percolation structure elements, the bridge and the interlayer. Let a_0 be the minimum size in the system (the characteristic size of nonuniformities). The local fields on the bridge and interlayer can then be written as

$$E_1 = \frac{\Delta\varphi_1}{a_0 N_1},\quad E_2 = \frac{\Delta\varphi_2}{a_0}. \tag{37}$$

Applying the Ohm law $j_1 = \sigma_1(E_1)E_1$ and $j_2 = \sigma_2 E_2$ and using (36) and (37), we can write the currents passing through the bridge and interlayer, J_1 and J_2, in the form

$$J_1 = a_0^2 j_1 = a_0^2 \sigma_1\left(\frac{\xi}{a_0}\frac{\langle E\rangle}{N_1}\right)\frac{\xi}{a_0}\frac{\langle E\rangle}{N_1}, \quad (38)$$

$$J_2 = a_0^2 N_2 j_2 = a_0 N_2 \sigma_2 \xi, \quad (39)$$

where the bridge cross section is taken to be a_0^2 and the field dependence of the second phase is omitted because this dependence is linear ($\mu_2 = \mu_0$). As total current J through the correlation volume is related to volume-average current density $\langle j\rangle$ as $J = \langle j\rangle\xi^2$, and as $J = J_1 + J_2$, we obtain

$$\langle j\rangle = \frac{a_0}{\xi}\frac{\langle E\rangle}{N_1}\sigma_1\left(\frac{\xi}{a_0}\frac{\langle E\rangle}{N_1}\right) + \frac{a_0}{\xi}N_2\sigma_2\langle E\rangle. \quad (40)$$

Correlation length ξ increases as the system approaches the percolation threshold ($p \longrightarrow p_c$) by the law

$$\xi = a_0|\tau|^{-\nu}, \quad \tau = (p - p_c)/p_c, \quad (41)$$

where τ is the closeness to the percolation threshold and ν is the critical correlation length index, $\nu = 0.9$ in the three-dimensional case. The numbers of elements in the bridge and interlayer, N_1 and N_2, increase as p_c is approached by the laws

$$N_1 = |\tau|^{-\alpha_1}, \quad N_2 = |\tau|^{-\alpha_2}, \quad (42)$$

where, according to the percolation structure model [23–28],

$$\alpha_1 = t - \nu, \quad \alpha_2 = q + \nu \quad (43)$$

in the three-dimensional case, in which $t = 2.0$ and $q = 0.7$ are the critical conductivity indices above and below the percolation threshold. Substituting (41)–(43) into (40) yields

$$\langle j\rangle = [\sigma_1(\langle E\rangle\tau^{t-2\nu})\tau^t + \sigma_2\tau^{-q}]\langle E\rangle, \quad (44)$$

where the expression in square brackets is the effective specific conductivity in the nonlinear case.

Passing to the notation of the problem of the relative effective magnetic permeability and substituting numerical critical index values, we obtain

$$\mu_{\text{eff}}^{(3D)}(\langle H\rangle) = \mu_1(\langle H\rangle\tau^{0.2})\tau^2 + \mu_0\tau^{-0.7}. \quad (45)$$

The effective magnetic permeability of a fiber composite across fibers (a two-dimensional problem) is calculated similarly,

$$\mu_{\text{eff}}^{(2D)}(\langle H\rangle) = \mu_1(\langle H\rangle\tau^{t_2-\nu_2})\tau^{t_2} + \mu_0\tau^{-q_2}, \quad (46)$$

where $t_2 = q_2 = 1.33$ and $\nu_2 = 4/3$.

The critical conductivity (t) and correlation length (ν) indices are almost equal in the two-dimensional case, whereas, at not superstrong fields, μ_1 is much larger than μ_0. Equation (46) can therefore be approximately rewritten in the form

$$\mu_{\text{eff}}^{(2D)}(\langle H\rangle) = \mu_1(\langle H\rangle)\tau^{t_2}, \quad (47)$$

which means that the field dependence of $\mu_{\text{eff}}^{(2D)}$ is identical to that for the pure phase and its dependence on the closeness to the percolation threshold is identical to that for a linear composite. Recall that (46) and (47) are only valid in the region of the applicability of percolation theory and outside the smearing region.

The determination of the effective properties of magnetic composites by percolation theory methods below the percolation threshold requires the introduction of the $\lambda_1(B(H)) = 1/\mu_1(H)$ function reciprocal to $\mu_1(H)$. Using the percolation structure models [28] and performing calculations similar to those described above, we obtain

$$\langle H\rangle = \left(\frac{|\tau|^q}{\mu_0} + \lambda_1(\langle B\rangle|\tau|^{-2\nu})|\tau|^{-t}\right)\langle B\rangle \quad (48)$$

for the three-dimensional case and

$$\langle H\rangle = \left(\frac{|\tau|^{q_2}}{\mu_0} + \lambda_1(\langle B\rangle|\tau|^{-\nu_2})|\tau|^{-t_2}\right)\langle B\rangle \quad (49)$$

for the two-dimensional case. Equation (48) determines the $\lambda_{\text{eff}}(\langle B\rangle)$ effective coefficient reciprocal to $\mu_{\text{eff}}(\langle H\rangle)$. As in standard (linear) percolation theory, the equations for the effective coefficients above and below the percolation threshold are valid at $|\tau| \ll 1$, on the one hand, and at $|\tau| > \Delta$, on the other. The latter condition means that the second terms in (45), (46) and in (48), (49) are much smaller than the first ones. It follows that the criterion of percolation description applicability at $p > p_c$ and outside the smearing region, for instance, for the three-dimensional case, can, according to (45), be written as

$$\mu_1(\langle H\rangle\tau^{0.2})\tau^2 > \mu_0\tau^{-0.7}. \quad (50)$$

This condition can be rewritten in the form

$$k_1(\langle H\rangle\tau) > 1, \quad (51)$$

where

$$k_1^{(3D)}(\langle H\rangle\tau) = \mu_1(\langle H\rangle\tau^{0.2})\tau^{2.7}/\mu_0. \quad (52)$$

Similarly, for the two-dimensional case, we have

$$k_1^{(2D)}(\langle H\rangle\tau) = \mu_1(\langle H\rangle\tau^{t_2-\nu_2})\tau^{t_2+q_2}/\mu_0. \quad (53)$$

One more condition of the applicability of percolation theory follows from the requirement of a strong nonuniformity of the local properties of the phases. Only when nonuniformity is substantial can the bridge ($p > p_c$) and interlayer ($p < p_c$) be percolation structure elements that determine the critical behavior of the effective coefficients. At very strong fields, the $\mu_1(H)/\mu_0$ ratio tends to one (the medium becomes uniform) and the condition under consideration therefore means that the local field in the first phase should not be smaller than some H^* value such that $\mu_1(H^*)/\mu_0 \gg 1$. This condition is most important for the field in the bridge, $H_1 = \langle H\rangle\tau^{t-\nu(D-1)}$ [see (37)] ($D = 2$ or 3 for the two- or three-dimensional case, respectively). It follows that the second condition of the applicability of the percolation approach can be written in the form

$$k_2(\langle H\rangle\tau) < 1, \quad (54)$$

where

$$k_2(\langle H\rangle\tau) = \frac{\langle H\rangle}{H^*}\tau^{t-\nu(D-1)}, \quad D = 2, 3. \quad (55)$$

Next, consider the behavior of the effective magnetic permeability at the percolation threshold itself; that is, in the smearing region. The smearing region can be found by equating the first and second terms in (45) and (46) or in (48) and (49). It is easy to see that all variants give (as they must) the same Δ value. The equation for Δ can therefore be written as

$$\mu_1(\langle H\rangle\Delta^{t-\nu(D-1)})\Delta^{t+q}/\mu_0 = 1, \quad D = 2, 3. \quad (56)$$

The Δ smearing region value in the nonlinear problem should and does depend on $\langle H\rangle$. Solving (56) and substituting the result (Δ) into the main term in (45) and (46) yields μ_{eff} in the smearing region,

$$\mu_{\text{eff}}(\langle H\rangle\Delta) = \mu_1(\langle H\rangle\Delta^{t-\nu(D-1)})\Delta^t, \quad D = 2, 3. \quad (57)$$

To compare the results obtained within percolation theory and by the methods of [13, 14] and the local linearization method, consider the dependence of μ_{eff} on $\langle\mathbf{H}\rangle$ above the percolation threshold (Fig. 6). Numerically solving nonlinear equation (56) for the selected $\mu_1(H)$ dependence (see Fig. 4) gives $\Delta \approx 0.1$ at $1000 < \langle H\rangle <$ 4000 A/m. The Δ value increases from 0.1 to 0.15 as $\langle H\rangle$ changes from 4000 to 12000 A/m. Figure 6 shows that the results obtained by all three methods for $\tau = 0.3$ qualitatively coincide. The wavy behavior of μ_{eff} is likely to be an artifact of the local linearization approximation in this region of parameters.

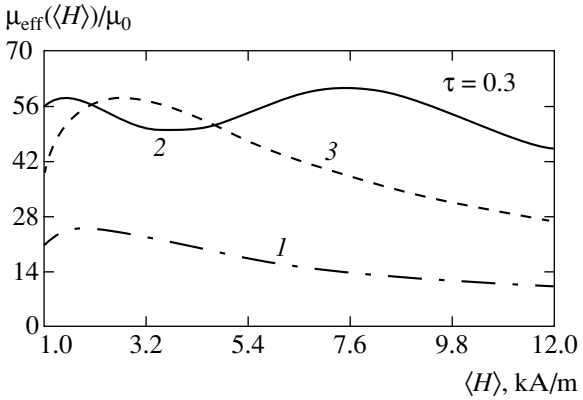

Fig. 6. Dependences of the relative effective permeability on $\langle\mathbf{H}\rangle$ above the percolation threshold, obtained at $\tau = 0.3$ by (*1*) the percolation theory method, (*2*) the local linearization method, and (*3*) the method suggested in [13, 14].

3. NONUNIFORM ORDERED MEDIA

Structures with periodically distributed inclusions are no less interesting objects. They have been extensively studied both theoretically [29–34] and experimentally (e.g., see [6]).

Numerical calculations of local fields and effective media with randomly arranged inclusions are virtually impossible even in the linear case, because it is then necessary to perform calculations for regions whose dimensions exceed the correlation radius, that is, regions containing a large number of inclusions. As inclusions have a certain form (let it be the simplest spherical form), the problem cannot be reduced to a mesh problem; that is, the inclusions cannot be replaced by a set of "shapeless" bonds and nodes, because the shape of inclusions strongly influences the field distribution and, therefore, conductivity. If the inclusions are arranged periodically, it suffices to perform calculations for a single unit cell.

The dependence of the effective magnetic permeability on $\langle H\rangle$ can be found using the solution [29] to the linear problem of the effective conductivity of a medium with periodically arranged inclusions of a circular shape. According to [29], the effective conductivity can be represented with an accuracy of 1% in the form

$$\sigma_e = \sigma_1\left(\alpha - \frac{\pi R^2}{4a^2}\delta\right)\left(\alpha + \frac{\pi R^2}{4a^2}\delta\right)^{-1}, \quad (58)$$

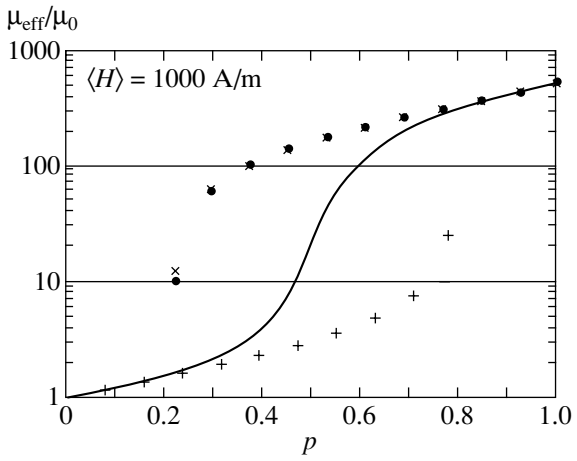

Fig. 7. Differences in the concentration behavior of the relative effective permeability between ordered and random media: the solid curve corresponds to theoretical calculations by the local linearization method with the use of the effective medium approximation for a randomly nonuniform medium, (+) numerical simulation results for ferromagnetic circular inclusions in a nonmagnetic matrix (ordered medium), (×) numerical simulation results for nonmagnetic circular inclusions in a ferromagnetic matrix and field directed along the diagonal of the square (see Fig. 8) (ordered medium), and (•) numerical calculation results for nonmagnetic circular inclusions in a ferromagnetic matrix and field directed parallel to the side of the square (see Fig. 8) (ordered medium).

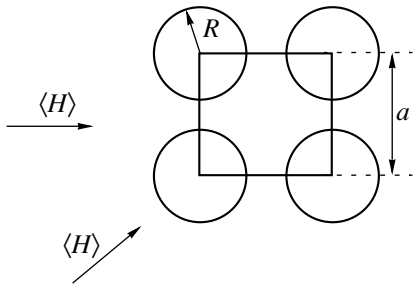

Fig. 8. Applied field directions.

where

$$\alpha = 1 - \frac{1}{3}(gR^4)^2\delta^2 - \frac{1}{63}(gR^4)^4\delta^2 - \frac{9}{5}\left(\delta^2 + \frac{4}{5\times 11\times 13^2}\right)(gR^4)^6\delta^2, \quad (59)$$

$$\delta = \frac{\sigma_1 - \sigma_2}{\sigma_1 + \sigma_2}, \quad g = \frac{1}{20a^4}K^4\left(\frac{1}{\sqrt{2}}\right), \quad K\left(\frac{1}{\sqrt{2}}\right) = 1.85407, \quad (60)$$

R is the radius of circular inclusions with conductivity σ_2, $2a$ is the size of the unit (square) cell, and $K(1/\sqrt{2})$ is the complete elliptic integral of the first kind with modulus $1/\sqrt{2}$. The concentration of the high-conductivity phase (σ_1) is $p = 1 - \pi R^2/4a^2$. Equation (58) for σ_e is valid (a) in the whole range of high-conductivity phase concentration variations $1 - \pi/4 \le p \le 1$ at $|\delta| \le 0.7$, that is, at $\sigma_1/\sigma_2 \le 5.67$, and (b) in the concentration range $0.291 \le p \le 1$ at an arbitrary σ_1/σ_2 ratio.

We will repeat the calculations described in Sections 2.1 and 2.2 for the two-dimensional case, but the effective medium theory approximation will everywhere be replaced by (58). Formula (6) is replaced by (58) with the substitutions

$$\frac{1}{\sigma_e} \longrightarrow \lambda_{\text{eff}}, \quad \delta = \frac{1/\tilde{\lambda}_1 - 1/\lambda_2}{1/\tilde{\lambda}_1 + 1/\lambda_2}, \quad \frac{1}{\sigma_1} \longrightarrow \tilde{\lambda}_1.$$

Next, (8) is replaced by (58) with similar substitutions,

$$\sigma_e \longrightarrow \mu_{\text{eff}}, \quad \delta = \frac{\tilde{\mu}_1 - \mu_2}{\tilde{\mu}_1 + \mu_2}, \quad \sigma_1 \longrightarrow \tilde{\mu}_1,$$

and (25) is replaced by (58) with the substitutions

$$\frac{1}{\sigma_e} \longrightarrow \lambda_e, \quad \delta = \frac{1/\lambda_d - 1/\lambda_2}{1/\lambda_d + 1/\lambda_2}, \quad \sigma_1 \longrightarrow \frac{1}{\lambda_d}.$$

Note that the use of the linear problem to determine the effective properties in the nonlinear problem by the local linearization method requires justification additional to that given above. The matter is that the structure of randomly distributed spheres (or circles) under consideration possesses cubic symmetry on average, and, as is well known [35], leaves for the conductivity, which is a second-rank tensor, the only possibility of degeneration into a scalar. Generally, this is not the case in the nonlinear problem [36]. An especially spectacular example of the difference in nonlinear properties (in the current–voltage characteristics) along and across a mesh with periodically distributed nonlinear bonds is given in [30]. The local linearization method and the method suggested in [13, 14] that we use cannot describe such a nonlinear "anisotropy." More precisely, they cannot be used to calculate the effective tensor of a higher rank generally required to describe nonlinear effective properties. In discussing the numerical experimental results, we will consider the problem of different properties for different applied field directions. Here, we give the numerical simulation results (Fig. 7). As is well known (e.g., see [12]), the effective medium theory approximation for circular inclusions coincides with the effective medium theory approximation for the mesh problem. Precisely this makes it possible to determine the concentration dependences of the effective coefficients in the whole concentration range. Real media, for instance, media with circular inclusions, have geometric limitations on the maximum concentration of inclusions. In media with a periodic arrangement of circular ferromagnetic phase inclusions under

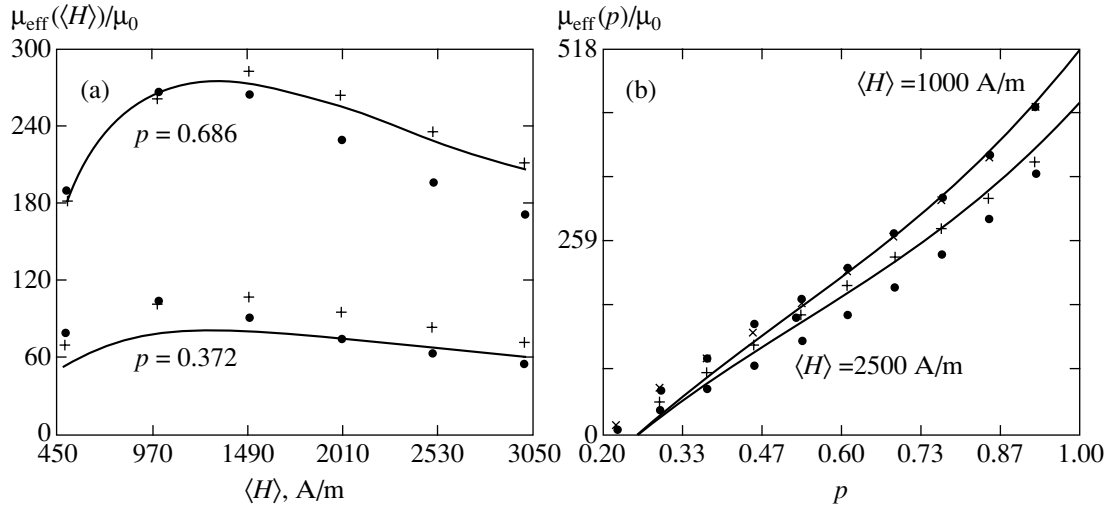

Fig. 9. Numerical experiment. Nonmagnetic circular inclusions in a ferromagnetic matrix. Dependences of the relative effective permeability on (a) external field $\langle \mathbf{H} \rangle$ and (b) ferromagnetic phase concentration p at various external field $\langle \mathbf{H} \rangle$ directions (see Fig. 8); the solid line corresponds to local linearization calculations based on [29], solid circles are for the field directed parallel to the side of the square (see Fig. 8), and crosses, for the field directed along the diagonal of the square (see Fig. 8).

consideration, the concentration of these inclusions cannot exceed $p_{\max} = \pi/4 \approx 0.785$. Naturally, the concentration dependences of the effective magnetic permeability for two fundamentally different structures (ferromagnetic inclusions in a nonmagnetic matrix and nonmagnetic inclusions in a ferromagnetic matrix) do not transform into each other.

4. NUMERICAL SIMULATION

For a composite with an ordered structure and for some field $\langle \mathbf{H} \rangle$ directions, symmetry considerations allow the Maxwell equations to be solved in one (unit) cell and the solution to be averaged over this cell. The straight lines connecting the centers of four neighboring circles form a square with side a. We considered two possible field directions (Fig. 8). Mean applied field $\langle \mathbf{H} \rangle$ is directed parallel to the side of this square in the first case and along its diagonal in the second (Fig. 8). In the first case, the cell side length is $a/2$ (the potential difference is $-\langle H \rangle a/2$ between the sides perpendicular to the direction of $\mathbf{H}$), and, in the second, it is $a\sqrt{2}$ (the potential difference is $\langle H \rangle a\sqrt{2}$). The Maxwell equations were numerically solved using the implementation of the finite element method described in [37]. This program proved itself advantageous in solving similar problems of magnetostatics for nonlinear ferromagnets, for which it provided excellent agreement with the experimental results [38]. The computations were performed on a standard personal computer. The time of computations for given ferromagnetic phase concentration p and applied field $\langle \mathbf{H} \rangle$ was of 5 to 45 min depending on p and $\langle \mathbf{H} \rangle$.

Importantly, the medium under consideration with air inclusions in a ferromagnetic matrix is only isotropic in the linear approximation. There is no isotropism in the nonlinear case, and the field dependences of μ_{eff} for the two selected applied field directions are different, as is well seen from Fig. 9. Shown in this figure are not only the results of theoretical calculations by the local linearization method based on [29] but also the numerical experimental results for nonmagnetic inclusions at different field directions. We see that the difference between the field dependences of μ_{eff} (Fig. 9a) amounts to 15% for different field directions and that the local linearization method provides close (for an analytic method) agreement with the numerical experimental results (especially for the concentration dependence of μ_{eff}, Fig. 9b).

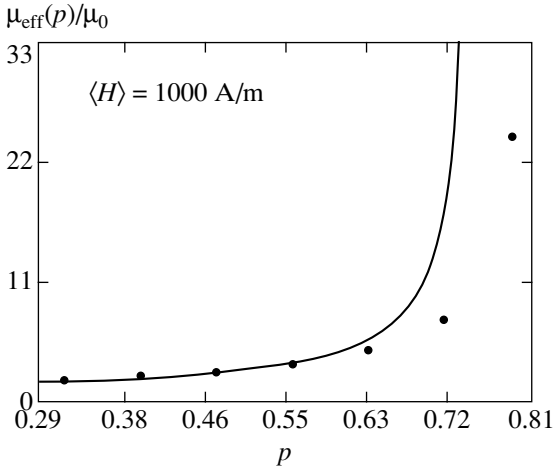

Fig. 10. Dependence of the relative effective permeability on concentration p of ferromagnetic circular inclusions; the solid curve corresponds to theoretical local linearization calculations based on [29], and the solid circles, to numerical experiment results.

There is virtually no anisotropy for ferromagnetic inclusions in a nonmagnetic matrix. The dependence of the effective magnetic permeability on external field **H** and its spatial orientation is then also vanishingly small. The plots obtained in theoretical calculations by the local linearization method based on [29] and in numerical simulation of a system with ferromagnetic inclusions are shown in Fig. 10.

5. CONCLUSION

It has been shown above that different approximate methods give qualitatively identical and quantitatively similar results (e.g., see Fig. 6). Different structures, randomly nonuniform and ordered (with periodically distributed inclusions), are described by fundamentally different laws (see Fig. 7). The transition from the linear to the nonlinear case also increases differences; this transition results in the appearance of anisotropy of the effective properties (see Fig. 9a). The approximate analytic methods that we used in this work were based on the well-known equations for the μ_{eff} and λ_{eff} effective parameters in the linear case; they were in principle incapable of describing the arising anisotropy of nonlinear properties. In the case under consideration, the anisotropy of magnetic properties for periodically distributed nonmagnetic inclusions in a ferromagnetic matrix (see Fig. 9a) and ferromagnetic inclusions in a nonmagnetic matrix is insignificant.

It would be interesting to study the influence of a weak disorder introduced by small displacements of inclusion centers. This problem is, however, beyond the scope of the present work and deserves special consideration.

ACKNOWLEDGMENTS

The authors thank P.-M. Hui and D. Kalyon for kindly providing reprints and V. Holod for his help in fitting Eq. (A.1). One of us (A.A.S.) thanks H. ROSEN Engineering GmbH for hospitality.

APPENDIX

The dependence shown in Fig. 4 is described by the equation

$$\mu_1(H) = \mu_0\left(1 + 1.56993\times 10^6\frac{\tanh(5.39\times 10^{-4}H)}{H} - 257731\frac{\tanh(3.25\times 10^{-3}H)}{10^{-2}H}\right), \quad \text{(A.1)}$$

where H is in A/m.

To obtain $\lambda_1(B)$, we must numerically solve the nonlinear equation

$$\mu_1(H)H = B, \quad \text{(A.2)}$$

find $H(B)$, and set

$$\lambda_1(B) = \frac{H(B)}{B}. \quad \text{(A.3)}$$

For analytic purposes, the curve obtained is approximated by the dependence

$$\lambda_1(B) = 267.404\left\{\frac{\arctan(296.322B) + \tan(0.9B)}{B} + 0.03[1 + \tan^2(0.92B)]\right\}, \quad \text{(A.4)}$$

where B is in Tesla units.

REFERENCES

1. T. J. Fiske, H. S. Gokturk, and D. M. Kalyon, J. Mater. Sci. **32**, 5551 (1997).
2. H. Gokturk, T. Fiske, and D. M. Kalyon, J. Appl. Phys. **73**, 5598 (1993).
3. E. Ganshina, A. Granovsky, V. Gushin, *et al.*, Physica A (Amsterdam) **241**, 45 (1997).
4. S. O. Gladkov, Pis'ma Zh. Tekh. Fiz. **26**, 50 (2000) [Tech. Phys. Lett. **26**, 115 (2000)].
5. V. Masheva, M. Grigorova, D. Nihtianova, *et al.*, J. Phys. D **32**, 1595 (1999).
6. É. S. Gorkunov, V. A. Zakharov, A. I. Ul'yanov, and A. A. Chulkina, Defektoskopiya **3**, 31 (2001).
7. *Proceedings of International Conference on Electrical Transport and Optical Properties of Inhomogeneous Media*, Vol. 3, Ed. by W. L. Mochan and R. G. Barrera, Physica A (Amsterdam) **207** (1994); Vol. 4, Ed. by A. M. Dykhne, A. N. Lagarkov, and A. K. Sarychev, Physica A (Amsterdam) **241** (1997); Vol. 5, Ed. by P. M. Hui, P. Sheng, and L.-H. Tang, Physica B (Amsterdam) **279** (2000).
8. K. J. Binns, P. J. Lawrenson, and C. W. Trowbridge, *The Analytical and Numerical Solution of Electric and Magnetic Fields* (Wiley, Chichester, England, 1992).
9. N. Ida, *Numerical Modeling for Electromagnetic Nondestructive Evaluation* (Chapman and Hall, London, 1995).
10. D. A. Bruggeman, Ann. Phys. (Leipzig) **24**, 636 (1935).
11. R. Landauer, J. Appl. Phys. **23**, 779 (1952).
12. M. I. Shvidler, *Statistical Hydrodynamics of Porous Media* (Nedra, Moscow, 1985).
13. P. M. Hui, Y. F. Woo, and W. M. V. Wan, J. Phys. C **7**, L593 (1995).
14. P. M. Hui, P. Cheung, and Y. R. Kwong, Physica A (Amsterdam) **241**, 301 (1997).
15. S. W. Kenkel and J. P. Straley, Phys. Rev. Lett. **49**, 767 (1982).
16. J. P. Straley and S. W. Kenkel, Phys. Rev. B **29**, 6299 (1984).
17. A. M. Dykhne, Zh. Éksp. Teor. Fiz. **59**, 110 (1970) [Sov. Phys. JETP **32**, 63 (1971)].

18. V. V. Bakaev, A. A. Snarskiĭ, and M. V. Shamonin, Zh. Tekh. Fiz. **71** (12), 84 (2001) [Tech. Phys. **46**, 1571 (2001)].
19. V. V. Bakaev, A. A. Snarskiĭ, and M. V. Shamonin, Zh. Tekh. Fiz. **72**, 129 (2002) [Tech. Phys. **47**, 125 (2002)].
20. A. A. Snarskii and M. I. Zhenirovsky, J. Phys. B **322**, 84 (2002).
21. I. Webman, J. Jortner, and M. H. Cohen, Phys. Rev. B **16**, 2959 (1977).
22. B. Ya. Balagurov, Fiz. Tekh. Poluprovodn. (Leningrad) **16**, 259 (1982) [Sov. Phys. Semicond. **16**, 1204 (1982)].
23. A. A. Snarskiĭ, Zh. Éksp. Teor. Fiz. **91**, 1405 (1986) [Sov. Phys. JETP **64**, 828 (1986)].
24. A. E. Morozovskiĭ and A. A. Snarskiĭ, Zh. Éksp. Teor. Fiz. **95**, 1844 (1989) [Sov. Phys. JETP **68**, 1066 (1989)].
25. A. E. Morozovskiĭ and A. A. Snarskiĭ, Pis'ma Zh. Éksp. Teor. Fiz. **52**, 871 (1990) [JETP Lett. **52**, 224 (1990)].
26. A. E. Morozovskiĭ and A. A. Snarskiĭ, Zh. Éksp. Teor. Fiz. **102**, 683 (1992) [Sov. Phys. JETP **75**, 366 (1992)].
27. A. E. Morozovsky and A. A. Snarskii, Int. J. Electron. **78**, 135 (1995).
28. A. A. Snarskii, A. E. Morozovsky, A. Kolek, and A. Kusy, Phys. Rev. E **53**, 5596 (1996).
29. B. Ya. Balagurov and V. A. Kashin, Zh. Éksp. Teor. Fiz. **117**, 978 (2000) [JETP **90**, 850 (2000)].
30. D. J. Bergman, Physica A (Amsterdam) **270**, 8 (1999).
31. N. S. Bakhvalov and G. P. Panasenko, *Averaging of Processes in Periodic Media* (Nauka, Moscow, 1984).
32. Yu. P. Emets, *Electrical Properties of Composites with Regular Structure* (Naukova Dumka, Kiev, 1986).
33. B. Ya. Balagurov and V. A. Kashin, Zh. Tekh. Fiz. **71**, 106 (2001) [Tech. Phys. **46**, 101 (2001)].
34. B. Ya. Balagurov, Zh. Éksp. Teor. Fiz. **120**, 668 (2001) [JETP **93**, 586 (2001)].
35. J. F. Nye, *Physical Properties of Crystals: Their Representation by Tensors and Matrices*, 2nd ed. (Clarendon Press, Oxford, 1964; Mir, Moscow, 1967).
36. A. M. Satanin, A. A. Snarskiĭ, K. V. Slipchenko, and I. V. Bessudnov, Zh. Tekh. Fiz. **68** (5), 132 (1998) [Tech. Phys. **43**, 602 (1998)].
37. D. C. Carpenter, Mater. Eval. 877 (2000).
38. M. Shamonin, M. Klank, O. Hagedorn, and H. Dötsch, Appl. Opt. **40**, 3182 (2001).

Translated by V. Sipachev

Journal of Experimental and Theoretical Physics, Vol. 96, No. 1, 2003, pp. 78–82.
Translated from Zhurnal Éksperimental'noĭ i Teoreticheskoĭ Fiziki, Vol. 123, No. 1, 2003, pp. 92–97.

SOLIDS
Electronic Properties

Effect of Binding Energy on the Kinetics of Radiative and Nonradiative Recombination of Bound Excitons

A. N. Starukhin* and B. S. Razbirin

Ioffe Physicotechnical Institute, Russian Academy of Sciences,
Politekhnicheskaya ul. 26, St. Petersburg, 194021 Russia
**e-mail: A.Starukhin@pop.ioffe.rssi.ru*

Received March 28, 2002

Abstract—Radiative and nonradiative lifetimes of bound excitons in GaSe with various binding energies are measured by the magnetooptical method using time-resolution spectroscopy. It is shown that both the radiative and nonradiative lifetimes of an exciton bound at an ionized center increase with the binding energy of an exciton with a defect. Possible reasons for this dependence are considered. The results of calculations obtained in the framework of the proposed model are in good agreement with experimental data. © *2003 MAIK "Nauka/Interperiodica".*

1. INTRODUCTION

Radiative and nonradiative recombination of electrons and holes determines to a considerable extent the electric and optical properties of semiconductors. Crystal lattice defects serve as effective centers of recombination of electrons and holes in semiconducting crystals. For this reason, an analysis of the peculiarities of electron–hole recombination at various types of centers is of considerable importance. In particular, bound excitons are effective centers for the electron–hole recombination at low temperatures. It is radiative recombination of electrons and holes in bound excitons that determines to a considerable extent the optical emission spectra of semiconductors in the region of their fundamental absorption edge [1].

Bound excitons can be formed in crystals by various types of impurity centers (excitons bound to neutral donors or acceptors, excitons bound to ionized centers or isoelectronic traps, etc.). An important characteristic of a bound exciton is its binding energy with a defect. In the optical spectrum of a semiconductor, this energy determines the energy shift of the spectral emission (absorption) line of a bound exciton relative to the emission (absorption) line of a free exciton. This study aims at analyzing the effect of the binding energy of bound excitons on their radiative and nonradiative lifetimes using as an example triplet excitons bound at ionized centers (isoelectron traps) in a GaSe crystal. Traditional methods for measuring lifetimes of excitons from an analysis of the kinetics of exciton luminescence decay [2–6] do not provide direct information on their radiative and nonradiative recombination lifetimes.[1] The estimation of these lifetimes involves the employment of additional indirect data. In our study, we measure the radiative and nonradiative lifetimes of bound excitons using a new method [7] based on an analysis of the afterglow spectra of triplet bound excitons in GaSe in a magnetic field under conditions of their spin sublevels anticrossing. In contrast to the traditional approach, this method makes it possible to directly obtain information on the radiative and nonradiative lifetimes of an excited state.

[1] These methods are used for determining the total lifetime of an excited state.

2. EXPERIMENTAL TECHNIQUE

Gallium selenide crystals were grown by the Bridgman method and were not purposefully doped. The samples for investigations were cut from ingots by cleaving along the plane of crystal layers at right angles to the optical *c* axis of the crystal. Exciton luminescence was excited by radiation emitted by a copper vapor pulsed laser with a pulse duration of $\tau_p = 20$ ns. The excitation density was about 200 W/cm^2. Exciting light with a photon energy of $h\nu_{exc} = 2.140$ eV $> E_g$ (E_g is the forbidden gap of the crystal) was incident at a small angle to the normal to the sample surface, and radiation was detected in the direction of the normal parallel to the *c* axis. The spectra were recorded using a diffraction spectrometer supplied with a photon counting system with a time resolution of about 30 ns. The mean value of dark current in the photon counting system was less than 1 pulse per second. In order to study radiation at different instants of the lifetime of a bound exciton, the pulse at the gate of the photon counting system was delayed relative to the exciting pulse. During the experiments, the samples were kept in liquid helium at 2 K. Magnetic fields were created by a super-

conducting solenoid. The magnetic field was oriented parallel to the optical *c* axis of the crystal.

3. EXPERIMENTAL RESULTS AND DISCUSSION

The emission spectrum of a GaSe crystal in the region of the fundamental absorption edge is shown in Fig. 1 (curve *a*) for the first 30 ns after an exciting pulse. The same figure shows for comparison the emission spectrum of the crystal 200 ns after the termination of the exciting pulse (curve *b*). The comparison obviously demonstrates a noticeable difference in the decay rates for different spectral lines. The spectral line corresponding to the shortest wave with a peak near $h\nu$ = 2.108 eV is due to radiative annihilation of direct free excitons, while lines α and β with peaks at the energies 2.096 and 2.089 eV correspond to the emission of triplet excitons bound at ionized centers (or isoelectron traps) [8]. Line β is accompanied by an intense acoustic wing whose peak is displaced to the long-wave region approximately by 0.001 eV relative to line β (the acoustic wing for line α is manifested less clearly). It can be seen from Fig. 1 that line β corresponding to a bound exciton with a higher binding energy is characterized by the longest decay time.

In a longitudinal magnetic field $B \geq 2$ T ($\mathbf{B} \parallel c \parallel \mathbf{k}_{\text{photon}}$, i.e., in Faraday geometry), the resonance absorption lines α and β of bound photons split into doublets whose components are strictly polarized according to the right (σ^+) and left (σ^-) circular polarizations. In weaker fields, the splitting of lines α and β is not observed in view of their relatively large widths, but the magnetic field dependence of the exciton emission intensity under continuous excitation has a peak due to the anticrossing of Zeeman sublevels of bound excitons in a magnetic field [8].

In GaSe crystals, the orbital-nondegenerate state Γ_4 of an exciton bound at an ionized center (or isoelectron trap), as well as the ground state of a direct free exciton [9], splits into two states (singlet and triplet) on account of exchange interaction. In the case of free excitons, the splitting Δ_1 between these states amounts to 2 meV [9]. In the singlet state, the total spin of the electron and the hole in an exciton is zero, and transitions to this state are allowed for the light polarization $\mathbf{E} \parallel c$. Under our experimental conditions ($\mathbf{E} \perp c$), the singlet state is not manifested.

Triplet excitons are characterized by the total spin $S = 1$ and by the spin components $S_z = 0, \pm 1$ along the *c* axis. Transitions to the state with $S_z = \pm 1$ are allowed for the light polarization $\mathbf{E} \perp c$; the state with $S_z = 0$ is optically inactive. In view of the crystal anisotropy, the state with $S_z = 0$ is split from the states with $S_z = \pm 1$ by $\Delta \ll \Delta_1$ [10]. The longitudinal magnetic field $\mathbf{B} \parallel c$ splits the level with $S_z = \pm 1$ into two sublevels with $S_z = +1$ and $S_z = -1$; radiation emitted from these sublevels has right or left circular polarization, respectively. The

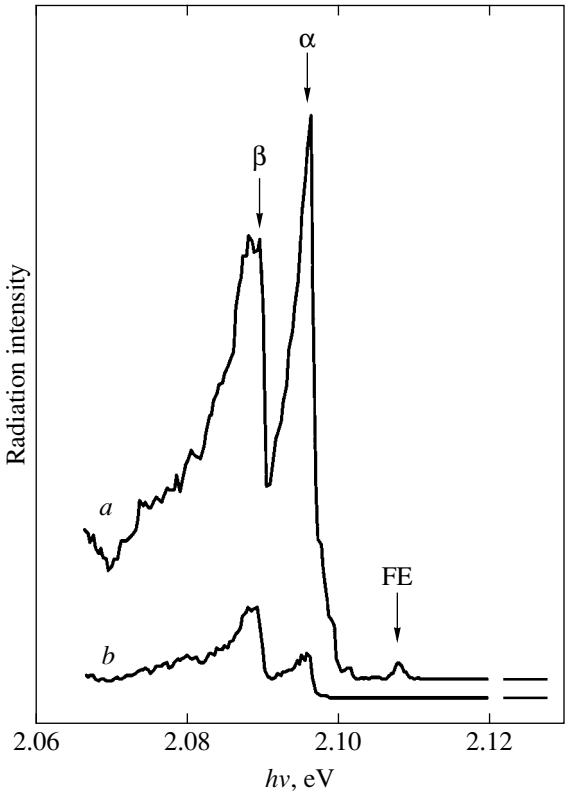

Fig. 1. Exciton emission spectra for a GaSe crystal recorded during the first 30 ns after the exciting pulse (*a*) and 200 ns after the termination of the exciting pulse (*b*); T = 2 K.

energy of the states of a triplet exciton in a longitudinal field is described as

$$E_{1,2} = E_0 \pm 0.5 g_{zz} \mu_0 B, \quad E_3 = E_0 - \Delta, \qquad (1)$$

where g_{zz} is the longitudinal component of the g factor of the exciton and μ_0 is the Bohr magneton. In accordance with relations (1), the energies of states 2 and 3 in the field $B = 2\Delta/g_{zz}\mu_0 \equiv B_c$ become identical; i.e., the corresponding energy levels intersect. However, a local field acting on a bound exciton may cause mixing of the exciton states $|0\rangle$ and $|\pm 1\rangle$ [11]. In this case, anticrossing of levels 2 and 3 is observed instead of their intersection (Fig. 2). For $B \approx 2\Delta/g_{zz}\mu_0$, states 2 and 3 (i.e., states $|-1\rangle$ and $|0\rangle$) will mainly be mixed since the difference between the energies of such states is considerably smaller than the energy difference between states 1 and 3. As a result of mixing, two new exciton states *a* and *b* are formed instead of the two initial states 2 and 3 (Fig. 2). States *a* and *b* are optically active in the light polarization σ^-, as well as state 2, since state 3 is optically inactive. Under steady-state excitation of the crystal by light with $h\nu_{\text{exc}} > E_g$, anticrossing of levels 2 and 3 is manifested in the form of a peak on the magnetic field, dependence $I_{\sigma^-}(B)$, of the intensity of the σ^- component of radiation emitted by a bound exciton for $B \approx B_c$. (It can be observed that the manifestation of the anti-

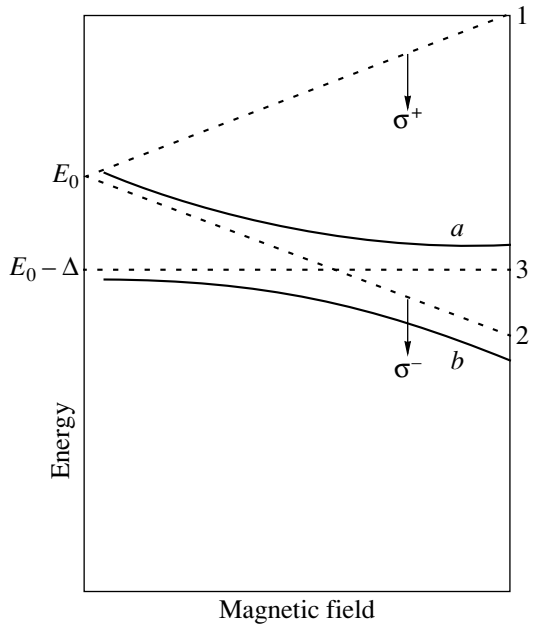

Fig. 2. Energy level diagram for a triplet exciton in GaSe in a magnetic field $\mathbf{B} \parallel c$.

crossing of levels in the form of a peak on the magnetic field dependence of the radiation intensity is typical of various systems from atoms to crystals [11–13].) However, an analysis of the shape of the signal from anticrossing of energy levels of triplet bound excitons in the afterglow spectra of GaSe crystals shows that the shape of the signal varies significantly during the lifetime of the excited state [7]. Figure 3 illustrates the variation of $I_{\sigma^-}(B, t)$ in the case of the emission of exciton α ($0 \le B < 1$ T, $\mathbf{B} \parallel c \parallel \mathbf{k}_{\text{photon}}$) for various delay times t relative to the excitation pulse (the duration of the pulse at the gate of the recording system was $\Delta t = 30$ ns).

It can be seen from Fig. 3 that, for $t \approx 0$, only a very small peak can be noticed on the curve describing the dependence $I_{\sigma^-}(B, 0)$ at $B = 0.36$ T $\equiv B_c'$. (For $\Delta t <$ 30 ns, the peak on the dependence $I_{\sigma^-}(B, 0)$ is practically unnoticeable.) As the delay time increases from 0 to 600 ns, the relative intensity of the peak at 0.36 T increases sharply (the absolute intensity of the α line in the afterglow spectra for $B = 0$ naturally decreases in this case) so that a clearly manifested peak is formed on the curve $I_{\sigma^-}(B, t)$ in the region $B = B_c'$ (see Fig. 3). Thus, in this interval of delay times, the dependence $I_{\sigma^-}(B, t)$ for a fixed t is similar to the magnetic field dependence $I_{\sigma^-}(B)$ of the intensity of the emission line α in the case of continuous excitation of luminescence. As the delay time increases further, the relative intensity of the peak continues to increase, but a shallow dip appears in the region of the maximum of the peak (Fig. 3). A further increase in t leads to an increase in the width and depth of the dip (Fig. 3) so that two well-defined peaks appear on the curve $I_{\sigma^-}(B, t)$ at $t \ge 1$ μs, and the separation between their maxima continues to increase with t (Fig. 3). The emergence of a dip at $B = B_c'$ on the magnetic field dependence of the intensity of exciton radiation for large values of t can be explained as follows. Since optical transitions from states a and b are not resolved in the spectra, the signal being recorded is the total intensity of exciton radiation in these states: $I_{\sigma^-}(B, t) = I_a(B, t) + I_b(B, t)$. For $B = B_c'$, the exciton lifetimes $\tau_a(B)$ and $\tau_b(B)$ in states a and b are identical; the total lifetime $\tau_a(B) + \tau_b(B)$ attains its minimum value in this case. Accordingly, the total population of these states also attains its minimum value. As a result, states a and b turn out to be depleted for $B \approx B_c'$ and for large values of t and do not make any significant contribution to radiation, while the population of one of these states for $B < B_c'$ and $B > B_c'$ remains quite high, manifested in the form of two emission peaks at $B < B_c'$ and $B > B_c'$. These symmetric relative to $B = B_c'$ (Fig. 3); one peak corresponds to emission from state b and the other to emission from state a. Thus, the shape of the signal from anticrossing of energy levels at different instants of the lifetime of bound photons changes significantly from nearly a complete absence of a signal (at $t = 0$) to a complex shape with two peaks (for large values of t). The behavior of the radiation intensity $I_{\sigma^-}(B, t)$ for exciton α with polarization σ^- is similar to the behavior of β exciton radiation under similar conditions [7] and can be described in the above model of anticrossing of spin sublevels of triplet bound excitons.

It was shown in [7] that a comparison of the experimental and theoretical dependences $I_{\sigma^-}(B, t)$ makes it possible to determine a number of important parameters of triplet excitons, including the radiative and nonradiative lifetimes (τ_r and τ_{nr}, respectively). If the effective g factor of the α exciton is known from an analysis of the Zeeman effect [8], all the remaining parameters characterizing the energy structure and kinetic properties of a bound exciton can be determined independently by comparing theory and experiment. Among other things, such an analysis shows that the delay time t' corresponding to the instant of dip formation for $B = B_c'$ is determined only by the radiative lifetime of a triplet exciton: $t' = 4\tau_r$. For given parameters of the energy structure and a value of τ_r, the quantity τ_{nr} is in fact the only fitting parameter determining the behavior of $I_{\sigma^-}(B, t)$ with time. The theoretical dependences $I_{\sigma^-}(B, t)$ corresponding to the best agreement between theory and experiment are presented by solid curves in

Fig. 3.[2] Theoretical dependences in Fig. 3 were obtained using the following parameters of the triplet bound exciton α: $\tau_{r\alpha} = 80 \times 10^{-9}$ s, $\tau_{nr\alpha} = 1.5 \times 10^{-6}$ s, other parameters characterizing the splitting of states *a* and *b* (Fig. 2) being practically the same for excitons α and β (this is confirmed by the magnetic resonance data [10]). Thus, bound excitons α and β differ, as regards the structure of energy levels, only in binding energies. At the same time, the radiative and nonradiative lifetimes $\tau_{r\beta} = 125 \times 10^{-9}$ s and $\tau_{nr\beta} = 7 \times 10^{-6}$ s of the bound exciton β [7] differ noticeably from those for the bound exciton α. We can assume that the noticeable difference in the radiative and nonradiative recombination lifetimes is determined to a considerable extent precisely by the difference in the binding energies of excitons α and β.

Indeed, according to Rashba and Gurgenishvili [14], the oscillator force f_d of an optical electron transition to the bound exciton state is defined as

$$f_d \sim \kappa^{-3} f_{ex} \sim |E|^{-3/2} f_{ex}, \qquad (2)$$

where E is the binding energy of a bound exciton; f_{ex} is the oscillator strength of a transition to the free exciton state; the quantity $\kappa^{-1} = \hbar/\sqrt{2m|E|}$ characterizes the wave function of a bound exciton (it is assumed that the forces of interaction of the exciton with a defect are short-range forces of radius R_0 and the wave function range for a bound exciton is noticeably larger than R_0 [14]); and m is the effective exciton mass. The radiative lifetime of a bound exciton is $\tau_r \sim f_d^{-1}$ [2]. Thus, the radiative lifetime for bound excitons in a given semiconductor (f_{ex} = const) must increase with their binding energy. It was shown above that exactly the same situation is obtained for the bound excitons α and β in GaSe. On the basis of relation (2), we can write the ratio of radiative lifetimes of two bound excitons with different binding energies in the form

$$\frac{\tau_{1r}}{\tau_{2r}} = \frac{f_{d2}}{f_{d1}} = \left|\frac{E_1}{E_2}\right|^{3/2}. \qquad (3)$$

In our case, the binding energy is $E_1 = E_\alpha \approx 12$ meV for exciton α and $E_2 = E_\beta \approx 19$ meV for exciton β. Consequently, the expected ratio of radiative lifetimes $\tau_{r\alpha}/\tau_{r\beta} = (12/19)^{3/2} = 0.5$, which is close to the experimentally obtained value $\tau_{r\alpha}/\tau_{r\beta} = 0.65 \pm 0.15$.

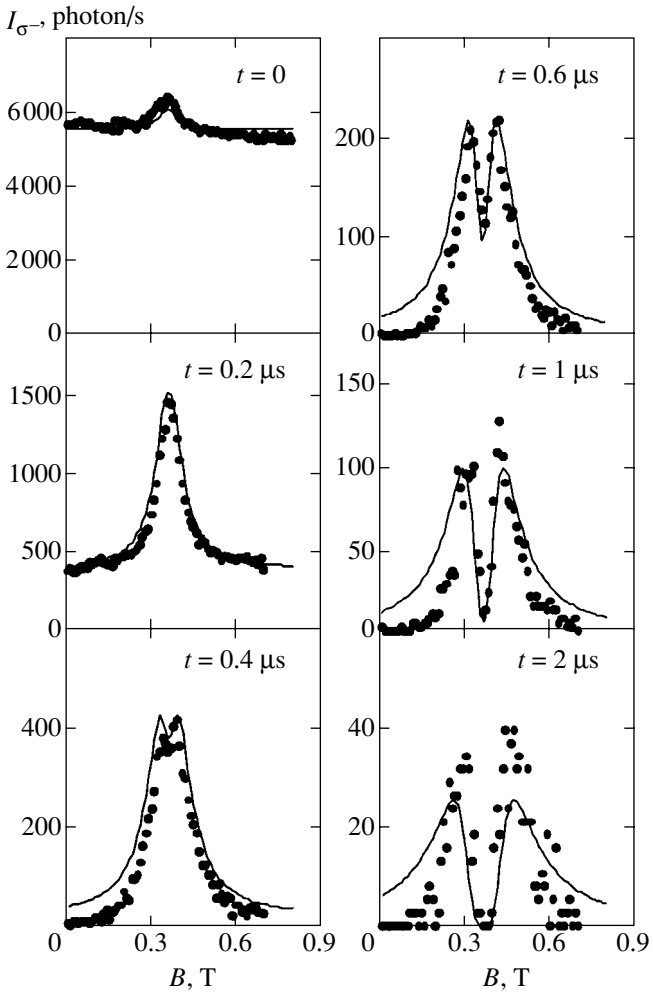

Fig. 3. Magnetic field dependence of the radiation intensity $I_{\sigma^-}(B, t)$ of a triplet bound exciton α in polarization σ^- at different instants in the lifetime of the excited state (time t is indicated in the figure), $\mathbf{B} \parallel c \parallel \mathbf{k}_{photon}$, T = 2 K. Dark circles correspond to experimental values, and curves, to the theoretical dependence.

We can assume that a dependence similar to relation (3) is also observed for nonradiative lifetimes of excitons bound at ionized centers and isoelectron traps. At low temperatures and low optical excitation density, the nonradiative decay of an exciton bound at an ionized center (or an isoelectron trap) is due to transition of one of the charge carriers (e.g., an electron) forming the exciton to a lower vacant electron energy level of another defect, which can be quite shallow on account of the energy of excitons α and β. The probability of such a transition depends, among other things, on the overlapping of the wave functions of the bound exciton and the defect under investigation. If the concentration of defects is quite high, the nonradiative lifetime of a bound exciton is determined by the number of "appropriate" (containing the above-mentioned electron level) defects in the crystal region where the wave function of

[2] It should be noted that, owing to the effect of anticrossing of spin levels observed in a magnetic field and associated with the mixing of optically active and optically inactive states, the luminescence signal $I_{\sigma^-}(B, t)$ can be reliably observed for delay times up to 10 μs, while the luminescence intensity for $B = 0$ becomes smaller than the detection threshold even for $t \geq 0.5$ μs. Such an increase in the time range for reliable observation of the luminescence signal significantly increases the accuracy of determining the lifetime of a bound exciton.

the bound exciton noticeably differs from zero. Denoting by N_t the concentration of such defects, we can write the dependence of the nonradiative lifetime of the bound exciton on its binding energy in the form

$$\tau_{nr} \sim \frac{1}{\kappa^{-3} N_t(E)} \sim \frac{|E|^{3/2}}{N_t(E)}. \quad (4)$$

The notation $N_t(E)$ shows here that the concentration of the defects that may participate in nonradiative decay of a bound exciton is a function of the exciton binding energy E. Indeed, it was noted above that the charge carrier constituting the exciton can, as a result of nonradiative decay, pass only to lower electron levels of other defects (as a last resort, a transition may occur without a change in the carrier energy). Consequently, the higher the binding energy of a bound exciton, the deeper must be the energy levels of the defects participating in the nonradiative decay of the exciton. Other conditions being the same, we have

$$n_t(E_1) > N_t(E_2) \quad (5)$$

if $E_1 < E_2$. In the framework of the above model, we obtain the following expression for the ratio of the nonradiative lifetimes of the bound excitons α and β:

$$\frac{\tau_{nr\alpha}}{\tau_{nr\beta}} = \left|\frac{E_\alpha}{E_\beta}\right|^{3/2} \frac{N_t(E_\beta)}{N_t(E_\alpha)}. \quad (6)$$

Since $E_\alpha < E_\beta$, the inequality $N_t(E_\beta)/N_t(E_\alpha) < 1$ holds in accordance with relation (5); taking into account relation (3), we obtain the following inequality from relation (6):

$$\frac{\tau_{nr\alpha}}{\tau_{nr\beta}} = \frac{\tau_{r\alpha}}{\tau_{r\beta}} \frac{N_t(E_\beta)}{N_t(E_\alpha)} < \frac{\tau_{r\alpha}}{\tau_{r\beta}}. \quad (7)$$

Experiments give $\tau_{nr\alpha}/\tau_{nr\beta} = (0.2 \pm 0.1) < \tau_{r\alpha}/\tau_{r\beta}$, which is in accord with relation (7). The total lifetimes $\tau_i = (\tau_{ri}^{-1} + \tau_{nri}^{-1})^{-1}$ ($i = \alpha, \beta$) of the bound excitons α and β calculated on the basis of the measured radiative and nonradiative lifetimes of these excitons are also in complete agreement with the experimental data presented in Fig. 1.

It is interesting to note that in the case of excitons bound at neutral donors or acceptors, for which the Auger decay is the main mechanism of nonradiative decay, the reverse (relative to excitons bound at ionized centers) dependence of the nonradiative lifetime of bound excitons on their binding energy is observed: the nonradiative lifetime decreases upon an increase in the binding energy of the exciton at a center [4].

4. CONCLUSIONS

Thus, we directly measured the radiative and nonradiative recombination times for bound excitons of the same type (excitons bound at ionized centers or isoelectron traps) with different binding energies. To our knowledge, these measurements were made for the first time. It is shown that the radiative and nonradiative lifetimes of an exciton bound at an ionized center (isoelectron trap) increase with the binding energy of the exciton. Possible reasons for such a dependence are considered.

REFERENCES

1. J. I. Pankove, *Optical Processes in Semiconductors* (Prentice-Hall, Englewood Cliffs, 1971; Mir, Moscow, 1973).
2. J. D. Cuthbert and D. G. Thomas, Phys. Rev. **154**, 763 (1967).
3. C. H. Henry and K. Nassau, Phys. Rev. B **1**, 1628 (1970).
4. W. Schmid, Phys. Status Solidi B **84**, 529 (1977).
5. I. S. Hauksson, J. Suda, M. Tsuka, *et al.*, J. Cryst. Growth **159**, 329 (1996).
6. N. Q. Vinh, M. A. J. Klik, and T. Gregorkiewicz, Physica B (Amsterdam) **308–310**, 414 (2001).
7. A. N. Starukhin, D. K. Nel'son, and B. S. Razbirin, Pis'ma Zh. Éksp. Teor. Fiz. **72**, 612 (2000) [JETP Lett. **72**, 427 (2000)].
8. E. M. Gamarts, E. L. Ivchenko, G. E. Pikus, *et al.*, Fiz. Tverd. Tela (Leningrad) **24**, 2325 (1982) [Sov. Phys. Solid State **24**, 1320 (1982)].
9. E. Mooser and M. Schlüter, Nuovo Cimento B **18**, 164 (1973).
10. B. C. Cavenett, P. Dawson, and K. Morigaki, J. Phys. C **12**, L197 (1979).
11. W. M. Chen, M. Godlewski, B. Monemar, and J. P. Bergman, Phys. Rev. B **41**, 5746 (1990).
12. A. Kana-ah, B. C. Cavenett, H. P. Gislason, *et al.*, J. Phys. C **19**, 1239 (1986).
13. E. B. Aleksandrov, G. I. Khvostenko, and M. P. Chaĭka, *Interference of Atomic States* (Nauka, Moscow, 1991).
14. É. I. Rashba and G. É. Gurgenishvili, Fiz. Tverd. Tela (Leningrad) **4**, 1029 (1962) [Sov. Phys. Solid State **4**, 759 (1962)].

Translated by N. Wadhwa

Journal of Experimental and Theoretical Physics, Vol. 96, No. 1, 2003, pp. 8–18.
Translated from Zhurnal Éksperimental'noĭ i Teoreticheskoĭ Fiziki, Vol. 123, No. 1, 2003, pp. 13–24.

NUCLEI, PARTICLES, AND THEIR INTERACTION

Magnetooptical Compression of Atomic Beams

V. I. Balykin and V. G. Minogin*

Institute of Spectroscopy, Russian Academy of Sciences, Troitsk, Moscow oblast, 142190 Russia
**e-mail: minogin@isan.troitsk.ru*

Received July 2, 2002

Abstract—We consider the propagation of an atomic beam in a quadrupole magnetic field under transverse irradiation by a cooling laser field. The cooling laser field was chosen in the form of a two-dimensional σ^+–σ^- configuration. We show that the sub-Doppler resonance in the radiation force can be used to reduce the diameter of the atomic beam to a value on the order of 10 μm. We establish that the simultaneous transverse cooling and compression of the atomic beam allow its phase density to be increased to values of the order of 10^{-4}–10^{-3}. The dipole interaction of an atom with the cooling and compressing laser field in a quadrupole magnetic field is analyzed in terms of a simple (3 + 5)-level model atom. © *2003 MAIK "Nauka/Interperiodica".*

1. INTRODUCTION

The compression of atomic beams to increase their phase density has been of considerable interest in recent years. One of the effective schemes is the compression of an atomic beam by a cooling laser field in a nonuniform magnetic field. Transverse cooling of an atomic beam in a potential well produced by a magnetic field causes the atomic oscillation amplitude in the potential and, accordingly, the atomic beam diameter to decrease. Previously, similar compression schemes were experimentally studied for transverse Doppler [1] and sub-Doppler [2] cooling of atomic beams. A deeper compression can be achieved in principle through a significant reduction in the beam temperature by using sub-Doppler cooling.

Attaining a high atomic beam phase density is of independent interest, because atomic beams are widely used in precision physical measurements, and of special interest in designing continuous-wave atomic lasers. The existing experimental schemes for attaining quantum degeneracy in atomic ensembles are known to be based on the evaporative cooling method [3, 4]. This cooling method can be applied to high-density atomic ensembles with a large number of atoms and with a low temperature. In all cases, the evaporative cooling method has been applied to laser-precooled atomic ensembles. All of the above three conditions in laser cooling of atoms are difficult to satisfy: low temperatures are reached at low atomic densities and, conversely, high densities prevent low temperatures from being reached. Despite these difficulties, the method has been effectively applied to atomic ensembles localized in magnetic or optical dipole traps. The long lifetime of the trapped atoms (on the order of 100 s) allows quantum degeneracy to be achieved even at a moderate initial phase density.

An atomic ensemble in the beam regime is of interest in that a continuous-wave atomic laser can be realized. However, quantum degeneracy in a beam is more difficult to achieve because of the limited preparation time of the atomic ensemble determined by the time of flight. Thus, for the evaporative cooling method to be applicable, the initial atomic phase density in the beams must be higher than that in the traps. Here, we consider a laser-cooling scheme that allows us to significantly increase the atomic beam phase density and, thereby, makes the subsequent evaporative cooling of the beam atoms possible to attain quantum degeneracy.

The effect of a magnetic field on the sub-Doppler cooling of atoms has previously been studied both theoretically [5–8] and experimentally [9, 10]. A magnetic field was used in experiments to extract atomic beams from magnetooptical traps [11–13]. The structure of the one-photon Doppler and two-photon sub-Doppler resonances in a magnetic field was investigated in [14, 15]. The multicomponent velocity distribution of the atomic cloud produced by the one- and two-photon resonances in a magnetooptical trap (MOT) was studied in [6, 7]. The authors of [6, 10] pointed out that under certain conditions, a magnetic field could even suppress the sub-Doppler cooling.

Here, our goal is to obtain analytical estimates for the maximum possible compression of an atomic beam in a nonuniform magnetic field and to estimate the atomic beam phase density reached in the case of transverse sub-Doppler cooling and compression.

We analyze the transverse compression of an atomic beam in a quadrupole axisymmetric magnetic field on which a cooling laser field was imposed. The laser field chosen as a two-dimensional σ^+–σ^- configuration produces transverse sub-Doppler cooling of the atomic beam, while the magnetic field produces a two-dimensional potential well across the atomic beam axis. The dipole interaction of the atoms with a nonuniform magnetic field and with a laser electric field is considered in a simple (3 + 5)-level model atom with the total

moments in the ground and excited states $F_g = 1$ and $F_e = 2$. In order that our results be applicable to real experimental schemes, the Lande g factors for the ground and excited states are assumed to be arbitrary. Our analysis reveals that the sub-Doppler resonances in the radiation force can be used for the simultaneous transverse cooling to sub-Doppler temperatures and the effective compression of the atomic beam to a diameter on the order of 10 μm.

2. THE COMPRESSION SCHEME AND THE MODEL ATOM

The scheme for transverse sub-Doppler compression of an atomic beam in a quadrupole magnetic field is shown in Fig. 1. In this scheme, four rectilinear currents I produce a magnetic field $\mathbf{B} = (B_x, B_y)$ near the electromagnetic quadrupole configuration axis whose components are defined by the standard relations [16]

$$B_y = -ay, \quad B_z = az. \tag{1}$$

Here, a is the magnetic field gradient on the quadrupole magnetic configuration axis, which depends on the currents I and on the distance R from the configuration axis to the currents.

The laser field was chosen in the form of two σ^+–σ^- configurations directed along the y and z axes. Each σ^+–σ^- configuration was composed of two counterpropagating, circularly polarized laser waves. In the coordinate system shown in Fig. 1, the electric field of the laser σ^+–σ^- configuration directed along the y axis is

$$\mathbf{E}^{(y)} = \frac{E_0}{2}[\mathbf{e}_+^y \exp(i(ky - \omega t)) - \mathbf{e}_-^y \exp(-i(ky - \omega t))] - \frac{E_0}{2}[\mathbf{e}_+^y \exp(i(ky + \omega t)) - \mathbf{e}_-^y \exp(-i(ky + \omega t))], \tag{2}$$

where

$$\mathbf{e}_\pm^y = \mp\frac{1}{\sqrt{2}}(\mathbf{e}_z \pm i\mathbf{e}_x)$$

are the unit circular vectors that correspond to the quantization y axis, $k = \omega/c$ is the magnitude of the wave vector, and ω is the laser field frequency. The first and second terms in Eq. (2) describe the waves with σ^+ and σ^- polarizations with respect to the quantization y axis, respectively. The electric field of the laser σ^+–σ^- configuration directed along the z axis in the coordinate system with the quantization z axis is

$$\mathbf{E}^{(z)} = \frac{E_0}{2}[\mathbf{e}_+^z \exp(i(kz - \omega t)) - \mathbf{e}_-^z \exp(-i(kz - \omega t))] - \frac{E_0}{2}[\mathbf{e}_+^z \exp(i(kz + \omega t)) - \mathbf{e}_-^z \exp(-i(kz + \omega t))], \tag{3}$$

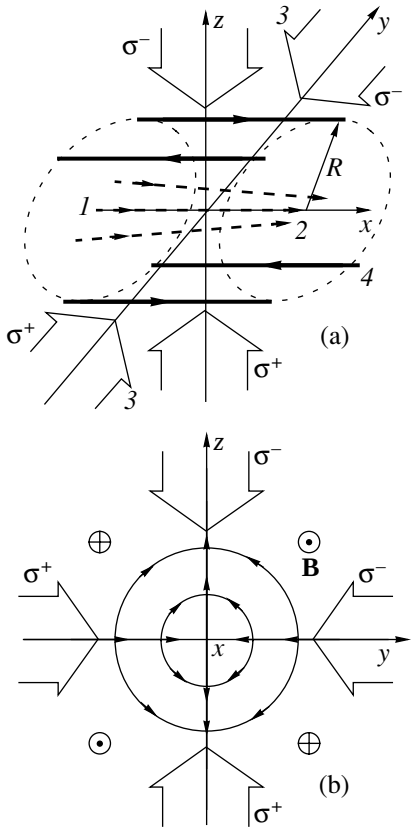

Fig. 1. (a) The scheme for laser sub-Doppler compression of an atomic beam in a quadrupole magnetic field: *1* incoming atomic beam, *2* outgoing atomic beam, *3* cooling laser beams, *4* electric currents producing a quadrupole magnetic field **B**. (b) The distribution of magnetic field **B** in the *yz* plane and the positions of the cooling laser beams.

where

$$\mathbf{e}_\pm^z = \mp\frac{1}{\sqrt{2}}(\mathbf{e}_x \pm i\mathbf{e}_y)$$

are the unit circular vectors that correspond to the quantization z axis. Similar to configuration (2), the first and second terms in Eq. (3) describe the waves with σ^+ and σ^- polarizations with respect to the quantization z axis, respectively.

Below, we estimate the basic parameters of the compressed atomic beam in a simple one-dimensional interaction model (see Fig. 2a). In this model, the atomic beam is compressed by the σ^+–σ^- configuration that propagates along the z axis. When the quantization z axis is chosen, this laser configuration induces the optical transitions in a (3 + 5)-level atom, shown in Fig. 2b. It should be immediately noted that all our estimates are also valid for the one-dimensional compression of the σ^+–σ^- configuration propagating along the y axis.

3. BASIC EQUATIONS

For the interaction scheme under consideration, the Hamiltonian can be written as

$$H = H_0 - \boldsymbol{\mu}\cdot\mathbf{B} - (\hbar^2/2M)\Delta - \mathbf{d}\cdot\mathbf{E}, \qquad (4)$$

where the Hamiltonian H_0 describes the quantized atomic states in the absence of a magnetic field and the second and last terms describe the dipole interaction of an atom with the nonuniform magnetic field $\mathbf{B} = B_z\mathbf{e}_z$ and with the laser field $\mathbf{E} = \mathbf{E}^{(z)}$, respectively.

A natural approach to describing the atomic motion in the chosen scheme is to use the atomic density matrix in the Wigner representation, $\rho = \rho(\mathbf{r}, \mathbf{p}, t)$. Below, we assume the density matrix $\rho_{\alpha\beta} = \langle\alpha|\rho|\beta\rangle$ to be determined from the time-independent eigenfunctions of the magnetic states α and $\beta = |F, m_F\rangle$. The energies E_{e_m} and E_{g_m} of the atomic Hamiltonian proper,

$$H_a = H_0 - \boldsymbol{\mu}\cdot\mathbf{B},$$

correspond to these eigenfunctions.

For a laser field composed of plane monochromatic traveling waves with a frequency ω close to the atomic transition frequencies $\omega_{mn} = (E_m - E_n)/\hbar$,

$$\mathbf{E} = \sum_a [\mathbf{E}^a \exp(i(\mathbf{k}_a\cdot\mathbf{r} - \omega t)) + \mathbf{E}^{a*}\exp(-i(\mathbf{k}_a\mathbf{r} - \omega t))], \qquad (5)$$

the equations of motion for the elements of the density matrix in Wigner representation and in the rotating-wave approximation can be written as [17, 18]

$$i\hbar\left(\frac{\partial}{\partial t} + \mathbf{v}\frac{\partial}{\partial\mathbf{r}}\right)\rho_{kl}(\mathbf{r}, \mathbf{p}) = (E_k - E_l)\rho_{kl}(\mathbf{r}, \mathbf{p})$$

$$- \sum_{a, m}(\mathbf{d}_{km}\cdot\mathbf{E}^a)\rho_{ml}\left(\mathbf{r}, \mathbf{p} - \frac{1}{2}\hbar\mathbf{k}_a\right)\exp(i\mathbf{k}_a\cdot\mathbf{r} - i\omega t)$$

$$+ \sum_{a, n}(\mathbf{d}_{nl}\cdot\mathbf{E}^a)\rho_{kn}\left(\mathbf{r}, \mathbf{p} + \frac{1}{2}\hbar\mathbf{k}_a\right)\exp(i\mathbf{k}_a\cdot\mathbf{r} - i\omega t)$$

$$- \sum_{a, m}(\mathbf{d}_{km}\cdot\mathbf{E}^{a*})\rho_{ml}\left(\mathbf{r}, \mathbf{p} + \frac{1}{2}\hbar\mathbf{k}_a\right)\exp(-i\mathbf{k}_a\cdot\mathbf{r} + i\omega t) \qquad (6)$$

$$+ \sum_{a, n}(\mathbf{d}_{nl}\cdot\mathbf{E}^{a*})\rho_{kn}\left(\mathbf{r}, \mathbf{p} - \frac{1}{2}\hbar\mathbf{k}_a\right)\exp(-i\mathbf{k}_a\cdot\mathbf{r} + i\omega t)$$

$$+ i\hbar\langle k|\Gamma\rho(\mathbf{r}, \mathbf{p})|l\rangle,$$

where $\mathbf{d}_{kl} = \langle k|d|l\rangle$ are the matrix elements of the atomic dipole moment operator. All four sums in Eqs. (6) are assumed to include terms that correspond only to positive atomic frequencies,

$$\omega_{pq} = \frac{E_p - E_q}{\hbar} > 0.$$

The first, second, third, and fourth sums include, respectively, the terms with frequencies

$$\omega_{km} = \frac{E_k - E_m}{\hbar} > 0,$$

$$\omega_{nl} = \frac{E_n - E_l}{\hbar} > 0,$$

$$\omega_{mk} = \frac{E_m - E_k}{\hbar} > 0,$$

$$\omega_{ln} = \frac{E_l - E_n}{\hbar} > 0.$$

The first term in Eqs. (6) describes the contributions from the radiative relaxation operator Γ.

Note that in Eqs. (6), we omitted the small magnetodipole forces

$$\mathbf{f}_\alpha = \partial\langle\alpha|\boldsymbol{\mu}\cdot\mathbf{B}|\alpha\rangle/\partial\mathbf{r},$$

which play no significant role in the dynamics of the atom.

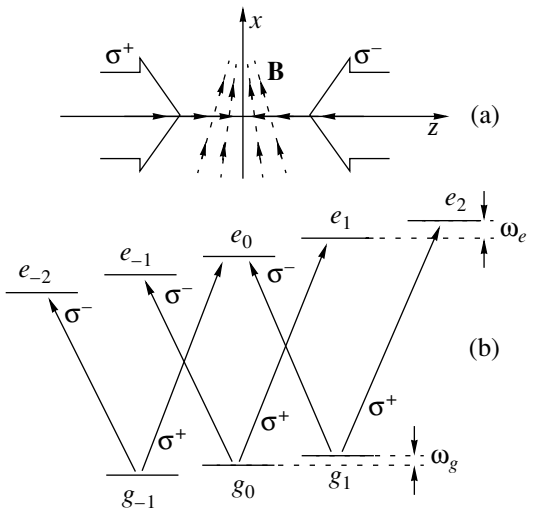

Fig. 2. (a) The one-dimensional compression of an atomic beam in the field of the laser σ^+–σ^- configuration propagating along the z axis. The magnetic field is directed along the z axis and the atomic beam propagates along the x axis. (b) Zeeman energy levels for the (3 + 5)-level atom in the coordinate system with the quantization z axis for positive Zeeman shifts, $\omega_g > 0$ and $\omega_e > 0$. The arrows indicate the transitions induced by the $\sigma^\pm$- and π-polarized laser waves.

Below, the Zeeman shifts of the magnetic states are considered in the simplest linear approximation in magnetic field strength. For the ground-state sublevels,

$$\langle F_g, m_g|-\boldsymbol{\mu}\cdot\mathbf{B}|F_g, m_g\rangle = \mu_B g_g B_z m_g; \quad (7)$$

for the excited-state sublevels,

$$\langle F_e, m_e|-\boldsymbol{\mu}\cdot\mathbf{B}|F_e, m_e\rangle = \mu_B g_e B_z m_e. \quad (8)$$

Here, μ_B is the Bohr magneton; g_g and g_e are the Lande g factors for the ground and excited states, respectively; $F_g = 1$, $m_g = -1, 0, 1$; $F_e = 2$, $m_e = -2, -1, 0, 1, 2$.

Below, we give Eqs. (6) for a (3 + 5)-level atom in explicit form in the practically important case of weakly saturated atomic transitions. In this case, it will suffice to take into consideration the equations only for the diagonal elements of the density matrix, for the nondiagonal one-photon elements describing optical coherences, and for one nondiagonal two-photon element describing the coherence between the sublevels g_{-1} and g_1 of the ground state g. Concurrently, we eliminate the explicit dependence on time and coordinate from the equations by the following simple substitutions:

$$\begin{aligned}
\rho_{g_{-1}e_{-2}} &= \sigma_{g_{-1}e_{-2}}\exp(i\omega t + ikz),\\
\rho_{g_{-1}e_0} &= \sigma_{g_{-1}e_0}\exp(i\omega t - ikz),\\
\rho_{g_0e_{-1}} &= \sigma_{g_0e_{-1}}\exp(i\omega t + ikz),\\
\rho_{g_0e_1} &= \sigma_{g_0e_1}\exp(i\omega t - ikz),\\
\rho_{g_1e_0} &= \sigma_{g_1e_0}\exp(i\omega t + ikz),\\
\rho_{g_1e_2} &= \sigma_{g_1e_2}\exp(i\omega t - ikz),\\
\rho_{g_{-1}g_1} &= \sigma_{g_{-1}g_1}\exp(-2ikz).
\end{aligned}$$

After these substitutions, the equations for the atomic density matrix elements that describe the dipole interaction of the (3 + 5)-level atom with the laser field $\mathbf{E} = \mathbf{E}^{(z)}$ in a nonuniform magnetic field $\mathbf{B} = B_z\mathbf{e}_z$ in the approximation of weak saturation are

$$\begin{aligned}
\frac{d}{dt}\rho_{g_{-1}g_{-1}} &= i\Omega(\sigma^{(-)}_{e_{-2}g_{-1}} - \sigma^{(-)}_{g_{-1}e_{-2}}) + \frac{i\Omega}{\sqrt{6}}(\sigma^{(+)}_{e_0g_{-1}} - \sigma^{(+)}_{g_{-1}e_0})\\
&+ \gamma\int\left(2\Phi_\sigma(\mathbf{n})\rho^{(\mathbf{n})}_{e_{-2}e_{-2}} + \Phi_\pi(\mathbf{n})\rho^{(\mathbf{n})}_{e_{-1}e_{-1}} + \frac{1}{3}\Phi_\sigma(\mathbf{n})\rho^{(\mathbf{n})}_{e_0e_0}\right)d^2n,\\
\frac{d}{dt}\rho_{g_0g_0} &= \frac{i\Omega}{\sqrt{2}}(\sigma^{(-)}_{e_{-1}g_0} - \sigma^{(-)}_{g_0e_{-1}} + \sigma^{(+)}_{e_1g_0} - \sigma^{(+)}_{g_0e_1})\\
&+ \gamma\int\left(\Phi_\sigma(\mathbf{n})\rho^{(\mathbf{n})}_{e_{-1}e_{-1}} + \frac{4}{3}\Phi_\pi(\mathbf{n})\rho^{(\mathbf{n})}_{e_0e_0} + \Phi_\sigma(\mathbf{n})\rho^{(\mathbf{n})}_{e_1e_1}\right)d^2n,\\
\frac{d}{dt}\rho_{g_1g_1} &= i\Omega(\sigma^{(+)}_{e_2g_1} - \sigma^{(+)}_{g_1e_2}) + \frac{i\Omega}{\sqrt{6}}(\sigma^{(-)}_{e_0g_1} - \sigma^{(-)}_{g_1e_0})\\
&+ \gamma\int\left(\frac{1}{3}\Phi_\sigma(\mathbf{n})\rho^{(\mathbf{n})}_{e_0e_0} + \Phi_\pi(\mathbf{n})\rho^{(\mathbf{n})}_{e_1e_1} + 2\Phi_\sigma(\mathbf{n})\rho^{(\mathbf{n})}_{e_2e_2}\right)d^2n,\\
\frac{d}{dt}\rho_{e_{-2}e_{-2}} &= i\Omega(\sigma^{(+)}_{g_{-1}e_{-2}} - \sigma^{(+)}_{e_{-2}g_{-1}}) - 2\gamma\rho_{e_{-2}e_{-2}},\\
\frac{d}{dt}\rho_{e_{-1}e_{-1}} &= \frac{i\Omega}{\sqrt{2}}(\sigma^{(+)}_{g_0e_{-1}} - \sigma^{(+)}_{e_{-1}g_0}) - 2\gamma\rho_{e_{-1}e_{-1}},\\
\frac{d}{dt}\rho_{e_0e_0} &= \frac{i\Omega}{\sqrt{6}}(\sigma^{(-)}_{g_{-1}e_0} - \sigma^{(-)}_{e_0g_{-1}} + \rho^{(+)}_{g_1e_0} - \rho^{(+)}_{e_0g_1}) - 2\gamma\rho_{e_0e_0},\\
\frac{d}{dt}\rho_{e_1e_1} &= \frac{i\Omega}{\sqrt{2}}(\sigma^{(-)}_{g_0e_1} - \sigma^{(-)}_{e_1g_0}) - 2\gamma\rho_{e_1e_1},\\
\frac{d}{dt}\rho_{e_2e_2} &= i\Omega(\sigma^{(-)}_{g_1e_2} - \sigma^{(-)}_{e_2g_1}) - 2\gamma\rho_{e_2e_2},\\
\frac{d}{dt}\sigma_{g_{-1}e_{-2}} &= i\Omega(\rho^{(-)}_{e_{-2}e_{-2}} - \rho^{(+)}_{g_{-1}g_{-1}})\\
&- (\gamma - i(\omega_g - 2\omega_e - \delta_1))\sigma_{g_{-1}e_{-2}},\\
\frac{d}{dt}\sigma_{g_{-1}e_0} &= -\frac{i\Omega}{\sqrt{6}}(\rho^{(-)}_{g_{-1}g_{-1}} + \sigma^{(+)}_{g_{-1}g_1} - \rho^{(+)}_{e_0e_0})\\
&- (\gamma - i(\omega_g - \delta_{-1}))\sigma_{g_{-1}e_0},\\
\frac{d}{dt}\sigma_{g_0e_{-1}} &= -\frac{i\Omega}{\sqrt{2}}(\rho^{(+)}_{g_0g_0} - \rho^{(-)}_{e_{-1}e_{-1}}) - (\gamma + i(\omega_e + \delta_1))\sigma_{g_0e_{-1}},\\
\frac{d}{dt}\sigma_{g_0e_1} &= -\frac{i\Omega}{\sqrt{2}}(\rho^{(-)}_{g_0g_0} - \rho^{(-)}_{e_{-1}e_{-1}}) - (\gamma - i(\omega_e - \delta_{-1}))\sigma_{g_0e_1},\\
\frac{d}{dt}\sigma_{g_1e_0} &= -\frac{i\Omega}{\sqrt{6}}(\rho^{(+)}_{g_1g_1} + \sigma^{(-)}_{g_1g_{-1}} - \rho^{(-)}_{e_0e_0})\\
&- (\gamma + i(\omega_g + \delta_1))\sigma_{g_1e_0},\\
\frac{d}{dt}\sigma_{g_1e_2} &= -i\Omega(\rho^{(-)}_{g_1g_1} - \rho^{(+)}_{e_2e_2})\\
&- (\gamma + i(\omega_g - 2\omega_e + \delta_{-1}))\sigma_{g_1e_2},\\
\frac{d}{dt}\sigma_{g_{-1}g_1} &= \frac{i\Omega}{\sqrt{6}}(\sigma^{(+)}_{e_0g_1} - \sigma^{(-)}_{g_{-1}e_0}) + 2i(\omega_g + kv)\sigma_{g_{-1}g_1}.
\end{aligned} \quad (9)$$

Above, we use the following notation for the density matrix elements:

$$\rho_{ab} = \langle a|\rho(\mathbf{r}, \mathbf{p}, t)|b\rangle,$$

$$\rho_{ab}^{(\pm)} = \left\langle a\left|\rho\left(\mathbf{r}, \mathbf{p} \pm \frac{1}{2}\hbar\mathbf{k}, t\right)\right|b\right\rangle,$$

$$\rho_{ab}^{(\mathbf{n})} = \langle a|\rho(\mathbf{r}, \mathbf{p} + \mathbf{n}\hbar k, t)|b\rangle,$$

where $\mathbf{k} = k\mathbf{e}_z$ and $\mathbf{n}$ is the unit vector that specifies the direction of the spontaneous photon emission. The total time derivative is

$$\frac{d}{dt} = \frac{\partial}{\partial t} + v\frac{\partial}{\partial \mathbf{r}}. \quad (10)$$

The Rabi frequency Ω and the spontaneous decay rate of the upper magnetic sublevels 2γ are defined as

$$\Omega = \frac{\|d\|E_0}{2\sqrt{5}\hbar}, \quad 2\gamma = W_{sp} = \frac{4}{3}\frac{\|d\|^2\omega_0^3}{\hbar c^3}, \quad (11)$$

where $\|d\|$ is the reduced matrix element. The main, δ, and two Doppler-shifted, $\delta_{\pm 1}$, detunings are given by the relations

$$\delta = \omega - \omega_0, \quad \delta_{\pm 1} = \omega - \omega_0 \pm kv, \quad (12)$$

where $v = v_z$ is the velocity component along the z axis. The frequencies

$$\omega_g = \mu_B g_g a z/\hbar, \quad \omega_e = \mu_B g_e a z/\hbar \quad (13)$$

define the Zeeman shifts of the magnetic sublevels, which depend on the atom coordinate and which can have any signs. The functions $\Phi_\sigma(\mathbf{n})$ and $\Phi_\pi(\mathbf{n})$ define the angular anisotropy in spontaneous emission:

$$\Phi_\sigma(\mathbf{n}) = \frac{3}{16\pi}(1 + n_z^2), \quad \Phi_\pi(\mathbf{n}) = \frac{3}{8\pi}(1 - n_z^2), \quad (14)$$

where $n_z = \cos\theta$ is the component of the unit vector $\mathbf{n}$ along the quantization z axis. The integration in the radiation arrival terms is performed over the directions of spontaneous emission specified by the unit vector $\mathbf{n}$, $d^2n = \sin\theta d\theta d\phi$.

4. THE KINETIC EQUATION

The difference differential equations (9), which do not include the explicit dependence on time and coordinate, can be analyzed in a standard way [19]. If the atom–field interaction time is much longer than the spontaneous decay time, $\tau_{\text{int}} \gg \tau_{sp} = 1/2\gamma$, then the momentum width of the density matrix elements can be assumed to exceed the photon momentum $\hbar k$. This assumption, which always holds below, allows the atomic density matrix elements to be expanded in terms of powers of the photon momentum $\hbar k$. Considering below the equations expanded in terms of sequentially increasing orders of the photon momentum $\hbar k$, we can infer that the diagonal (ρ_{aa}) and nondiagonal (σ_{ab}) density matrix elements are the functionals of the Wigner distribution function $w(\mathbf{r}, \mathbf{p}, t)$,

$$w = \sum \rho_{g_\alpha g_\alpha} + \left(\sum \rho_{e_\beta e_\beta}\right), \quad (15)$$

where $\alpha = -1, 0, 1$ and $\beta = -2, -1, 0, 1, 2$.

The general structure of the functional dependence can be directly determined from the structure of the expanded equations:

$$\begin{aligned}\rho_{aa} &= \left(R_{aa}^0 + \frac{1}{2}\hbar k R_{aa}^1 + \ldots\right)w \\ &\quad + \frac{1}{2}\hbar k(Q_{aa}^1 + \ldots)\frac{\partial w}{\partial p_z} + \ldots, \\ \sigma_{ab} &= \left(S_{ab}^0 + \frac{1}{2}\hbar k S_{ab}^1 + \ldots\right)w \\ &\quad + \frac{1}{2}\hbar k(T_{ab}^1 + \ldots)\frac{\partial w}{\partial p_z} + \ldots,\end{aligned} \quad (16)$$

where R_{aa}^0, R_{aa}^1, Q_{aa}^1, …, S_{ab}^0, S_{ab}^1, T_{ab}^1, … are the functions of momentum $\mathbf{p}$ (or velocity $\mathbf{v} = \mathbf{p}/M$), which are determined by the solution procedure. By the definition of the distribution function (15), the unknown diagonal functions satisfy the normalization conditions

$$\sum R_{g_\alpha g_\alpha}^0 + R_{e_\beta e_\beta}^0 = 1, \quad (17)$$

$$\sum R_{g_\alpha g_\alpha}^1 + R_{e_\beta e_\beta}^1 = 0, \quad (18)$$

$$\sum Q_{g_\alpha g_\alpha}^1 + Q_{e_\beta e_\beta}^1 = 0. \quad (19)$$

Taking into account the structure of solution (16), we can see from the expanded equations that the Wigner function $w(\mathbf{r}, \mathbf{p}, t)$ satisfies the closed equation. To within the second order in photon momentum $\hbar k$, the closed equation for the distribution function is the Fokker–Planck equation:

$$\frac{\partial w}{\partial t} + \mathbf{v}\frac{\partial w}{\partial \mathbf{r}} = -\frac{\partial}{\partial p_z}(Fw) + \sum \frac{\partial^2}{\partial p_i^2}(D_{ii}w), \quad (20)$$

where $i = x, y, z$. The kinetic coefficients F and D_{ii} in Eq. (20) define the radiation force and the momentum diffusion tensor:

$$\begin{aligned}F = \hbar k\Omega\Big[&i(S_{g_1e_2}^0 - S_{e_2g_1}^0 + S_{e_{-2}g_{-1}}^0 - S_{g_{-1}e_{-2}}^0) \\ &+ \frac{i}{\sqrt{2}}(S_{g_0e_1}^0 - S_{e_1g_0}^0 + S_{e_{-1}g_0}^0 - S_{g_0e_{-1}}^0) \\ &+ \frac{i}{\sqrt{6}}(S_{g_{-1}e_0}^0 - S_{e_0g_{-1}}^0 + S_{e_0g_1}^0 - S_{g_1e_0}^0)\Big],\end{aligned} \quad (21)$$

$$D_{ii} = \hbar^2 k^2 \gamma \times \Big[\alpha_{ii}^{\sigma} \Big(R^0_{e_{-2}e_{-2}} + \frac{1}{2} R^0_{e_{-1}e_{-1}} + \frac{1}{3} R^0_{e_0 e_0} + \frac{1}{2} R^0_{e_1 e_1} + R^0_{e_2 e_2} \Big) + \alpha_{ii}^{\pi} \Big(\frac{1}{2} R^0_{e_{-1}e_{-1}} + \frac{2}{3} R^0_{e_0 e_0} + \frac{1}{2} R^0_{e_1 e_1} \Big) \Big] + \frac{1}{2} \delta_{iz} \hbar^2 k^2 \Omega \Big[i (T^1_{g_{-1}e_{-2}} - T^1_{e_{-2}g_{-1}} + T^1_{e_2 g_1} - T^1_{g_1 e_2}) + \frac{i}{\sqrt{2}} (T^1_{g_0 e_{-1}} - T^1_{e_{-1}g_0} + T^1_{e_1 g_0} - T^1_{g_0 e_1}) + \frac{i}{\sqrt{6}} (T^1_{e_0 g_{-1}} - T^1_{g_{-1}e_0} + T^1_{g_1 e_0} - T^1_{e_0 g_1}) \Big]. \quad (22)$$

In these equations, the coefficients α_{ii}^{σ} and α_{ii}^{π} take into account the angular anisotropy in spontaneous photon emission,

$$\alpha_{ii}^{\sigma} = \int \Phi_{\sigma}(\mathbf{n}) n_i^2 d^2 n, \quad \alpha_{ii}^{\pi} = \int \Phi_{\pi}(\mathbf{n}) n_i^2 d^2 n. \quad (23)$$

In explicit form, the angular anisotropy coefficients are

$$\alpha_{xx}^{\sigma} = \alpha_{yy}^{\sigma} = \frac{3}{10}, \quad \alpha_{zz}^{\sigma} = \frac{2}{5}, \quad \alpha_{xx}^{\pi} = \alpha_{yy}^{\pi} = \frac{2}{5}, \quad \alpha_{zz}^{\pi} = \frac{1}{5}. \quad (24)$$

The force F and the diffusion tensor D_{ii} can be explicitly determined from the solution of the steady-state equations that follow from the expanded equations for the atomic density matrix elements considered separately in the zero and first orders in photon momentum $\hbar k$. The steady-state equations for the functions R^0_{aa} and S^0_{ab}, as well as for Q^1_{aa} and T^1_{ab} in the case of weakly saturated transitions, are given in Appendices A and B.

5. FORCES ACTING ON AN ATOM

The radiation force that acts on an atom in the scheme under consideration depends both on the velocity and on the coordinate of the atom. In the approximation of weak saturation, the one-photon optical processes described by the coherences between the sublevels g_α and $e_{\alpha \pm 1}$ and the two-photon processes described by the coherences between the ground-state sublevels g_{-1} and g_1 contribute to the force.

Below, we consider the radiation force in the practically important case of large negative detunings ($-\delta \gg \gamma$), where the radiation force produces the deepest sub-Doppler cooling of an atomic beam [20, 21]. Restricting our analysis to low velocities ($kv \ll \gamma$) and small Zeeman shifts ($|\omega_g|, |\omega_e| \ll \gamma$), we can derive the following approximate expression for the radiation force near the axis of the compressing configuration ($z = 0$), which reduces to the sum of the forces due to one- and two-photon processes (Fig. 3):

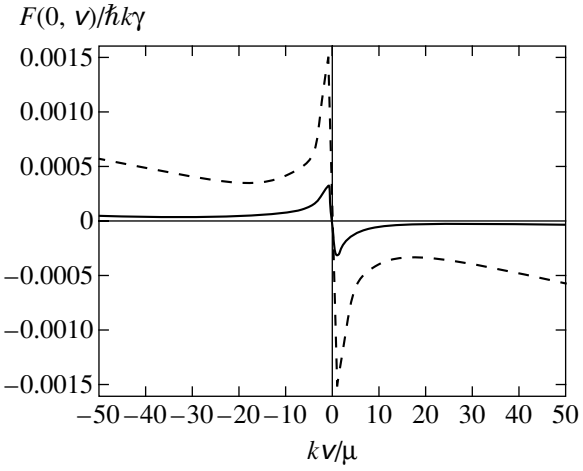

Fig. 3. Radiation force versus velocity at $z = 0$, the detuning $\delta = -10\gamma$, and the saturation parameter $G = 0.1$ (solid line) and 0.5 (dashed line). The sub-Doppler resonance line halfwidths $\mu = 0.18\gamma$ (solid line) and 0.90γ (dashed line) correspond to the chosen detuning and saturation parameter.

$$F(0, v) = -\frac{25}{11} \hbar k \gamma \frac{G\gamma^2}{\delta^2} \frac{(88/85) + (kv/\mu)^2}{1 + (kv/\mu)^2} \frac{kv}{|\delta|} - \frac{60}{17} \hbar k \gamma \frac{kv/|\delta|}{1 + (kv/\mu)^2}, \quad (25)$$

where

$$G = \frac{2\Omega^2}{\gamma^2} = \frac{1}{10} \Big(\frac{\|d\| E_0}{\hbar \gamma} \Big)^2 \quad (26)$$

is the dimensionless saturation parameter and

$$\mu = \frac{1}{4} \sqrt{\frac{17}{33}} \frac{G\gamma^2}{|\delta|} = \frac{1}{2} \sqrt{\frac{17}{33}} \frac{\Omega^2}{|\delta|} \quad (27)$$

is the sub-Doppler resonance halfwidth for $|\delta| \gg \gamma$.

Under the same conditions, the force acting on a static atom is also the sum of the forces due to one- and two-photon processes (Fig. 4):

$$F(z, 0) = -\frac{5}{11} \hbar k \gamma \frac{G\gamma^2}{|\delta|^3} \times \frac{(44/17)(3\omega_e - \omega_g) + (8\omega_e - 3\omega_g)(\omega_g/\mu)^2}{1 + (\omega_g/\mu)^2} - \frac{60}{17} \hbar k \gamma \frac{\omega_g/|\delta|}{1 + (\omega_g/\mu)^2}. \quad (28)$$

Recall that the Zeeman shifts ω_g and ω_e are proportional to the z coordinate.

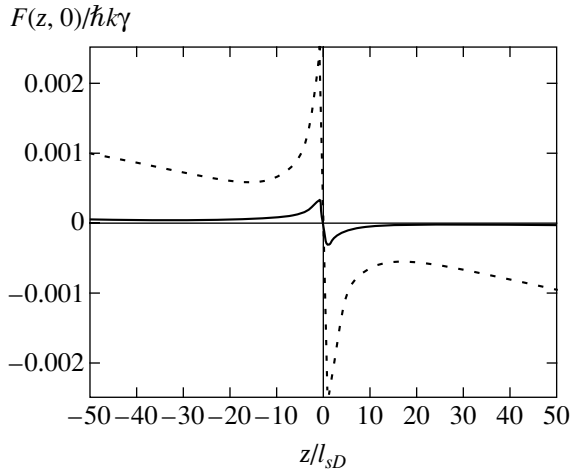

Fig. 4. Radiation force versus coordinate at a zero velocity, the detuning $\delta = -10\gamma$, and the saturation parameter $G = 0.1$ (solid line) and 0.5 (dotted line) for the Lande factors $g_g = 1/3$ and $g_e = 1/2$. The value of l_{sD} defined by (30) was chosen as the scale length.

The broad parts of the velocity and coordinate dependences of the radiation force are attributable to the one-photon absorption (emission) weakly perturbed by two-photon processes. In our case of large detunings ($|\delta| \gg \gamma \gg \mu$), the broad velocity dependence originates from the two resonances of one-photon absorption (emission) located at the velocities $kv_{\text{res}} = \pm\delta$. The broad spatial dependence of the radiation force originates from the one-photon resonances related to the Zeeman shift frequencies.

The narrow resonances in the field are attributable to two-photon processes. For an atom that moves in a zero magnetic field, i.e., at $z = 0$, the two-photon processes are effective at two-photon resonance velocities

$$(\omega \pm kv) - (\omega \mp kv) \approx 0,$$

i.e., at velocities $v \approx 0$. For a static atom ($v = 0$), the two-photon processes are effective for

$$(\omega \pm \omega_g) - (\omega \mp \omega_g) \approx 0,$$

i.e., for $\omega_g \approx 0$ or for $z \approx 0$ (Fig. 4).

The characteristic velocity scale of the change in the force due to the sub-Doppler resonance is determined by the characteristic velocity $v_{sD} = \mu/k$, which for weak saturation and for a large negative detuning is

$$v_{sD} = \frac{1}{4}\sqrt{\frac{17}{33}}\frac{G\gamma\gamma}{|\delta|}\frac{\gamma}{k}. \tag{29}$$

The characteristic spatial scale of the change in the force due to the sub-Doppler resonance is determined by the length l_{sD} on which the Zeeman ground-state sublevel splitting is equal to the two-photon resonance width. For weak saturation and for a large negative detuning, the condition $\omega_g = \mu$ specifies the scale length

$$l_{sD} = \frac{\hbar\mu}{\mu_B g_g a}. \tag{30}$$

For definiteness, we estimate the degree of beam compression for ^{85}Rb atoms that interact with laser radiation on the $5^2S_{1/2}(F = 3) - 5^2P_{3/2}(F = 4)$ dipole transition at the wavelength $\lambda = 780$ nm. In general, this scheme is described by a (7 + 9)-level model atom. However, since the higher order multiphoton processes give small contributions to the radiation force, a simple (3 + 5)-level model can be used to estimate the main effects. For the optical transition under consideration, $g_g = 1/3$ and $g_e = 1/2$. If, for example, we choose the saturation parameter $G = 0.5$ and the detuning $d = -10\gamma$, then the characteristic velocity interval is $v_{sD} = 2.1$ cm s^{-1}. For a moderate magnetic field gradient, $a = 10$ G cm^{-1}, the characteristic spatial scale is $l_{sD} = 50$ μm.

6. BEAM COMPRESSION

The radiation force (28) produces a potential well across the atomic beam axis:

$$U(z) = -\int F(z, 0)dz.$$

For large detunings ($|\delta| \gg \gamma$) and for the Lande factors $g_g = 1/3$ and $g_e = 1/2$, this potential well is described by the approximate expression

$$U(z) \approx \frac{15}{22}\hbar\gamma\frac{G\gamma^3}{|\delta|^3}\frac{k}{z_m}z^2 + \frac{15}{88}\hbar\gamma\frac{G^2\gamma^3}{|\delta|^3}kz_m \times \ln\left(1 + \frac{176}{51}\left(\frac{\delta}{G\gamma}\right)^2\left(\frac{z}{z_m}\right)^2\right), \tag{31}$$

where we introduced the characteristic length on which the Zeeman shift frequency is equal to the natural line width,

$$z_m = \frac{\hbar\gamma}{\mu_B a}. \tag{32}$$

The shape of the potential well (31) near the bottom is determined by the two-photon sub-Doppler resonance and its wings are determined by the Doppler resonance (Fig. 5). At the magnetic field gradient $a = 10$ G cm^{-1}, the characteristic length for the transition in ^{85}Rb with the natural line halfwidth $\gamma/2\pi = 2.95$ MHz under consideration is $z_m \approx 2.1$ mm.

The atomic oscillation frequency near the bottom of the potential well where the sub-Doppler resonance is effective is

$$\omega_v = \left(\frac{\gamma}{|\delta|}\right)^{1/2}\sqrt{\frac{40}{17}\frac{\lambda}{2\pi z_m}\gamma\omega_r}, \tag{33}$$

where $\omega_r = \hbar k^2/2M$ is the recoil frequency. At the same detunings $\delta = -10\gamma$ and the magnetic field gradient a = 10 G cm^{-1}, the oscillation frequency for the chosen transition with the characteristic recoil frequency $\omega_r/2\pi$ = 3.8 kHz is $\omega_v \approx 400$ Hz.

Let us now estimate the parameters of the compressed atomic beam. For a negative detuning ($\delta < 0$), radiation force (25) reduces to the frictional force

$$F = -M\beta v$$

with the coefficient of friction β, which at large detunings ($|\delta| \gg \gamma, \Omega$) is proportional to the recoil frequency:

$$\beta = \frac{120}{17}\frac{\gamma}{|\delta|}\omega_r. \quad (34)$$

The velocity dependence of the momentum diffusion tensor also includes the two-photon sub-Doppler resonance localized at zero velocity. For our purposes, it will suffice to use the diffusion coefficient D_{zz} at zero velocity and zero coordinate, $D_0 = D_{zz}(0, 0)$. This value of the diffusion coefficient, together with the coefficient of friction β, determines the atomic temperature near the quadrupole configuration axis according to the steady-state solution of the Fokker–Planck equation:

$$T = \frac{D_0}{M\beta}.$$

At large detunings ($|\delta| \gg \gamma, \Omega$), the momentum diffusion coefficient D_0 is estimated as

$$D_0 = \frac{23}{17}\hbar^2 k^2 \gamma \frac{G\gamma^2}{\delta^2}. \quad (35)$$

Accordingly, the transverse velocity distribution of the atomic beam near the quadrupole configuration axis is described by the Maxwellian distribution with the characteristic temperature

$$T = \frac{D_0}{M\beta} = \frac{23}{60}\frac{\hbar\gamma}{k_B}\frac{G\gamma}{|\delta|}. \quad (36)$$

The spatial distribution is described by the Boltzmann distribution

$$W(z) = \text{const} \cdot \exp\left(-\frac{U(z)}{k_B T}\right). \quad (37)$$

Since the potential has the form (31), the beam size near the bottom of the potential well depends only on the saturation parameter G and on the characteristic length z_m. For the chosen Lande factors, the beam width is estimated as

$$\Delta z = \sqrt{8k_B T/M\omega_v^2} = \sqrt{\frac{391}{150}G\frac{\lambda z_m}{2\pi}}. \quad (38)$$

For detuning $\delta = -10\gamma$, saturation parameter G = 0.5, and magnetic field gradient a = 10 G cm^{-1}, the temperature is 3 μK and the beam size is 18 μm.

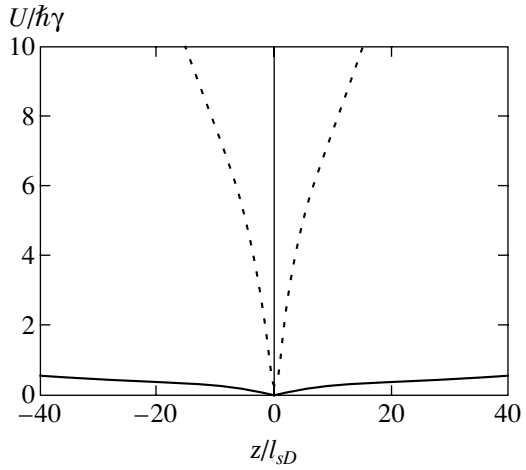

Fig. 5. The potential well for an atom at the same parameters as in Fig. 4.

It should be particularly emphasized that the above estimates are also retained for the beam compression along any other direction. Thus, in describing the compression of an atomic beam along the y axis, substituting the laser field (2) for field (3) in the basic equations does not change the above estimates. The estimates of the compression for any other directions include additional geometrical factors on the order of unity.

The widths of the velocity and spatial distributions determined above can be used to estimate the phase density of the compressed atomic beam. We give an estimate of the dimensionless phase density [22]:

$$\Lambda = \frac{N_a h^3}{(\Delta r \Delta p)^3}, \quad (39)$$

where N_a is the number of atoms in the beam and $(\Delta r \Delta p)^3$ is the phase volume occupied by the atoms. In the case of an atomic beam, it is convenient to express the phase density in terms of the mean atomic density n_a and to separate out the widths of the atomic momentum distribution along, Δp_l, and across, Δp_{tr}, the beam axis:

$$\Lambda = \frac{n_a h^3}{\Delta p_l (\Delta p_{tr})^2}. \quad (40)$$

The atomic density in the magnetic system under consideration is limited by the dipole–dipole atomic interaction, by the repulsive potential produced by scattered laser radiation, and by the attractive potential produced by the absorption of laser radiation. All these factors were studied in reasonable detail, because they play an important role in magnetooptical traps [23–26]. The most important factor is the reabsorption of photons inside the atomic ensemble. Multiple photon reabsorption causes the frictional and compressing forces to

decrease. A characteristic feature of an axisymmetric magnetic system is its small cross section. This circumstance shows that the atomic medium can remain optically transparent in the transverse direction at a relatively high density. A standard estimate for the atomic density $n_a = 1/\sigma\Delta z$ (where σ is the resonance absorption cross section) and available data on the atomic density in magnetooptical traps show that the maximum atomic density in the beam is limited to a value on the order of $n_a = 10^{12}$ cm^{-3}. If we take the realistic Doppler value of $\Delta p_l = M\gamma/k$ for the width of the longitudinal momentum distribution and the sub-Doppler value that corresponds to the temperature of 3 μK for the width of the transverse momentum distribution, we then obtain $\Lambda = 5 \times 10^{-4}$ for the ^{85}Rb atomic beam phase density.

7. CONCLUSION

Our analysis shows that the sub-Doppler resonances in the radiation force allow atomic beams to be compressed to values on the order of several tens of microns. Such a significant compression is, naturally, possible for slow atomic beams where the time of flight of the atoms is enough for the atomic temperature to be reduced to the sub-Doppler value.

Thus, we found that an atomic beam in a nonuniform magnetic field could be compressed to a diameter on the order of several tens of microns and the phase density could be increased to a value on the order of 10^{-4}–10^{-3}. Such a high expected atomic phase density in the compressed beam enables the subsequent evaporative cooling of the atoms down to quantum degeneracy for a realistic length of the magnetic trapping system [27]. In turn, the realization of this possibility may allow a continuous-wave atomic laser to be produced.

APPENDIX A

Below, we give the system of equations that defines the steady-state values of the functions $R^0_{g_\alpha g_\alpha} = N_\alpha$, $R^0_{e_\alpha e_\alpha} = n_\alpha$, and $S^0_{ab} = c_{ab}$:

$$\sum N_\alpha + \sum n_\alpha = 1, \tag{A.1}$$

$$i\Omega(c_{e_{-2}g_{-1}} - c_{g_{-1}e_{-2}}) + \frac{i\Omega}{\sqrt{6}}(c_{e_0g_{-1}} - c_{g_{-1}e_0}) + \gamma\left(2n_{-2} + n_{-1} + \frac{1}{3}n_0\right) = 0,$$

$$\frac{i\Omega}{\sqrt{2}}(c_{e_{-1}g_0} - c_{g_0e_{-1}} + c_{e_1g_0} - c_{g_0e_1}) + \gamma\left(n_{-1} + \frac{4}{3}n_0 + n_1\right) = 0,$$

$$i\Omega(c_{e_2g_1} - c_{g_1e_2}) + \frac{i\Omega}{\sqrt{6}}(c_{e_0g_1} - c_{g_1e_0}) + \gamma\left(\frac{1}{3}n_0 + n_1 + 2n_2\right) = 0,$$

$$i\Omega(c_{g_{-1}e_{-2}} - c_{e_{-2}g_{-1}}) - 2\gamma n_{-2} = 0,$$

$$\frac{i\Omega}{\sqrt{2}}(c_{g_0e_{-1}} - c_{e_{-1}g_0}) - 2\gamma n_{-1} = 0,$$

$$\frac{i\Omega}{\sqrt{6}}(c_{g_{-1}e_0} - c_{e_0g_{-1}} + c_{g_1e_0} - c_{e_0g_1}) - 2\gamma n_0 = 0,$$

$$\frac{i\Omega}{\sqrt{2}}(c_{g_0e_1} - c_{e_1g_0}) - 2\gamma n_1 = 0,$$

$$i\Omega(c_{g_1e_2} - c_{e_2g_1}) - 2\gamma n_2 = 0,$$

$$i\Omega(n_{-2} - N_{-1}) - (\gamma + i(\delta_1 - \omega_g + 2\omega_e))c_{g_{-1}e_{-2}} = 0,$$

$$\frac{i\Omega}{\sqrt{6}}(N_{-1} + c_{g_{-1}g_1} - n_0) + (\gamma + i(\delta_{-1} - \omega_g))c_{g_{-1}e_0} = 0,$$

$$\frac{i\Omega}{\sqrt{2}}(N_0 - n_{-1}) + (\gamma + i(\delta_1 + \omega_e))c_{g_0e_{-1}} = 0,$$

$$\frac{i\Omega}{\sqrt{2}}(N_0 - n_1) + (\gamma + i(\delta_{-1} - \omega_e))c_{g_0e_1} = 0,$$

$$\frac{i\Omega}{\sqrt{6}}(N_1 + c_{g_1g_{-1}} - n_0) + (\gamma + i(\delta_1 + \omega_g))c_{g_1e_0} = 0,$$

$$i\Omega(N_1 - n_2) + (\gamma + i(\delta_{-1} + \omega_g - 2\omega_e))c_{g_1e_2} = 0,$$

$$\frac{i\Omega}{\sqrt{6}}(c_{e_0g_1} - c_{g_{-1}e_0}) + 2i(\omega_g + kv)c_{g_{-1}g_1} = 0. \tag{A.2}$$

Equations (A.2) were derived from Eqs. (9) considered in the zero order in photon momentum. Normalization condition (17) was written as the first equation of system (A.1).

APPENDIX B

Below, we give the system of equations for the functions $Q^1_{g_\alpha g_\alpha} = Q_\alpha$, $Q^1_{e_\alpha e_\alpha} = q_\alpha$, and $T^1_{ab} = t_{ab}$:

$$\sum Q_\alpha + \sum q_\alpha = 0, \tag{B.1}$$

$$i\Omega(t_{e_{-2}g_{-1}} - t_{g_{-1}e_{-2}}) + \frac{i\Omega}{\sqrt{6}}(t_{e_0g_{-1}} - t_{g_{-1}e_0})$$
$$+ \gamma\left(2q_{-2} + q_{-1} + \frac{1}{3}q_0\right) = i\Omega(c_{e_{-2}g_{-1}} - c_{g_{-1}e_{-2}})$$
$$-\frac{i\Omega}{\sqrt{6}}(c_{e_0g_{-1}} - c_{g_{-1}e_0}) - fN_{-1},$$

$$\frac{i\Omega}{\sqrt{2}}(t_{e_{-1}g_0} - t_{g_0e_{-1}} + t_{e_1g_0} - t_{g_0e_1}) + \gamma\left(q_{-1} + \frac{4}{3}q_0 + q_1\right)$$
$$= \frac{i\Omega}{\sqrt{2}}(c_{e_{-1}g_0} - c_{g_0e_{-1}} - c_{e_1g_0} + c_{g_0e_1}) - fN_0,$$

$$i\Omega(t_{e_2g_1} - t_{g_1e_2}) + \frac{i\Omega}{\sqrt{6}}(t_{e_0g_1} - t_{g_1e_0}) + \gamma\left(\frac{1}{3}q_0 + q_1 + 2q_2\right)$$
$$= i\Omega(c_{g_1e_2} - c_{e_2g_1}) + \frac{i\Omega}{\sqrt{6}}(c_{e_0g_1} - c_{g_1e_0}) - fN_1,$$

$$i\Omega(t_{g_{-1}e_{-2}} - t_{e_{-2}g_{-1}}) - 2\gamma q_{-2}$$
$$= i\Omega(c_{e_{-2}g_{-1}} - c_{g_{-1}e_{-2}}) - fn_{-2},$$

$$\frac{i\Omega}{\sqrt{2}}(t_{g_0e_{-1}} - t_{e_{-1}g_0}) - 2\gamma q_{-1} = \frac{i\Omega}{\sqrt{2}}(c_{e_{-1}g_0} - c_{g_0e_{-1}}) - fn_{-1},$$

$$\frac{i\Omega}{\sqrt{6}}(t_{g_{-1}e_0} - t_{e_0g_{-1}} + t_{g_1e_0} - t_{e_0g_1}) - 2\gamma q_0 \qquad \text{(B.2)}$$
$$= \frac{i\Omega}{\sqrt{6}}(c_{g_{-1}e_0} - c_{e_0g_{-1}} - c_{g_1e_0} + c_{e_0g_1}) - fn_0,$$

$$\frac{i\Omega}{\sqrt{2}}(t_{g_0e_1} - t_{e_1g_0}) - 2\gamma q_1 = \frac{i\Omega}{\sqrt{2}}(c_{g_0e_1} - c_{e_1g_0}) - fn_1,$$

$$i\Omega(t_{g_1e_2} - t_{e_2g_1}) - 2\gamma q_2 = i\Omega(c_{g_1e_2} - c_{e_2g_1}) - fn_2,$$

$$i\Omega(q_{-2} - Q_{-1}) - (\gamma + i(\delta_1 - \omega_g + 2\omega_e))t_{g_{-1}e_{-2}}$$
$$= i\Omega(N_{-1} + n_{-2}) - fc_{g_{-1}e_{-2}},$$

$$\frac{i\Omega}{\sqrt{6}}(Q_{-1} - q_0 + t_{g_{-1}g_1}) + (\gamma + i(\delta_{-1} - \omega_g))t_{g_{-1}e_0}$$
$$= \frac{i\Omega}{\sqrt{6}}(N_{-1} + n_0 - c_{g_{-1}g_1}) + fc_{g_{-1}e_0},$$

$$\frac{i\Omega}{\sqrt{2}}(q_{-1} - Q_0) - (\gamma + i(\delta_1 + \omega_e))t_{g_0e_{-1}}$$
$$= \frac{i\Omega}{\sqrt{2}}(N_0 + n_{-1}) - fc_{g_0e_{-1}},$$

$$\frac{i\Omega}{\sqrt{2}}(q_1 - Q_0) - (\gamma + i(\delta_{-1} - \omega_e))t_{g_0e_1}$$
$$= -\frac{i\Omega}{\sqrt{2}}(N_0 + n_1) - fc_{g_0e_1},$$

$$\frac{i\Omega}{\sqrt{6}}(q_0 - Q_1 - t_{g_1g_{-1}}) - (\gamma + i(\delta_1 + \omega_g))t_{g_1e_0}$$
$$= \frac{i\Omega}{\sqrt{6}}(N_1 + n_0 - c_{g_1g_{-1}}) - fc_{g_1e_0},$$

$$i\Omega(q_2 - Q_1) - (\gamma + i(\delta_{-1} + \omega_g - 2\omega_e))t_{g_1e_2}$$
$$= -i\Omega(N_1 + n_2) - fc_{g_1e_2},$$

$$\frac{i\Omega}{\sqrt{6}}(t_{e_0g_1} - t_{g_{-1}e_0}) + 2i(\omega_g + kv)t_{g_{-1}g_1}$$
$$= -\frac{i\Omega}{\sqrt{6}}(c_{e_0g_1} + c_{g_{-1}e_0}) - fc_{g_{-1}g_1}.$$

Equations (B.2) were derived from Eqs. (9) considered in the first order in photon momentum. The first equation of system (B.1) is normalization condition (19). The quantity $f = F/\hbar k\gamma$ is the normalized force.

ACKNOWLEDGMENTS

This study was supported in part by the Russian Foundation for Basic Research (project nos. 01-02-16337, 02-02-17014) and INTAS (grant no. 479).

REFERENCES

1. J. Nellessen, J. Werner, and W. Ertmer, Opt. Commun. **78**, 300 (1990).
2. M. Schiffer, M. Christ, G. Wokurka, and W. Ertmer, Opt. Commun. **134**, 423 (1997).
3. W. Ketterle and N. J. van Druten, in *Advances in Atomic, Molecular and Optical Physics*, Ed. by B. Bederson and H. Walther (Academic, San Diego, 1996), Vol. 37, p. 181.
4. J. T. M. Walraven, in *Quantum Dynamics of Simple Systems*, Ed. by G. L. Oppo and S. M. Barnett (Institute of Physics, London, 1996), p. 315.
5. G. Nienhuis, P. van der Straten, and S.-Q. Shang, Phys. Rev. A **44**, 462 (1991).
6. M. Walhout, J. Dalibard, S. L. Rolston, and W. D. Phillips, J. Opt. Soc. Am. B **9**, 1997 (1992).
7. J. Werner, H. Wallis, and W. Ertmer, Opt. Commun. **94**, 525 (1992).
8. P. van der Straten, S.-Q. Shang, B. Sheehy, *et al.*, Phys. Rev. A **47**, 4160 (1993).
9. C. Valentin, M.-C. Gagne, J. Yu, and P. Pillet, Europhys. Lett. **17**, 133 (1992).
10. M. Walhout, U. Sterr, and S. L. Rolston, Phys. Rev. A **54**, 2275 (1996).
11. S. Weyers, E. Aucouturier, C. Valentin, and N. Dimarcq, Opt. Commun. **143**, 30 (1997).

12. P. Berthoud, A. Joyet, G. Dudle, *et al.*, Europhys. Lett. **41**, 141 (1998).
13. Y. Fukuyama, H. Kanou, V. I. Balykin, and K. Shimizu, Appl. Phys. B **70**, 561 (2000).
14. S.-Q. Shang, B. Sheehy, P. van der Straten, and H. Metcalf, Phys. Rev. Lett. **65**, 317 (1990).
15. S.-Q. Shang, B. Sheehy, P. van der Straten, *et al.*, Phys. Rev. Lett. **67**, 1094 (1991).
16. R. Golub and J. M. Pendlebury, Rep. Prog. Phys. **42**, 439 (1979).
17. S. G. Rautian, G. I. Smirnov, and A. M. Shalagin, *Nonlinear Resonances in Atomic and Molecular Spectra* (Nauka, Novosibirsk, 1979).
18. S. Chang and V. Minogin, Phys. Rep. **365/2**, 65 (2002).
19. V. G. Minogin and V. S. Letokhov, *Laser Light Pressure on Atoms* (Gordon and Breach, New York, 1987).
20. S. Chang, T. Y. Kwon, Ho S. Lee, and V. Minogin, Phys. Rev. A **60**, 2308 (1999).
21. S. Chang, T. Y. Kwon, Ho S. Lee, and V. G. Minogin, Phys. Rev. A **60**, 3148 (1999).
22. F. Lison, P. Schuh, D. Haubrich, and D. Meshede, Phys. Rev. A **61**, 013405 (1999).
23. D. W. Sesko, T. G. Walker, and C. E. Wieman, J. Opt. Soc. Am. B **8**, 946 (1991).
24. A. M. Steane, M. Chowdhurry, and C. J. Foot, J. Opt. Soc. Am. B **9**, 2142 (1992).
25. M. Drewsen, P. Laurent, A. Nadir, *et al.*, Appl. Phys. B **59**, 283 (1994).
26. C. G. Townsend, N. H. Edwards, C. J. Cooper, *et al.*, Phys. Rev. A **52**, 1423 (1995).
27. E. Mandonnet, A. Minguzzi, R. Dum, *et al.*, Eur. Phys. J. D **10**, 9 (2000).

Translated by V. Astakhov

Journal of Experimental and Theoretical Physics, Vol. 96, No. 1, 2003, pp. 83–92.
Translated from Zhurnal Éksperimental'noĭ i Teoreticheskoĭ Fiziki, Vol. 123, No. 1, 2003, pp. 98–108.

SOLIDS
Electronic Properties

EPR and Longitudinal Response Signals in Spin Systems Consisting of Localized (S = 1/2) and Delocalized Spins

N. P. Fokina* and K. O. Khutsishvili**
Tbilisi State University, Tbilisi, 380028 Georgia
**e-mail: augst@caucasus.net*
***e-mail: garemo@hotmail.com*
Received May 24, 2002

Abstract—The spin system of many new promising materials, such as high-temperature superconductors, fullerenes, fullerides, or manganites with colossal magnetoresistance, consists of localized spins (*s*-spins of impurity paramagnetic centers) and delocalized spins (*e*-spins of charge carriers). The two sorts of spins are coupled by exchange interaction, which leads to coupled precession of the corresponding magnetizations. When the materials mentioned above are investigated by EPR methods, the measured longitudinal (T_1) and transverse (T_2) relaxation times provide the most valuable information. However, the presence of inhomogeneous broadening of the EPR of *s*-spins often makes it difficult to measure T_2, while small values of T_1 do not allow one to measure it by conventional methods. Atsarkin and colleagues [4, 7, 8] proposed a new version of the method for measuring T_1 by longitudinal response signals induced in a longitudinal spin coil (oriented along the constant magnetic field) under low-frequency modulation of the microwave power, which saturates the EPR, even though very weakly. Earlier, the results obtained in experiments on measuring the longitudinal response for samples containing interacting *s*- and *e*-spins were interpreted using formulas for an individual sort of spins. In this paper, the magnetization of *s*- and *e*-spins that precess under the condition of relaxational coupling is considered, which is characteristic, for example, of fullerides. The complete EPR susceptibility is represented in a form that makes it possible to determine the origin (from *s*- or *e*-spins) of two Lorentzians, each of which is characterized by one of the normal decay rates of two coupled oscillators (i.e., of precessing transverse magnetization components). The common EPR line analytically decomposed into those Lorentzians, and special factors take into account the influence of the other sort of spins on the amplitude of the signal generated by the sort under consideration. Similarly to the EPR absorption signals, the expressions for the longitudinal response are decomposed into parts originating from *s*- and *e*-spins, and each part is proportional to the form factor of one of the modes (*s*- or *e*-like). The qualitative comparison shows good agreement with experimental data in terms of EPR and longitudinal response in a fulleride. © *2003 MAIK "Nauka/Interperiodica".*

1. INTRODUCTION

New materials, such as high-temperature superconductors, fullerenes, fullerides, or manganites with colossal magnetoresistance, which exhibit interesting and promising (from the practical point of view) magnetic and electric properties [1, 2], have been successfully investigated by EPR methods [3, 4]. In these materials, there are usually several types of paramagnetic centers, which are coupled by spin–spin interactions with each other. In conducting systems, these are, first of all, charge carriers (electrons and holes) (which are usually denoted as *e*-spins) and localized paramagnetic centers of impurities or the host lattice (*s*-spins). The fulleride RbC_{60} in the polymer phase is an example of such a material. Here, the role of localized spins with S = 1/2 is played by the torn ends of polymer chains.

From the viewpoint of understanding the nature of phase transitions in such materials, investigation of their internal fluctuating magnetic fields is of major interest. Information about their amplitudes and correlation times is obtained by measuring the time of longitudinal (T_1) and transverse (T_2) spin relaxation. The transverse relaxation time is usually measured by the EPR linewidth; however, the existing inhomogeneous broadening often conceals the contribution of fluctuating fields, and small values of the longitudinal relaxation time (10^{-10}–10^{-7} s) are impossible to measure by the conventional method of registration of the EPR signal recovery time after its stationary saturation.

In studies [5, 6], a technique was suggested for measuring such small time intervals by longitudinal response signals induced in a longitudinal coil (oriented along the constant magnetic field) under low-frequency modulation of microwave power, which saturates the EPR, even though very weakly. This technique was improved and used for measuring the times T_1 and T_2 for various materials [7–10]. However, the results for samples containing interacting *s*- and *e*-spins were interpreted using formulas obtained in [4–6] from the Bloch equations for one sort of spins. At the same time, long-term experimental and theoretical studies of the EPR in metals with paramagnetic impurities [11] show

that the exchange interaction of *s*- and *e*-spins in these materials leads to two clear-cut specific features in the precession of magnetizations. The first feature is related to the dynamic shift of unperturbed (partial) resonance frequencies of *s*- and *e*-spins. The second one, which is most important for our purposes, is related to the shift of partial decay rates, i.e., with the change in the width of EPR lines. Evidently, these properties of magnetization precession must affect the behavior of longitudinal magnetization components, whose motion induces longitudinal response. Therefore, the further development of the longitudinal response method in systems with interacting *s*- and *e*-spins requires theoretical investigation of longitudinal response signals with regard for the *s*–*e* coupling. Such an investigation is the purpose of this paper.

The EPR of two sorts of coupled spins in metals with paramagnetic impurities was studied on the basis of the Bloch–Hasegawa equations in [11, 12]. In those papers, the spectra of coupled precessing transverse magnetization components (i.e., the frequencies and widths of EPR lines) were thoroughly studied, and the EPR susceptibility was numerically calculated for certain particular samples. Since the investigation of EPR saturation was not the purpose of studies [11, 12], the evolution of longitudinal magnetization components was not considered.

In contrast to study [11], we compute the complete EPR susceptibility in a form that makes it possible to determine the origin (from *s*- or *e*-spins) of each of the two Lorentzians into which the common EPR line is analytically decomposed. Each of these Lorentzians is characterized by one of the normal decay rates of two coupled oscillators (i.e., of precessing transverse magnetization components). Special factors, which include the amplification and attenuation factors of EPR signals, contain complete information about the influence of the other sort of spins on the amplitude of the signal under consideration.

However, interpretation of the experiments on the longitudinal response requires consideration of saturation effects, i.e., the nutation of magnetization vectors relative to the *z* axis. Thus, we face the problem of matching the coupled precession of transverse magnetization components of two sorts of spins with coupled evolution of their longitudinal components. This problem must be solved under the conditions when all components of the two magnetizations vary due to the effect of an external modulated saturating microwave field and the inherent relaxation processes.

Assuming that the coupling between *s*- and *e*-spins is purely relaxational (which is the case in the majority of experimental situations), we change the variables so as to ensure that the disentangled equations in the new variables be characterized by normal decay rates (widths of EPR lines). Then, we complement equations for slow amplitudes of the normal transverse magnetization components with equations for individual longitudinal components; this will provide a basis for considering nutation in the spin system. In the process of nutation, there appears a kind of relaxation resonance between the external low-frequency periodic action on the spin system (modulation of the microwave power that saturates the EPR) and the natural motion of magnetization components under the influence of relaxation processes. As this takes place, time-dependent corrections to the stationary values of individual magnetizations appear.

The computed sum of individual in-phase and out-of-phase corrections decomposes into the sum of signals, which are proportional to the form factors of two EPR modes and are characterized by two sets of transverse and longitudinal normal decay rates. These are the decay rates measured when the longitudinal response is observed by the techniques developed in [7–10].

The first attempts to implement the program described above were made in [13]. In this paper, we solve the problem more consistently, thus creating a theoretical basis for extending the longitudinal response method to the case of relaxationally coupled *s*- and *e*-spins, which is especially important for studying promising new materials.

The results are qualitatively compared with experimental data concerning the EPR and longitudinal response in a fulleride.

2. STATEMENT OF THE PROBLEM AND COMPUTATION OF THE EPR ABSORPTION SIGNAL IN A COUPLED SYSTEM OF *s*- AND *e*-SPINS

Consider the spin system of a sample containing localized (*s*) spins ($S = 1/2$) and delocalized (*e*) spins coupled by the exchange interaction

$$H_{\text{ex}} = -2J\sum_{i,j}\mathbf{S}_{si}S_{ej}\delta(\mathbf{R}_i - \mathbf{R}_j), \qquad (1)$$

where $\mathbf{S}_{si}$ is the localized spin occupying the *i*th lattice site and $\mathbf{S}_{ej}$ is the delocalized spin. The sample is in the constant magnetic field $\mathbf{H}_0 \parallel z$ and in the variable field $H^x = 2H_1\cos\omega t$ oriented along the *x* axis; *s*- and *e*-spins possess Zeeman energy; in addition, *e*-spins possess kinetic energy. In experiments, we often encounter the situation (see [7, 8]) with no dynamic shifts in the frequencies of the *s*- and *e*-spins precession. Below, we consider precisely this case. We also assume that the *g*-factors of *s*- and *e*-spins are equal. Then, the precession frequencies of *s*- and *e*-spins are equal, and the coupling between the corresponding magnetizations is purely relaxational. Due to the huge predominance of the kinetic energy of *e*-spins over the Zeeman energies of *s*- and *e*-spins, there is no distinguished direction in such a system [14]; therefore, the Bloch–Hasegawa equations, which describe the evolution of *s*- and *e*-spin magnetization, are characterized by the isotropy of the

relaxation behavior of the *x*, *y*, and *z* components of the magnetization vectors of *s*- and *e*-spins; in what follows, they are denoted by $M_{s,e}^{x,y,z}$.

For convenience, we pass, in the original Bloch–Hasegawa equations [11] for the transverse magnetization components, to second-order differential equations, while leaving the equations for longitudinal components in the form of first-order differential equations. Thus, we have

$$\begin{aligned}\ddot{M}_s^x + \omega_0^2 M_s^x + 2\omega_\delta'' \dot{M}_s^x + 2\omega_\alpha'' \dot{M}_e^x &= -\omega_0 \frac{g_s \mu_B}{\hbar} H^x M_s^z,\\ \ddot{M}_e^x + \omega_0^2 M_e^x + 2\omega_\gamma'' \dot{M}_e^x + 2\omega_\beta'' \dot{M}_s^x &= -\omega_0 \frac{g_e \mu_B}{\hbar} H^x M_e^z,\end{aligned} \tag{2}$$

$$\begin{aligned}\dot{M}_s^z + T_s^{-1} M_s^z - T_{es}^{-1} M_e^z &= T_{sL}^{-1} M_s^0 - \frac{g_s \mu_B}{\hbar} H^x M_s^y,\\ \dot{M}_e^z + T_e^{-1} M_e^z - T_{se}^{-1} M_s^z &= T_{eL}^{-1} M_e^0 - \frac{g_e \mu_B}{\hbar} H^x M_e^y,\end{aligned} \tag{3}$$

where ω_0 is the common Larmor frequency of *s*- and *e*-spins,

$$\omega_\delta'' = T_{se}^{-1} + T_{sL}^{-1}, \quad \omega_\gamma'' = T_{es}^{-1} + T_{eL}^{-1},$$

$$\omega_\alpha'' = -T_{es}^{-1}, \quad \omega_\beta'' = -T_{se}^{-1},$$

T_s^{-1} coincides with ω_δ'' for the homogeneous broadening of the EPR of both sorts of spins with $S = 1/2$, and T_e^{-1} coincides with ω_γ''. However, this coincidence is violated in the presence of inhomogeneous broadening or the fine structure of localized spin EPR. We will take into account the inhomogeneous broadening of *s*-spins in final formulas, which implies a change in the transverse partial decay rate ω_δ'', but not a change in the longitudinal relaxation of T_e^{-1}; therefore, it seems reasonable to distinguish by special notation the quantities describing the decay rate of transverse magnetization components and, on the other hand, the relaxation rates of longitudinal components.

Furthermore, T_{se}^{-1} and T_{es}^{-1} are the kinetic coefficients, which describe the coupling of the *s*- and *e*-systems (for metals, they are conventionally called the Korringa and Overhauser relaxation rates). When the *g*-factors of spins are equal, they are connected by the relation $T_{se}/T_{es} = \chi_s/\chi_e$ [11], where χ_s and χ_e are the static susceptibilities of the *s*- and *e*-spins, respectively. T_{sL}^{-1} and T_{eL}^{-1} are the relaxation rates of the *s*- and *e*-spins to the lattice.

It follows from these equations that the precession of magnetizations in the transverse plane is an oscillatory motion of two relaxationally coupled oscillators. The motion of coupled longitudinal components in the absence of inhomogeneous broadening and the fine structure of EPR has a relaxation rate equal to the decay rate of the transverse components.

We assume that the constant magnetic field is strong; i.e, the Larmor frequency is much greater than all decay rates. Then, the coupled relaxation motion is slow, and we can pass to slow amplitudes (see [15]):

$$\begin{aligned}M_{s,e}^x &= \frac{1}{2}\tilde{M}_{s,e}^x(t)e^{-i\omega t} + \text{c.c.}\\ &= \frac{1}{2}(u_{s,e\perp}(t) + iv_{s,e\perp}(t))e^{-i\omega t} + \text{c.c.}\\ &= u_{s,e\perp}(t)\cos\omega t + v_{s,e\perp}(t)\sin\omega t,\\ \tilde{M}_{s,e}^x(t) &\equiv u_{s,e\perp}(t) + iv_{s,e\perp}(t),\\ \left|\dot{\tilde{M}}_{s,e}^x(t)\right| &\ll \left|\omega_0 \tilde{M}_{s,e}^x(t)\right|,\end{aligned} \tag{4}$$

where ω is the frequency of the variable field

$$H^x = \frac{1}{2}\tilde{H}^x e^{-i\omega t} + \text{c.c.}, \quad \tilde{H}^x = 2H_1. \tag{5}$$

Applying transformations (4), (5) to Eqs. (2), we obtain the following equations describing the evolution of coupled complex transverse slow amplitudes:

$$\begin{aligned}\dot{\tilde{M}}_s^x + \omega_\delta'' \tilde{M}_s^x + \omega_\alpha'' \tilde{M}_e^x - i(\omega - \omega_0)\tilde{M}_s^x &= -i\frac{g_s \mu_B}{\hbar} H_1 M_s^z,\\ \dot{\tilde{M}}_e^x + \omega_\gamma'' \tilde{M}_e^x + \omega_\beta'' \tilde{M}_s^x - i(\omega - \omega_0)\tilde{M}_e^x &= -i\frac{g_e \mu_B}{\hbar} H_1 M_e^z.\end{aligned} \tag{6}$$

The equations for the longitudinal magnetization components are slow by their nature.

In order to compute the spectrum of decay rates of motion in the transverse plane, we seek the solution of system (6) in the form

$$\tilde{M}_{s,e}^x = m_{s,e}^x e^{-\omega'' t}$$

(the quantities of decay rate ω'' have the dimension of frequency). Substituting this expression into Eqs. (6), provided that there is no variable field, we discover that the transverse slow amplitudes have the spectrum of decay rates, which is given by solutions to the equation

$$(\omega'' - \omega_\delta'')(\omega'' - \omega_\gamma'') - \omega_\alpha'' \omega_\beta'' = 0. \tag{7}$$

These solutions are transverse normal decay rates $\omega_{(t)}''$ and $\omega_{(-t)}''$ [16] (the index *t* takes plus or minus values: $\omega_{(+)}''$ is the normal decay rate that is greater than the largest transverse partial decay rate, and $\omega_{(-)}''$ is the one that is less than the smallest transverse partial decay rate). These are precisely the widths of EPR lines observed in experiments in the linear case (when the

longitudinal magnetization components are equal to their equilibrium values).

The system of differential equations (3)–(6) exhibits the saturation effect, and its general solution seems impossible to be written explicitly. To solve it, we first extricate the equations for transverse slow amplitudes. For this purpose, we make the following linear transformation:

$$\begin{aligned}\tilde{M}_s^x &= \tilde{M}_{(t)}^x + k_{(-t)}^{-1}\tilde{M}_{(-t)}^x,\\ \tilde{M}_e^x &= k_{(t)}\tilde{M}_{(t)}^x + \tilde{M}_{(-t)}^x,\end{aligned} \tag{8}$$

where the quantities

$$\begin{aligned}k_{(t)} &= \frac{\omega''_{(t)} - \omega''_\delta}{\omega''_\alpha} = \frac{\omega''_\beta}{\omega''_{(t)} - \omega''_\gamma},\\ k_{(-t)} &= \frac{\omega''_{(-t)} - \omega''_\delta}{\omega''_\alpha} = \frac{\omega''_\beta}{\omega''_{(-t)} - \omega''_\gamma}\end{aligned} \tag{9}$$

are the amplitude distribution coefficients at the frequencies $\omega''_{(t)}$ and $\omega''_{(-t)}$ [17]. If we specify the relaxation oscillator that has the greater partial decay rate, then the quantities $k_{(t)}$ and $k_{(-t)}$ acquire the known meaning. For example, if the *e*-system has the greater partial decay rate, then

$$k_{(t=-)} = \eta_{s-enh}, \quad k_{(-t=+)} = -\eta_{e-suppr}^{-1},$$

where η_{e-enh} is the amplification factor [13, 18] of the transverse slow amplitude of *s*-spins and $\eta_{e-suppr}$ is the suppression factor of the transverse slow amplitude of *e*-spins. If, on the other hand, the *s*-system has the greater partial decay rate, then

$$k_{(-t=-)} = \eta_{e-enh}^{-1}, \quad k_{(t=+)} = -\eta_{s-suppr}.$$

Substituting (8) into Eqs. (6) with a driving force, we obtain disentangled equations for the new variables:

$$\begin{aligned}\dot{\tilde{M}}_{(t)}^x + \omega''_{(t)}\tilde{M}_{(t)}^x - i(\omega-\omega_0)\tilde{M}_{(t)}^x &= -i\frac{g\mu_B}{\hbar}H_1 M_s^z \tilde{K}_{s(t)},\\ \dot{\tilde{M}}_{(-t)}^x + \omega''_{(-t)}\tilde{M}_{(-t)}^x - i(\omega-\omega_0)\tilde{M}_{(-t)}^x &= -i\frac{g\mu_B}{\hbar}H_1 M_e^z \tilde{K}_{e(-t)},\end{aligned} \tag{10}$$

where

$$\begin{aligned}\tilde{K}_{s(t)} &= \frac{(\omega''_{(t)} - \omega''_\gamma)(1+k_{(t)})}{\omega''_{(t)} - \omega''_{(-t)}},\\ \tilde{K}_{e(-t)} &= \frac{(\omega''_{(-t)} - \omega''_\delta)(1+k_{(-1)}^{-1})}{\omega''_{(-t)} - \omega''_{(t)}}.\end{aligned} \tag{11}$$

Since these equations are disentangled, the new variables are normal (i.e., mode variables). Equations (10) indicate that the *t*-mode is *s*-like and the (–*t*)-mode is *e*-like. This implies that, in the absence of relaxation coupling ($\omega''_\alpha = \omega''_\beta = 0$), the normal decay rates $\omega''_{(t)}$ and $\omega''_{(-t)}$ turn into the partial decay rates ω''_δ and ω''_γ of *s*-spins and *e*-spins, respectively.

The imaginary part of the dynamic susceptibility (the EPR absorption signal) can be found by the formula (see [19])

$$\begin{aligned}\chi'' &= -\frac{v_{s\perp}^{st} + v_{e\perp}^{st}}{2H_1}\\ &= -\frac{1}{2H_1}[(1+k_{(t)})v_{(t)}^{st} + (1+k_{(-t)}^{-1})v_{(-t)}^{st}],\end{aligned} \tag{12}$$

where $v_{(t)}^{st}$ and $v_{(-t)}^{st}$ are the stationary values of the mode Bloch absorption signals in the linear case, when the longitudinal magnetization components do not differ from their equilibrium values. As a result, we have

$$\begin{aligned}\chi''_{ESP} &= \frac{\pi g\mu_B}{2\hbar}\\ &\times [M_s^0 K_{s(t)} g_{(t)}(\omega-\omega_0) + M_e^0 K_{e(-t)} g_{(-t)}(\omega-\omega_0)],\end{aligned} \tag{13}$$

where

$$\begin{aligned}g_t(\omega-\omega_0) &= \frac{\omega''_{(t)}}{\pi}\frac{1}{(\omega-\omega_0)^2 + \omega''^2_{(t)}},\\ K_{s(t)} &= \tilde{K}_{s(t)}(1+k_t),\\ K_{e(-t)} &= \tilde{K}_{e(-t)}(1+k_{(-t)}^{-1}).\end{aligned} \tag{14}$$

If we pass to the conventional amplification–attenuation factors in (14), then (13) will coincide with expression (8) in [13] obtained using Green's function.

3. THE LONGITUDINAL RESPONSE SIGNAL IN A COUPLED SYSTEM OF *s*- AND *e*-SPINS

In order to compute the longitudinal response signal, we complement Eqs. (10) with Eqs. (3) for the individual longitudinal magnetizations, which are slow variables by their nature. To relate the evolution of individual longitudinal components with the evolution of two transverse modes, we substitute transformation (8) into the equations for the longitudinal magnetization

components. As a result, we have the system consisting of Eqs. (10) and the equations

$$\begin{aligned} &\dot{M}_s^z + T_s^{-1}M_s^z - T_{es}^{-1}M_e^z \\ &= T_{sL}^{-1}M_s^0 + \frac{g\mu_B}{\hbar}H_1(\nu_t + k_{(-t)}^{-1}\nu_{(-t)}), \\ &\dot{M}_e^z + T_e^{-1}M_e^z - T_{se}^{-1}M_s^z \\ &= T_{eL}^{-1}M_e^0 + \frac{g\mu_B}{\hbar}H_1(k_{(t)}^{-1}\nu_t + \nu_{(-t)}). \end{aligned} \tag{15}$$

We stress that Eqs. (10) and (15) are exact when assuming a strong magnetic field (ω_0 is much greater than all decay rates). These equations describe the EPR saturation in the system of exchange-coupled *s*- and *e*-spins under an arbitrary magnitude of the interaction between them.

In order to compute the signals registered by the longitudinal coil under the modulation of the microwave field power, we set

$$\frac{g\mu_B}{\hbar}H_1 = \sqrt{a + b\cos\Omega t}$$

in the resulting equations. Here, $a\hbar^2(g\mu_B)^{-2}$ is the squared amplitude of the microwave field that saturates the EPR, b/a is the modulation depth of the corresponding microwave power, and the modulation frequency Ω is much less than ω_0.

As in studies [5, 6], we assume that the modulation leads only to small time-dependent corrections to the stationary values of longitudinal components:

$$M_{s,e}^z = M_{s,e}^{zst} + m_{s,e}^z(t).$$

The response in the longitudinal coil, a part of which is in phase with the modulation and the other part is shifted by $\pi/2$ in phase, is due to the sum of these time-dependent corrections:

$$\begin{aligned} m_{sz} + m_{ez} &= (u_s + u_e)\cos\Omega t + (\nu_s + \nu_e)\sin\Omega t \\ &\equiv (u + i\nu)e^{-i\Omega t} + (u - i\nu)e^{i\Omega t}, \end{aligned} \tag{16}$$

where $u_{s,e}$ and $\nu_{s,e}$ are Bloch-type longitudinal amplitudes.

In what follows, we assume that one of the following constraints holds: (i) the modulation frequency Ω is much less than all decay rates for arbitrary detuning of the microwave field frequency relative to the resonance frequency of spins; (ii) the EPR detuning is small compared to linewidths for arbitrary frequency modulation. Then, we can get by with second-order differential equations for $m_{s,ez}(t)$. Under the condition of weak EPR saturation, we obtain the following coupled second-order differential equations for the time-dependent corrections:

$$\begin{aligned} &\ddot{m}_{sz} + (T_s^{-1} + \omega_\delta'')\dot{m}_{sz} + [\omega_\delta''T_s^{-1} + T_{se}^{-1}T_{es}^{-1}]m_{sz} \\ &- 2T_{es}^{-1}\dot{m}_{ez} - T_{es}^{-1}(\omega_\delta'' + T_e^{-1})m_{ez} \\ &= B_s[\Omega(2\omega_{(t)}'')^{-1}\sin\Omega t - \cos\Omega t] \\ &+ k_{(-t)}^{-1}B_e[\Omega(2\omega_{(-t)}'')^{-1}\sin\Omega t - \cos\Omega t] \equiv B_s(t), \\ &\ddot{m}_{ez} + (T_e^{-1} + \omega_\gamma'')\dot{m}_{ez} + [\omega_\gamma''T_e^{-1} + T_{se}^{-1}T_{es}^{-1}]m_{ez} \\ &- 2T_{se}^{-1}\dot{m}_{sz} - T_{se}^{-1}(\omega_\gamma'' + T_s^{-1})m_{sz} \\ &= k_{(t)}B_s[\Omega(2\omega_{(t)}'')^{-1}\sin\Omega t - \cos\Omega t] \\ &+ B_e[\Omega(2\omega_{(-t)}'')^{-1}\sin\Omega t - \cos\Omega t] \equiv B_e(t), \end{aligned} \tag{17}$$

where

$$\begin{aligned} B_s &= bM_s^0\tilde{K}_{s(t)}\pi\omega_{(t)}''g_{(t)}(\omega - \omega_0), \\ B_e &= bM_e^0\tilde{K}_{e(-t)}\pi\omega_{(-t)}''g_{(-t)}(\omega - \omega_0); \end{aligned}$$

for the other notation see Section 2.

Substitute expression $m_{sz,\,ez} = \tilde{m}_{sz,ez}e^{-kt}$ into Eqs. (17) and equate the determinant of the resulting algebraic equation to zero to obtain the following secular equation for the characteristic decay rates of coupled time-dependent corrections to the stationary values of the longitudinal magnetization components caused by modulation of the microwave power:

$$\begin{aligned} &(k - \omega_{(t)}'')(k - \omega_{(-t)}'') \\ &\times [k^2 - (T_s^{-1} + T_e^{-1})k + T_s^{-1}T_e^{-1} - T_{se}^{-1}T_{es}^{-1}] = 0. \end{aligned} \tag{18}$$

Solutions of this equation have the form

$$k_{1,2} = \omega_{(t),(-t)}'', \quad k_{3,4} = \omega_{(L),(-L)}'' \tag{19}$$

(the last two solutions solve the equation obtained by equating the expression in square brackets in (18) to zero). Note that the quantities $\omega_{(t),(-t)}''$ include decay rates of the transverse magnetization components and $\omega_{(L),(-L)}''$ include the relaxation rate of longitudinal components. If there are no causes for breaking the isotropy of the relaxation behavior of the longitudinal and transverse magnetization components, then $\omega_t'' = \omega_L''$ and $\omega_{-t}'' = \omega_{-L}''$. The quantities k_1, k_2, k_3, and k_4 yield the "relaxation spectrum" of longitudinal "oscillators." Thus, the longitudinal response signal must have singularities at the modulation frequencies that are equal to those decay rates. We stress that the use of the term

"oscillator" for the longitudinal magnetization components is justified by the fact that, in the course of the observation of longitudinal response, the longitudinal components vary periodically under the effect of the periodic driving force (modulation of the microwave power that saturates the EPR).

Now, we take into account the fact that the localized spins in metals are usually spectrally inhomogeneous. For the first time, this fact was taken into account while calculating the EPR signal of a coupled system of *s*- and *e*-spins in the study [20]. In that paper, every *s*-spin was assigned an individual resonance frequency and the kinetic equations included, along with the magnetization of *e*-spins, the spectral magnetization density of *s*-spins as a dynamic variable. In the calculation of the EPR signal, the integration was performed over all resonance frequencies of *s*-spins. The technique for calculating the EPR spectrum proposed in [20] was used to estimate spectra in [7, 8]. These spectra were in good agreement with the two Lorentzians obtained by the numerical decomposition of the EPR intensity.

The approach to the allowance for inhomogeneous broadening proposed in [20] is the most consistent one. However, this model is very cumbersome, and we try to take into account the inhomogeneous broadening in a simplified way. More precisely, we add the inhomogeneous width to T_{sL}^{-1} in Eqs. (10) for the transverse magnetization components (but not in Eqs. (15) for longitudinal components). Note that due to the competition between the Korringa relaxation and the distribution of localized spins in resonance frequencies, the magnitude of the effective inhomogeneous width in the case of a strong *s*–*e* coupling (see the criterion below) differs from the width of this distribution (see Appendix).

The quantity $u + iv$ obtained with the allowance for the inhomogeneous broadening using expressions (16) and (17) and multiplied by Ω and the instrumental factor A gives the complex longitudinal response signal, i.e., the voltage measured at the ends of the longitudinal coil

$$U + iV = A\Omega(u_s + u_e + iv_s + iv_e).$$

It has the form

$$\begin{aligned} U + iV &= -A\Omega\pi b M_s^0 K_{s(t)} f(\Omega, \omega''_{(t)}, \omega''_{(L)}) \\ &\times \frac{\Omega + i(\omega''_{(-t)} - \delta^* k_{(t)}/(1 + k_{(t)}))}{\Omega + i\omega''_{(-L)}} g_{(t)}(\omega - \omega_0) \\ &- A\Omega\pi b M_e^0 K_{e(-t)} f(\Omega, \omega''_{(-t)}, \omega''_{(-L)}) \\ &\times \frac{\Omega + i(\omega''_{(t)} - \delta^*/(1 + k_{(-t)}^{-1}))}{\Omega + i\omega''_{(L)}} g_{(-t)}(\omega - \omega_0), \end{aligned} \tag{20}$$

where

$$\begin{aligned} f(\Omega, \omega''_{(t)}, \omega''_{(L)}) &= \frac{\omega''_{(L)}\omega''^2_{(t)}}{(\Omega^2 + \omega''^2_{(t)})(\Omega^2 + \omega''^2_{(L)})} \\ &\times \left\{1 - \frac{\Omega^2(\omega''_{(t)} - \omega''_{(L)})}{2\omega''_{(L)}\omega''^2_{(t)}} \right. \\ &\left. + \frac{i\Omega}{\omega'_{(L)}}\left[1 + \frac{\omega''_{(L)}}{2\omega''_{(t)}}\left(1 + \frac{\Omega^2}{\omega''_{(L)}\omega''_{(t)}}\right)\right]\right\}. \end{aligned} \tag{21}$$

Formula (20) is the main result of the present paper. This result is valid for arbitrary coupling of *s*- and *e*-spins and is exact under the assumption that the detuning or (and) the frequency modulation is small compared with the decay rates.

Note that, for $\Omega \ll \omega''_{(t)}, \omega''_{(L)}$, when (20) is valid for arbitrary detunings, expression (21) becomes simpler:

$$f(\Omega, \omega''_{(t)}, \omega''_{(L)}) \approx \frac{1}{\omega''_{(L)}}\left[1 + \frac{i\Omega}{\omega''_{(L)}}\left(1 + \frac{\omega''_{(L)}}{2\omega''_{(t)}}\right)\right]. \tag{22}$$

In the absence of inhomogeneous broadening, one must take into account the equality $\omega''_{(\pm t)} = \omega''_{(\pm L)}$ (which becomes automatically true in this case) in (20); in addition, the fractions in both terms in (20) turn into unity. We also note that in the total absence of coupling, both the EPR signal and the longitudinal response signal are sums of the contributions of individual *s*- and *e*-spins, and these contributions are equal to the corresponding expressions for the one sort of spins obtained in [3, 8].

We analyze the result obtained using the metal–insulator transition in the polymer linear phase of the fulleride RbC_{60} as an example [3, 7, 8]. It was shown in [7] that this transition, which occurs when the material is cooled below $T_c = 55$ K, is accompanied by a sharp attenuation of the relaxation coupling between the spin subsystem of localized paramagnetic centers formed by torn polymer bonds (*s*-spins) and conduction electrons (*e*-spins). As a result, there occurs the transition from the situation of a "relaxation-dominated bottleneck" [11] ($T > 55$ K) to the intermediate *s*–*e* coupling ($T < 55$ K) and, finally, to isolated spin subsystems at even lower temperatures. The coupling of *s*- and *e*-subsystems is quantitatively characterized by the "connectedness" parameter [17], which in our case of relaxationally coupled oscillators can be determined as

$$\sigma = \frac{T_{se}^{-1} + T_{es}^{-1}}{\left|\delta^* + T_{sL}^{-1} - T_{eL}^{-1}\right|}, \tag{23}$$

where δ^* is the effective width of the distribution of localized spins in resonance frequencies (see below). It is seen from (23) that parameter σ is determined by the ratio of the quantity describing the coupling of the two

sorts of spins to the difference of their partial decay rates coupling.

Consider the case when the connectedness is weak for longitudinal magnetization components, i.e., $\sigma \ll 1$. In this case, the inhomogeneous width δ^*, which appears in transverse normal decay rates, coincides with the width (δ_s^0) of the *s*-spin distribution in resonance frequencies (see Appendix). Then, assuming that $T_{eL}^{-1} < \delta_s^0 + T_{sL}^{-1}$, we have the following expressions for the normal EPR decay rates:

$$\omega''_{(t=+)} \approx T_{se}^{-1} + T_{sL}^{-1} + \delta_s^0 + \frac{\sigma}{4}(T_{es}^{-1} + T_{se}^{-1}),$$
$$\omega''_{(-t=-)} \approx T_{es}^{-1} + T_{eL}^{-1} - \frac{\sigma}{4}(T_{es}^{-1} + T_{se}^{-1}) \quad (24)$$

(the normal longitudinal decay rates are obtained from (24) if we set $\delta_s^0 = 0$ there).

The EPR signal is a sum of two terms:

$$\chi''_{ESR} \approx \frac{\pi g \mu_B}{\hbar} M_s^0 \left(1 - \frac{\sigma}{4}\frac{\chi_s + \chi_e}{\chi_s}\right)^2 g_{(t=+)}(\omega - \omega_0)$$
$$+ \frac{\pi g \mu_B}{\hbar} M_e^0 \left(1 + \frac{\sigma}{4}\frac{\chi_s + \chi_e}{\chi_e}\right)^2 g_{(-t=-)}(\omega - \omega_0). \quad (25)$$

Every term is proportional to (i) the equilibrium magnetization of the sort of spins that produces this term; (ii) the Lorentzian that is characterized by the corresponding normal decay rate (the EPR linewidth); (iii) factors that contain the complete information about the influence of the other sort of spins on the amplitude of the observed sort.

The longitudinal response signal is approximately written as

$$U + iV \approx -A\Omega\pi b M_s^0 \left(1 - \frac{\sigma}{4}\frac{\chi_s + \chi_e}{\chi_s}\right)^2$$
$$\times f(\Omega, \omega''_{(t=+)}, \omega''_{(L=+)}) g_{(t=+)}(\omega - \omega_0)$$
$$- A\Omega\pi b M_e^0 \left(1 + \frac{\sigma}{4}\frac{\chi_s + \chi_e}{\chi_e}\right)^2 \quad (26)$$
$$\times f(\Omega, \omega''_{(t=-)}, \omega''_{(-L=-)}) g_{(-t=-)}(\omega - \omega_0).$$

At lower temperatures, it is possible that *e*-spins relax to the lattice so quickly that they possess equilibrium magnetization at every instant of time (in the literature, this case is called isothermal [9]) and only *s*-spins with their partial decay rates evolve. Then, the longitudinal response signal is determined by the first term in (26) with $\sigma = 0$.

If the connectedness is strong, i.e., $\sigma \gg 1$ (in other terms, the effect of a strong relaxation-dominated bottleneck [11] takes place), which is characteristic of temperatures greater than T_c [7], then normal decay rates of the slow transverse amplitudes are approximately written as

$$\omega''_{(t=+)} \approx T_{se}^{-1} + T_{es}^{-1} + \frac{\chi_e T_{sL}^{-1} + \chi_s T_{eL}^{-1}}{\chi_s + \chi_e} + \frac{\chi_e}{\chi_s + \chi_e}\delta^*,$$
$$\omega''_{(-t=-)} \approx \frac{\chi_s T_{sL}^{-1} + \chi_e T_{eL}^{-1}}{\chi_s + \chi_e} + \frac{\chi_s}{\chi_s + \chi_e}\delta_s^0, \quad (27)$$

where the effective inhomogeneous width δ^* appearing in the normal decay rate of the *s*-like mode is related to the width of the distribution of *s*-spins in spin packets as (see formula (A.10) in the Appendix)

$$\delta^* \sim \frac{(\delta_s^0)^2}{T_{se}^{-1}}.$$

The comparison of expressions (27) with the partial decay rates shows that, in the case of strong connectedness, the larger normal decay rate is much greater than the larger partial one and the smaller normal decay rate is much less than the smaller partial one.[1] In the case of strong connectedness, a narrow EPR line is observed, which corresponds to the mode that is due to the sort of spins with a smaller partial decay rate ("weak" mode). Because of the effect of *s*–*e* coupling, the EPR linewidth of this mode becomes even smaller, and the amplitude increases. For the second mode, which arises from the sort of spins with a greater partial decay rate ("strong" mode), the amplitude is significantly attenuated by the *s*–*e* coupling; therefore, this mode is not observed. Since

$$K_{\text{weak}} \approx \frac{\chi_{\text{strong}} + \chi_{\text{weak}}}{\chi_{\text{weak}}},$$

regardless of which individual spin system has the smaller partial decay rate, the EPR signal comes from the combined equilibrium magnetizations and has the form of a line of a narrow transverse mode:

$$\chi''_{ESR} \approx \frac{\pi}{2\hbar} g \mu_B (M_s^0 + M_e^0) g_-(\omega - \omega_0). \quad (28)$$

A similar combination of magnetizations in the narrow line also occurs for the longitudinal response signal (when calculating the longitudinal response signal, we assume that $\delta^* \ll T_{es}^{-1}$, which is in agreement with the condition of the relaxation-dominated bottleneck effect ($\sigma \gg 1$) under inhomogeneous broadening):

$$(U + iV) \approx -A\Omega\pi b (M_e^0 + M_s^0)$$
$$\times f(\Omega, \omega''_{(-t=-)}, \omega''_{(-L=-)}) g_{(-t=-)}(\omega - \omega_0). \quad (29)$$

Using formulas (28) and (29), we easily find the ratios that were experimentally measured in [4, 7–10] (we

[1] This situation is similar to the presence of a great dynamic shift of the NMR frequency in magnets, which was thoroughly studied in [21].

write them out for the case of small modulation frequencies):

$$\frac{V}{U} \approx \frac{\Omega}{\omega''_{(-L=-)}}\left(1 + \frac{\omega''_{(-L=-)}}{2\omega''_{(-t=-)}}\right),$$
$$\frac{U}{\chi''_{ESR}} \approx -\frac{2Ab\hbar}{g\mu_B}\frac{\Omega}{\omega''_{(-L=-)}}. \quad (30)$$

Note that in experiments with a fulleride [7–10], the major contribution to the integral EPR intensity was made by the narrowed and enhanced *e*-like mode. The magnitude and temperature dependence of its width correspond to the narrow normal decay rate, which is obtained from (7) both above and below T_c; this is also supported by computer analysis for the particular case of the fulleride. This implies that the characteristic time measured from the ratio *V*/*U* (30) for the narrow line corresponds to the normal decay rate of the narrow *e*-like "longitudinal oscillator" (i.e., this is the effective time of *e*-spins, T_1).

For the intermediate connectedness, the general formulas (20) should be used to calculate the longitudinal response signals.

4. CONCLUSIONS

For samples containing localized ($S = 1/2$) and delocalized spins with purely relaxational coupling, we have calculated both the EPR signal and the longitudinal response (which is registered by a longitudinal coil) to the modulation of the microwave power saturating the EPR. The EPR signal analytically decomposes into two Lorentzians with normal decay rates of relaxationally coupled transverse magnetization components. Equations for the corresponding mode variables along with equations for individual longitudinal magnetization components are derived. These equations describe the saturation effect in the coupled system of *s*- and *e*-spins.

Equations for longitudinal coupled "relaxation oscillators" that are affected by external low-frequency periodic action (modulation of the saturation factor) and by natural relaxation processes are obtained. Longitudinal response signals analytically decompose into two parts that are derived from *s*- and *e*-spins, and each of them is proportional to the form factor of one of the modes (*s*- or *e*-like). The longitudinal response signals are analyzed for various cases of *s*–*e*-spin coupling. The effect of inhomogeneous broadening of *s*-spins is taken into account.

The results are in good qualitative agreement with experimental data concerning EPR and longitudinal response reported in [7–10].

ACKNOWLEDGMENTS

We are grateful to V.A. Atsarkin for many stimulating discussions and valuable remarks. We are also grateful to M. Elizbarashvili for help in computer and analytical calculations. The work was supported by the Swiss National Research Foundation, grant no. 7GEPJ062429.

APPENDIX

Here, we analyze in more detail the issue of broadening of the EPR spectrum of *s*-spins, which can be caused by microscopic inhomogeneities of the crystal structure, superfine fields of neighboring nuclei, and the like. Take into account that the distribution of resonance frequencies of *s*-spins caused by these factors leads to breaking the correlation of their Larmor precession, while the relaxation by the Korringa mechanism encourages this correlation. Therefore, the issue of the correction describing the inhomogeneous broadening requires special consideration. For this purpose, we use the Kubo–Tomita relaxation function [22] (a similar technique was used in [23]). To analyze the results of the competition mentioned above, we assume that *e*-spins form a thermostat, and we represent the complete magnetization of *s*-spins in the form

$$M_s^+ = \sum_n \rho_n M_{sn}^+,$$

where M_{sn}^+ is the magnetization of the set of *s*-spins correlated by the Korringa relaxation mechanism and ρ_n is the density of the distribution of magnetization in those groups. The distribution is assumed to be uniform. Then, $\rho_n = N^{-1}$, where *N* is the number of groups. The equation of motion for M_{sn}^+ has the form

$$\dot{M}_{sn}^+ = -i\omega_n M_{sn}^+ - \sum_{n'} k_{nn'} M_{sn'}^+. \quad (A.1)$$

Here, $\omega_n = \omega'_n + i\omega''_n$ is the complex frequency of M_{sn}^+ precession whose imaginary part, in the isothermal case, is the Korringa relaxation rate T_{se}^{-1} and the distribution width of spin packets, δ_s^0, is considered as a source of fluctuations; $k_{nn'}$ are kinetic coefficients, which have, under our assumptions, the form

$$k_{nn'} = \delta_s^0/N.$$

The correlation function is given by the expression (see [23])

$$\Phi_n(t) = \frac{\langle \tilde{M}_{sn}^+(t)\tilde{M}_{sn}^-(0)\rangle}{\langle \tilde{M}_{sn}^+(0)\tilde{M}_{sn}^-(0)\rangle}, \quad (A.2)$$

where

$$\tilde{M}^{+}_{sn} = M^{+}_{sn}\exp(i\omega_n t) \quad \text{(A.3)}$$

and the angle brackets denote the equilibrium average. The integration of Eq. (A.1) yields

$$\langle \tilde{M}^{+}_{sn}(t)\tilde{M}^{-}_{sn}(0)\rangle = \langle \tilde{M}^{+}_{sn}(0)\tilde{M}^{-}_{sn}(0)\rangle - \frac{\delta_s^0}{N}\sum_{n'}\int_0^t dt' \exp[i(\omega_n - \omega_{n'})t']\langle \tilde{M}^{+}_{sn'}(t')\tilde{M}^{-}_{sn'}(0)\rangle. \quad \text{(A.4)}$$

The iteration of expression (A.4) on δ_s^0/T_{se}^{-1} up to the second order inclusive yields

$$\Phi_n(t) \approx 1 + \frac{(\delta_s^0)^2}{N}\sum_{n'}\int_0^t dt'\int_0^{t'} dt'' \exp[i(\omega_n - \omega_{n'})(t' - t'')] \quad \text{(A.5)}$$

or the equivalent expression

$$\Phi_n(t) \approx 1 + \frac{(\delta_s^0)^2}{N}\sum_{n'}\int_0^t d\tau(t-\tau)\exp[i(\omega_n - \omega_{n'})\tau]. \quad \text{(A.6)}$$

For infinitely small time values, the latter expression is reduced to

$$\Phi_n(t) = 1 - \frac{1}{2}(\delta_s^0)^2 t^2. \quad \text{(A.7)}$$

For finite time values much less than $(\delta_s^0)^{-1}$, expression (A.7) is a good approximation if $|\omega_n - \omega_{n'}|t \ll 1$. Since

$$|\omega'_n - \omega'_{n'}|_{\max} \sim \delta_s^0, \quad |\omega''_n - \omega''_{n'}|_{\max} \sim T_{se}^{-1},$$

expression (A.7) is true for $T_{se}^{-1} \ll \delta_s^0$. Since the fulfillment of this inequality assists in the fulfillment of the weak coupling condition, it is evident that, under weak coupling, the inhomogeneous width coincides with the square root of the second moment of the distribution of *s*-spins in packets; i.e., it is equal to δ_s^0.

On the other hand, it is known from nonstationary perturbation theory that the long-term behavior of the relaxation function is exponential with the correlation time η_n^{-1} such that $\eta_n t \ll 1$. Therefore, we can write the approximate relation

$$\Phi_n(t) \approx 1 - \eta_n t. \quad \text{(A.8)}$$

This follows from (A.6) under the condition $T_{se}^{-1} \gg \delta_s^0$ for large time values (in this case, for $t \sim (\delta_s^0)^{-1} \gg T_{se}$). The corresponding value of η_n obtained by calculating the integral in (A.6) is given by the formula

$$\eta_n \approx \frac{(\delta_s^0)^2}{N}\sum_{n'}\frac{1}{\omega''_n - \omega''_{n'}}, \quad \text{(A.9)}$$

which yields the following estimate of the effective inhomogeneous width of *s*-spins under the relaxation-dominated bottleneck effect (the conditions under which this effect takes place are consistent with the condition $T_{se}^{-1} \gg \delta_s^0$):

$$\delta^* \sim (\delta_s^0)^2/T_{se}^{-1}. \quad \text{(A.10)}$$

Note that this expression is obtained by the reasoning similar to that used in [24] for deriving the effective inhomogeneous width of nuclear spins in the presence of both nuclear spin waves and dynamic shift of the NMR frequency in the case when this shift is considerably greater than microscopic inhomogeneities of local fields on the nuclei. In contrast to the situation discussed in [23–25], here, the role of the dynamic frequency shift is played by the quantity T_{se}^{-1}. We believe that this is quantity (A.10) that determines the effective width of the inhomogeneously broadened line added to T_{sL}^{-1} in the expression for the width of the *s*-like mode under the relaxation-dominated bottleneck effect. Note that this quantity coincides with the result obtained in [4, 20] by other techniques under the same conditions (see Section 3).

REFERENCES

1. F. Bommeli, L. Degiorgi, P. Wachter, *et al.*, Phys. Rev. B **51**, 14794 (1995).
2. V. Brouet, H. Alloul, Y. Yoshinaru, and L. Forro, Phys. Rev. Lett. **76**, 3638 (1996).
3. O. Chauvet, G. Oszlanyi, L. Forro, *et al.*, Phys. Rev. Lett. **72**, 2721 (1994).
4. V. A. Atsarkin, G. A. Vasneva, and V. V. Demidov, Zh. Éksp. Teor. Fiz. **108**, 927 (1995) [JETP **81**, 509 (1995)].
5. J. Herve and J. Pescia, C. R. Hebd. Seances Acad. Sci. **251**, 665 (1960).
6. J. Pescia, Ann. Phys. (Paris) **10**, 389 (1965).
7. V. A. Atsarkin, V. V. Demidov, and G. A. Vasneva, Phys. Rev. B **56**, 9448 (1997).
8. V. A. Atsarkin and V. V. Demidov, Zh. Éksp. Teor. Fiz. **113**, 1048 (1998) [JETP **86**, 572 (1998)].
9. V. A. Atsarkin, V. V. Demidov, and G. A. Vasneva, Appl. Magn. Reson. **15**, 323 (1998).
10. V. A. Atsarkin, V. V. Demidov, G. A. Vasneva, and K. Conder, Phys. Rev. B **63**, 092405 (2001).
11. S. E. Barnes, Adv. Phys. **30**, 801 (1981).
12. T. Plefka, Phys. Status Solidi B **55**, 129 (1973).
13. N. P. Fokina and K. O. Khutsishvili, Appl. Magn. Reson. **17**, 503 (1999).
14. M. B. Walker, Phys. Rev. B **7**, 2920 (1973).

15. N. N. Bogolyubov and Yu. A. Mitropol'skii, *Asymptotic Methods in the Theory of Nonlinear Oscillations* (Nauka, Moscow, 1974; Gordon and Breach, New York, 1962), § 1.
16. M. I. Rabinovich and D. N. Trubetskov, *Introduction to the Theory of Oscillations and Waves* (Nauka, Moscow, 1984), p. 85.
17. V. V. Migulin, V. I. Medvedev, E. R. Mustel', and V. N. Parygin, *Foundations of the Theory of Oscillations* (Nauka, Moscow, 1978), p. 245.
18. E. A. Turov and M. P. Petrov, *Nuclear Magnetic Resonance in Ferro- and Antiferromagnets* (Nauka, Moscow, 1960; Wiley, New York, 1972), Chap. III.
19. A. Abragam, *The Principles of Nuclear Magnetism* (Clarendon, Oxford, 1961; Inostrannaya Literatura, Moscow, 1963).
20. L. R. Tagirov and K. F. Trutnev, Zh. Éksp. Teor. Fiz. **86**, 1092 (1984) [Sov. Phys. JETP **59**, 638 (1984)].
21. T. G. Vardosanidze and K. O. Khutsishvili, Fiz. Tverd. Tela (Leningrad) **26**, 1546 (1984) [Sov. Phys. Solid State **26**, 941 (1984)]; Fiz. Tverd. Tela (Leningrad) **26**, 1567 (1984) [Sov. Phys. Solid State **26**, 955 (1984)].
22. R. Kubo and K. Tomita, J. Phys. Soc. Jpn. **9**, 888 (1954).
23. P. Richards, Phys. Rev. **173**, 581 (1968).
24. M. I. Kurkin and E. A. Turov, *Nuclear Magnetic Resonance in Magnetoordered Substances and Its Applications* (Nauka, Moscow, 1990), p. 152.
25. T. G. Vardosanidze and K. O. Khutsishvili, Fiz. Met. Metalloved. **53**, 1065 (1982).

Translated by A. Klimontovich

Journal of Experimental and Theoretical Physics, Vol. 96, No. 1, 2003, pp. 93–101.
Translated from Zhurnal Éksperimental'noĭ i Teoreticheskoĭ Fiziki, Vol. 123, No. 1, 2003, pp. 109–119.

SOLIDS
Electronic Properties

On Resonance and Nonresonance Interactions between Electrons and Spatially Periodic Clusters

A. V. Gordeev[a, *], I. A. Gordeev[b], and T. V. Losseva[c]

[a]*Russian Research Centre Kurchatov Institute, pl. Kurchatova 1, Moscow, 123182 Russia*
[b]*Moscow Institute of Steel and Alloys, Leninskiĭ pr. 4, Moscow, 119049 Russia*
[c]*Institute for Dynamics of Geospheres, Russian Academy of Sciences, Leninskiĭ pr. 38-1, Moscow, 119334 Russia*
**e-mail: gordeev@dap.kiae.ru*

Received May 29, 2001

Abstract—The effects of resonance and nonresonance interactions between electrons and spherical structures with spatial periodicity in the radial direction (clusters) were studied. It was shown analytically and by numerical calculations that the δ_l phase shift of the wave function, which arises in resonance electron scattering by such a periodic structure of a fairly large radius r_0, was not small even at a small ratio between the U_0 amplitude of the periodic potential and scattered electron energy E ($\varepsilon_0 = U_0/E \ll 1$) and equaled $|\delta_l| = \pi/4$ (modulo π). This phase shift corresponded to the limiting case of a large Born parameter for the cluster, $\xi_0 = r_0 U_0/\hbar v \gg 1$, where v is the characteristic velocity of the electron. The effect of nonresonance electron scattering by a periodic potential whose spatial period was incommensurate with the Brillouin wavelength of the scattered electron was considered analytically. The effect of nonresonance scattering was shown to be of a higher order in the $\varepsilon_0 \ll 1$ parameter than resonance scattering. The cross section of electron scattering by a cluster was calculated, which allowed the conductivity of a medium containing clusters to be estimated. © *2003 MAIK "Nauka/Interperiodica".*

1. In recent years, the electron transport properties of quasicrystalline films have been discussed in terms of the possibility of resonance electron scattering by cluster structures of the Al–Cu–Fe and Al–Pd–Re types [1, 2]. According to [2], strong scattering of electrons by such structures is possible if the Brillouin wavelength of scattered electrons coincides with the characteristic spatial scale of the cluster in the radial direction or is multiple to it. Because of the absence of strict periodicity in such clusters, the resonance between the electron wavelength and suitable characteristic lengths is considered in [1, 2]. In [1], an analogy between resonance interactions in quasi-crystals and phenomena in crystals in which resonance interaction creates an energy gap in the spectrum is directly stated. As follows from [2], such scattering would be able to considerably decrease the electron conduction of films in which cluster structures arise [3–5]. There are experiments [3–5] describing the conductivity of films which substantially decreases after the annealing of the amorphous phase and its transition to the quasi-crystalline phase possessing high symmetry according to the X-ray data [3]. All these results suggest a possibility of effects related to resonance electron scattering by an onion-shell-like local ionic arrangement, where successive atomic shells form spheres embedded into each other. In this work, we make an attempt to give a calculational and analytical counterpart to the qualitative physical considerations contained in [1, 2] and construct a model for calculating electron scattering in media with cluster structures. Below, clusters with spherical-periodic order (SPO) are considered.

The general theoretical concepts described above imply that low medium conductivity in the presence of cluster structures can be related to electron scattering by cluster structures with a high degree of ordering in the radial direction. Let medium conductivity Σ be estimated by the modified Drude formula for solids [6–8],

$$\Sigma = e^2 n_e \tau/m. \quad (1)$$

Here, n_e is the concentration of electrons, m is the mass of the electron, and τ is the characteristic time of electron scattering by a cluster structure. We have

$$\tau^{-1} = n_c \langle \sigma v \rangle,$$

where n_c is the number of clusters in unit volume, σ is the cross section of electron scattering by a cluster, v is the velocity of electrons, and angle brackets denote averaging over the velocity distribution of electrons.

Below, we estimate cross section σ for elastic resonance scattering of electrons by a cluster. The velocity v of electrons corresponds to the Fermi limit in the medium under consideration [9] because of the low temperatures at which measurements are taken [4].

2. In this section, we give some estimates for spherical clusters. As the first step in understanding resonance effects, we consider electron scattering by a clus-

ter structure with SPO. The characteristic potential energy related to ions in such a structure will be estimated by the Poisson equation for electric field E_r in the cluster,

$$\frac{1}{r^2}\frac{\partial}{\partial r}r^2E_r = 4\pi e(Zn_i - n_e), \quad (2)$$

where Z is the charge of the ion, n_i is the concentration of ions, and the cluster is assumed to have spherical symmetry.

Let ions be arranged locally on equidistant spherical shells with distances Δ between the shells. Equation (2) then gives the following estimate for potential energy amplitude U:

$$U \sim \frac{4\pi}{3}Zn_ie^2\Delta^2\eta. \quad (3)$$

Here, ions with the characteristic density n_i are arranged on the surface of a sphere of radius R and the coefficient $\eta < 1$ corresponds to the neutralization of the ionic charge by conduction electrons [10].

If N atoms are distributed over a sphere of radius R, the mean density of ions is given by

$$n_i \sim N(R)/4\pi R^2\Delta. \quad (4)$$

Let us introduce the surface density of ions,

$$\nu \equiv \frac{N(R)}{4\pi R^2}. \quad (5)$$

The potential energy can then be written as

$$U \sim \frac{4\pi}{3}Ze^2\Delta\nu\eta. \quad (6)$$

In (5), radius R is actually the number of the spherical surface.

It will be seen from further estimates that the $E > U$ inequality, where E is the kinetic energy of the electron,

$$E = \frac{1}{2m}\left(\frac{2\pi\hbar}{\lambda}\right)^2, \quad (7)$$

holds for electron scattering by a cluster structure. Therefore, the inequality

$$n^2 = \frac{\lambda^2}{\Delta^2} < \frac{\pi a}{\nu\Delta^3\eta}, \quad n = 1, 2, \ldots \quad (8)$$

is valid under resonance conditions. Here, a is the Bohr radius,

$$a = \hbar^2/Ze^2m. \quad (9)$$

3. Consider electron scattering by a separate cluster whose $U(r)$ potential is a periodic function of radius r. In accordance with general theory, the wave function that corresponds to scattering by a center has the asymptotic form [11, 12]

$$\psi \approx e^{ikz} + \frac{f(\theta)}{r}e^{ikr}, \quad (10)$$

where z is the direction of the initial motion of electrons and θ is the angle made by axis z and the direction of motion of scattered particles.

The exact equation for such a function is given by the series [11, 12]

$$\psi = \sum_{l=0}^{\infty}A_lP_l(\cos\theta)R_{kl}, \quad A_l = \frac{1}{2k}(2l+1)i^le^{i\delta_l}, \quad (11)$$

where $P_l(\cos\theta)$ are spherical functions and the R_{kl} function satisfies the Schrödinger equation

$$\frac{1}{r^2}\frac{d}{dr}r^2\frac{dR_{kl}}{dr} + \left[k^2 - \frac{l(l+1)}{r^2} - \frac{2m}{\hbar^2}U(r)\right]R_{kl} = 0, \quad k^2 = \frac{2mE}{\hbar^2}, \quad (12)$$

and, at large r, has the asymptotic

$$R_{kl} \approx \frac{2}{r}\sin\left(kr - \frac{l\pi}{2} + \delta_l\right). \quad (13)$$

Phase shifts δ_l determine the total cross section of scattering by the scattering center,

$$\sigma = \frac{4\pi}{k^2}\sum_{l=0}^{\infty}(2l+1)\sin^2\delta_l. \quad (14)$$

Clearly, potential energy $U(r)$ in (12) is the sum of the potential energies of separate ions, which are Coulomb centers in nature and are situated on spherical surfaces. Taking into account spherical symmetry assumed above, we will, however, treat the $U(r)$ function as some smooth periodic function of r devoid of Coulomb potential singularities. This corresponds to the approach based on the method of orthogonalized plane waves in the theory of solids [13], where the wave functions of electrons scattered by an ionic lattice are orthogonal to the wave functions of bound electrons and are insensitive to Coulomb potential singularities. For this reason, we use a periodic function free of Coulomb singularities to represent potential energy $U(r)$; this function is nonzero at $r \le r_0$,

$$U(r) = U_0\cos\frac{2\pi r}{\Delta}, \quad U_0 = \text{const}, \quad (15)$$

and is zero at $r > r_0$. Here, r_0 is the radius of the cluster.

Let us introduce the function $y = rR_{kl}$ and the new variable $x = kr$. We can then rewrite (12) in the form

$$y'' + \left[1 - \frac{l(l+1)}{x^2} - \varepsilon\cos 2x\right]y = 0, \quad (16)$$

where $\varepsilon = \varepsilon_0 \equiv U_0/E$ at $x \le x_0$, $\varepsilon = 0$ at $x > x_0$, and primes denote the differentiation with respect to x. Here, $\lambda = 2\Delta$, which corresponds to the resonance condition for $n = 2$ [see (8)] (here, Δ coincides with the Friedel wavelength λ_{Fr} [2]).

As follows from (6)–(8), the $\varepsilon_0 \sim 4\Delta^3\nu\eta/\pi a$ value is expressed via the universal ν function. In a cluster atoms are onion-shell-like radially ordered around any ad-atom, and it follows from (5) that, in the vicinity of the central ad-atom, $\nu \sim 1/4\pi\Delta^2$ and the estimate $\varepsilon_0 \sim \Delta\eta/\pi^2 a$ is valid. Usually, Δ is of the order of several a; this gives $\varepsilon_0 < 1$, which is in agreement with the $E > U$ inequality given above.

Note that the ionic core potential is positive, but, because of the presence of the neutralizing electronic background, the mean potential U value for the cluster in (2) is zero.

At $l = 0$, (16) is a particular case (for $\varphi = \pi$) of the equation

$$y'' + [1 + \varepsilon\cos(2x + \varphi)]y = 0, \qquad (17)$$

which transforms into the Mathieu equation at $\varphi = 0$ [14, 15].

Further, we consider (17) at $\varepsilon < 1$. This equation describes above-the-barrier scattering of electrons by a radially periodic cluster structure at $l = 0$. Equation (17) is a Mathieu-type equation, and, because the ε value is predetermined by the physical characteristics of the problem, solutions to (17) are not periodic. A theory studying aperiodic solutions to the Mathieu equation is described in [15] in the general form. Equation (16) actually generalizes the Mathieu equation to $l \ne 0$. Below, phase shift calculations by (16) are performed both numerically and analytically by expanding solutions to (16) in series in the εx parameter.

4. We studied (16) and (17) numerically and analytically for several $\varepsilon_0 < 1$ values in a wide range of dimensionless cluster radius x_0 variations, which corresponded to above-the-barrier electron scattering by a spherical structure with a periodic potential. This scattering was related to the resonance between the spatial period of the structure and the Brillouin wavelength of scattered electrons.

The mathematical statement of the problem for (16) and (17) was as follows. At $x = x_0$, the "external" solution of the form $y = \sin(x + \delta_l - l\pi/2)$ and its derivative were sewed together with the solution to (16) [or (17)] in the interval $0 \le x \le x_0$ under the additional condition that $y = 0$ in the center of the cluster $x = 0$ [11, 12],

$$\begin{aligned} y(x_0) &= \sin(x_0 + \delta_l - l\pi/2), \\ y'(x_0) &= \cos(x_0 + \delta_l - l\pi/2), \\ y(0) &= 0. \end{aligned} \qquad (18)$$

These boundary conditions allow the solution to (16) and (17) and the δ_l phase shift to be found.

First, consider the solution to (17) for $l = 0$. The δ_0 phase calculated for $l = 0$ as a function of dimensionless cluster radius x_0 at two ε_0 values is shown in Fig. 1. The calculations were performed for the $\varepsilon_0 = 0.5$ and 0.1 values at $x_0 > 100$. The δ_0 phase experienced rapid oscillations under these conditions and, in addition, monotonically changed (decreased or increased) starting with the $\delta_0(x_0 = 0) = \pi$ value, which corresponded to wave reflection in the center of the cluster. The phase shift increased as x_0 grew, which corresponded to strengthening of the effect of electron scattering by the cluster. The whole array of data obtained in the numerical calculations can be fairly closely approximated by the formula [16]

$$\begin{aligned} \delta_0 = \pi &+ f_1\frac{\pi}{16}\varepsilon_0\sin(2x_0 + \varphi) \\ &- f_2\frac{\pi}{4}\cos\varphi\tanh\frac{x_0\varepsilon_0}{\pi}. \end{aligned} \qquad (19)$$

The results of numerical calculation are shown by thick lines in Fig. 1; thin lines are the δ_0 phase values calculated by (19) at $\varphi = 0$ and $\varphi = \pi$ for $f_i \equiv f_i(\cos^2\varphi, \varepsilon_0) = 1$ corresponding to the $\varepsilon_0 = 0.1$ and 0.5 values. The results of calculations by (19) closely agree with the numerical calculation data. Equally close agreement was obtained for $\varphi = \pi/2$. At intermediate φ values, f_i somewhat different from one should be taken into account in (19).

The main feature of (19) is the universal phase shift value for scattering corresponding to large cluster dimensions $x_0 \gg 1$. A comparison of the results of numerical calculations and calculations by (19) shows that this phase shift, which to high accuracy equals $\pi/4$ (modulo π), weakly depends on ε_0 at a fairly large x_0 value and remains unchanged even at $\varepsilon_0 \ll 1$. It follows from (19) that such a δ_0 phase value is formed along the $x_0 \sim 3\pi/\varepsilon_0$ length. This is a consequence of spatial resonance between the Brillouin electron wavelength $\lambda = 2\pi/k$ and the Δ spatial period of the cluster.

5. In item 4, we showed by numerical calculations that, in the $x_0 = kr_0 \longrightarrow \infty$ limit (r_0 is the geometric size of the cluster), the δ_0 phase shift at a zero angular momentum equals $\pi/4$ (modulo π). Estimating the total scattering cross section, however, requires the determination of phase shifts δ_l for $l \ne 0$. For electron scattering by a cluster, the characteristic impact parameter r_0 then corresponds to [11]

$$l \approx \frac{r_0 m v}{\hbar} = kr_0\frac{mv}{k\hbar} = x_0. \qquad (20)$$

For this reason, the cross section at $x_0 \gg 1$ is determined by the limiting $l_{max} \approx x_0$ value. Here, we give the results obtained in calculations by (16) with boundary conditions (18) at $l \ne 0$. The calculations show that the absolute values of phase shifts for modulo π coincide in

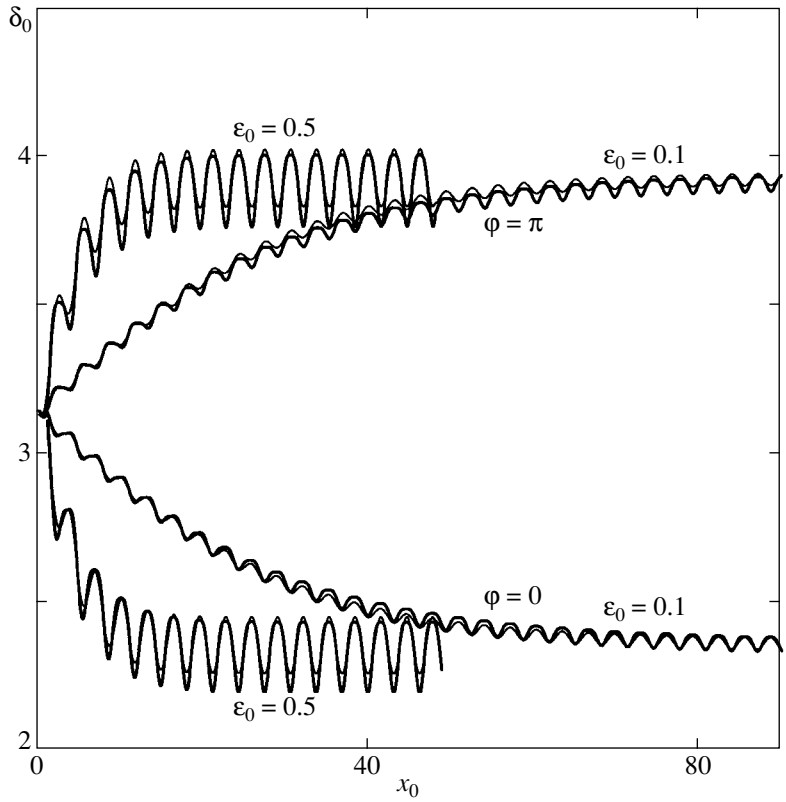

Fig. 1. Dependence of phase shift δ_0 on the radial size of the structure, $x_0 = kr_0$, for two different $\varepsilon_0 = U_0/E$ values at $\varphi = 0, \pi$ in (17) for electron scattering by a periodic structure.

magnitude for all l in the asymptotic case of $x_0 \gg 1$. The phase shift values can be approximated by the equation

$$\delta_l \approx \pi + (-1)^l \frac{\pi}{4}. \tag{21}$$

By way of illustration, phase shifts δ_l for the first several l values are shown in Fig. 2. The only difference in phase shift formation is that increasing l increases x values at which the asymptotic is attained. This means that, at $l \gg 1$, cross section σ (14) with δ_l given by (21) becomes

$$\sigma \approx 2\pi r_0^2 l_{\max}^2 / x_0^2. \tag{22}$$

In view of the estimate obtained above ($l_{\max} \approx x_0$), this gives the scattering cross section $\sigma = 2\pi r_0^2$, which corresponds to the "optical" approximation at a large Born parameter ξ value [11],

$$\xi_0 = \frac{r_0 U_0}{\hbar v} \sim \frac{U_0}{E}\frac{r_0 m v}{\hbar} \approx \varepsilon_0 l \gg 1. \tag{23}$$

Note that, although the obtained expression for the cross section of electron scattering by a periodic structure coincides with the scattering cross section for an absorbing sphere, this cross section is the sum of the terms that describe resonance electron scattering by a periodic cluster structure at different l, and the problem cannot initially be stated as the problem of scattering by a "hard" sphere.

Set cluster radius $r_0 \sim 10^{-5}$ cm and characteristic electron velocity $v \approx 3 \times 10^7$ cm/s, which corresponds to the Fermi energy for a conduction electron density on the order of 10^{21} cm^{-3} [3]. Equation (1) for conductivity then takes the form

$$\Sigma[\text{CGS units}] \approx 2.5 \times 10^{10} n_e/n_c. \tag{24}$$

The conductivity on the order of 300 $(\Omega\ \text{cm})^{-1}$ observed in [4] corresponds to 2.7×10^{14} CGS units. Such a conductivity can be attained if the number of electrons per cluster n_e/n_c is on the order of 10^4.

6. Next, let us theoretically justify (21) for $l \geq 1$. For this purpose, write differential equation (16) in the integral form

$$\begin{aligned} y(x) &= C_0 \sqrt{x} J_{l+1/2}(x) \\ &- \varepsilon \frac{\pi}{2} \sqrt{x} J_{l+1/2}(x) \int_0^x dx' \cos(2x') \sqrt{x'} N_{l+1/2}(x') y(x') \\ &+ \varepsilon \frac{\pi}{2} \sqrt{x} N_{l+1/2}(x) \int_0^x dx' \cos(2x') \sqrt{x'} J_{l+1/2}(x') y(x'), \end{aligned} \tag{25}$$

where J_ν and N_ν are the Bessel and Neumann functions [17].

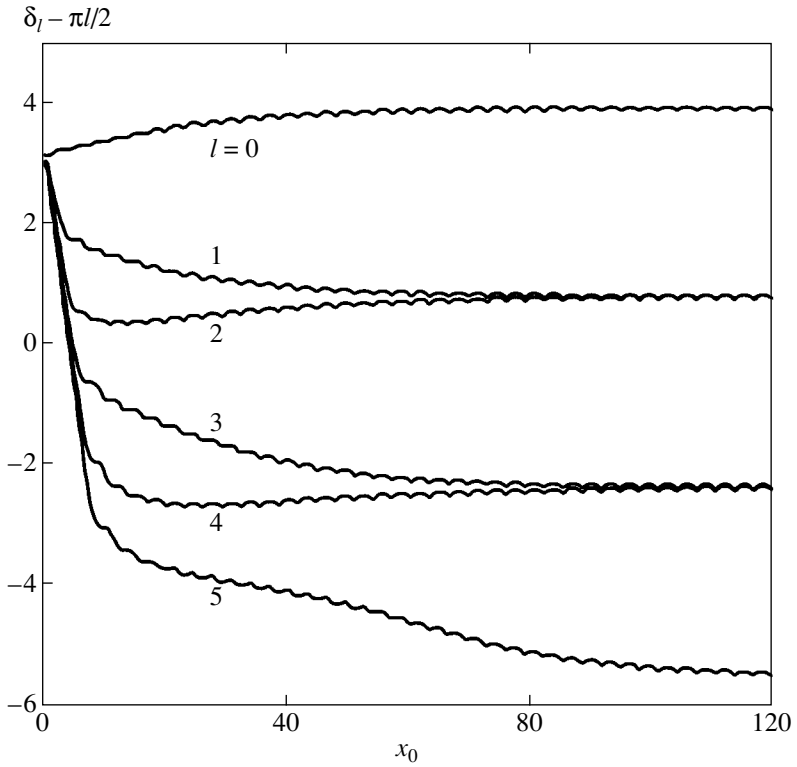

Fig. 2. Dependence of phase shift δ_l for the first six l values on the radial structure size $x_0 = kr_0$ at $\varepsilon_0 \equiv U_0/E = 0.1$.

The solution to (16) at $\varepsilon = 0$ has the form

$$y(x) = C_0\sqrt{x}J_{l+1/2}(x),$$

which satisfies the condition $y(0) = 0$. It follows from (25) that the terms proportional to ε can be significant at $\varepsilon \ll 1$, because the actual expansion parameter is εx. For this reason, generally, an infinite series in powers of εx should be taken into account in (25).

Integral equation (25) will be used to demonstrate a simple technique for obtaining the most significant, nonoscillating contribution to phase shift δ_l. For this purpose, we will sequentially substitute the expression for y into the right-hand side of (25) to obtain an increasing number of chains of multiple integrals of an arbitrary order with respect to the ε parameter. Among such chains of multiple integrals of order p, a single chain only containing the squares of cylindrical functions in the integrands corresponds to the nonoscillating contribution. Using the asymptotics of cylindrical functions for large x to calculate the multiple integrals, we can obtain simple expressions for the coefficients of J_ν and N_ν in the $y(x)$ solution in the vicinity of $x = x_0$.

It is easy to see that one of the expressions,

$$g_1(x) = xJ_{l+1/2}(x)N_{l+1/2}(x), \quad g_2(x) = xJ^2_{l+1/2}(x),$$

$$g_3(x) = xN^2_{l+1/2}(x),$$

multiplied by $\cos 2x$ appears in the chain of sequential integrations in each of the integrals. Clearly, given the p order in ε, the unique chain of multiple integrals where the integrands contain only the quadratic expressions in $J_{l+1/2}(x)$ or $N_{l+1/2}(x)$ should be taken into account in calculating the nonoscillating contribution to phase shift $\bar{\delta}_l$. A consideration of such chains of multiple integrals in each successive order p in ε shows that, because of different signs of the integral terms in (25), the $\sqrt{x}N_{l+1/2}(x)$ term multiplied by $(-1)^{(p-1)/2}$ appears for odd powers of ε ($p = 2q + 1$), and the $\sqrt{x}J_{l+1/2}(x)$ term multiplied by $(-1)^{p/2}$ appears for even powers of ε ($p = 2q$). As the unperturbed solution to (25) is $\sqrt{x}J_{l+1/2}(x)$, the $xJ^2_{l+1/2}(x)$ factors prevail in the integrands of the multiple integral having $\sqrt{x}N_{l+1/2}(x)$ as a factor, whereas equal numbers of $xJ^2_{l+1/2}(x)$ and $xN^2_{l+1/2}(x)$ multipliers appear in the multiple integral at the $\sqrt{x}J_{l+1/2}(x)$ function. Note that, in the asymptotic case $x \gg l \geq 1$, the $(\pi/2)xJ^2_{l+1/2}(x)\cos 2x$ product gives the multiplier $(-1)^{l+1}/4$, and the $(\pi/2)xN^2_{l+1/2}(x)\cos 2x$ product gives the multiplier $(-1)^l/4$.

The integration of sequential powers of x in calculations of the nonoscillating contribution gives $1/p!$, and the

common term at arbitrary p is therefore $(-1)^{lp}(\varepsilon x/4)^p/p!$. Clearly, the $(-1)^{lp}$ multiplier should be taken into account only for odd p; we then have $(-1)^{lp} \equiv (-1)^l$. It turns out that all the nonoscillating terms contain the $\sqrt{x}\,J_{l+1/2}(x)$ function without the $(-1)^l$ multiplier and the $\sqrt{x}\,N_{l+1/2}(x)$ function multiplied by $(-1)^l$.

Combining the numerical coefficients and signs of the nonoscillating terms obtained in sequential integrations yields

$$\begin{aligned}\bar{y}(x) &= C_0\sqrt{x}J_{l+1/2}(x)\cosh\frac{\varepsilon_0 x}{4}\\ &-(-1)^l C_0\sqrt{x}N_{l+1/2}(x)\sinh\frac{\varepsilon_0 x}{4}.\end{aligned} \tag{26}$$

Using the asymptotic equations for cylindrical functions [17] in the region $x \gg l \geq 1$, we can recast (26) as

$$\begin{aligned}\bar{y}(x) &= C_0\sqrt{\frac{2}{\pi}\left(\cosh^2\frac{\varepsilon_0 x}{4}+\sinh^2\frac{\varepsilon_0 x}{4}\right)}\\ &\times\sin\left(x-l\frac{\pi}{2}+\bar{\delta}_l\right).\end{aligned} \tag{27}$$

Here, the nonoscillating phase shift part is

$$\bar{\delta}_l = (-1)^l \arctan\tanh\frac{\varepsilon_0 x}{4}. \tag{28}$$

The oscillating phase shift part of δ_l contains the $\varepsilon_0 \ll 1$ smallness and is not taken into account in this formula.

Two points should be mentioned. First, it was assumed that $x \gg l$ in the derivation of (28) for $\bar{\delta}_l$. At the same time, in the summation in (14), the asymptotic phase shift value up to $l \leq x$ was used. A consideration of asymptotic equations for cylindrical functions at $l \leq x$ shows that the passage to this limit is continuous and the inaccuracy under consideration only weakly influences the summation result. Secondly, it follows from the form of the nonoscillating $\bar{y}(x)$ function (27) that the modulus of the $\bar{y}(x)$ function exponentially grows as the cluster boundary is approached. This can create the impression that the shape of the boundary substantially influences the effect under consideration. It is, however, easy to show that the δ_l phase shift value is formed in the $x < x_0$ region, where boundary shape effects on the phase shift are negligible.

Note that the expression for $\bar{\delta}_l$ transforms into (21) in the $x \longrightarrow \infty$ limit. The calculations performed above show that (28) also describes the case $l = 0$. For δ_0, however, we use (19) given in [16], especially since the obtained approximation to δ_0 does not strongly differ from the equation for $\bar{\delta}_l$ at $l = 0$ (the largest discrepancy between these functions at $\varepsilon_0 x/4 \sim 1$ does not exceed 3%).

Equation (16) is a generalization of the usual Mathieu equation to $l \neq 0$. Here, nonperiodic solutions to this equation are used.

7. It was assumed above that the resonance term corresponding to the potential in (15) is $\cos 2x$. Exact resonance is, however, only attained for particles from a very narrow energy range. For this reason, below we consider electron scattering by a potential that does not satisfy the resonance condition. Here, we calculate the phase shift for the potential containing the $\cos(\lambda x)$ nonresonance term, where λ is an irrational number and, hence, resonance is absent in all orders. This is, of course, an idealization to a certain degree, but such an approximation can be used to calculate the nonresonance contribution to scattering averaged over spatial oscillations in all orders in the ε parameter.

The assumption introduced above will be used to calculate the phase shift only for $l = 0$ to obtain information about the magnitude of the corresponding effect. We assume that an arbitrary number of multipliers of the form of $\cos(\lambda x)$ trigonometric functions with irrational λ and of the form of $\sin(sx)$ and $\cos(sx)$ trigonometric functions with integer s are always averaged independently over space. Let us calculate the scattering effect in this approximation using an integral representation of $y(x)$ similar to (25) but for $l = 0$. Because of the nonresonance character of scattering, it is expedient to write the integral representation of the solution accurate to terms on the order of ε^2,

$$\begin{aligned}y(x) &= C_0\sin x-\varepsilon\sin x\int_0^x dx'\cos x'\cos(\lambda x')\\ &\times\left[C_0\sin x'-\varepsilon\sin x'\int_0^{x'}dx''\cos x''\cos(\lambda x'')y(x'')\right.\\ &\left.+\varepsilon\cos x'\int_0^{x'}dx''\sin x''\cos(\lambda x'')y(x'')\right]\\ &+\varepsilon\cos x\int_0^x dx'\sin x'\cos(\lambda x')\\ &\times\left[C_0\sin x'-\varepsilon\sin x'\int_0^{x'}dx''\cos x''\cos(\lambda x'')y(x'')\right.\\ &\left.+\varepsilon\cos x'\int_0^{x'}dx''\sin x''\cos(\lambda x'')y(x'')\right].\end{aligned} \tag{29}$$

We must at once note that, in the nonresonance approximation, one power of x only arises from two sequential integrations, and the expansion parameter is therefore $\varepsilon^2 x$ in this case. Indeed, a power of x only appears when two sequential integrals, apart from

obligatory $\cos(\lambda x)$, contain integrands of two essentially different types: $\sin x\cos x$ or $\cos^2 x$ ($\sin^2 x$). In the approximation under consideration, the $\sin^2 x$ and $\cos^2 x$ multipliers give contributions equal within the sign. It is easy to see that only the second part of the expression for $y(x)$, which is proportional to $\cos x$, corresponds to a nonzero contribution in the approximation quadratic in ε in (29).

Calculations of higher even orders in ε require sequentially substituting expressions for $y(x)$ into the right-hand side of (29). To simplify calculations of the same type, each chain of multiple integrals will be symbolically characterized by multipliers $\sin x$ or $\cos x$ of sequential integrals. In calculating the chain starting with $\sin x$ and giving a maximum number of powers of x in averaging over space, it is necessary to select the following sequences of trigonometric functions preceding the integrals,

$$\sin x,\ \cos x \text{ or } \cos x,\ \cos x \tag{30}$$

within the block corresponding to the second order in ε. In calculating the block starting with the $\cos x$ multiplier, other sequences of trigonometric functions preceding the integrals should be selected, namely,

$$\sin x,\ \sin x \text{ or } \cos x,\ \sin x. \tag{31}$$

Note that the $\sin x$ multiplier, which is last in sequences (31) in the block of the lowest order in expansion (29), does not correspond to any integral. All the other $\sin x$ multipliers in sequences (30) and (31) have a minus sign by virtue of (29).

It should be stressed that the number of terms doubles each time in passage to the next order in ε^2. To show this, let us introduce the matrix notation for each second-order block taking into account the signs determined by (29). The initial block second order in ε then corresponds to the matrix

$$\begin{pmatrix} -\sin x & \sin x \\ \cos x & \sin x \end{pmatrix}, \tag{32}$$

and the block fourth order in ε, to the sequence of matrices

$$-\begin{pmatrix} -\sin x & \cos x \\ \cos x & \cos x \end{pmatrix}\begin{pmatrix} -\sin x & \sin x \\ \cos x & \sin x \end{pmatrix}. \tag{33}$$

The minus sign preceding the sequence of matrices (33) is taken from the $-\sin x$ multiplier preceding the fourth-order term in (29).

(Specially note that, here and throughout, multiplying the matrices makes no sense!) The obtained matrix structure (32) allows calculations to be performed in the second order in ε. In each block, the first integration should change $\sin[(2 \pm \lambda)x]$ into $\cos[(2 \pm \lambda)x]$ with sign change or $\cos[(2 \pm \lambda)x]$ into $\sin[(2 \pm \lambda)x]$ without sign change. This causes the appearance of terms quadratic in trigonometric functions, which are then averaged over space as a result of the integration.

It follows that one row of matrix (32) corresponds to the term

$$-\frac{1}{2}\frac{\varepsilon^2 x}{16}\frac{4}{4-\lambda^2}, \tag{34}$$

where the appearance of the multiplier 1/2 is caused by averaging of the squares of trigonometric functions.

As has been mentioned above, two matrix rows cause doubling of the result, and the multiplier 1/2 present in (34) therefore disappears. This occurs in calculating each block because of the presence of two rows in the corresponding matrix.

Taking the aforesaid into account, we find that calculations corresponding to the sequence of matrices (33) give the following result:

$$-\frac{1}{2}\left[\frac{\varepsilon^2 x}{4(4-\lambda^2)}\right]^2, \tag{35}$$

where the multiplier 1/2 appears because of the repeat integration in x.

We therefore arrive at the conclusion that the second-order contribution is the multiplier preceding $\cos x$, and the fourth-order contribution is the multiplier preceding $\sin x$. It is easy to see that this rule remains valid in higher orders and $\cos x$ and $\sin x$ will be preceded by terms of the form $\varepsilon^{2(2q+1)}$ and ε^{4q}, respectively, where q is a natural number.

Let us apply these rules to calculate the sixth-order contribution in ε, which precedes $\cos x$. It is easy to see from (29) by applying sequential iterations that a structure of sequential chains of multiple integrals is formed, which can be represented by the following sequence of matrices:

$$-\begin{pmatrix} -\sin x & \sin x \\ \cos x & \sin x \end{pmatrix}\begin{pmatrix} -\sin x & \cos x \\ \cos x & \cos x \end{pmatrix}\begin{pmatrix} -\sin x & \sin x \\ \cos x & \sin x \end{pmatrix}. \tag{36}$$

Here, the minus, which corresponds to $\sin x$ preintegral multipliers in the leftmost matrix, is placed before the sequence of matrices to restrict calculations to the introduction of only two matrices. Calculations similar to those performed previously yield

$$\frac{1}{6}\left[\frac{\varepsilon^2 x}{4(4-\lambda^2)}\right]^3. \tag{37}$$

The obtained sequence of matrices (36) suggests the idea that calculations of the contribution of arbitrary order p in $\varepsilon^2 x$ reduces to a consideration of only two basis matrices, which strictly alternate and form a sequence of p matrices. It can be proved that this rule is also valid for higher orders. The calculations show that each basis matrix gives the $-\varepsilon^2 x/[4(4-\lambda^2)]$ multiplier. Sequential integrations in x increase the power of x by

one, and calculations of the contribution of order p in the $\varepsilon^2 x$ parameter give the $1/p!$ multiplier.

The summation of the terms of all orders in the $\varepsilon^2 x$ parameter taking into account their signs gives the following final result:

$$y = C_0 \sin\left[x - \frac{\varepsilon_0^2 x}{4(4-\lambda^2)}\right]. \quad (38)$$

It follows that the equation for the nonresonance phase averaged over fast spatial oscillations gives a value of a higher order in the $\varepsilon_0 \ll 1$ parameter as compared to the resonance phase.[1] In addition, averaging the equation obtained for the nonresonance phase over the distribution of electron velocities causes mutual compensation of the contributions of electrons with opposite shifts with respect to the resonance energy. Naturally, there is no exponential growth of the amplitude of the wave function.

8. It should be emphasized that the effect under consideration of the formation of a resonance phase shift on periodic potential U cannot be obtained from the well-known formula for the phase shift δ_l of the wave function at large $l \gg 1$ values [11, 18],

$$\delta_l = -\int_{r_*}^{\infty} \frac{mU(r)dr}{\hbar^2\sqrt{k^2 - (l+1/2)^2/r^2}}, \quad (39)$$

where r_* is the root of the radicand.

Clearly, if function $U(r)$ decreases at infinity more slowly than $1/r$, phase δ_l becomes formally infinite (actually indeterminate!) and cannot be calculated for the $U(r)$ potential given by (15) that we are considering. At the same time, it has been shown above analytically and by numerical calculations that, asymptotically, at $x_0 \gg 1$, all δ_l values are finite and determined by (21). As follows from numerical calculations for (17), which is a Mathieu-type equation, the asymptotic phase δ_0 value does not change as ε_0 decreases, and the formation of this phase shift occurs at distances of the order of $x_0 \sim 1/\varepsilon_0$. It follows from the character of nonperiodic solutions to the Mathieu equation that the phase shift is formed as a result of the accumulation of small resonance effects on sequential periods and is related to parametric resonance [15]. Precisely the infinite series in powers of εx forms a nonperiodic Mathieu-type function, which ensures a certain finite value of the resultant phase shift δ_l. Of course, our reasoning refers to the spatial resonance between the Brillouin wavelength and the cluster structure period. Calculations of δ_l for (16) at $l \neq 0$ show that, in the $x_0 \longrightarrow \infty$ asymptotic limit, the absolute value of the phase shift (modulo π) is a universal constant. As follows from analytic calculations, the δ_l phase shift is formed precisely in the region where the radicand in (39) is negative. It follows that (39) is inapplicable to clusters with potential (15), because calculations of phase shift δ_l in the quasi-classical approach exclude the major contribution of the large $x_0 \sim l$ region.

9. Let us briefly discuss the results obtained above. In [8], the characteristic relaxation time τ is identified with the characteristic time of resonance electron scattering by a cluster. This characteristic time is essentially determined by the n_c number of clusters in unit volume. Clusters of size on the order of 10^{-5} cm [1, 19], which have been selected above, contain about 3×10^7 atoms, and there are less than 10^{-3} electrons per atom, as is typical of icosahedral crystals [20]. We stress that, in this work, the concentration of clusters (n_c) is a free parameter. The properties of thin films, however, differ insignificantly from those of quasi-crystalline large-sized samples [1]. Such films offer advantages for preparing samples and measuring their properties and allow the transition from the amorphous to icosahedral phase to be easily performed. The icosahedral phase can therefore in both cases be treated as a system of strongly interpenetrating clusters; that is, the whole quasi-crystalline sample can be considered as consisting of clusters representing elementary structures. The n_c value should then be selected consistently. The characteristic cluster size can be fixed by a disturbance of spatial symmetry or inelastic collisions [1]. Importantly, elastic scattering should be predominant, which is attained at very low temperatures of about several K [1, 21].

It follows from the above analytic calculations that the modulus square of the wave function $|\psi|^2$ exponentially increases to the cluster boundary when electrons experience resonance scattering by a periodic cluster. This results in exponential electron density localization at the cluster boundary,

$$|\psi(r)|^2 \propto e^{\xi(r)}, \quad (40)$$

where $\xi(r) = rU_0/\hbar v$ is the Born parameter depending on the coordinate.

The δ_l phase value obtained is, however, insensitive to the shape of the cluster boundary, because the δ_l value is already formed at $x \sim 3\pi/\varepsilon_0$; that is, far from the cluster boundary.

Because the $E > U$ inequality is valid for typical cluster structures, the suggested method can be used to calculate resonance electron scattering close to the Fermi surface for a structure consisting of clusters with a small potential amplitude U_0 but large size r_0. This can result in electron localization in quasi-crystals with predominant elastic scattering, which manifests itself by the metal–dielectric transition. The suggested method for calculating the cross section of scattering offers an alternative to the commonly used methods for calculations, in particular, in determining the conduc-

[1] Note that, according to the results of calculations, the fast spatial oscillations of the nonresonance phase possess a significant amplitude.

tivity of quasi-crystals with the use of approximants [20]. Indeed, if the limiting δ_l value is formed already at $x \sim 3\pi/\varepsilon_0$, considering approximants of a substantially larger size makes no sense.

10. We showed that strong above-the-barrier resonance electron scattering by spherical structures periodic along the radius occurs even at a small ratio between the potential energy of the periodic cluster and the incident electron energy, $\varepsilon = U/E \ll 1$, because of the resonance between the Brillouin wavelength of electrons and the spatial period of the cluster. Phase shifts δ_l for such resonance scattering were obtained both analytically and by direct numerical calculations. For a zero electron angular momentum, $l = 0$, a formula for the phase shift was suggested. This formula fairly accurately reproduced the calculation results at a small ratio between the potential energy of the cluster and the kinetic energy of electrons for various cluster sizes. The approximation suggested in [16] was in complete agreement with analytic calculations. It was shown that, under these conditions, the universal phase shift value was $\pi/4$ (modulo π) for fairly large clusters. Phase shift values for $l \neq 0$ were found, and the cross section of electron scattering by such clusters was calculated. The cross section values obtained offer a possibility of estimating electron gas conductivity in a medium filled by clusters with structures periodic along their radii. The conductivity values that follow from (24) do not contradict the experimental conductivity values reported in [4, 5], the number of conduction electrons per cluster being $n_e/n_c \sim 10^4$.

Preliminary calculations show that potential $U(r)$ periodicity disturbances, phase "breakdown" in the expression for the $U(r)$ potential (15), decrease the phase shift in scattering. Phase shift calculations for clusters with the $U(r)$ potential structure corresponding to quasi-crystals can be performed by a method similar to that described above. However quantitatively, the suggested approach can only be compared with experimental data after a consideration of electron scattering by self-similar clusters.

ACKNOWLEDGMENTS

The authors thank Prof. V.I. Kogan for useful comments and Prof. P. Häussler for kindly providing recent papers on cluster problems.

REFERENCES

1. R. Haberkern, in *Quasicrystals—an Introduction to Structures, Physical Properties and Applications*, Ed. by J.-B. Suck, M. Schreiber, and P. Häussler (Springer-Verlag, Berlin, 2002), p. 364.
2. J. Barzola-Quiquia, M. Lang, R. Haberkern, and P. Häussler, in *Aperiodic Structures 2001* (University of Mining and Metallurgy, Krakow, 2001), pp. 11–19.
3. T. Klein, A. Gozlan, C. Berger, *et al.*, Europhys. Lett. **13**, 129 (1990).
4. R. Habernkern, C. Roth, R. Knöfler, *et al.*, in *Proceedings of the 6th International Conference on Quasicrystals*, Ed. by S. Takeuchi and T. Fujiwara (World Sci., Singapore, 1998), p. 643.
5. F. S. Pierce, S. J. Poon, and Q. Guo, Science **261**, 737 (1993).
6. C. Janot, Phys. Rev. B **53**, 181 (1996).
7. B. D. Basov, T. Timusk, F. Barakat, *et al.*, Phys. Rev. Lett. **72**, 1937 (1994).
8. J. M. Ziman, *Principles of the Theory of Solids* (Cambridge Univ. Press, Cambridge, 1972; Mir, Moscow, 1974).
9. L. D. Landau and E. M. Lifshitz, *Course of Theoretical Physics*, Vol. 5: *Statistical Physics* (Nauka, Moscow, 1976; Pergamon, Oxford, 1980), Part 1.
10. C. Kittel, *Introduction to Solid State Physics* (Wiley, New York, 1976; Nauka, Moscow, 1978).
11. L. D. Landau and E. M. Lifshitz, *Course of Theoretical Physics*, Vol. 3: *Quantum Mechanics: Non-Relativistic Theory* (Nauka, Moscow, 1989, 4th ed.; Pergamon, New York, 1977, 3rd ed.).
12. N. F. Mott and H. S. W. Massey, *The Theory of Atomic Collisions* (Clarendon, Oxford, 1965; Mir, Moscow, 1969).
13. W. A. Harrison, *Solid State Theory* (McGraw-Hill, New York, 1970; Mir, Moscow, 1972).
14. *Higher Transcendental Functions (Bateman Manuscript Project)*, Ed. by A. Erdelyi (McGraw-Hill, New York, 1955; Nauka, Moscow, 1967), Vol. 3.
15. V. A. Yakubovich and V. M. Starzhinskiĭ, *Linear Differential Equations with Periodic Coefficients and Their Applications* (Nauka, Moscow, 1972), p. 718.
16. A. V. Gordeev, I. A. Gordeev, and T. V. Losseva, Preprint IAÉ-6241/1, Moscow (2001).
17. I. S. Gradshteyn and I. M. Ryzhik, *Table of Integrals, Series, Sums, and Products* (Nauka, Moscow, 1971; Academic, New York, 1980).
18. S. Flugge, *Practical Quantum Mechanics* (Springer-Verlag, Berlin, 1971; Mir, Moscow, 1974), Vol. 1.
19. C. Janot, J. Phys.: Condens. Matter **9**, 1493 (1997).
20. S. J. Poon, Adv. Phys. **41**, 303 (1992).
21. R. Haberkern, G. Fritsch, and J. Schilling, Z. Phys. B **92**, 383 (1993).

Translated by V. Sipachev